NASA Contractor Report 172594

REVISION 1

Issued for Removal of Proprietary Information on pages 35, 36, and 37.

P-284

Development of Rotorcraft Interior Noise Control Concepts

IN-71

Phase II Full Scale Testing

117215

(NASA-CR-172594-Rev-1) DEVELOPMENT OF ROTORCRAFT INTERIOR NOISE CONTROL CONCEPTS. PHASE 2: FULL SCALE TESTING, REVISION 1
Contractor Report, May 1983 - Dec. 1985
(Sikorsky Aircraft) 284 p CSCL 20A G3/71

N88-14769

Unclas
0117215

C.A. Yoerkie
P.J. Gintoli
United Technologies Corporation
SIKORSKY AIRCRAFT DIVISION
STRATFORD, CT 06601

J.A. Moore
Cambridge Collaborative, Inc.
CAMBRIDGE, MA 02138

Contract NAS1-16932
February 1986

National Aeronautics and Space Administration
Langley Research Center
Hampton, Virginia 23665

Date for general release February, 1988

NASA Contractor Report 172594

REVISION 1

Issued for Removal of Proprietary Information on pages 35, 36, and 37.

Development of Rotorcraft Interior Noise Control Concepts

Phase II Full Scale Testing

C.A. Yoerkie
P.J. Gintoli
United Technologies Corporation
SIKORSKY AIRCRAFT DIVISION
STRATFORD, CT 06601

J.A. Moore
Cambridge Collaborative, Inc.
CAMBRIDGE, MA 02138

Contract NAS1-16932
February 1986

NASA
National Aeronautics and Space Administration

Langley Research Center
Hampton, Virginia 23665

Date for general release February, 1988

TABLE OF CONTENTS

TABLE OF CONTENTS (Cont'd)

TABLE OF CONTENTS (Cont'd)

LIST OF FIGURES

LIST OF FIGURES (Cont'd)

LIST OF FIGURES (Cont'd)

LIST OF FIGURES (Cont'd)

LIST OF FIGURES (Cont'd)

LIST OF FIGURES (Cont'd)

LIST OF FIGURES (Cont'd)

LIST OF FIGURES (Cont'd)

LIST OF PHOTOS

LIST OF PHOTOS (Cont'd)

LIST OF TABLES

FOREWORD

Scientific prediction of helicopter cabin noise has long been a challenge. This is understandable in light of the complex, compact, and highly interconnected nature of the power plant, drive train, airframe, and cabin. The major predictive tools which have been available utilize general trending parameters, such as aircraft horsepower, transfer functions, panel transmission loss, and radiation efficiency. While these descriptors could be tailored to existing aircraft, it became very difficult when the time came for application to conceptual aircraft in the design stages.

One of the basic design concepts for both military and commercial helicopter viability is to achieve as large a payload to design gross weight ratio as practically feasible. This forces the entire structure to be a highly efficient, compact design. In general, this translates into high cabin noise levels, interfering with speech and passenger comfort, and raising the possibility of hearing damage. Acceptable solutions must be light weight, inexpensive, and durable. These qualities can not be optimized without a thorough understanding of the phenomenon, leading to a design which addresses each facet of the noise problem from source to receiver with the appropriate concern for overall end use objectives.

The objective of this research effort is to conduct a multi-phase study to develop practical rotorcraft interior noise control concepts and predictive techniques for concept evaluations. This will result in the implementation of a prediction method which permits acoustic sources and energy paths to be identified and treated using information acquired early in the aircraft development/fabrication cycle. The Phase I effort [1][1] consisted of a review of dominant rotorcraft interior noise sources and the synthesis of an analytical interior noise prediction model capable of predicting cabin noise levels due to various sources and structural energy paths for an untreated aircraft. The Phase II effort included full scale ground and flight testing of a commercial rotorcraft for validation of the analytical model developed in Phase I and development of diagnostic techniques for identifying noise and vibration energy paths. Analytic model improvements were developed in Phase II for frame junction vibration transmission and panel/frame/acoustic space coupling loss factors. Phase III involves the analytical modeling and development of noise control concepts via extension of the analytical model to include acoustic trim panels, damping treatments, and isolation. This provides the link to the completed helicopter by predicting the benefits of various noise control treatment concepts and allowing the parametric evaluations which are demanded by the noise, weight, and cost constraints of future helicopter customers. Phase IV is intended to contain additional laboratory testing and some full scale demonstration of the noise control concepts developed in Phase III.

[1]References will appear enclosed in square brackets.

The overall philosophy of this contracted effort is shown in Figure 1. The four conceptual stages required for solution of the helicopter interior cabin noise problem very closely parallel the four contractual phases just described.

Specifically, the Phase I effort consisted of a review of information relevant to dominant rotorcraft interior noise sources and transmission paths responsible for noise in the passenger compartment (cabin), and a rank ordering of these noise sources. This study established the main rotor transmission gearbox gear tooth loading variations at gear clash frequencies and their harmonics as the primary source of cabin noise levels. A detailed analytic modeling approach with capabilities for evaluating a variety of noise control concepts (exclusive of source modification) was developed. This required a model containing details of the energy transfer from various sources, via a multitude of structural and acoustic paths, to the cabin acoustic space. Since the number of structural and acoustic resonances in the frequency range of interest is large, a statistical approach (Statistical Energy Analysis - or SEA) was applied [1].

The Phase II effort consisted of a series of ground and flight test measurements to obtain data for validation of the SEA model. The general scope and purpose of this validation process is indicated in Figure 2. Included in the ground tests were various transfer function measurements between vibratory and acoustic subsystems, vibration and acoustic decay rate measurements, and coherent source measurements. The bulk of these, the vibration transfer functions, were used for SEA model validation, while the others provided information for characterization of damping and reverberation time of the subsystems. The flight test program included measurements of cabin and cockpit sound pressure level, frame and panel vibration level, and vibration levels at the main transmission attachment locations (for input power determination and final prediction comparisons). Comparisons between measured and predicted subsystem excitation levels from both ground and flight testing were evaluated. The ground test data show good correlation with predictions of vibration levels throughout the cabin overhead for all excitations. The flight test results also indicate excellent correlation of in-flight sound pressure measurements to sound pressure levels predicted by the SEA model, where the average aircraft speech interference level (SIL-4) is predicted within 0.2 dB.

The Phase II effort reported herein provides the necessary validation of the SEA model. The data required for validation were acquired through full scale measurements performed on the Sikorsky S-76 (Photo P1), both on the ground (Photos P2 through P22) and in flight (Photo P23), and in laboratory experiments. SEA predictions are shown to correlate well with full scale data (see Appendix E, for example) and the material presented represents reasonable verification that the Statistical Energy Analysis method of rotorcraft cabin noise prediction is a feasible and relatively accurate approach. The methodology provides output which, in addition to predicting sound pressure levels, predicts power flow information that reveals vibratory energy paths leading to the

PROBLEM

- CABIN NOISE INFLUENCES
  - SPEECH, COMFORT, HEARING

SOLUTION

- UNDERSTAND
  - SOURCES, PATHS, RECEIVERS
- MODEL
  - ANALYSIS, VALIDATION
- DESIGN
  - OPTIMIZE NOISE, WEIGHT, COST
- DEMONSTRATE
  - QUIET, LOW WEIGHT/COST INSTALLATION

Figure 1. Noise Control Concept Development Program Philosophy

MEASUREMENT/VALIDATION PROGRAM

TASK	PURPOSE
• GROUND TEST	
• LOSS FACTOR	1. PARAMETERS
• SOURCE SUBSTITUTION	2. VALIDATION
• SEA PREDICTIONS	
• FLIGHT TEST	
• VIBRATION/SOUND PRESSURE	1. INPUTS
• SEA PREDICTIONS	2. VALIDATION
• POWER FLOW	

Figure 2. Major Tasks and Related Purposes of the Phase II Measurement and Validation Program

creation of cabin noise. It is now possible to assess the influence structural modifications have on energy flow and the resulting changes in cabin acoustic levels. Additionally, an efficient and systematic approach is available for evaluation of structural damping.

SEA MODEL OF THE SIKORSKY S-76

The Sikorsky S-76, shown in Photo P1, is a twin turbine powered helicopter which has a certified maximum speed of 80 m/s, a normal flight cruise speed of 75 m/s, a range of over 740 km, a maximum certified gross weight of 45 kN, and a useful load to weight empty ratio of 0.84. The S-76, with 4.2 square meters of passenger cabin space, can accommodate up to 12 passengers in the standard utility configuration and 5 to 8 passengers in the executive (VIP) configuration.

Helicopter cabin noise in an untreated configuration is dominated by the main gearbox [1]. It is a source of both acoustic and vibratory energy which is subsequently transmitted into the cabin acoustically through intervening panels and spaces and vibrationally through the airframe structure to panel and frame surfaces that radiate directly into the cabin. The gearbox on the S-76 is pad mounted directly to the airframe at four attachment points. Internal details of the S-76 airframe structure are displayed and quantified in Appendix B. The overhead framing in the cabin consists of two main fore/aft members that reach from the rear bulkhead forward to the pilot's windows (see Photos P3, P14, P17, P18). Cross frames in the cabin overhead extend down the sides (Photo P3) to support the floor structure and they connect to the keel beam under the floor (Photo P2). The skin panels are of a lightweight honeycomb construction riveted to the frames (Photo P6).

In a compact structure, such as a helicopter airframe which has been specifically designed for load sharing and efficient stress distribution at minimum weight, there is a high degree of interconnectedness between the possible paths from sources to receivers. It is therefore difficult to describe the overall transmission in terms of paths that are independent of each other. The extent to which this is possible depends on the existence of a sequence of strongly coupled subsystems with relatively larger modal energies than surrounding subsystems. In this case the power flow will be along the path of the strongly coupled subsystems with lateral flow out into the surrounding subsystems.

The first step in developing SEA subsystems for the helicopter is to physically section the total structure into individual components called structural subsections that are characterized dynamically by a consistent deformation type. This is accomplished by considering the physical discontinuities that occur within the structure. Skin panels are sectioned by the framing to which they are attached. Framing is sectioned by junctions with cross frames.

SUBSECTION TYPES

Panel	53	
Frame	35	130 Degrees of Freedom
Acoustic Space	7	
Total Subsections	95	

JUNCTION TYPES

Line	99
Area	86
Point	29
Frame	21
Total Junctions	235

Figure 3. S-76 SEA Model Subsection and Junction Summary

In general, these junctions are also the locations where changes in frame cross-sectional geometry occur in the S-76. Acoustic spaces are sectioned by bulkheads, cowlings, and other panel surfaces which physically define these spaces. The structural subsectioning of the S-76 airframe for the SEA model is detailed in Appendix B. Subsectioning of the airframe is shown schematically in Figure B1.

A summary of the subsection and junction types contained in the SEA model of the S-76 is shown in Figure 3. A total of 95 subsections are used in describing the S-76 helicopter (35 frames, 53 panels, and 7 acoustic spaces). Since two types of motion are considered for each frame, the SEA model contains a total of 130 subsystems (i.e. degrees of freedom). Subsections are joined together using 235 junctions (29 point, 99 line, 21 frame, and 86 area junctions) which account for the interconnectedness of this highly compact structure. An example of this would be the cabin acoustic space which receives energy from 110 subsystems in the model.

One can obtain a feel for the extent of the model by looking at which helicopter components are not physically included in the model. There are only three! These are: 1) the propulsion system, 2) the tailcone, and 3) the landing gear. The first is accounted for in the source power input term to the model while the other two are aircraft extremities which are considered to not influence cabin noise. Therefore, virtually the entire helicopter is contained in the model.

PHASE II OBJECTIVES

The Phase I effort produced a comprehensive SEA model of the S-76 helicopter. At that point the model was analytic in nature and had yet to be faced with comparisons with the real world. An integral part of any model development must be the validation process involving a case study. Data generation for this complex case study is an involved process which includes stationary ground tests (where vibration shakers and acoustic speakers take the place of actual sources) and in-flight measurements under various operating conditions. In addition, selected laboratory testing was performed to fine tune the state-of-the-art knowledge on coupling loss factors and transmission coefficients for these structures. The testing was designed to achieve several broad objectives, which were to:

1. demonstrate the utility of SEA in understanding complex vibro/acoustic systems,

2. validate the SEA model for the S-76 helicopter, and

3. develop an understanding of the dominant structural vibratory energy paths in the S-76 airframe.

Commercial helicopters in the same class as the S-76 are of generally similar construction. Understanding the vibration energy transmission developed for the S-76 expands the overall understanding of aircraft cabin noise since it has relevance for other airframes. Important transmission paths and key parameters controlling power flow along these paths are readily identified using the SEA model. Comparisons of measured data with SEA predictions and insights gained from detailed descriptions of the vibration transmission process provided by the model also serve as a basis for refining and extending the model. The ground, flight, and laboratory tests were selected to support these requirements. A more detailed set of objectives for this effort would be to:

a. provide data relevant to assessing the validity of general presumptions in the model (e.g. source coherence),

b. define or validate values of important dynamic parameters in the model (e.g. structural damping, acoustic absorption, vibration coupling loss factor),

c. establish intermediate vibration levels along transmission paths for comparison with model predictions,

d. conduct specific laboratory tests to determine coupling and damping loss factors for frame/panel configurations,

e. refine the model as new information is verified,

f. measure panel and frame vibration levels on those surfaces which radiate into the cabin acoustic space,

g. obtain in-flight acoustic and vibration source levels to define the inputs required by the analytic model, and

h. gain insight relative to major contributing factors of helicopter cabin noise.

The measurements required to meet these objectives can be obtained from tests which fall into the following two categories: 1) ground or laboratory tests, with the in-flight sources simulated by either electro-mechanical shakers or acoustic speakers, and 2) flight tests with the real in-flight sources fully operational. These tests and the associated measurements are summarized later in the text and described in more detail in Appendixes C, D, and F. In general, ground testing requires substantially fewer support personnel and doesn't have the time, safety, and weather restrictions associated with flight testing. Therefore, the test plans were formulated to maximize information generated from ground and laboratory testing. Flight testing was reserved for obtaining essential information on source power levels and the corresponding in-flight cabin sound pressure levels required for final model validation.

An additional objective of the Phase II effort was to formulate the model with the future requirements of Phase III in mind. This would facilitate the implementation of noise control models consistent with the untreated model in a cost efficient fashion. All of these tests and related objectives are intended to implement the overriding philosophy of this program, which is to gain insight into the complex acoustic environment of helicopter cabin noise. The interaction of these diverse parts is depicted in Figure 4.

MODEL REFINEMENTS

As the modeling and investigation of a system as complicated and extensive as a helicopter airframe proceeds, new insights and understanding are developed which form the basis for refining the model. The original SEA model of the S-76 developed during Phase I [1] has been revised in several important areas. These are described in greater detail in Appendix F and include the following four situations: 1) frame vibration transmission across a frame junction; 2) direct coupling between panels across a frame; 3) radiation coupling between a frame and an acoustic space; and, of a more practical nature, 4) modeling of the structural member that extends around the perimeter of the cabin overhead as a panel subsystem whereas originally it was modeled as a frame. Each of these items is briefly discussed in the following paragraphs.

As originally developed the modeling of frame vibration transmission included three motion types: torsion and bending deformation about the two axes perpendicular to the frame axis. This does not account directly for the constraint placed on in-plane motion of the frames as a result of their attachment to the skin panels. The high in-plane stiffness of the skin panels can be expected to significantly prohibit frame motion at the elevation where they are attached. The constraint has the effect of coupling torsional and in-plane bending motions in a fixed geometric relation (see Figure F1). The modified frame subsystem also accounts for out-of-plane bending motion.

The direct coupling between panels across a frame occurs due to non-resonant mass controlled response of the frame. Resonant frame response has been taken into account by the coupling loss factors between the frame and the respective panels on both sides. The mass controlled frame response includes both an out-of-plane translational motion and a rotational motion associated with the combined torsion and in-plane bending.

Framing in the cabin overhead structure of the S-76 is of a relatively deep web construction with significant web area (see Photos P3, P13, P16) and potential for radiation into the cabin. In an untreated cabin environment, the transverse motion of the webs (associated with the combined in-plane frame motion) and of the lower flanges (due to out-of-plane bending) are unbaffled acoustically and therefore will radiate with a lesser efficiency than a baffled panel.

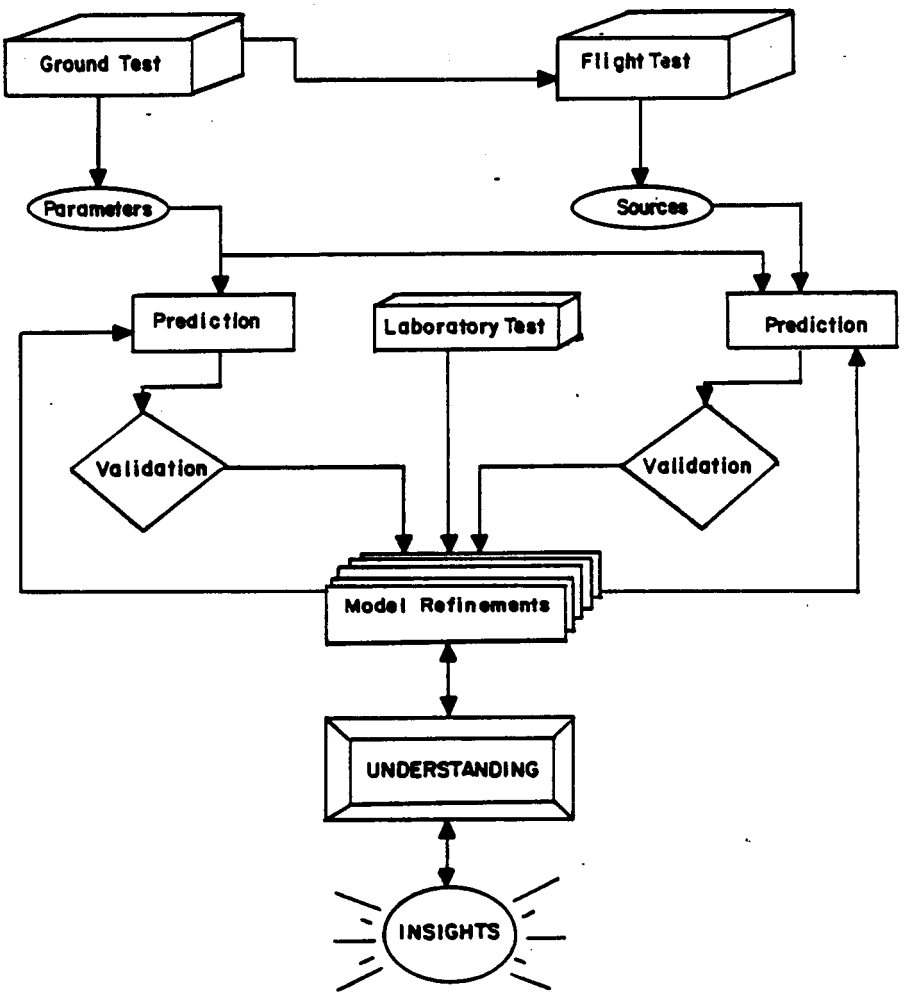

Figure 4. Phase II Philosophy

The final area of modification involves the characterization of the perimeter member around the cabin overhead. This member consists of a light weight, open channel, sheet metal construction (Figure F8) that is situated at the seam between overhead and side wall skin panels (see Photos P3, P10, P17, P18, P19). It was originally modeled [1] as a relatively stiff frame subsystem in the S-76 SEA model. Using this model, it was found that the dominant transmission path forward into the front windshield and overhead panels above the pilot/co-pilot was through the perimeter "frame", which was fed by aft cross frames that attach to the main gearbox support frames. This was felt to be unrealistic and so the "frame" was remodeled as a panel subsystem as if the channel were opened flat. The "softer" panel model reduced the transmission forward through the perimeter member consistent with one's physical intuition.

A more complete discussion for each of the above modifications is presented in Appendix F.

GROUND TEST MEASUREMENT PROGRAM

The SEA model, which contains virtually the entire helicopter structure, must be validated using measured data. This validation involves investigation of SEA modeling considerations and comparisons of vibro/acoustic ground test measurements with predicted subsystem response levels. The following sections describe the concepts associated with this ground test program along with some of the related concerns each test attempts to answer.

Multiple sources in the helicopter are treated in the SEA model as being statistically independent, or incoherent. In reality, the individual gearbox foot vibratory loads are likely to be highly coherent with one another. Additional testing was performed to evaluate questions relating to the effects of source coherence on the frame and panel vibration response levels in the cabin. Specifically, shakers were placed at several gearbox attachment locations on the airframe (and in several orientations), while measurements were made at selected subsystems. Appendixes C and D describe these measurements and the conclusions derived.

As shown in Figure 2, the major purpose of this phase of the measurement program was to generate the dynamic model parameters and provide the data required for the validation of the analytic SEA model for the Sikorsky S-76. Ground test measurements were the prime source of information whenever feasible. The basis for these ground test measurements was source substitution (i.e. shakers to simulate vibratory sources and speakers to simulate acoustic sources) at various locations on and about the helicopter. Vibration and acoustic data were acquired while these simulated sources were being applied to the aircraft.

Analytical estimates of damping related parameters (important dynamic characteristics for any vibratory model) are often obtained with great difficulty and uncertainty. Mechanical damping loss factors and acoustic absorption estimates are therefore commonly based on direct measurement. The ground test measurements provide a useful opportunity to compare measured damping levels with general empirical estimates.

The measurement program primarily focused on vibratory source substitution for the gearbox, as it had been established to be the major source of cabin noise [1]. The test program involved multiple direction, multiple location, vibration simulation of the gearbox at the gearbox/airframe interface. Gearbox casing acoustic radiation was considered to be a much less significant source due in part to the high transmission loss associated with the airframe upper deck and the relatively stiff and massive gearbox housing sidewalls. Hydraulics line attachment points also were considered as vibratory source locations. Measurements were made in the frequency range of 350 Hz to 10 kHz to characterize the high frequency vibratory and acoustic properties of the S-76 airframe for model validation. These included transfer function measurements between subsections, decay rate measurements of free standing and in-situ subsections, and acoustic reverberation time measurements in the cabin. The measurements were taken on an aircraft having the main transmission and engines removed for easy access to the transmission mounting locations on the airframe. Test descriptions for each event are described in Appendix C, test results are presented in Appendix D, and comparisons with SEA model predictions are shown and discussed in Appendix E.

GROUND TEST RESULTS AND COMPARISONS WITH SEA PREDICTIONS

Introduction

The preliminary ground test measurements were concerned with multiple coherent source experiments. The remaining ground tests were organized into the following two major categories: 1) parameter estimation measurements, and 2) vibration and acoustic transfer function measurements. The first category, which includes the energy decay measurements of mechanical and acoustic loss factors, forms the basis for estimates of some of the dynamic parameters in the SEA model; while the second is primarily used for model validation.

Investigation of Coherent Source Effects

An important consideration in modeling vibration transmission due to the gearbox is whether coherence between the excitations at the different attachment points and in the different directions has a significant effect on the

resulting vibration levels at distant locations on the airframe. A SEA model typically treats excitations at different source points as being statistically independent. The input power for a particular source is typically estimated based on the dynamic behavior at that point independently of any mutual coupling with sources at other points. Several coherent source tests were conducted. The results indicate that, in general, the coherent source effect is very localized (see Appendixes C and D), and for the highly interconnected, three-dimensional helicopter structure, coherent sources appear non-coherent at relatively short distances removed from the sources.

Parameter Estimation Measurements

Structural damping loss factor. - The damping loss factor is an important SEA parameter governing the distribution of energy levels within the system. Built-up aerospace structures have damping values over a broad range around the value 0.01. The values are larger than the inherent damping for the base material as a result of joints and riveted connections.

Damping measurements on an actual airframe are complicated by the fact that energy leaves the excited subsystem due to its structural connections to adjacent subsystems as well as due to internal mechanical dissipation. Detaching the subsystem from the overall structure does away with the energy loss associated with power flow to adjacent subsystems but also removes the dissipation occurring at the connections due to riveted joints or other forms of mechanical connection.

For this reason measurements of the damping of frame and panel structures were performed in-situ within the S-76 airframe and with the components detached from the airframe and freely suspended in air. The measurements were performed using the procedures described in the ground test descriptions section of Appendix C by tapping the structure with a blunt object and monitoring the decay using a decay rate meter.

The in-situ measurements included several different construction types and materials. Representative panel sections are of composite construction with relatively thick aluminum cores and thin aluminum or composite material face sheets. The bonding is achieved using a raised temperature and pressure process, where the components are primed and laid up with an adhesive film sheet applied between layers. Other panel sections, such as the drip pan (immediately beneath the gearbox) and the rear passenger bulkhead, are of a more conventional riveted single aluminum sheet construction, with lightweight, riveted aluminum angles for added stiffening (see Photos P9 through P13). Most frames, except immediately underneath the gearbox, are riveted constructions with separate pieces for the webs and top and bottom flanges. The frame webs are additionally stiffened with riveted on lightweight angles that are oriented perpendicular to the frame axis (see Photos P14, P15, P16). Windows are constructed of a plexiglas type material.

Damping loss factor results are given in Table D1 (Appendix D) for both the in-situ measurements of the airframe subsections and the individual structural subsections suspended freely in air. Values for the composite and riveted panels and frame constructions are, for the most part, in close agreement with each other. The absolute values of the in-situ measurements are larger than 0.01, which is a general rule of thumb for aerospace structures. The coupling to adjacent structures is the likely explanation for the in-situ levels being higher. The plexiglas windows exhibit in-situ damping values significantly larger than for other structural elements.

Damping values for the different constructions when suspended in air, free from the airframe, are also consistent with each other, and the absolute values are lower than when measured in the airframe. Damping loss factor values of from 0.01 to 0.02 were therefore used in characterizing both panel and frame subsystems which connected with other modeled subsystems in the SEA model. Damping loss factors for subsystems which connected to structural components not modeled (and thus represented energy flowing out of the spacial modeling range) were made artificially higher (approximately 0.05) to form a proper termination for the model.

Cabin reverberation and absorption. - Energy dissipation characteristics of an acoustic space are typically described by a reverberation time or average energy absorption coefficient for the bounding surfaces of the space, including absorbing acoustic treatments. An SEA model of the acoustic space requires a value for the loss factor, which is straightforwardly obtained from the reverberation time, T_r, according to:

$$\eta_a = \frac{2.2}{f_o T_r}$$

As was the case for structural subsystems, an in-situ energy decay measurement includes energy which is transmitted out of the cabin through skin panels, windows, bulkheads, etc., to adjoining spaces and the exterior and, as well, energy which is coupled into resonant structural vibration. Energy transmission into structures or spaces which are subsystems in the SEA model is already accounted for in the model by the appropriate coupling loss factor and should not be included in the "measured" damping loss factor. It is not feasible to remove this energy transmission and so the experiment relies on this energy being small in comparison with the energy actually dissipated due to absorption within the cabin and that energy which is transmitted to spaces which are not included within the SEA model, such as the exterior.

Measured reverberation times for the S-76 cabin in a bare interior condition are shown in Figure D15 (Appendix D) along with the corresponding average wall absorption coefficient values. Spaces with absorption coefficient values in the range from 0.1 to 0.2 are typically described as being from medium live to medium dead.

Vibration Transfer Functions

The most substantive body of data from the ground test measurements was the transfer functions resulting from shaker locations at the different gearbox and hydraulics system attachment points. The measured data is in the form of the ratio of measured acceleration levels on different substructures throughout the airframe relative to the acceleration at the shaker attachment location. These measurements were performed at relatively low dynamic excitation levels to avoid problems with non-linear effects in riveted structures and therefore the transfer function levels are independent of the excitation level. In addition, no large static loads were applied to the airframe upper deck.

The input to the SEA model is the power injected into the airframe at the shaker attachment. The power flow is scaled by the velocity and the real part of the airframe impedance at the shaker attachment. Experimental estimates of the real component of input impedance are inherently a more difficult measurement requiring accurate phase discrimination. The more complicated the structural geometry in the region near the attachment point the more difficult it is to model the input impedance characteristics in either deterministic or statistical terms, in order to obtain the input power.

The approach used to compare SEA predictions with measured transfer function data was to scale the predicted levels based upon measured levels for structural subsystems limited to the region near the shaker attachment. This approach (consistent with the approach described in the Phase I report) utilizes the measured vibratory response of a directly excited subsystem to evaluate the subsystem modal energy which then becomes a source term on the right hand side of the system equations. This in effect eliminates the direct force excitation from the system equations, replacing it with the modal energy of the directly excited subsystems as the source.

Four subsystems adjacent to and including the longitudinal frame section that the gearbox attaches to were used in scaling the SEA predictions. These included the frame section, LF14, and adjacent panels OP12, OP23, and OP34. The panels connect directly to the frame section. A scaling factor, in dB, at each frequency was determined by shifting up or down predicted levels for these subsystems so that the net difference between measured and predicted levels was zero. The scale factor was then applied to the predictions for all subsystems at the particular frequency in generating the subsequent comparisons.

The comparisons are presented as spatial distributions of levels for various subsystems for a particular octave frequency band. This form of presentation assists in developing an understanding of how energy spreads out from a localized source , i.e., a gearbox attachment point into a complicated structure such as the helicopter airframe. To further develop this understanding the

SEA model was utilized to generate a quantative description of the power flow into and out of different subsystems. This information helps describe the "paths" by which the input power disperses throughout the structure. A "path" description, implying sequentially connected subsystems, is somewhat of a simplification for the highly interconnected and compact helicopter airframe.

Gearbox attachment shaker locations: measured results. - Measured vibration transfer functions for gearbox attachment locations are shown in Figures D16 through D21. Comparing results for only the rear right side attachment location with shaker excitation in different directions (RRV, RRLT, RRLNG) reveals a remarkable comparability. A unit motion at this attachment location produces comparable response at different locations in the cabin regardless of the direction of the source motion.

For the left front attachment locations (FLV, FLLT) the cabin structure response levels are significantly different depending on direction of motion. Lateral motion at this attachment location produced 15 - 20 dB less response in the cabin structure than for vertical excitation. It was not possible to measure with longitudinal excitation at this location. Measurements of impedance magnitudes show the lateral direction at the front attachment points to be of generally lower input impedance.

Lateral constraint is provided at the forward gearbox attachment locations by two cross frames (CF3L and CF3R) and at the rear attachment locations by the rear passenger bulkhead (RB) and two cross frames (CF2L and CF2R). The forward location is dynamically softer in the lateral direction (compared to the rear location) because CF3 terminates at the relatively soft perimeter member PP14.

Excitation of the frame member to which the gearbox attaches in the vertical direction and longitudinally along the frame axis would be expected to be dynamically of higher impedance, since for these directions the drive is directly into the load bearing strength of these frames.

Absolute transfer function levels for the source side panels are significantly greater than zero, by as much as 20-30 dB for frequencies above 500 Hz and panels immediately adjacent to the excited frame member. For the 500 Hz octave band the levels are in the range of 10-15 dB. Transfer function levels drop below zero for the panels overhead of the forward passenger and pilot seating locations.

For strongly connected structures that are not heavily damped the modal energies of the different subsystems will tend to be more nearly equal. In general within the S-76 airframe the structure is of lighter construction at further distance from the gearbox. For a given modal energy this corresponds to higher response vibration levels for the lighter subsystem.

Overhead panels on the side opposite to the source also show the lower levels for the forward left attachment point when driven in the lateral direction (see Figures D21a to D21d). The levels are 8-12 dB lower than for the source side panels regardless of excitation direction and location which is indicative of the fall off in level laterally across the cabin overhead.

Comparisons of measured transfer functions with SEA predictions. - Comparisons between SEA predictions and measured transfer functions are shown in Figures E1 to E25. The figures cover five different excitation cases involving two shaker locations and three directions of force application, as well as four octave frequency bands. The gearbox attachment structural configuration can be seen in Photos P4 through P6. Discerning trends in the comparisons is difficult.

Overall, the agreement is consistently good though there are cases where significant discrepancies of 10 dB or more occur. There may be a slight tendency for the SEA model to over predict panel response levels for higher frequency bands and for panels that are further forward in the cabin or on the opposite side from the attachment and down onto the cabin sidewall. The model predicts frame out-of-plane bending response levels with similar agreement as it does skin panel levels.

Particular panel structures including the read bulkhead and drip pan appear to shown greater discrepancies than other, composite honeycomb panels. Both are conventional riveted aluminum single sheet panels with angle stiffeners. The panels are less "homogeneous" than the honeycomb panels and this may affect estimation of the measured average response over the surface of the panel. The SEA prediction is of an average response level. Greater numbers of measurement points would reduce uncertainties in the measurement of average subsystem response.

The SEA model provides a description of the power flow between the subsystems of the model. Where consistent discrepancies do exist, this feature, which is distinctive of SEA modeling, can be utilized to identify possible sources of the problems with the model. A power flow description of "transmission" paths through the cabin overhead structure is illustrated in Table F2. Starting with the front windshield the primary power flow contributions are identified. The description is extended by looking at the contributions for each of these subsystems. In this manner paths are traced back to the source subsystem.

For the windshield the primary path leads from the windshield to the overhead skin panels above the pilot that are adjacent to the windshield, and then along the main longitudinal frame on the left side back to the gearbox attachment point. An over prediction of the windshield response level may be associated with the structural connections along the primary power flow path. Predicted coupling loss factors may be too large.

Damping also plays a very important role in controlling the distribution of response. Larger effective damping results in a more rapid decrease in response away from a source. The damping in structures adjacent to those that form the primary power transmission path can also be important dependent on the degree of coupling to the primary path structure.

The power flow path description is also useful if the primary paths identified are implausible and to not fit with one's intuitive understanding and experience concerning the structure as a whole or individual subsystems. This was the case for an early version of the S-76 SEA model. A perimeter frame structure between the overhead and side wall panels was originally modeled as a frame whereas the actual structure is considerably softer and more appropriately characterized by plate like bending deformation of its cross-section. As originally modeled a primary power flow path is illustrated in Table F1 was along the perimeter frame and resulted in a more pronounced over prediction of response levels forward in the cabin.

Hydraulics attachment shaker locations. - As described in the Phase I report [1], hydraulics noise is present in the bare cabin configuration. The mechanism for this transmission of energy follows several paths. The hydraulic system consists of gear driven piston pumps which are driven by (and located on) the main gearbox. The gear mesh forces transmit through the bearing supports to the gearbox housing and then down to the gearbox/airframe attachment points. This is probably the strongest path into the airframe for hydraulics vibratory energy. A secondary energy path is provided by the hydraulics tubing attachment points along the airframe structure (at approximately 0.5m separations).

Several typical upper deck frame and panel hydraulics line attachment locations were excited using the shaker and a variety of transfer functions to other subsystems were measured (see Figures D22 to D26).

Vibro/Acoustic Transfer Functions

Measurements of the sound pressure levels created by vibratory inputs were performed to characterize the main gearbox attachment locations/cabin acoustic transfer functions. Vibration exciters attached at three main gearbox attachment locations and directions provided the input acceleration, while microphones in the cabin and luggage compartment measured the resulting sound pressure. These measurements, performed with the main gearbox removed, provide information about the airframe response.

The measurement data is presented in the form of the ratio of sound pressure level (dB re 20 micropascals) to input acceleration level (dB re 1 x 10^{-6} m/s^2). For example given an acceleration level of 130 dB and a transfer function level of -30 dB in a given octave band, the resulting sound pressure

would be (-30) + 130 = 100 dB sound pressure. This data is presented in Figures D27 through D29, and shows that the vertical inputs (FAL and RAL) provide nearly equal response, while the lateral FAL input yields approximately 20 dB less response in the cabin and luggage compartment. The aft cabin location shows its closeness to the source (main gearbox attachments are directly overhead) by having the highest transfer function values for each attachment location and direction. Also, the luggage compartment, as expected, shows lower response than the cabin. Response level decreases with increasing frequency for all locations measured.

Acoustic Transfer Functions

Acoustic transfer functions characterize the difference in sound pressure level between a source cavity and a receiver cavity, which are separated by an intervening subsystem or set of subsystems. This data is shown as the difference in level between source and receiver (see Figure D30). These results are complicated by the fact that the powertrain (engines and main gearbox) were removed during these tests, as well as some of the gearbox cowling. Source locations included the "racecar", which is above the forward and mid cabin center locations, the gearbox space which is above the center aft cabin, and the luggage compartment, which is aft of the cabin.

The data shows lowest response levels from the racecar source, and highest from the gearbox source location. These results follow general mass law trends, as the racecar source is separated from the cabin by thick aluminum honeycomb panels with flight controls hardware attached, while the gearbox source space sees the drip pan, a relatively lightweight intervening panel.

Ground Test Comparisons-Statistical Data

The comparison of measurements with predictions of ground test data is a task complicated by the amount of information needing summary. Some basic statistics, therefore, can reveal the general trends of the predictions for cursory examination. The statistical data reveals that there exists a group of subsystems that are mis-predicted for each excitation and frequency. These subsystems generally are at a significant distance from the source either forward on the aircraft or across the airframe laterally, or are relatively lightweight panels whose junction modeling may be suspect. These subsystems generally include CPM, RB and OP14D, and SP14L for right side excitation. The overall average measured minus predicted delta's range from +7.7 dB at 500 hz for FAL lateral excitation to -7.2 dB at 4000 hz for RAR lateral, and the trend towards increasing overprediction with increasing frequency is evident. (See Figures E32 through E37 and Table E1.)

FLIGHT TEST MEASUREMENT PROGRAM

The primary objectives for the flight test measurement program were to: 1) obtain measurements from which source levels could be determined and 2) measure the frame, panel, and acoustic spatial response levels corresponding to those in-flight source levels. As indicated in Figure 2, the purpose for these measurements was to provide input power levels and data for overall, in-flight validation of the model. Measurements were made to obtain vibration levels of various subsystems and noise levels of the cabin acoustic space on an S-76 during hover and 75 m/s forward flight. Vibration levels at the four main transmission attachment locations in each of three principal directions were measured. These have been used to scale the vibratory power flow into the airframe. Vibration levels were measured by mounting accelerometers onto various subsystems. Acoustic level measurements were performed at twelve different locations in the cabin, concurrently with the vibration measurements.

FLIGHT TEST RESULTS AND COMPARISONS WITH SEA PREDICTIONS

Introduction

The flight test results are divided into two parts, the first of which describes simply the results of the measurements taken in terms of velocity or sound pressure levels. The second describes comparison of the SEA predictions with flight test measurements which includes the input source scaling into the airframe under flight conditions, and calculation of SEA predictions.

Cabin Acoustic Environment Survey

The in-flight bare (i.e. untreated) acoustic environment of the passenger cabin and pilot/copilot cockpit spaces is dominated by main gearbox gear clash related noise. This can be seen in the narrowband spectra shown Figure D55, where these gearbox tones are apparent. As can be seen, these tone levels are highest in the aft cabin (under the gearbox) and progressively diminish in level moving forward in the aircraft. The cabin average SIL4 measured during flight was 99.7 dB, which is typical for this aircraft and configuration.

When the aircraft is completed with an executive type interior treatment (Photo P25), the cabin average noise levels are in the 72 to 78 dB SIL4 range, depending on customer options and some aircraft to aircraft variation. This bare vs. treated difference leads naturally to the next phase in the model development: inclusion of interior treatment types in the SEA model. Its subsequent validation is required for a complete description of the finished aircraft and a complete prediction capability. This capability is important for the efficient redesign of more effective acoustic treatment on current aircraft and the design of treatment for new aircraft which have not yet been built.

In Flight Acoustic and Vibratory Measurements

In-flight measurements of noise and vibration during hover and 75m/s forward flight are summarized in Figures D31 to D55. Vibration measurements taken in-flight are summarized in Figures D31 to D46. Vertical, lateral, and longitudinal measurements were made at the four attachment locations for the main transmission on the airframe. These measurements are summarized in Figures D31 through D41. These show the left side front and rear attachment points in the lateral direction to be the highest in both forward flight and hover, in the 500 and 1000 Hz octave bands. Measurements taken on various subsystems are shown in Figures D42 to D46.

The aircraft octave band noise levels during hover and 75m/s forward flight are shown in Figure D47 through D54. In both conditions, the 1000 Hz octave, which contains the main transmission bull gear clash and the main bevel gear clash frequencies, dominates. In general, the sound pressure levels during 75m/s forward flight and hover are approximately equal. The measurement locations are shown in Figure C10.

Comparison of SEA Predictions With Flight Test Measurements

The flight test measurement program produced data for both vibratory and acoustic levels in the S-76. SEA predictions are made for the airframe structure relative to the source input direction and magnitude. Main gearbox excitation of the longitudinal frames LF14L and LF14R is represented in the model by in-plane (lateral) and out-of-plane (vertical/longitudinal) energy input. The estimation of input energy levels is thus a key element in making comparisons of actual levels. An additional element in these comparisons is the relative trends associated with the predictions, both in frequency and spatial extent. A description of the source scaling procedure is contained in Appendix E.

Error Discussion

There are many items which can contribute to differences between measurements and predictions of subsystem energy and vibratory levels. The first obvious one is that the SEA predicts the energy level of each subsystem while a singular measurement (e.g., an accelerometer placed on a panel to measure vibration level) can only measure the energy at that local point. This is probably the largest cause of discrepancies. To reduce this source of disagreement, several measurement points were selected for each subsystem and the combined results are those reported as the measured value.

Other reasons for disagreement include: a) structural discontinuities within a subsystem element which are converted to "average" values in the model, b) curvature of panels, and c) background noise during ground testing. Even in a "quiet" facility, low level airborne noise excites lightweight subsystems.

CONCLUDING COMMENTS

Since this is the first comprehensive comparison of SEA predictions with measured aircraft data, there are several important conclusions to be mentioned. First, SEA modeling has now been shown to provide a complete description of the energy flow within the structure with a relatively small number of degrees of freedom while retaining the high frequency prediction capability required for acoustics. Second, vibration trends for structural elements (panels and frames) agree well with predictions. Third, predicted cabin sound pressure levels are in good agreement with measured levels. Fourth, the SEA modeling technique provides insight into the energy flow through the structure and therefore highlights areas where treatment can be most effective.

RECOMMENDATIONS

The next logical step will be to: 1) incorporate acoustic treatment models into the SEA model and 2) to apply the modeling technique to other aircraft to demonstrate the generic aspects of SEA. The first recommendation is now underway as Phase III of this NASA contract and applications to other aircraft are being pursued.

APPENDIX A

LIST OF SYMBOLS

A	-	frame cross-sectional area
B	-	bending rigidity
c	-	wavespeed-subscripts refer to type of motion
C^{bl}	-	blocked force/moment coefficient, subscripts refer to type of motion
e	-	Naperian base
E	-	Young's modulus
f	-	frequency
F	-	force
G	-	shear modulus
h	-	frame height
H	-	defined by Equations (F9b) and (F15b)
i	-	imaginary number, $\sqrt{-1}$
I	-	area moment of inertia of frame cross-section
J	-	torsional rigidity of cross-section
k	-	wave number
L	-	length
m	-	mass
M	-	moment
n	-	mode density
r	-	reflection coefficient
$Re( )$	-	real part of a complex function
R_r	-	radiation resistance

LIST OF SYMBOLS (Cont'd)

S	-	spectral density
t	-	time
T_r	-	reverberation time of subsystem
U	-	partical displacement
V	-	velocity
x, y, z	-	coordinate positions
Y	-	mechanical mobility
Z	-	individual frame junction impedance, ( ) identifies frame number

Greek

γ	-	shear strain
ε	-	normal strain
$\eta_{i,d}$ -	-	damping loss factor for subsystem i
η_{ij}	-	coupling loss factor between subsystems i and j
$\eta_{x,y,z}$	-	displacements in the respective coordinate directions
θ	-	angular displacement
π	-	pi
Π	-	power
ρ	-	density
σ	-	normal stress
Σ	-	summation
τ	-	shear stress
τ_{ij}	-	transmission coefficient

Greek (Cont'd)

ϕ	-	orientation angle of frame with respect to source frame
ω	-	radian frequency, $2\pi f$

Subscripts

a	-	acoustic
d	-	decaying, or damping
f	-	transverse force
f, θ	-	cross terms
fr	-	frame
g	-	group
i, j	-	subsystem index numbers
inc	-	incident
m	-	moment
p	-	propagating wave, or polar
rad	-	radiated
trans	-	transmitted
x, y, z	-	coordinate axis directions

Superscripts

a	-	about the frame/panel intersection junction
bl	-	blocked
fr	-	frame
free	-	unattached
inc	-	incident
ip	-	in-plane frame motions

Superscripts (Cont'd)

J	-	junction
op	-	out-of-plane frame motions
p	-	panel
*	-	complex conjugate
•	-	time derivative

Subsystems

LFijL,R	-	main longitudinal frame between cross frames i&j, left and right
CFiL,M,R	-	cross frame number i, left, middle, and right
OPijL,M,R	-	overhead panel between cross frames i&j, left, middle, and right
PPijL,R	-	perimeter panel between cross frames i&j, left and right
SPijL,R	-	side panel between cross frames i&j, left and right
FWL,R	-	front windshields, left and right
RB	-	rear bulkhead

Shaker attachment

FL___	-	front left gearbox/airframe attachment location (FAL)
RR___	-	rear right gearbox/airframe attachment location (RAR)

Shaker direction

___V	-	vertical
___LT	-	lateral
___LNG	-	longitudinal

APPENDIX B

SEA MODEL OF THE SIKORSKY S-76

TABLE OF CONTENTS

Introduction

Appendix B covers the general structural description of the S-76 helicopter, selection of SEA subsystems, and tabulation of physical properties related to these SEA subsystems.

Description of the S-76 Airframe.

As previously described, the primary source of helicopter cabin noise in an untreated configuration is the gearbox. It is a source of both acoustic and vibratory energy that is transmitted into the cabin acoustically through intervening panels and spaces and vibrationally through the airframe structure to panel surfaces that radiate directly into the cabin. Internal details of the S-76 airframe structure [1] are displayed schematically in Figure B1. The overhead framing in the cabin consists of two main fore/aft members that reach from the gearbox mounting locations forward to the pilot's windows. The gearbox is pad mounted directly onto these fore/aft frames. Immediately underneath the gearbox the frames are an integral I beam construction with added plating for additional support. Forward of the gearbox the framing is a riveted, lighter weight construction and the mass per unit length continuously decreases moving forward on the airframe structure.

Cross frames in the cabin overhead are of a riveted construction and extend down around the sides of the cabin to support the floor structure. The skin panels for both the overhead and sides of the cabin are of lightweight honeycomb construction and are riveted to the frames. In the bare condition with no interior treatment the framing and honeycomb skin panels are completely exposed to the cockpit and cabin acoustic space. The entire nose section of the helicopter extending forward from the top framing section above the pilot/copilot's position is of composite material construction.

The space around the gearbox is enclosed by a fiberglass cowling which also covers the control linkages mounted to the exterior skin surfaces forward of the gearbox (also known as the top deck). A bulkhead separates the gearbox space from a plenum chamber for the turbine inlet air supply. The plenum chamber is also separated from the turbines themselves by a bulkhead. Immediately aft of the rear passenger bulkhead is a luggage compartment that lies below the gearbox and turbine inlet spaces. Behind it and beneath the turbines is a space occupied by the environmental control unit.

Selection of SEA Subsections

Subsystems in a SEA model consist of groups of resonant modes in component sections of the total structure which exhibit similar dynamic behavior. The dynamic behavior is characterized by the type of deformation within the struc-

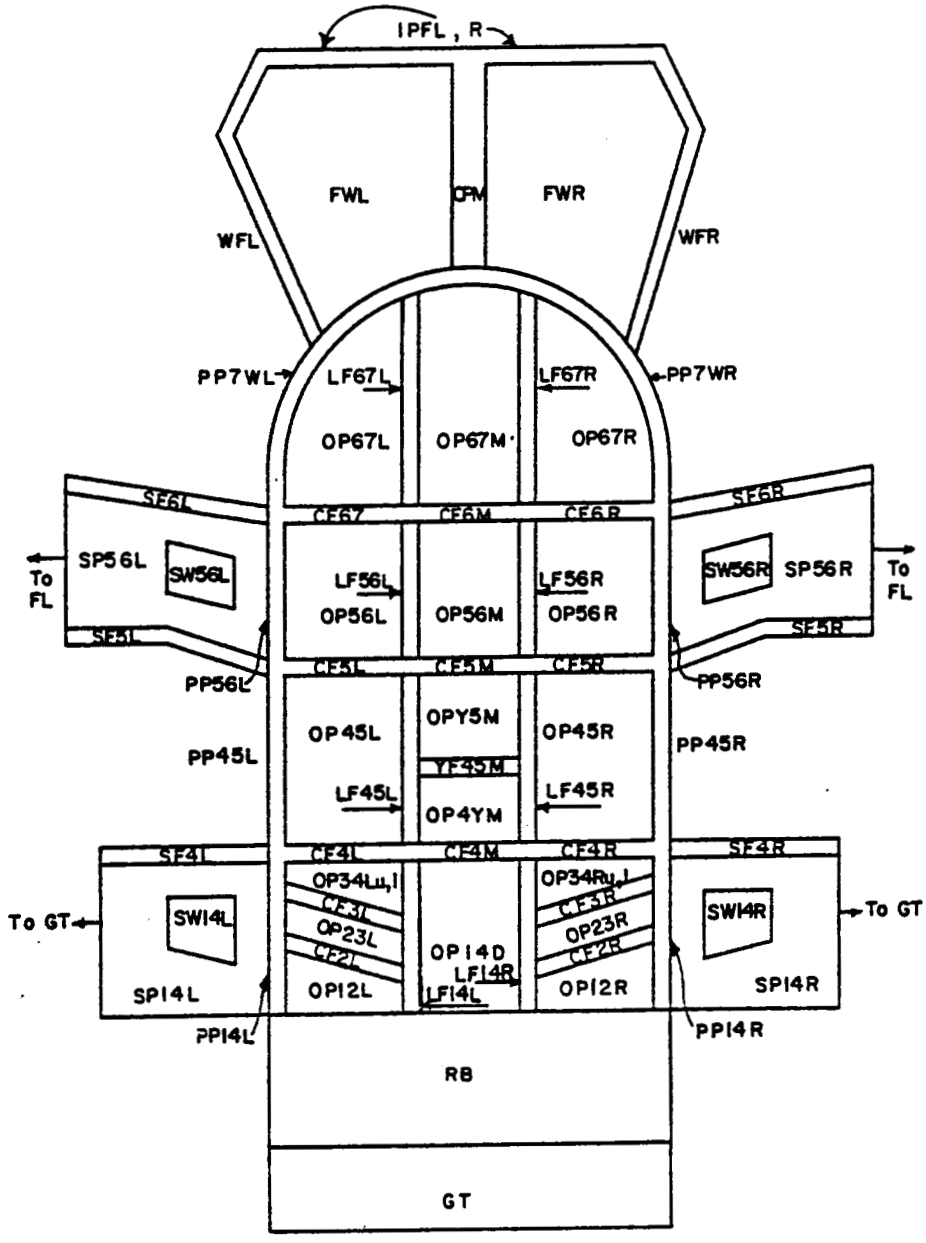

Figure B1. Structural SEA Subsections - Airframe Foldout

ture as well as the nature of the coupling to adjacent structures. Possible types of deformation include bending or flexural, torsional, longitudinal, and shear motions. Each differs in the way in which energy is stored within the structure.

In structures with extremely complicated geometries these motions are often internally well coupled by changes in cross-section, bends, attached brackets, etc. In such cases the modes with different types of motion have comparable modal energies and can be treated collectively as a single subsystem within the SEA model.

The selection of SEA subsections is accomplished by considering the physical discontinuities that occur within the structure. Skin panels are sectioned by the framing to which they are attached. Framing is sectioned by junctions with cross frames. This is also where changes in frame cross-sectional geometry occur on the S-76. Acoustic spaces are sectioned by bulkheads, cowlings, and other panel surfaces which physically define these spaces.

The structural subsectioning of the S-76 airframe for the SEA model is given in Table B1. It includes the panel sections between frames, frame sections between junctions, bulkheads, window and door panels, and assorted other structural elements. There are several important acoustic spaces in the helicopter. In addition to the cabin itself, other acoustic spaces include the different overhead compartments around the gearbox, turbines, inlet air plenum, luggage, and ECU compartments. These acoustic subsections are listed in Table B2.

Within each structural subsection, subsystems have been included which account for mode groups containing different types of motion. This occurs primarily for the framing at lower frequencies where the final subsystem selection accounts for out-of-plane bending and the combined in-plane bending and torsion. The SEA model, as formulated for the S-76, does not account for longitudinal motions in the frame due to the nature of the gearbox motions, which predominantly excite the attachment frames in bending and torsion.

A total of 88 structural subsections are used in describing the S-76 airframe. Of these 35 are frame structures and 53 are panel structures. For each frame two types of motion are considered, yielding a total of 70 frame subsystems in the SEA model. In addition there are 7 acoustic spaces (listed in Table B2) that are included as subsystems in the SEA model. This brings the total number of SEA subsystems for the S-76 to 130. This also represents the number of degrees of freedom in the model.

The cabin is the primary space for establishing the interior noise environment. The other spaces act as sources (e.g., gearbox and turbine spaces) or as connecting spaces (e.g., luggage compartment). Others, such as the nose compartment and environmental control unit space, are less important as connecting spaces since they physically are not on a direct path from the source to the cabin.

Table B1. S-76 Structural Subsections

I.D.	DESCRIPTION
"LF"	Main Long. Frame Members
LF14L,R	Between Cross Frames 1 & 4, left and right.
LF45L,R	Between Cross Frames 4 & 5, left and right.
LF56L,R	Between Cross Frames 5 & 6, left and right.
LF67L,R	Between Cross Frame 6 & the top of the front window.
"CF"	Cross Frame Members
CF2L,R	Location #2, left and right sides
CF3L,R	Location #3, left and right sides
CF4L,M,R	Location #4, left and right sides
CF5L,M,R	Location #5, left and right sides
CF6L,M,R	Location #6, left and right sides
-	Miscellaneous Overhead Frames
YF45M	Tail Rotor Yoke Cross Frame, between 4 & 5, mid only
"OP"	Cabin Overhead Panel Subsections
OP12L,R	Between 1 & 2, left and right sides
OP23L,R	Between 2 & 3
OP34Lu,Ru	Between 3 & 4 upper
OP34Ll,Rl	Between 3 & 4 lower (interior facing shear panel)
OP14D	Drip Pan
OP45L,R	Between 4 & 5, left and right sides
OP4YM, OPY5M	Between 4 & Y, Y & 5, middle
OP56Lu,M,Ru	Between 5 & 6, left, middle and right upper
OP67L,M,R	Between 6 & windshield, left, middle, and right
"PP"	Perimeter Panel Members
PP14L,R	Between Cross Frames 1 & 4, left and right.
PP45L,R	Between Cross Frames 4 & 5, left and right.
PP56L,R	Between Cross Frames 5 & 6, left and right.
PP7WL,R	From 6 to CPM along top front window.

Table B1. S-76 Structural Subsections (Cont'd)

I.D.	DESCRIPTION
	Cabin Wall Subsections
RB	Rear Passenger Bulkhead
SP14L,R	Rear Passenger Side Panel, left and right
SW14L,R	Rear Passenger Side Window, left and right
DF45L,R	Rear Passenger Door - Upper Frame
DW45L,R	Rear Passenger Door - Window
DP45L,R	Rear Passenger Door - Lower Panel Section
SP56L,R	Mid Passenger Side Panel
SW56L,R	Mid Passenger Window
DF67L,R	Pilot/Copilot Door - Upper Frames
DW67L,R	Pilot/Copilot Door - Window
DP67L,R	Pilot/Copilot Door - Lower Panel Section
FWL,R	Pilot/Copilot Windshields
NC	Nose Cone
	Sidewall Frame Subsections
SWF4L,R	At Frame #4 location
SWF5L,R	At Frame #5 location
SWF6L,R	At Frame #6 location
SWF7L,R	At Frame #7 location, lower front frame, crew doors
CPM	Center Post Between Windshields
WFL,R	At Frame #7 location, outer windshield frames.
	Miscellaneous Subsections
IPW	Instrument Panel Window
BC	Broom Closet
GT	Gas Tank
FL	Floor
IPFL,R	Instrument Panel Frame
LCPL,R	Luggage Compartment Panel
TDP	Top Deck Panel
IWP	Luggage Compartment Ceiling Panel

Table B2. S-76 Acoustic Subsections

I.D.	DESCRIPTION
GBA	Around MGB under racecar
TIA	Turbine Inlet Air Plenum
TA	Space around turbines
LCA	Luggage Compartment
ECUA	ECU Space
CA	Cabin
NCA	Nose Compartment

Evaluation of Subsection Physical Properties

The SEA formulation requires that the geometric and material properties of each of the SEA subsections be known. For frame subsections, this includes the length, cross sectional area, out-of-plane and in-plane area moment of inertia, polar moment of inertia, and the height and width of the cross section (see Table B3). For panel subsections, the area and thickness is needed (see Table B4). Acoustic spaces require that the volume and surface area be known (see Table B5).

The material of construction for each subsection, along with its density, longitudinal and shear wavespeeds, and internal loss factor must also be specified. A summary of these parameters for the S-76 is given in Table B6. Material models 3 through 5 represent different composite panel configurations that are of various aluminum honeycomb and facesheet thicknesses.

Another important physical property involves the joining of SEA subsystems consistent with the physical connections in the helicopter structure. Junction information describes the type of junction, i.e. point, line or area, junction dimension, i.e. area or line length, and identifies the connected subsystems. Point junctions occur at connections between frame subsystems. Line junctions occur between frames and adjacent panels, area junctions between panels, frames, and adjacent acoustic spaces. The model of the untreated configuration contains 235 junctions.

APPENDIX C

DESCRIPTION OF MEASUREMENT PROCEDURES

TABLE OF CONTENTS

35, 36, 37, 38

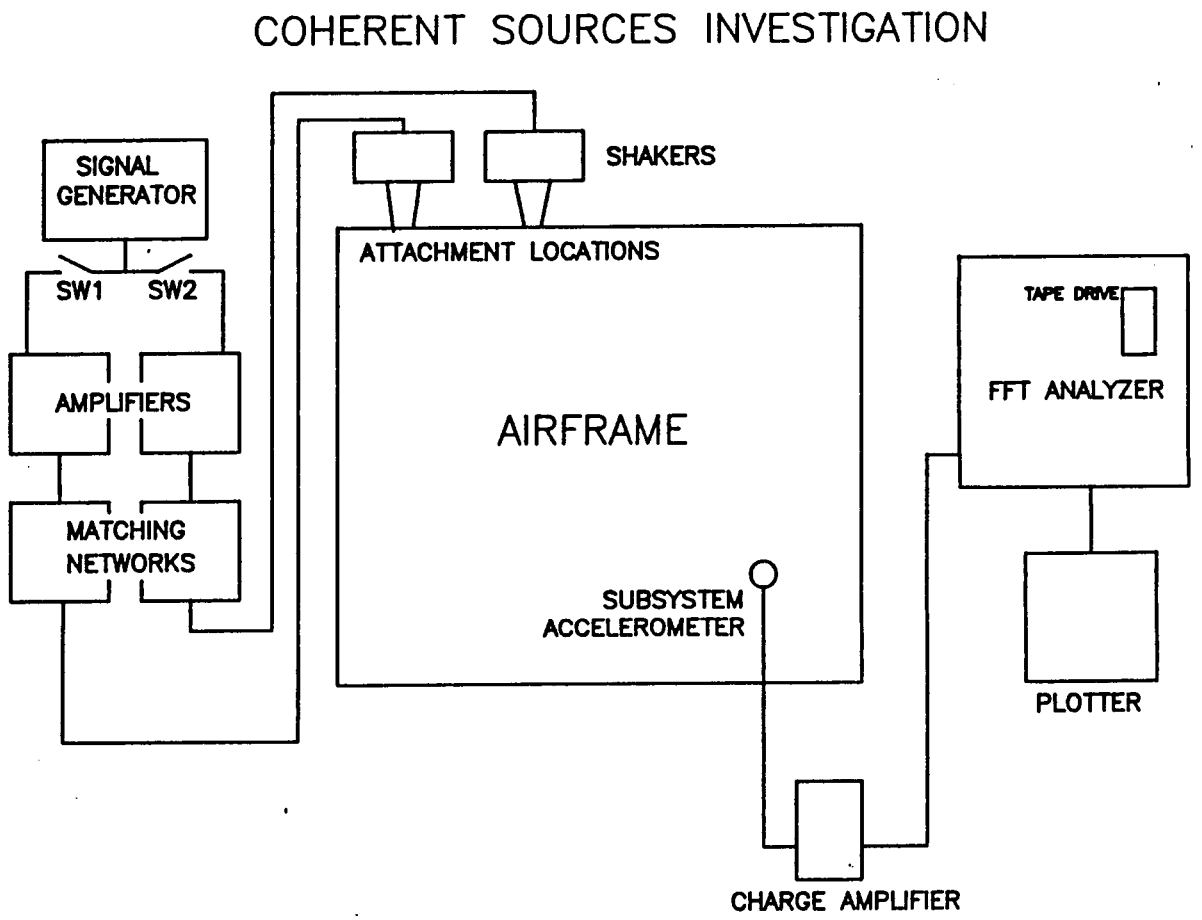

Figure C1. Coherent Sources Measurements Schematic

Introduction

The following paragraphs describe the measurement program performed on an S-76 helicopter for this effort. In general, a description of the ground and flight test measurements used for both structural and non-structural parameter evaluation, SEA model validation, and development of in-flight noise level prediction is included.

Ground Test Measurements

Coherent sources - Two electromagnetic shakers were mounted in two different position-direction configurations, at the transmission mounting locations on the S-76 airframe (see Figures C1 and C8). A broadband noise signal is shaped and amplified to produce a nearly uniform acceleration spectral level at various remote locations from each shaker. Acceleration measurements are taken at the remote locations for vibration inputs for both shakers active, one shaker active, and the other shaker active, keeping the input level to each shaker constant and supplying a coherent electrical excitation to each shaker. These data were stored on magnetic tape for later reference.

Vibration decay rate. - Vibratory decay rates were measured for both the free-standing and in-situ conditions on various subsections, to approximate the amount of damping present as a function of frequency. In each case a vibratory impulse was input into the subsection and the acceleration was monitored on a storage oscilloscope, which was triggered by the input impulse. A decay meter was then employed on the oscilloscope to approximate the rate of decay, and subsequently the amount of damping present. Each measurement was repeated a number of times to provide an averaged estimate of damping level. Free-standing measurements were made with the subsections suspended by shock cord from a nearby structure. (See Figure C2).

Acoustic decay rate - An acoustic signal was supplied by driving a small speaker via a signal generator and amplifier. The speaker was located in the closed cabin, along with two microphones. The microphones were connected through a microphone power supply into the 4-channel recorder. The noise signal in octave bandwidths, centered on 500, 1000, 2000, 4000 and 8000 hz was abruptly switched off and the pressure decays were recorded and subsequently analyzed using a graphic level recorder with a logarithmic potentiometer. The tape recorder speed was slowed by a factor of ten for the data reduction to improve the accuracy of the decay slope measurement. (See Figures C3 and C8).

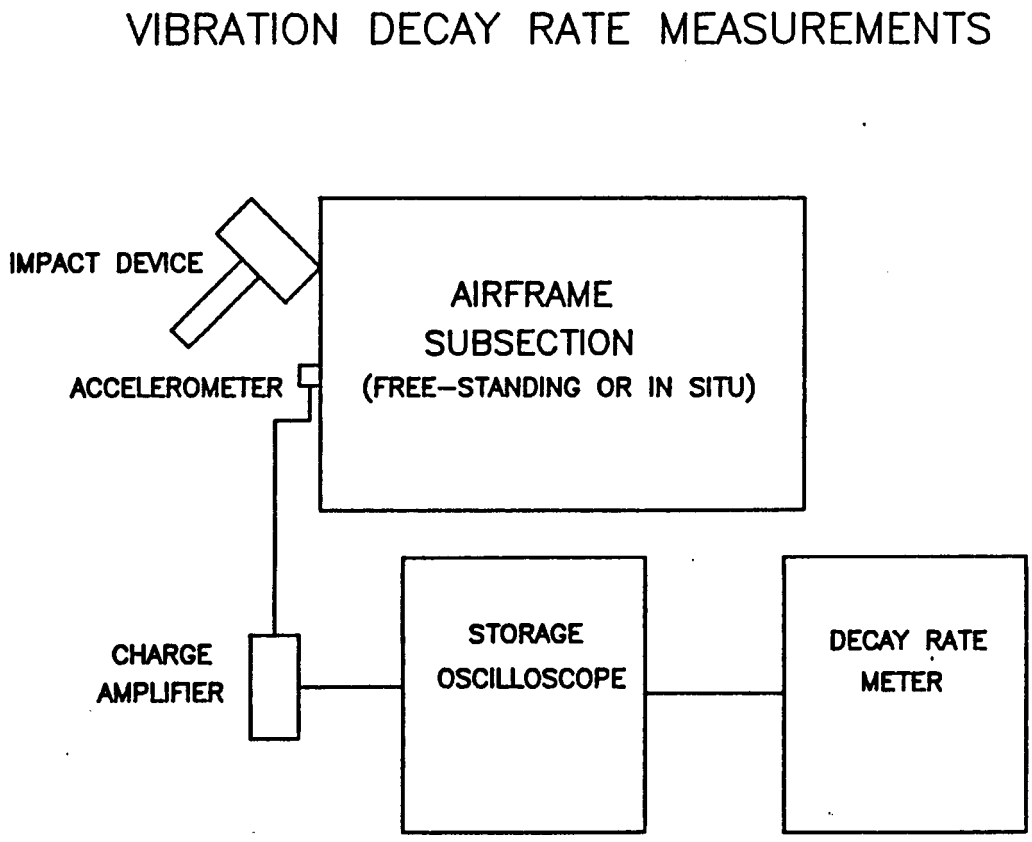

Figure C2. Vibration Decay Rate Measurement Schematic

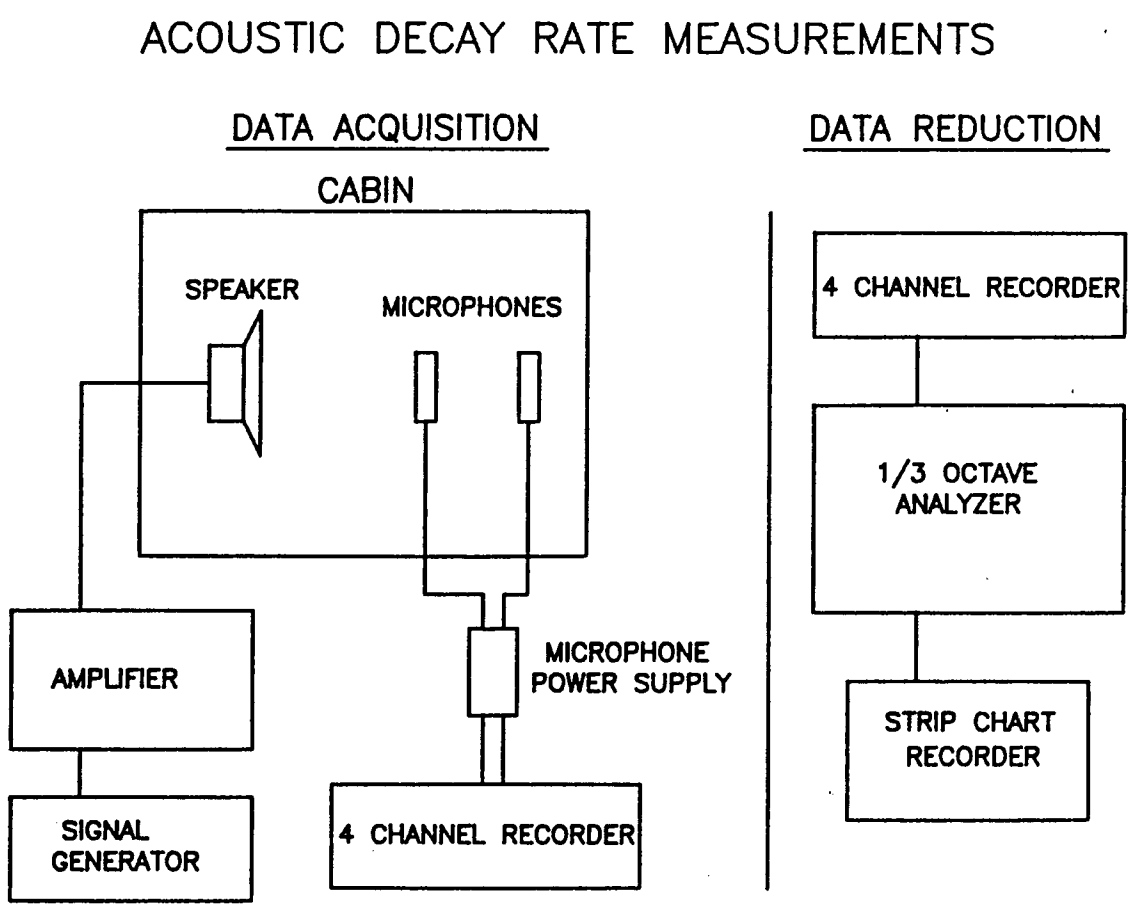

Figure C3. Acoustic Decay Rate Measurement Schematic

Vibration transfer functions. - In this type of test (Figures C4 and C9) a vibratory signal was input into the airframe via a small shaker. The shaker was attached to two transmission mounting locations alternately in each of three directions (x, y, and z), and to two hydraulic line mounting locations. At the hydraulic locations the shaker was mounted normal to the surface. At each location a white noise signal was shaped and amplified to produce a remote acceleration spectrum of approximate uniform level across the frequency range of interest. One accelerometer was moved around the aircraft while a second accelerometer was left at the input (shaker) location. These signals were conditioned and fed into a 2-channel digital signal analyzer, and transfer functions (subsystem acceleration/source acceleration), and coherence measurements were stored on digital tape. A complete subsystem survey was performed for each shaker attachment.

Vibro/acoustic transfer functions. - For this condition a vibratory signal was input into the airframe via the small shaker (See Figures C5 and C8). The shaker was attached to two transmission mounting locations alternately in each of three directions (x, y, and z). A white noise signal for each location was shaped and amplified to produce an input acceleration spectrum of approximately uniform level across the frequency range of interest. Two microphones were suspended at various locations in the cabin, and connected through microphone power supplies into a 4-channel portable tape recorder. The input accelerometer was connected through a charge amplifier into the 4-channel recorder. Transfer functions and coherence measurements were calculated by a 2-channel digital signal analyzer, and stored on digital tape.

Acoustic transfer functions. - An acoustic source level was created by driving a small speaker via a signal generator and amplifier. The speaker and one microphone were located in the source cavity, while another microphone was located in the receiving cavity. Both microphones were connected to the 4-channel recorder through a microphone power supply. Sound pressure levels were recorded for cabin to luggage compartment, gearbox space to cabin and gearbox space to luggage compartment. Subsequently, transfer function and coherence measurements were generated by a 2-channel digital signal analyzer and stored on digital tape (see Figures C6 and C8).

Compliance - airframe. - A vibratory signal was input into the airframe via the small shaker equipped with an impedance head located at one of the main transmission attachment locations in any of the three principal directions (see Figure C7). Accelerometers are placed at all of the four transmission mounting locations in each of three directions. Frequency response functions are measured by utilizing a two channel FFT analyzer to divide the acceleration and input force spectral levels, and store these records on digital tape. The shaker is moved through all the positions and directions until a matrix of frequency response functions is filled.

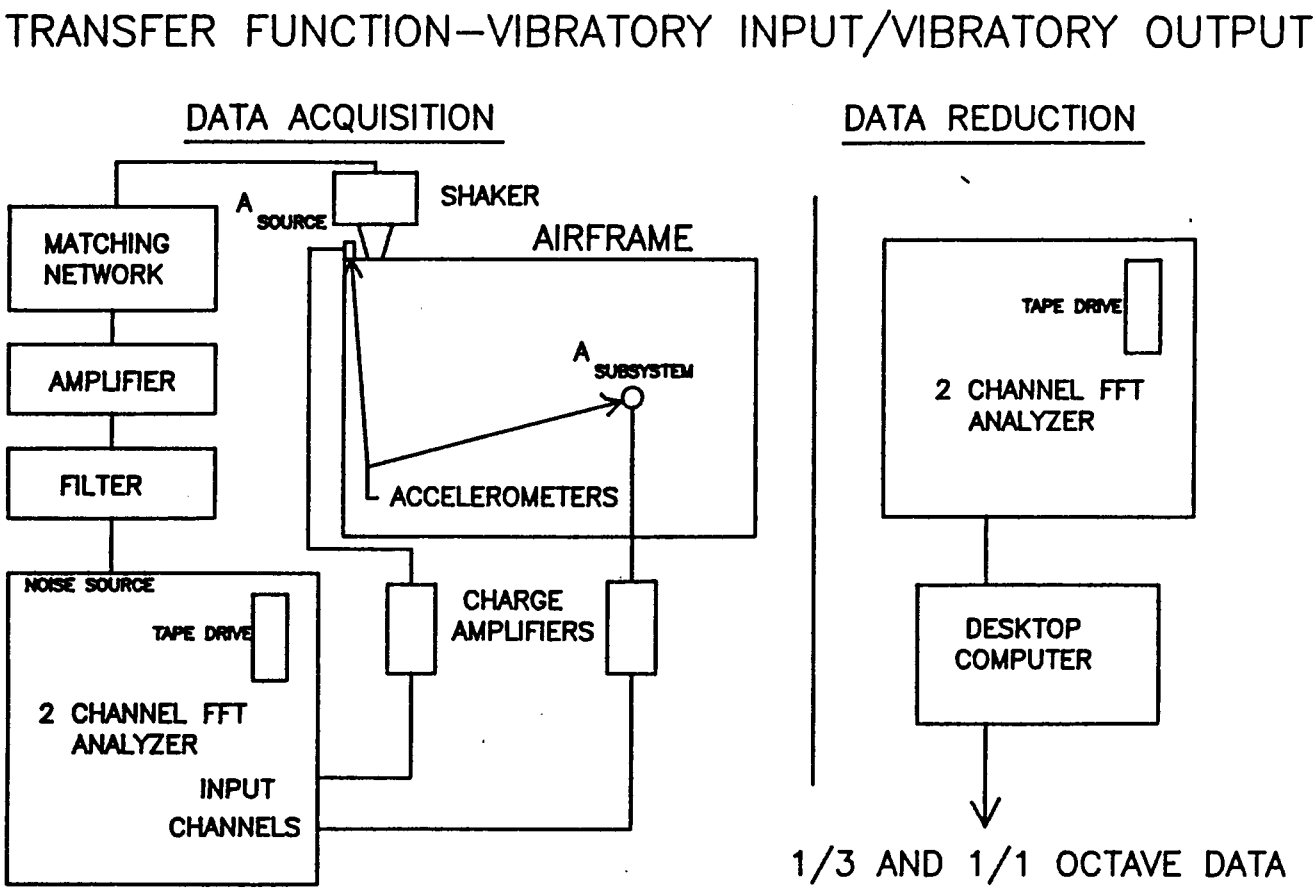

Figure C4. Transfer Function Measurement Schematic - Vibratory Input/Vibratory Output

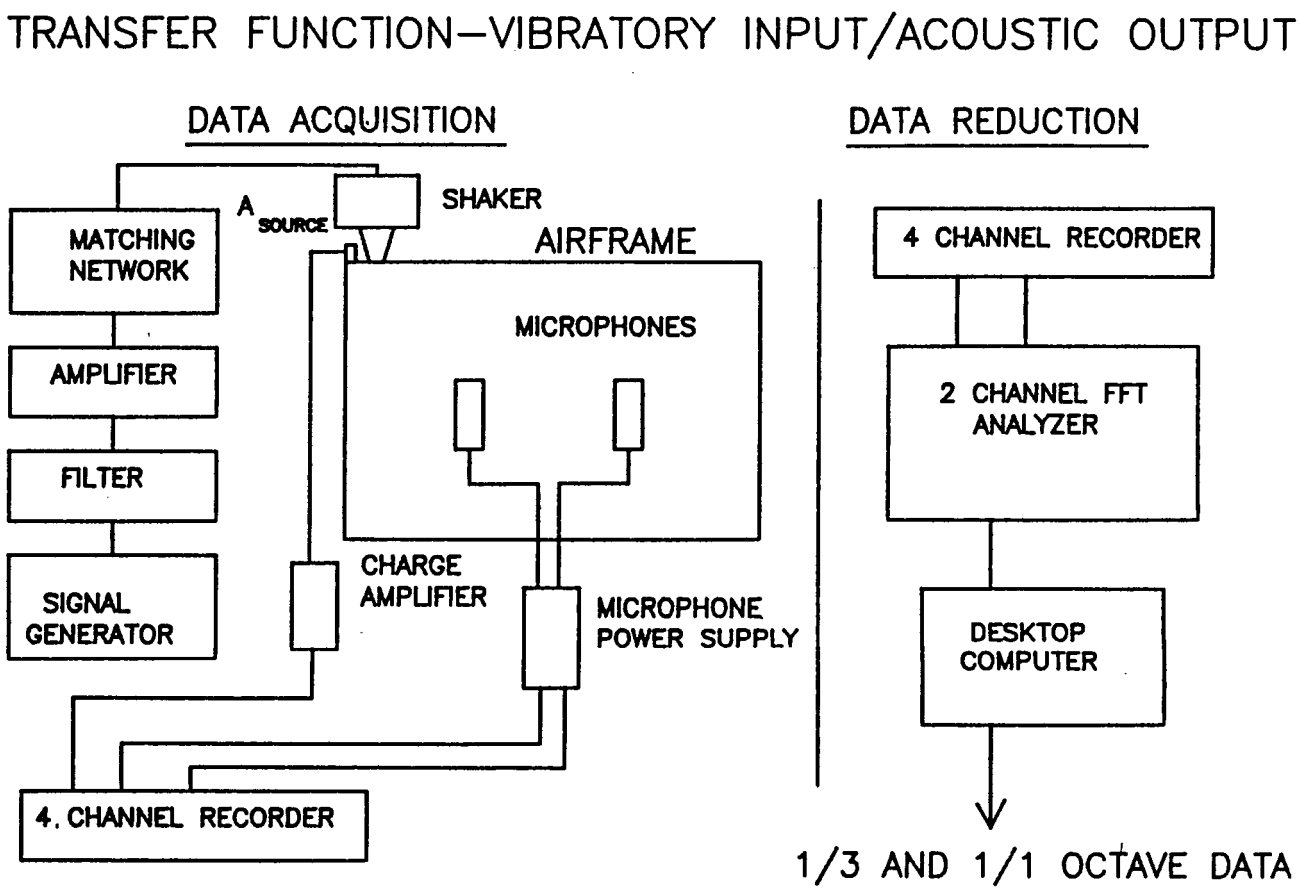

Figure C5. Transfer Function Measurement Schematic - Vibratory Input/Acoustic Output

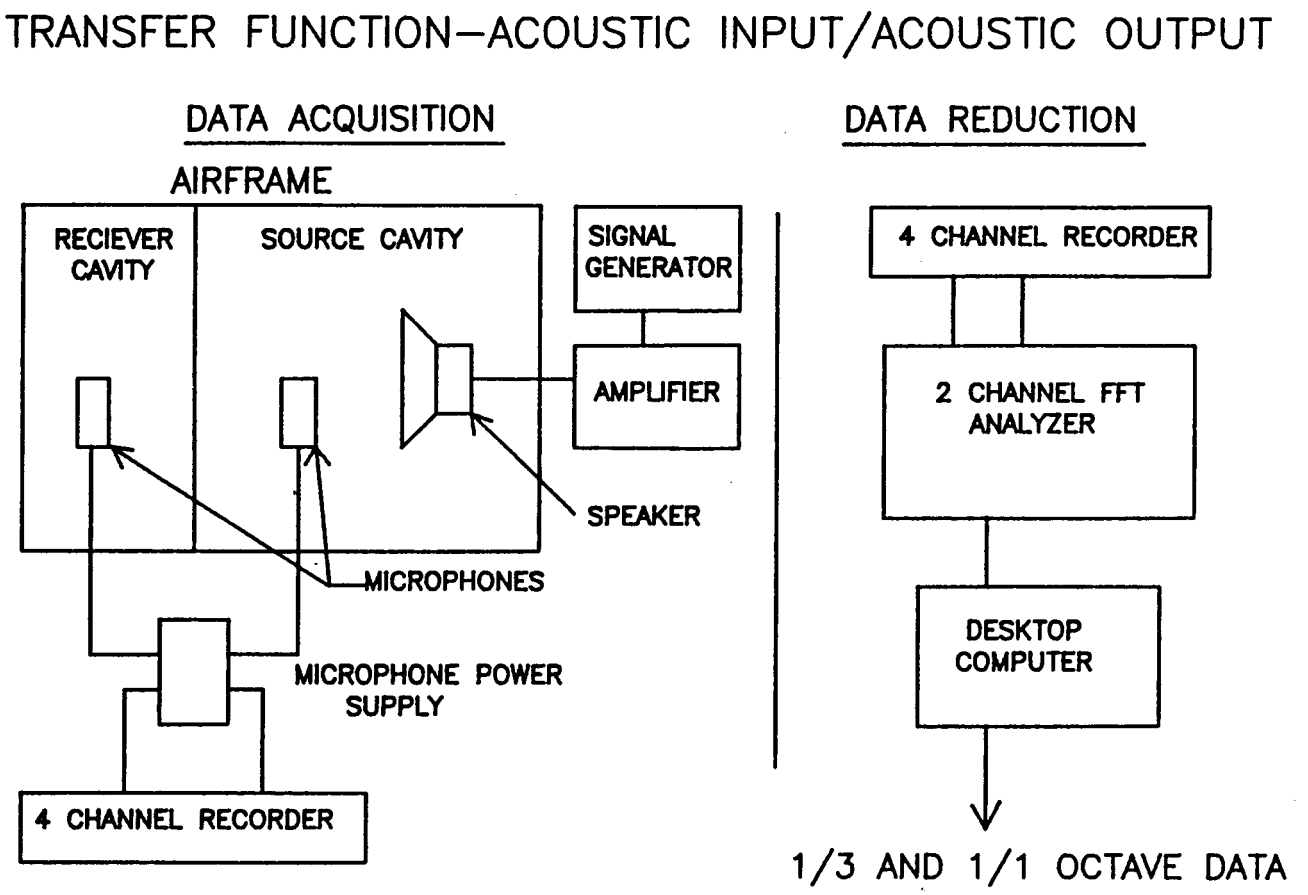

Figure C6. Transfer Function Measurement Schematic - Acoustic Input/Acoustic Output

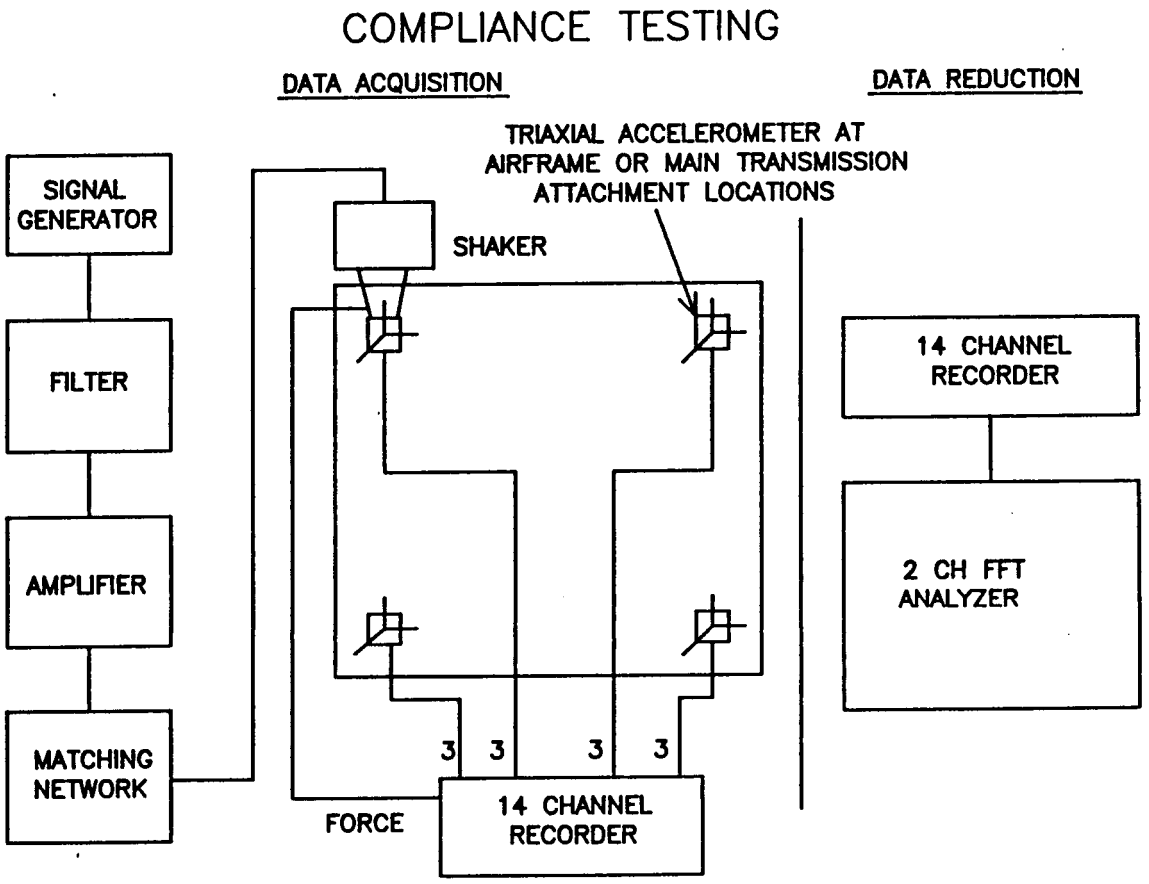

Figure C7. Compliance Measurement Schematic

LOCATION KEY

m microphone
S Shaker
Sp Speaker

SUBSCRIPTS

c Cabin
rc Racecar Area
GB Gearbox Area
Lug Luggage Compartment Area

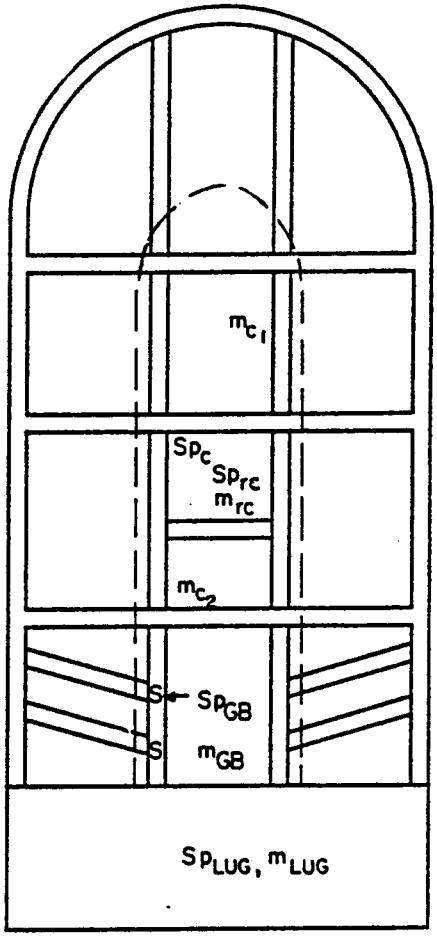

Note: Shaker Locations (s)
Were: FAL Vertical
FAL Lateral
RAL Vertical

Figure C8. Ground Test Measurement Locations - Acoustic Decay Rate, Acoustic and Vibro/Acoustic Transfer Functions

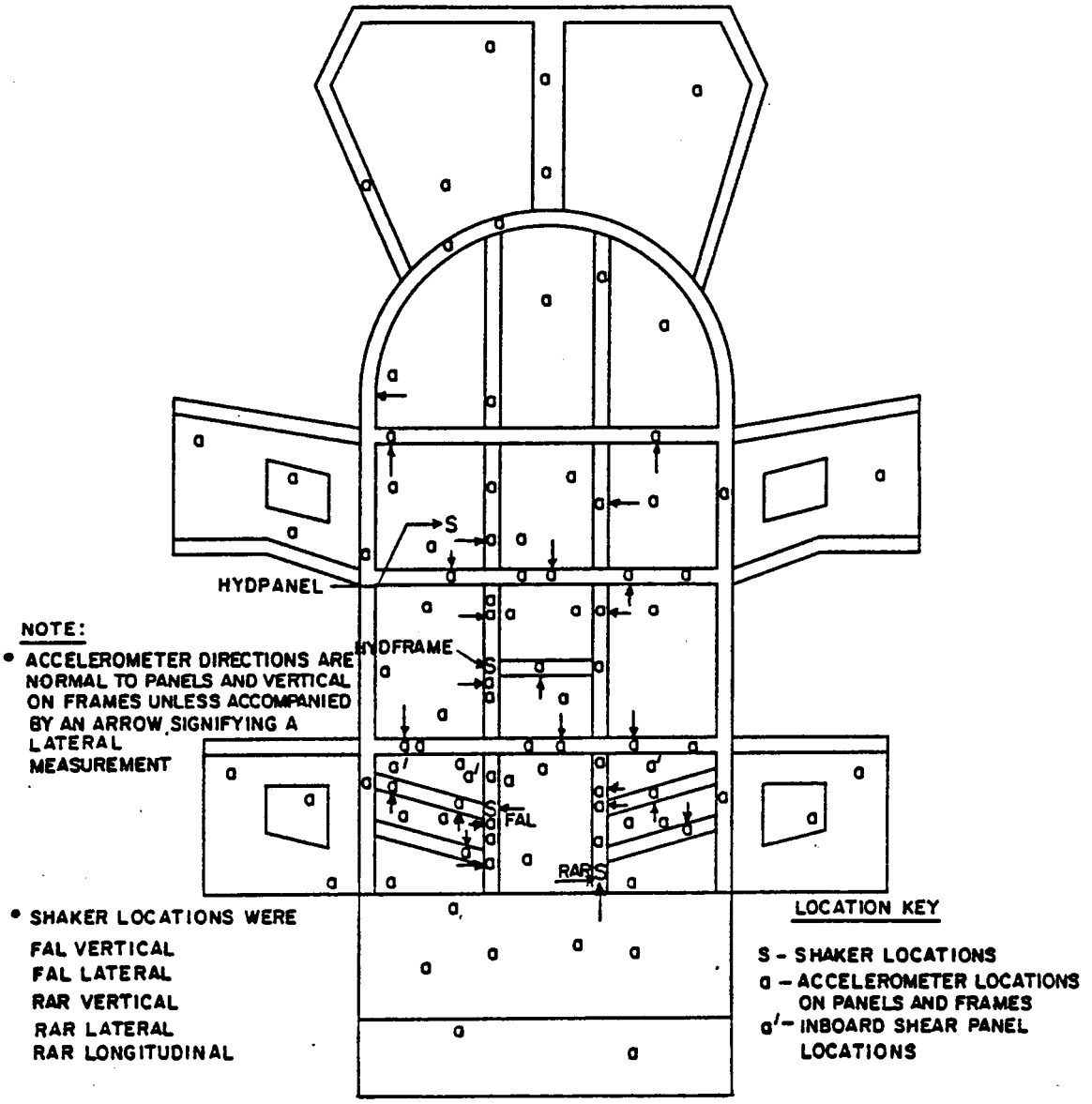

Figure C9. Ground Test Measurement Locations - Vibration Transfer Functions

Note that the matrix of frequency responses is assumed to be symmetric. That is, the frequency response of the front left main gearbox attachment location in the vertical direction when the airframe is excited at the same location but in the lateral direction, is assumed to be the same as the frequency response of the front left main gearbox attachment location in the lateral direction, when the shaker is located at the same foot in the vertical direction. Also, because of physical constraints, the point frequency response of the two front attachment locations in the longitudinal (fore and aft) direction are assumed to be equal to the frequency response functions of the aft mounting location longitudinal values, for each side respectively.

Compliance - main gearbox. - These measurements are similar to those described in the preceeding sections and a similar matrix of frequency response functions are then generated. All data was integrated twice using the two channel FFT analyzer, to yield units of displacement over force.

Data analysis. - All transfer function data were analyzed on a 2-channel digital signal analyzer, using a frequency range of 350-6750 hz. After storage onto digital tape, the data were converted to 1/3 and 1/1 octave band levels via software developed for a desktop computer. These levels are stored on disk for future reference.

Flight Test Measurements

The flight test measurement program objectives were to: 1) determine in-flight source levels, 2) determine the corresponding in-flight acoustic levels, and 3) provide data for overall validation of the SEA model. The following sections describe these efforts (see Figure C10 for measurement locations).

Vibration levels. - Accelerometers were mounted onto various subsystems and vibration signals were amplified and recorded onto magnetic tape. Also recorded were vibration levels in three principal directions at all four transmission mounting locations, which will be used later to formulate source levels into the airframe. The data is reduced using an octave band analyzer, to formulate 1/3 and 1/1 octave levels.

Sound pressure levels. - A microphone was positioned at twelve different locations in the cabin at passenger ear elevation, and noise levels were recorded onto magnetic tape. The data was reduced using a 1/3 octave analyzer and desktop computer to average over the length of the record and to print the results.

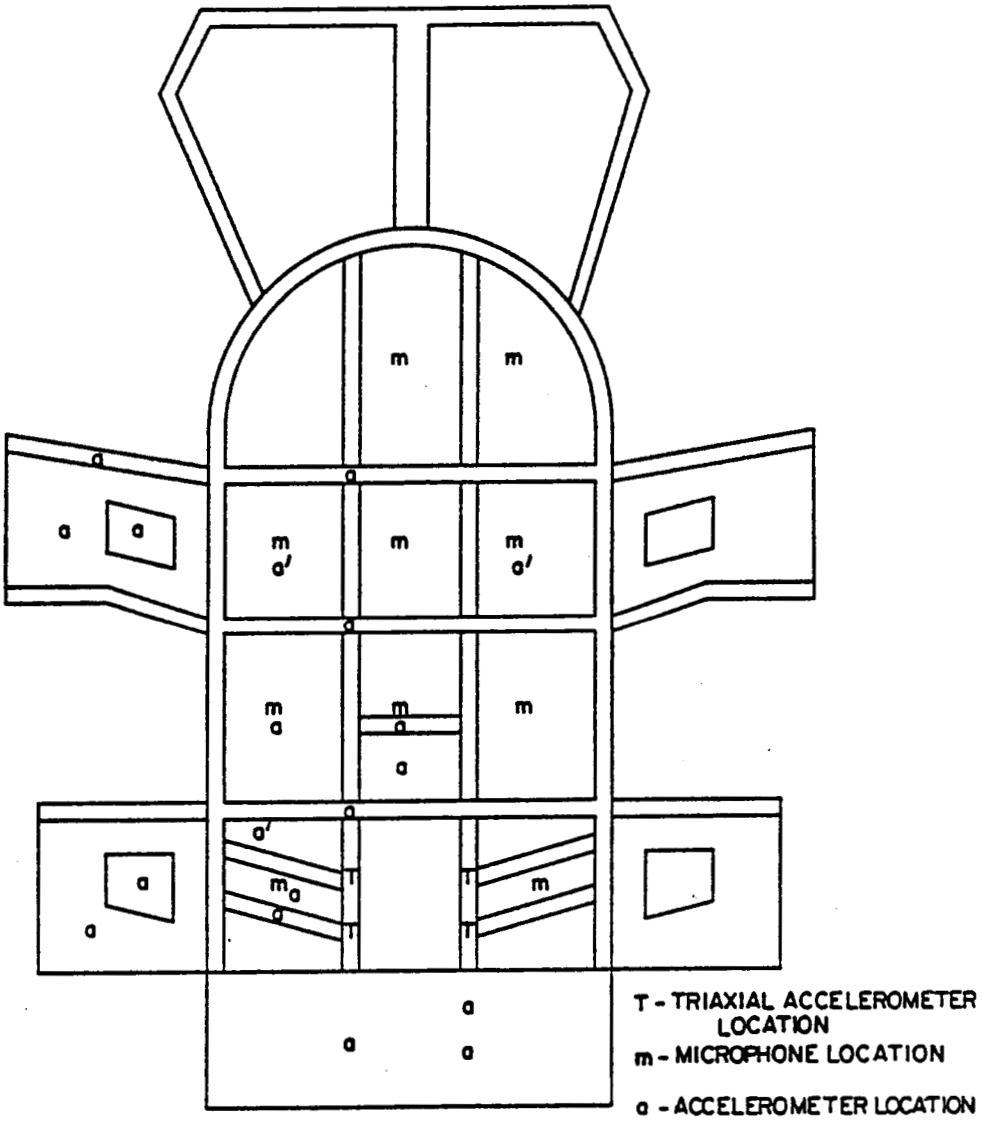

Figure C10. Flight Test Measurement Locations - Acoustic and Vibratory Response

APPENDIX D

TEST RESULTS

TABLE OF CONTENTS

Introduction

This appendix describes the results of laboratory, ground, and flight testing designed to supply key information to and validation of the SEA prediction of noise and vibration in the S76 helicopter. Coupling loss factor assessment is a key portion of the model development. A laboratory experiment was designed to focus on the accurate representation of the coupling loss factor in a general sense without the extraneous discontinuities that appear in the actual airframe. Tests included the evaluation of panel to panel coupling across a frame, and direct frame excitation and panel coupling.

The ground test measurements section covers the coherent sources investigation, parameter loss factor estimation, and transfer function measurements, for both input to and the validation of the SEA model. Flight test information focuses on vibration and sound pressure levels measured during flight for estimation of source input levels and final flight prediction comparison of cabin noise.

SEA Coupling Loss Factor Validation Measurements

A series of laboratory measurements were carried out to validate particular coupling loss factor estimations that are important in the overall SEA model of the S-76. These measurements focused on the coupling between frame members and adjacent panels that connect along the length of the frame. The coupling loss factors between resonant frame and panel vibrations and between panels on opposite sides of a frame as a result of non-resonant or mass controlled response of the frame is of particular interest.

Laboratory experiment. - Actual frame and panel structures representative of the S-76 were not used for reasons of generality, parameter control, cost, and simplicity. Instead, frames of a simple rectangular cross-section and uniform panels were used to provide more controlled test structures, thereby focusing on the coupling loss factor estimations with reduced concern about the effects of inhomogeneities and cross-sectional asymmetries that characterize the actual built-up riveted frames and composite panels on the S-76.

The measurements involved: 1) shaker excitation of a source subsystem, either the frame or the panel on one side of the frame; and 2) the measurement of average vibration levels in the source subsystem and also the receiving panel subsystem(s). Sketches of the test structures are shown on the appropriate figures containing the test data. Comparison of source and receiver subsystem average vibration levels provides the desired information for validating the estimation of coupling loss factors of interest.

This is illustrated for a model with only two subsystems where the ratio of vibrational energies is given by the following expression:

$$\frac{e_2}{e_1} = \frac{\eta_{21}}{\eta_{2,d} + \eta_{21}} \tag{D1}$$

where e_1, e_2 are the modal energies of the subsystems, $\eta_{2,d}$ is the damping loss factor of the receiving subsystem and η_{21} is the coupling loss factor of interest. From this expression it is seen that

$$\text{if:} \quad \eta_{2,d} < \eta_{21}$$

$$\text{then:} \quad \frac{e_2}{e_1} \cong 1 \tag{D2}$$

and the measurement has a very weak dependence on the coupling loss factor. Therefore, a damping treatment was added to the receiving panel subsystem for all test cases, thus enhancing the coupling loss factor as a measurable quantity. With the damping treatment, if $\eta_{21} < \eta_{2,d}$ then:

$$\frac{e_2}{e_1} \cong \frac{\eta_{21}}{\eta_{2,d}} \tag{D3}$$

and the experiment provides a direct validation of the coupling loss factor. The expression relating source and receiver subsystem energies becomes more involved when additional structural elements and subsystems are included within the model. Measured results from these controlled tests were compared with predictions generated from SEA models of the respective test structures.

The test structures were fabricated from aluminum having a material loss factor of approximately 0.002. Loss factor measurements were performed on a 0.0064 m thick aluminum panel, damped over its' entire surface with a free extensional damping treatment. The damping material, EAR C-2003-05, consisted of a 0.0013 m thick sheet bonded to the panel. The measured loss factors for this damped plate are shown in Figure D1 along with the curve fit used in the SEA model.

An alternative check on the damping loss factor estimations involved a measurement of the differences in average vibrational levels on two halves of a large (1.22 m by 2.44 m by 0.0016 m thick) panel where the receiver side was treated with the damping material while the source side (or subsystem) was left untreated. The coupling loss factor between treated and untreated halves of the same panel is relatively straight-forwardly modeled. The difference in level is attributed to the high damping levels in the receiving half panel, according to Equation (D3).

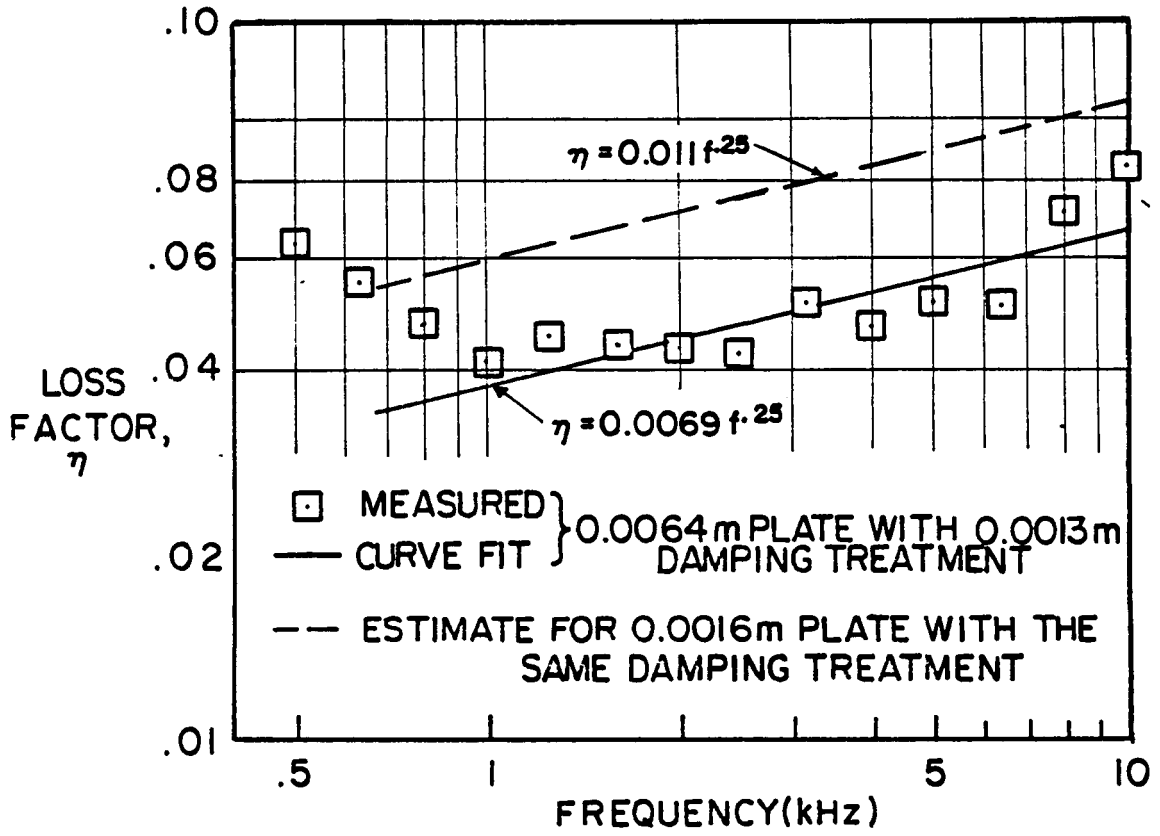

Figure D1. Damped Panel Loss Factors

The predicted results shown in Figure D2 are based on loss factors for the 0.0016 m thick panel that have the same frequency dependence as for the damped 0.0064 m thick panel (Figure D1), but with increased loss factor corresponding to the greater effectiveness of the same thickness treatment when applied to a thinner panel. Loss factor levels were scaled to provide the close agreement to the measured data shown in Figure D2.

An additional consideration accounted for in the modeling of the treated panel subsystem was the effect of treatment mass and stiffness on panel dynamics. The treatment will shift the neutral axis for panel bending, thereby altering its' bending rigidity, though the dominant effect is due to the additional mass it adds to the panel.

Panel-to-panel coupling across a frame. - Two physically different frame cross sections were used to conduct the following set of measurements. One was 0.013 m square while the other was a narrow rectangle, 0.152 m by 0.0064 m. The frame/panel attachment was made, in all cases, with the narrow dimension of the "frame" cross-section attached to the panel. Cross-sectional deformation for the 0.013 m square frame does not occur within the frequency band of interest for these experiments. However, for the 0.152 m by 0.0064 m "frame", cross-sectional deformation or plate-like bending deformation will occur at a frequency within the measurement band. This second frame provides a test case more representative of S-76 frames which have relatively thin webs with angle stiffeners that can be expected to undergo cross-sectional deformation in the audible frequency range. The frame model, as currently configured for the S-76, does not account for cross-sectional deformation.

Damped panels were connected to the ends of the frame which extended beyond the source and receiving panels, thus providing damping for frame resonances and a smoothing of the panel vibration level differences. Measurements obtained with and without these damping panels did not exhibit significant changes in the results which would indicate that the frame connection to the source and receiving panels, and in particular, the damped receiving panel, provided for adequate smoothing.

Figure D3 shows results for the 0.013 m square frame. Using the presumption that frame rotational motion occurs about the frame/panel junction, SEA predictions track the measured data quite well at lower frequency. Near 1.6 to 2.5 kHz the increase in transmission reduction across the frame becomes more pronounced. The predicted transition to faster increase in vibration reduction occurs at a lower frequency than experimentally observed. The transition is associated with the non-resonant, mass-controlled, rotational inertia of the frame. The panel moment impedances along the line connection (junction) to the frame have an imaginary component that is stiffness controlled. The transition near 2 kHz to a more rapid increase in vibration reduction at higher frequency is due to the cancellation of panel stiffness-controlled and frame mass-controlled behavior. The effect is similar to the increasingly reduced response of a simple resonator at frequencies above resonance. This discussion relates

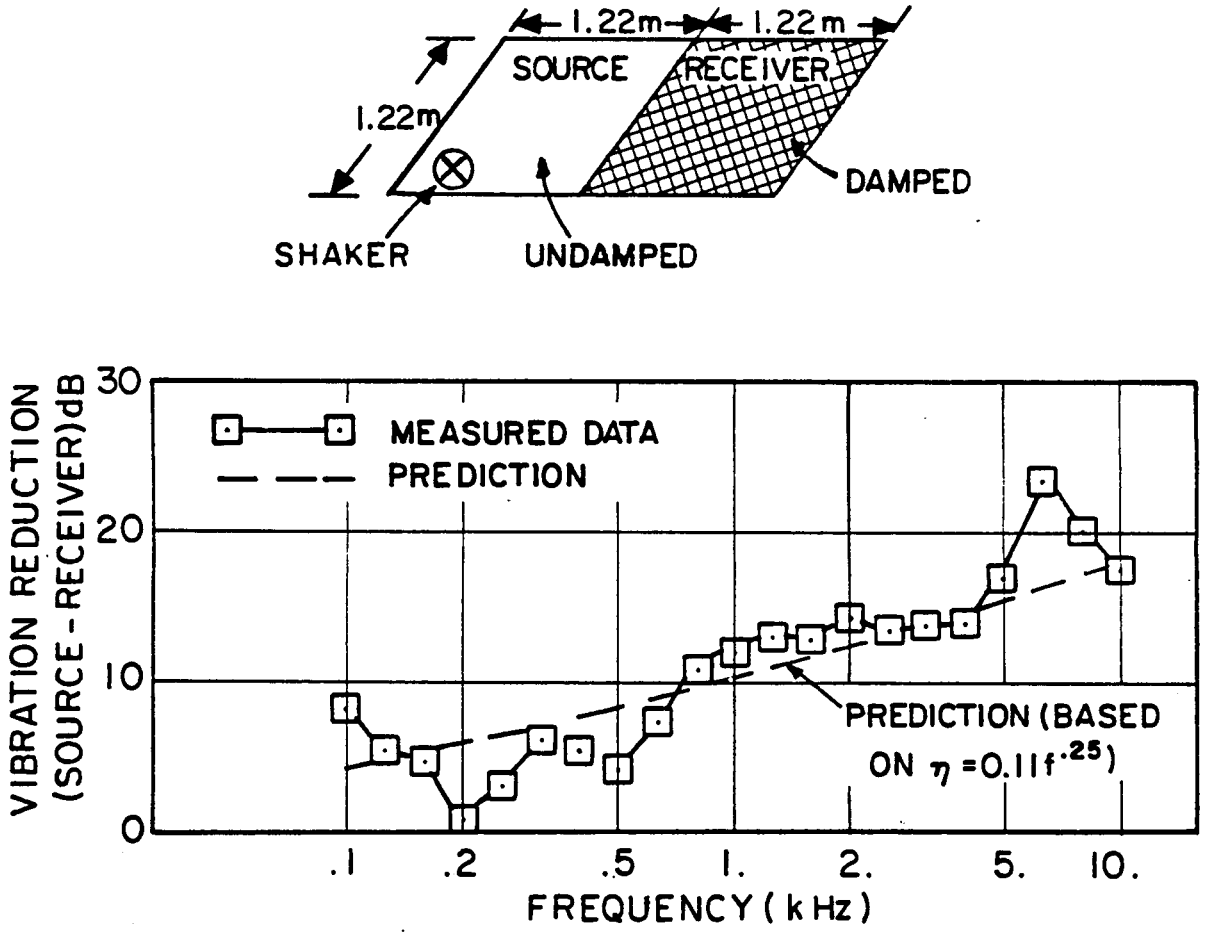

Figure D2. Undamped vs. Damped Panel Vibration Reduction (Without a Frame)

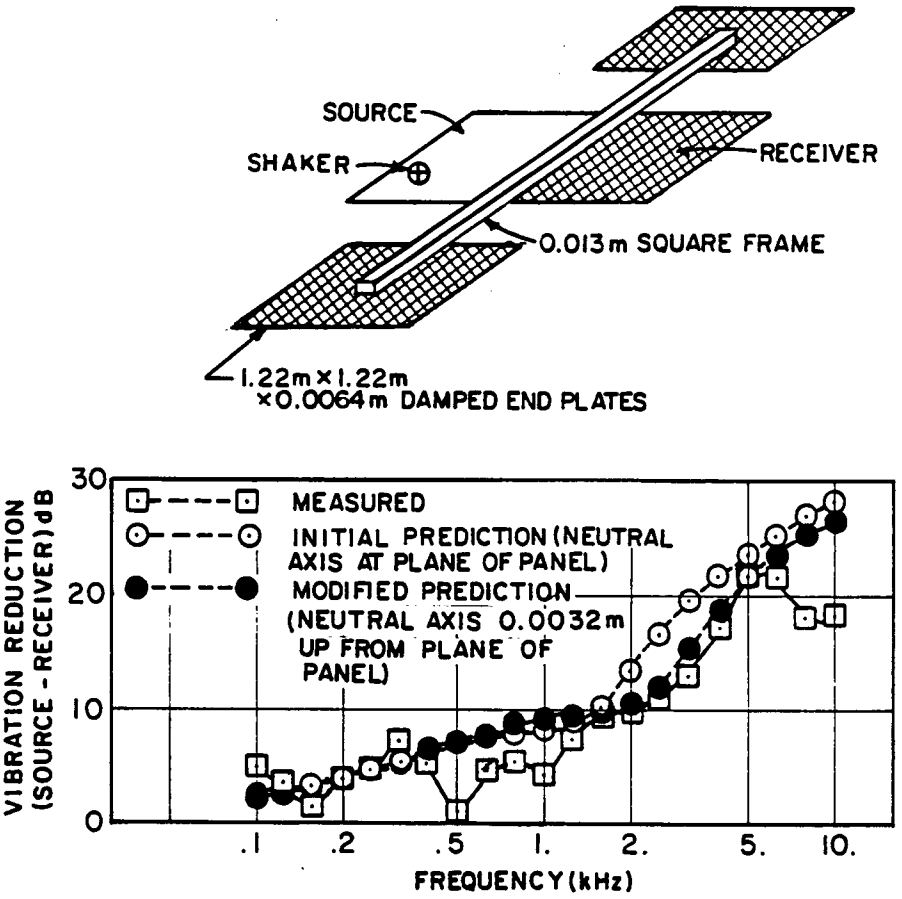

Figure D3. Panel-to-Panel Coupling Across a 0.013 m Square Frame

to the direct coupling between the panels associated with mass controlled rotation of the frame. Transmission to the receiving panel due to mass controlled transverse motion of the frame is effectively blocked down to very low frequency.

Also shown in Figure D3 is a prediction where the rotational inertia of the frame was arbitrarily reduced. This shifted the transition point to higher frequency, in better agreement with the measured data. The current frame model specifies that rotation take place about a neutral axis at the location where the frame connects to the panel. This is as a result of the presumed high in-plane impedance of the panels. For the asymmetric configuration tested, this axis is at the base of the frame. Rotation about this extreme neutral axis results in a greater moment of inertia of the cross-section.

If the actual neutral axis for frame rotation (when attached to the panels) is at an elevation between the base and the centroid of the rectangular cross-section, then the moment of inertia is reduced. This will have the effect of shifting the cancellation between frame mass-controlled and panel stiffness-controlled behavior to a higher frequency, resulting in an improved fit to the measured data, as shown. The neutral axis for the frame in the modified prediction was placed half way between the base and centroid. The measured leveling of vibration reduction at very high frequency is not understood at present and may be the result of anomalous behavior in the measurement.

Results for the 0.152 m by 0.0064 m "frame" are shown in Figure D4. The measured vibration reduction is characterized by steadily increasing values at a rate of approximately 1.5 dB per octave change in frequency, or proportional to the square root of frequency. Predicted results (modeling the "frame" as a frame with no cross-sectional deformation) increase at a rate of 3 dB per octave or proportional to frequency. This behavior corresponds to the predictions for the 0.013 m square frame at high frequencies above the transition point. The 0.152 m by 0.0064 m frame has substantially greater rotational polar moment of inertia resulting in a significantly reduced transition frequency.

A second prediction was generated where the frame was modeled as a narrow plate. This allows for plate-like cross-sectional deformation. Out-of-plane bending in the "frame" model is not accounted for in these "plate" predictions as it would correspond to in-plane deformation of the plate. Cross-modes of the plate in the 0.152 m direction appear as dips in the vibration reduction. These cross-modes "soften" the 0.152 m by 0.0064 m plate, allowing additional transmission between the source and receiver plates.

As shown in Figure D4, these two otherwise significantly different modeling approaches result in very similar predictions for this case. Both, though, suffer a discrepancy (in comparison with the measured data) that appears related to the frequency dependence of the behavior which is controlling the

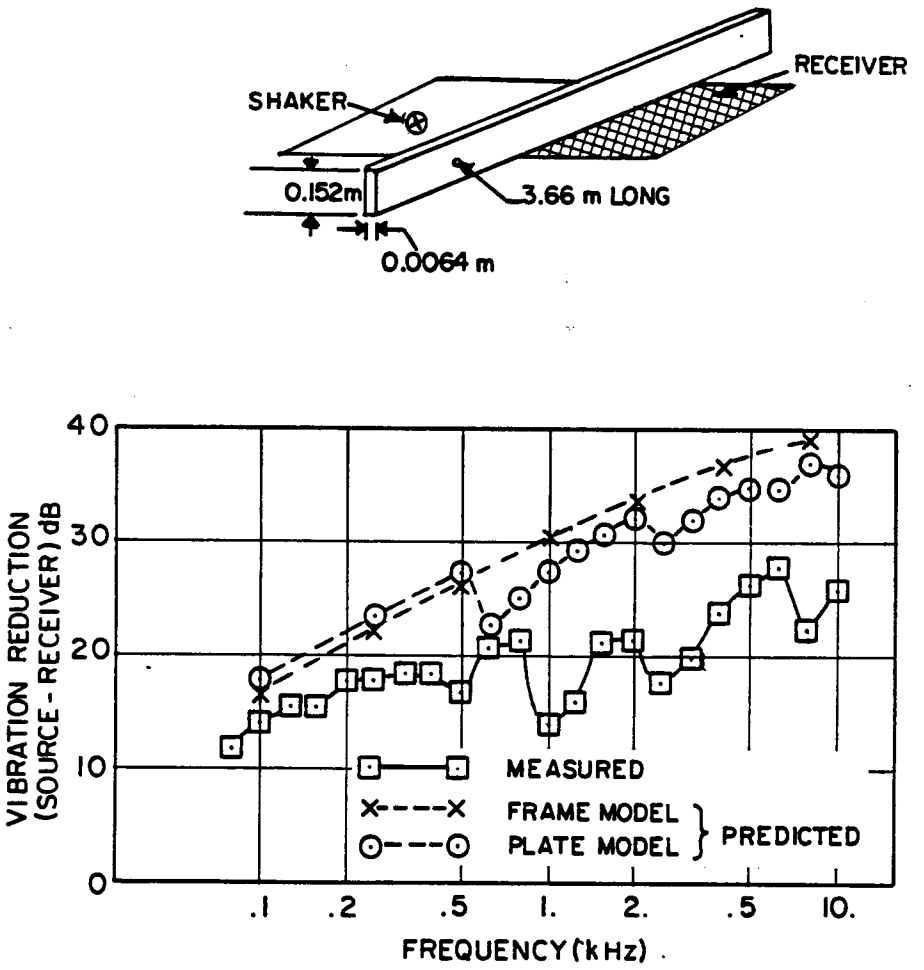

Figure D4. Panel-to-Panel Coupling Across a 0.152 m by 0.0064 m Frame

transmission process. As yet, no consistent explanation has been formulated to account for this or which would suggest refinements to the modeling of the frame as either a "frame" or a "panel".

Direct frame excitation and panel coupling. - The previous experiments focused on the coupling between panels across a frame including both non-resonant and resonant frame response. This experiment provided for direct excitation of the frame and measurements of the difference in vibration response between average levels in the source frame and average levels in the receiver panels on both sides of the frame. Both panels have been treated with the damping material. The frame in this case had a 0.025 m by 0.013 m rectangular cross-section.

These comparisons apply directly for the coupling loss factor between resonant frame motion and panel bending. Since there are difficulties in generating a purely moment excitation of the frame, out-of-plane motion was the only excitation considered for this experiment.

As will be seen, excitation of only out-of-plane bending with no induced frame rotation is also difficult. This difficulty is illustrated in Figure D5 which shows out-of-plane bending vibration levels and in-plane vibration levels measured laterally near the top and bottom of the frame cross-section. The shaker was carefully positioned in an attempt to excite only out-of-plane bending. At low frequencies, in-plane motion is negligible and only out-of-plane bending is excited. As frequency increases, a rapid increase in the in-plane motion occurs, peaking in the region near 2.5 kHz. Above 2.5 kHz the different motions are comparable in level.

The behavior near 2.5 kHz is presumed to involve a resonant interaction between the rotational inertia of the frame and the stiffness of the attached panels for rotational motion at their edges. This is the same behavior observed in the data for transmission across the frame with panel excitation. The frame in this case has twice the height and therefore greater moment of inertia so that the location of the resonance would be shifted to lower frequency relative to the shorter height frame. Again, there is an uncertainty about the elevation of the neutral axis for frame rotation due to the panel attachments, and also therefore, concerning the appropriate rotational inertia for the frame.

Vibration level differences between the attached panel and the excited frame are shown in Figure D6. The measured results at low frequencies decrease at a rate of 1.5 dB per octave or inversely proportional to the square root of frequency. Peaks in the 1.6 to 2.5 kHz region are apparently related, in part, to the rotational resonance of the frame on the panels. Excitation of resonant rotational frame motion by the shaker would increase the panel levels relative to the predictions which have power input only into out-of-plane bending of the frame.

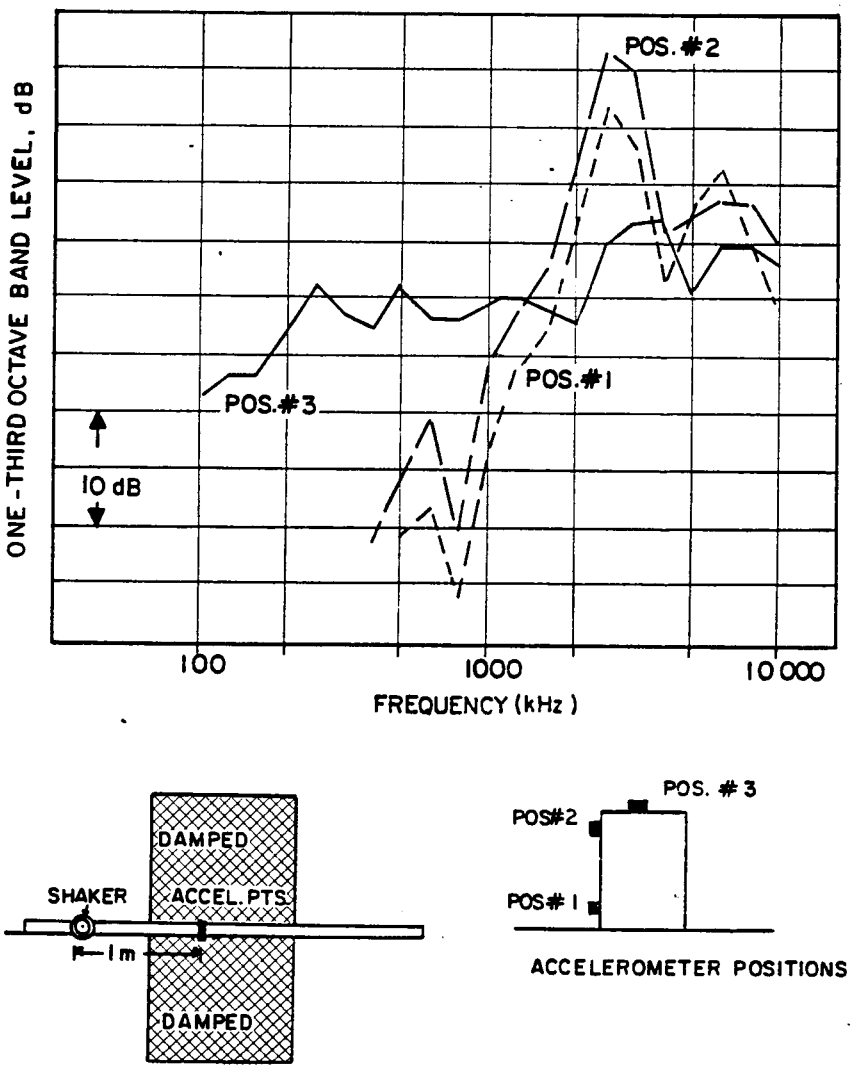

Figure D5. Frame Motions for Out-of-Plane Frame Excitation

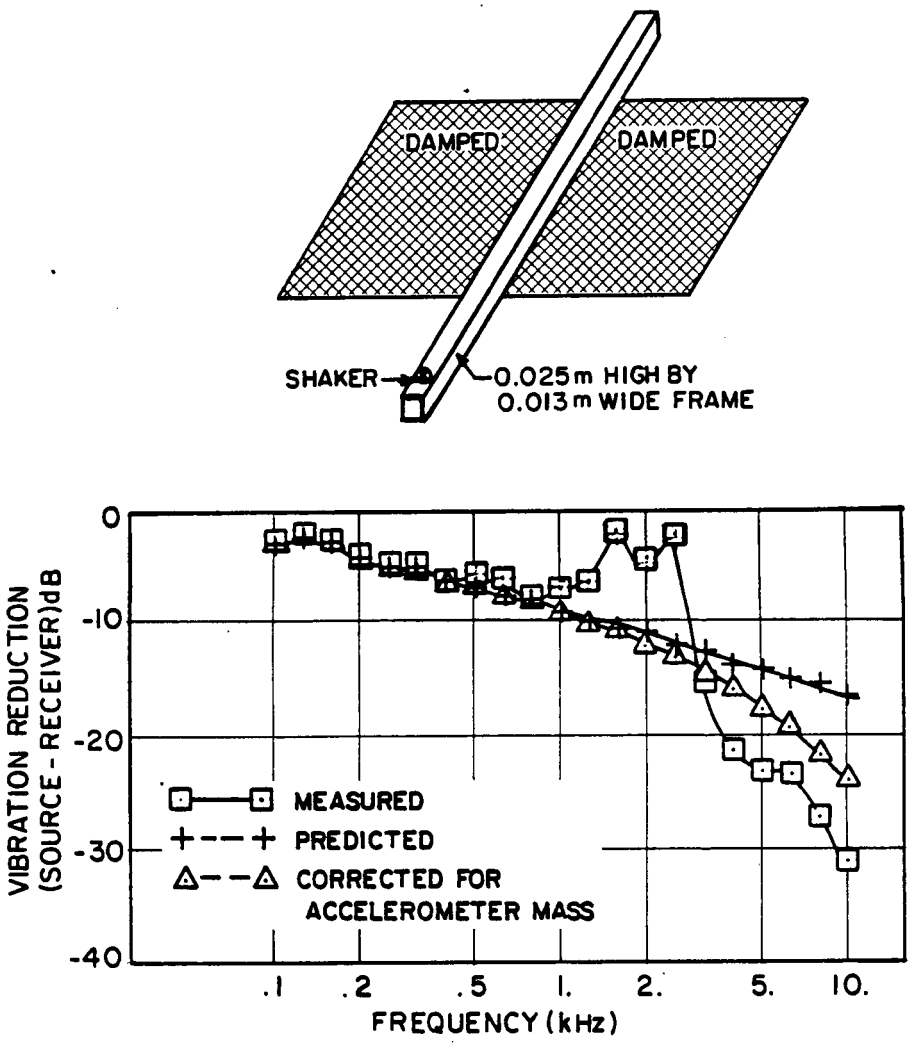

Figure D6. Frame-to-Panel Coupling for Out-of-Plane Frame Excitation

Above the 1.6 to 2.5 kHz region the panel level falls off relative to the frame at a rate inversely proportional to frequency. This in part can be attributed to the mass of the accelerometer used to measure the panel vibration levels, as the effect is more pronounced at higher frequencies. A 2.7 gm. accelerometer was used for the measurements on panels which were 0.0016 m thick. The mass becomes significant near 2 kHz, with an estimated reduction in panel levels of 1 dB. The effect increases at a rate of 6 dB per octave, resulting in a reduction of approximately 7.4 dB at 10 kHz.

Predicted results agree quite well with the measured data at low frequencies. The discrepancy in the region from 1.6 to 2.5 kHz is attributed to the effect of the rotational resonance of the frame attached to the panels. Above 2.5 kHz the added accelerometer mass correction results in a consistent frequency dependence between the measured and predicted behavior. The 5 dB difference is unexplained at present. In the low frequency region, where only out-of-plane bending is being excited, the modeling of resonant coupling between the frame out-of-plane bending and panel bending provides an excellent agreement with measured results.

Ground Test Measurements

The ground test measurements performed involved the validation of some basic assumptions, the estimation of damping level parameters for inclusion into the SEA model, and measurements of transfer functions for the validation of the ground based predictions.

Coherent sources investigation. - Coherence effects between multiple sources are dependent on the degree of mutual coupling between the excited locations on the structure as well as the coherence between the sources. The mutual coupling is quantitatively represented by non-zero transfer mobilities relating forces and velocities at the source points. For the simplified case of two source points (1 and 2) and a single distant receiving point (3), the equations become:

$$\begin{Bmatrix} V_1 \\ V_2 \\ V_3 \end{Bmatrix} = \begin{bmatrix} Y_{11} & Y_{12} \\ Y_{12} & Y_{22} \\ Y_{13} & Y_{23} \end{bmatrix} \begin{Bmatrix} F_1 \\ F_2 \end{Bmatrix} \tag{D4}$$

where $Y_{i,j}$'s are the mobilities characterizing the dynamic behavior of the system, V_1, V_2, F_1, F_2 are velocities and forces at two source points and V_3, the response at a distant point on the airframe. Vibration transmission to the distant point is characterized by the transfer mobilities Y_{13} and Y_{23} while the coupling between the sources F_1 and F_2 depends on the transfer mobility Y_{12}.

The input power is given in general by the following:

$$\Pi_{in} = \frac{1}{2} \text{Re } (FV^*) \tag{D5}$$

with Equation (D4) this gives the following for the total power:

$$\Pi_{in} = \frac{1}{2} \text{Re } (Y_{11})|F_1|^2 + \frac{1}{2} \text{Re } (Y_{22})|F_2|^2 + \frac{1}{2} \text{Re } (Y_{12}) (F_1 F_2^* + F_1^* F_2) \tag{D6}$$

The magnitude of the response of the structure at point 3 is given by:

$$|V_3|^2 = |Y_{13}|^2|F_1|^2 + |Y_{23}|^2|F_2|^2 + Y_{13}Y_{23}^* F_1 F_2^* + Y_{13}^* Y_{23} F_1^* F_2 \tag{D7}$$

In both expressions the first two terms are associated with the individual sources treated independently of each other. In Equation (D6) the third term represents the effects of source coherence. For random excitations the various terms are statistically described in terms of spectral densities:

$$\begin{aligned} S_{v3}(\omega) = {} & S_{F_1}(\omega)|Y_{13}(\omega)|^2 + S_{F_2}(\omega)|Y_{23}(\omega)|^2 \\ & + S_{F_1, F_2}(\omega) \left(Y_{13}^*(\omega) Y_{23}(\omega) + Y_{13}(\omega) Y_{23}^*(\omega)\right) \end{aligned} \tag{D8}$$

and

$$\Pi_{in}(\omega) = \text{Re}(Y_{11}) S_{F_1}(\omega) + \text{Re}(Y_{22}) S_{F_2}(\omega) + \text{Re}(S_{F_1, F_2}(\omega)\, Y_{12}^*(\omega)) \tag{D9}$$

where the functions S_{F_1}, etc., are two sided spectra.

It is seen from Equations (D8) and (D9) that the condition that the applied forces are incoherent, i.e., the cross spectrum is zero, produces a simple incoherent sum of mean square responses at the receiver location and also of the power input to the structure associated with each source estimated independently.

The SEA approach evaluates the response at the receiving location based on the input powers associated with the force spectra, $S_{F_1}(\omega)$ and $S_{F_2}(\omega)$. In this sense it yields results to be compared with the quantities $|Y_{13}(\omega)|^2$ and $|Y_{23}(\omega)|^2$ which are otherwise evaluated experimentally. Coherence between multiple sources results in an additional term in the expression for the total power and also the receiving location response that is otherwise unaccounted for by the SEA model. The impact of the term depends on the degree of coherence as quantified by the cross spectral density S_{F_1}, $S_{F_2}(\omega)$ as well as the magnitude of coupling between source points given by $\mathrm{Re}(Y_{12}(\omega))$.

In the absence of measurements of the complex quantities Y_{12}, Y_{13}, Y_{23} for a helicopter airframe, and without information defining the degree of coherence between the excitations at the gearbox attachment locations, a straightforward experimental approach was adopted to assess the potential importance of coherence effects for gearbox excited airframe transmission. Actual gearbox excitations were replaced with two mechanical shakers at different attachment locations. The response at two distant locations on the airframe was measured when the same random voltage was coherently applied to the two shakers. This is the coherent excitation case. The response spectrum from this case was compared with the incoherent energy sum of responses at the same point from two measurements where shakers were excited one at a time. The voltage levels to each shaker where individually adjusted to produce comparable response levels at the receiver locations.

If the incoherent sum is comparable to the coherent excitation result then the conclusion can be drawn that coherence effects are not of general importance for helicopter vibration transmission associated with gearbox excitations and additional consideration is not required in the SEA model. The experiment performed is conservative in that in the coherent excitation case the two sources were perfectly coherent because the same random noise source was applied to both shakers.

The results of the measurements are shown in Figures D7 to D14. Two source configurations were evaluated: in one the shakers were located at the same gearbox attachment point but were driving in different directions and in the other the shakers point in the same direction but at different gearbox attachment locations. Responses were measured at two airframe locations: one a frame member, LF45R, for out-of-plane bending, and the other on a overhead skin panel, OP56M.

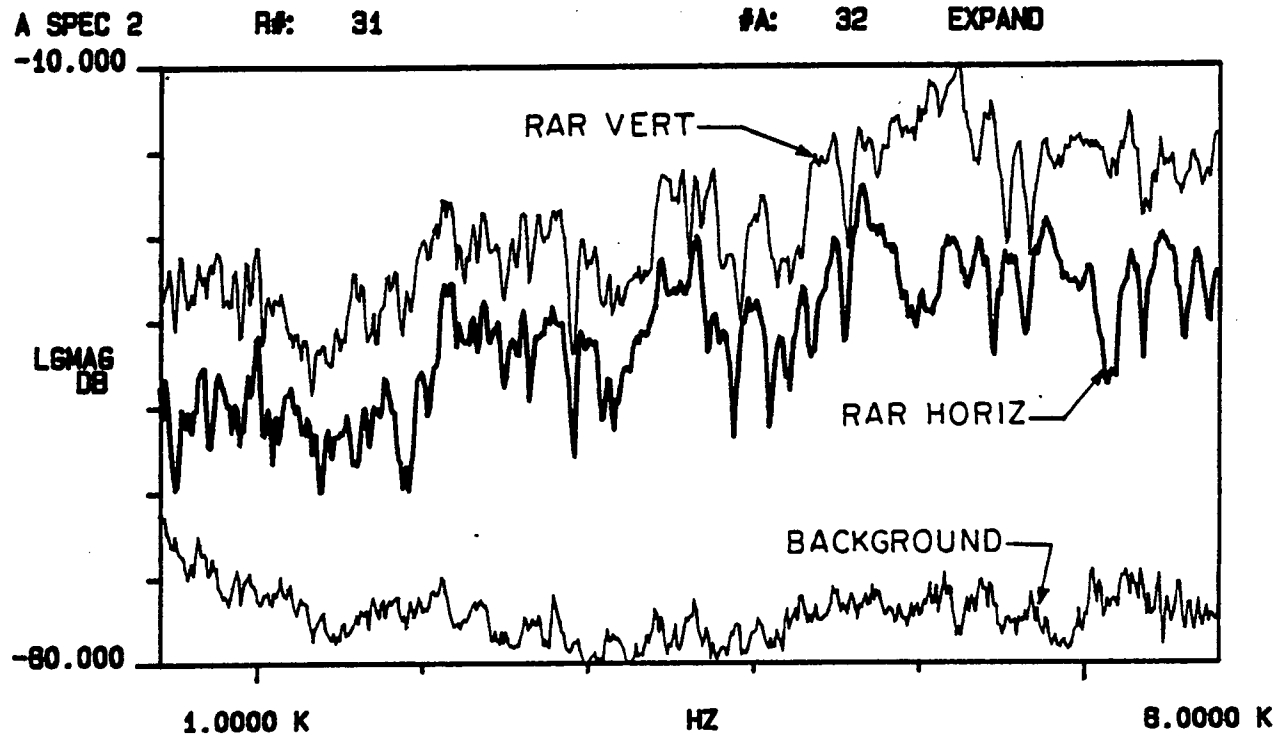

Figure D7. Overhead Panel OP56M Vibration Levels for Individual Inputs at RAR Vertical and RAR Horizontal, and Panel Vibration Background Level

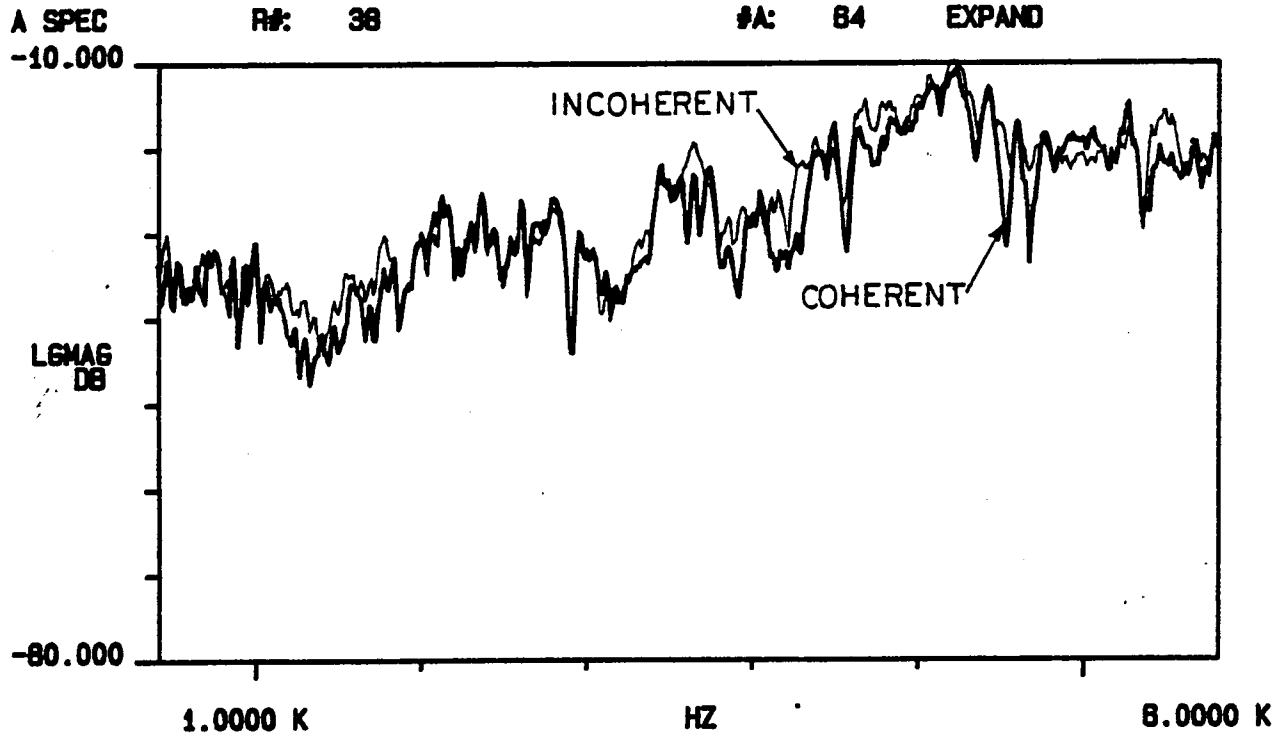

Figure D8. Coherent and Incoherent Sum at OP56M for RAR Vertical and RAR Horizontal Input

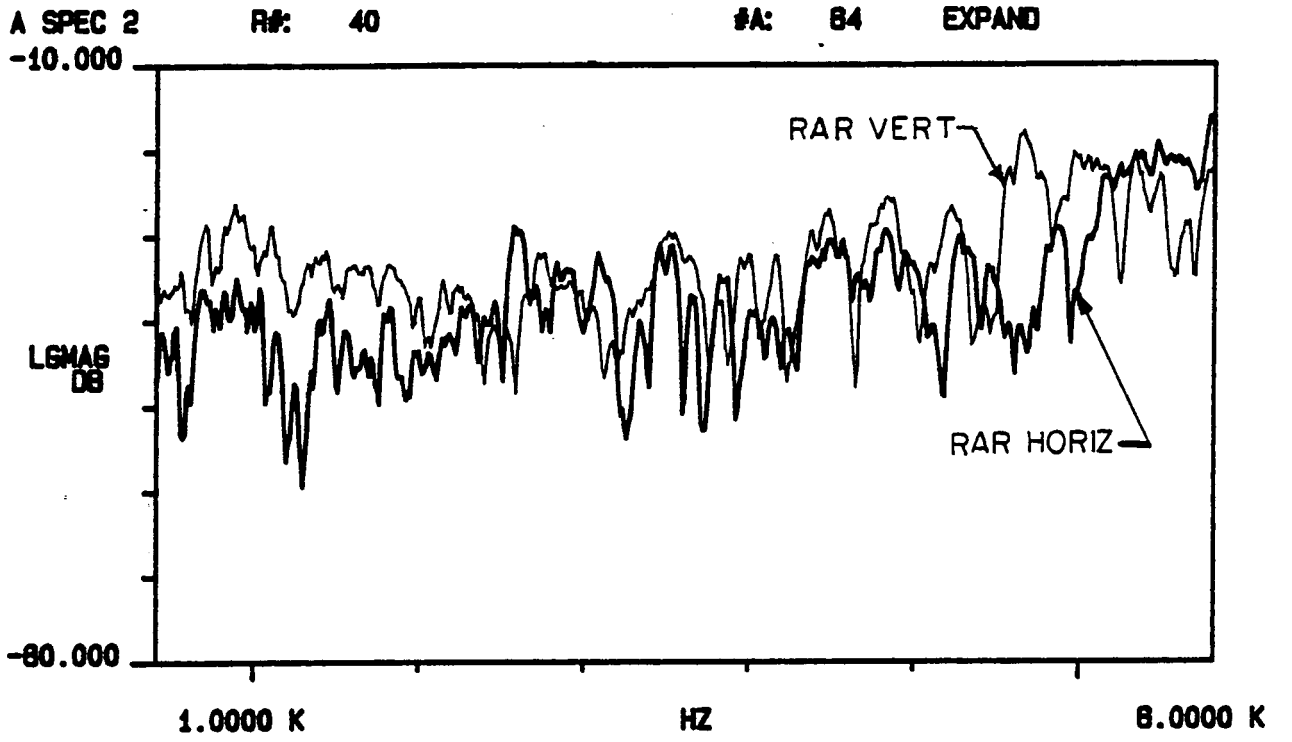

Figure D9. Overhead Frame LF45RV Vibration Levels for Individual Inputs at RAR Vertical and RAR Horizontal

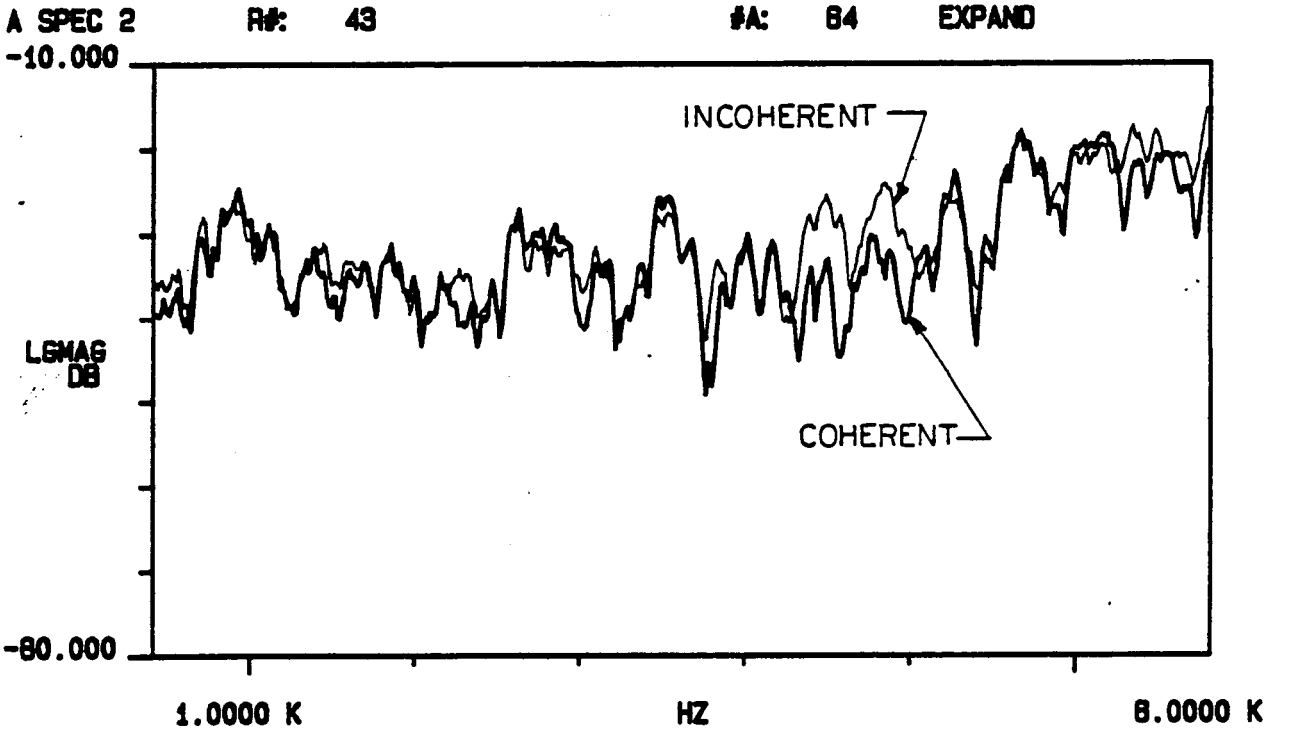

Figure D10. Coherent and Incoherent Sum at LF45RV for RAR Vertical and RAR Horizontal Input

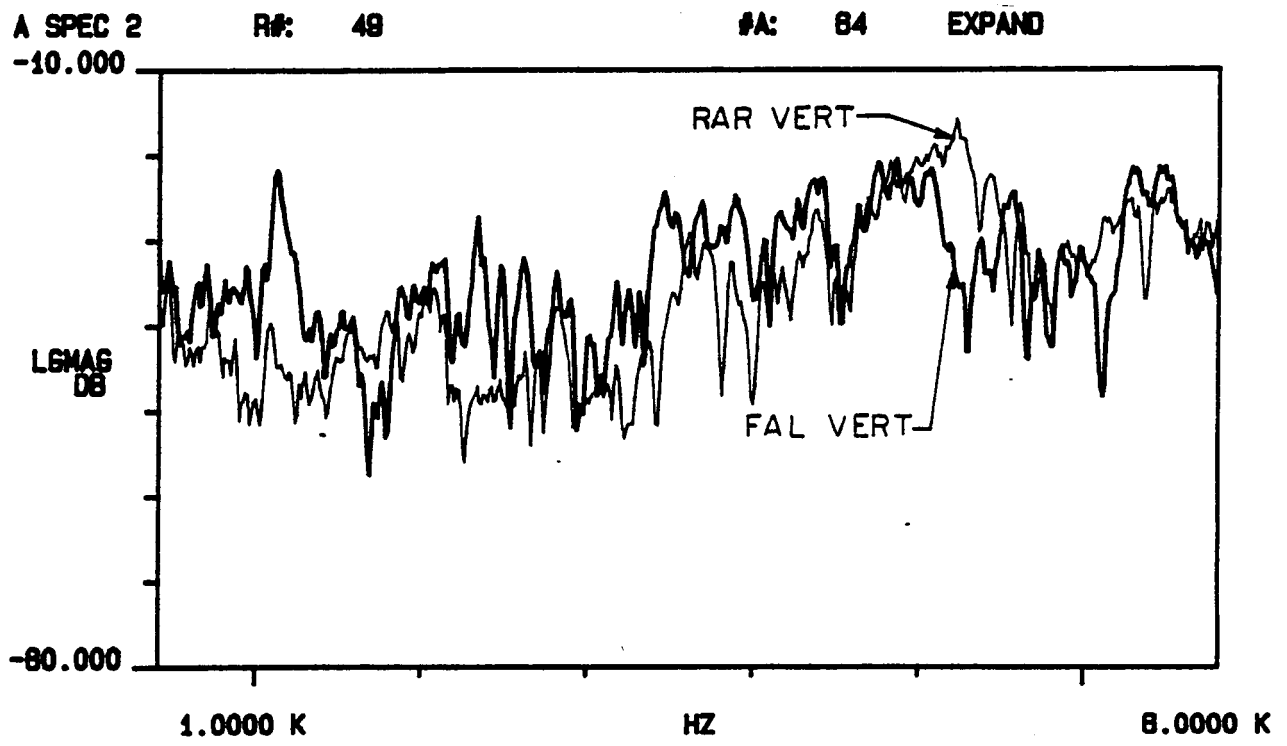

Figure D11. Overhead Panel OP56M Vibration Levels for Individual Inputs at RAR Vertical and FAL Vertical

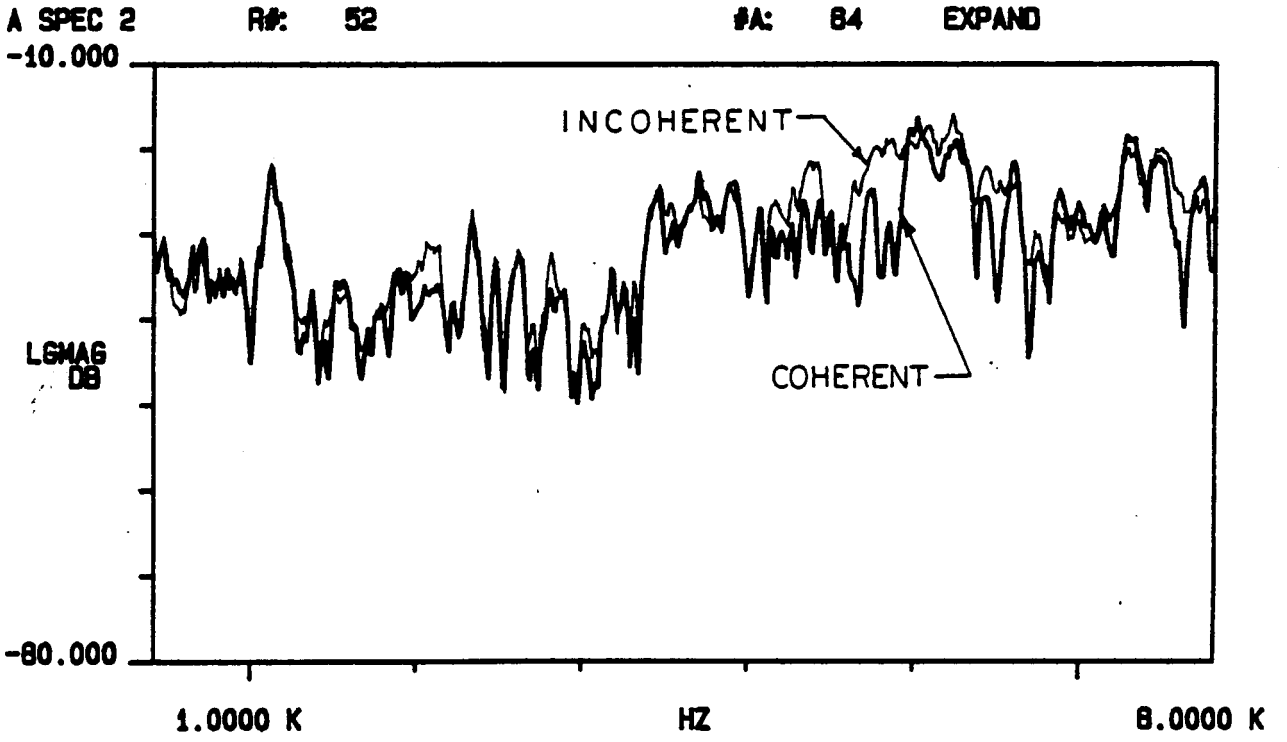

Figure D12. Coherent and Incoherent Sum at OP56M for RAR Vertical and FAL Vertical Input

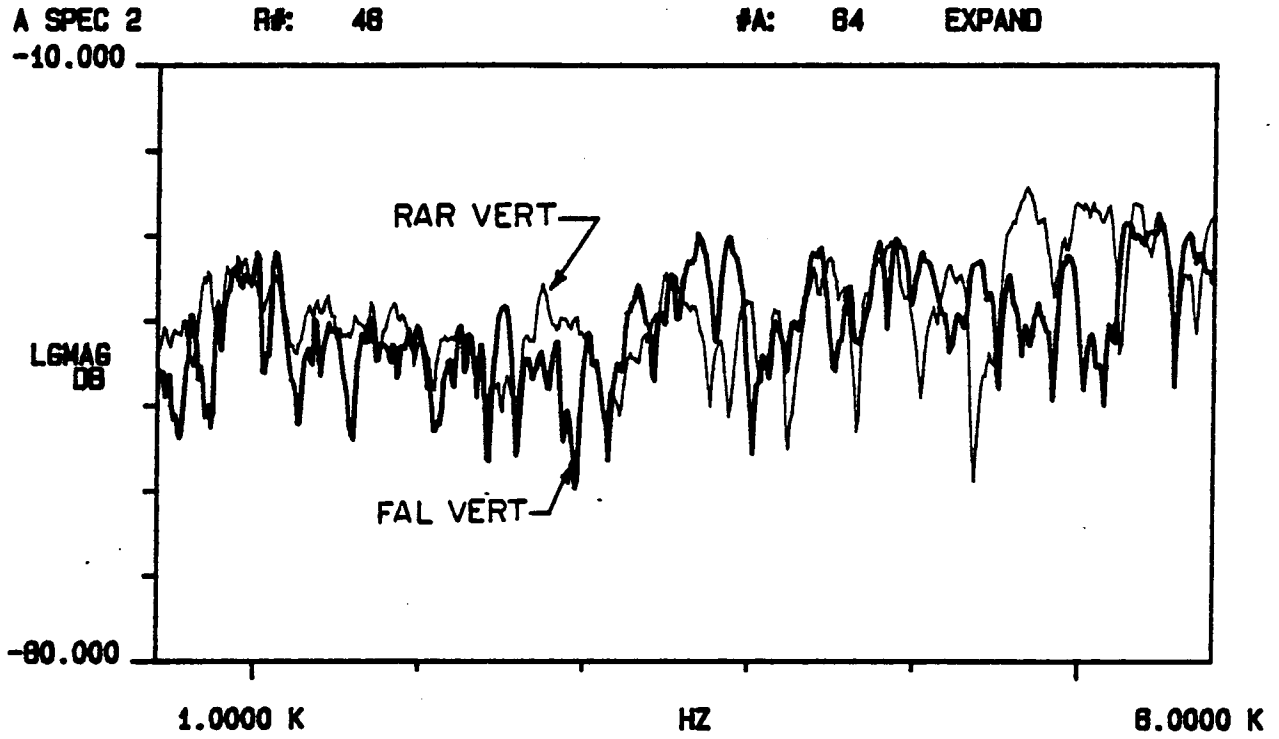

Figure D13. Overhead Frame LF45RV Vibration Levels for Individual Inputs at RAR Vertical and FAL Vertical

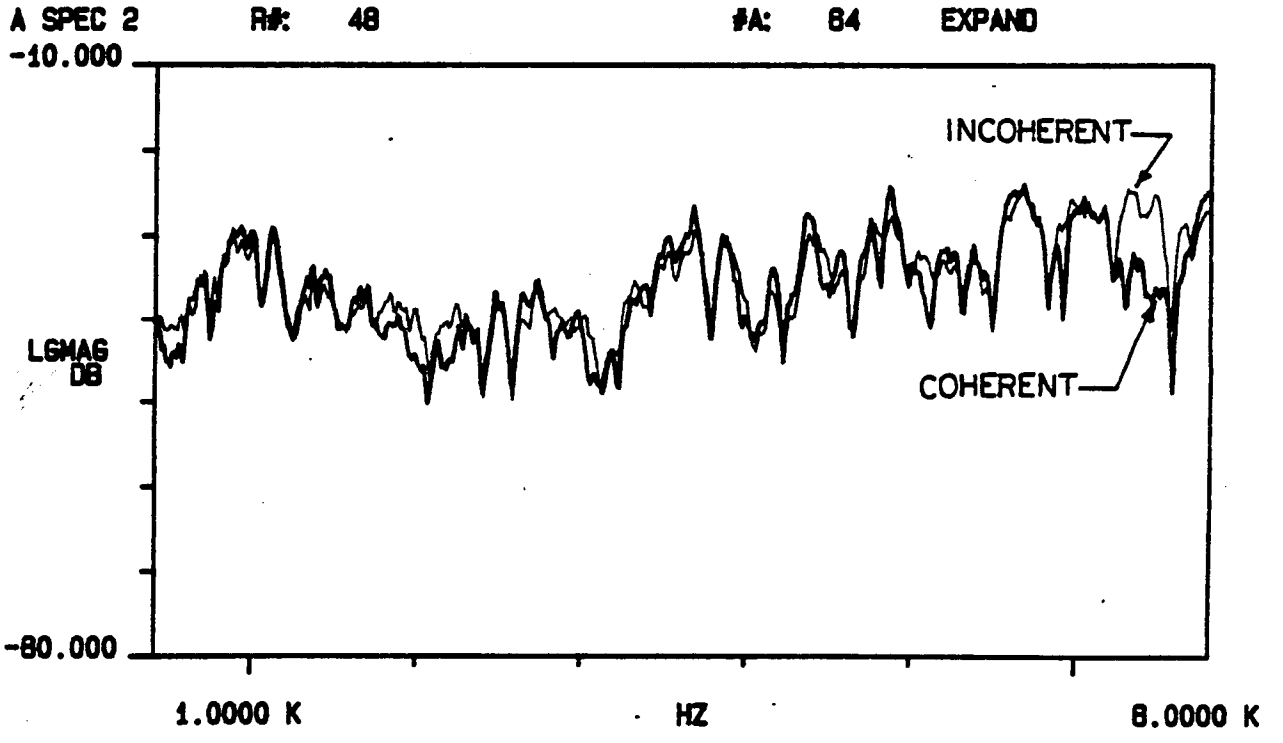

Figure D14. Coherent and Incoherent Sum at LF45RV for RAR Vertical and RAR Horizontal Input

Narrowband spectra, Figures D7 through D14, for the different cases comparing the incoherent sum for separate excitation with the coherent sum with simultaneous excitation show scattered frequency regions where the two differ by as much as 10 dB, but in general there is quite close agreement between these data. On a 1/3 octave band basis, the results would exhibit an even closer comparison. The results support the conclusion that coherence effects are not of particular importance when considering gearbox excitation of airframe vibration transmission.

Structural damping loss factor. - As can be seen from Photos P1 and P2, the S-76 airframe is fabricated in fixtures as a built up structure. The individual webs and flanges, for each of the frames, are clamped in place in the fixture and, after aligning holes, riveted together. This procedure is repeated from the rear bulkhead forward to the cockpit. This type of construction precludes, in general, the availability of individual subassemblies. The damping measurements, therefore, concentrated on the in-situ rather than freely suspended.

It should be mentioned that neither the in-situ nor the freely suspended damping measurements provide the appropriate information for the model. Structural damping in the S-76 airframe is dominated by dissipation at the riveted joints. Some subsections (e.g., frames) have riveting throughout, while others (e.g., panels) do not. They all have rivets at the junctions. What does this mean? It means that subsystem damping loss factor values lie somewhere between the freely suspended data (without the joint damping) and the in-situ data (with the coupling loss factors to adjoining subsystems). The damping loss factor measurements performed on various S-76 subsystems are summarized in Table D1.

TABLE D1. STRUCTURAL DAMPING LOSS FACTORS

	500	1k	2k	4k	8k
IN-SITU ON AIRFRAME					
Composite Panels					
OP56M	.055	.022	.018	.012	.013
OP34Lu	.028	.020	.018	.010	.013
OP45L	.037	.020	.019	.029	.023
SP56L	.052	.063	.031	.037	.034
Single Sheet Panels (Riveted)					
OP14D	.024	.022	.020	.018	.018
RB2	.014	.021	.018	.017	.015
RB3	.018	.013	.010	.010	.009
Riveted Frame Sections					
LF14L (Web)	.028	.022	.019	.016	.011
LF14L (Flange)	.028	.028	.020	.013	.016
LF56L (Flange)	.023	.016	.011	.014	.009
LF56R (Web)	.023	.018	.013	.010	.009
Window (Plexiglas)					
SW14L	.071	.073	.069	.046	.138
SUSPENDED FREE FROM AIRFRAME					
Composite Panels					
SP14R	.006	.010	.010	.007	.008
SP56L	.004	.007	.006	.006	.006
Single Sheet Panel (No Riveting)					
Luggage Compartment Cover Plate	.006	.006	.006	.008	.006
Riveted Frame Sections					
Cross Frame #5					
Web	.008	.010	.009	.009	.008
Flange	.014	.011	.010	.009	.007
"Broom Closet"	.013	.018	.011	.017	.007
Window (Plexiglas)					
"Chin Window"	.050	.040	.042	.037	.034

In-situ measurements on composite panels are consistent with one another, with higher damping loss factors recorded on subsystems which have substantial discontinuities (fastening locations for various avionic assemblies and flight hardware). These locations, typically, are through-holes in the panels, with the honeycomb core removed locally and an insert, threaded or straight, is then installed by filling the core void with an epoxy, and installing the insert. Discontinuities such as these occur throughout the airframe, with more on the center overhead panels such as OP4YM, Y5M, and 56M, which have the flight controls mechanisms and hardware attached on a completed airframe. Photos P13 and P14 show some of these mounting locations, with views of the overhead panels from the cabin. As evident from these photos, OP56M has many of these discontinuities, as does OP45L. These panels exhibit somewhat more damping than OP34Lu, which, in contrast, does not have any attachment discontinuities. All composite honeycomb panels have a certain amount of discontinuity in the form of the closeout of the core along the panel perimeter. This closeout occurs where the core and inboard facesheet end, and an aluminum "Z" section is bonded and connects them to the outer face sheet, which is then riveted to an adjoining frame and/or panel. SP56L also contains various mounting locations, and a window is attached.

The single sheet riveted panels display similar damping levels to the composite panels in all but the 500 hz octave, where the composite panels dominate. These panels are manufactured from aluminum sheet, and are stiffened with riveted on angle stock and/or stamped beads formed in the base metal. The drip pan, OP14D (see Photo P11) and caulked for water integrity. This is believed the main reason for the higher in-situ damping levels in all five octaves as compared to damping measured on RB. The RB2 location, the higher of the two RB measurements, was made on a luggage compartment access cover that is riveted on all four edges to the rest of RB, and is flat and unstiffened. The other RB location measured (RB3) is between vertical and horizontal (on the luggage compartment side) stiffeners (see Photo P8).

Riveted frame sections measured include LF14L and LF56L, on both the web and flange. These data show LF14L exhibits slightly higher damping levels than LF56L in both locations. The forward longitudinal frames in the S-76 are lighter in cross section than the aft frames on the airframe (see Photo P14). This means that LF56L is of substantially thinner and lighter cross section than LF14L, and contains less added stiffening by riveted angle or plate (see Photo P4).

The clear thermoplastic window measurement made in-situ shows much higher damping levels than any of the other in-situ measurements in all the octaves measured. It is installed in SP14L by screws and has a rubber gasket for water integrity. This installation method along with the comparatively higher loss factors found in the base material provides the reason for higher damping levels.

Measurements were also made on freely suspended components. Two composite panels were suspended by shock cord and damping loss factors were measured. The data shows similar loss factors for SP14R and SP56L, with SP14R slightly higher in all five octaves measured. Comparison of these levels to the in-situ loss factors measured show the in-situ levels to be approximately five to ten times that of the free hanging subsystem. This represents the damping added by the riveted junctions, and the energy transferred to adjoining subsystems. Note that all of this components rivets are at the junctions, thus producing a large difference between freely suspended and in-situ measurements.

The luggage compartment cover plate (a portion of RB) was measured while detached from RB. Its damping values measured resemble that of the material damping present in aluminum, with values of 0.006 to 0.008.

The riveted frame subsection measured, CF5, is of approximately the same construction as LF56L. The measurement of damping in CF5 free standing is made on an assembly that represents SWF5L, CF5L, CF5M, CF5R, and SWF5R together. This frame is manufactured as one continuous piece but sectioned in the SEA model at its major connection to longitudinal frames and perimeter panels. The damping values recorded appear relatively constant with frequency for the web measurement, while the flange measurement shows eta's slightly higher at low frequency. The 8 Khz octave values are very close to those measured in-situ on LF56L, while the difference between the in-situ and free hanging loss factor values increase with decreasing frequency. At 500 hz, the in-situ loss factor measured is approximately two to three times the freely suspended values. Note that approximately two-thirds of this components rivets are already in place for the in-situ measurement since it is a built-up sheet metal construction. Thus the increase in loss factor, when measured in-situ, is much smaller than the increase experienced by a panel component, such as SP56L discussed above.

Another measurement made with a subsystem free hanging was performed on the "broom closet", a lightweight structure of riveted aluminum and composite construction which houses flight control rods and circuit breaker panels (see Photo P16). The loss factor data acquired show values slightly higher than that of the CF5 measurements. The broom closet has many attachment brackets and such riveted to it, and has a composite material center section that has a higher material loss factor than aluminum.

The "chin window" is a clear thermoplastic panel with a compound curvature, which mounts to either side of the nose cone, near the pilot's feet. The free standing loss factor values are approximately within the material loss factor values typically referenced in the literature (0.02 to 0.04), and are much lower than the values measured in-situ on SW14L.

In general, the damping loss factor values measured confirm that the rule of thumb damping values used for aerospace structures applies to rotorcraft, with the possible exception of members subjected to many discontinuities.

Acoustic decay rate. - Measurements of cabin acoustic decay rates and calculation of absorption coefficient are shown in Figure D15. These values represent the average of decay rate measurements made at two locations in the cabin. The aft cabin measurement location was at cross frame four approximately on the aircraft centerline (CF4M), while the forward location was between cross frames five and six, approximately six inches to port from the aircraft centerline. Both microphones were at approximately seated head level.

As noted previously, this decay rate measurement includes energy transmitted into subsystems adjacent to the cabin as well as the energy absorbed in the acoustic space. The panel subsystems that create the cabin boundaries are mainly of aluminum honeycomb construction, (> 50%), with clear thermoplastic windows installed as windshields, door and side panel windows representing approximately 20%. Stiffened aluminum sheet comprises the drip pan (OP14D), rear bulkhead (RB), and miscellaneous other small subsystems totaling approximately 10%, and composite material panels and sections of the cockpit and cabin doors representing the remaining bounding surface area. Within the cabin, the longitudinal and cross frames protrude from the outer skin bounding surface, defining "bays" which are approximately 0.2m deep in the overhead, and 0.1m deep in the sidewalls. These bays contain various electronic assemblies and many wire bundles and connectors routed through them. The instrument panel and broom closet assembly are of light sheet aluminum construction, and provide an interruption of the forward cabin volume.

The acoustic decay rates measured were slightly shorter for the aft cabin microphone position, compared to the forward cabin location. This difference is very little at 500 hz and 8 Khz (~ 1%), but as much as 8% at 2 Khz. The 1 Khz octave delta is 5% and the 4 Khz octave 2.5% lower. Physically, the aft microphone position is surrounded by lightweight sheet aluminum construction panel subsystems such as OP14D and RB, whereas the forward microphone is not. The transfer of energy into these subsystems may be a factor in this consistent difference in decay rate values.

Table D2. Acoustic Loss Factor Measurements
Time for 60 dB SPL Decay, seconds

Microphone Location	500	1k	2k	4k	8k
Forward	0.225	0.275	0.382	0.364	0.258
Aft	0.222	0.262	0.350	0.355	0.256

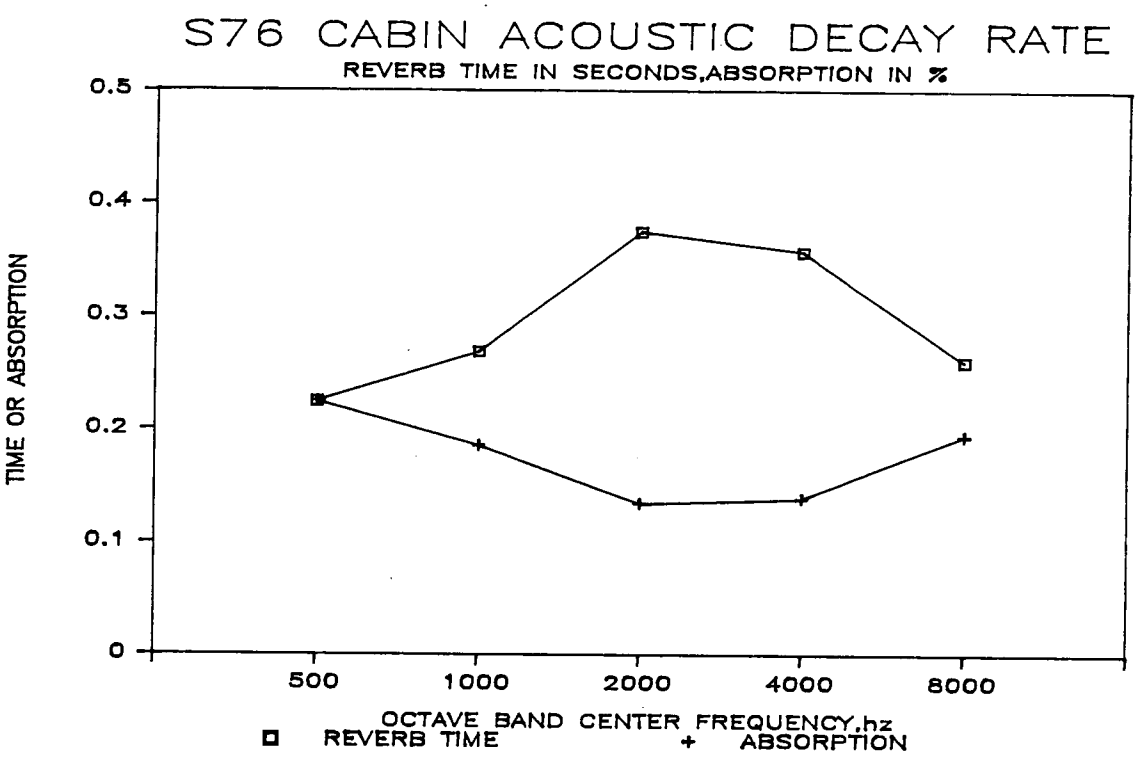

Figure D15. S-76 Untreated Cabin Acoustic Decay Rate Data

Vibration transfer functions. - Vibratory transfer functions were measured between the majority of panel and frame subsystems and seven shaker attachment locations. The shaker attachment set was comprised of a vertical, lateral and longitudinal direction at the right rear main gearbox attachment location (RAR), vertical and lateral at the front left main gearbox attachment (FAL), and two shaker locations related to hydraulics line hard mounting locations (HYD). The data acquired is displayed in Figures D16 to D25.

The overhead frames in the S-76 consist of two longitudinal members and three main cross frames (see Figure B1 and Photo P2). The longitudinal frames extend from the main gearbox forward to the cockpit and windshield area, and are physically sectioned by the cross frames at the rear and front edges of the cabin doors, and at the aft edge of the cockpit doors. These cross frames attach to side frames at the junction between the upper deck and the side walls in the cabin, which then attach to the cabin floor. Adjacent to the main gearbox support frames are two cross frames on either side of the drip pan, which attach to the perimeter panel structure. Overhead frame transfer functions measured in the out-of-plane direction are shown in Figure D16. The 500 and 1 Khz octave measurements appear similar in that FALV has the highest level transferred up to LF56L, where RARLong then excites LF67Lo and CPM to a higher degree. CPM is a frame that is the center post between windshields. These transfer function levels are consistently greater than zero, meaning that the ratio of output vibration to input (source) vibration is greater than one. FAL lateral is consistently the lowest level vibration transfer location/direction in all four octaves. An interesting observation is that the RAR lateral excitation produces higher output on the left side frames out-of-plane than FAL lateral does, which is a left side input. At 500 hz, the remaining three source locations, RAR lateral, vertical and longitudinal, are nearly equal at LF14L and LF45L, separate slightly at LF56L, but keep the same trend of high LF67L response. The 1 Khz octave shows more of a trend towards lower transfer function levels with distance from the source, with a slight rise in response at LF67L. The 2 Khz plot shows the two FAL sources and the RAR vertical responses decreasing with distance from the source, but the RAR lateral and longitudinal responses rise and peak at LF56L and decrease towards the front of the aircraft. This is also true at 4 Khz, and implies a distinct path across the airframe in that location. Also at 4 Khz, the FAL vertical excitation shows a substantial increase in response of the CPM subsystem.

In-plane transfer function measurements are shown in Figure D17. At 500 hz, RAR lateral produces good response in LF14Li, with a substantial drop in response in LF45Li. FAL vertical excitation provides a nearly constant response in all three frames measured. The only point below zero is from FAL lateral, as the response of LF45Li is less than the input supplied. At 1 Khz, RAR vertical and longitudinal exhibit the same response, while FAL vertical dominates and FAL and RAR lateral produce similar response levels from LF14Li to LF45Li. The 2 Khz and 4 Khz responses are similar with 4 Khz of lower level. FAL vertical dominates, decreases with distance from the source. FAL lateral shows a substantial decrease from LF14 to LF45, and the right side excitations show increase in response with forward distance.

The perimeter panel, a lightweight structure located on either side of the aircraft (see Photos P2, P9, P12), separating the overhead from the side panels and connecting cross frames, is discussed next. The left side measurements (Figure D18) made show, at 500 hz, highest response of PP14L from FAL vertical, while RAR longitudinal dominates PP56L, PP67L, and PP7WL. FAL lateral produces the least response in all four octaves. As frequency increases, the rise in response of PP56 and 67L diminishes where at 4 Khz, the responses decrease almost linearly with distance from the source frames. Between 1 Khz and 2 Khz, response to FAL vertical remains nearly constant, while the distant subsystem dominance of RAR longitudinal diminishes. The 2 Khz and 4 Khz octaves show RAR excitations close together, with FAL vertical dominating the near-source and FAL lateral generating the least response at the subsystems furthest from the source.

The left side overhead panel transfer function measurements are shown in Figure D19. These subsystems extend from the panels adjacent to the source frames (OP12, 23, 34 lower and upper) to the cockpit and windshield area (FWL). They are constructed mainly of aluminum honeycomb, with OP12L and OP34L1 as aluminum sheet, and the windshields of clear thermoplastic (see Figure B2). In the 500 hz octave, OP34L1 gets the highest response from each of the excitations. FAL lateral produces the lowest response levels, and the three RAR excitations result in nearly equal response levels (within approximately 5 dB) from subsystem to subsystem, peaking at OP34L1 with a slight increase from RAR longitudinal input for OP67L and FWL. FAL vertical yields the highest response on panels up to the cockpit, where RAR longitudinal then dominates. At 1 Khz, these trends remain the same, with the RAR group of excitation widening its spread to approximately 10 dB. FAL lateral response is up in the subsystems adjacent to LF14L. At 2 Khz, FAL vertical response is approximately 10 to 15 dB higher than all other excitations. RAR inputs remain within 10 dB response of each other for all subsystems and FAL lateral is lowest, particularly at OP56L and OP67L. The 4 Khz octave is dominated by FAL vertical up to OP56L, where the RAR excitations merge with it at nearly equal response level. RAR lateral and longitudinal produce less response at the panels adjacent to LF14L. Also, the high response of OP34L1 is not evident here, and has diminished with increasing frequency. Response levels of +20 to +30 dB at subsystems near-source with a healthy rolloff beginning with OP45L is the general trend.

Panels in the center include light, stiffened sheet aluminum panels such as OP14D and the rear bulkhead, RB, and more forward panels are of aluminum honeycomb construction (see Photos P8 through P14). At 500 hz, the FAL vertical input response increases from OP14D to OP5YM, then declines towards the front of the aircraft. RAR vertical response, however, decreases smoothly towards the cockpit. The other out-of-plane input, RAR longitudinal, resulted in high responses from all but OP5YM, and markedly at OP67M. The two lateral responses show very similar trends for each subsystem, with FAL lateral approximately 15 dB less in response level for all subsystems overhead panel subsystems measured. At 1 Khz, these trends appear the same, with the OP14D response from

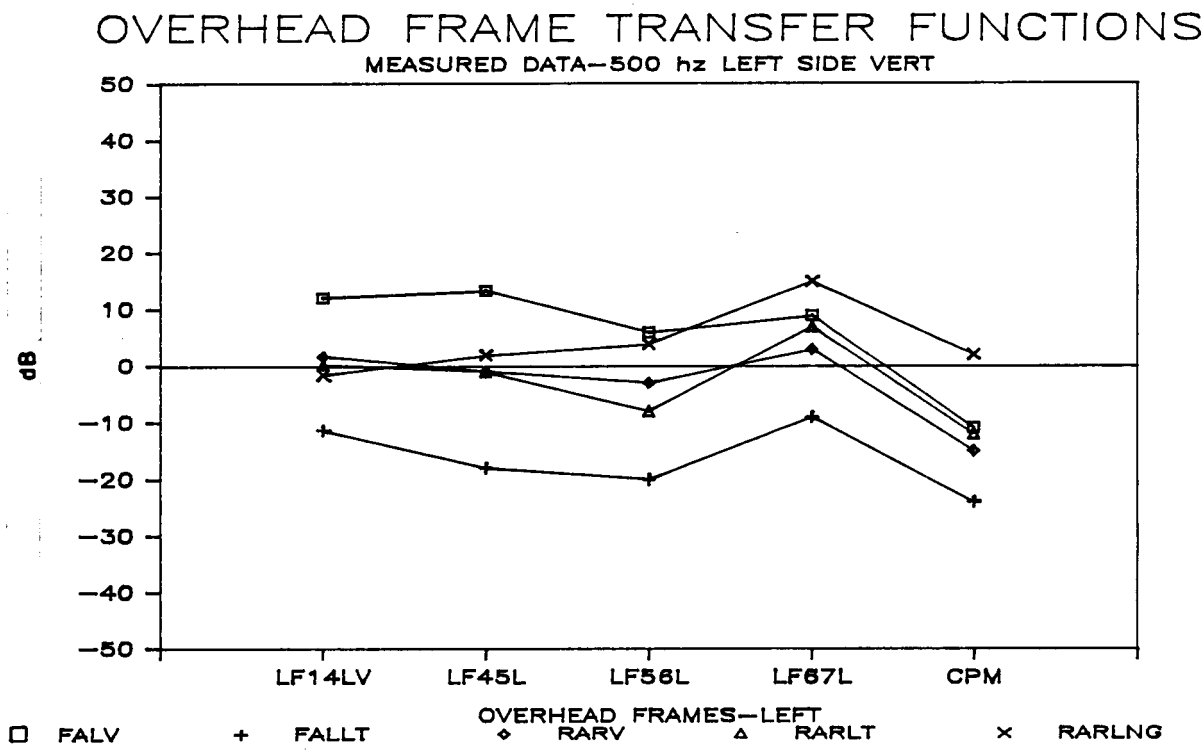

Figure D16a. Overhead Frame Out-of-Plane Transfer Function Measurements, Left Side, .5 kHz

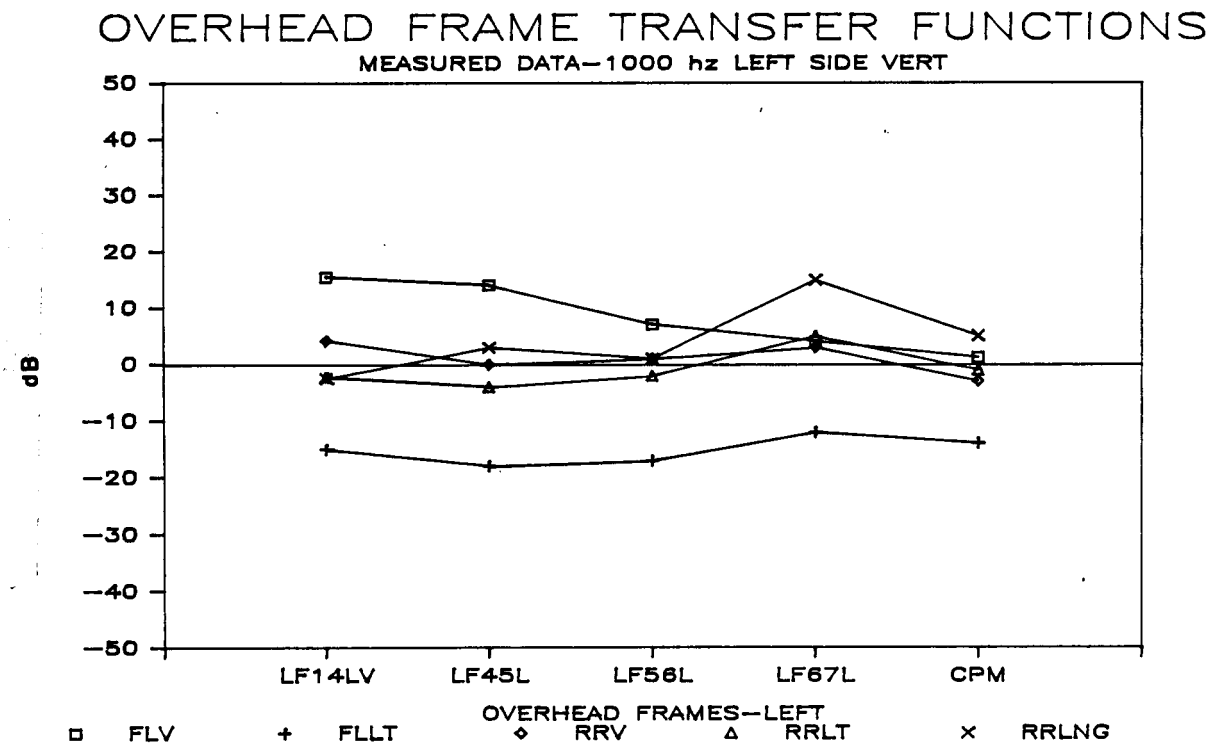

Figure D16b. Overhead Frame Out-of-Plane Transfer Function Measurements, Left Side, 1 kHz

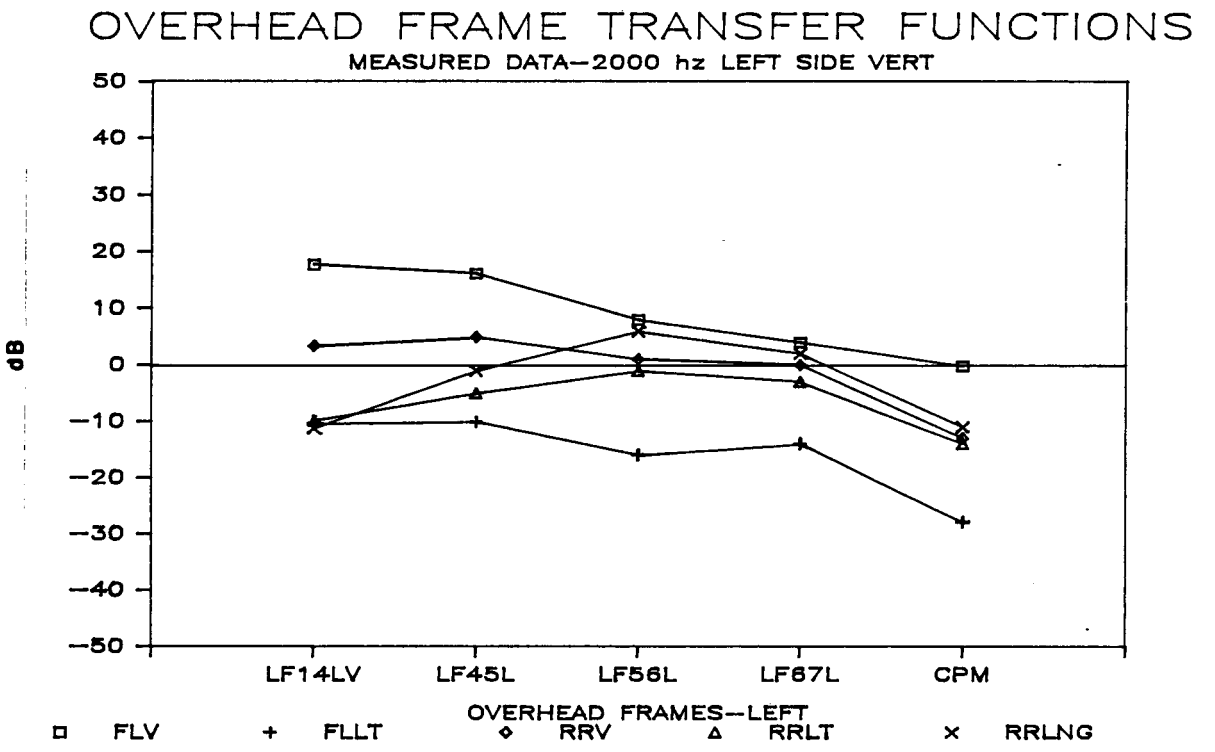

Figure D16c. Overhead Frame Out-of-Plane Transfer Function Measurements, Left Side, 2 kHz

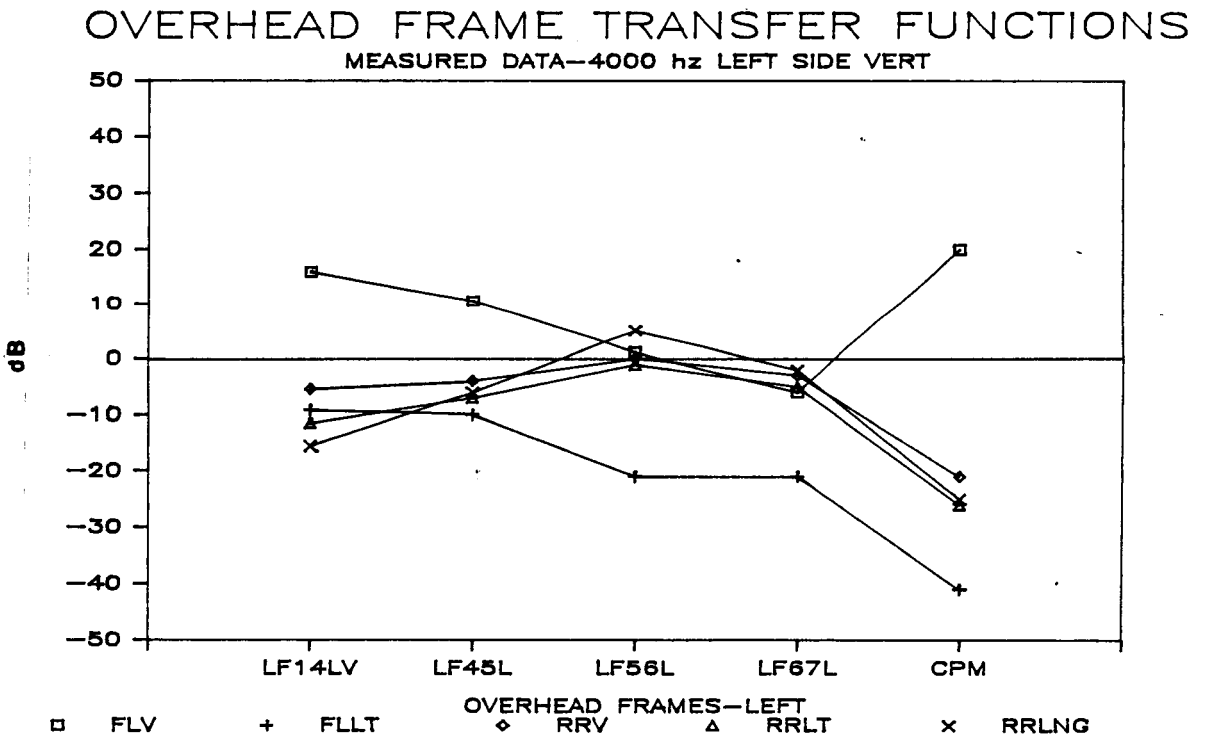

Figure D16d. Overhead Frame Out-of-Plane Transfer Function Measurements, Left Side, 4 kHz

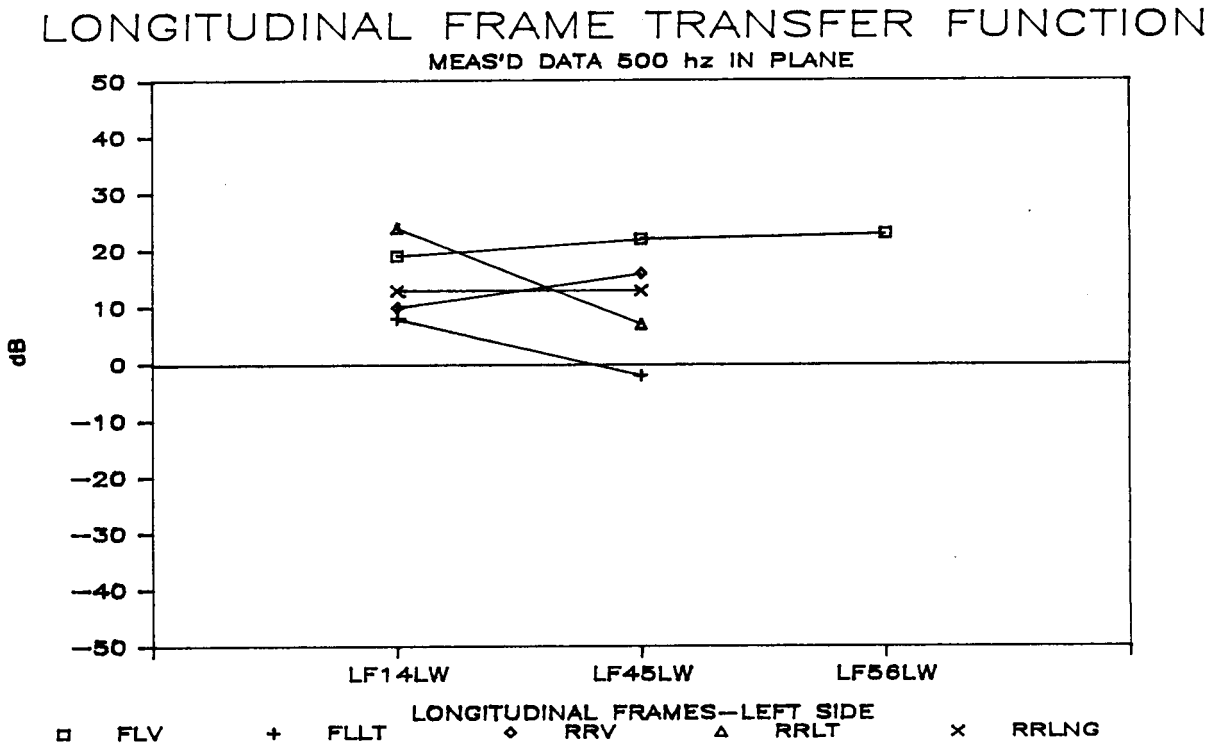

Figure D17a. Overhead Frame In-Plane Transfer Function Measurements, Left Side, .5 kHz

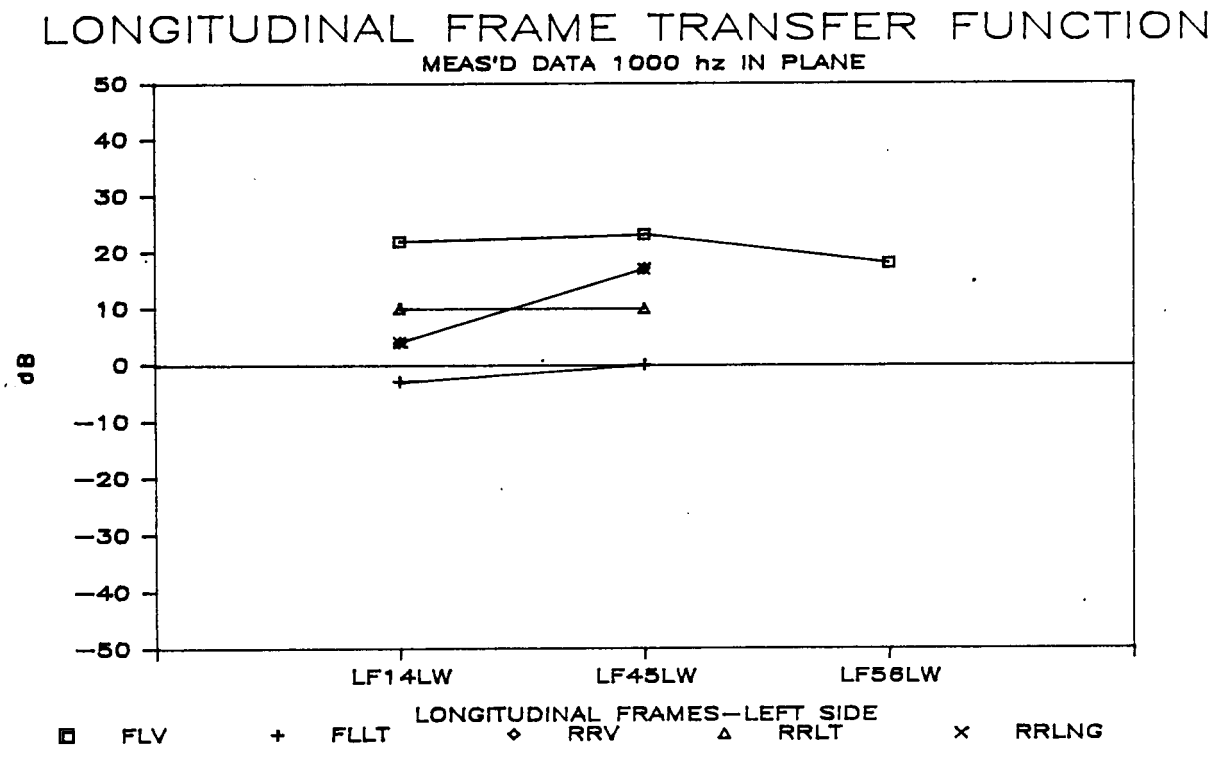

Figure D17b. Overhead Frame In-Plane Transfer Function Measurements, Left Side, 1 kHz

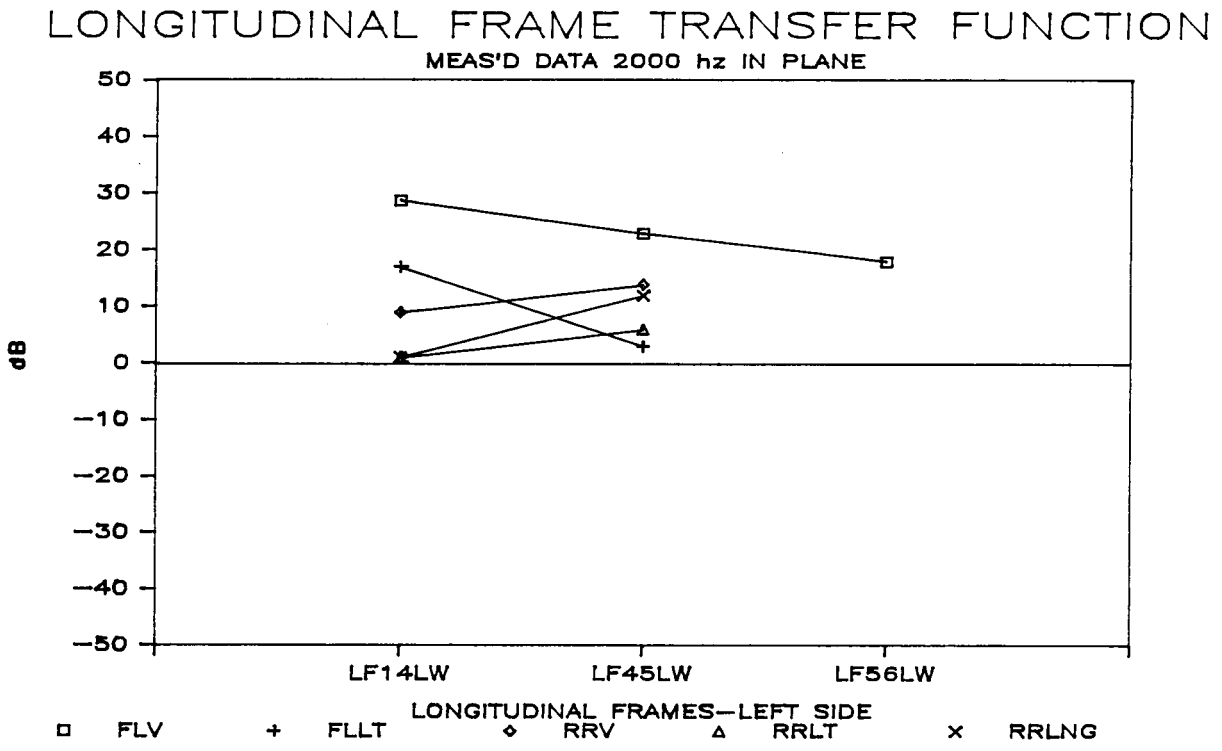

Figure D17c. Overhead Frame In-Plane Transfer Function Measurements, Left Side, 2 kHz

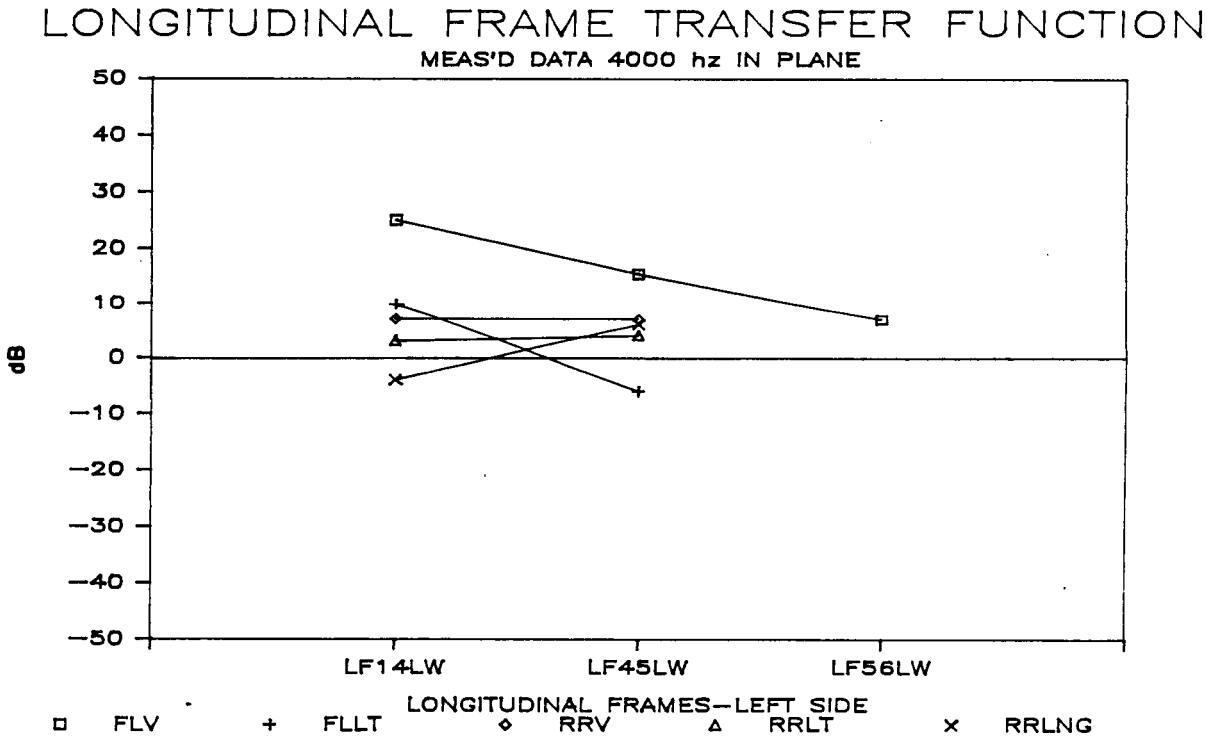

Figure D17d. Overhead Frame In-Plane Transfer Function Measurements, Left Side, 4 kHz

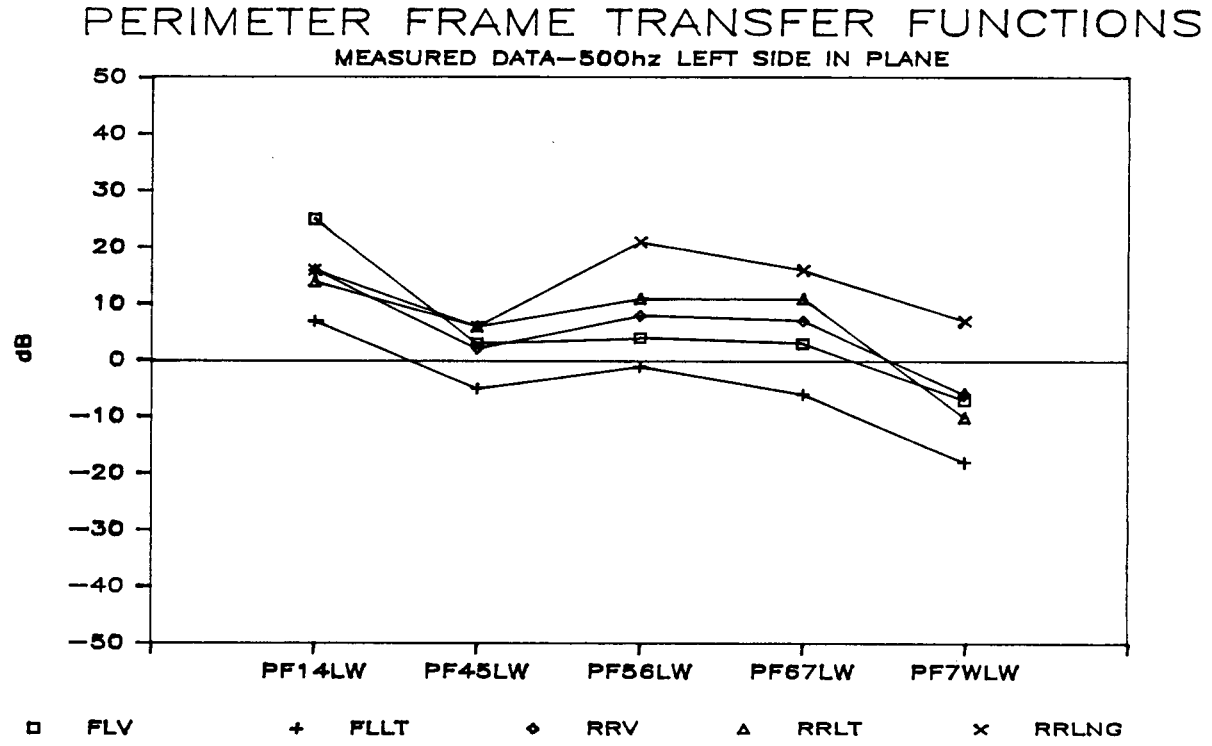

Figure D18a. Perimeter Member In-Plane Transfer Function Measurements, Left Side, .5 kHz

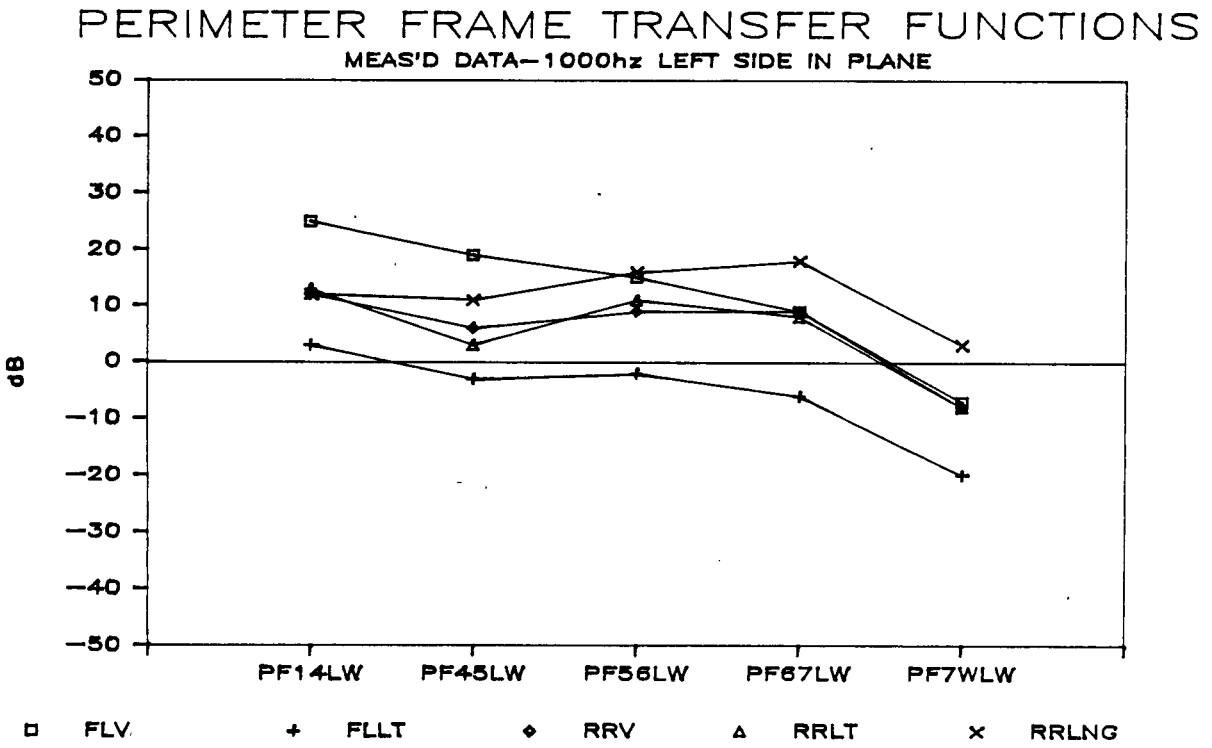

Figure D18b. Perimeter Member In-Plane Transfer Function Measurements, Left Side, 1 kHz

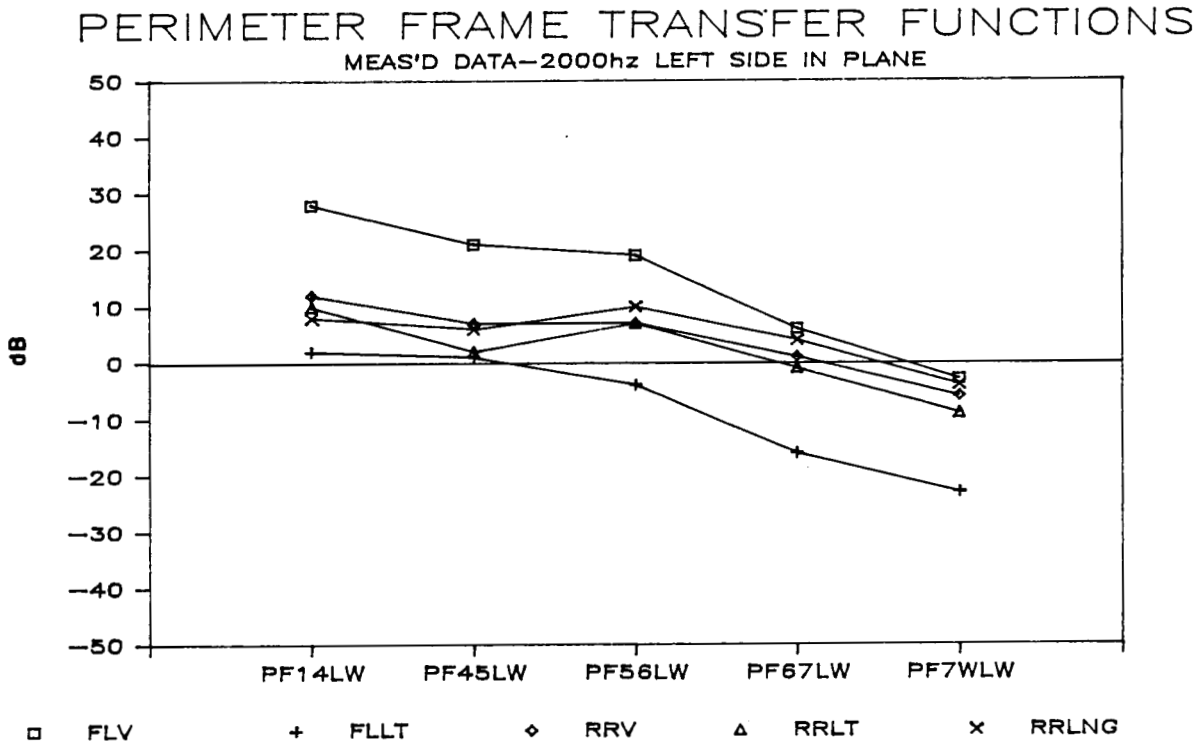

Figure D18c. Perimeter Member In-Plane Transfer Function Measurements, Left Side, 2 kHz

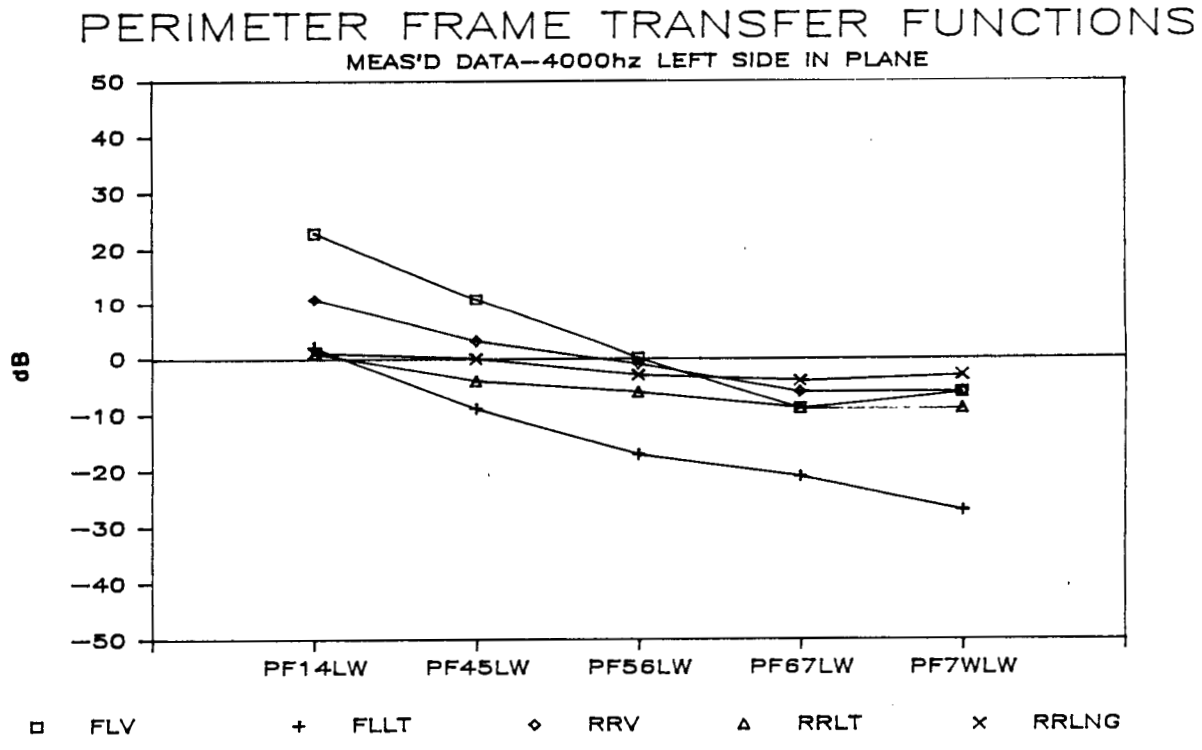

Figure D18d. Perimeter Member In-Plane Transfer Function Measurements, Left Side, 4 kHz

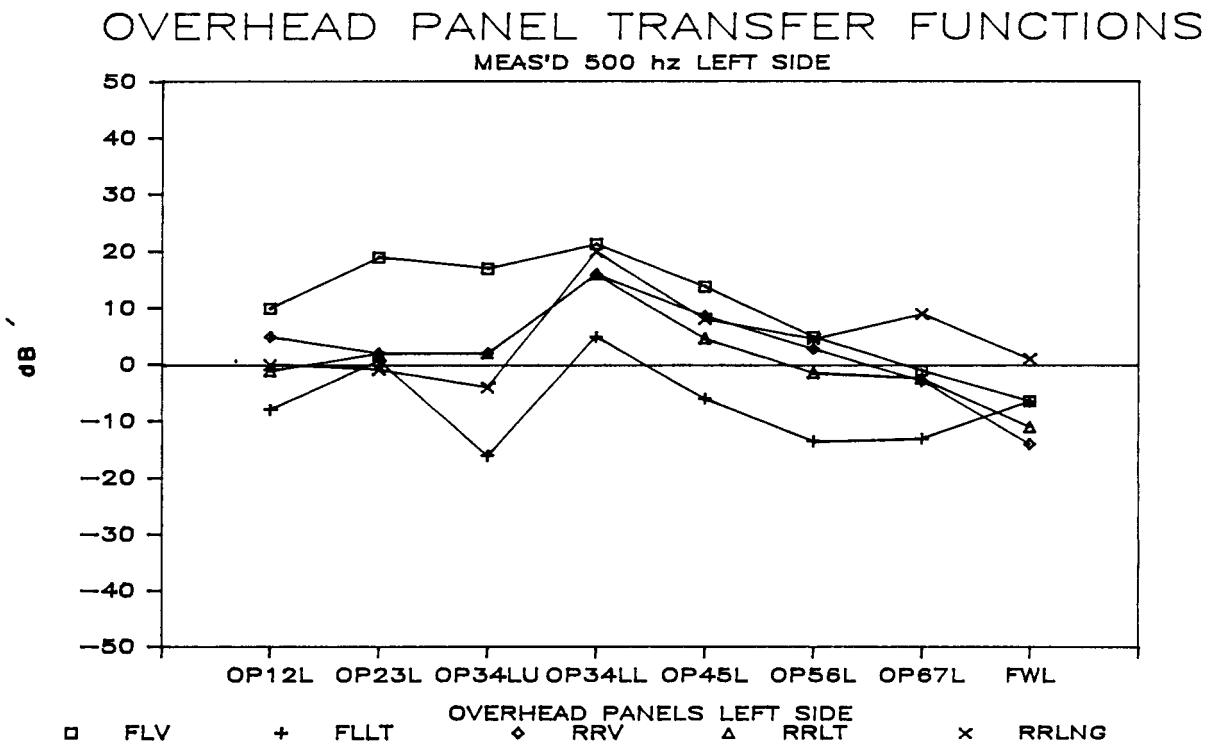

Figure D19a. Overhead Panel Transfer Function Measurements, Left Side, .5 kHz

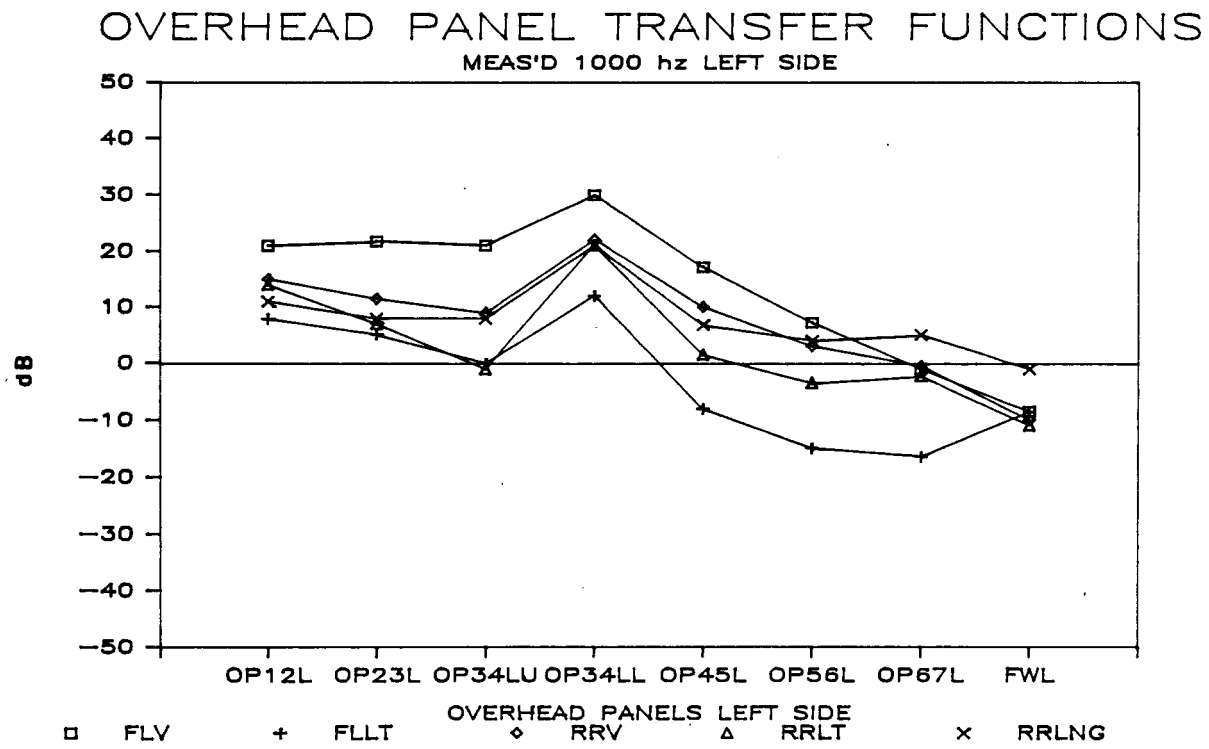

Figure D19b. Overhead Panel Transfer Function Measurements, Left Side, 1 kHz

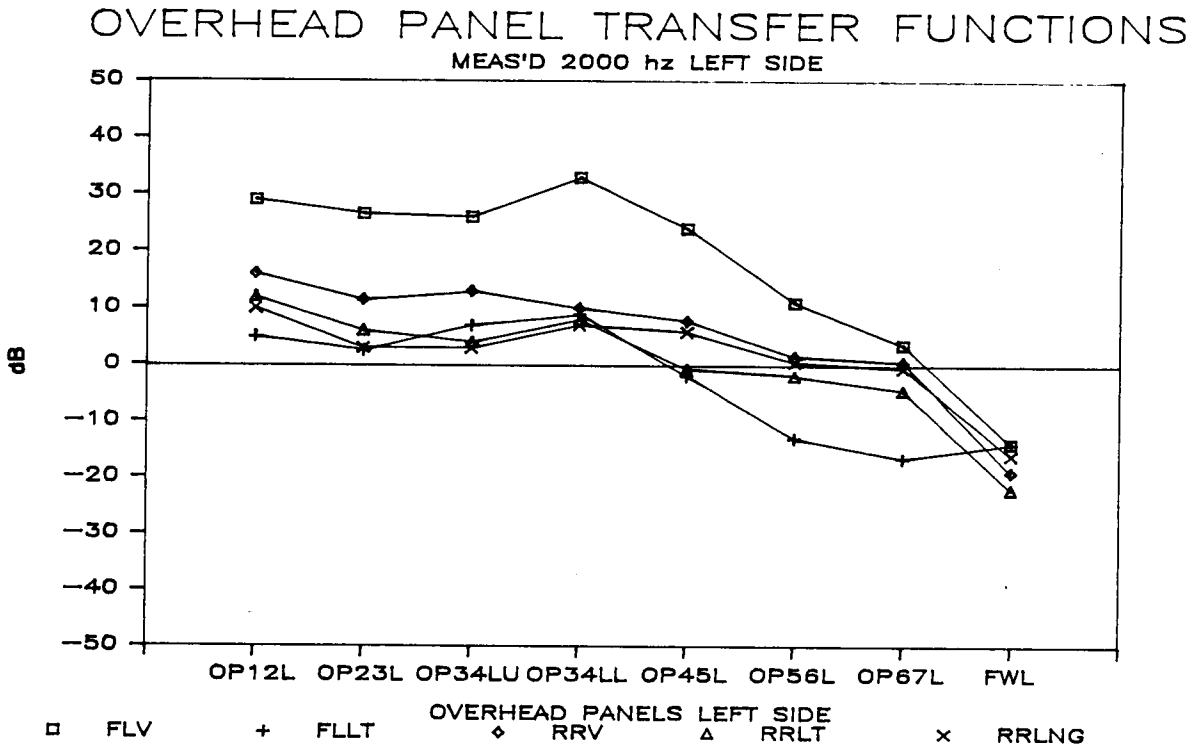

Figure D19c. Overhead Panel Transfer Function Measurements, Left Side, 2 kHz

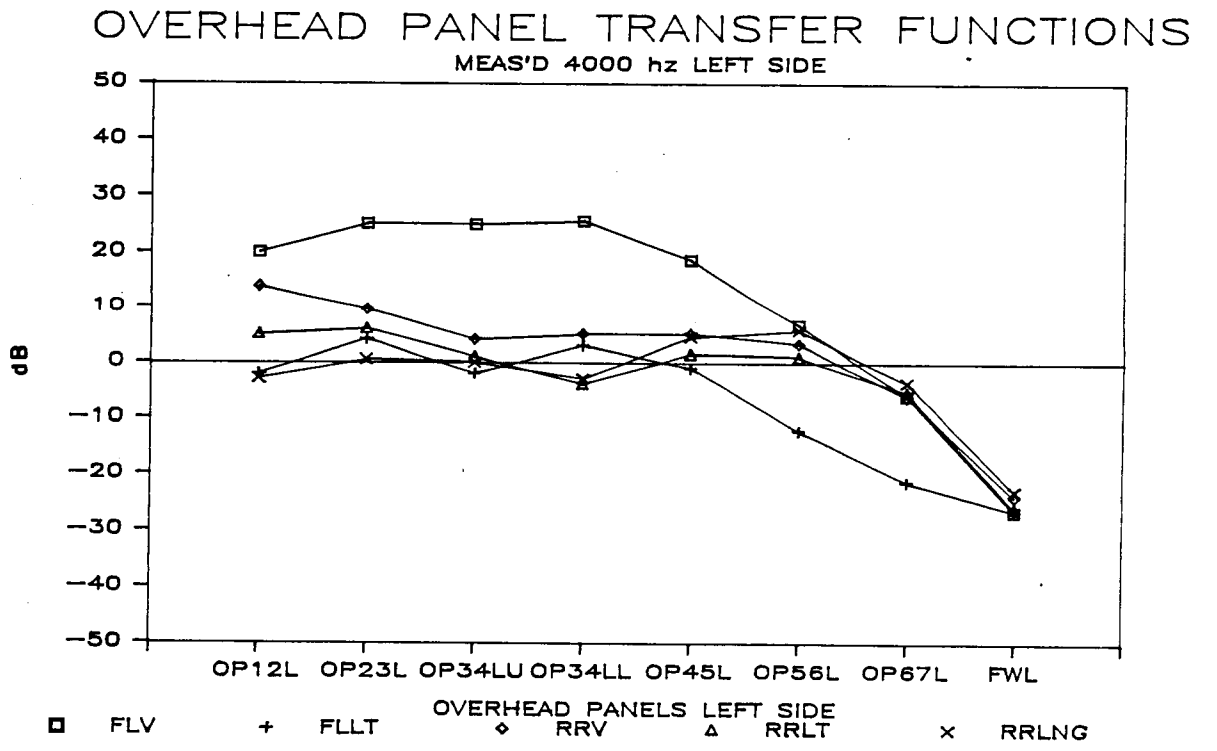

Figure D19d. Overhead Panel Transfer Function Measurements, Left Side, 4 kHz

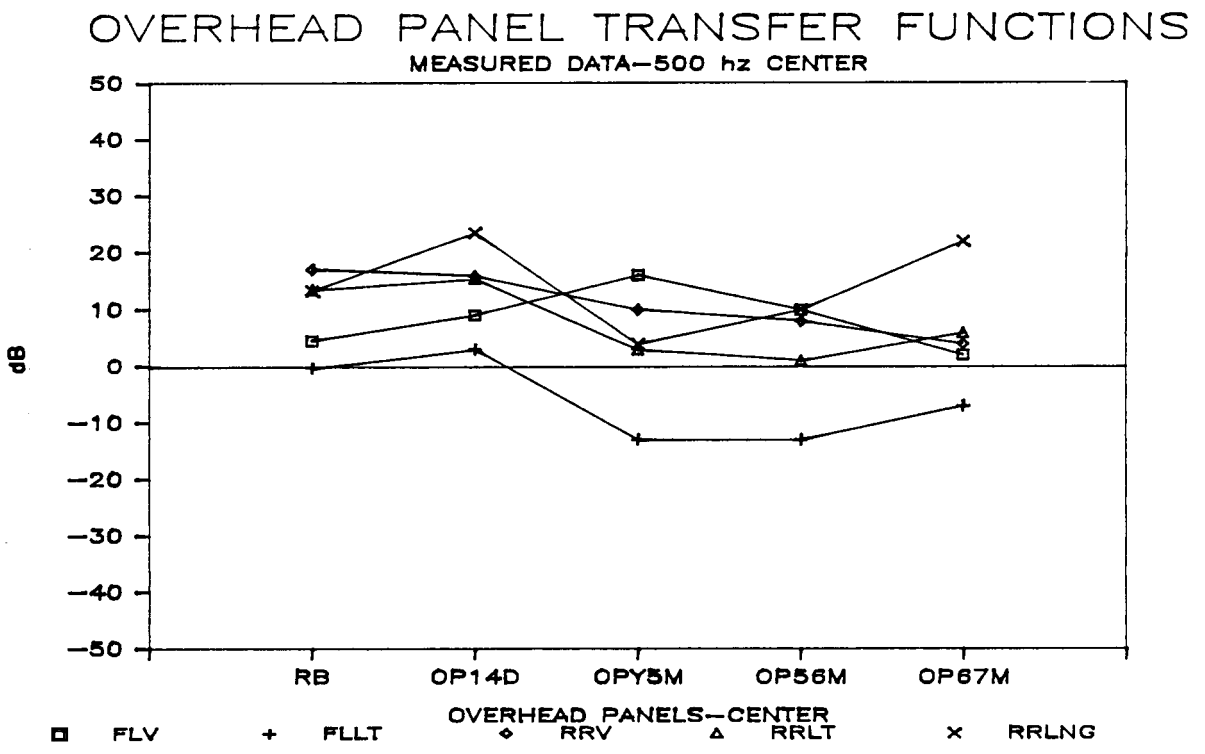

Figure D20a. Overhead Panel Transfer Function Measurements, Middle, .5 kHz

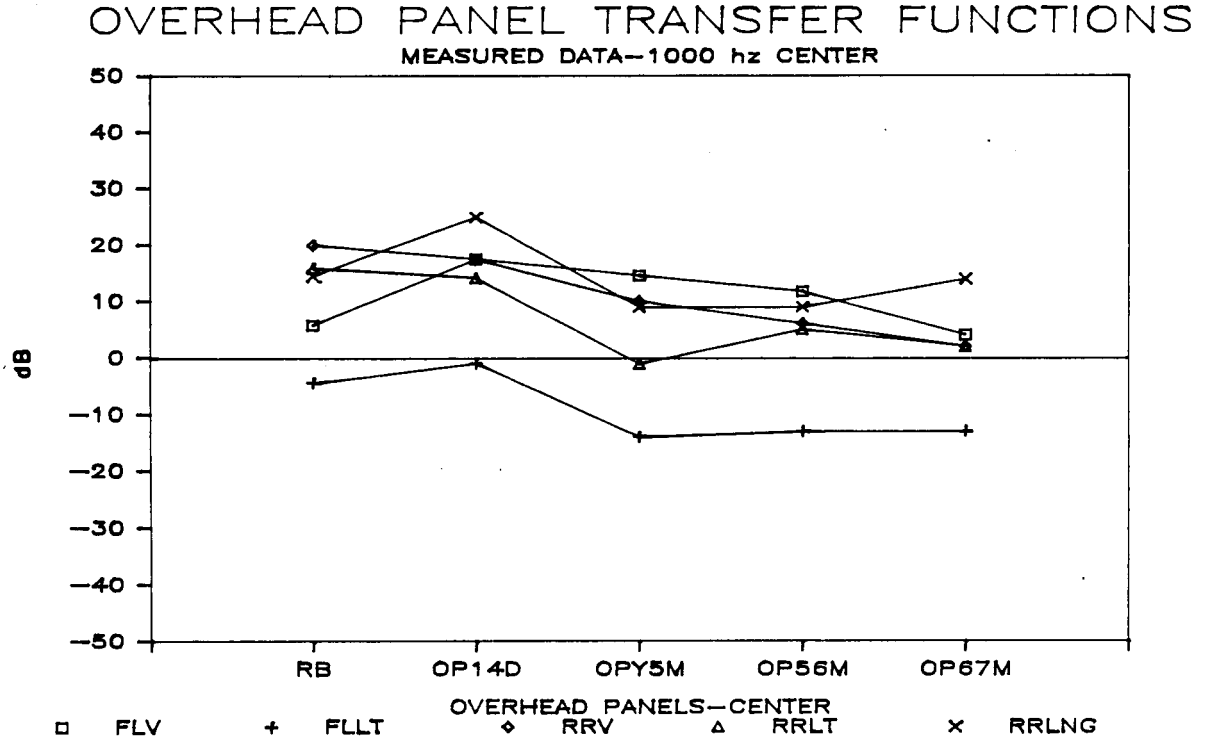

Figure D20b. Overhead Panel Transfer Function Measurements, Middle, 1 kHz

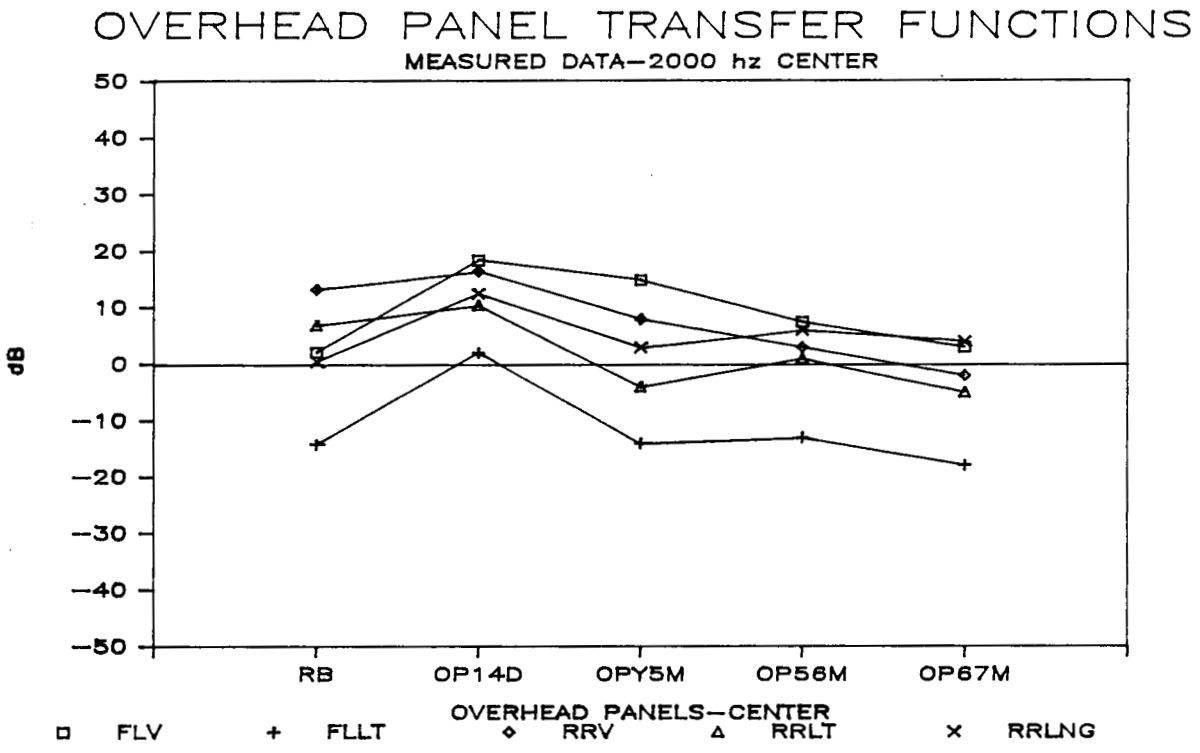

Figure D20c. Overhead Panel Transfer Function Measurements, Middle, 2 kHz

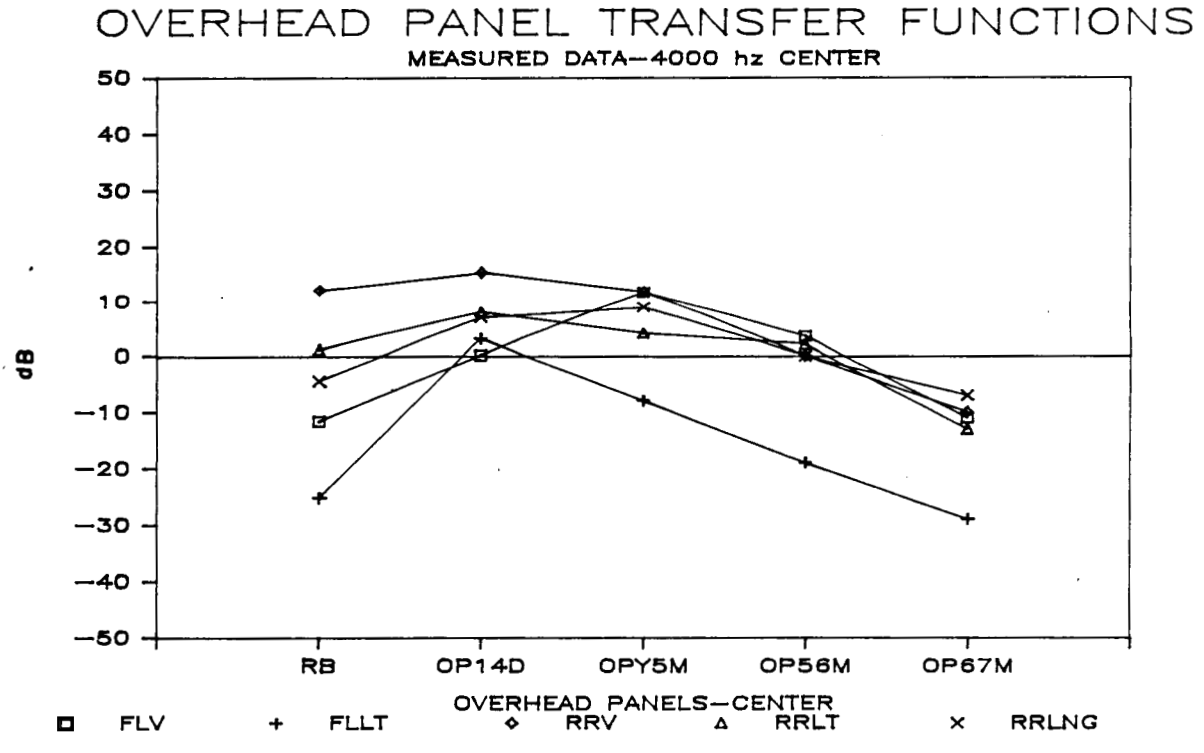

Figure D20d. Overhead Panel Transfer Function Measurements, Middle, 4 kHz

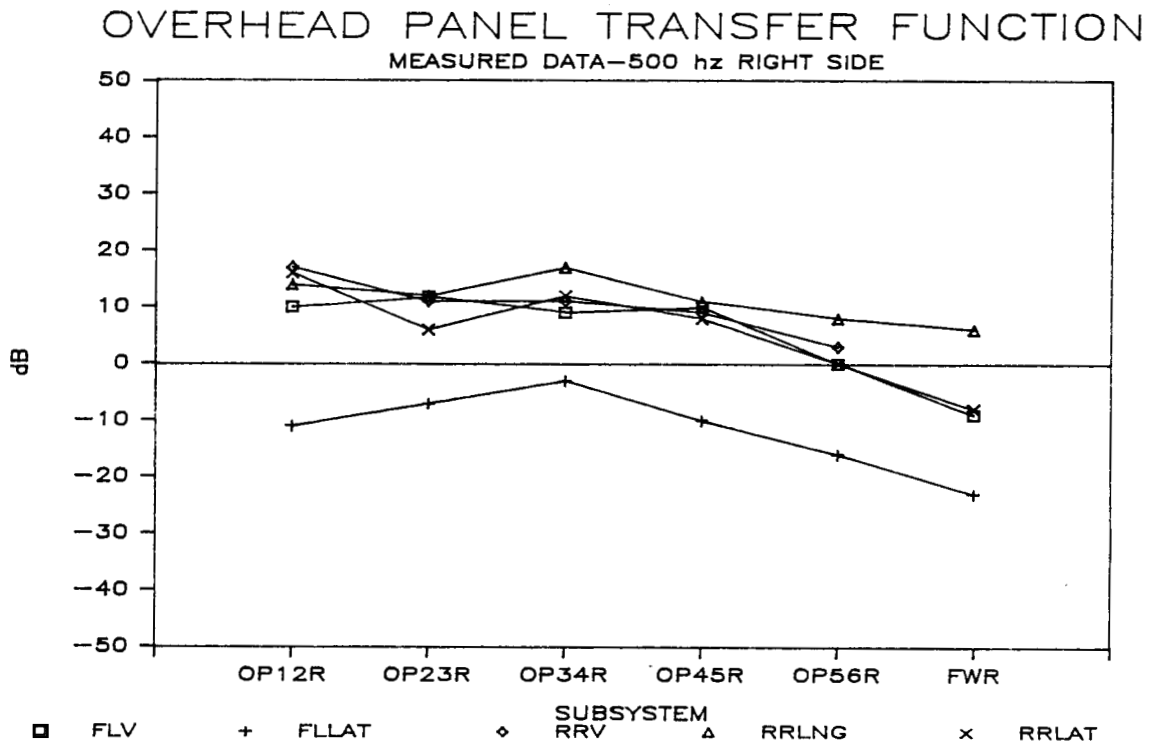

Figure D21a. Overhead Panel Transfer Function Measurements, Right Side, .5 kHz

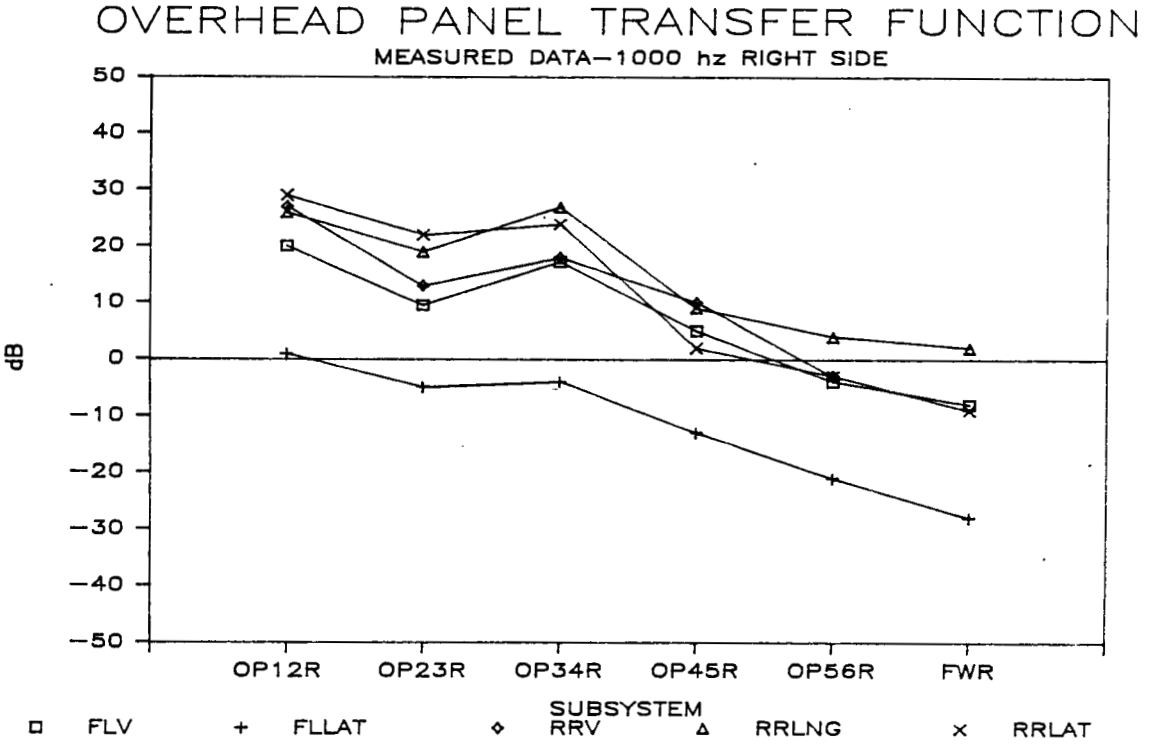

Figure D21b. Overhead Panel Transfer Function Measurements, Right Side, 1 kHz

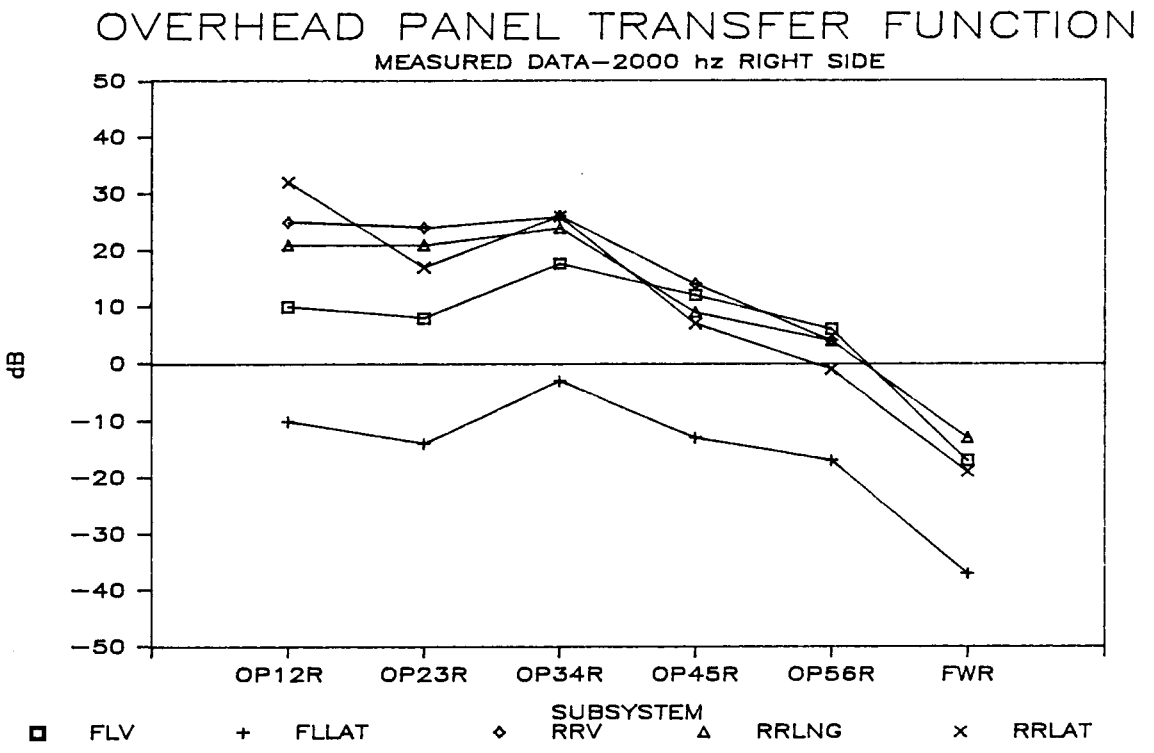

Figure D21c. Overhead Panel Transfer Function Measurements, Right Side, 2 kHz

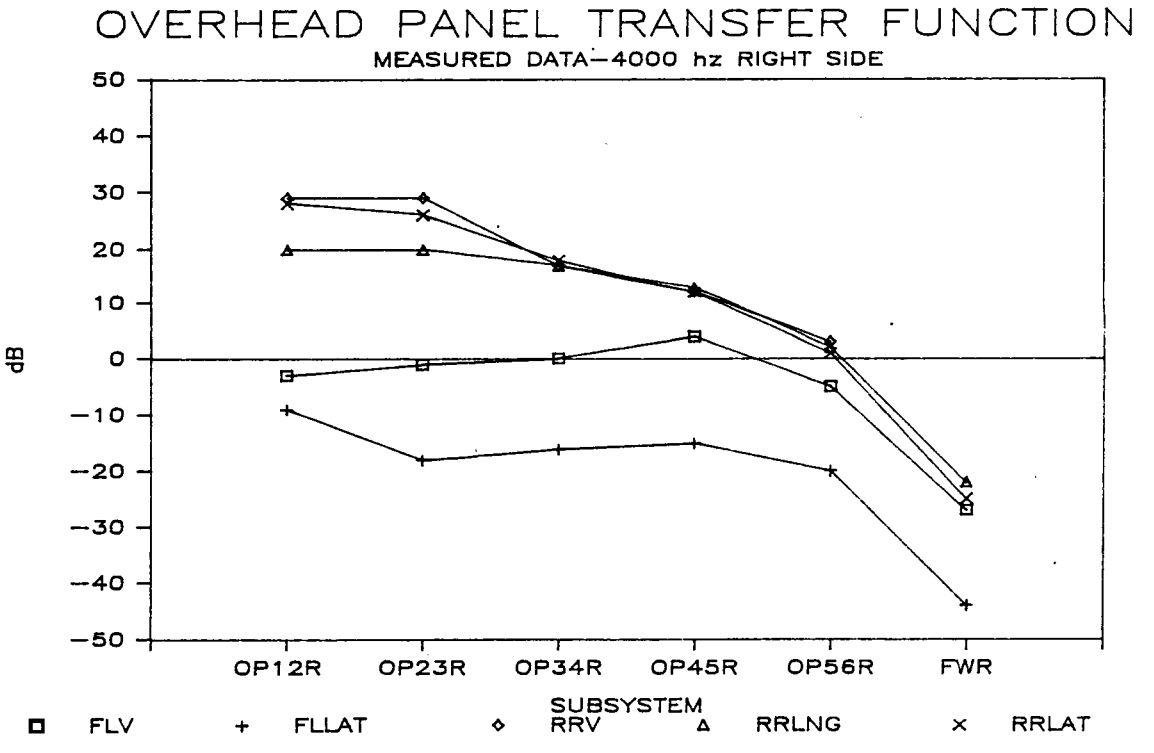

Figure D21d. Overhead Panel Transfer Function Measurements, Right Side, 4 kHz

FAL vertical up and the RAR longitudinal response at OP67M lower. At 2 Khz, RB response is nearly unity from FAL vertical and RAR longitudinal. The OP14D response then is between 10 and 18 dB for all excitations except FAL lateral, which is slightly positive. Response of OP5YM is varied from -14 dB from lateral to +15 dB from FAL vertical. OP56M and OP67M show response levels within 8 to 10 dB for all excitations except for FAL lateral, which is lowest across these measurements. At 4 Khz, a wide variation in response at RB occurs, with RAR vertical highest and FAL lateral lowest. Response to OP14D is greater than zero for all excitations, headed again by RAR vertical with FAL vertical slightly higher than unity. The remaining subsystems have similar responses for all but FAL vertical, with OP56M response within 3 dB.

The low response to FAL lateral excitation, seen in all of the previous measured data, may be attributable to the construction of the forward portion of LF14L and R (see Photos P3 through P5). The forward gearbox mounting location is stiffened vertically by the addition of plate and angle structure riveted along the inboard side of this beam, and continuing around to the top edge. Access, therefore, to the forged portion of the beam, which the gearbox is bolted directly to, is very limited, and not adequate for the mounting of the shaker in that location and direction. Mounting the shaker alternately to the uppermost portion of this stiffening structure provided the data shown in the figures referenced is the preceeding paragraphs. Upon comparison of the front to the rear attachment structure, the rear locations do not have this added structure, and RAR lateral excitation produced consistently higher response levels. Also, when comparing FAL and RAR lateral response of the center overhead panels, a distinct similarity in shape is present, although the FAL response remains much lower in level.

Hydraulics excitation. - The hydraulics excitation locations were on the upper deck of the aircraft, at two points where hydraulic pressure lines were attached. The HYDFRME location was on the upper flange of LF45L at the YF45M junction, while the HYDPANL excitation was located on OP56L, approximately 0.15m outboard of LF56L and 0.1m forward of CF5L. This deck is where much of the flight controls hardware is attached.

The miscellaneous frame in-plane measurement of response to these inputs are shown in Figure D21. In the 500 hz octave, the HYDFRME excitation produces more response with decreasing distance from the source along the longitudinal frames, LF14Li, and 45Li, measured. The response of LF56Ri, a right side longitudinal frame, is higher for either input than LF45Li, which is the source location for HYDFRME, and is very close to HYDPANL. CF3Li excitation is unity for HF but approximately -16 dB for HYDPANL. Response levels at CF6Li and CF5Mi are nearly the same for all four octaves measured. In the 1 Khz octave, HYDFRME gets higher response than HYDPANL at LF14Li and LF45Li, response is equal for LF56Ri, CF6Li, and CF5Mi, and CF3Li remains dominated by HYDFRME. At 2 Khz and 4 Khz, HYDFRME produces higher response in all but CF6Li, with LF45Li at levels of 20 to 25 dB. Also, HYDFRME produces nearly equal response levels for all but LF45Li in both octaves, while HYDPANL results in high response at CF6Li. 4 Khz responses are approximately 10 dB lower than 2 Khz levels.

Left side overhead panel transfer function measurements with RB included, appear in Figure D22. HYDFRME produces higher response at all four octaves in the subsystems RB, OP23L, OP34Lu, and OP45L by approximately 15 dB. Response at OP67L and FWL is nearly equal for both excitations and all octaves, with HYDPANL consistently slightly higher. OP56L is dominated by HYDPANL by as much as 15 dB, and on average 10 dB. RB response to either excitation decreases with increasing frequency.

Center overhead panel response measurements are shown in Figure D23. HYDFRME dominates all positions except CPM (note RB is echoed here) by approximately 15 dB with relatively constant response levels at all octaves for OP14D and OPY5M.

The right side overhead panel response levels are dominated by HYDFRME at all measurement locations and octaves (see Figure D24). These data show levels that are mainly negative, as these panels are on the opposite side of the airframe from the source locations. Highest response levels occur at OP45R at 500 and 4 Khz, while OP34Lu dominates 1K and 2K hz.

Miscellaneous panels measured with HYDFRME and HYDPANL input appear in Figure D25. SP56L and SW56L are the side panel and window nearest these excitation points, and FWL and FWR are the windshields left and right respectively. RB is added for comparison. The response to either input appears nearly the same within each octave, with the response at SP56L and SW56L close to unity, and FWL and FWR responses in the range of -20 dB in all octaves for both excitations.

Vibro/acoustic transfer function measurements. - Measurements of resulting sound pressure from a vibratory source input at three main gearbox mounting locations are shown in Figures D27, D28, and D29. The data is presented as the ratio of pressure level to acceleration level. The pressure level measured during vibratory input is referenced to 20 micropascals, the source acceleration level is referenced to one micrometer per second squared, and the ratio of these two quantities is calculated. Therefore, a $1 m/s^2$ input (120 dB acceleration) would yield 70 dB sound pressure if the transfer function level is -50 dB. The microphone positions utilized were forward and aft cabin and luggage compartment locations.

Figure D27 shows the response of the microphone locations to FAL vertical excitation. The rear cabin microphone response is highest at all octaves and excitation locations, followed by the front cabin, and baggage locations. Frequency trend is generally lower response with increasing frequency. RAL vertical excitation (see Figure D29) produces nearly the same rear cabin levels, and higher front cabin levels than FAL vertical. FAL lateral excitation response is much lower than the two vertical inputs by approximately 20 dB. In general, the luggage compartment is approximately 10 dB less than the

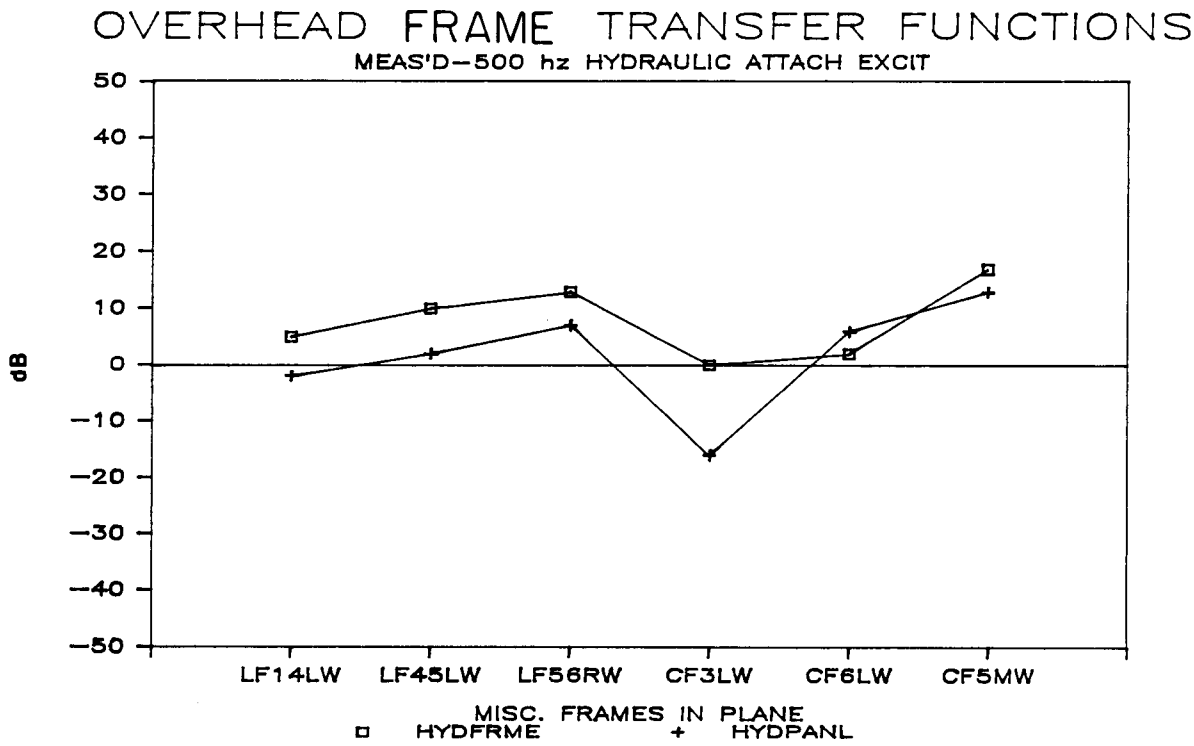

Figure D22a. Miscellaneous Frame In-Plane Transfer Function Measurements, Hydraulic Attachment Excitation, .5 kHz

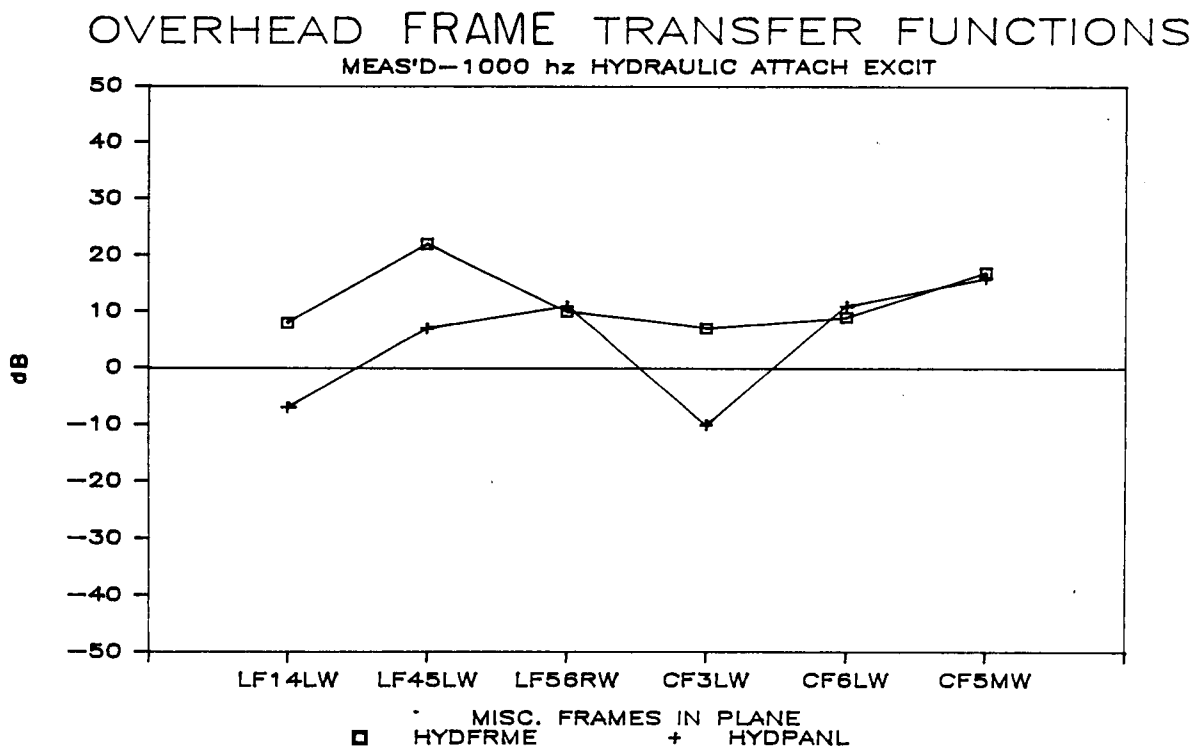

Figure D22b. Miscellaneous Frame In-Plane Transfer Function Measurements, Hydraulic Attachment Excitation, 1 kHz

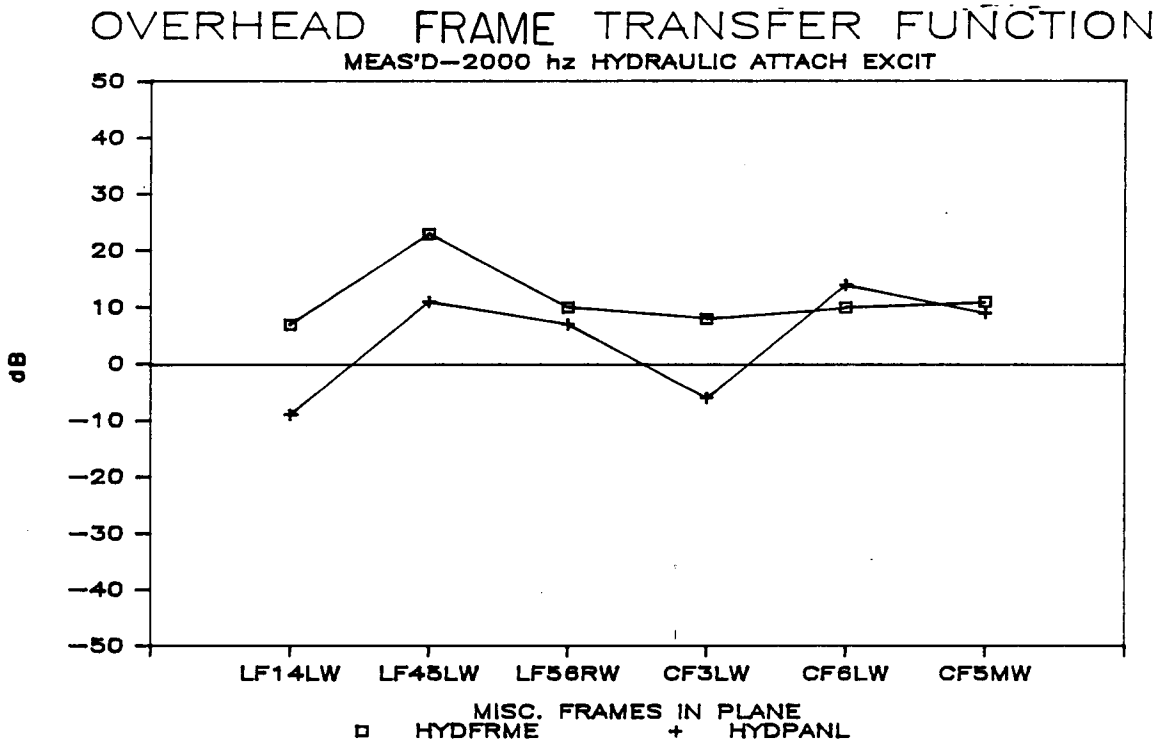

Figure D22c. Miscellaneous Frame In-Plane Transfer Function Measurements, Hydraulic Attachment Excitation, 2 kHz

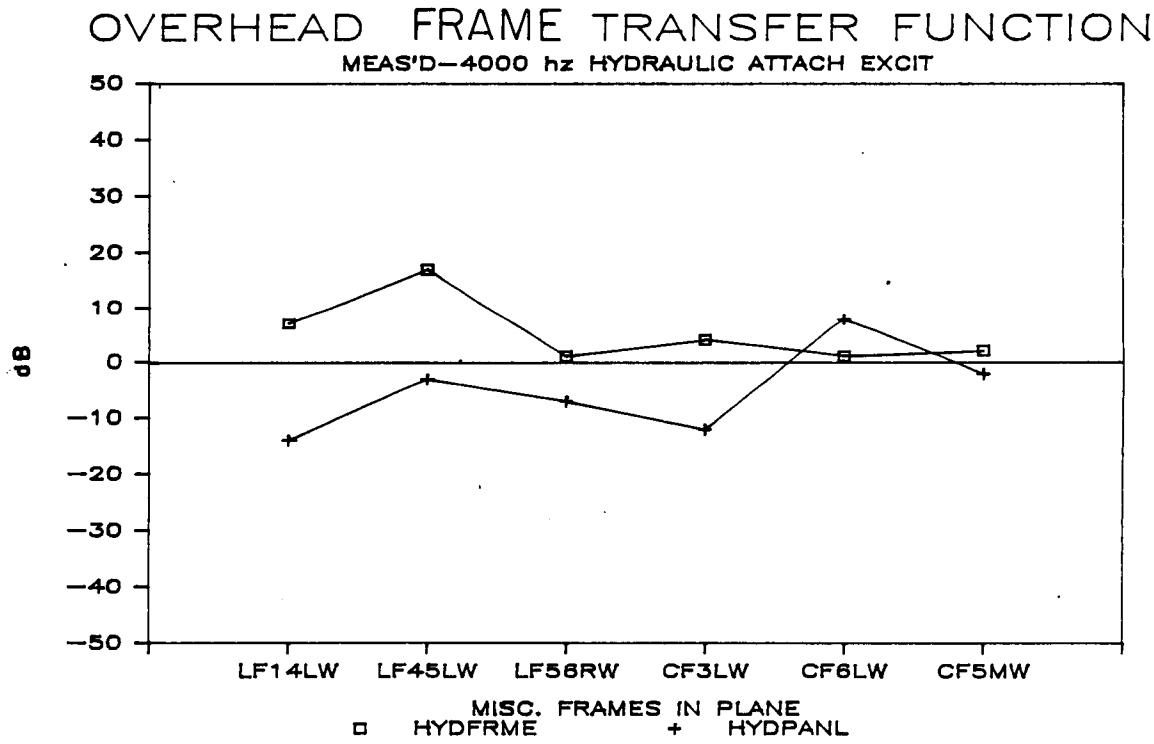

Figure D22d. Miscellaneous Frame In-Plane Transfer Function Measurements, Hydraulic Attachment Excitation, 4 kHz

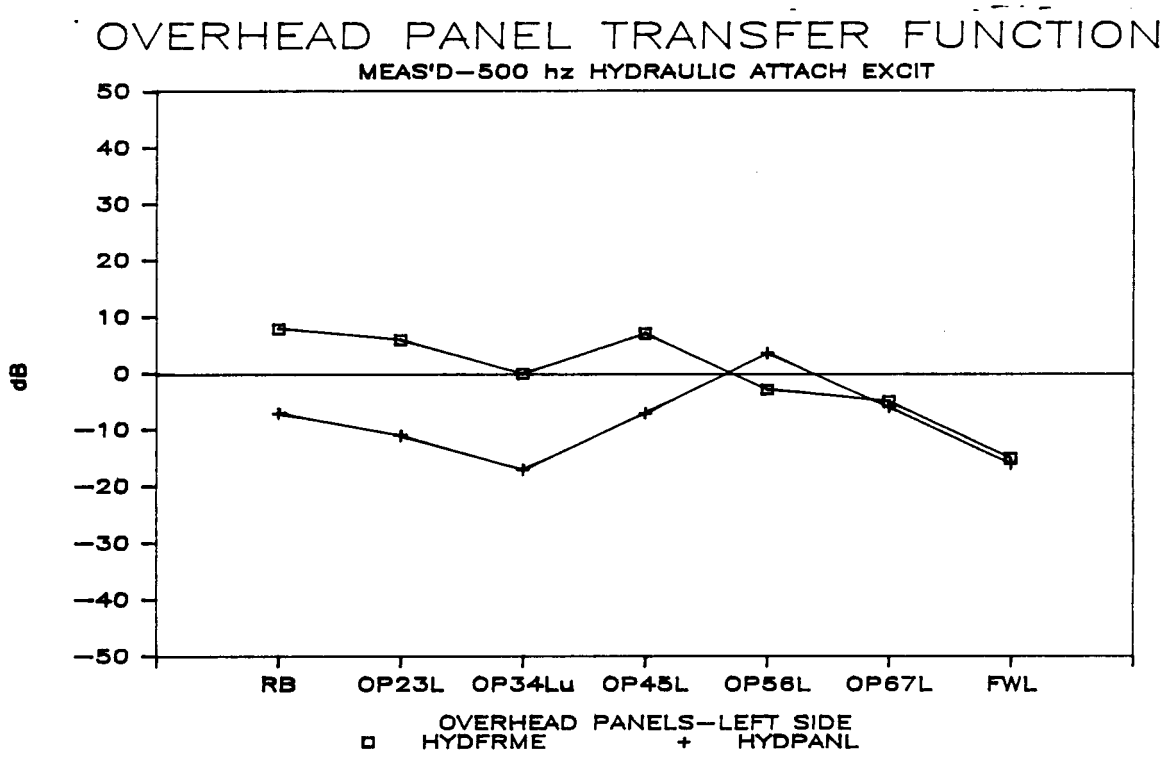

Figure D23a. Overhead Panel Transfer Function Measurements, Left Side, Hydraulic Attachment Excitation, .5 kHz

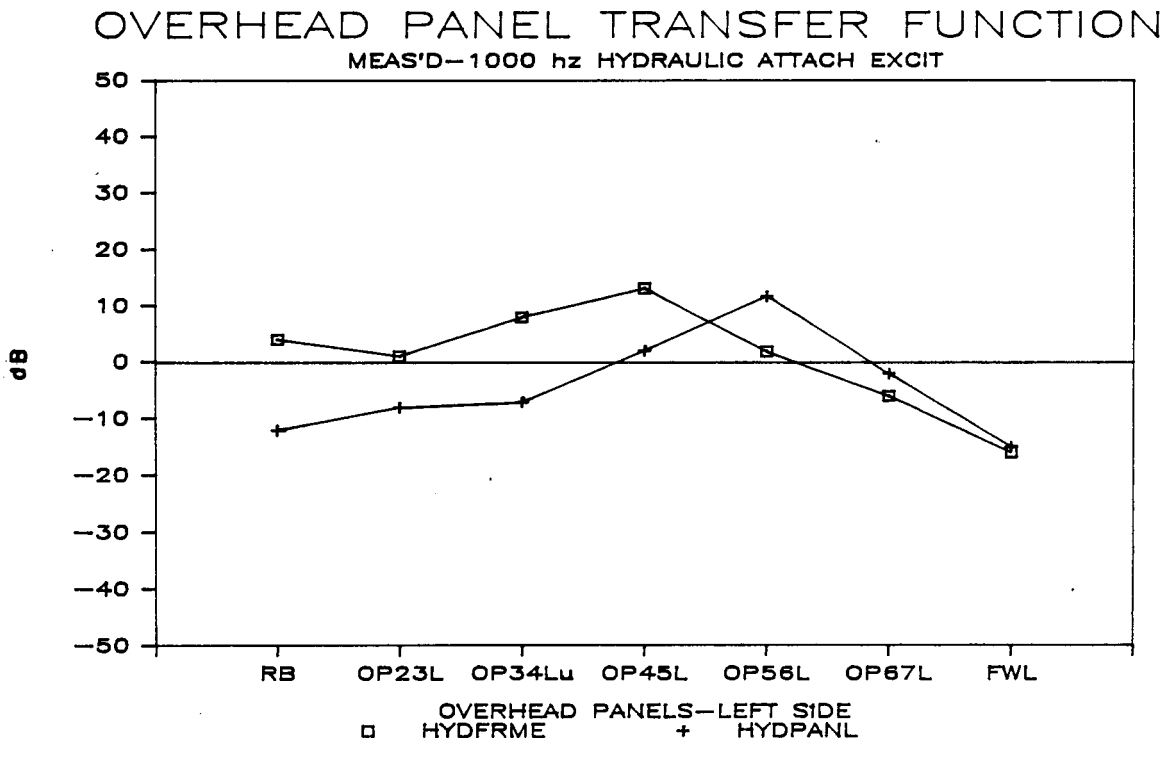

Figure D23b. Overhead Panel Transfer Function Measurements, Left Side, Hydraulic Attachment Excitation, 1 kHz

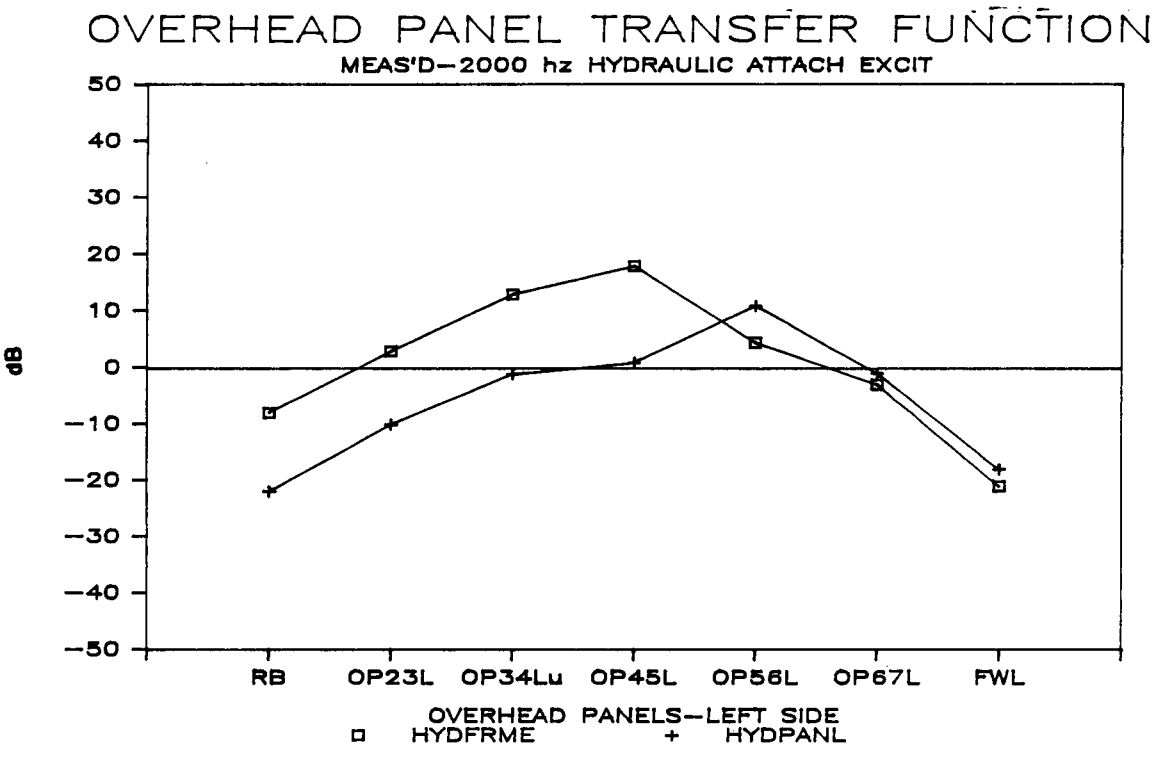

Figure D23c. Overhead Panel Transfer Function Measurements, Left Side, Hydraulic Attachment Excitation, 2 kHz

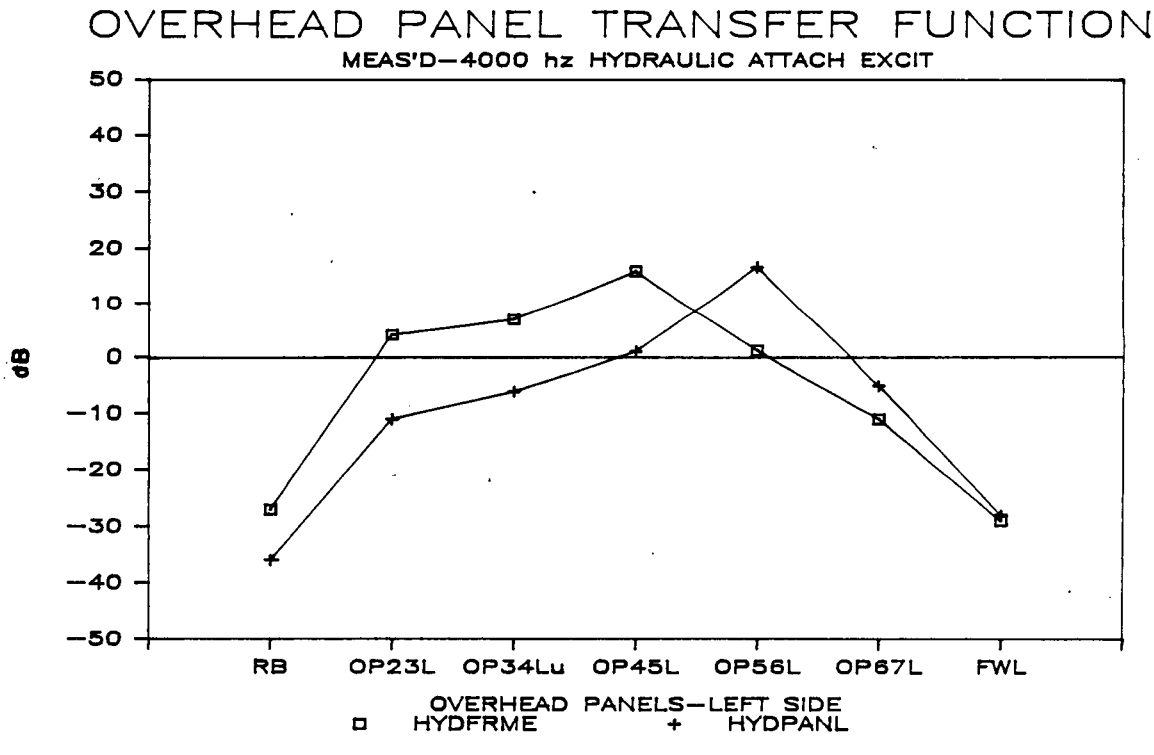

Figure D23d. Overhead Panel Transfer Function Measurements, Left Side, Hydraulic Attachment Excitation, 4 kHz

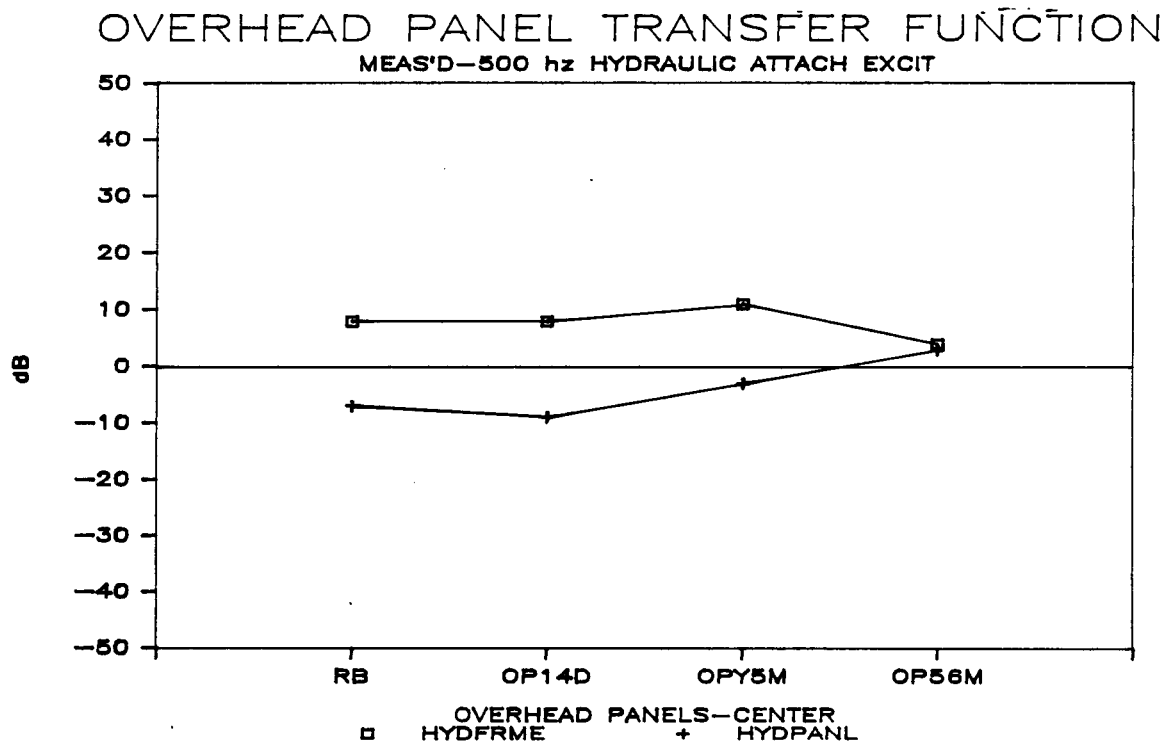

Figure D24a. Overhead Panel Transfer Function Measurements, Middle, Hydraulic Attachment Excitation, .5 kHz

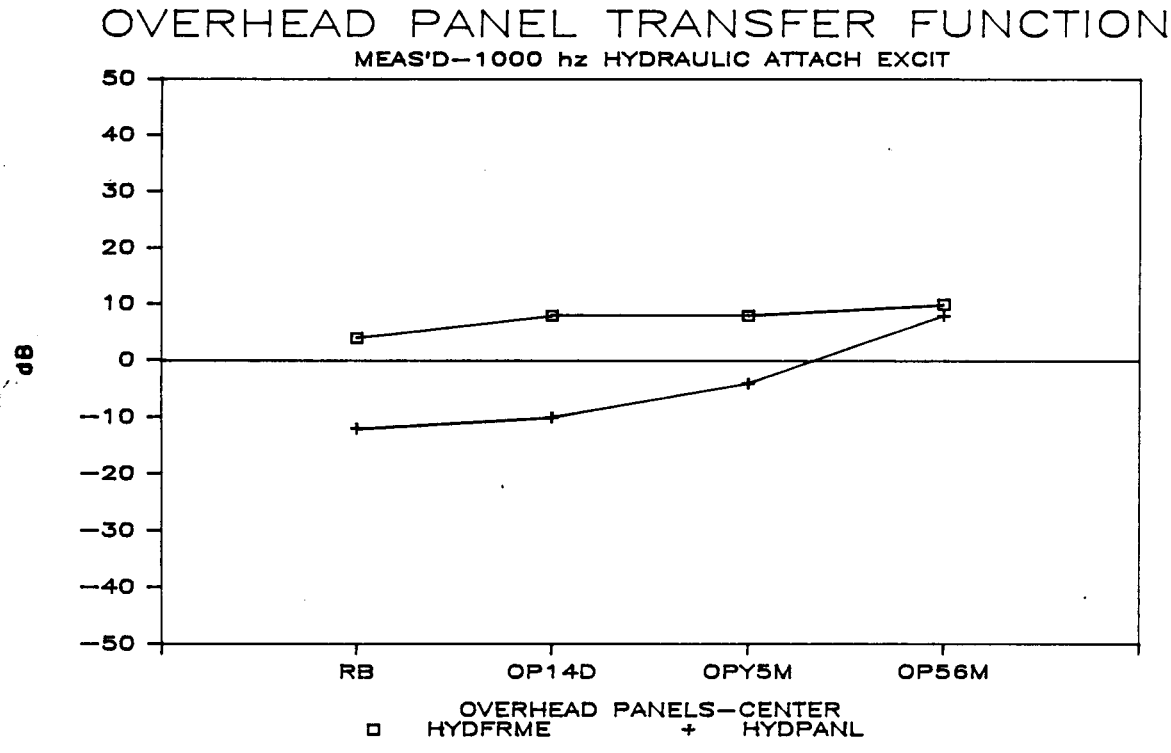

Figure D24b. Overhead Panel Transfer Function Measurements, Middle, Hydraulic Attachment Excitation, 1 kHz

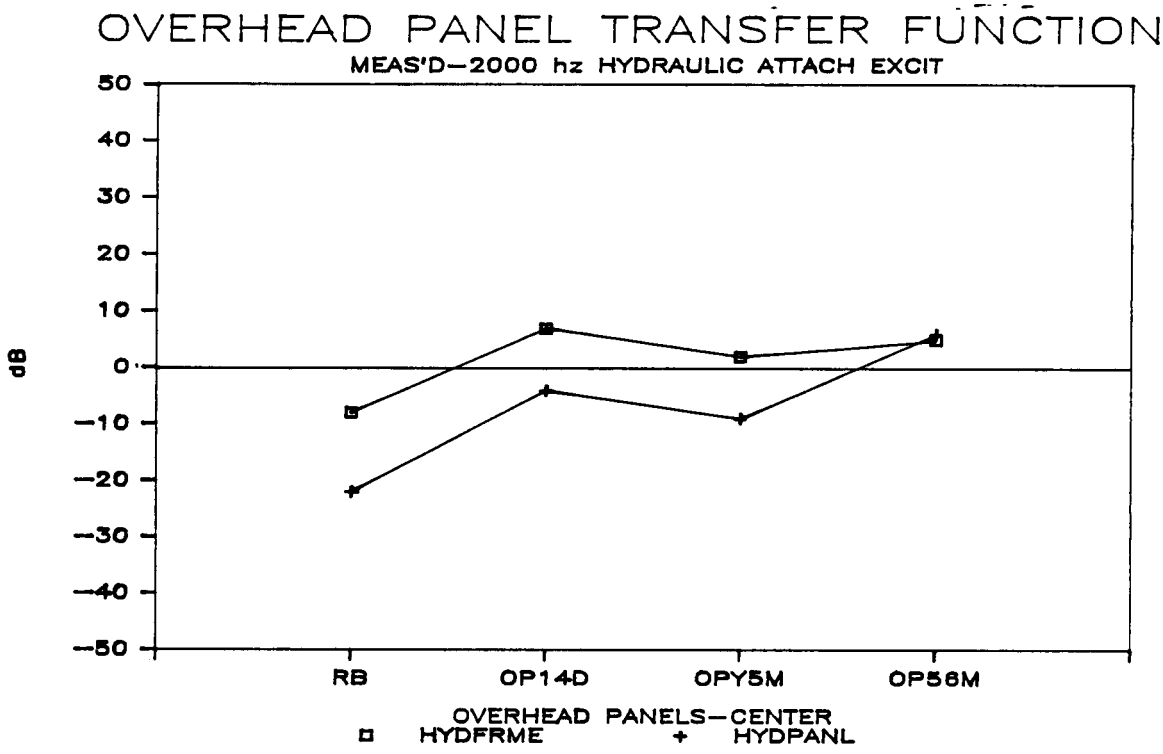

Figure D24c. Overhead Panel Transfer Function Measurements, Middle, Hydraulic Attachment Excitation, 2 kHz

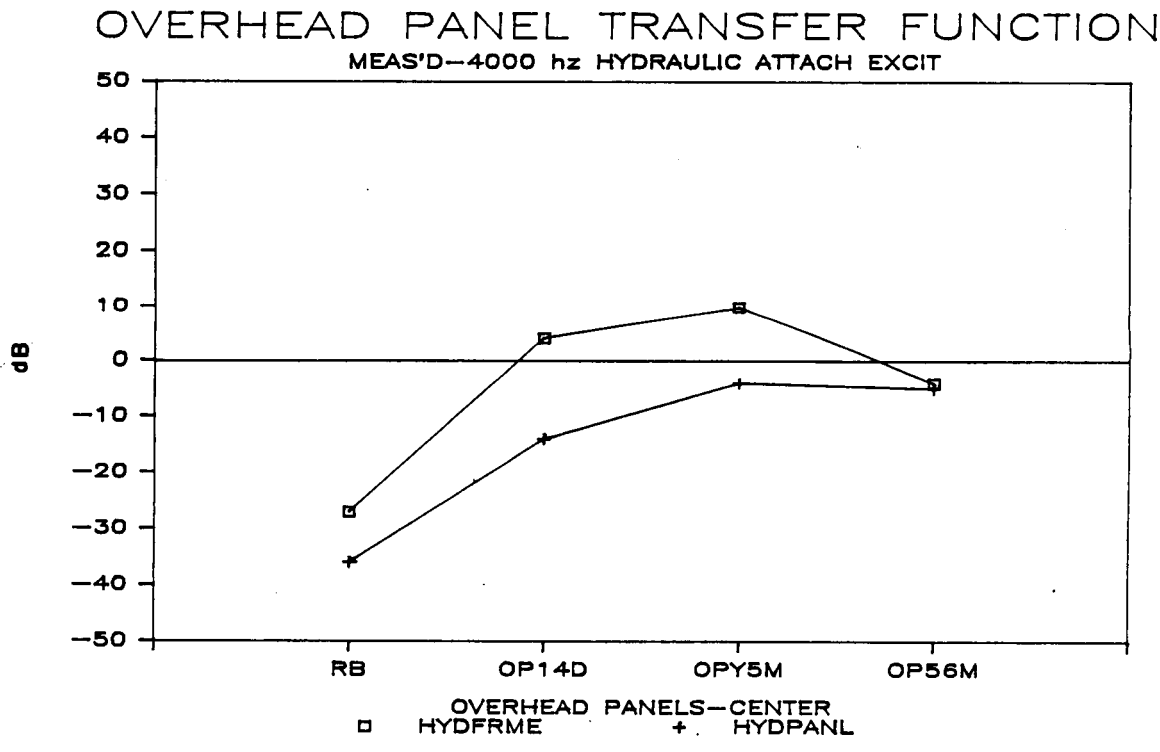

Figure D24d. Overhead Panel Transfer Function Measurements, Middle, Hydraulic Attachment Excitation, 4 kHz

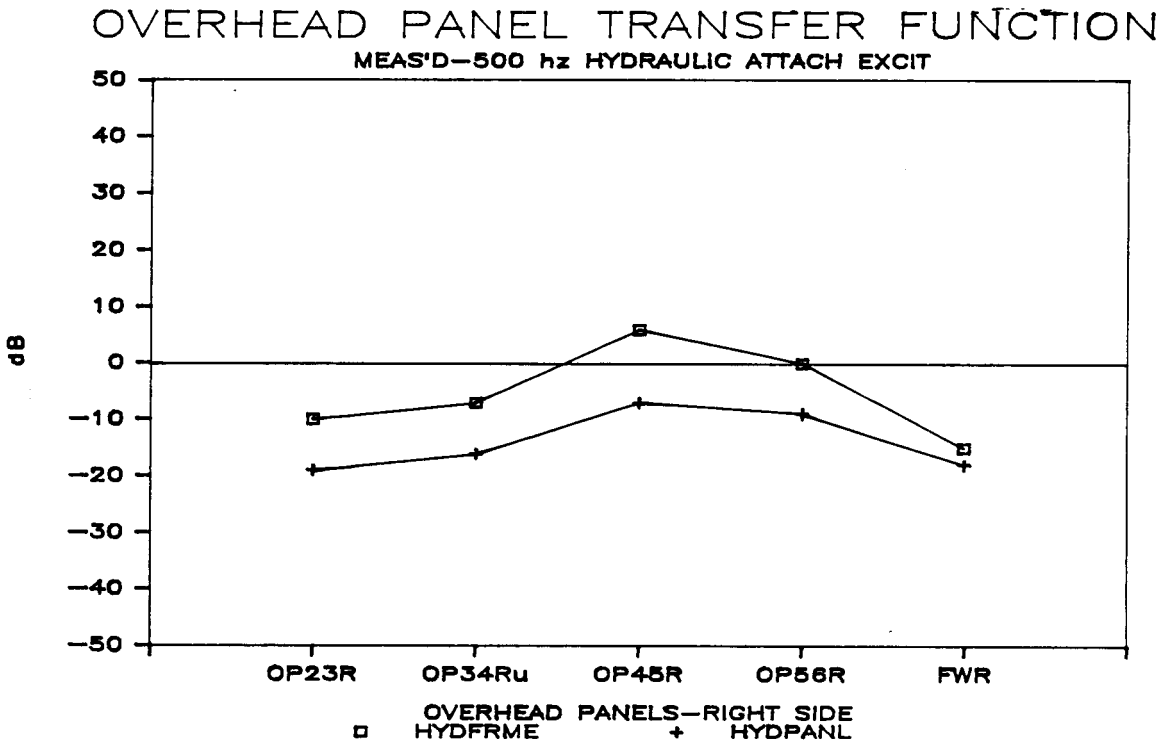

Figure D25a. Overhead Panel Transfer Function Measurements, Right Side, Hydraulic Attachment Excitation, .5 kHz

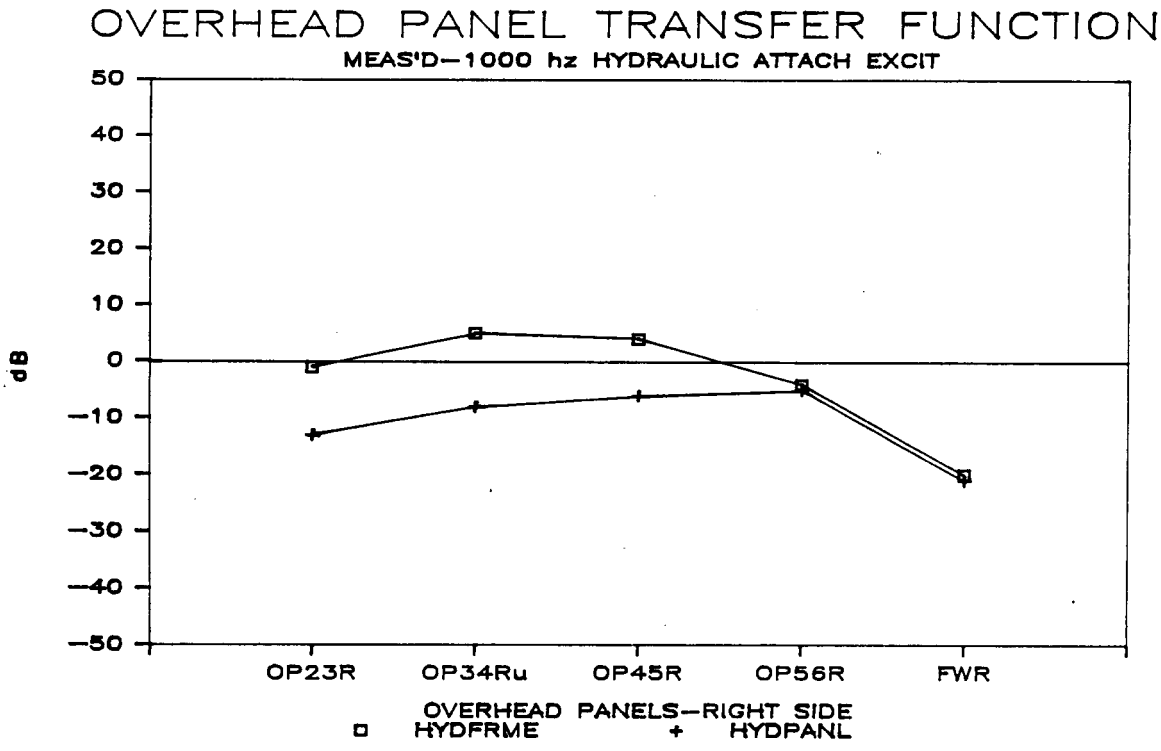

Figure D25b. Overhead Panel Transfer Function Measurements, Right Side, Hydraulic Attachment Excitation, 1 kHz

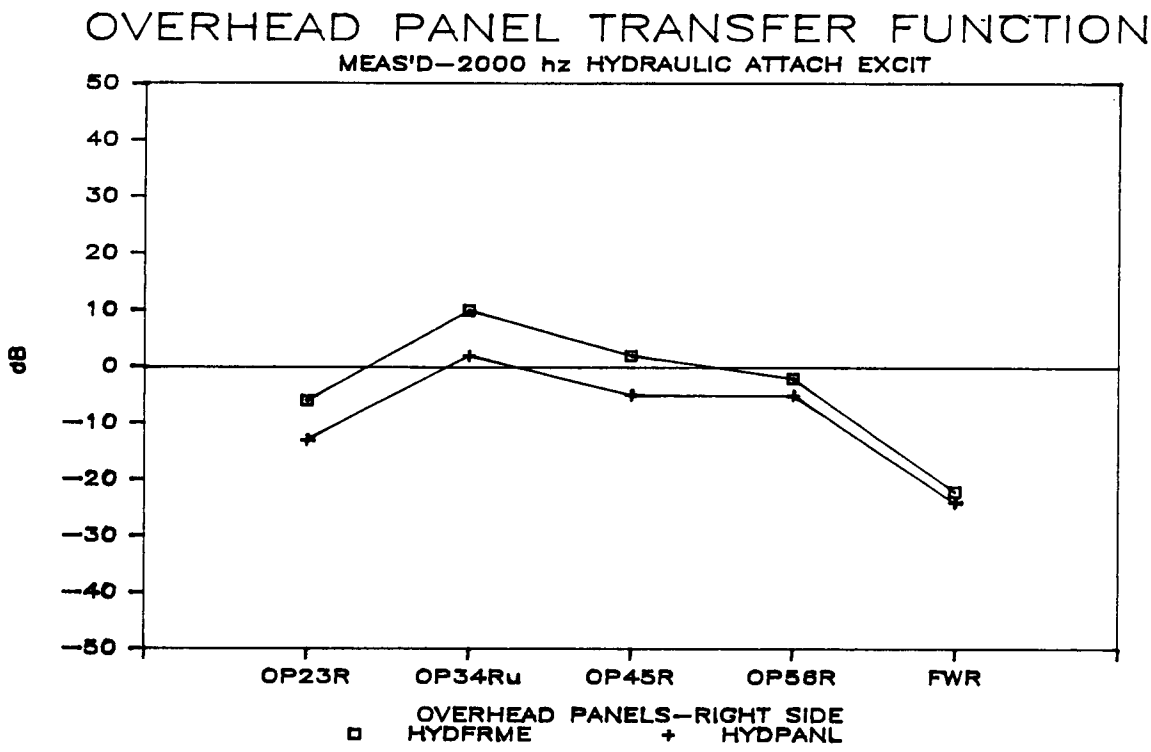

Figure D25c. Overhead Panel Transfer Function Measurements, Right Side, Hydraulic Attachment Excitation, 2 kHz

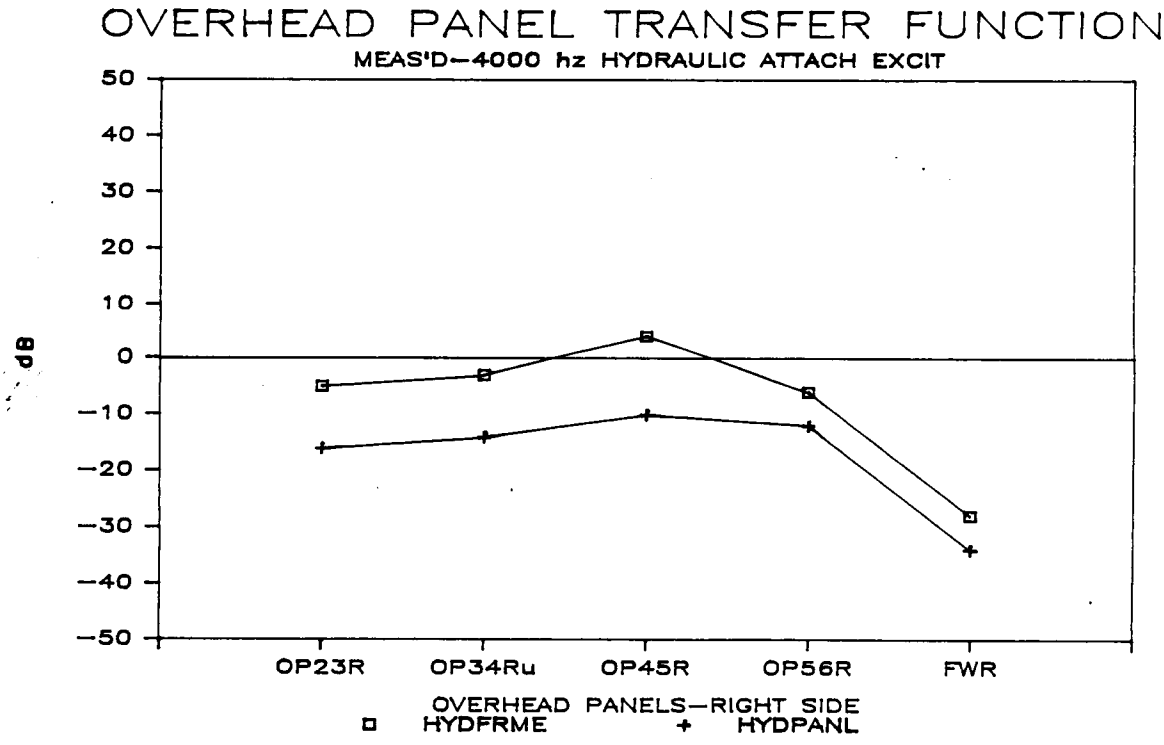

Figure D25d. Overhead Panel Transfer Function Measurements, Right Side, Hydraulic Attachment Excitation, 4 kHz

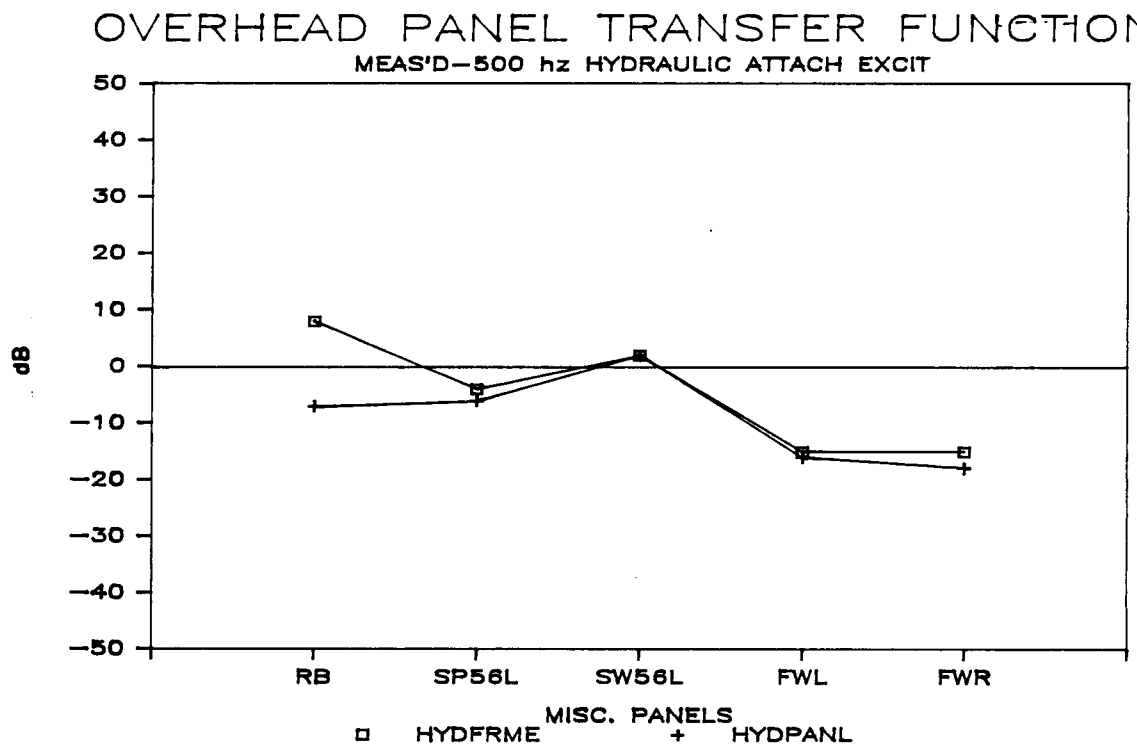

Figure D26a. Miscellaneous Panel Transfer Function Measurements, Hydraulic Attachment Excitation, .5 kHz

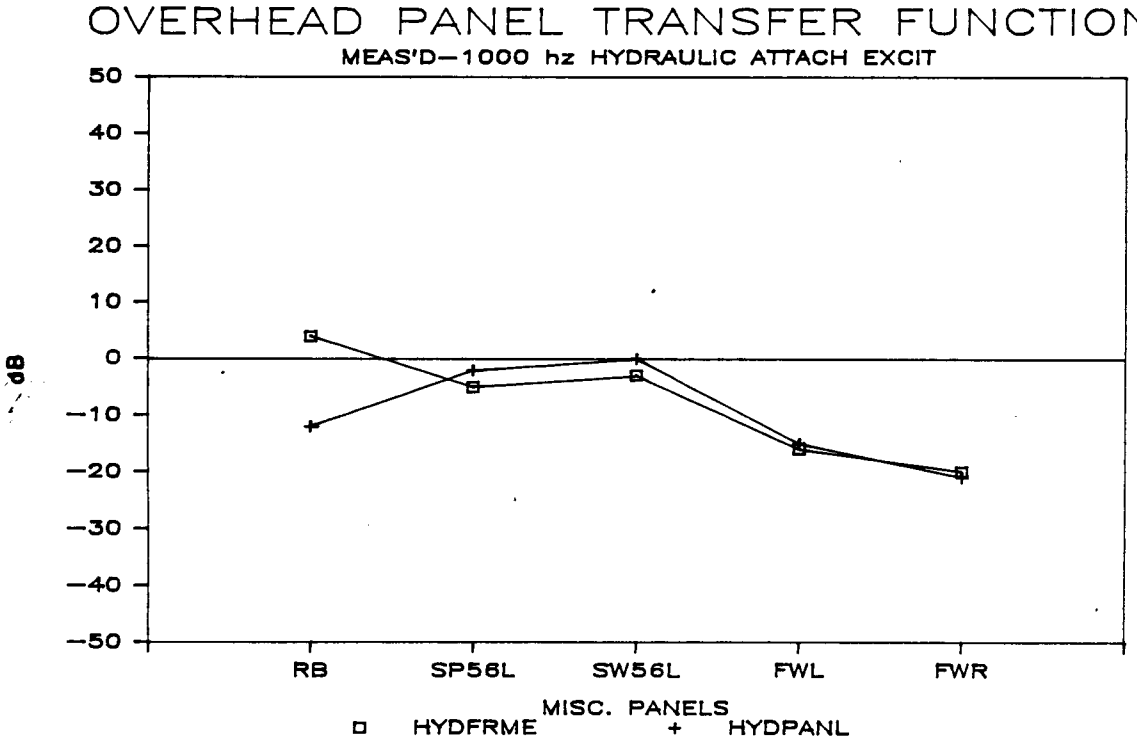

Figure D26b. Miscellaneous Panel Transfer Function Measurements, Hydraulic Attachment Excitation, 1 kHz

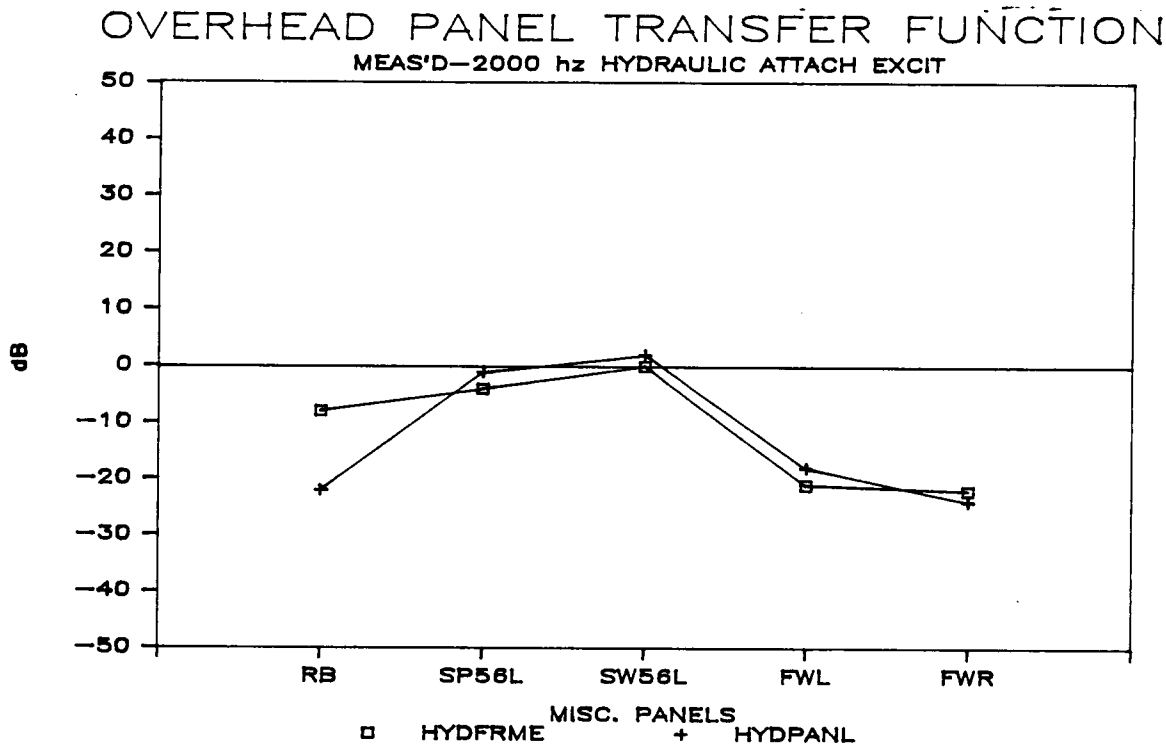

Figure D26c. Miscellaneous Panel Transfer Function Measurements, Hydraulic Attachment Excitation, 2 kHz

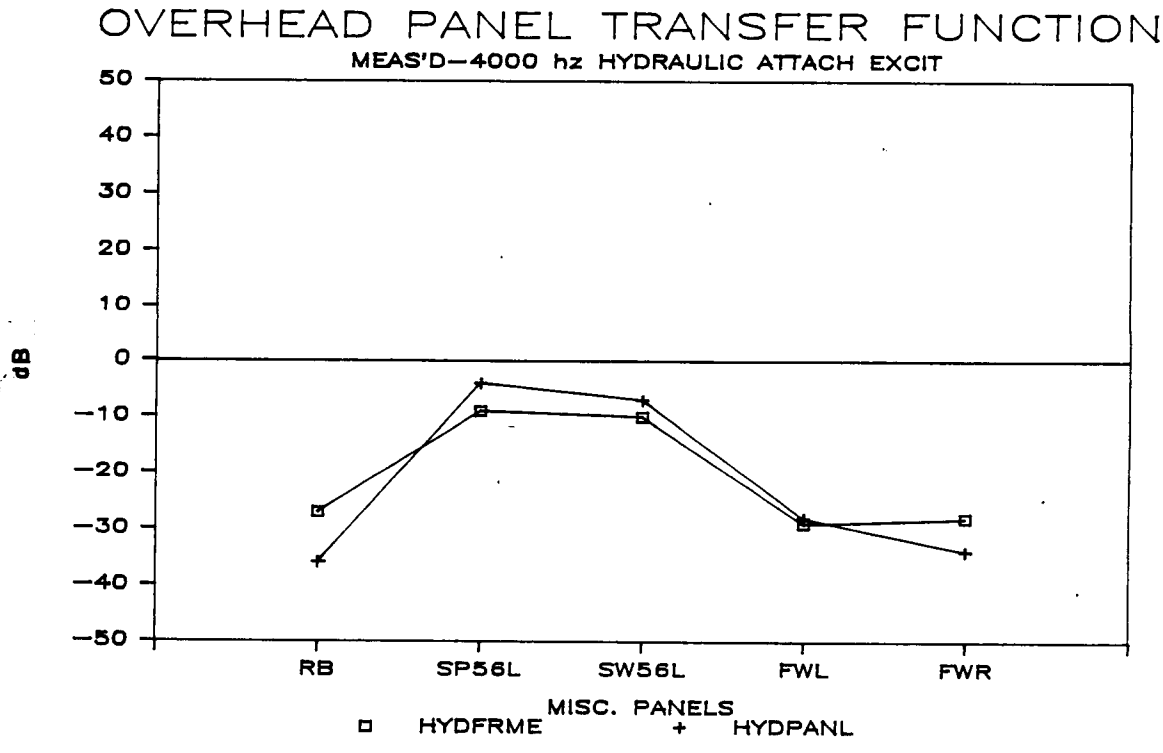

Figure D26d. Miscellaneous Panel Transfer Function Measurements, Hydraulic Attachment Excitation, 4 kHz

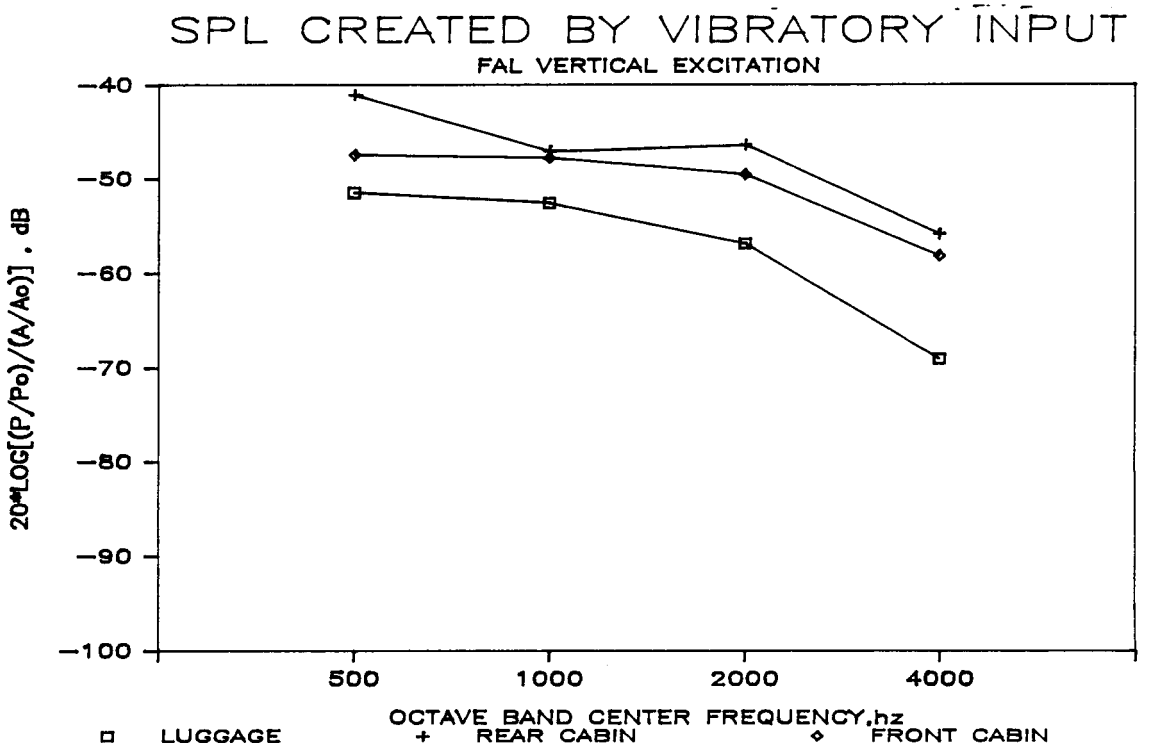

Figure D27. Vibratory Input/Acoustic Output Transfer Function Measurements, FAL Vertical Excitation

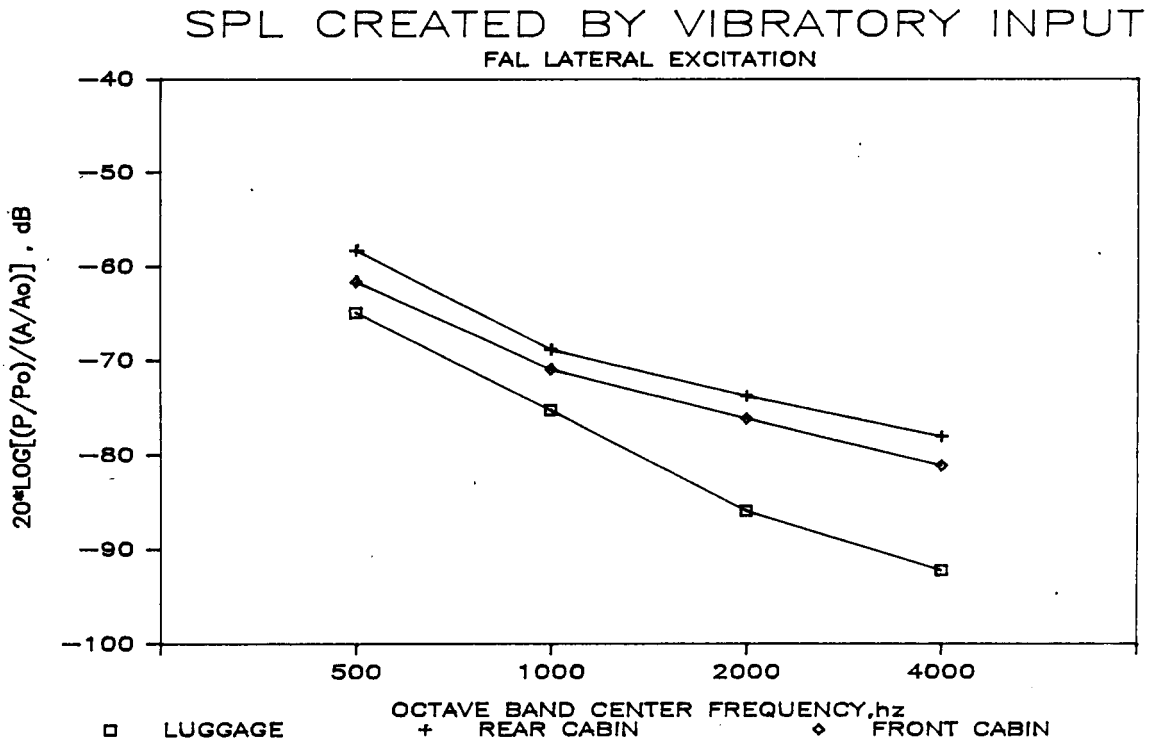

Figure D28. Vibratory Input/Acoustic Output Transfer Function Measurements, FAL Lateral Excitation

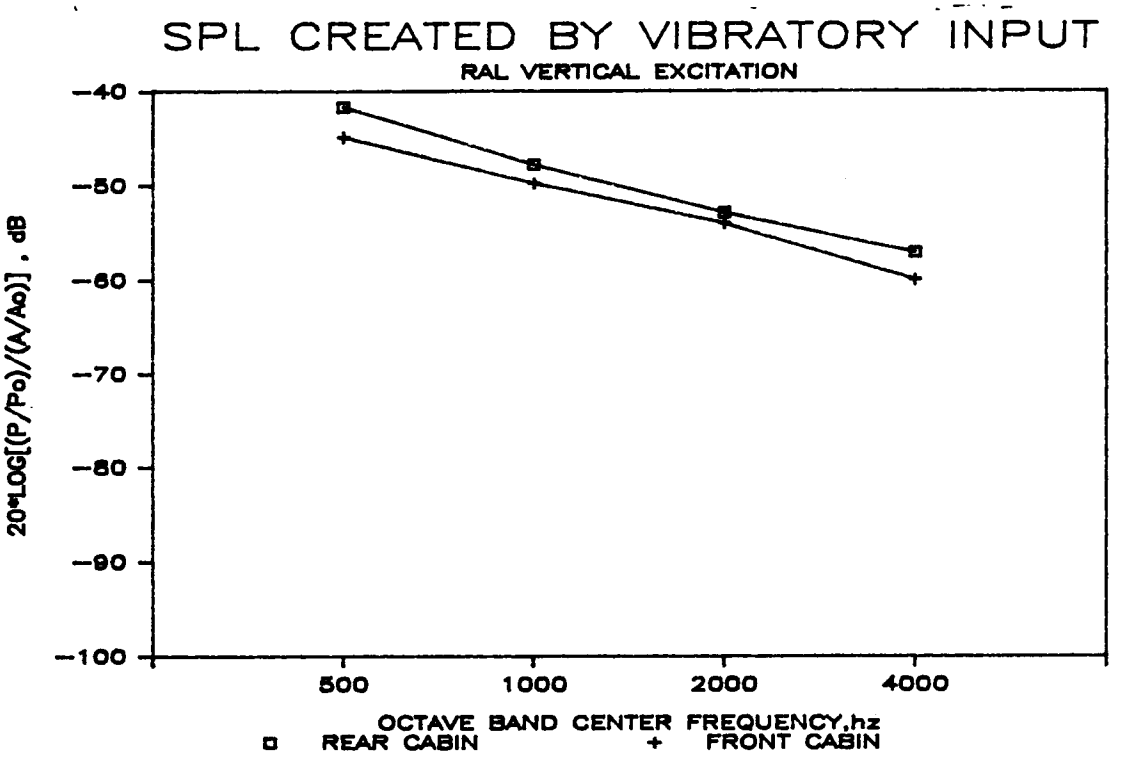

Figure D29. Vibratory Input/Acoustic Output Transfer Function Measurements, RAL Vertical Excitation

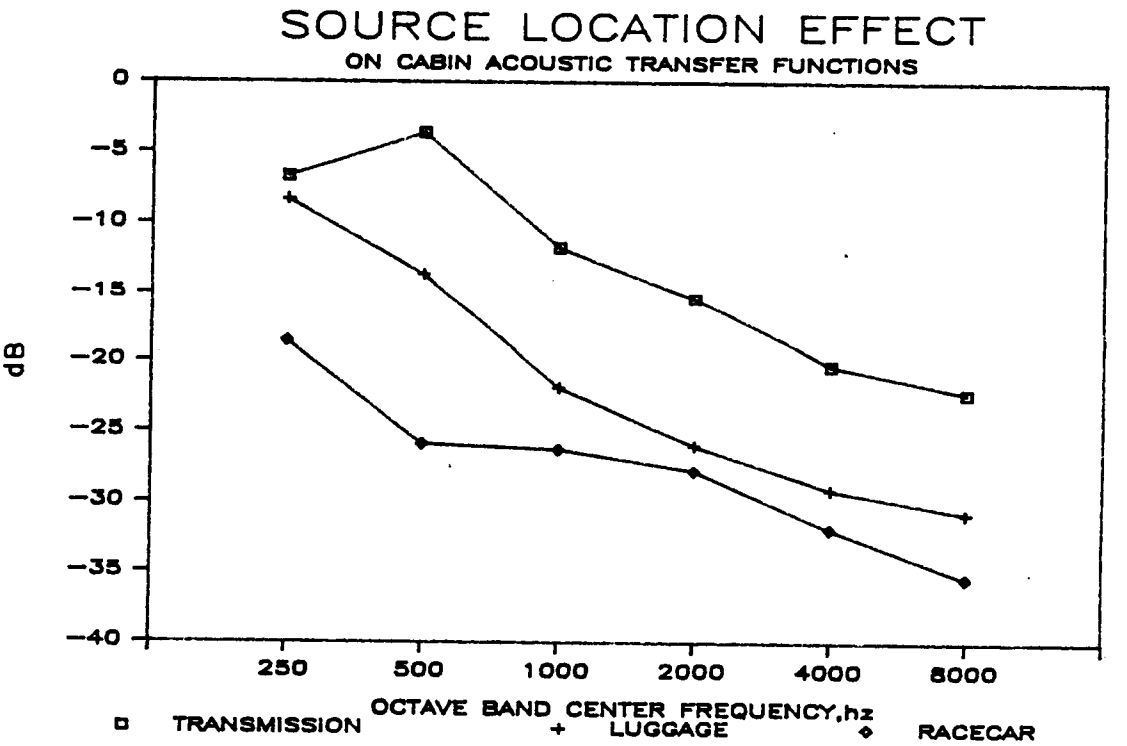

Figure D30. Acoustic Input/Acoustic Output Transfer Function Measurements

rear cabin microphone, while the front cabin microphone is 3 dB less than the rear on the average. The FAL vertical dominance of vibratory transfer functions, along with the much lower FAL lateral response levels correlates well with these results.

Acoustic transfer functions. - Acoustic transfer functions were measured between the rear cabin microphone location and three source locations. The source locations included the gearbox area, the luggage compartment, and the racecar, which is the cowling forward of the gearbox and covers the flight control hardware attached to the center overhead panels. The main gearbox and its adjacent cowlings were not in place during this test.

The data is shown in Figure D29. The gearbox source location dominates the response in all octaves measured, with the luggage compartment 10 dB less in the SIL-4 octaves and the racecar source 5 dB below that. The gearbox source location is bounded from the cabin by OP14D, a lightweight aluminum panel, while the luggage compartment connects to the cabin through RB, and the racecar source through the heavier center overhead panels. These descriptions correlate directly with the observed trends.

Flight Test Measurements

Vibration Levels. - Vibration measurements made in flight are shown in Figures D30 through D46. Main gearbox attachment location vibration levels were measured for approximation of the power input into the airframe during forward flight. This measurement data is shown in Figures D30 to D36. In the vertical direction, (see Figure D30) the 500 hz levels are close for all four mounting locations, at 146 to 147 dB. The 1kHz levels all fall between 151 and 154 dB, again very similar. At 2Khz, the rear attachments become higher than the front, by 2 to 5 dB and at 4Khz, the left front is highest at 152 and the right front lowest at 142 dB. In general, the vertical direction levels are comparable for all locations with exception at 4000 hz. The lateral direction (Figure D31) shows a much wider variation in levels than the vertical. The left side dominates, with front and rear within 1dB in level at 400, 1k and 2kHz, with the left front 3dB higher than the rear in the 4Khz octave. The right side measurements are 10 and 20 dB below the left at the rear and front in both the 500 and 1000 hz octaves. The rear levels are approximately 150 dB across the frequency range while the front averages in the low 140's. At 2 and 4 Khz, the right rear levels nearly equal those of the left side. The longitudinal excitation (Figure D32) has no dominant location for all four octaves. FAL is highest at 500 hz at 153 dB, where RAR is lowest at 136 dB. At 1000 hz FAL and RAL are both approximately 156 dB and FAR the lowest at 147 dB. At 2000 hz, RAR and RAL are high at 155 dB and at 4000 hz, FAL is high at 152 dB. In short, the lateral is dominated by the left side, vertical is approximately equal for all locations, and the longitudinal is mixed across the SIL-4 octaves.

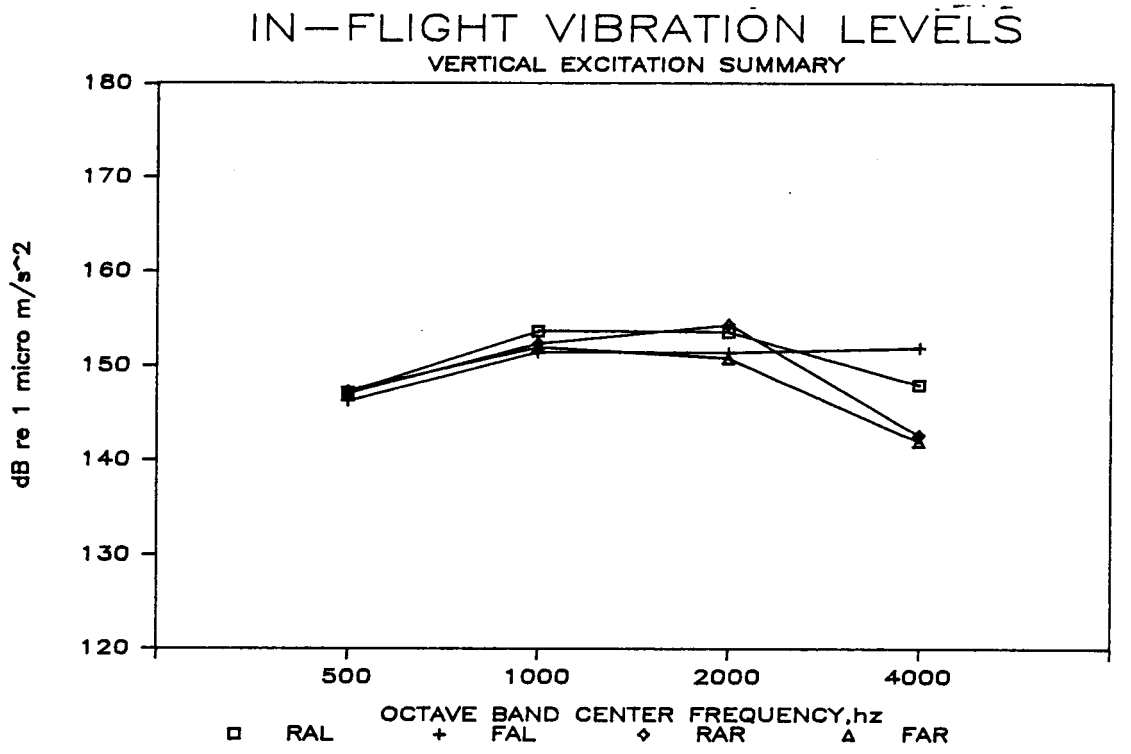

Figure D31. S-76 In-Flight Vibration Measurements, Vertical Transmission Interface Summary, 75 m/s

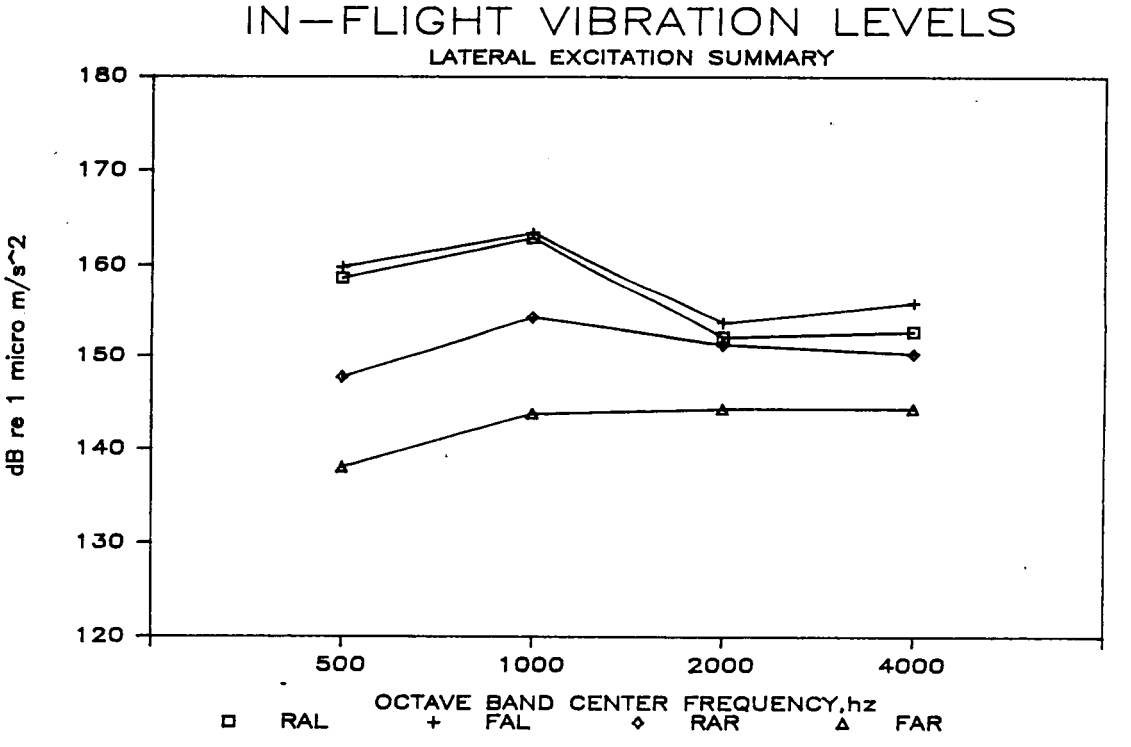

Figure D32. S-76 In-Flight Vibration Measurements, Lateral Transmission Interface Summary, 75 m/s

Figures D33 through D36 depict this same data, except grouped by foot location and compared in each plot by direction. The left front location, (Figure D33) shows the lateral levels highest in all octaves, with particular dominance in 500 and 1000 hz. The longitudinal and vertical are 8 and 12 dB below in these two octaves. The 2000 and 4000 octaves show nearly equal level in each direction. The right front location (Figure D34) has the vertical dominate the 500, 1k and 2k octaves, with approximately 9dB spread in level between each of the three directions. The lateral levels show an increase in levels with increasing frequency, while the vertical and longitudinal levels peak at 1k and 2k respectively. At the left rear location (see Figure D35) the lateral dominates the lower octaves (500 and 1000 hz) with levels around 160 dB while the 2 Khz octave is approximately equal for all three directions within 3dB. At 4Khz, is dominated by the lateral direction again, followed by the vertical 5dB lower and the longitudinal approximately 8dB down. At the right rear attachment the lateral and vertical levels are approximately equal at 500 and 1000 hz. The lateral drops off at 2000, and the longitudinal and vertical become equal and highest. The 4000 hz octave shows these two octaves dropping off and the lateral becoming highest by 8dB at 150 dB. In general, these data show the lateral measurements on the left side dominant at 1000 hz, the octave that generally controls the SIL-4 values in bare or fully treated cabins.

The vibration levels measured at the gearbox attachment during in-ground effect hover are shown in Figures D37 through D40. This data indicates for all locations and directions that the vibration levels measured in hover are within 5 dB of the forward flight levels, with trends with frequency and direction exceedingly similar, but generally of lower level.

The frame junctions measured during 75 m/s forward flight were the vertical or out-of-plane levels at longituindal frame junctions between LF14-45L, LF45-56L, LF56-67L on the left side, and LF56-67R on the right side. The data is shown in Figure D41. It reveals that the levels generally decrease with distance away from the main gearbox attachment. The station 4 junction (between LF14 and LF45) is less than 5 dB higher than the station 5 levels in the 500, 1k and 2k hz octaves, with the 4khz octave lower by approximately 3dB. The station 6 junctions show lower 500 and 1khz levels, and display an increasing trend with frequency much like the less stiff sheet aluminum panel levels when compared to the honeycomb construction. Other frames measured included YF45M, a lightweight frame that divides OP4YM from OPY5M and connects LF46L and LF45R. SF6L is the side frame between SP56L and the copilot's door, and CF2Lw is an in-plane measurement on a cross frame adjacent to the left rear gearbox mounting location. These measurements are shown in Figure D42. The levels measured on YF45M in the web direction are high, between 150 and 160 db for all four octaves. This frame is fairly close to the source locations, equidistant from LF14L and R. SF6L measured relatively low, as it is fairly far from the gearbox in path. CF2L shows extremely high levels in-plane, with the 1khz level approx. 173 dB (re 1 micrometer per second squared) and other octaves above 160 dB. These levels reflect accelerations of greater than 100 meters per second squared.

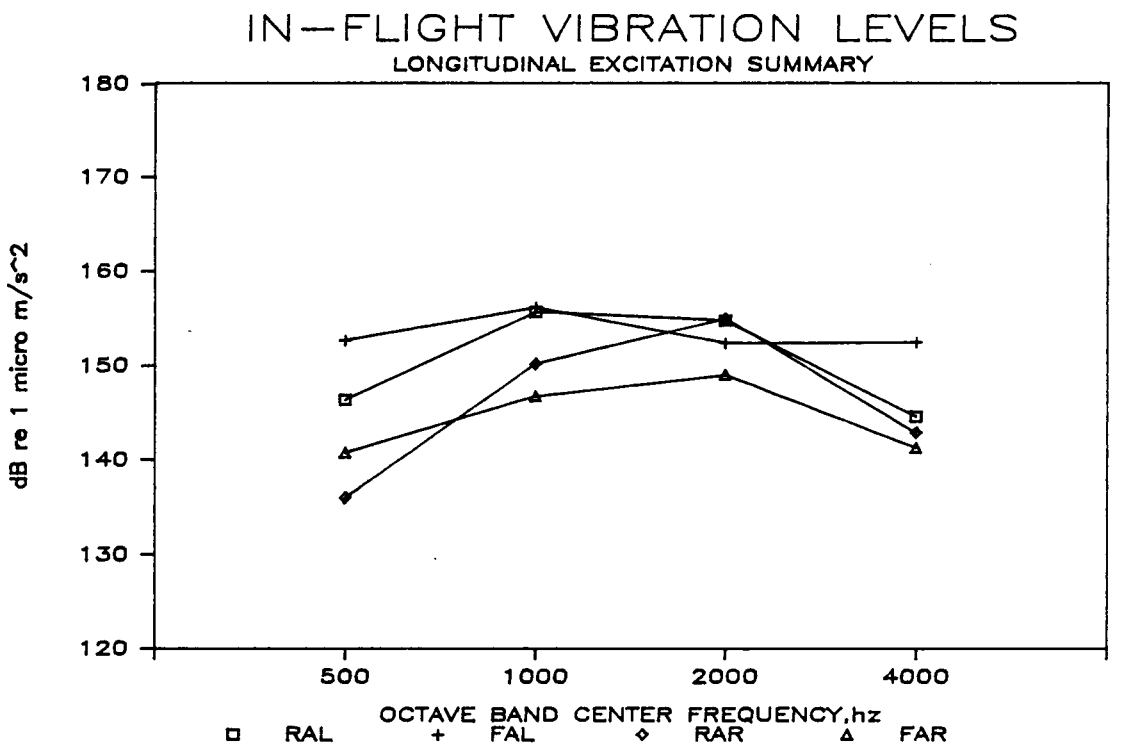

Figure D33. S-76 In-Flight Vibration Measurements, Longitudinal Transmission Interface Summary, 75 m/s

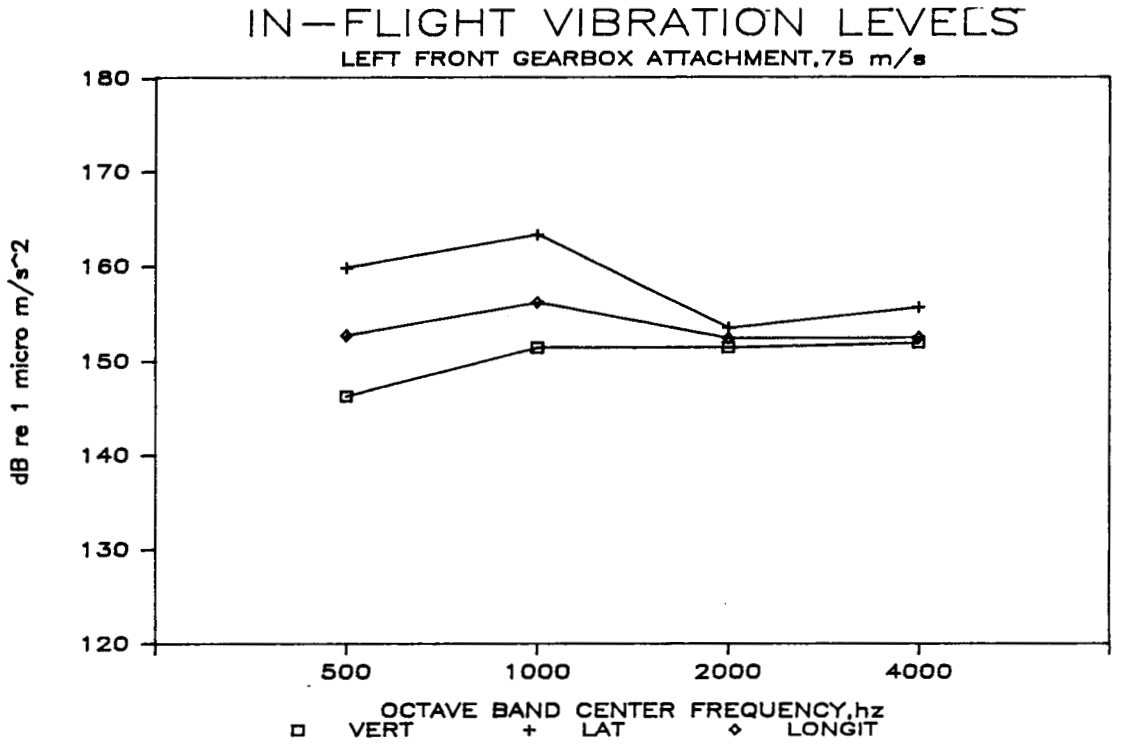

Figure D34. S-76 In-Flight Vibration Measurements, Left Front Transmission Interface Summary, 75 m/s

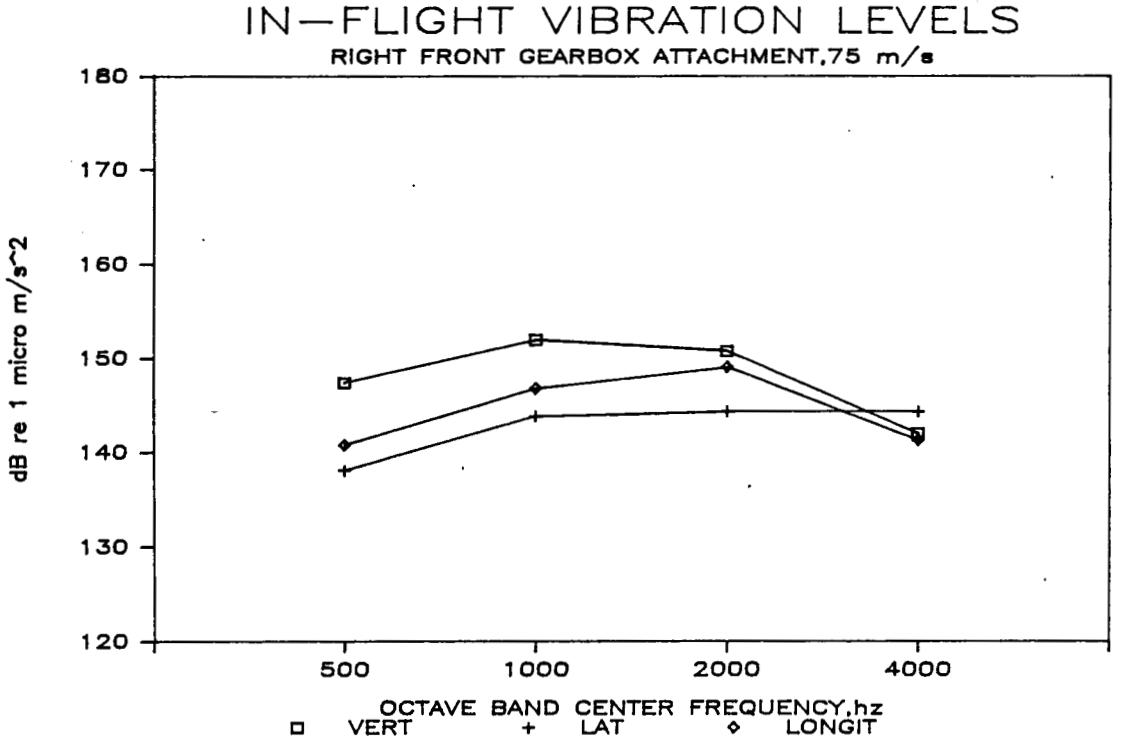

Figure D35. S-76 In-Flight Vibration Measurements, Right Front Transmission Interface Summary, 75 m/s

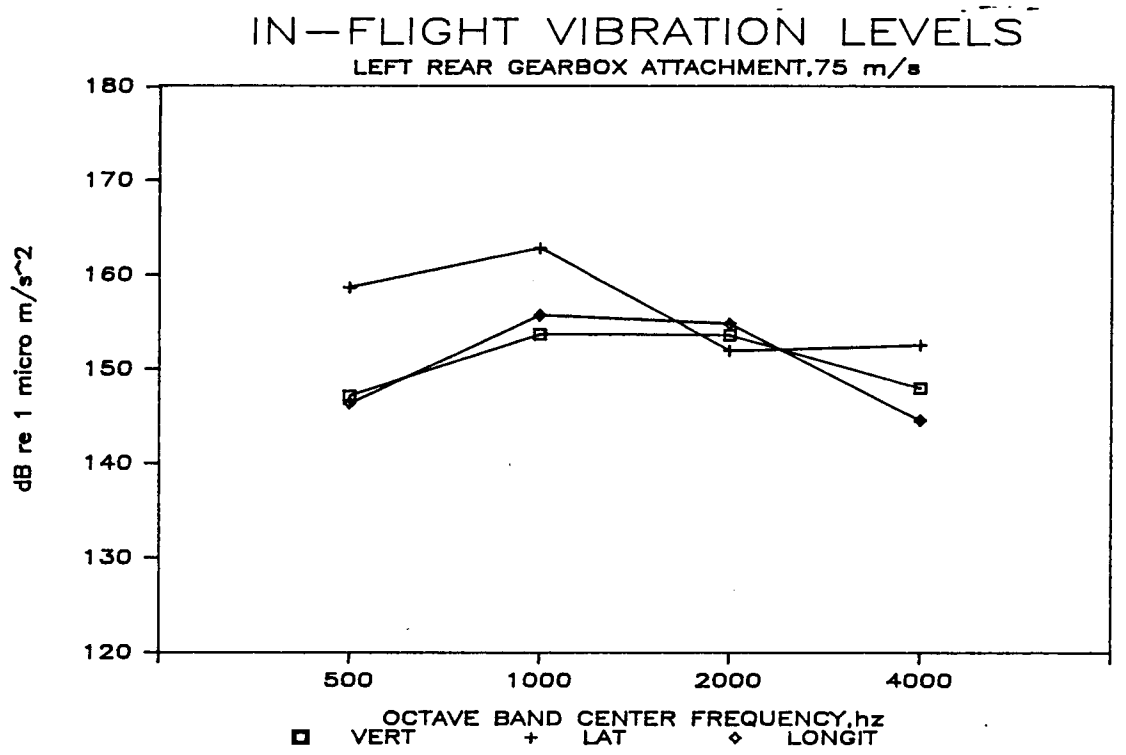

Figure D36. S-76 In-Flight Vibration Measurements, Left Rear Transmission Interface Summary, 75 m/s

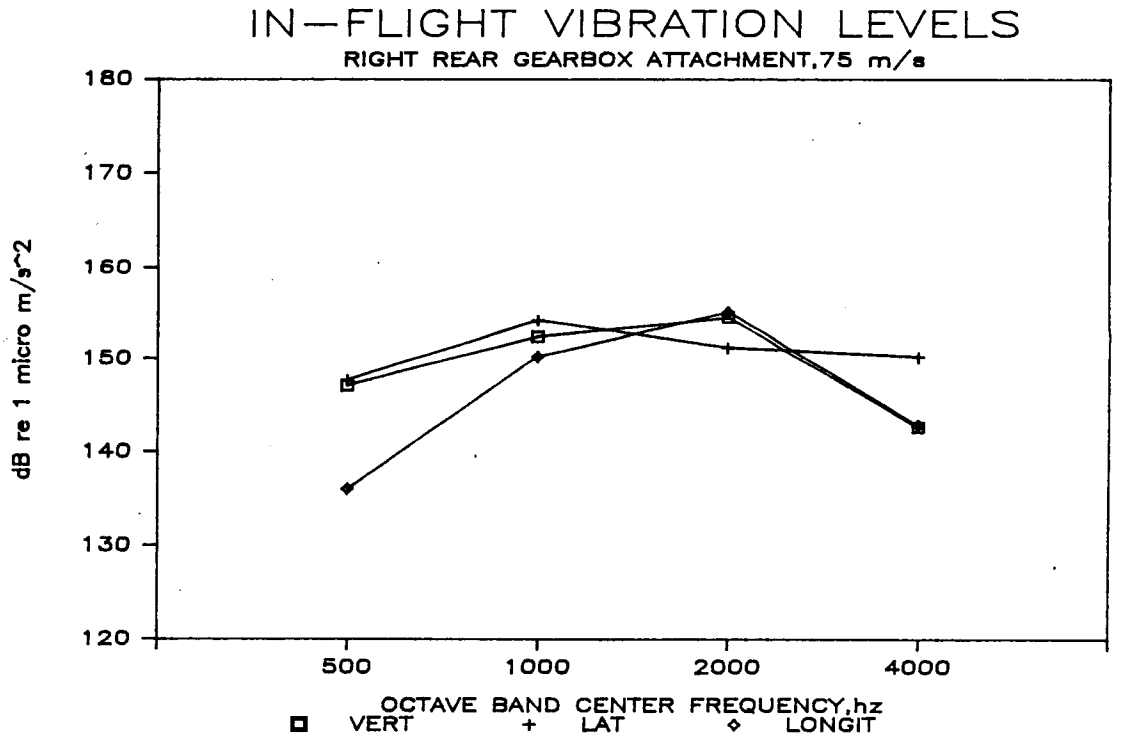

Figure D37. S-76 In-Flight Vibration Measurements, Right Rear Transmission Interface Summary, 75 m/s

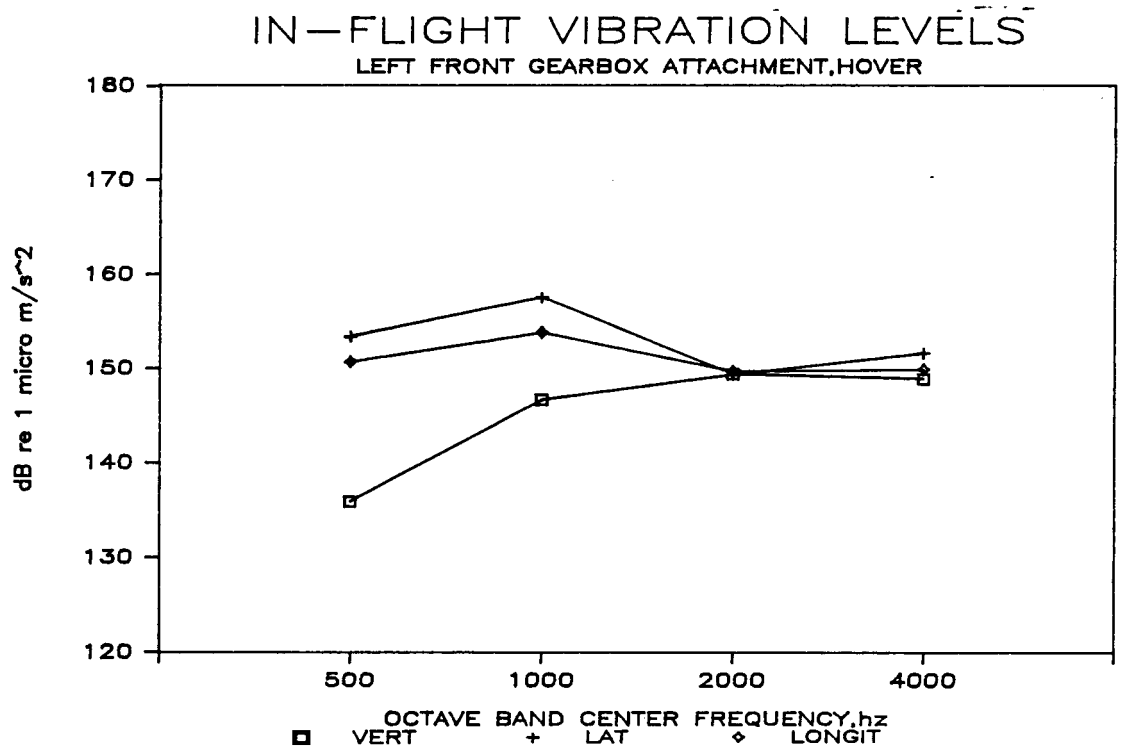

Figure D38. S-76 In-Flight Vibration Measurements, Left Front Transmission Interface Summary, Hover

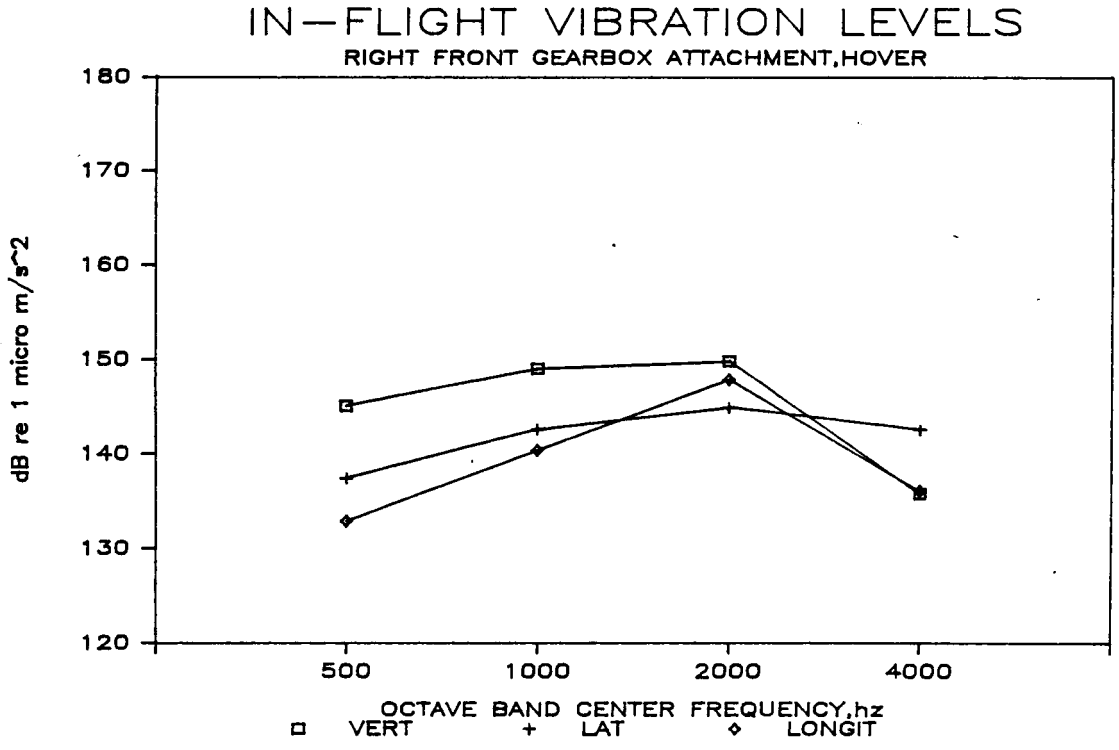

Figure D39. S-76 In-Flight Vibration Measurements, Right Front Transmission Interface Summary, Hover

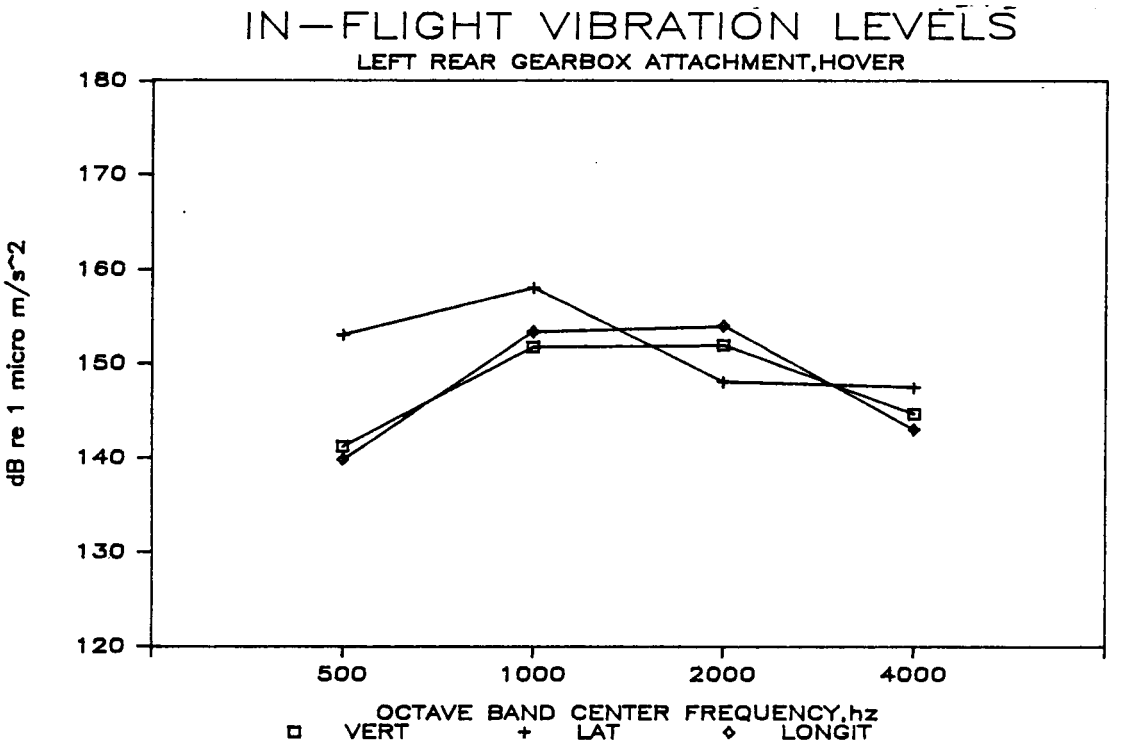

Figure D40. S-76 In-Flight Vibration Measurements, Left Rear Transmission Interface Summary, Hover

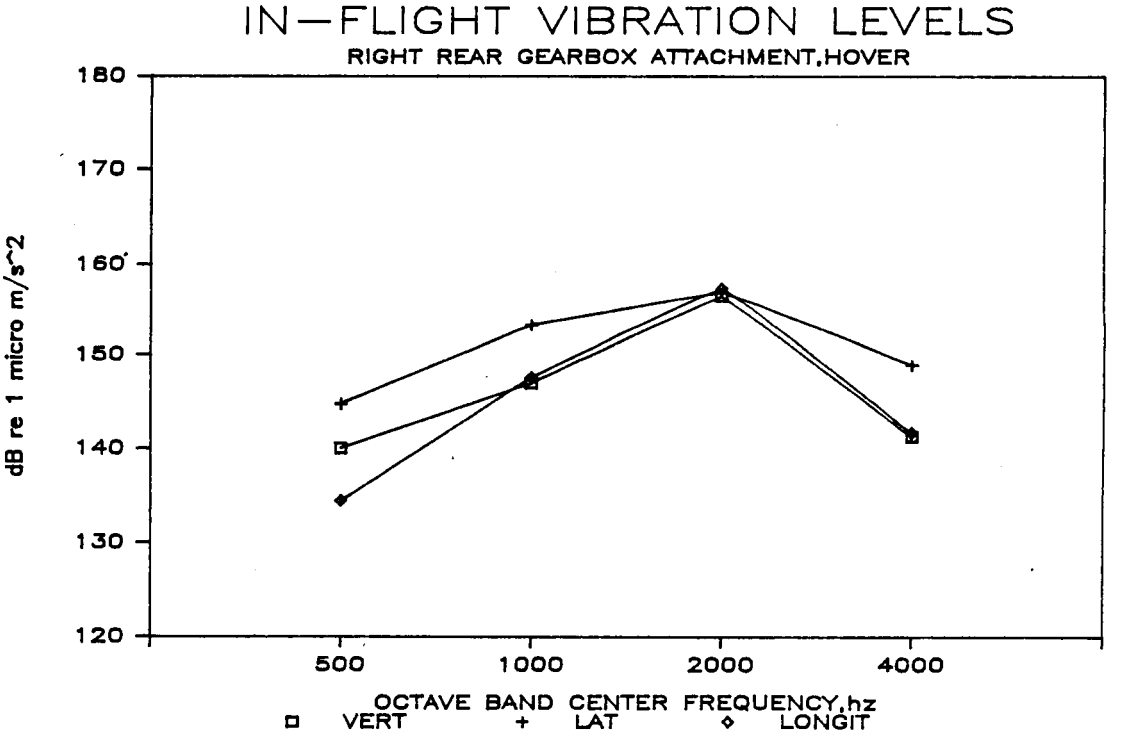

Figure D41. S-76 In-Flight Vibration Measurements, Right Rear Transmission Interface Summary, Hover

Side panel and window vibration levels measured in flight are shown in Figure D43. SP14L and SP56L represent cabin side panels that are aluminum honeycomb construction, and follow the same trend as the previous figure with vibration level increasing with frequency. The levels measured on SP14L are 5-15 dB higher than those measured on SP56L, with the 500 hz octave the most similar and the 1k and 2k approximately 15 dB different. The remaining subsystems are clear thermoplastic windows that are installed in the aft and forward side panels and the left side cabin door. They display a level distribution with frequency similar to that of the sheet aluminum shear panels refered to previously. The aft side panel window, SW14L is 10-20 dB higher than both DW45L and SW56L, and has higher 500 hz, and 1khz levels, and is equal to 2khz to the levels measured on the panel that it mounts to, SP14L. This trend is apparent at the forward side panel and window, SP56L and SW56L, with the levels approximately 15-20 dB lower.

The rear bulkhead positions measured were located on each of the left, middle, and right thirds of its span, on areas of different structural character (see Figure D44). Position 1 was located on a stiffening rib in the starboard third, position 2 on a thin cover plate approximately in the center, and position 3 in the port third in between stiffeners. These data are shown in Figure D45, and show higher levels in the center on the unstiffened cover plate in the 500, 1000 and 2000 hz octaves. Position 1 data shows the lowest levels across the frequency range, with competition at 2000 hz, and position 3 shows levels similiar to position 1 in all but the 4000 hz octave, where it increases to dominate the octave.

The overhead panel measurements performed during flight are shown in Fig. D45. OP23L is an external skin panel adjacent to the source frame LF14L, while OP34L1 is a shear panel, located adjacent to the source frames but riveted to the inboard flange of the surrounding cross frames (see Photo P9). OP4YM is the skin panel forward of CF4M, in between LF451 and R (see Photo P14). OP45L is the skin panel adjacent to the left cabin door and LF45L. OP56L1 is the shear panel inboard at the 56L location, and OP56R1 is the opposite right side panel. The data indicates that OP34L1 has the highest panel vibration levels of the panels measured in the 500, 1k and 2k octaves, with the OP23L panel having the highest 4k octave. Two trends are apparent from this graph, with the panels of aluminum sheet construction and the honeycomb panels setting distinct patterns. The aluminum honeycomb construction panels show vibration levels that increase with frequency, with a slight leveling between the 1k and 2k octave bands. Meanwhile, the aluminum sheet construction panels tend to have the 1Khz octave highest with levels decreasing with increasing frequency above 1k. The bending rigidity of these two constructions is substantially different, with the honeycomb panels the stiffer of the two.

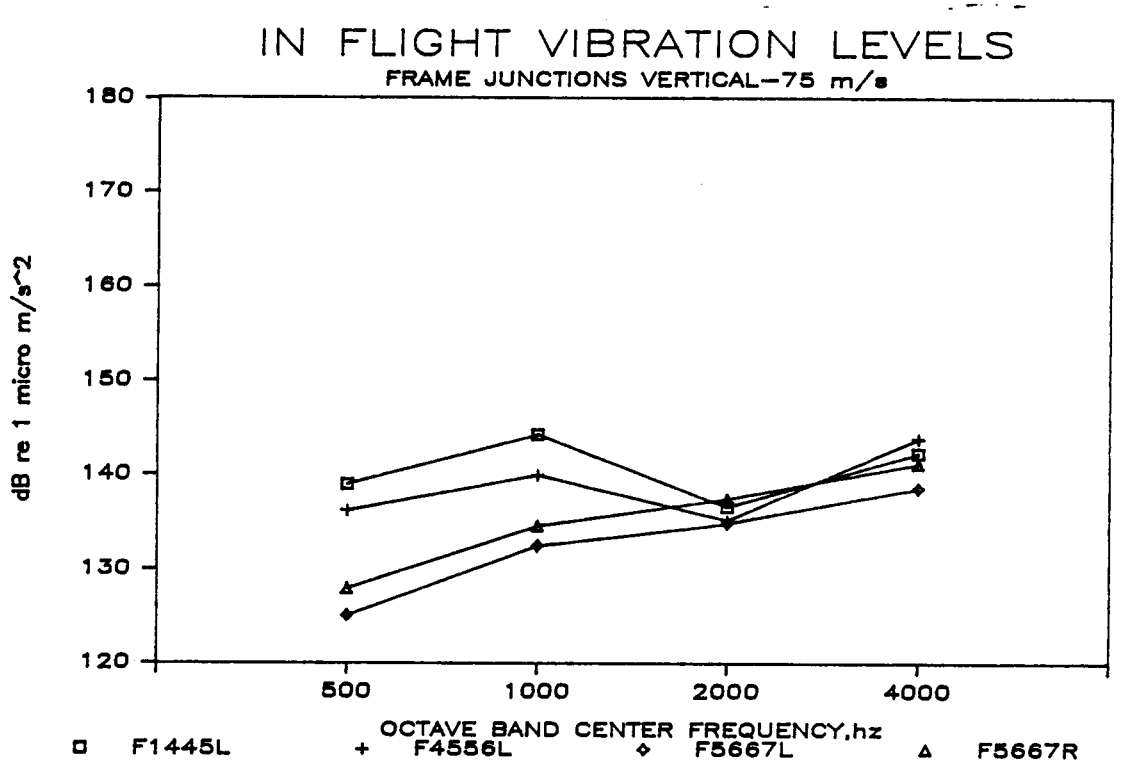

Figure D42. S-76 In-Flight Vibration Measurements, Frame Junctions, Left Side, 75 m/s

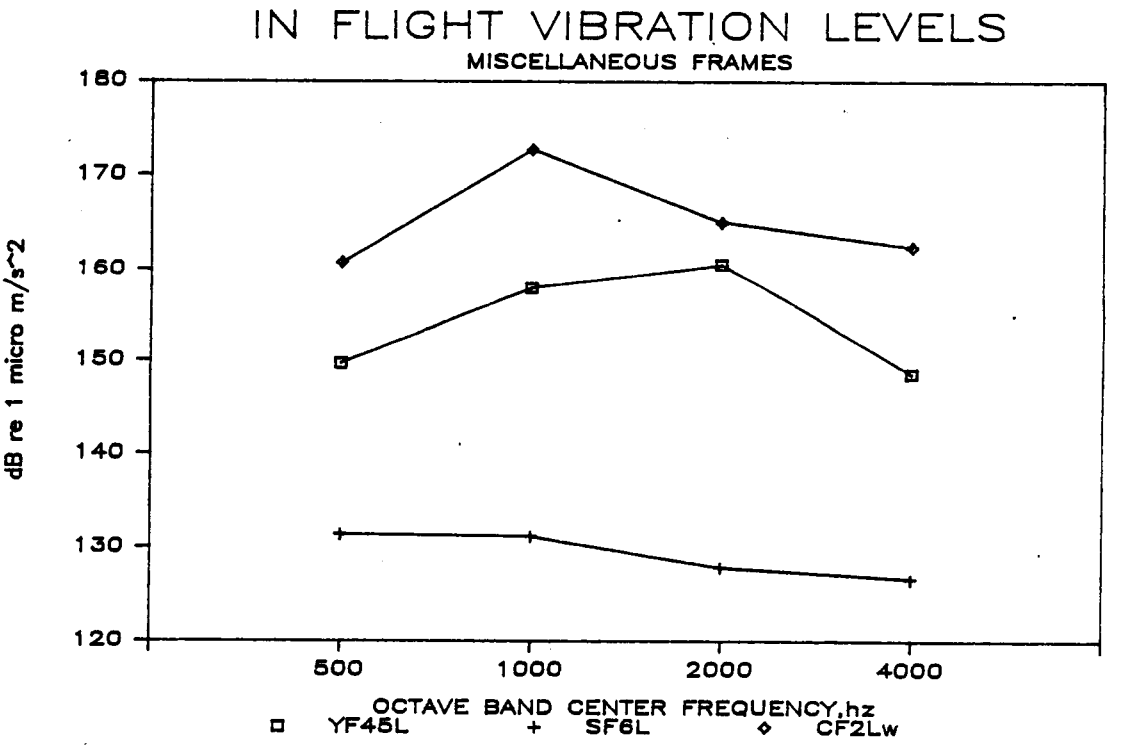

Figure D43. S-76 In-Flight Vibration Measurements, Miscellaneous Frames, 75 m/s

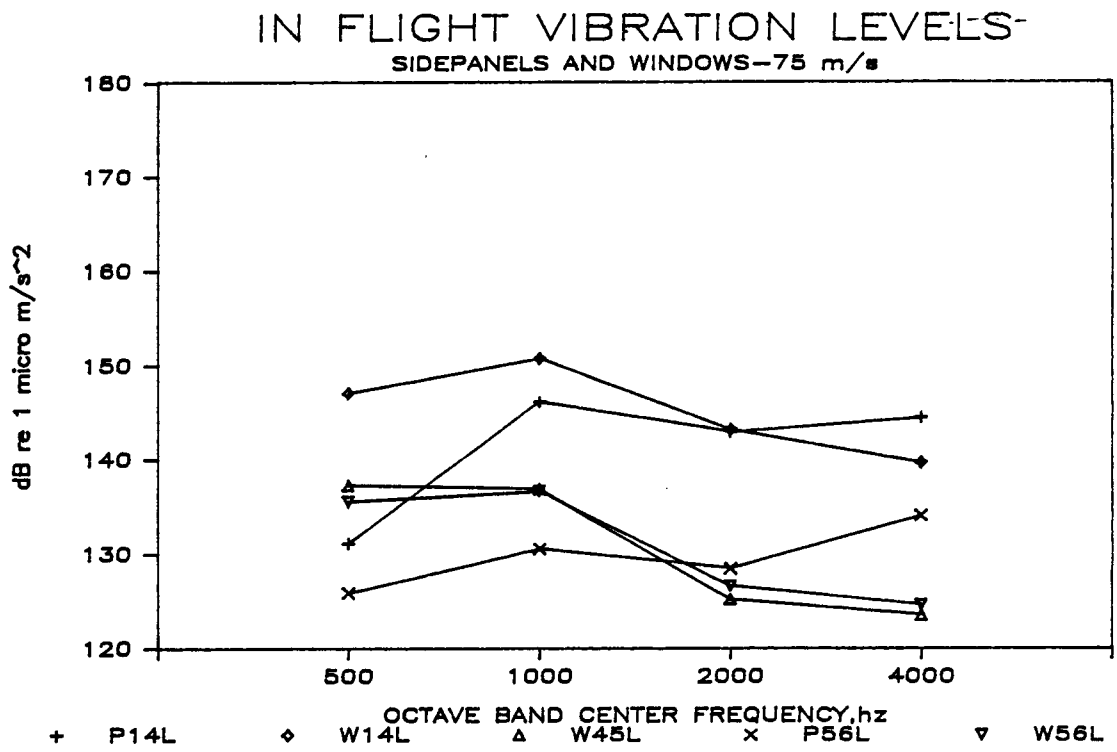

Figure D44. S-76 In-Flight Vibration Measurements, Miscellaneous Side Panels, 75 m/s

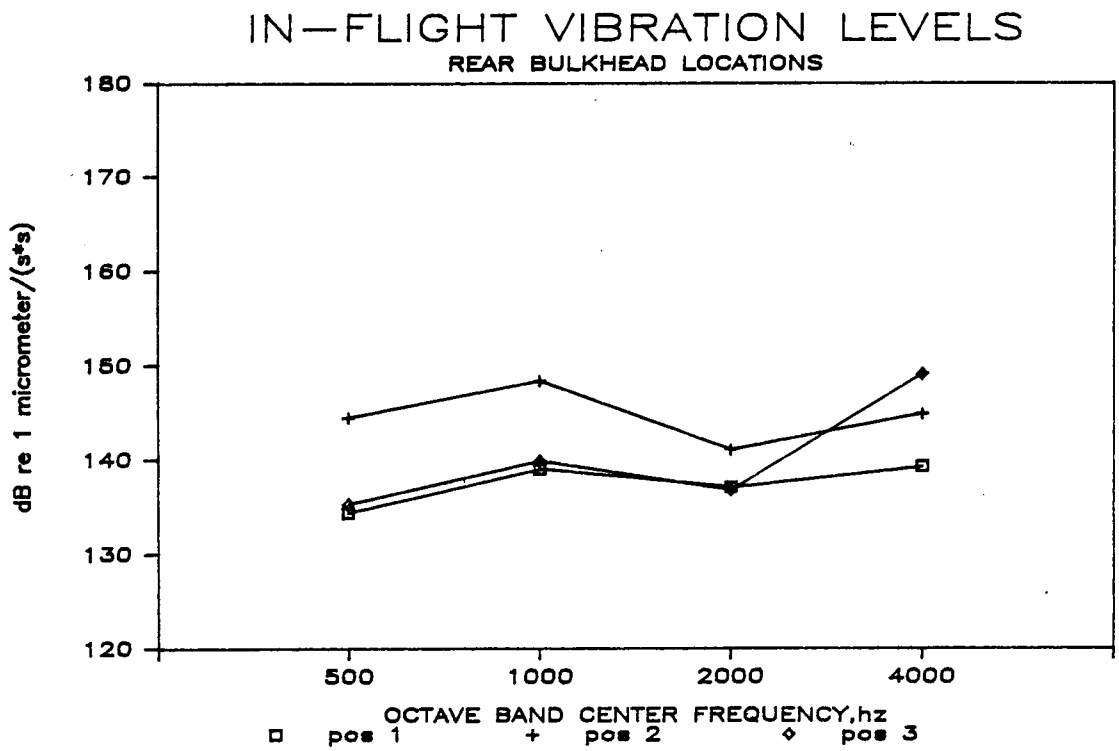

Figure D45. S-76 In-Flight Vibration Measurements, Rear Bulkhead Positions, 75 m/s

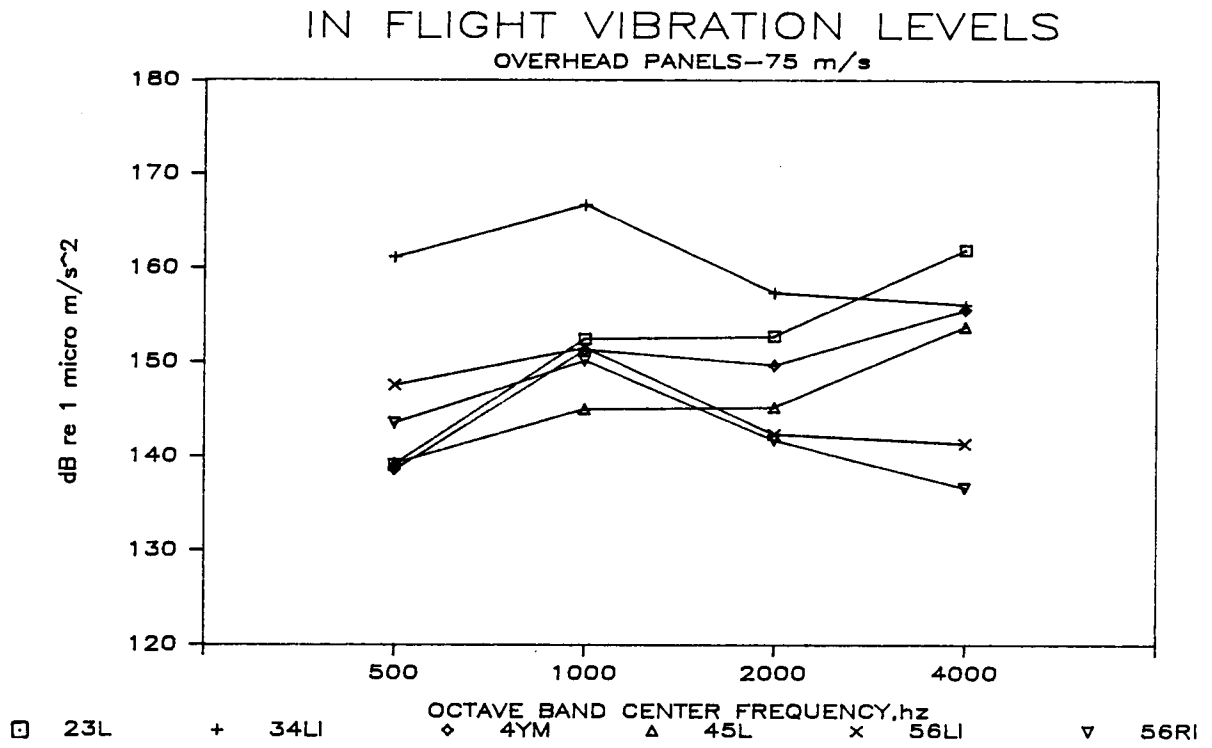

Figure D46. S-76 In-Flight Vibration Measurements, Overhead Panels, 75 m/s

Sound Pressure Levels. - Measurements of sound pressure during 75 m/s forward flight and in-ground effect hover were performed at approximate head level on an S-76 aircraft that was in the bare or untreated cabin configuration. This data is displayed in Figures D47 to D53. During 75 m/s forward flight (see Figures D47 through D50), the aircraft average sound pressure level was 98.7 dB SIL-4. This average includes nine cabin and two (pilot and center) cockpit locations. The cabin average during forward flight was 99.7 dB SIL-4, which includes only the aft, mid, and forward rows (nine seat locations) in the cabin (see Figure D54). The highest speech interference levels (SIL-4) measured were at the starboard mid and port aft, at 102.8 and 102.7 dB SIL-4 respectively (see Figures D49 and D50). Starboard aft, center mid and center aft follow closely at 102.0, 101.6, and 101.0 dB SIL-4 respectively. The center aft seat location is directly beneath the main gearbox, while the other mid and aft seats are adjacent to it. The lowest SIL-4 values measured were recorded in the center cockpit location with a 92.4 dB level. The pilot seat locations and the forward cabin seating location measurements range from 96.6 dB SIL-4 at the starboard forward location to 95.4 dB SIL-4 at the center forward position (see Figures D47 and D48). Note that the starboard mid and forward locations offer a 6.2 dB SIL-4 difference in sound pressure level within 1 meter distance between the two measurements.

The main gearbox bull gear clash frequency of 727.5 hz at 100% rotor speed lies within the 1 Khz octave, as well as the main bevel gear clash at 1221 hz. These gear meshes transfer the main rotor power from the input gears to the main rotor shaft. These make the 1 Khz octave the dominant of the four SIL octaves. The highest 1 Khz octave level recorded was at the starboard mid location, with a level of 110.9 dB. The port aft, center mid, starboard aft, center aft, port mid and pilot locations range from 108.7 to 105.4 dB in descending order. The remaining seat locations, the forward cabin and center cockpit range from 102.3 to 97.1 dB at the starboard forward and center cockpit locations. The average measurement made in this octave was 104.9 dB.

The 500 hz levels range from 103.7 dB to 93.5 dB at the starboard mid and center cockpit seat locations respectively. The seat location sound pressure level ranking follows the 1 Khz ranking closely. The average level in this octave is 98.6 dB, and the grouping of levels is similar to that of the 1 Khz octave, with the aft and mid locations the highest of the eleven measured. The high measurements in the 2K and 4Khz octaves are the starboard aft and port aft, respectively, while the lowest levels were measured in the center cockpit and pilot locations. Changes of note are that the high seat for the higher frequency octaves changes to the aft row, with the starboard mid levels 3.5 dB below the high seat, and the pilot location levels are down in rank with the forward cabin location gaining slightly. Average levels in these two octaves are 97.2 and 94.2 dB for 2Khz and 4Khz, respectively.

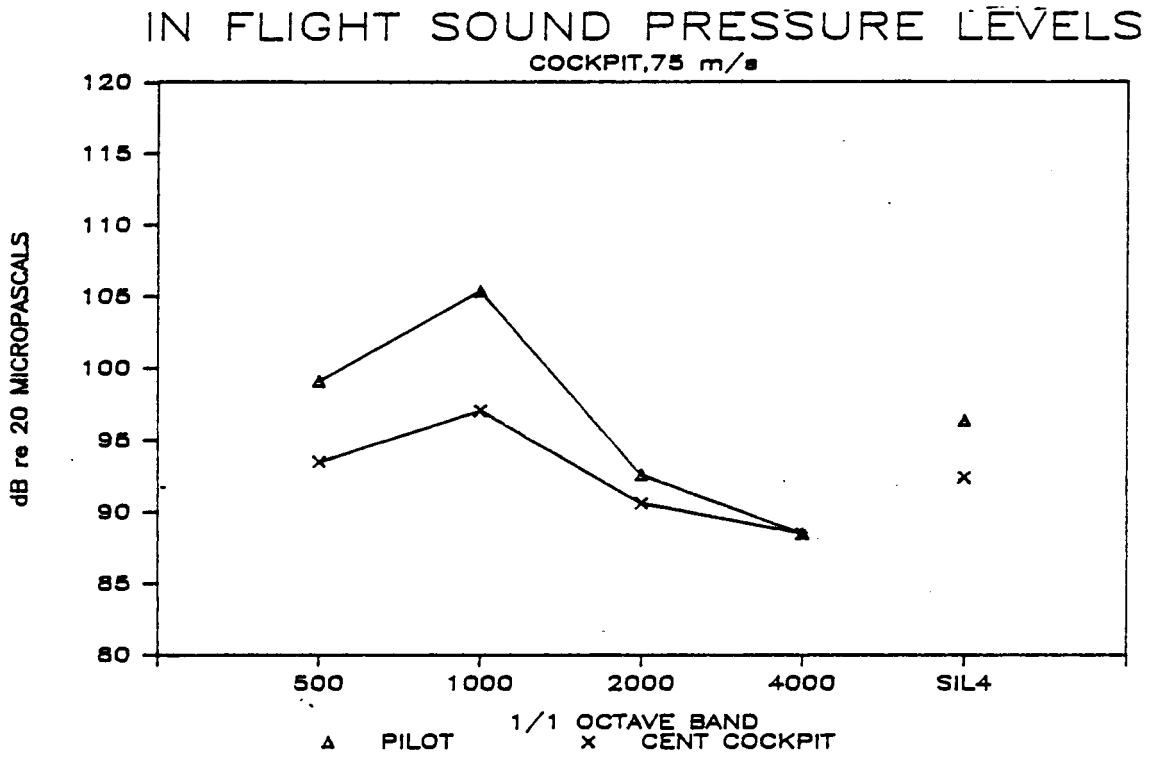

Figure D47. S-76 In-Flight Sound Pressure Measurements, Cockpit Locations, 75 m/s

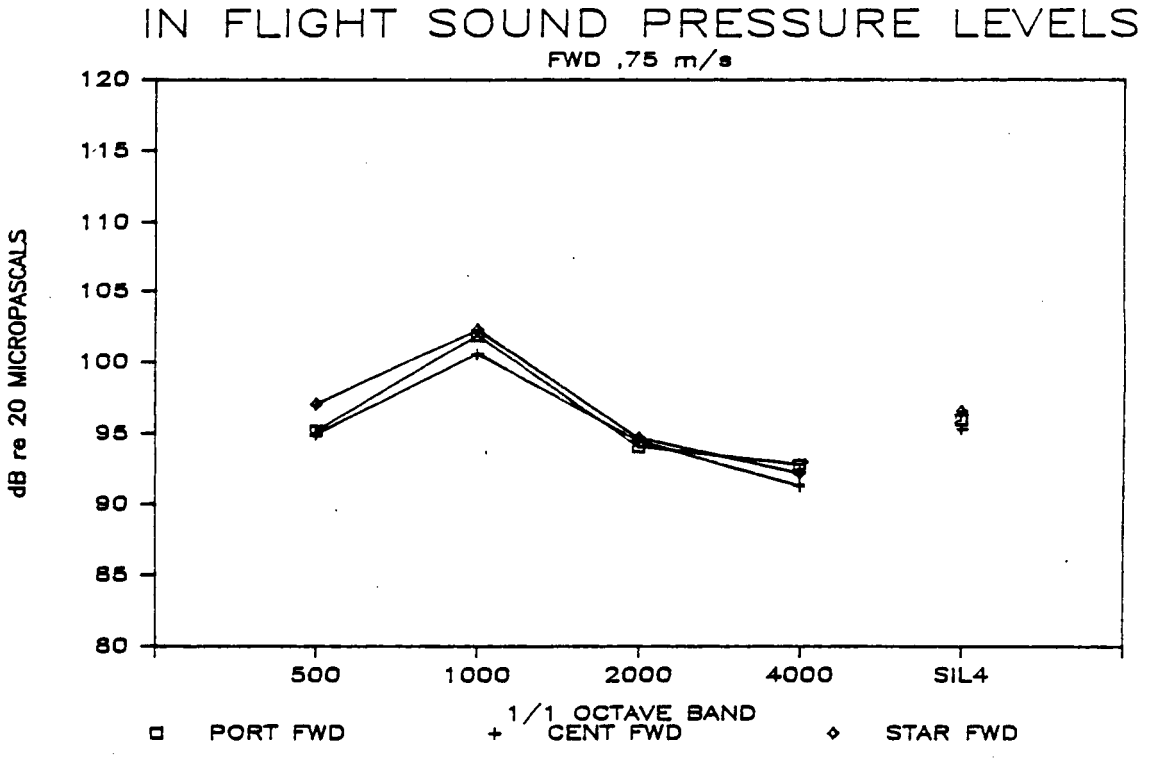

Figure D48. S-76 In-flight Sound Pressure Measurements, Forward Cabin Seating Locations, 75 m/s

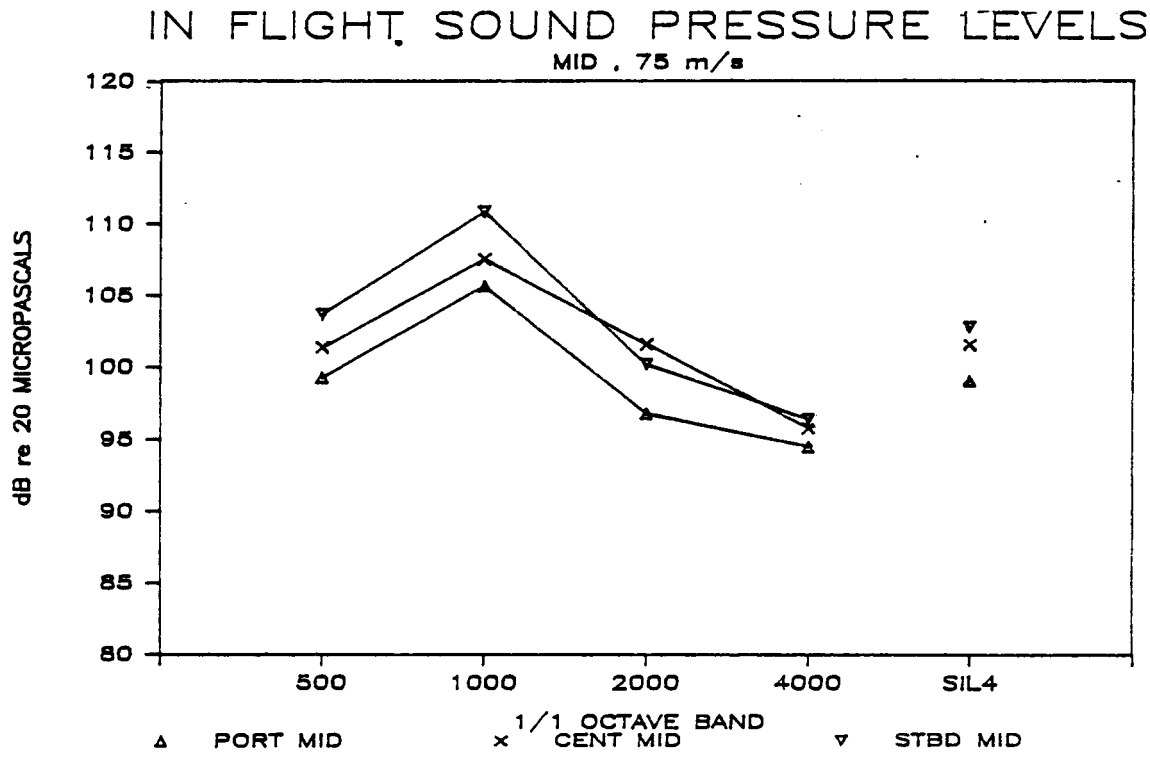

Figure D49. S-76 In-flight Sound Pressure Measurements, Mid Cabin Seating Locations, 75 m/s

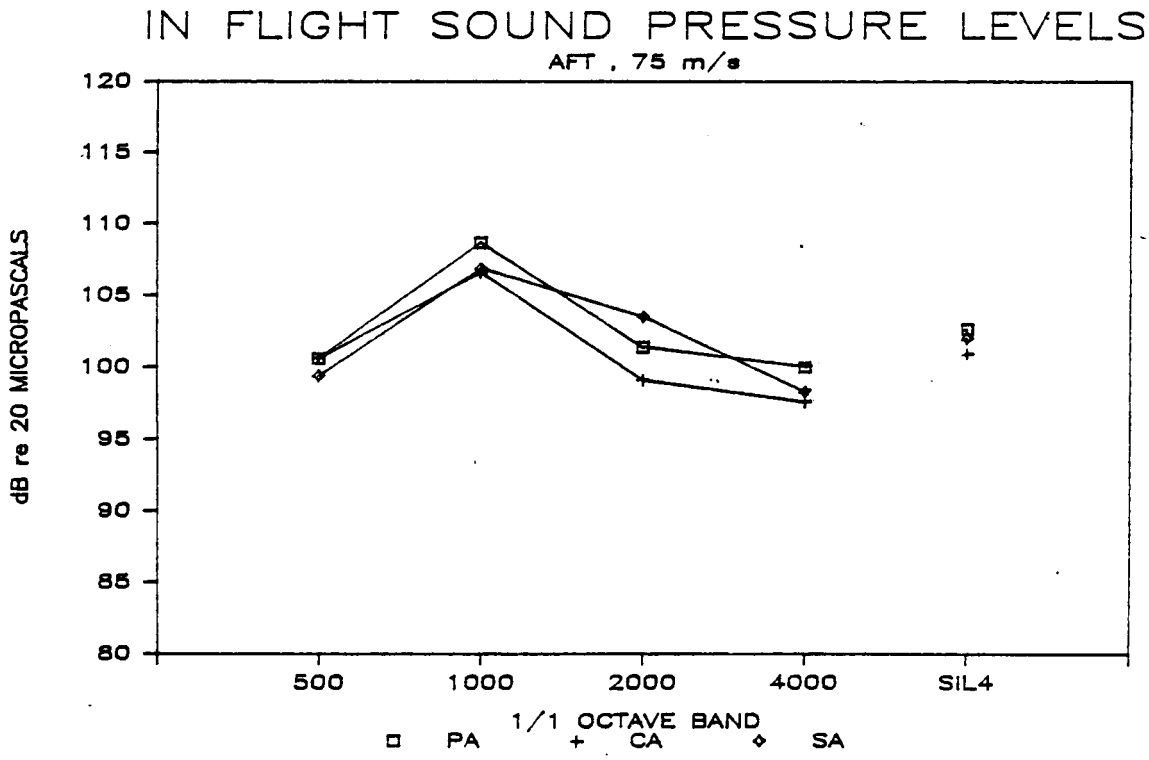

Figure D50. S-76 In-flight Sound Pressure Measurements, Aft Cabin Seating Locations, 75 m/s

Measurements performed during hover are shown in Figures D50 through D53. The cabin average sound pressure levels measured were 99.4 dB SIL-4 (see Figure D53). The port aft seat has the highest SIL-4 value while the port mid seat shows higher 500 hz and 1 Khz levels, and 1 dB less on the SIL-4. The aft and mid rows show the dominance in level (see Figures D50 and D51), much like the forward flight data, except with the port aft and mid, adjacent seats, the two highest locations. The forward seat locations represent the lowest measurements made in hover (see Figure D52), with the port forward lowest at 95.3 dB. The 1 Khz octave level measured at the port mid location was 112.1 dB, 6 dB greater than the cabin average and highest of either flight condition. The next highest 1 Khz octave was measured at the port aft location, at 108.9 dB and the remaining aft and mid locations ranging down to 105.8 dB. The forward locations show 1khz octave levels from 102.6 to 101.7, starboard forward and port forward, respectively.

In the 500 hz octave, the cabin average is 98.5 dB, with the port mid location 7.1 dB above this and the port forward 3.9 dB below. The 2 Khz and 4 Khz octaves have 97.9 and 95.2 dB cabin averages respectively. Both have the port aft as the highest at 103.8 and 101.2 dB, and the port forward the lowest at 93.5 and 91.4 dB respectively.

Figure D54 shows the comparison between hover and 75 m/s flight data to be very similar in level at all frequencies. This is interesting because the horsepower required for the two conditions are nearly the same. Figure D55 contains the narrowband acoustic spectra under typical flight conditions for a bare aircraft. The obvious pure tone contributions from main gearbox gear clash are present and one also notices a decrease in level further from the dominant source.

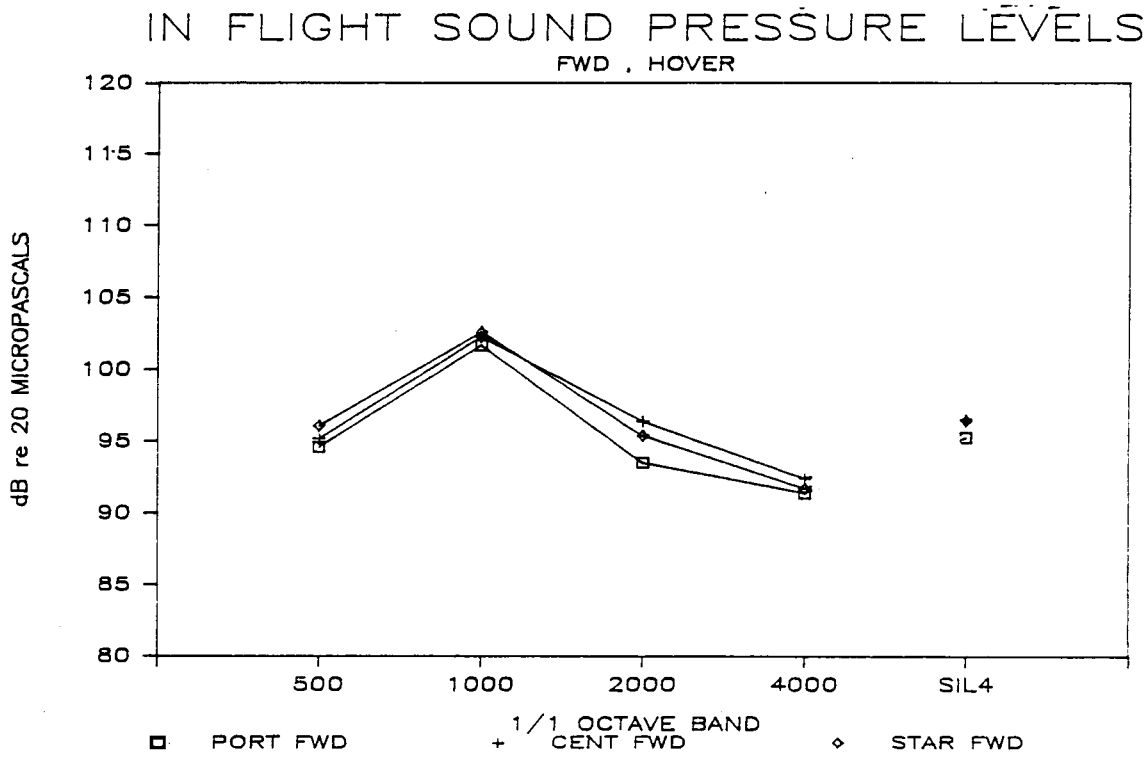

Figure D51. S-76 In-flight Sound Pressure Measurements, Forward Cabin Seating Locations, Hover

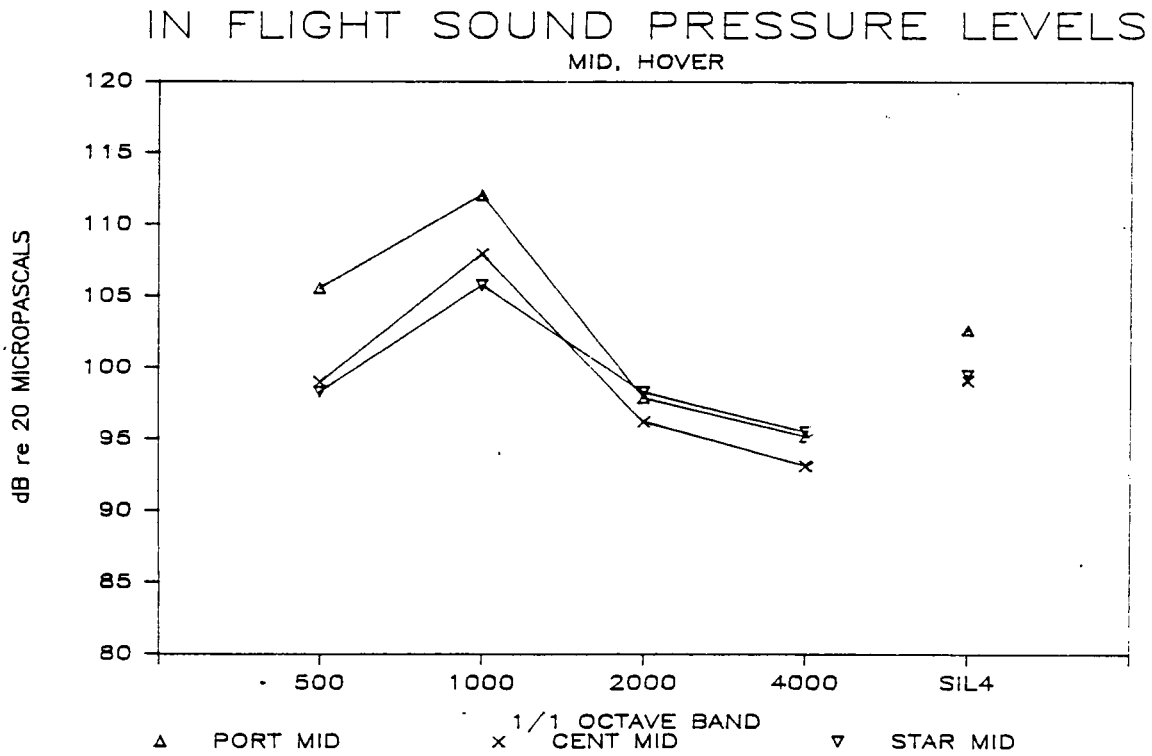

Figure D52. S-76 In-flight Sound Pressure Measurements, Mid Cabin Seating Locations, Hover

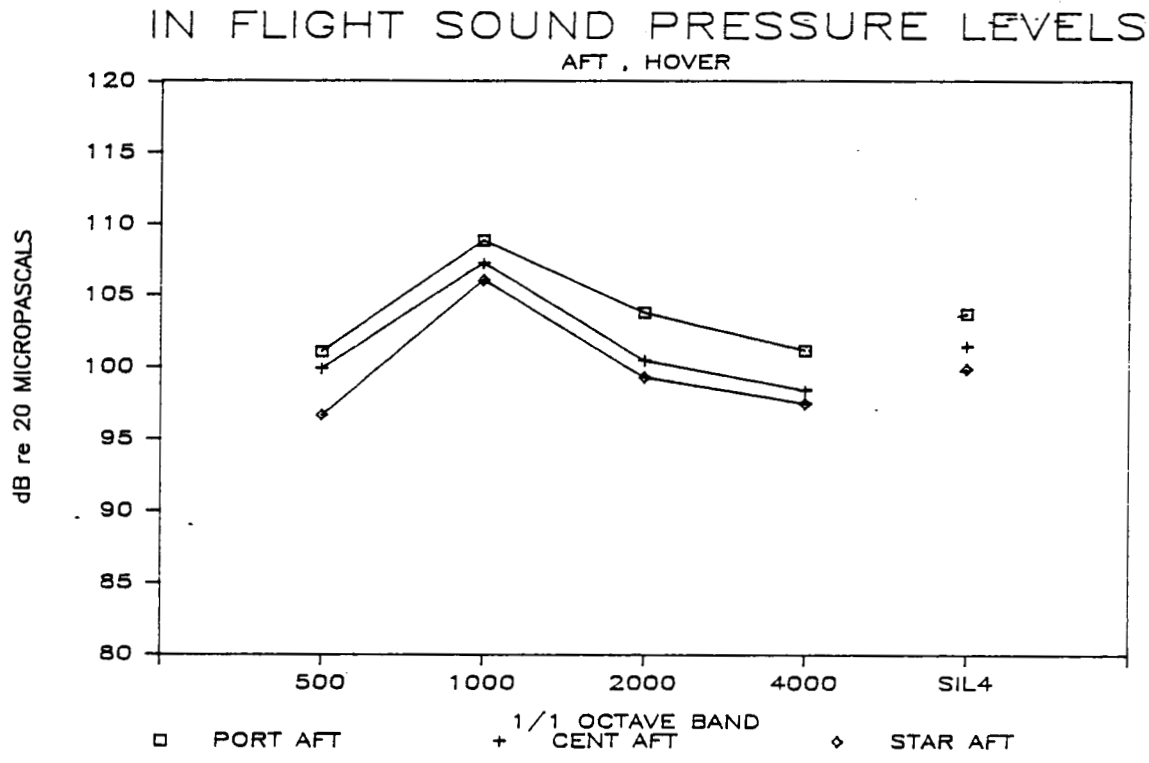

Figure D53. S-76 In-flight Sound Pressure Measurements, Aft Cabin Seating Locations, Hover

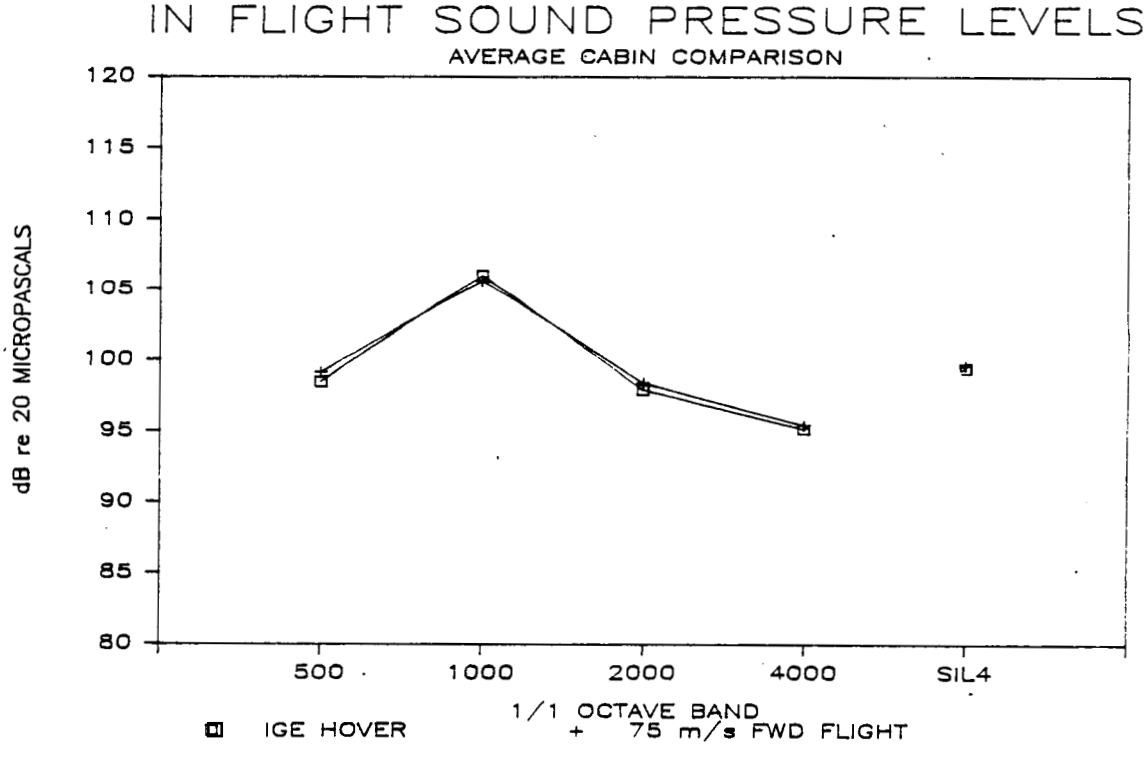

Figure D54. In-Flight Cabin Average Sound Pressure

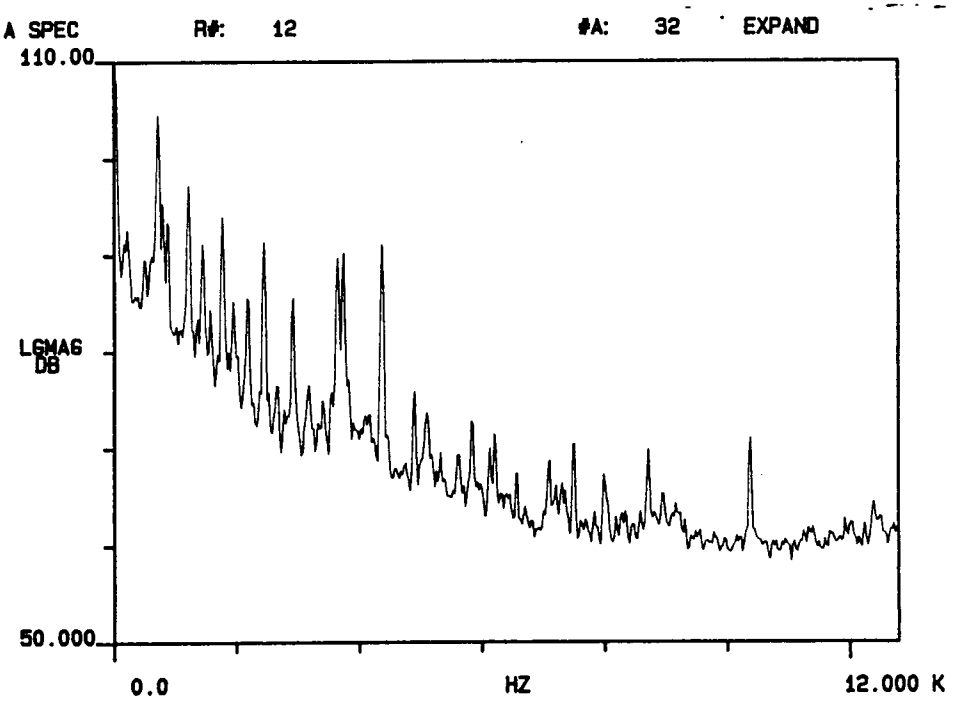

a. Center aft

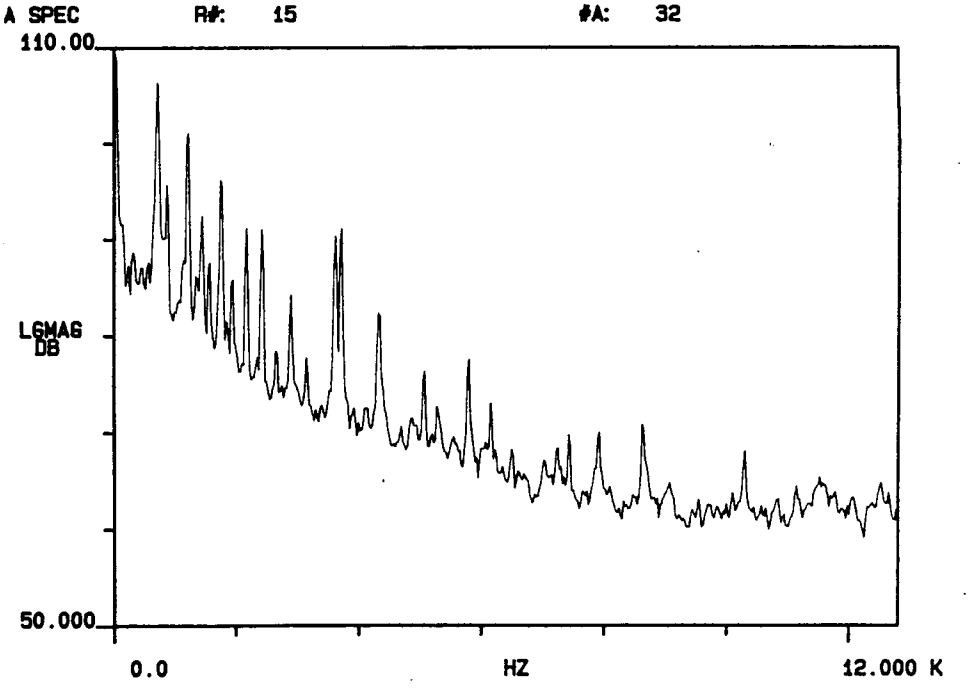

b. Center mid

Figure D55. S76 In-flight Sound Pressure Measurements, Narrowband Spectra, Center aft, Center mid, Center fwd., and Center cockpit

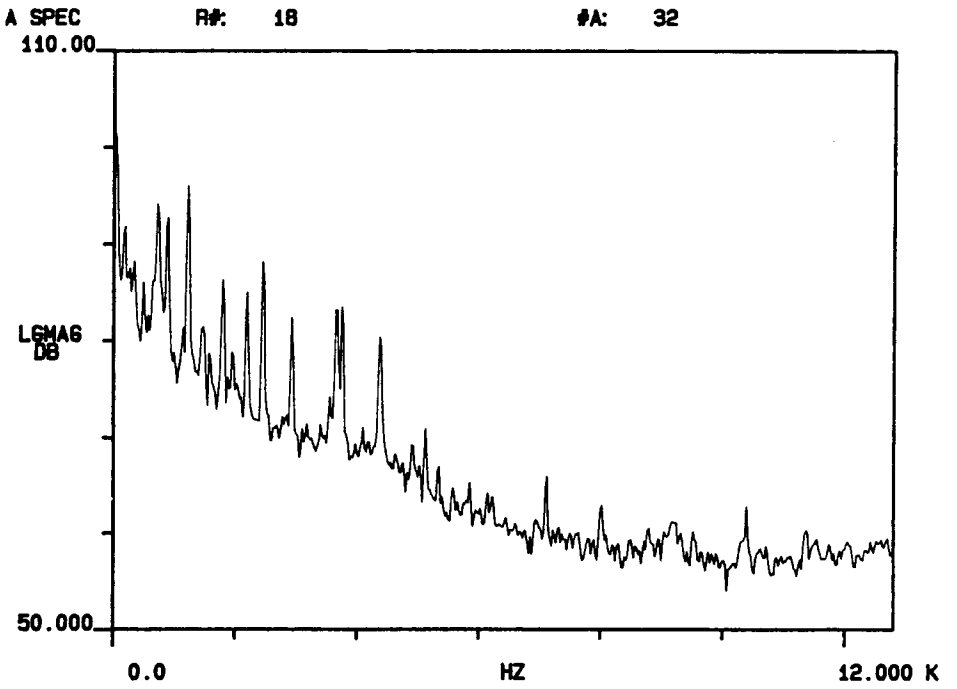

c. Center fwd.

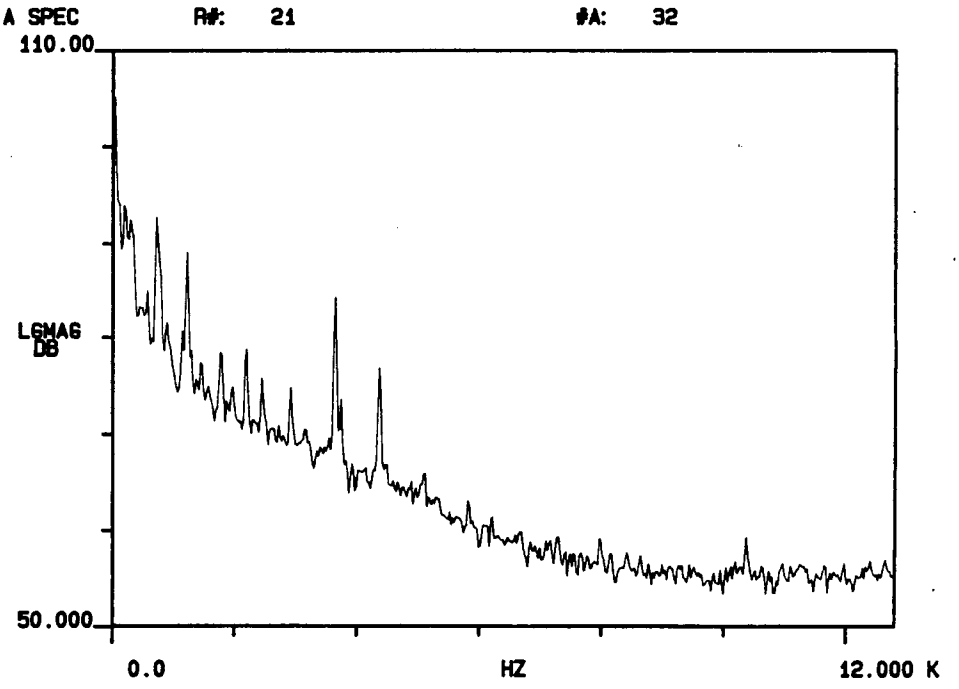

d. Center cockpit

Figure 55. Concluded

APPENDIX E

COMPARISON OF SEA PREDICTIONS WITH MEASURED DATA

TABLE OF CONTENTS

Introduction

The information provided in this appendix is comprised of ground and flight test comparison of measured vibration and noise on an S-76 and predicted vibration and noise using the SEA method. These results provide validation of this method and its application to a rotorcraft structure. Ground test measurements of subsystem response to vibratory excitation are compared to predictions and results are discussed, and a brief statistical analyses is provided. Flight test comparisons of cabin sound pressure is presented as well as the method of input vibratory source power determination for the flight condition.

Ground Test Measurements

The extensive combinations of ground test measurements described in Appendixes C and D will be compared with SEA predictions. The SEA predictions start with an input power into either the combined in-plane motion or the out-of-plane motion at LF14, the main gearbox support. Due to the structural geometry, it is very difficult to excite the structure purely in one of these analytic inputs. One would thus expect some differences between measured and predicted values.

Vibration transfer functions. - The comparison of measured ground test data with SEA predictions is shown in Figures E1 through E31. These data represent the majority of the validation information important to the application of the SEA method to rotorcraft structure and the accuracy that can be expected. As mentioned in previous sections, the predictions for unity input are scaled to the measurement by zeroing the average difference between the measured and predicted levels for four near source subsystems, for each octave.

The left front vertical excitation position (FALV) comparisons are shown in Figures E1 through E8. These data show generally good agreement in all cases except possibly the high frequency (4kHz) octave, which tends to be overpredicted. Figure E1 shows comparison of vertical frame response levels, and indicates differences of 5 dB max at 500 Hz, 2 and 4 dB up to CPM at 1k and 2khz, and 6 dB at 4khz. The CPM levels are underpredicted by 18 dB at 1khz and 2khz. This subsystem is of composite construction, as is the entire cockpit outer structure, and connects to the longitudinal frame through PP7wL, a subsystem with questions associated with its modeling (see Appendix F). Figure E2 shows the right side vertical frame response from FALV to be very similar in measurements and predictions, with lower levels as it is opposite from the source side. Here, in the 2k and 4k octaves, the tendency to overpredict is apparent, at all but the cockpit subystems, well downstream of the source. Note the CPM issue is apparent here also.

Figure E3 shows the left side overhead panel comparisons, which include the rear bulkhead and windshields for comparison. These two subsystems, being very near and far from the source respectively, provide the greatest difference between measured and predicted levels with 12 dB for RB at 500 hz and -12 dB for FWL at 4000 hz. In general, however, these data show good agreement in all four octaves. Figure E4 shows the center overhead panel comparisons. The 500 hz and 1khz octaves show good agreement for all panels measured, while the 2k and 4khz shows tendency to overpredict by an average of 7 dB in all subsystems except OP14D. Predictions for OP14D are consistently lower than measurements by an average of 10 dB across these four octaves. Figures E5 displays the right side overhead panel response to FALV excitation. Comparisons for 500 hz match predictions well with RB an exception. General trends in 1k, 2k, and 4khz are preserved, with the differences increasing with increasing frequency. The overprediction is evident in 2k and 4k, with 4k an average of 10 dB overpredicted. Figure E6 shows the panels between cross frames 5 and 6, going left to right up, across and down the airframe. For these subsystems, the average predictions minus measurement delta increases with increasing frequency. The trend of these data is higher response levels on the left and center than right side. At high frequencies, a tendency to overpredict the right side panel and overhead panel becomes apparent. Figure E7 shows the cockpit overhead panels left to right. The measured vs. predicted comparison, is quite reasonable considering the fact that these subsystems are at a substantial distance from the source. The maximum deviation occurs in the 4000 hz octave at OP67M, which is 11 dB overpredicted. The remaining predictions are within 5 dB of measurements. Figure E8 shows the variation in levels at panels clockwise around the aircraft, from the right windshield (FWR) to the right side panels, the rear bulkhead, the left side panels and left windshield. Although some over and under prediction occurs, the general trends are in agreement.

The left front lateral excitation (FAL Lat) transfer function comparisons are shown in Figures E9 through E14. The lower response levels associated with this excitation are accounted for by the near-source scaling of the SEA predictions with measurements. Figure E9 shows the results for the left side longitudinal frames in the vertical or out-of-plane direction. The delta between predictions and measurements decreases with increasing frequency. Although the LF67 and CPM levels are underpredicted, the remaining subsystems are predicted very well, especially at the higher frequencies. The input into the SEA model for this excitation is power into the in-plane subsystem of LF14L.

Figure E10 shows that predictions compare favorably with measurements for the left side overhead panels at frequencies above 500 hz. The 500 hz octave shows inconsistent RB and OP34L predictions, as the SEA model predicts a smooth response curve for adjacent subsystems with a decrease in level with distance from the source. Figure E11 shows the center overhead panels are underpredicted at 500 hz, but gradually move towards overprediction with increasing

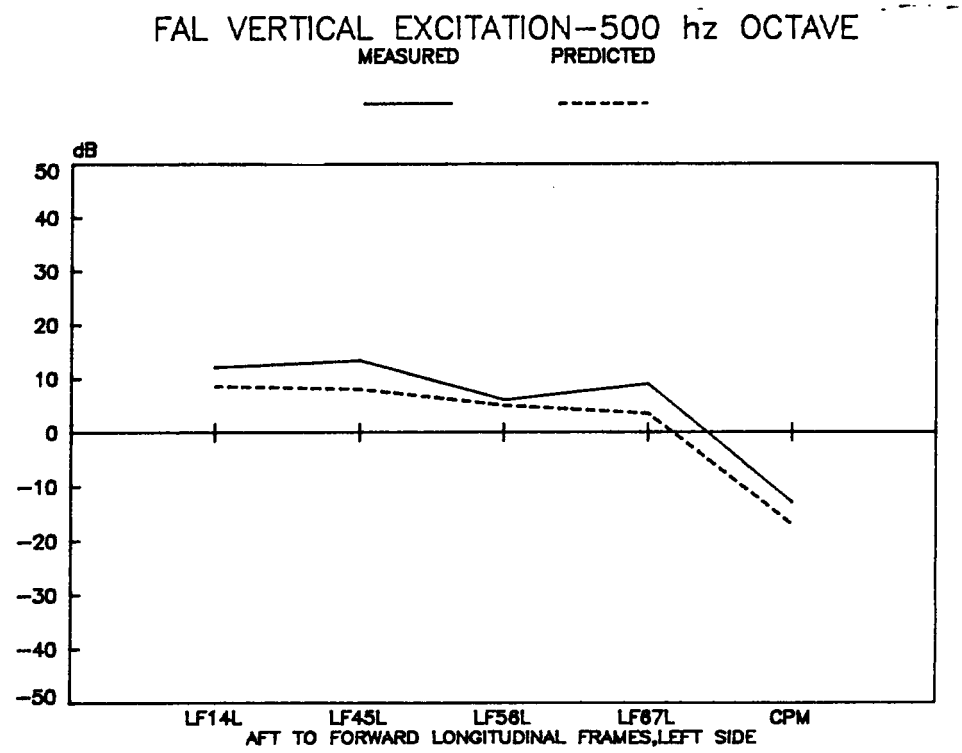

Figure E1a. Measured vs. Predicted Overhead Frame Vibration, Left Side, FAL Vertical Excitation, .5 kHz

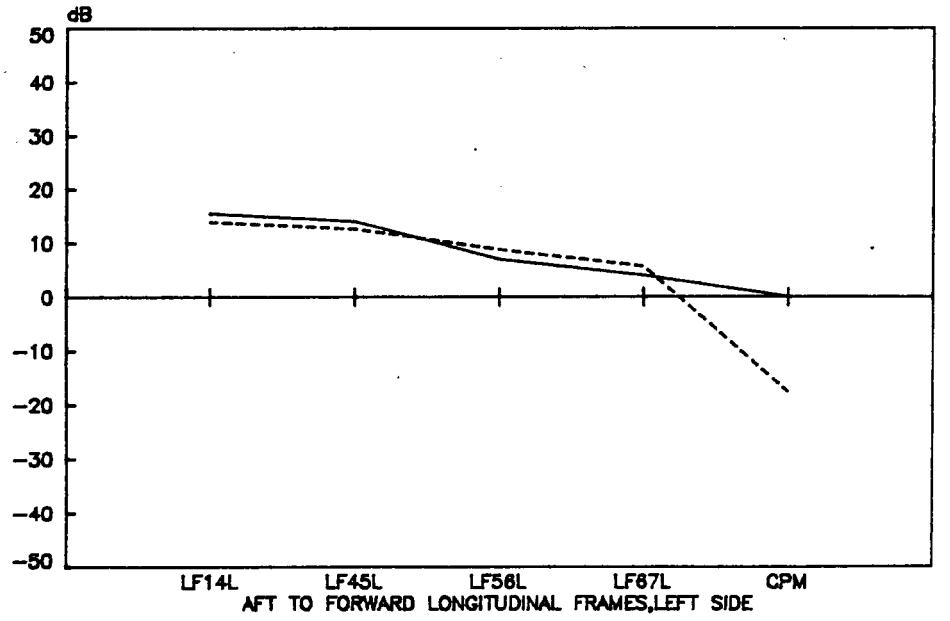

Figure E1b. Measured vs. Predicted Overhead Frame Vibration, Left Side, FAL Vertical Excitation, 1 kHz

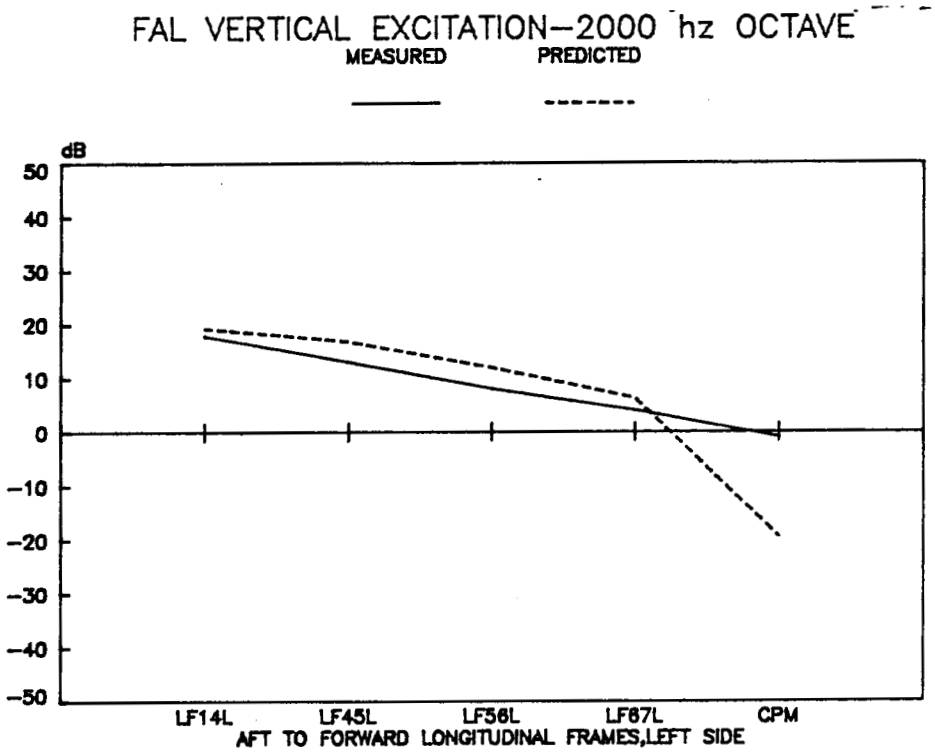

Figure E1c. Measured vs. Predicted Overhead Frame Vibration, Left Side, FAL Vertical Excitation, 2 kHz

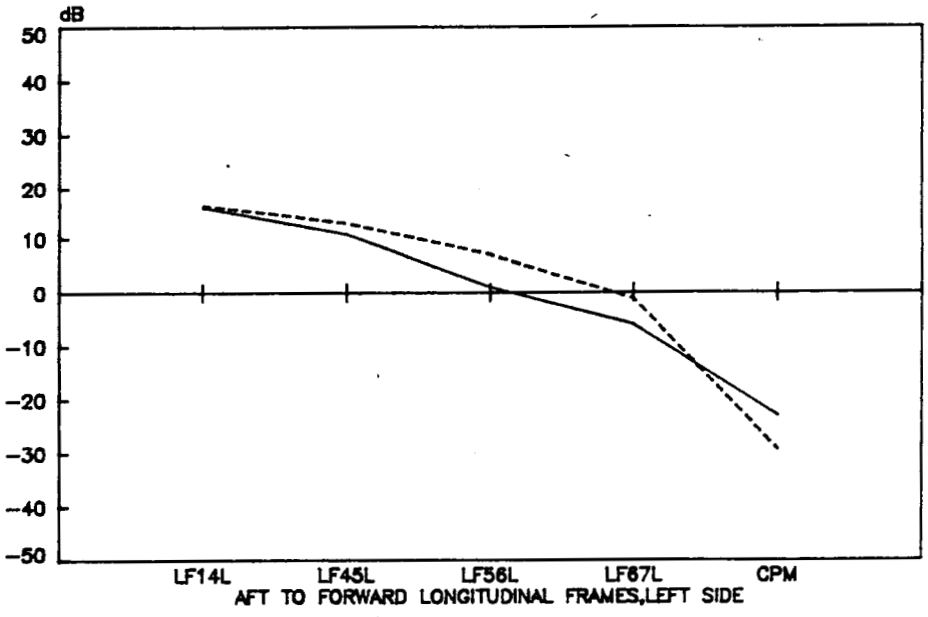

Figure E1d. Measured vs. Predicted Overhead Frame Vibration, Left Side, FAL Vertical Excitation, 4 kHz

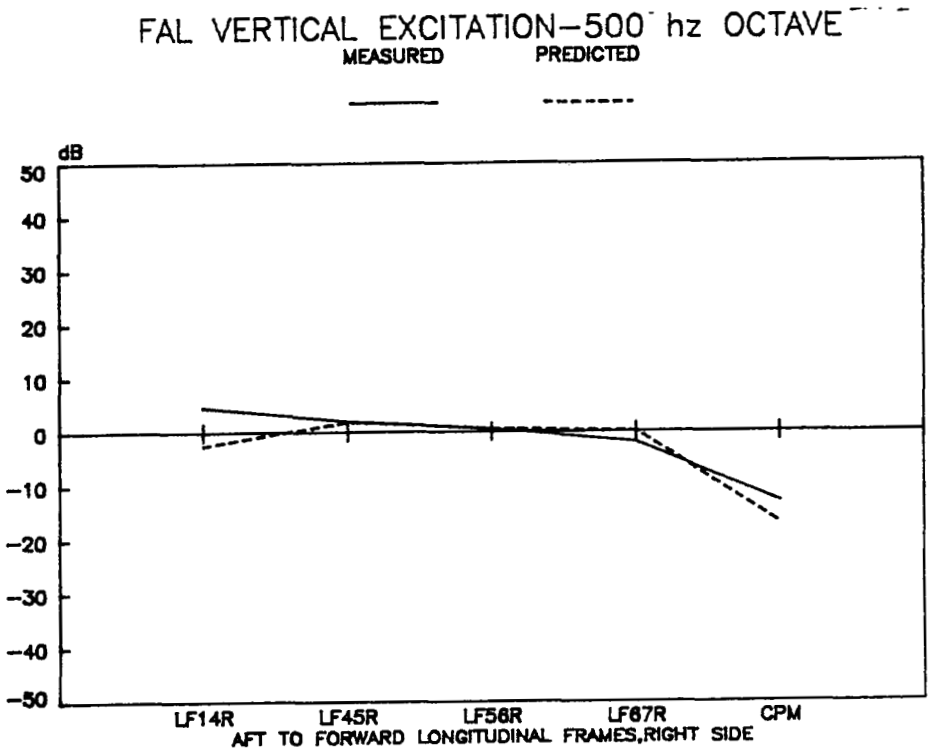

Figure E2a. Measured vs. Predicted Overhead Frame Vibration, Right Side, FAL Vertical Excitation, .5 kHz

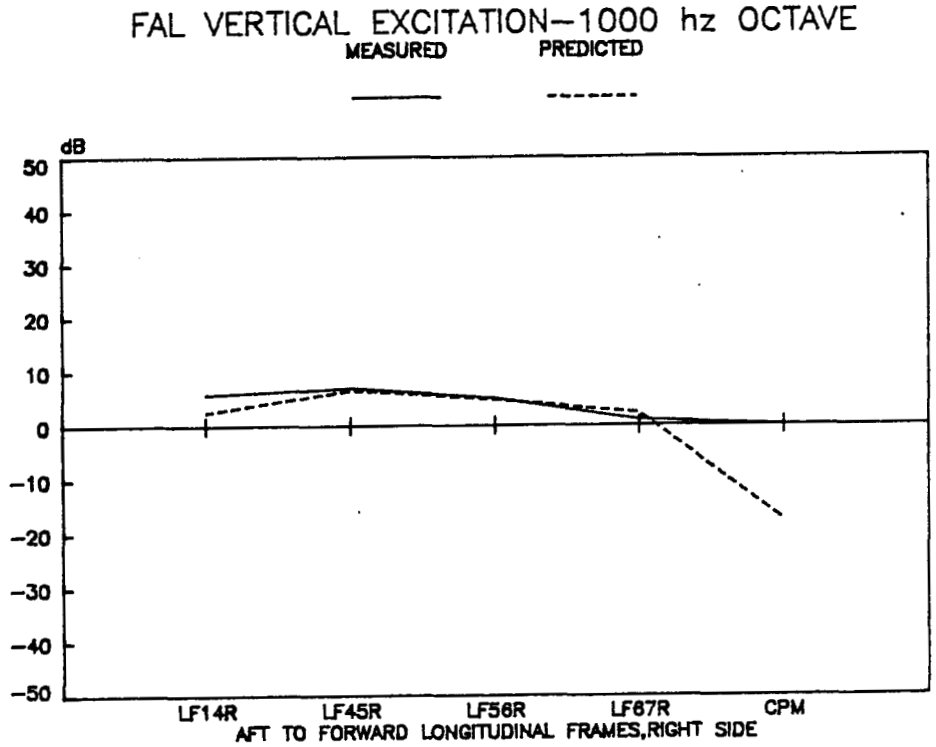

Figure E2b. Measured vs. Predicted Overhead Frame Vibration, Right Side, FAL Vertical Excitation, 1 kHz

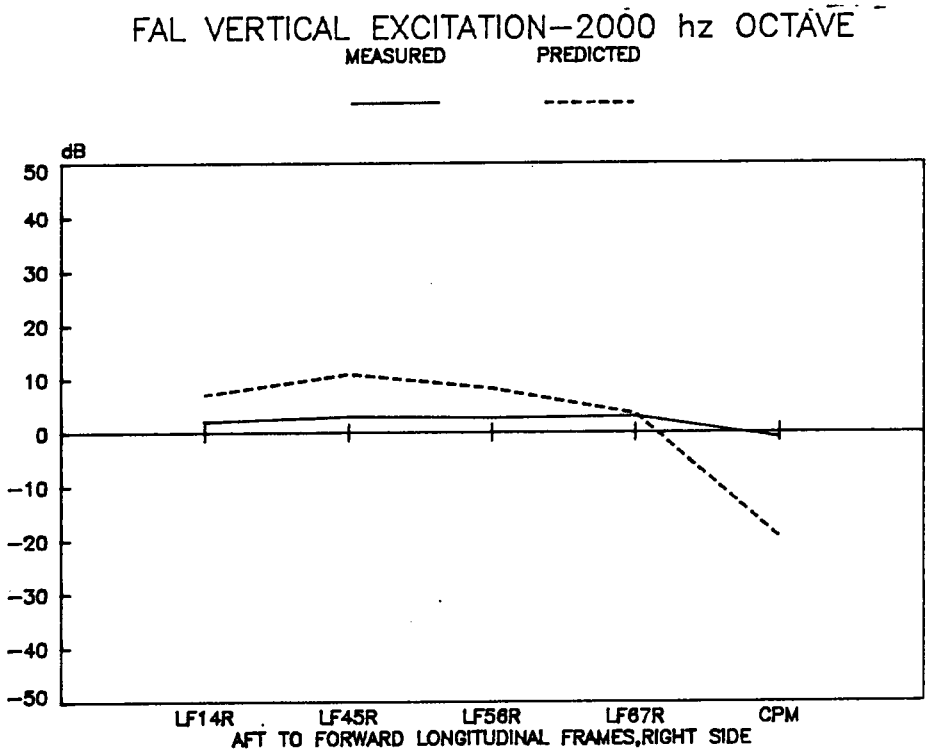

Figure E2c. Measured vs. Predicted Overhead Frame Vibration, Right Side, FAL Vertical Excitation, 2 kHz

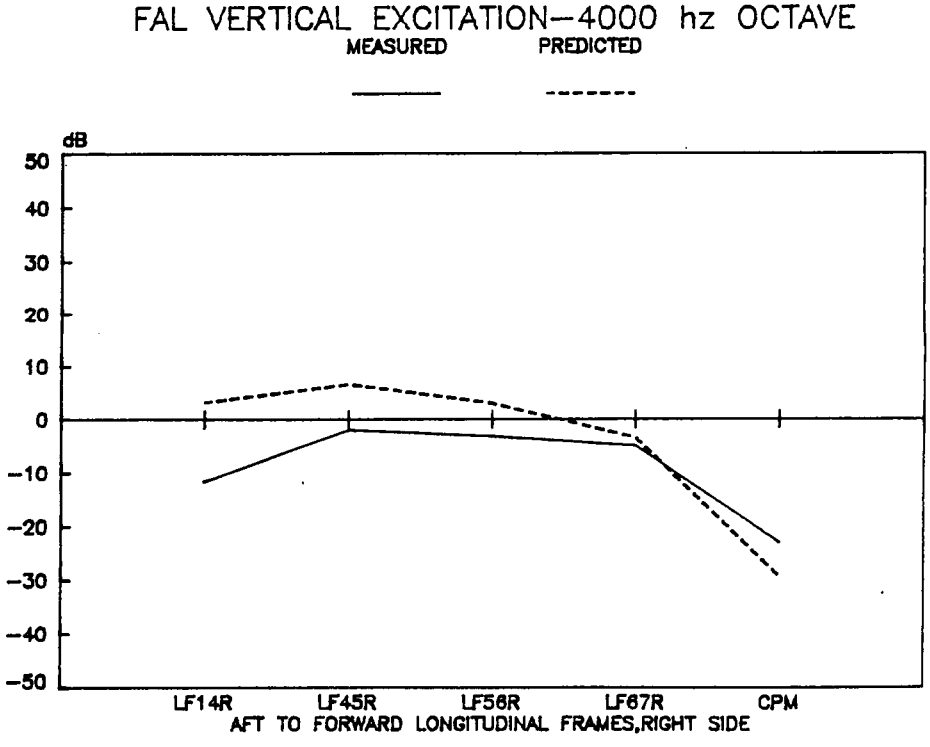

Figure E2d. Measured vs. Predicted Overhead Frame Vibration, Right Side, FAL Vertical Excitation, 4 kHz

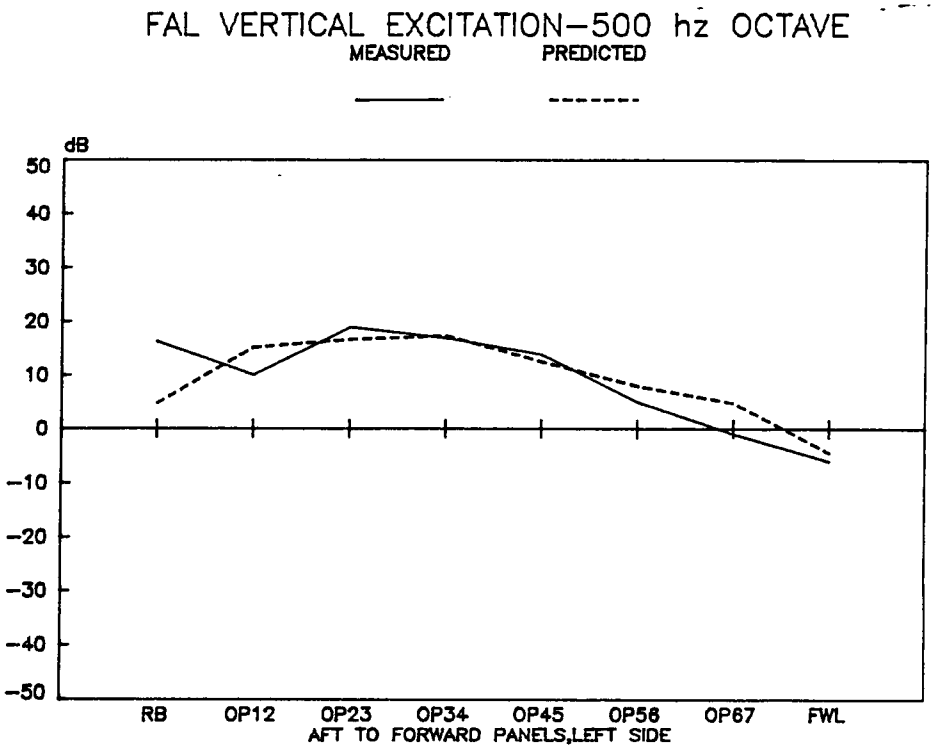

Figure E3a. Measured vs. Predicted Overhead Panel Vibration, Left Side, FAL Vertical Excitation, .5 kHz

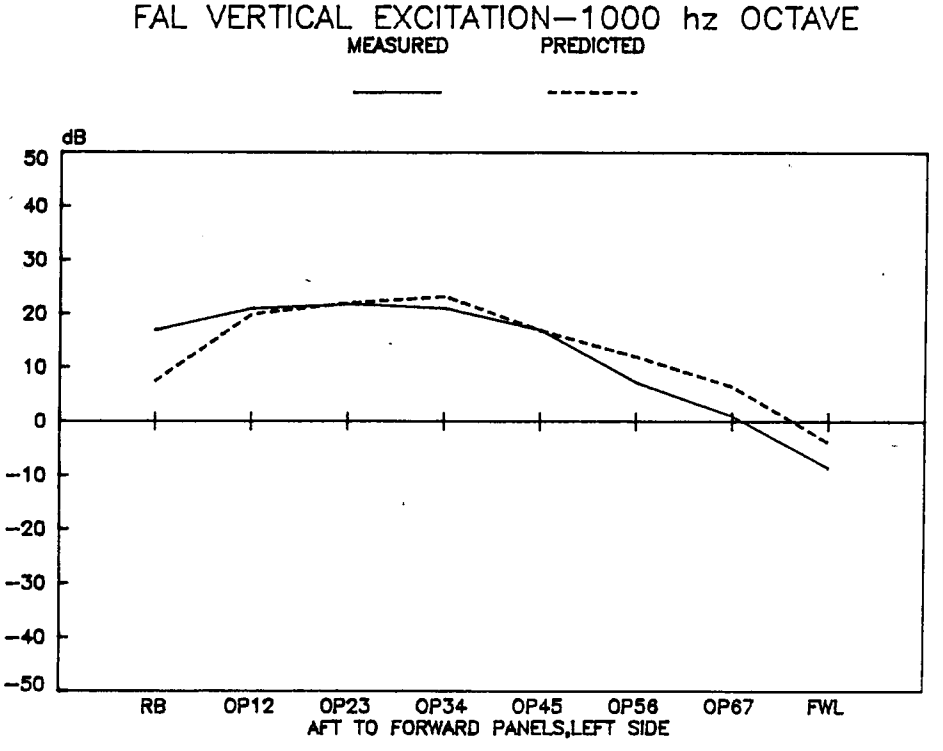

Figure E3b. Measured vs. Predicted Overhead Panel Vibration, Left Side, FAL Vertical Excitation, 1 kHz

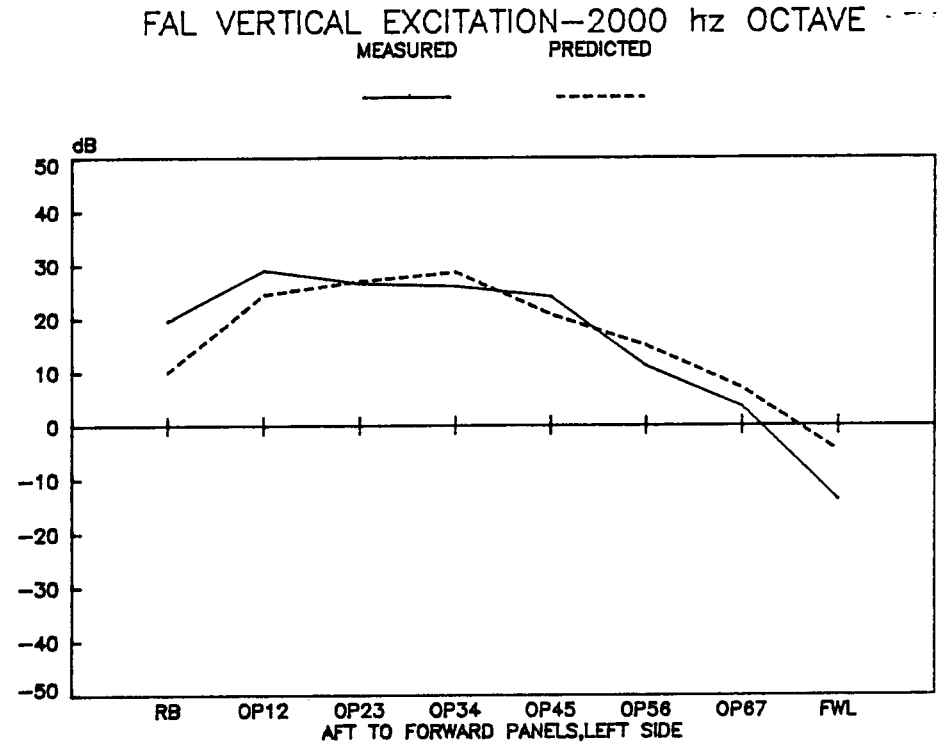

Figure E3c. Measured vs. Predicted Overhead Panel Vibration, Left Side, FAL Vertical Excitation, 2 kHz

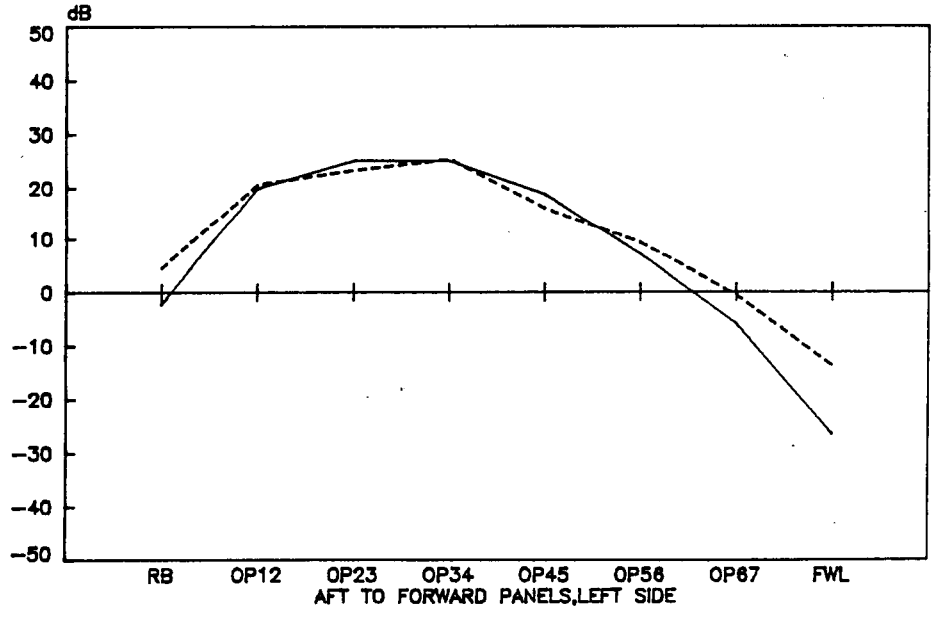

Figure E3d. Measured vs. Predicted Overhead Panel Vibration, Left Side, FAL Vertical Excitation, 4 kHz

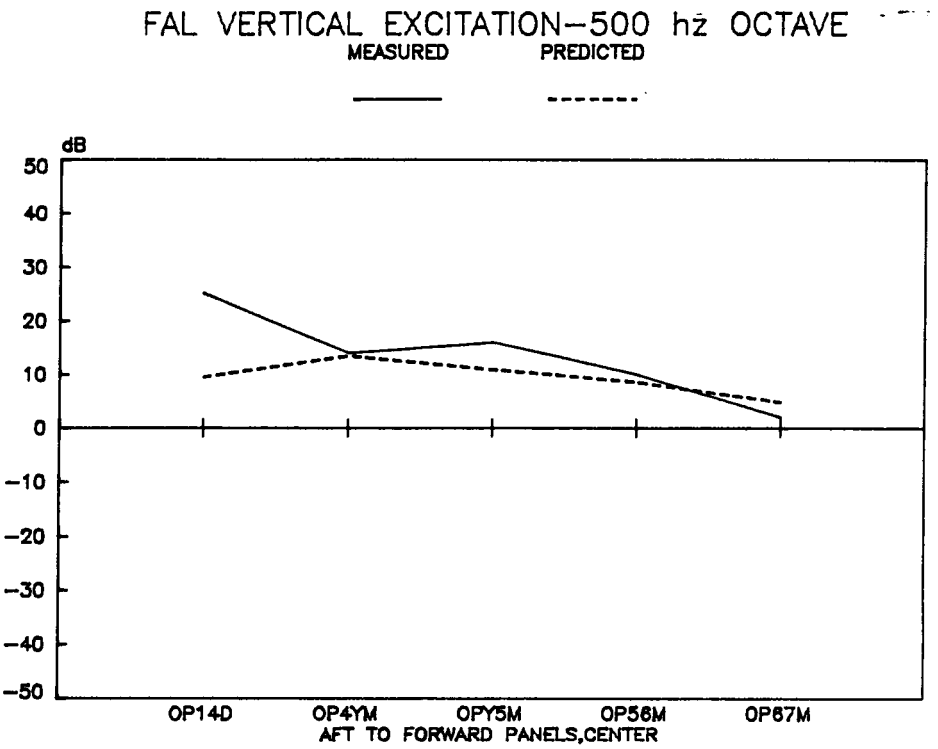

Figure E4a. Measured vs. Predicted Overhead Panel Vibration, Middle, FAL Vertical Excitation, .5 kHz

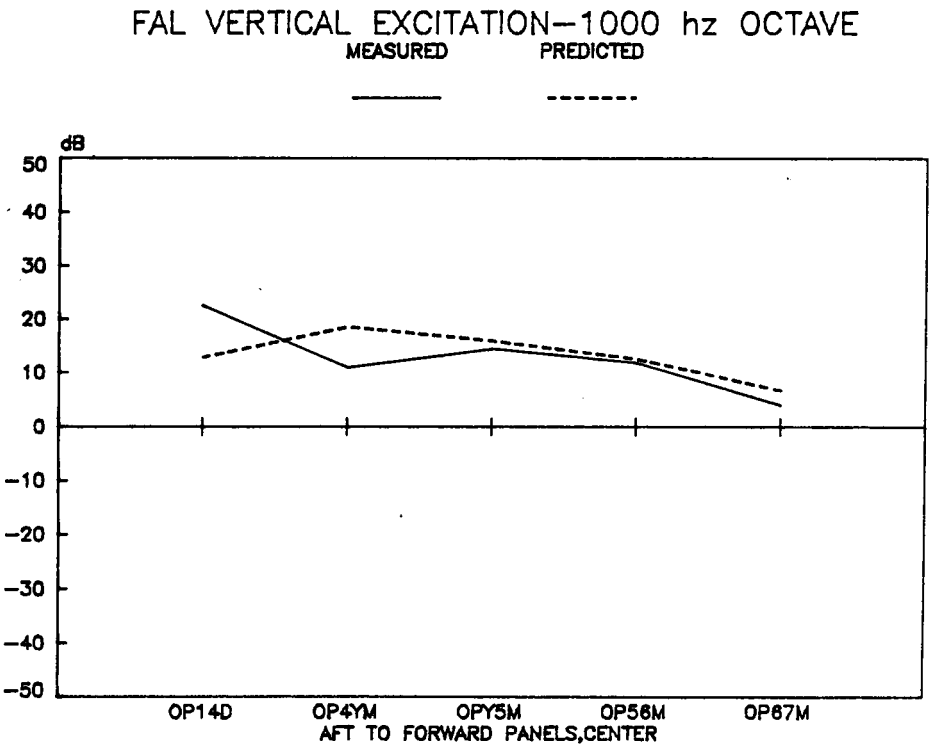

Figure E4b. Measured vs. Predicted Overhead Panel Vibration, Middle, FAL Vertical Excitation, 1 kHz

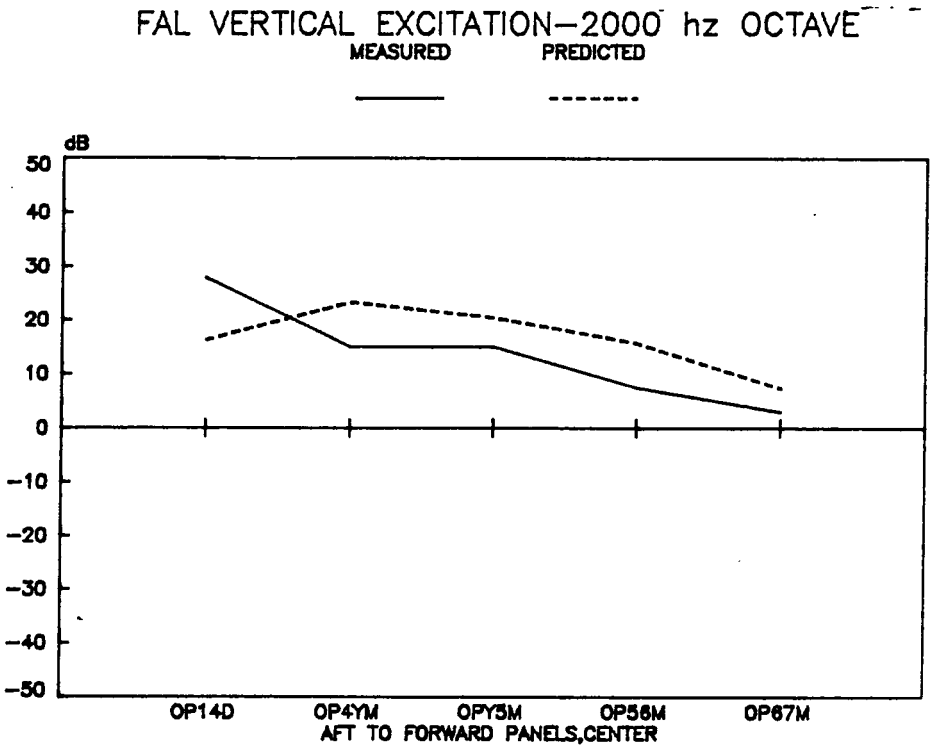

Figure E4c. Measured vs. Predicted Overhead Panel Vibration, Middle, FAL Vertical Excitation, 2 kHz

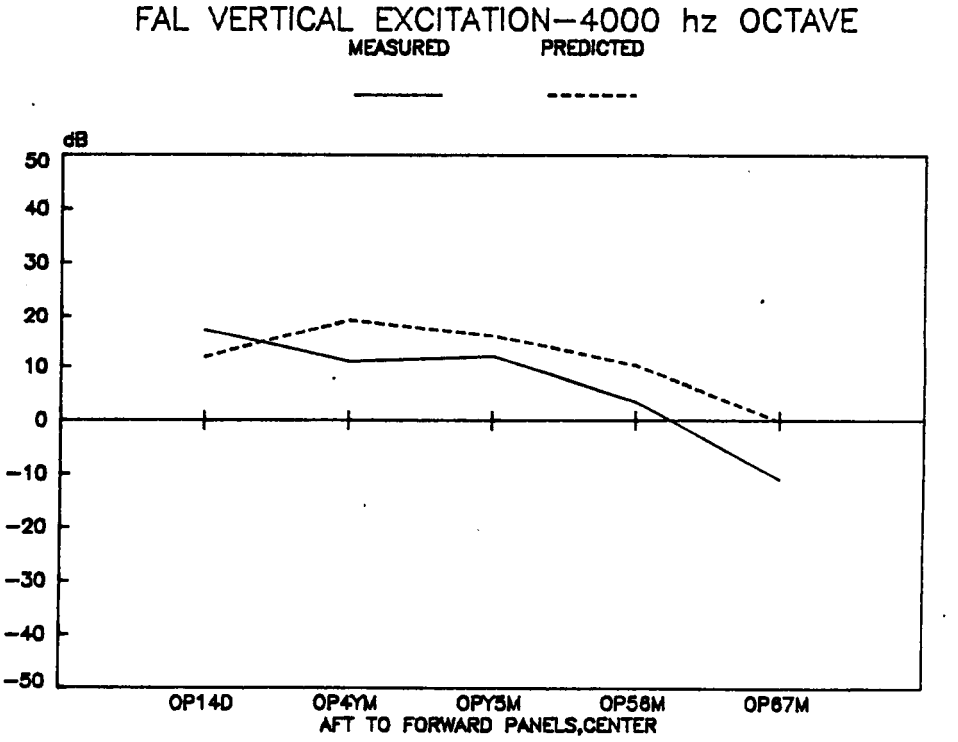

Figure E4d. Measured vs. Predicted Overhead Panel Vibration, Middle, FAL Vertical Excitation, 4 kHz

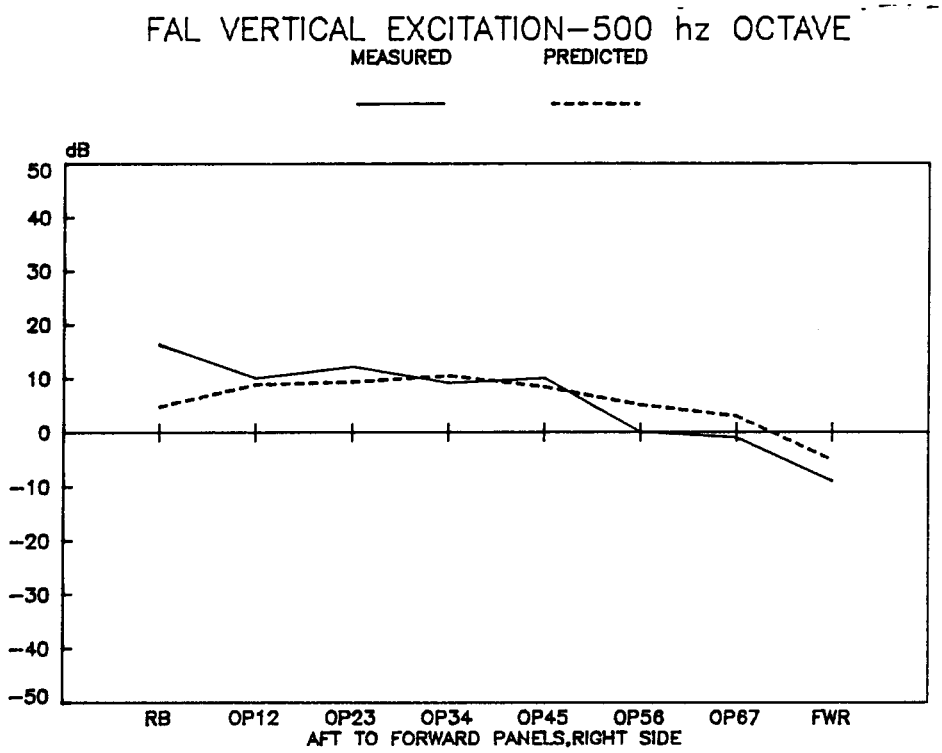

Figure E5a. Measured vs. Predicted Overhead Panel Vibration, Right Side, FAL Vertical Excitation, .5 kHz

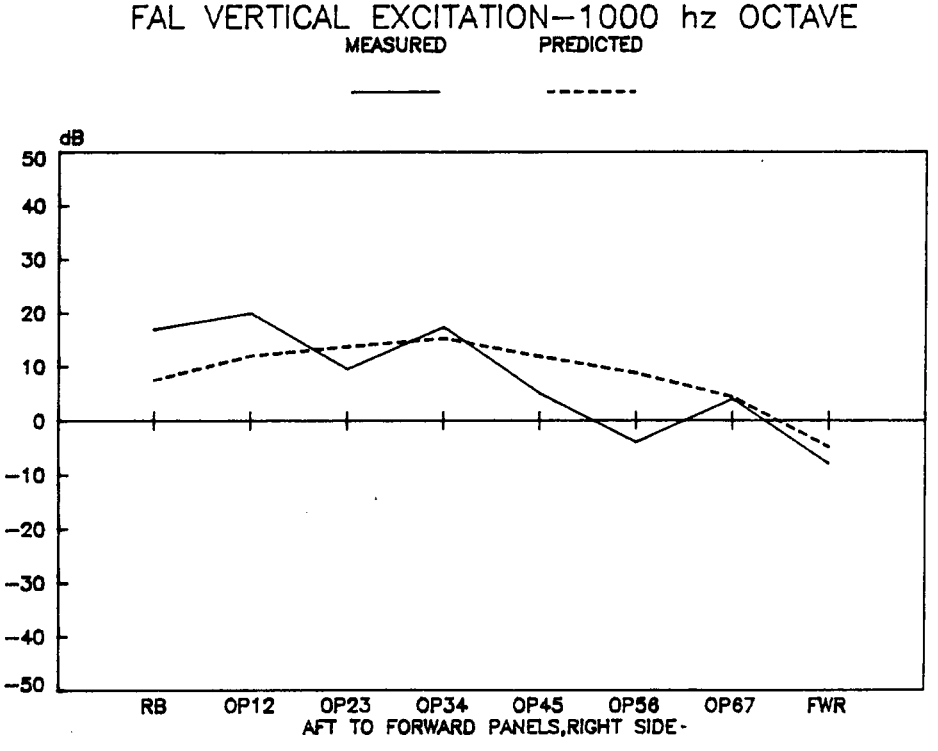

Figure E5b. Measured vs. Predicted Overhead Panel Vibration, Right Side, FAL Vertical Excitation, 1 kHz

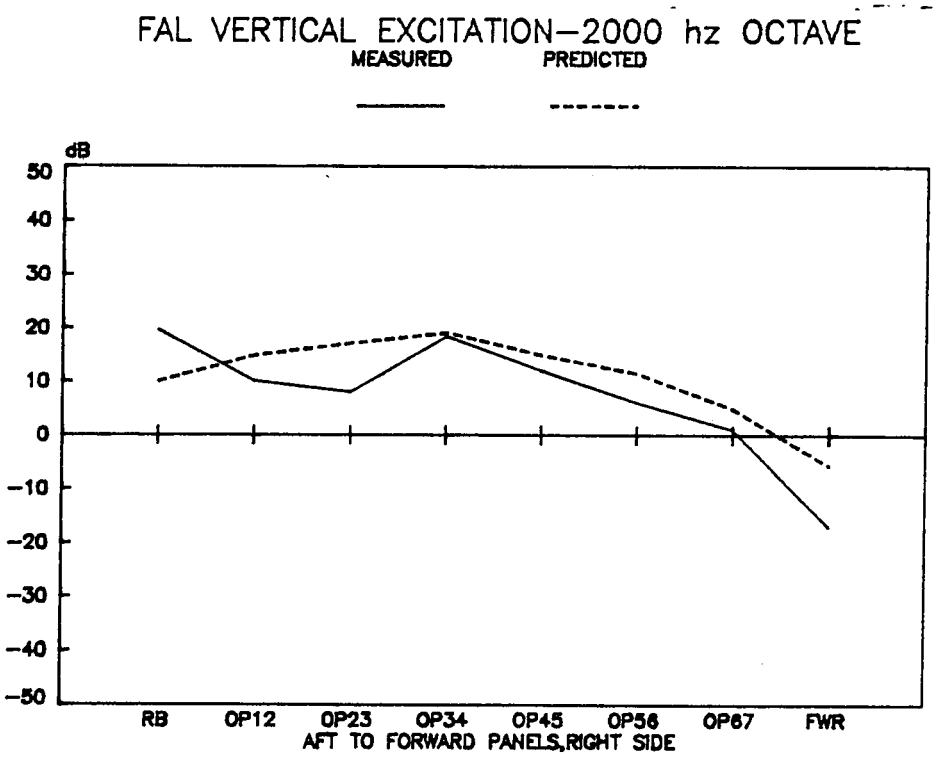

Figure E5c. Measured vs. Predicted Overhead Panel Vibration, Right Side, FAL Vertical Excitation, 2 kHz

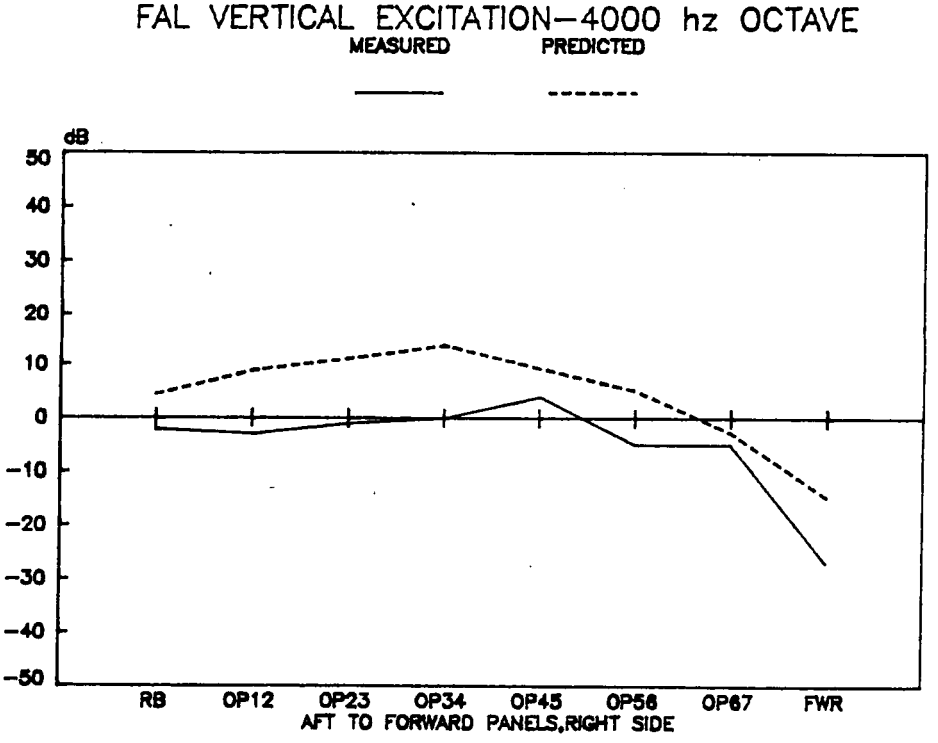

Figure E5d. Measured vs. Predicted Overhead Panel Vibration, Right Side, FAL Vertical Excitation, 4 kHz

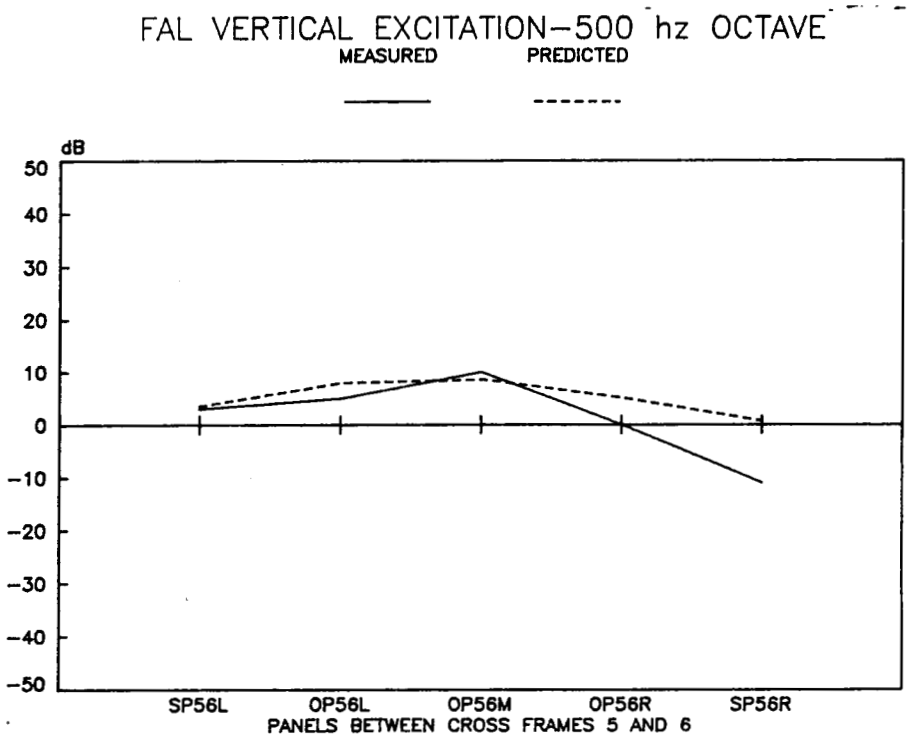

Figure E6a. Measured vs. Predicted Panel Vibration, Between CF5&6, FAL Vertical Excitation, .5 kHz

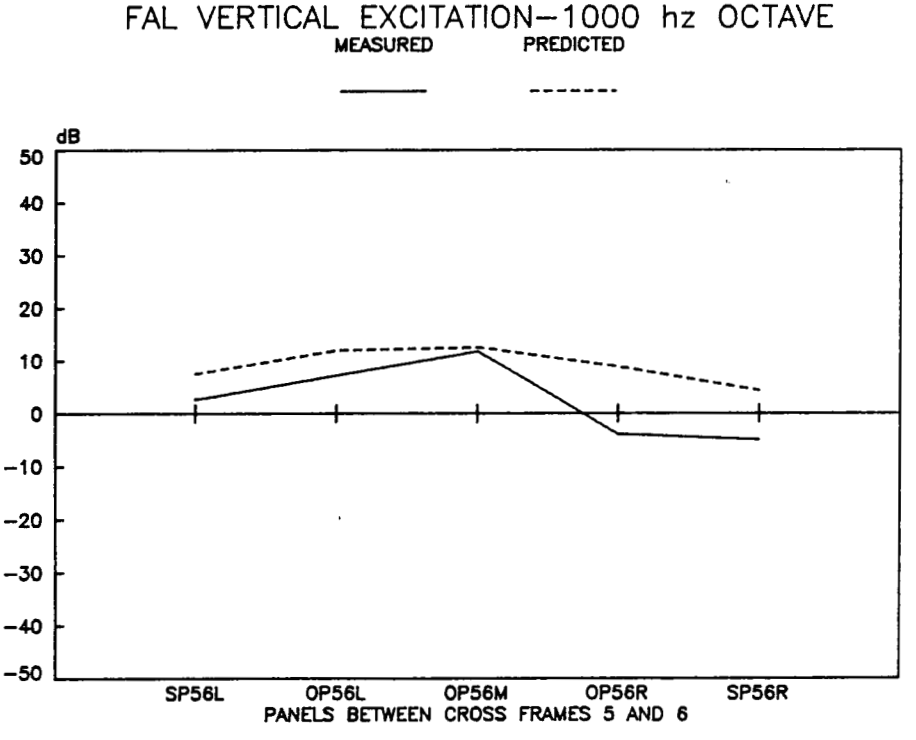

Figure E6b. Measured vs. Predicted Panel Vibration, Between CF5&6, FAL Vertical Excitation, 1 kHz

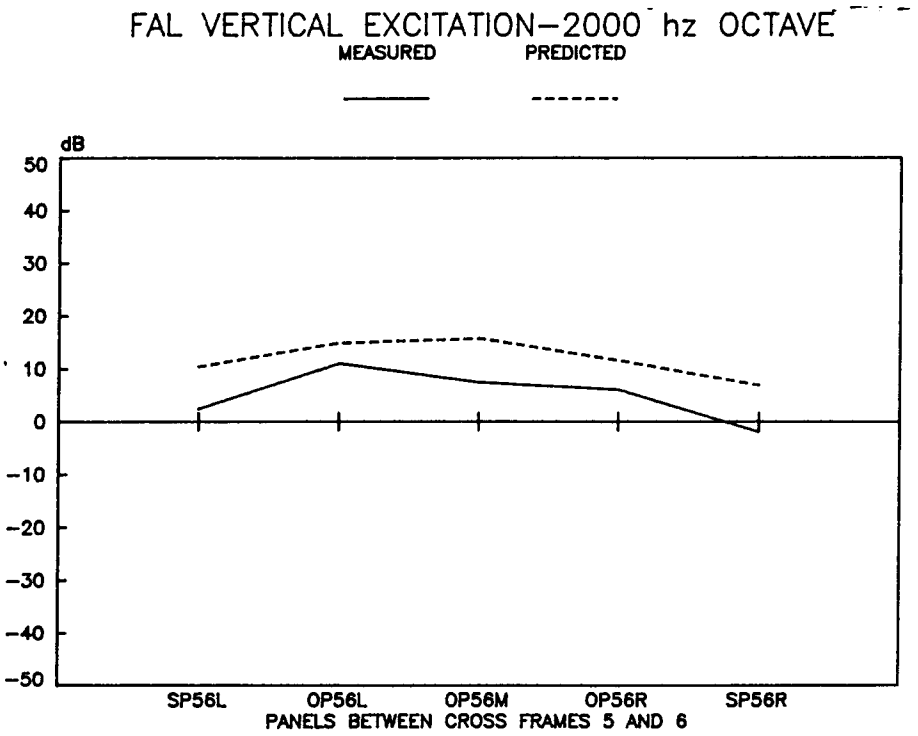

Figure E6c. Measured vs. Predicted Panel Vibration, Between CF5&6 FAL Vertical Excitation, 2 kHz

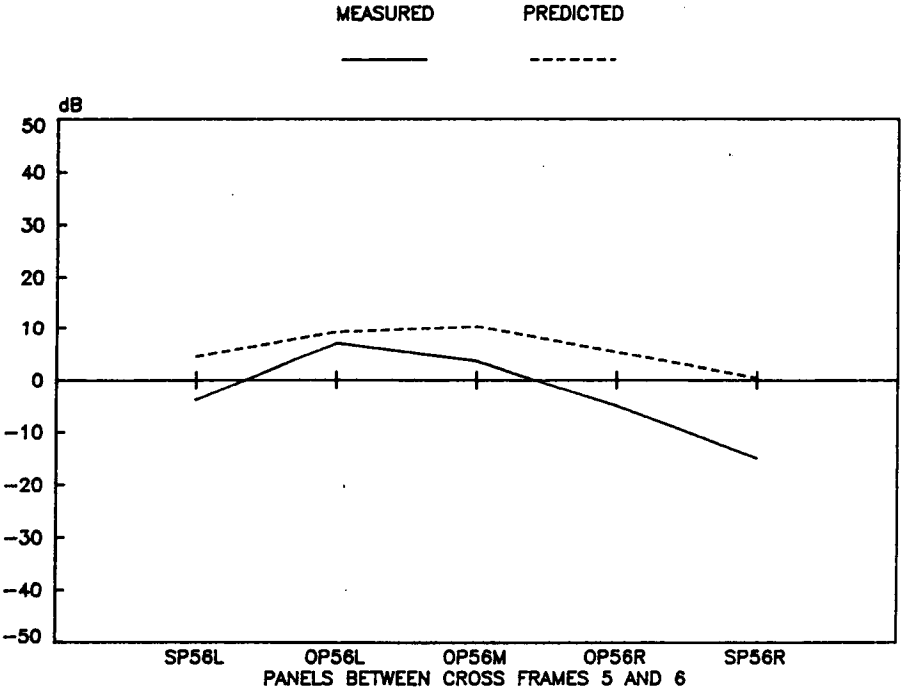

Figure E6d. Measured vs. Predicted Panel Vibration, Between CF5&6 FAL Vertical Excitation, 4 kHz

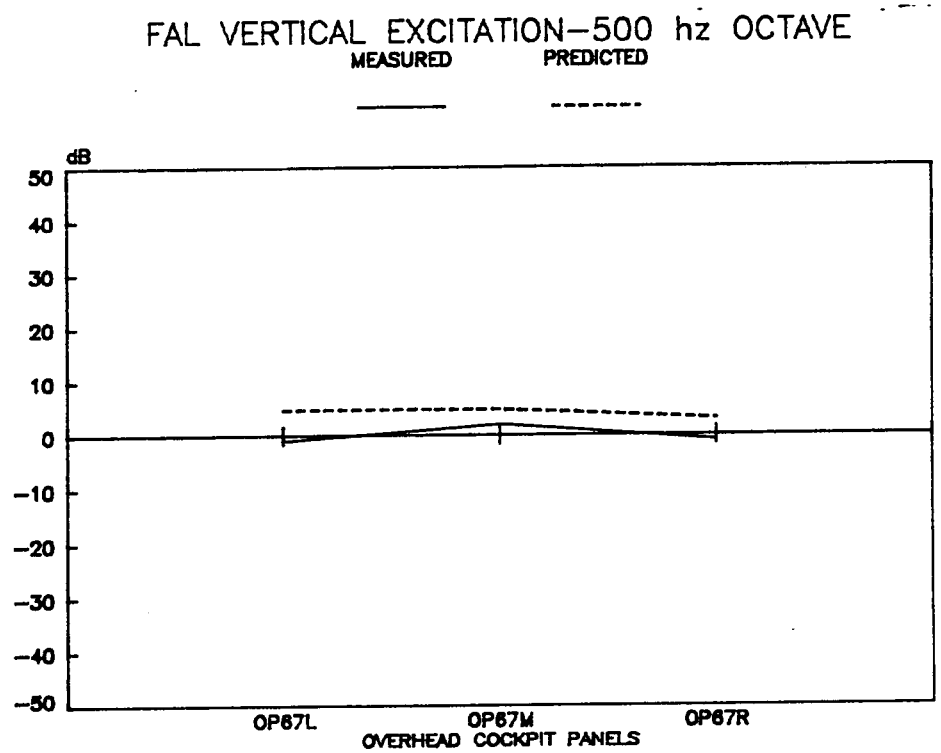

Figure E7a. Measured vs. Predicted Overhead Panel Vibration, Cockpit, FAL Vertical Excitation, .5 kHz

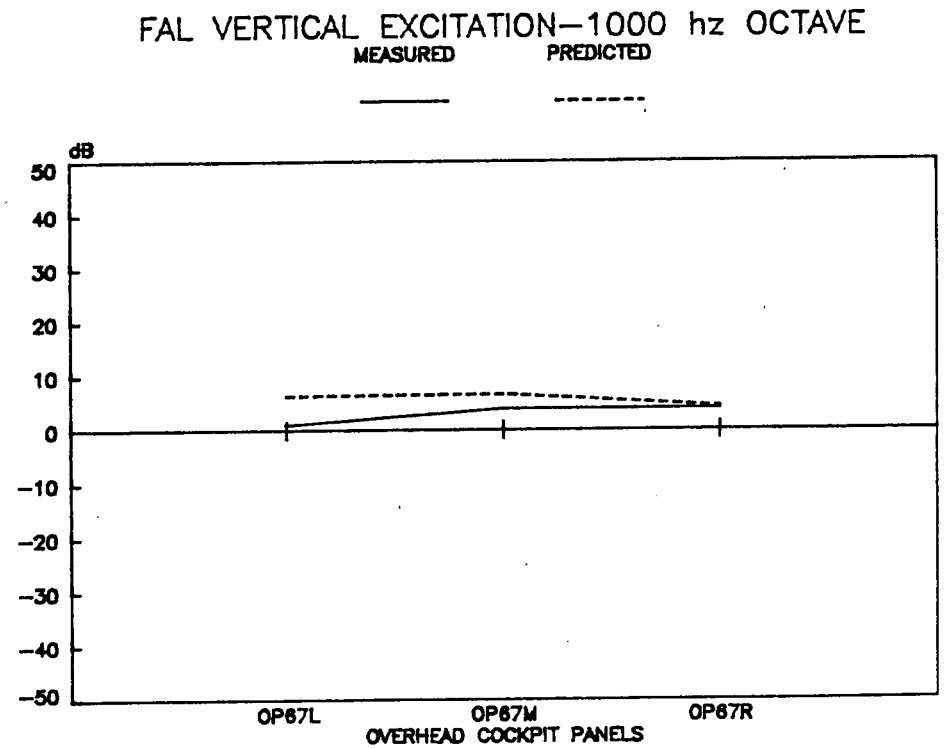

Figure E7b. Measured vs. Predicted Overhead Panel Vibration, Cockpit, FAL Vertical Excitation, 1 kHz

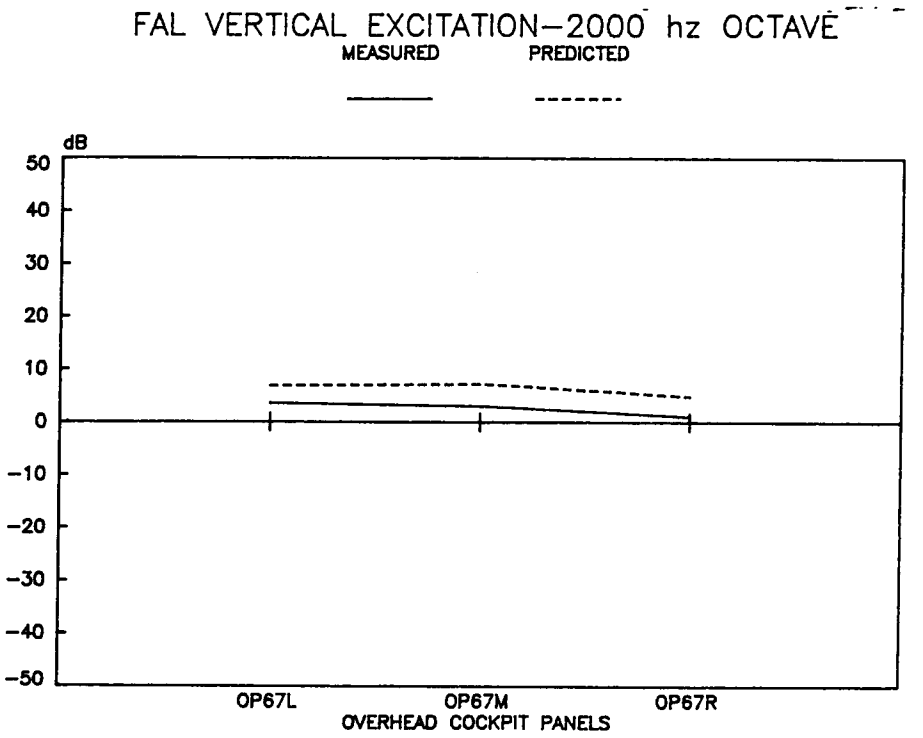

Figure E7c. Measured vs. Predicted Overhead Panel Vibration, Cockpit, FAL Vertical Excitation, 2 kHz

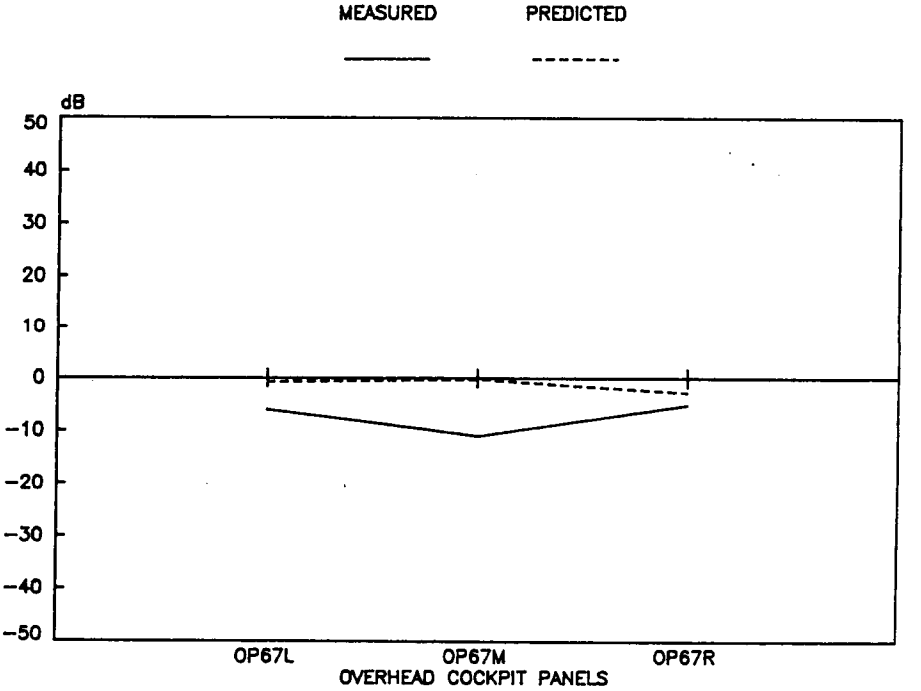

Figure E7d. Measured vs. Predicted Overhead Panel Vibration, Cockpit, FAL Vertical Excitation, 4 kHz

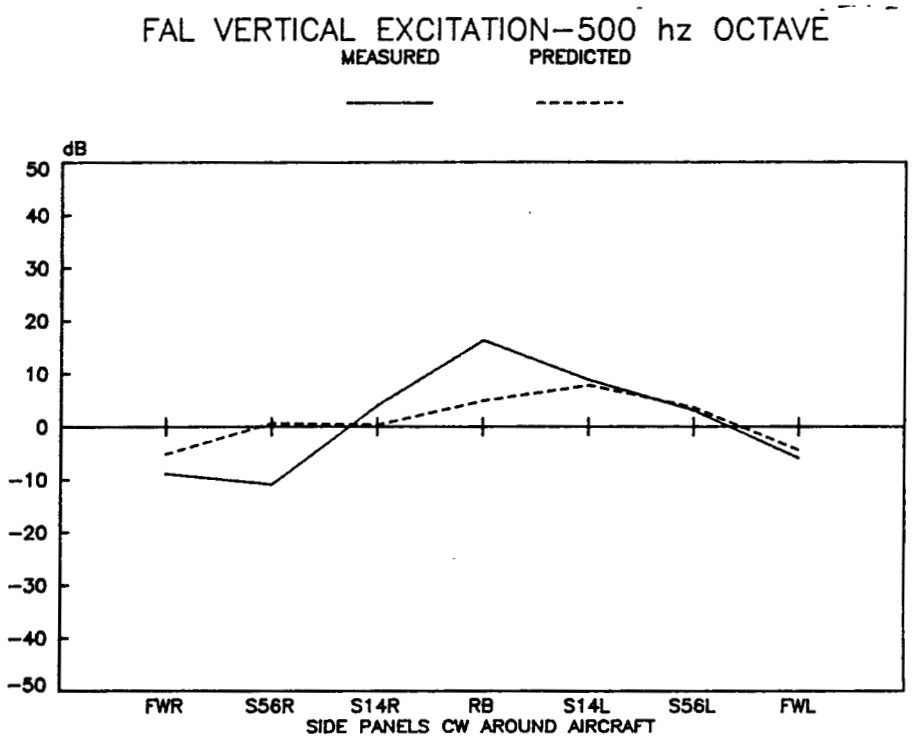

Figure E8a. Measured vs. Predicted Side Panel Vibration, FAL Vertical Excitation, .5 kHz

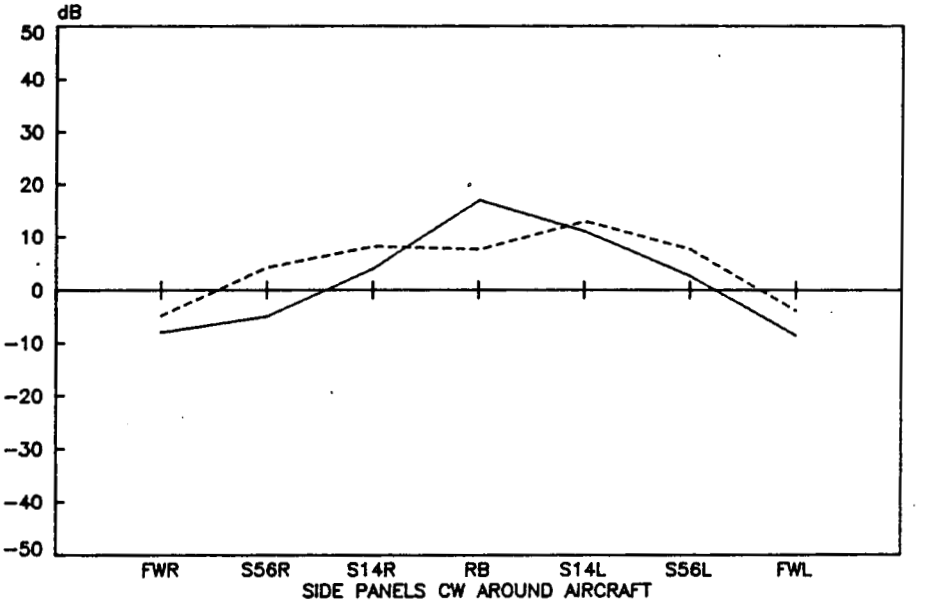

Figure E8b. Measured vs. Predicted Side Panel Vibration, FAL Vertical Excitation, 1 kHz

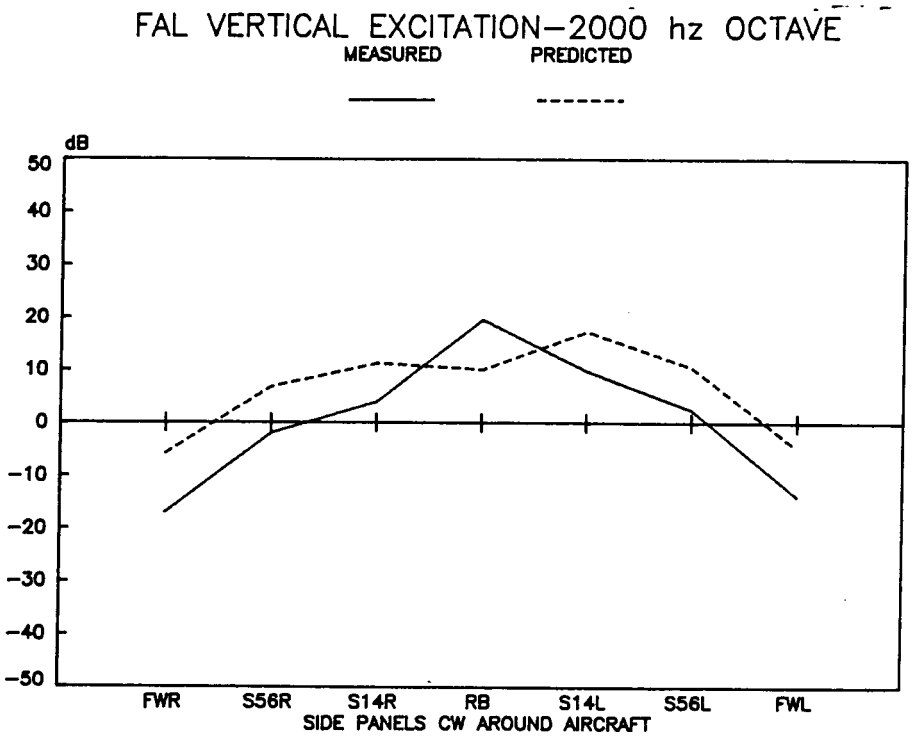

Figure E8c. Measured vs. Predicted Side Panel Vibration, FAL Vertical Excitation, 2 kHz

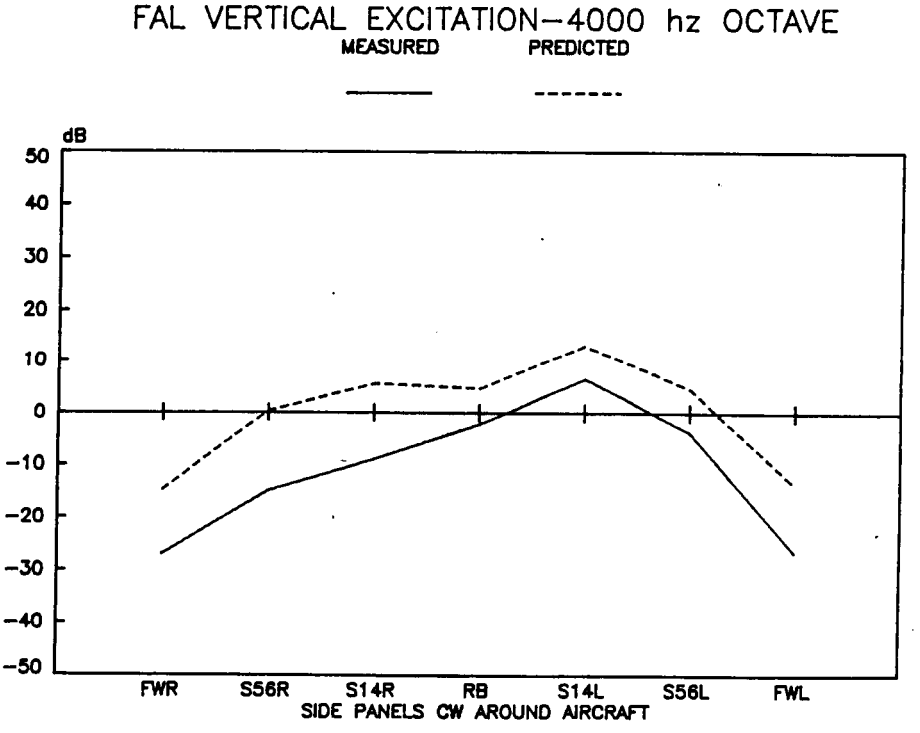

Figure E8d. Measured vs. Predicted Side Panel Vibration, FAL Vertical Excitation, 4 kHz

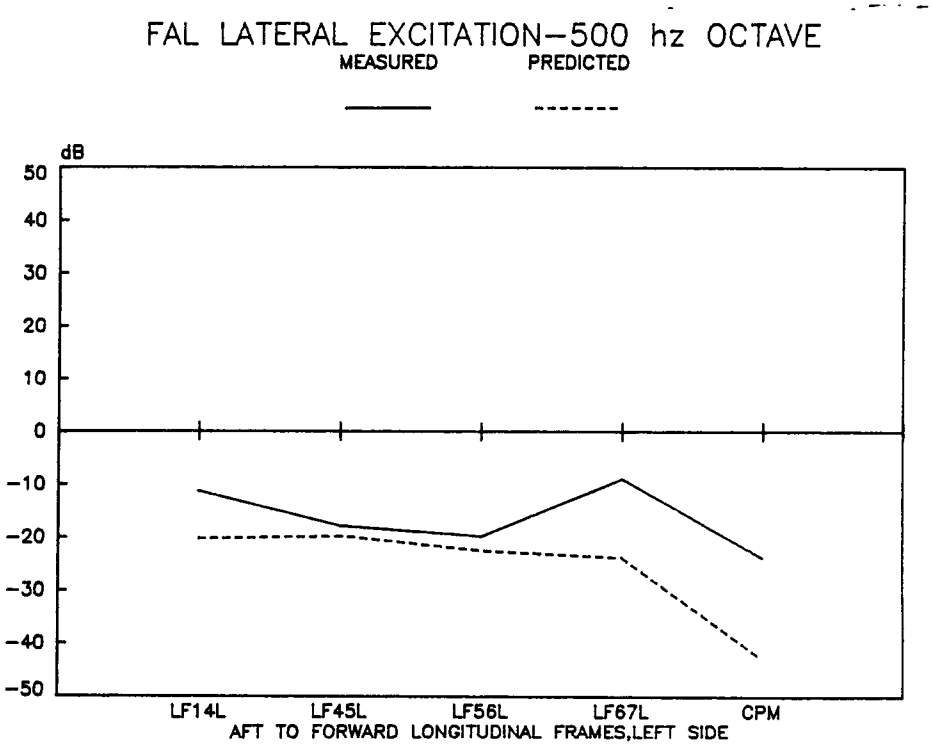

Figure E9a. Measured vs. Predicted Overhead Frame Vibration, Left Side, FAL Lateral Excitation, .5 kHz

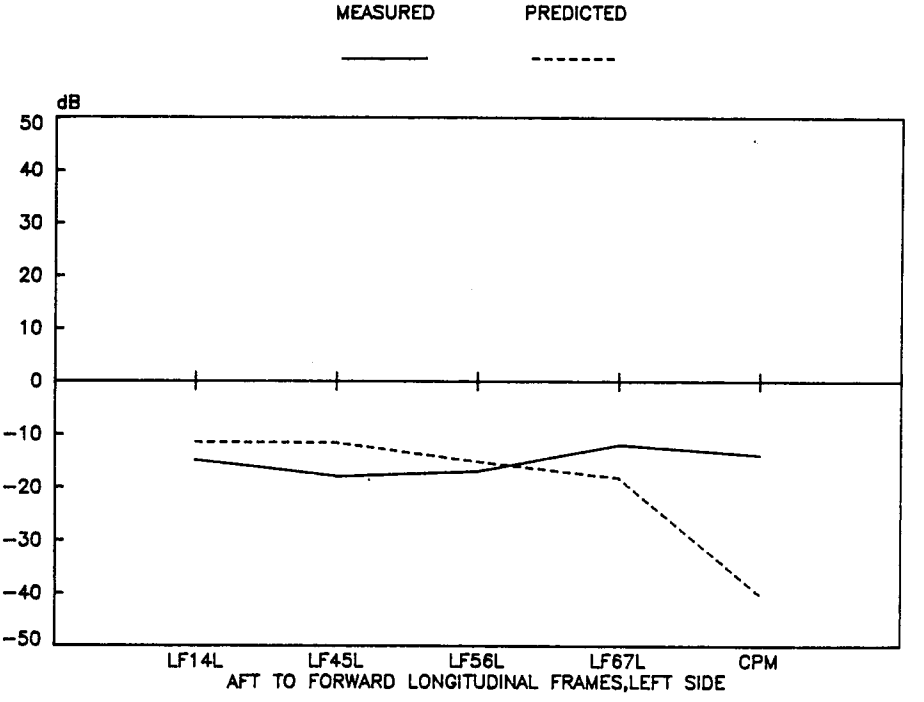

Figure E9b. Measured vs. Predicted Overhead Frame Vibration, Left Side, FAL Lateral Excitation, 1 kHz

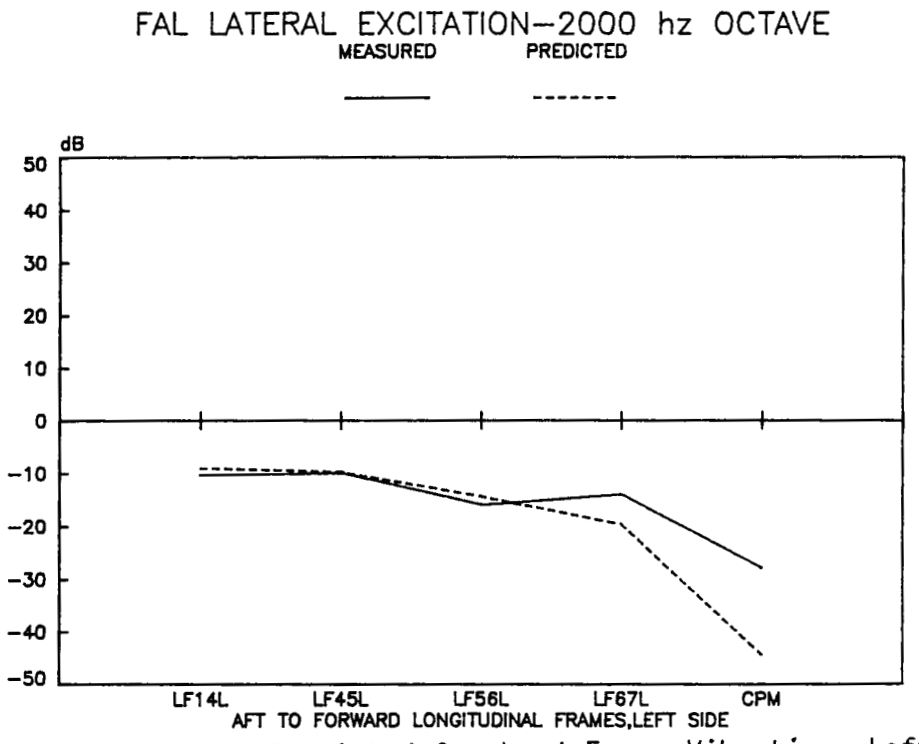

Figure E9c. Measured vs. Predicted Overhead Frame Vibration, Left Side, FAL Lateral Excitation, 2 kHz

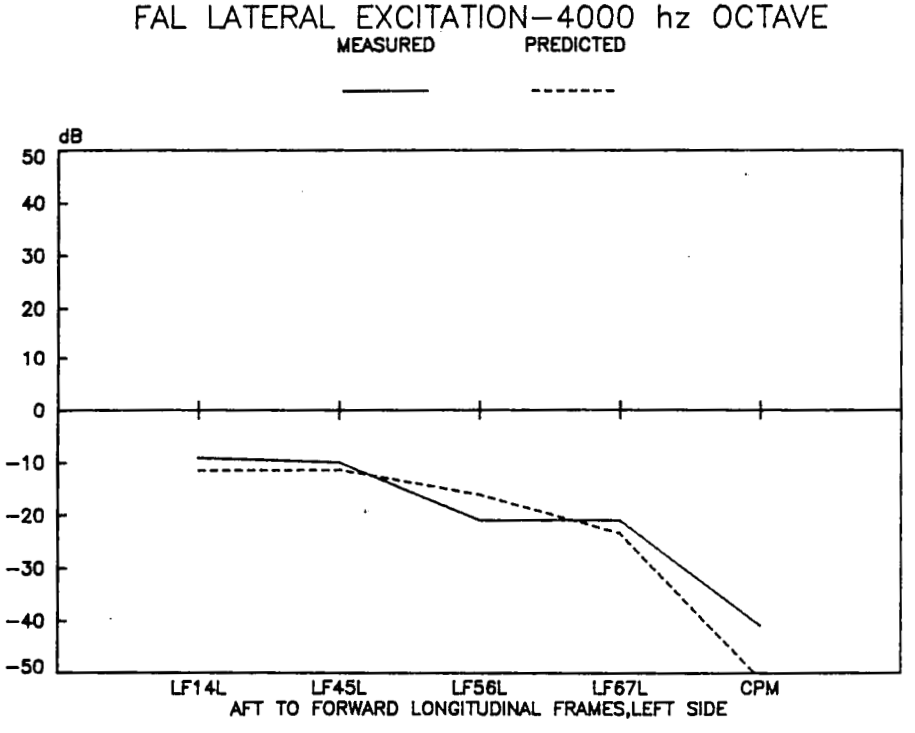

Figure E9d. Measured vs. Predicted Overhead Frame Vibration, Left Side, FAL Lateral Excitation, 4 kHz

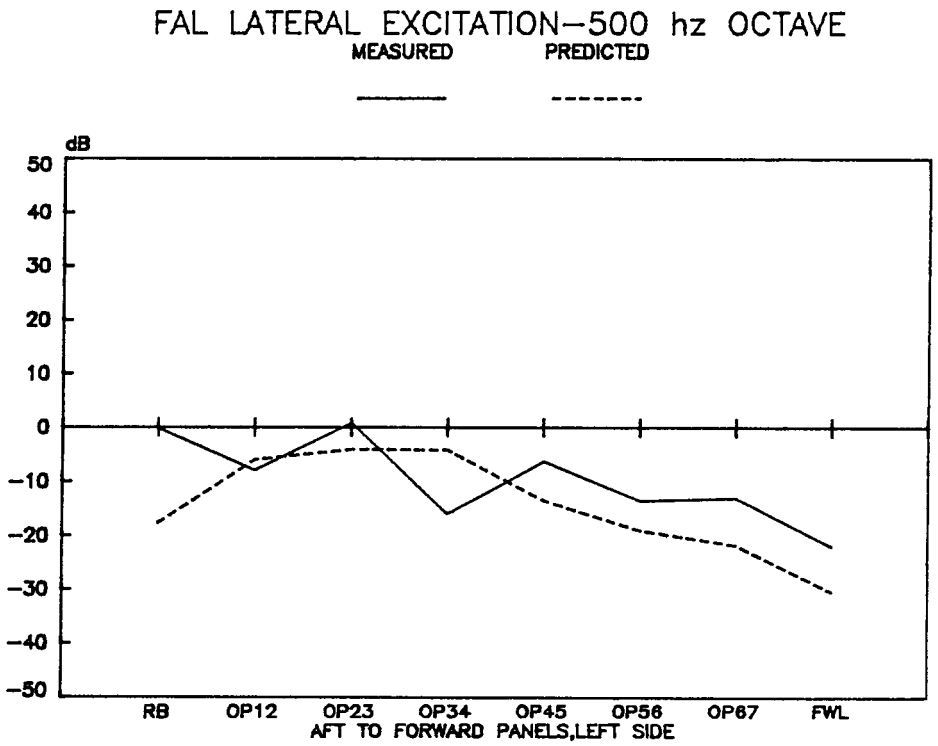

Figure E10a. Measured vs. Predicted Overhead Panel Vibration, Left Side, FAL Lateral Excitation, .5 kHz

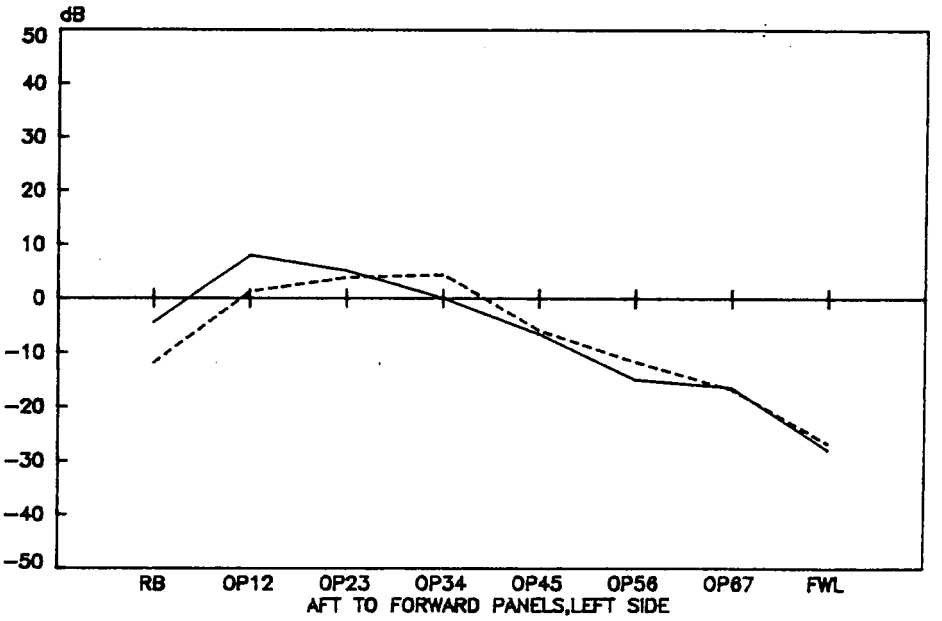

Figure E10b. Measured vs. Predicted Overhead Panel Vibration, Left Side, FAL Lateral Excitation, 1 kHz

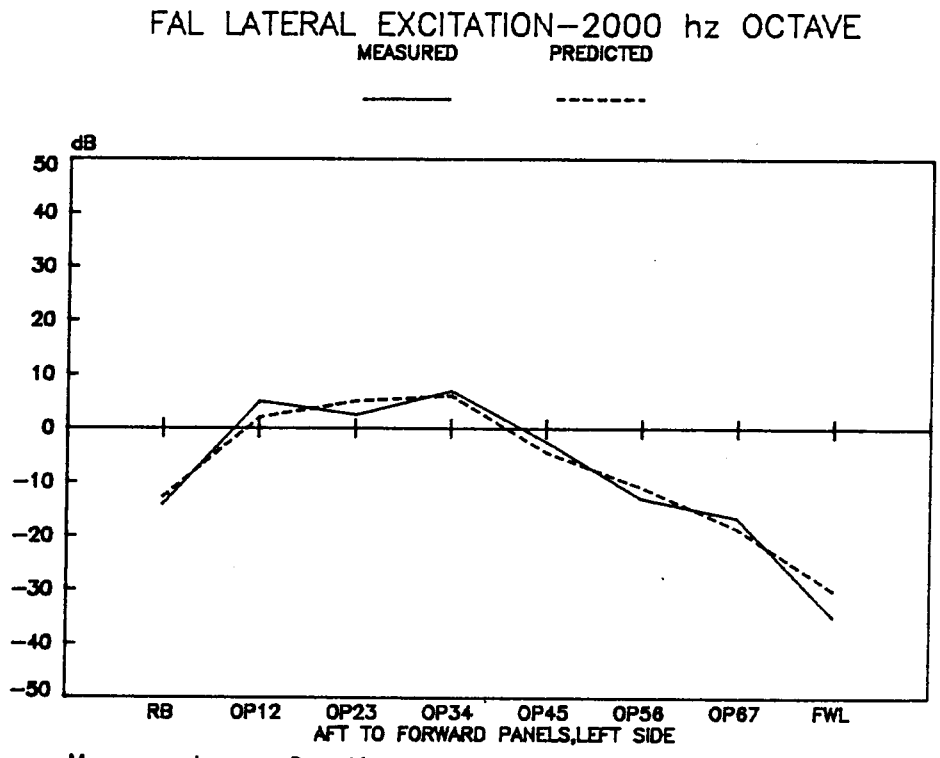

Figure E10c. Measured vs. Predicted Overhead Panel Vibration, Left Side, FAL Lateral Excitation, 2 kHz

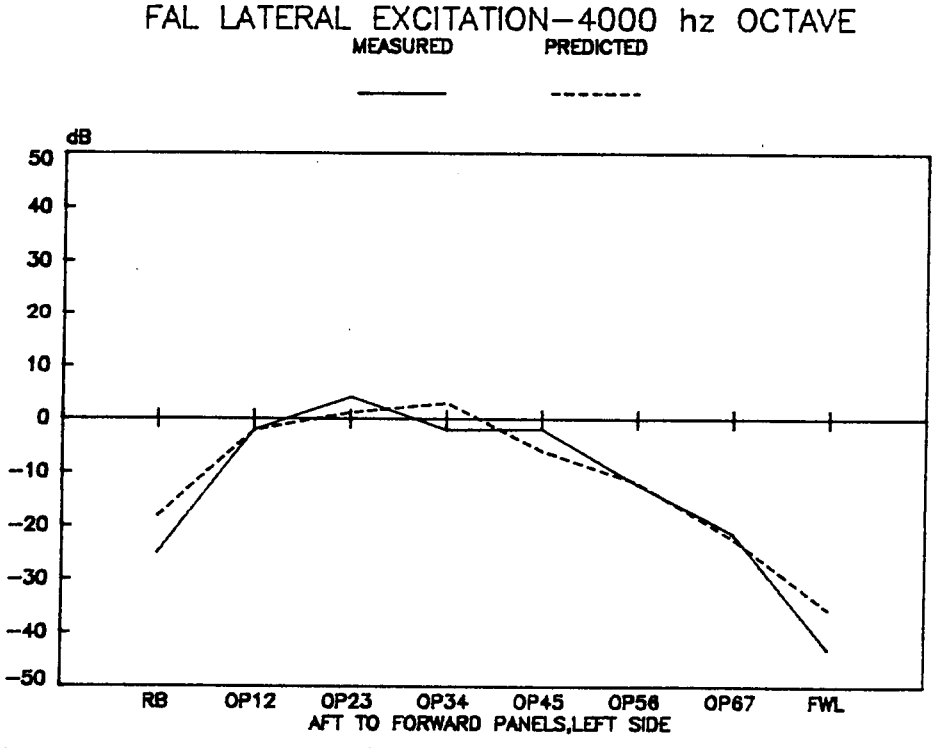

Figure E10d. Measured vs. Predicted Overhead Panel Vibration, Left Side, FAL Lateral Excitation, 4 kHz

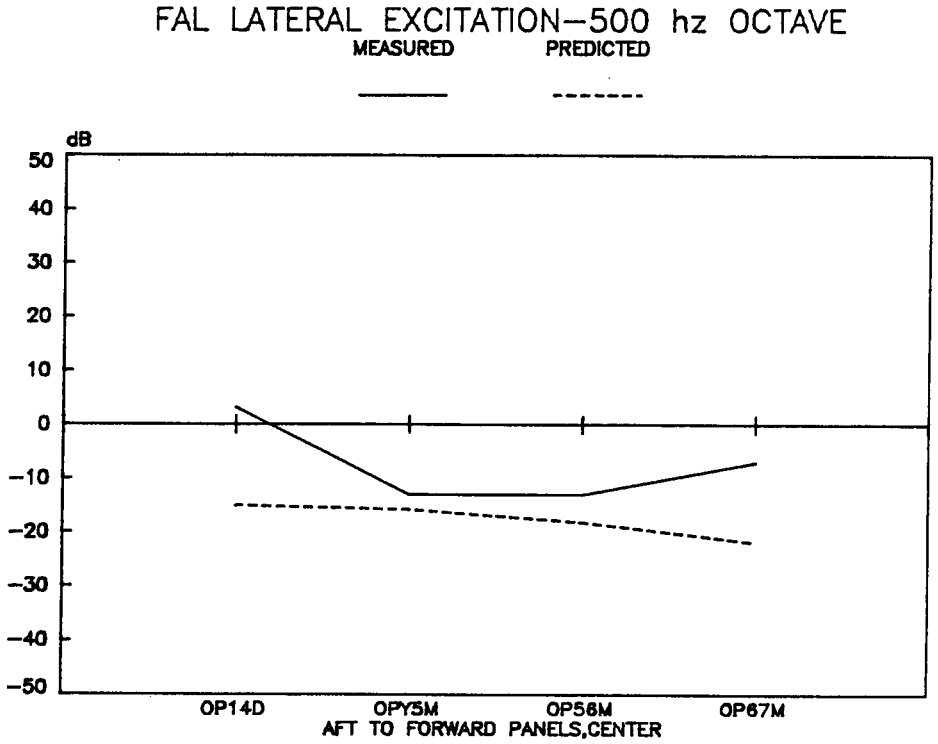

Figure E11a. Measured vs. Predicted Overhead Panel Vibration, Middle, FAL Lateral Excitation, .5 kHz

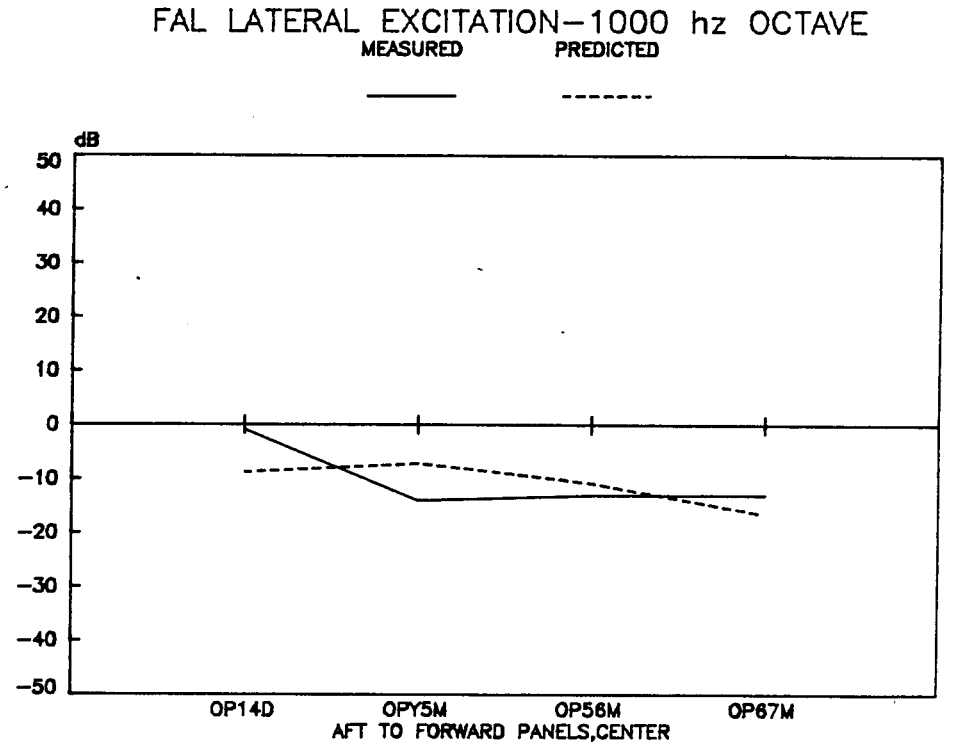

Figure E11b. Measured vs. Predicted Overhead Panel Vibration, Middle, FAL Lateral Excitation, 1 kHz

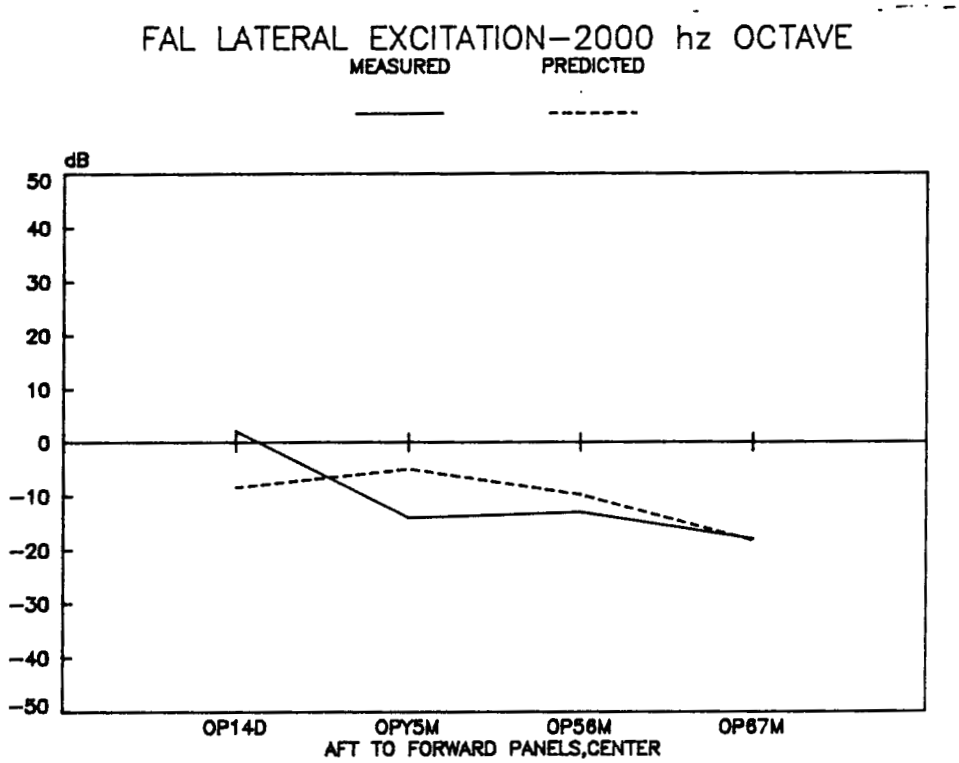

Figure E11c. Measured vs. Predicted Overhead Panel Vibration, Middle, FAL Lateral Excitation, 2 kHz

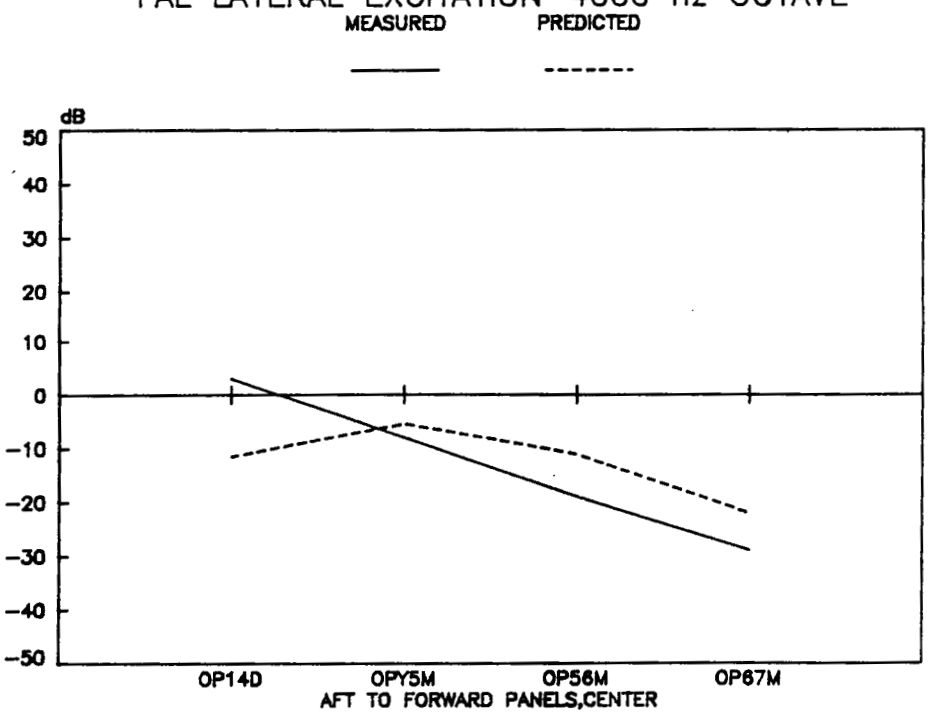

Figure E11d. Measured vs. Predicted Overhead Panel Vibration, Middle, FAL Lateral Excitation, 4 kHz

frequency, with OP14D the exception. The construction of this subsystem is lightweight aluminum with some stiffening angle and beads, but remains fairly flexible. A panel such as this may require more than the three point measurements (see Figure C9) spread out spacially to approximate the response level predicted by the SEA method.

Figure E12, the right side overhead, shows trending similar to Figure E11 as the delta between the measured data and the predictions starts off positive (underprediction) and becomes negative with increasing frequency. The lower frequency octaves again show measurement variation between subsystems, with the predictions remaining smooth. Figure E13 shows the panels between cross frames 5 and 6, and reveals that the side panel SP56L is underpredicted by 25 dB at 500 hz, but steadily improves with increasing frequency. The three overhead panels shown compare well except for OP56M at 4000 hz, which predicts high by approximately 8 dB. Figure E14 shows the side panels and windows around the aircraft, which shows some interesting results. At 500 hz, the aft side panels are underpredicted. On the average, 19 dB is the difference for this octave. As frequently increases, results improve dramatically with 8 dB average delta at 1000 hz and windshield predictions that match measurement well. The 2000 and 4000 hz octaves show good results. Note the decrease in measured levels with increasing frequency shows up slightly in the higher frequency predictions, and the trends are predicted very well.

The right rear vertical (RARV) excitation comparisons are shown in Figures E15 through E18. The results for the left side longitudinal frames are shown in Figure E15. The predictions follow measurements well with CPM at 1000 hz and the rear frames, LF14 and LF56 at 4000 hz showing some discrepancy. Figure E16, overhead panels left side, show the 500 and 1000 hz to agree well, with RB the exception. The higher frequencies tend towards overprediction forward of OP23 with 12 dB at FWL the highest delta. Figure E17 shows the center overhead panels, which show decent results at low frequency but again tend toward overprediction at 2000 and 4000 hz. OP14D stands out with underpredicted levels at 500 and 1000 hz but levels that match better at higher frequency where other subsystems are overpredicted. Figure E18 shows the source side overhead panel results for RAR vertical excitation. Measurements and predictions compare well in general, with RB underpredicted in the 500 and 1000 hz octaves. The 2000 hz octave agrees well, with OP56R and FWR overpredicted by 10 and 12 dB. At 4000 hz, the near-source subsystems are underpredicted, while the subsystems forward of OP23R are overpredicted. In general, the trends are in good agreement.

The RAR lateral input comparisons are shown in Figures E19 through E22. The left side longitudinal frame results are shown in Figure E19. The SEA model predicts more dropoff in level with distance than measurements indicate in general. At 500 hz the predictions are lower than measurements for all but LF56L, while the higher frequency octaves show a crossover where the predictions go from over to underprediction. The crossover point moves forward with

increasing frequency, indicating better forward predictions but diminishing results for the rear subsystems. Figure E20 shows left side overhead panel results that are excellent at 500 hz but diminish as frequency increases, toward overprediction in all subsystems in the 4000 hz octave by 7 dB on the average. The center overhead panels, Figure E21, again shows best results at 500 and 1000 hz, with a trend towards overprediction with increasing frequency, with a 10 dB average overprediction at 4000 hz. Figure E22 shows the results for the right side overhead panels. The predictions follow the measurements well in general, with some overprediction at the more forward subsystems in the 1K, 2K, and 4K octaves.

The RAR longitudinal excitation results are shown in Figures E23 through E25. Figure E23 shows the left side overhead panels. The 500 hz octave shows some overprediction in the rear and underprediction in OP67L and FWL. The 1k octave shows overprediction in all but RB and OP67 and FWL by an average of 6 dB. 2000 hz shows overprediction in all subsystems, by 5 dB average, and 4 khz shows OP56 and OP67 to be underpredicted by 5 dB in the midst of overpredictions at that octave. These predictions, in general, follow the measurements well. Figure E24, center overhead panels, show fair results at higher frequencies. The 500 hz octave shows OP14D and OP67M underpredicted by 16 and 19 dB respectively. The 1000 and 2000 hz octaves shows a maximum deviation of 12 dB. The 4000 hz octave compares well, with 6 dB overprediction at OP56M the highest deviation. Figure E25 shows better than average results for the right side overhead panels with RAR longitudinal excitation.

The narrow band spectrum of cabin noise level for the S-76[1], shows prominent tones associated with the hydraulics system. Hydraulics noise is generated at the pump and transmits down the hydraulics lines as pressure fluctuations in the hydraulics fluid. The hydraulics lines are supported directly from the skin panels and frames of the cabin overhead at 0.5m intervals and are therefore a potentially important path from the pump, which is mounted on the gearbox, to the panel surfaces that radiate into the cabin. The alternative path is through the gearbox casing and out into the airframe through the gearbox attachment locations.

During the ground test, measurements were taken with the shaker positioned at two of the support locations for the hydraulics lines (see Figure C9). One location was on overhead skin panel OP56L and the other was on frame section LF45L, with the shaker oriented to excite out-of-plane bending. Vibration transfer functions were measured at different locations on the airframe relative to the levels at the shaker location.

Predictions were generated using the SEA model with the power input to the excited subsystems, OP56L or LF45L. The predicted levels were scaled as before. Scaling of the transfer functions for the panel excitation location OP56L was accomplished by using only the response levels for this subsystem. Out-of-plane bending levels for frame subsystem LF45L and response levels for adjacent panel subsystems OP45L and OPY5M, for which measured data existed, were used for the scaling of predicted levels for the frame excitation case.

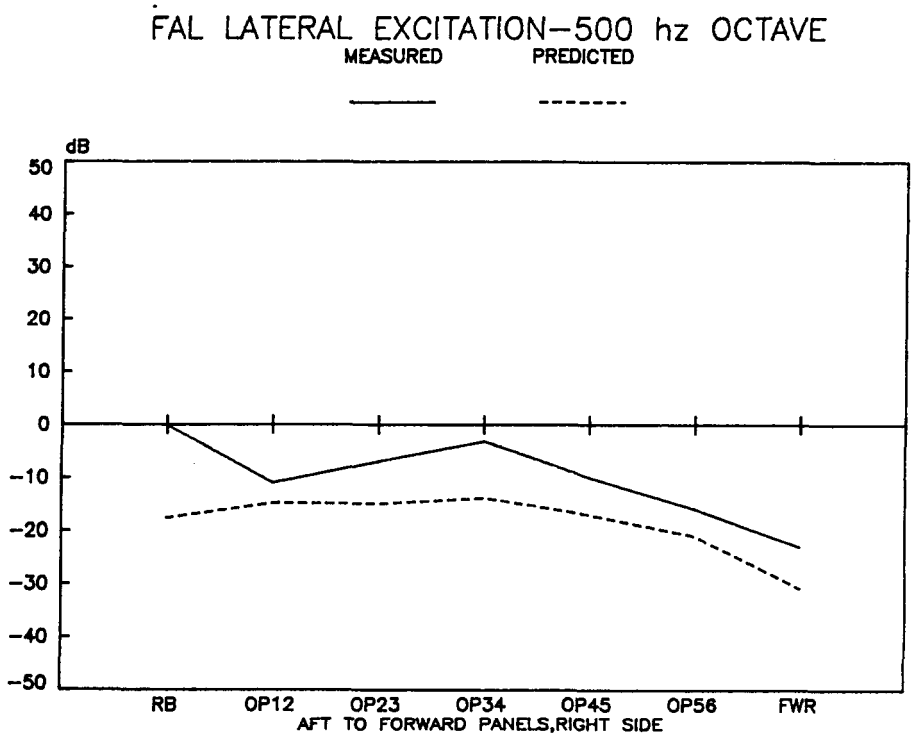

Figure E12a. Measured vs. Predicted Overhead Panel Vibration, Right Side, FAL Lateral Excitation, .5 kHz

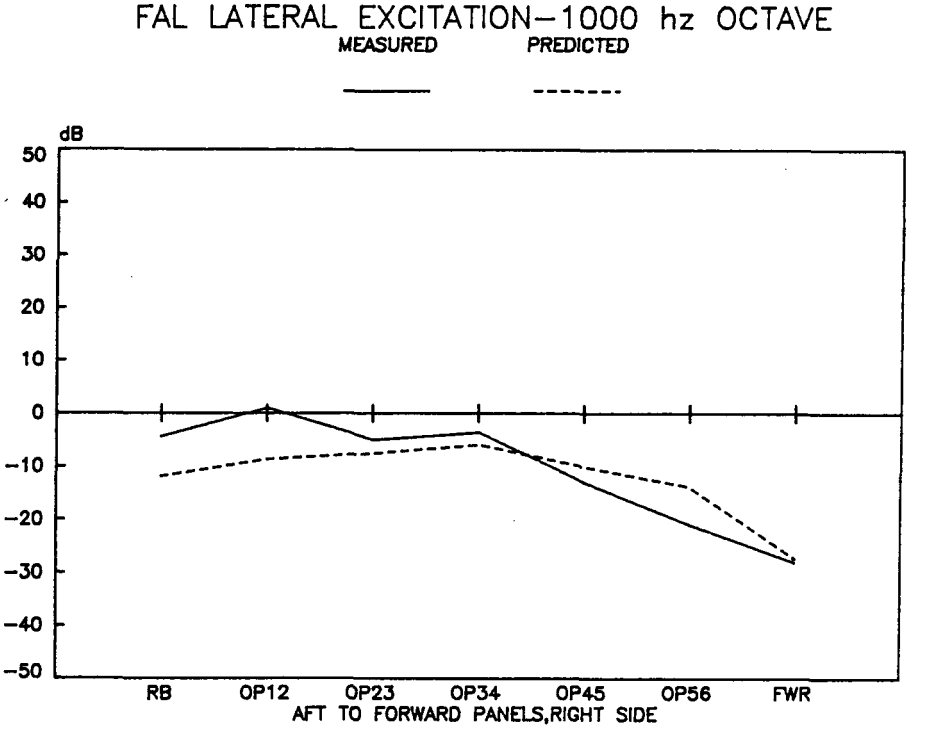

Figure E12b. Measured vs. Predicted Overhead Panel Vibration, Right Side, FAL Lateral Excitation, 1 kHz

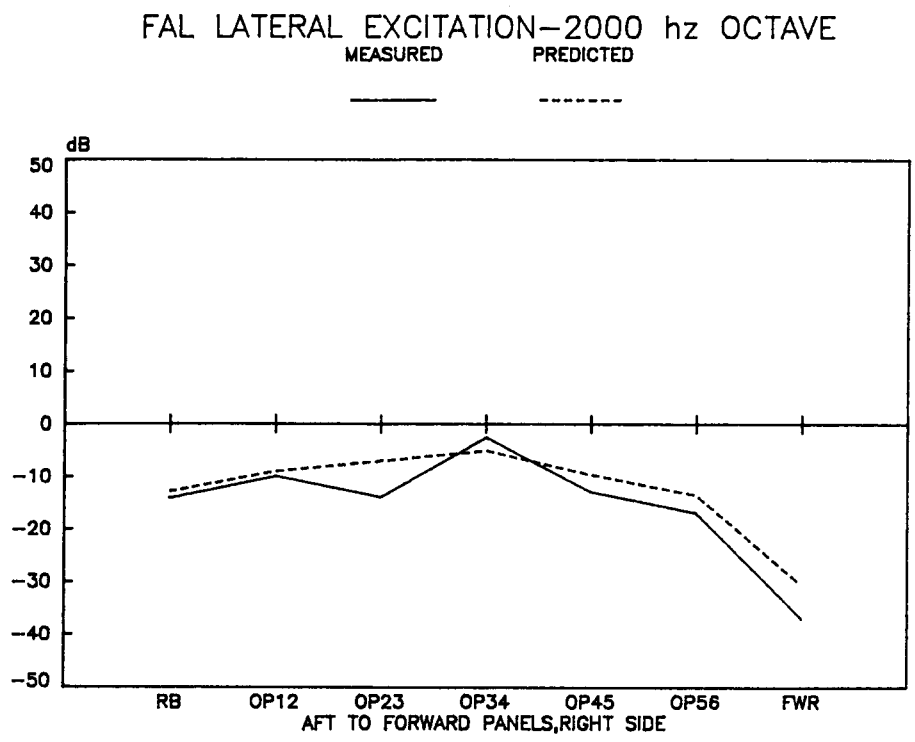

Figure E12c. Measured vs. Predicted Overhead Panel Vibration, Right Side, FAL Lateral, Excitation, 2 kHz

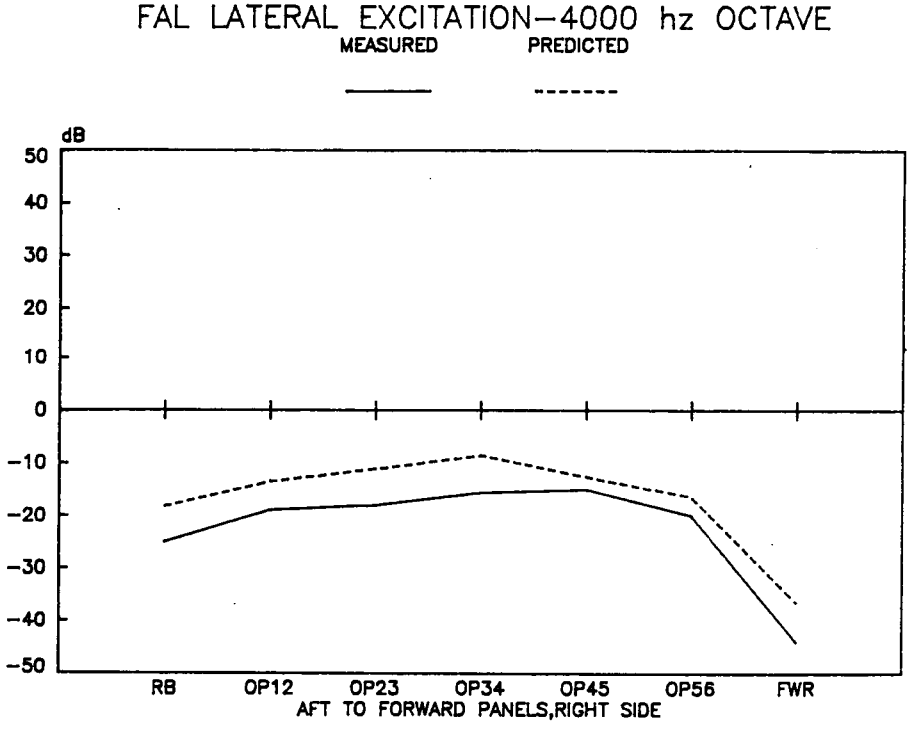

Figure E12d. Measured vs. Predicted Overhead Panel Vibration, Right Side, FAL Lateral Excitation, 4 kHz

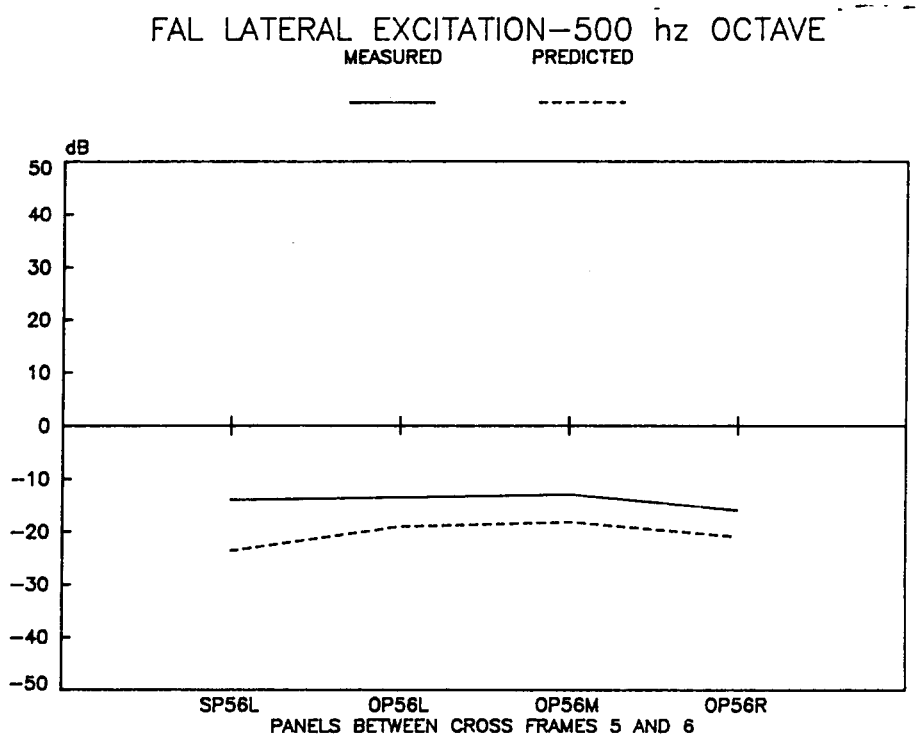

Figure E13a. Measured vs. Predicted Panel Vibration, Between CF5&6, FAL Lateral Excitation, .5 kHz

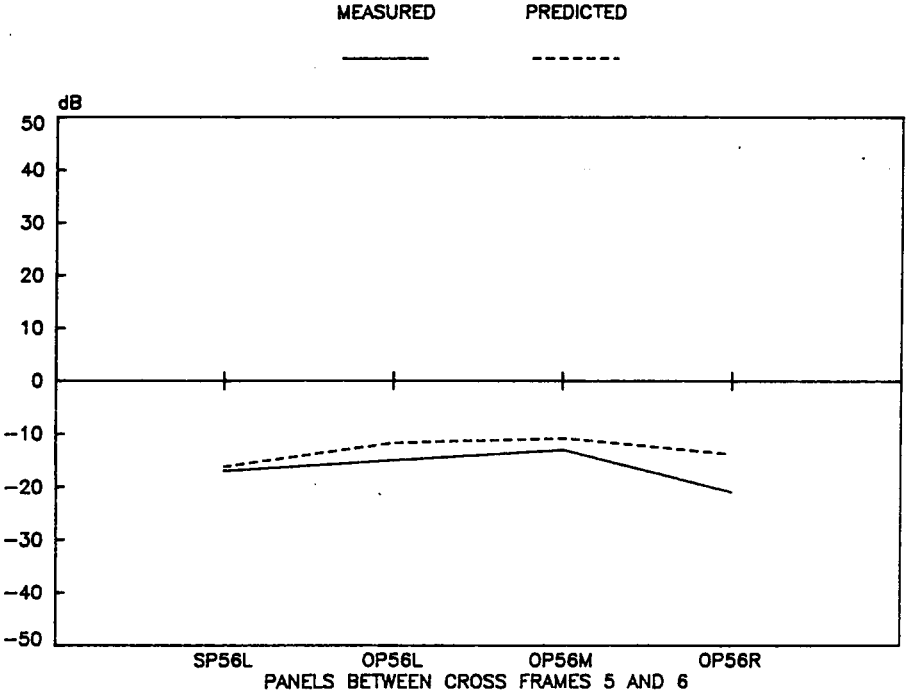

Figure E13b. Measured vs. Predicted Panel Vibration, Between CF5&6, FAL Lateral Excitation, 1 kHz

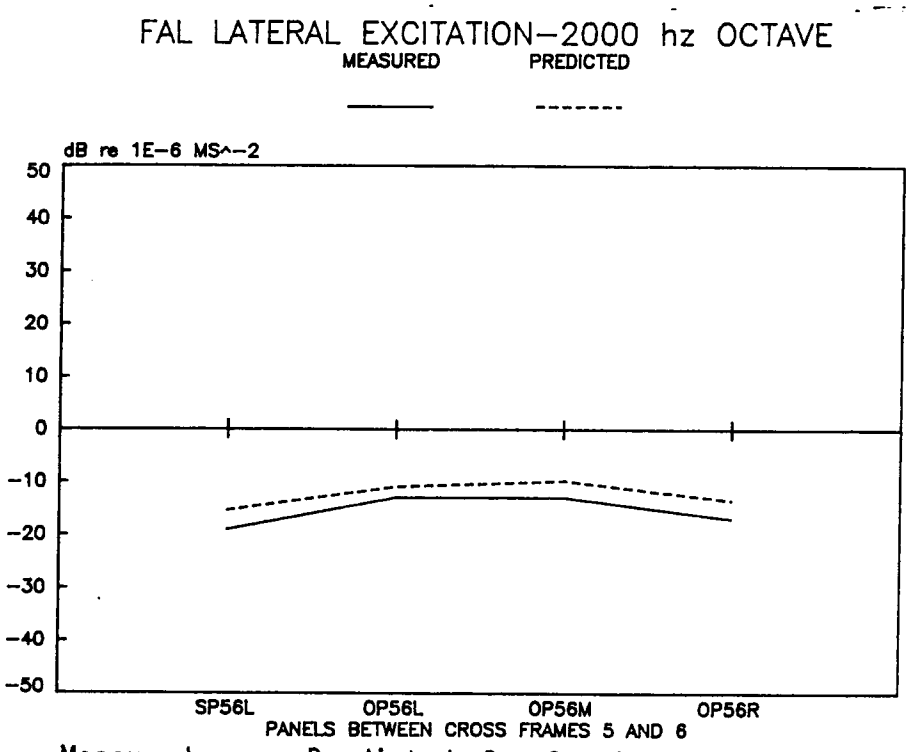

Figure E13c. Measured vs. Predicted Panel Vibration, Between CF5&6, FAL Lateral Excitation, 2 kHz

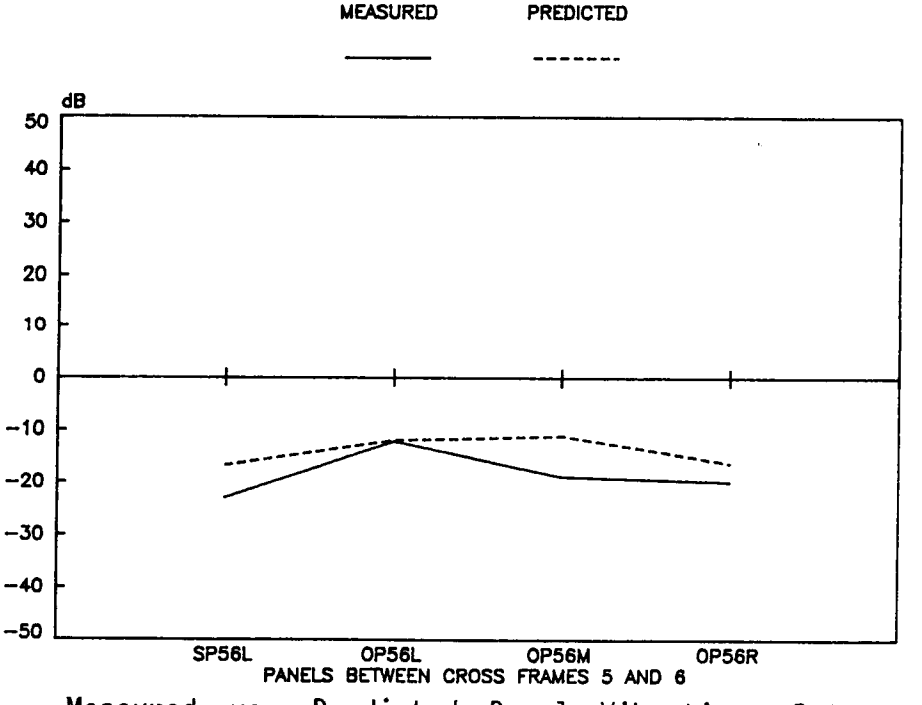

Figure E13d. Measured vs. Predicted Panel Vibration, Between CF5&6, FAL Lateral Excitation, 4 kHz

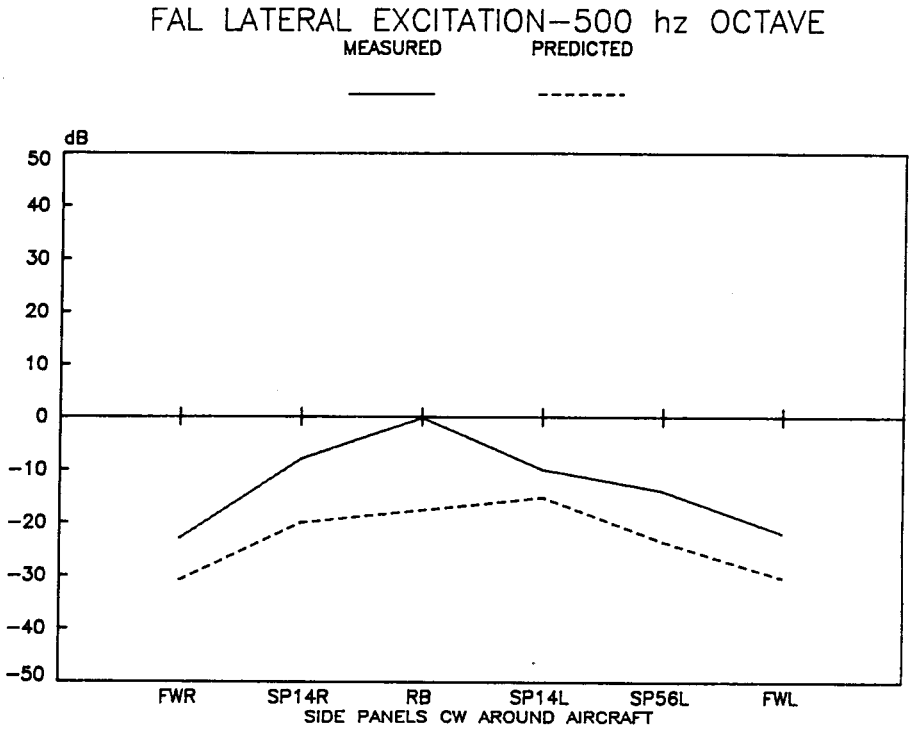

Figure E14a. Measured vs. Predicted Side Panel Vibration, FAL Lateral Excitation, .5 kHz

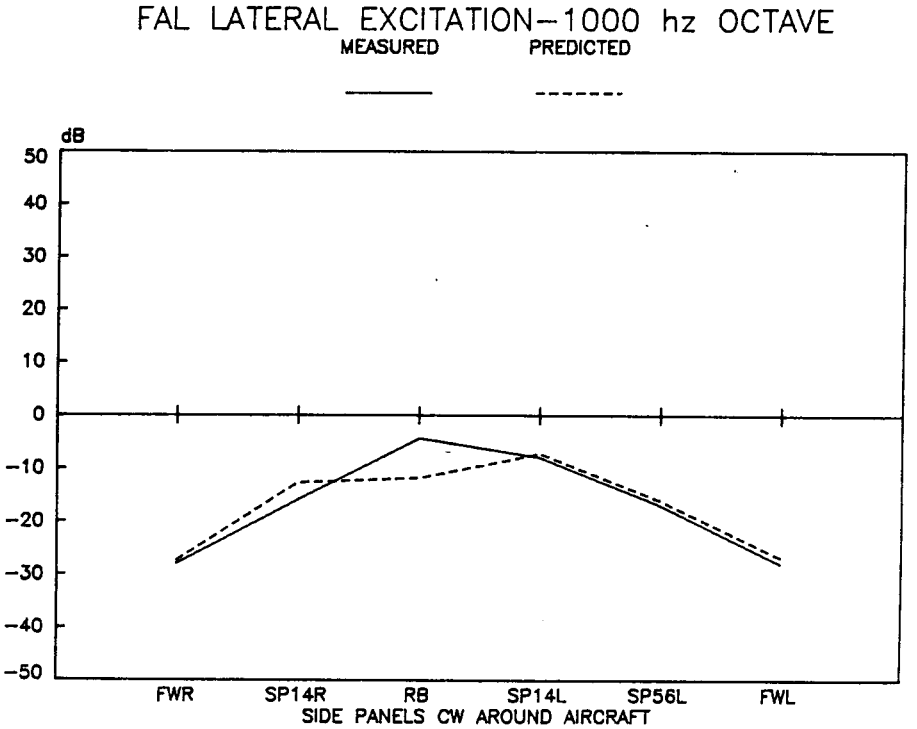

Figure E14b. Measured vs. Predicted Side Panel Vibration, FAL Lateral Excitation, 1 kHz

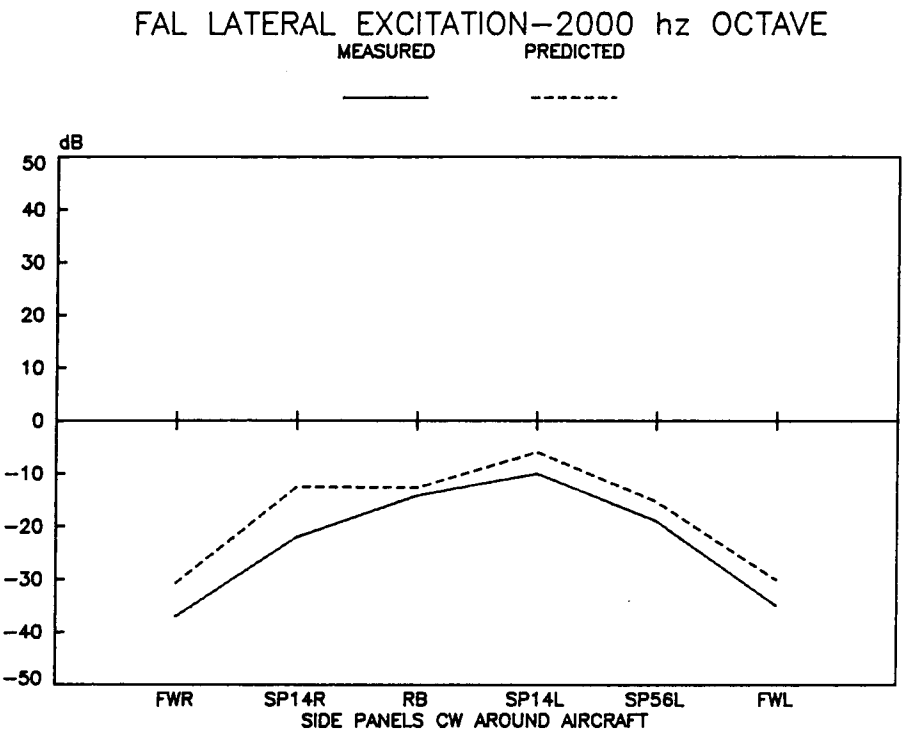

Figure E14c. Measured vs. Predicted Side Panel Vibration, FAL Lateral Excitation, 2 kHz

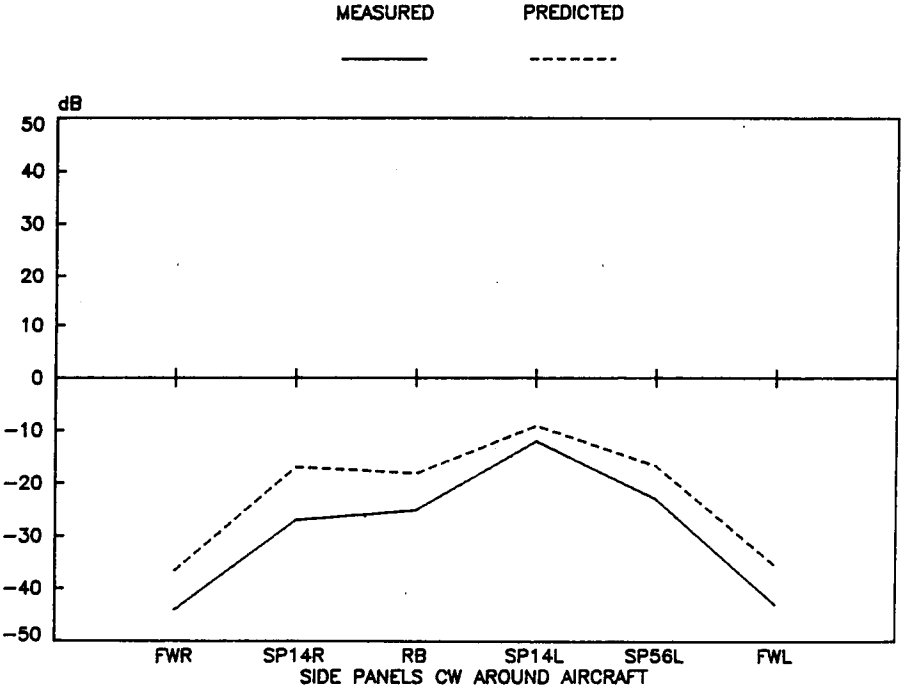

Figure E14d. Measured vs. Predicted Side Panel Vibration, FAL Lateral Excitation, 4 kHz

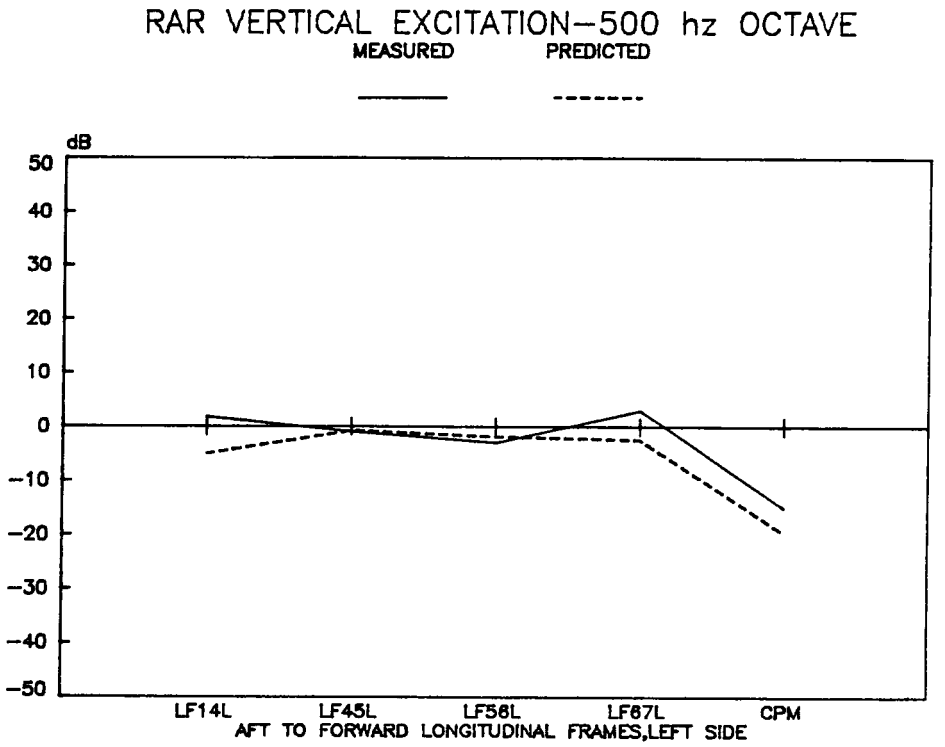

Figure E15a. Measured vs. Predicted Overhead Frame Vibration, Left Side, RAR Vertical Excitation, .5 kHz

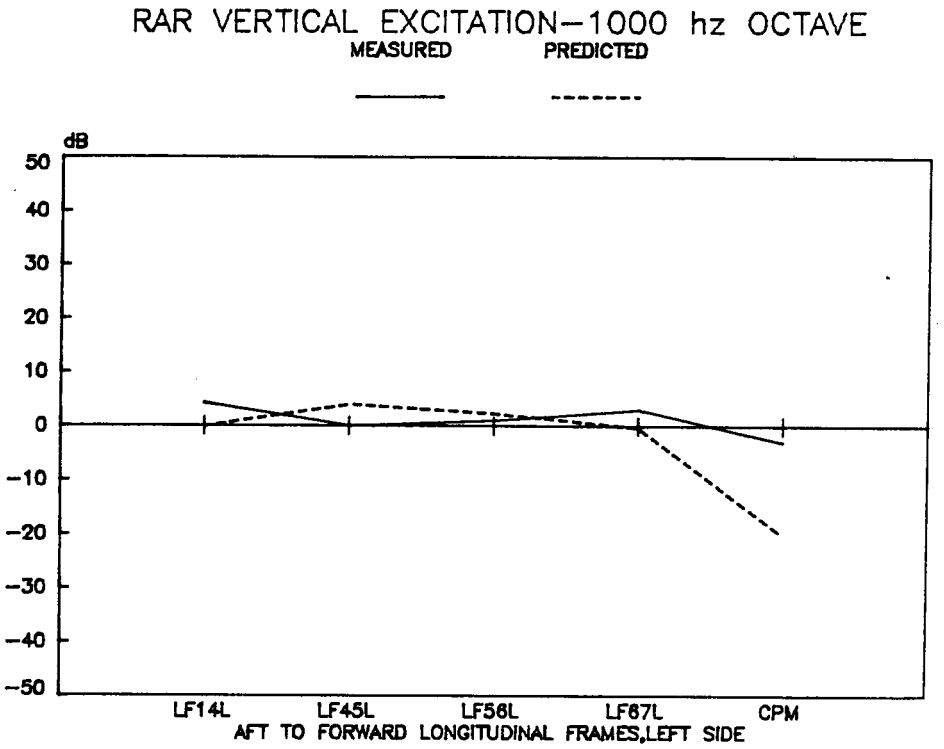

Figure E15b. Measured vs. Predicted Overhead Frame Vibration, Left Side, RAR Vertical Excitation, 1 kHz

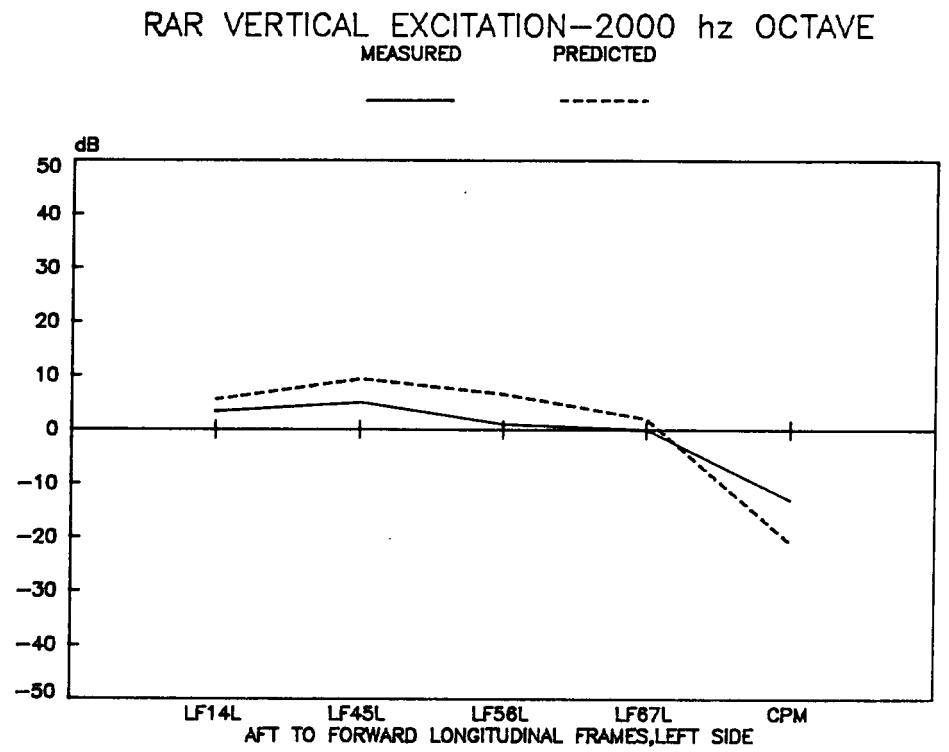

Figure E15c. Measured vs. Predicted Overhead Frame Vibration, Left Side, RAR Vertical Excitation, 2 kHz

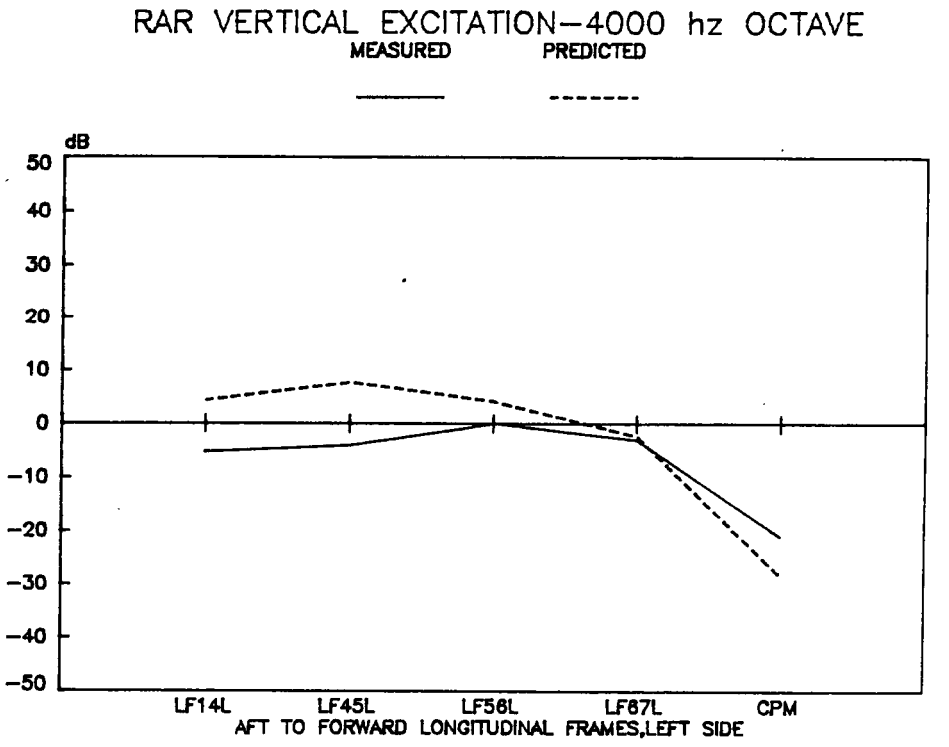

Figure E15d. Measured vs. Predicted Overhead Frame Vibration, Left Side, RAR Vertical Excitation, 4 kHz

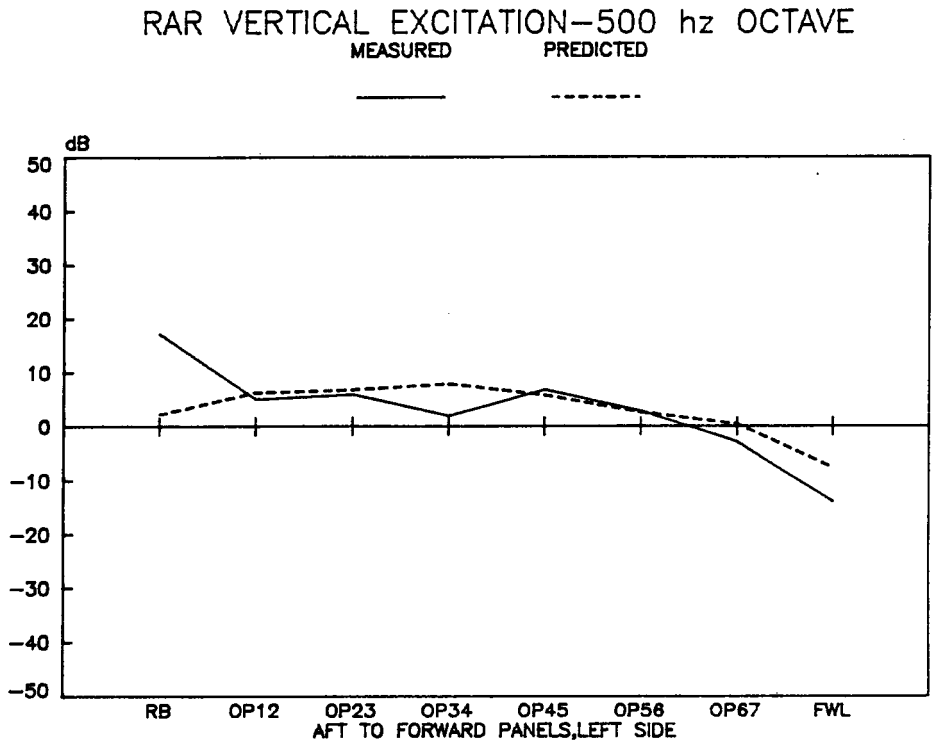

Figure E16a. Measured vs. Predicted Overhead Panel Vibration, Left Side, RAR Vertical Excitation, .5 kHz

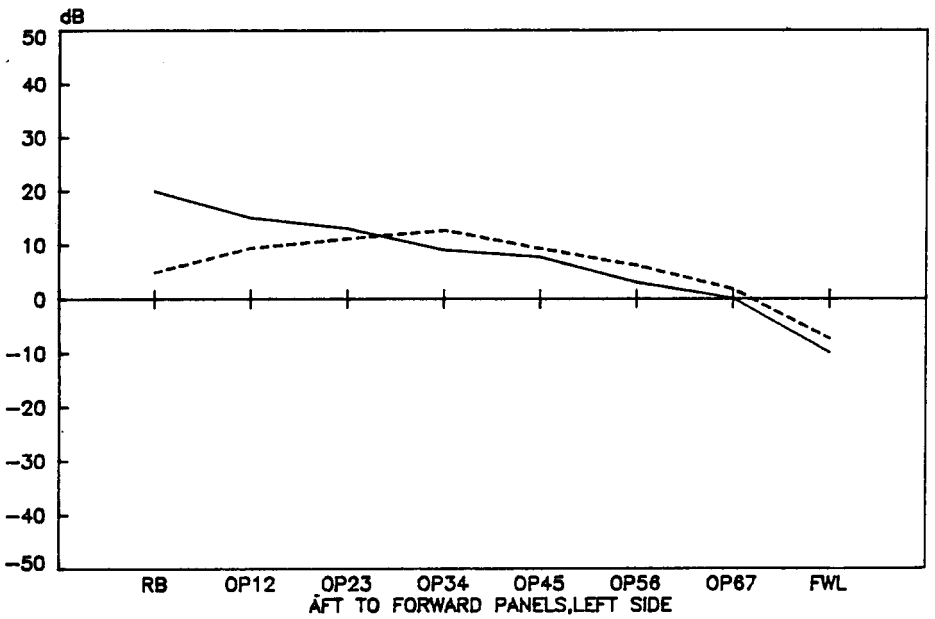

Figure E16b. Measured vs. Predicted Overhead Panel Vibration, Left Side, RAR Vertical Excitation, 1 kHz

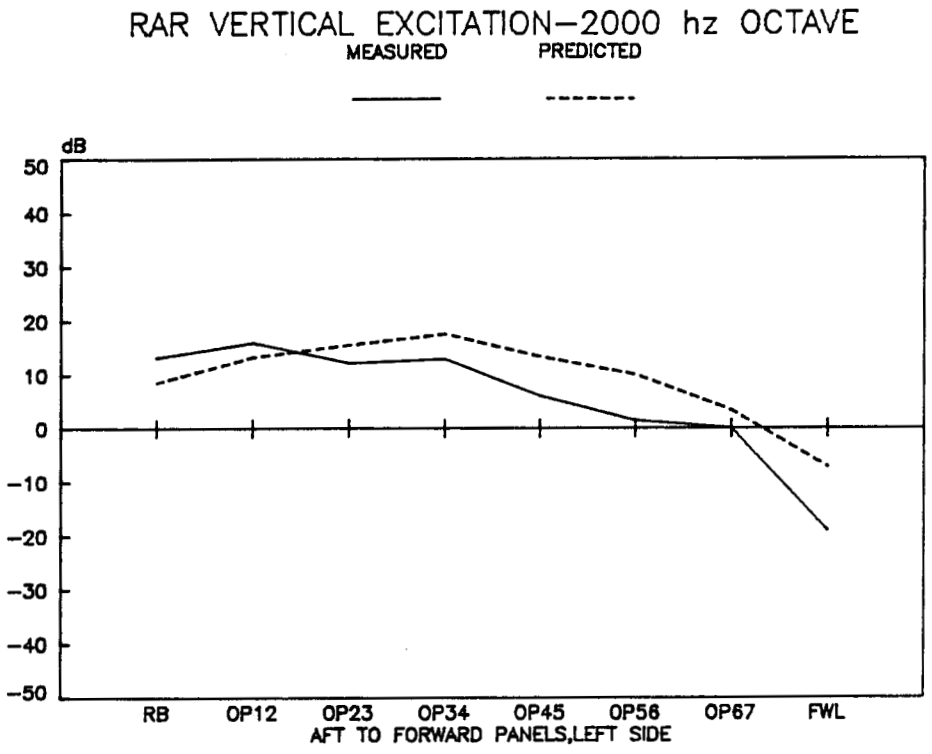

Figure E16c. Measured vs. Predicted Overhead Panel Vibration, Left Side, RAR Vertical Excitation, 2 kHz

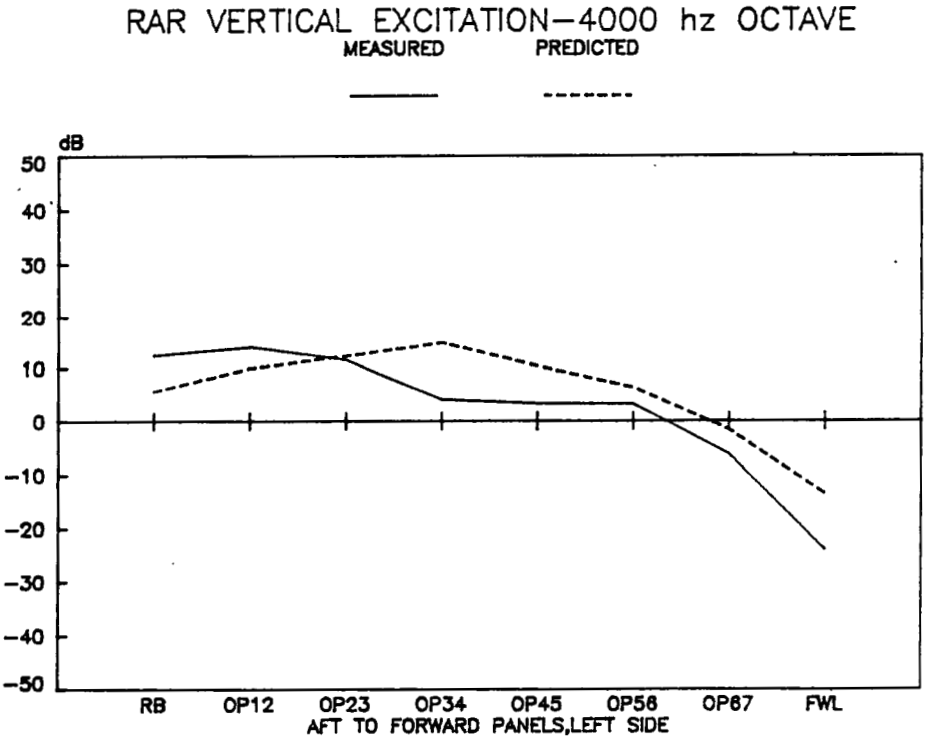

Figure E16d. Measured vs. Predicted Overhead Panel Vibration, Left Side, RAR Vertical Excitation, 4 kHz

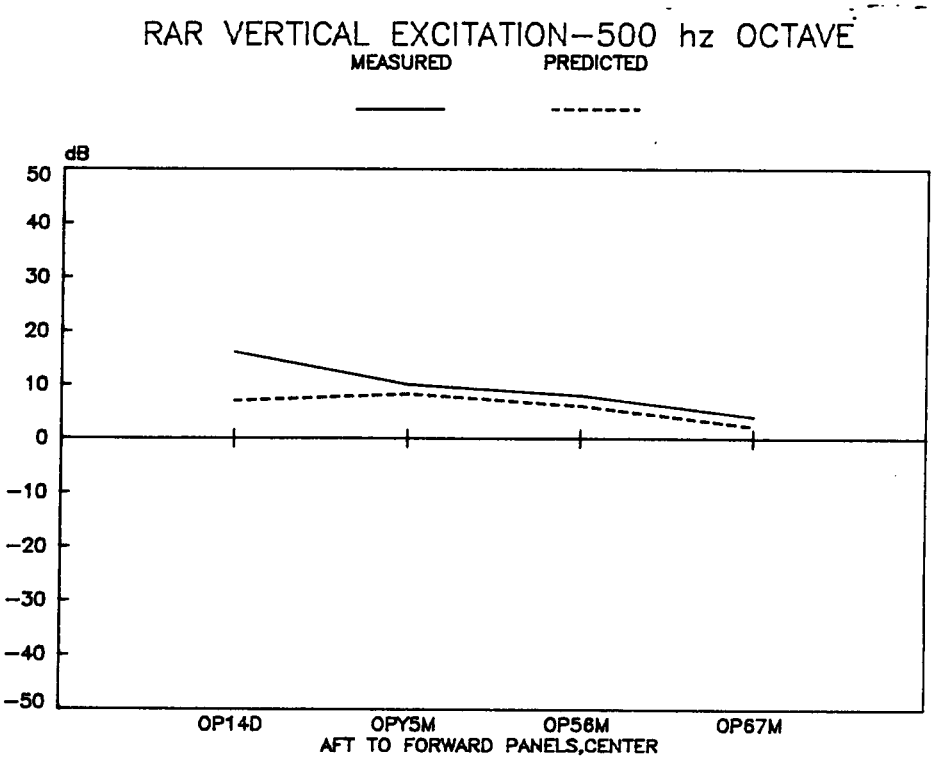

Figure E17a. Measured vs. Predicted Overhead Panel Vibration, Middle, RAR Vertical Excitation, .5 kHz

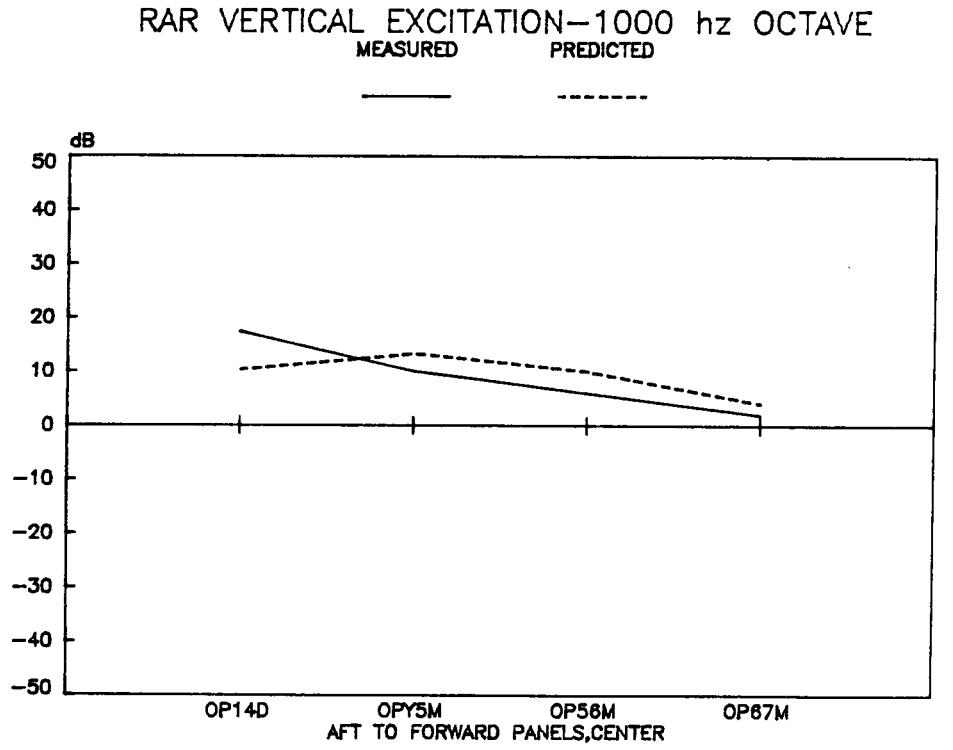

Figure E17b. Measured vs. Predicted Overhead Panel Vibration, Middle, RAR Vertical Excitation, 1 kHz

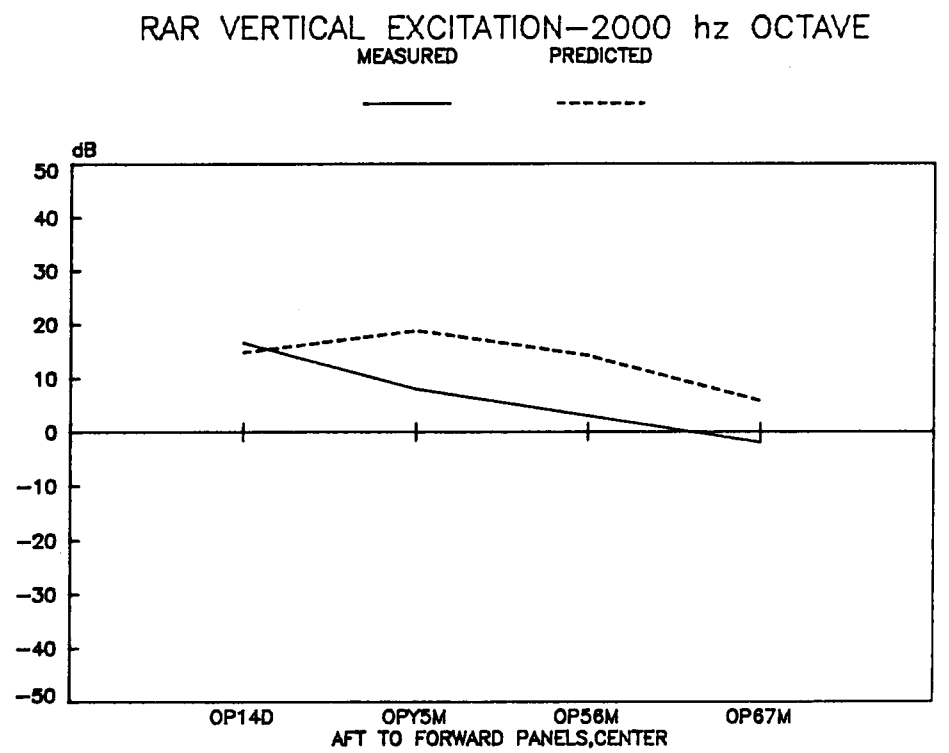

Figure E17c. Measured vs. Predicted Overhead Panel Vibration, Middle, RAR Vertical Excitation, 2 kHz

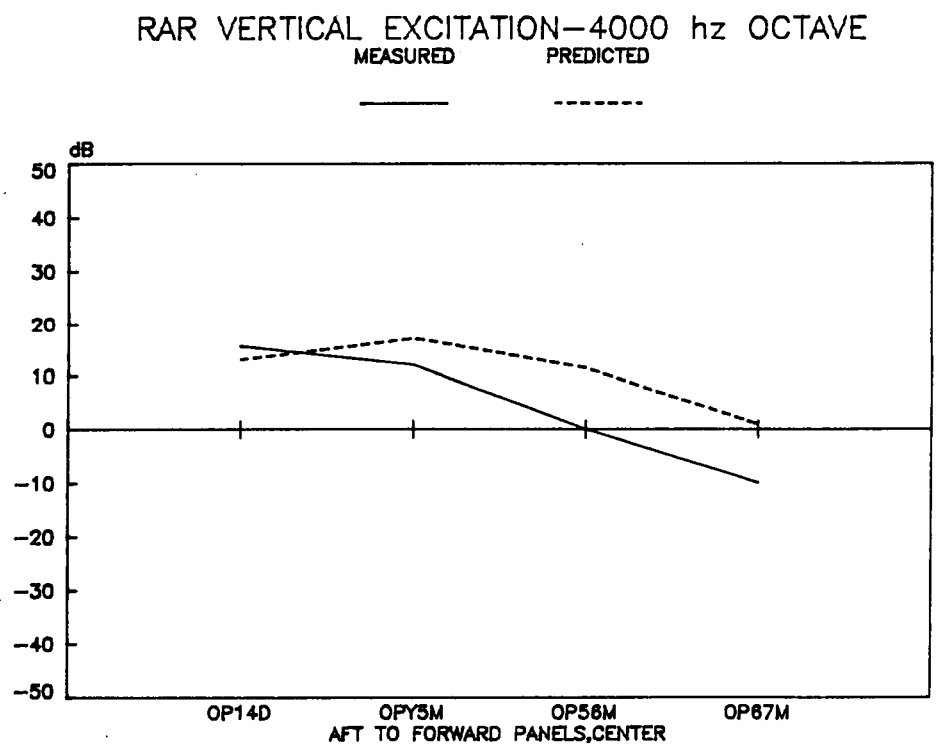

Figure E17d. Measured vs. Predicted Overhead Panel Vibration, Middle, RAR Vertical Excitation, 4 kHz

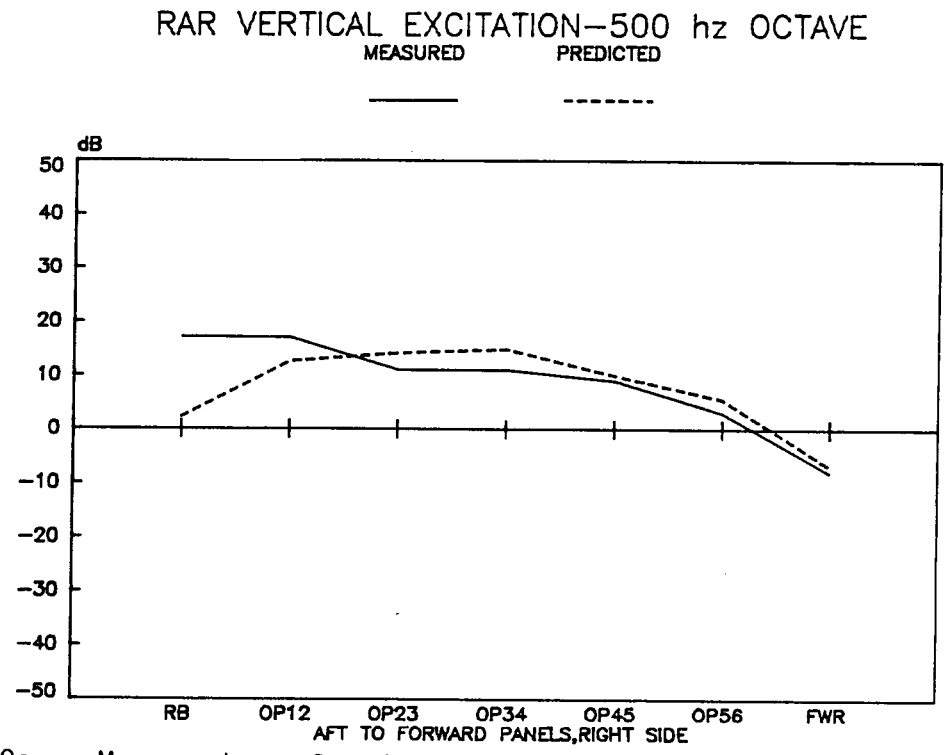

Figure E18a. Measured vs. Predicted Overhead Panel Vibration, Right Side, RAR Vertical Excitation, .5 kHz

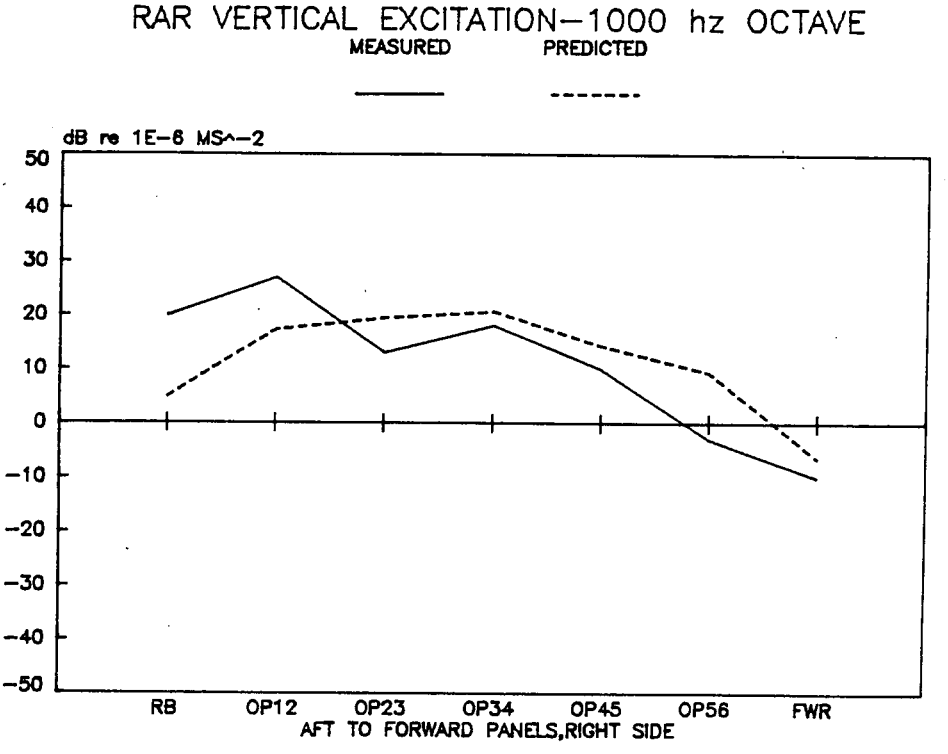

Figure E18b. Measured vs. Predicted Overhead Panel Vibration, Right Side, RAR Vertical Excitation, 1 kHz

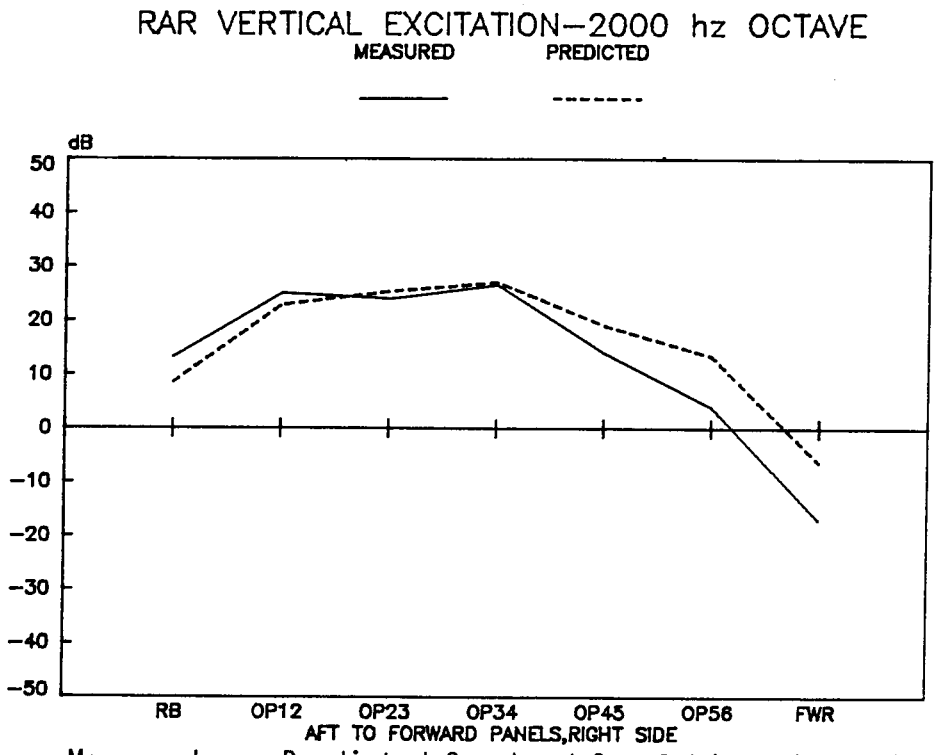

Figure E18c. Measured vs. Predicted Overhead Panel Vibration, Right Side, RAR Vertical Excitation, 2 kHz

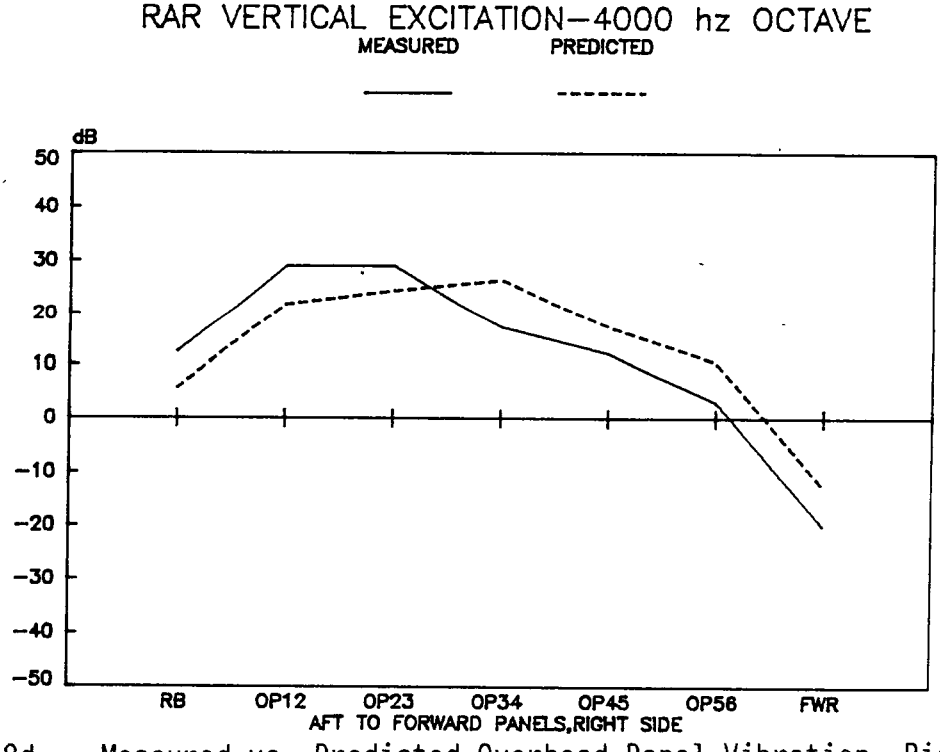

Figure E18d. Measured vs. Predicted Overhead Panel Vibration, Right Side, RAR Vertical Excitation, 4 kHz

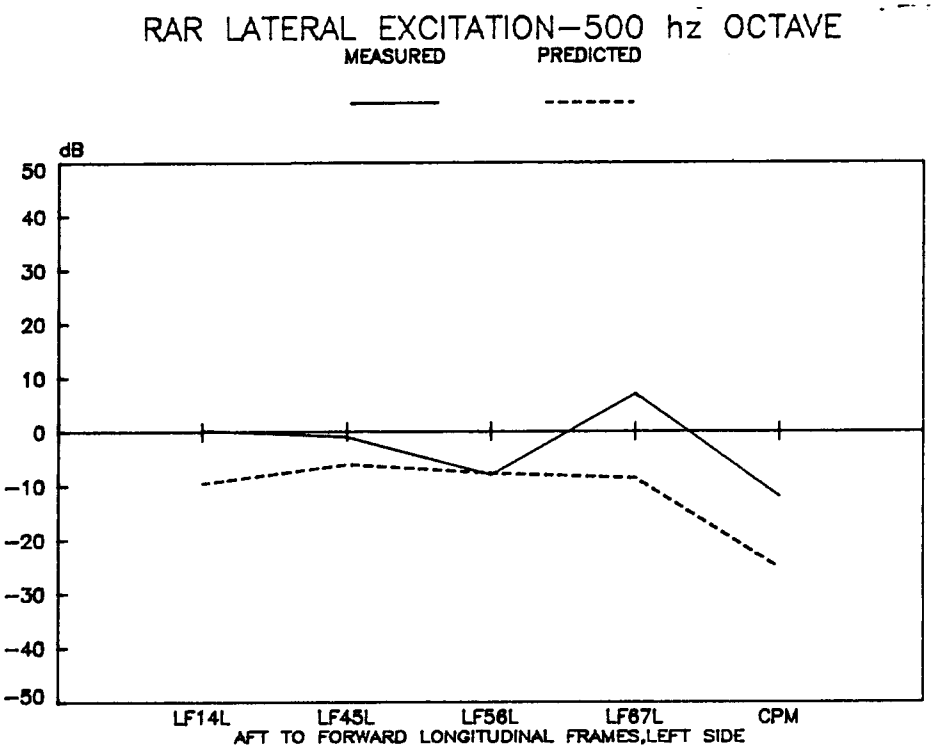

Figure E19a. Measured vs. Predicted Overhead Frame Vibration, Left Side, RAR Lateral Excitation, .5 kHz

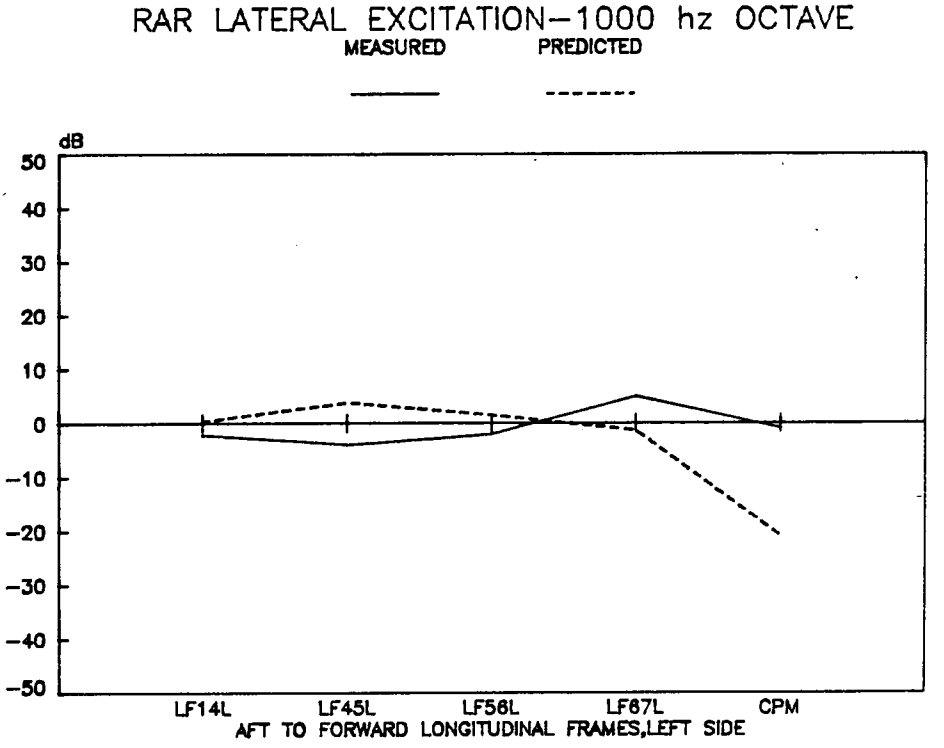

Figure E19b. Measured vs. Predicted Overhead Frame Vibration, Left Side, RAR Lateral Excitation, 1 kHz

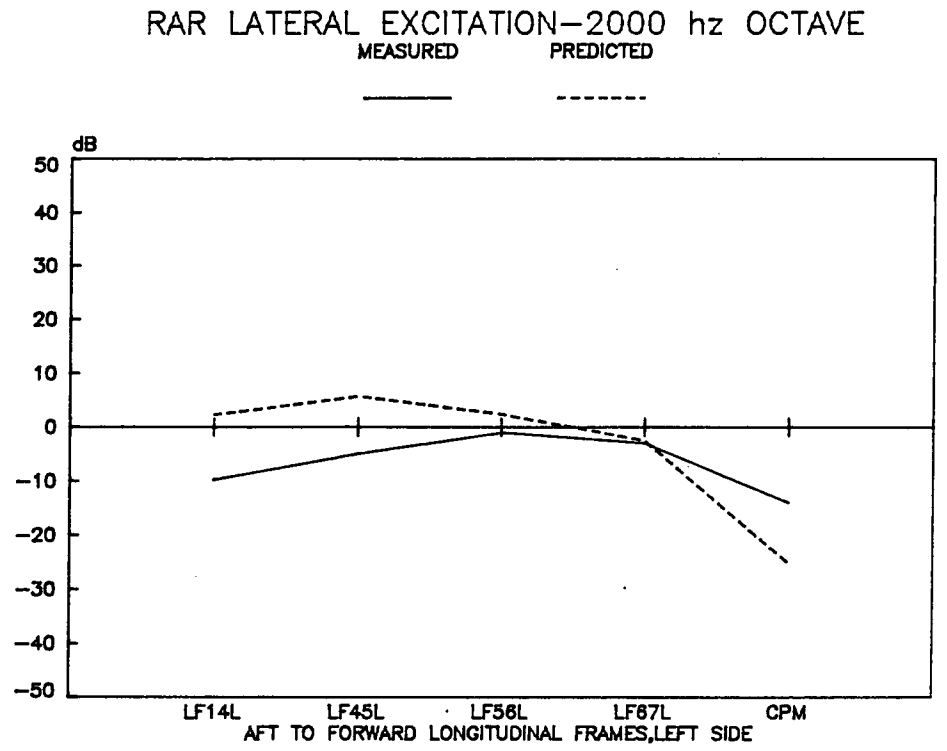

Figure E19c. Measured vs. Predicted Overhead Frame Vibration, Left Side, RAR Lateral Excitation, 2 kHz

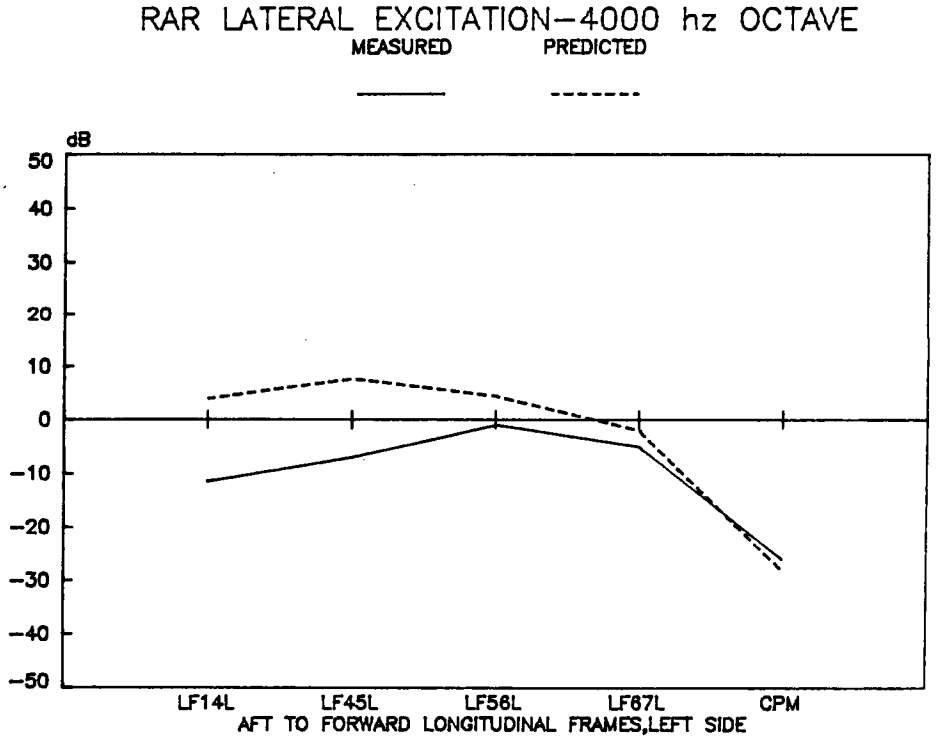

Figure E19d. Measured vs. Predicted Overhead Frame Vibration, Left Side, RAR Lateral Excitation, 4 kHz

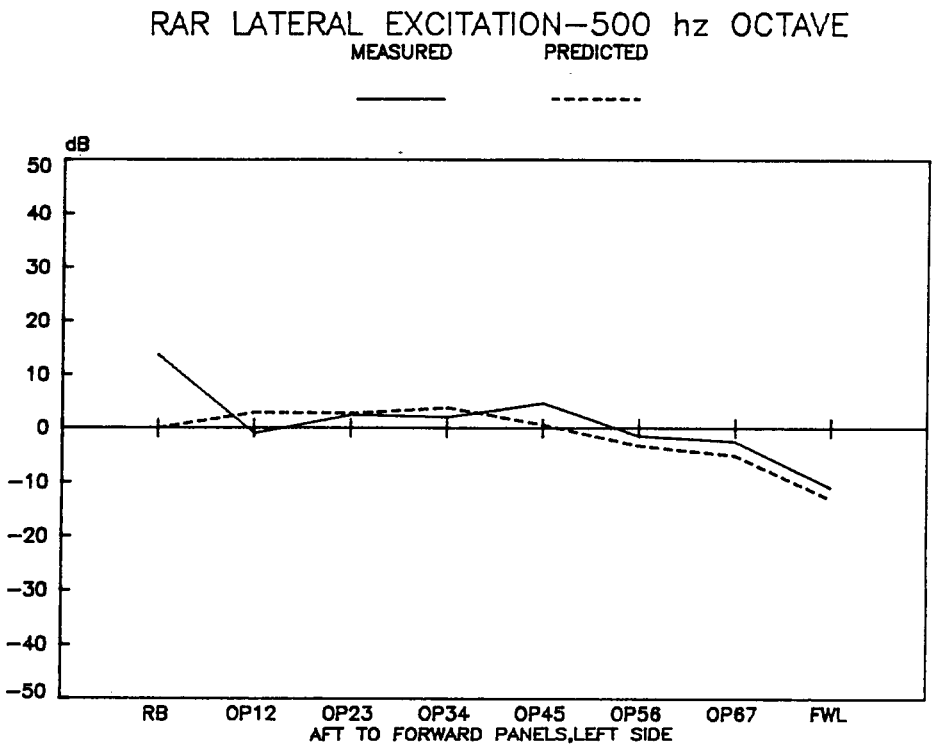

Figure E20a. Measured vs. Predicted Overhead Panel Vibration, Left Side, RAR Lateral Excitation, .5 kHz

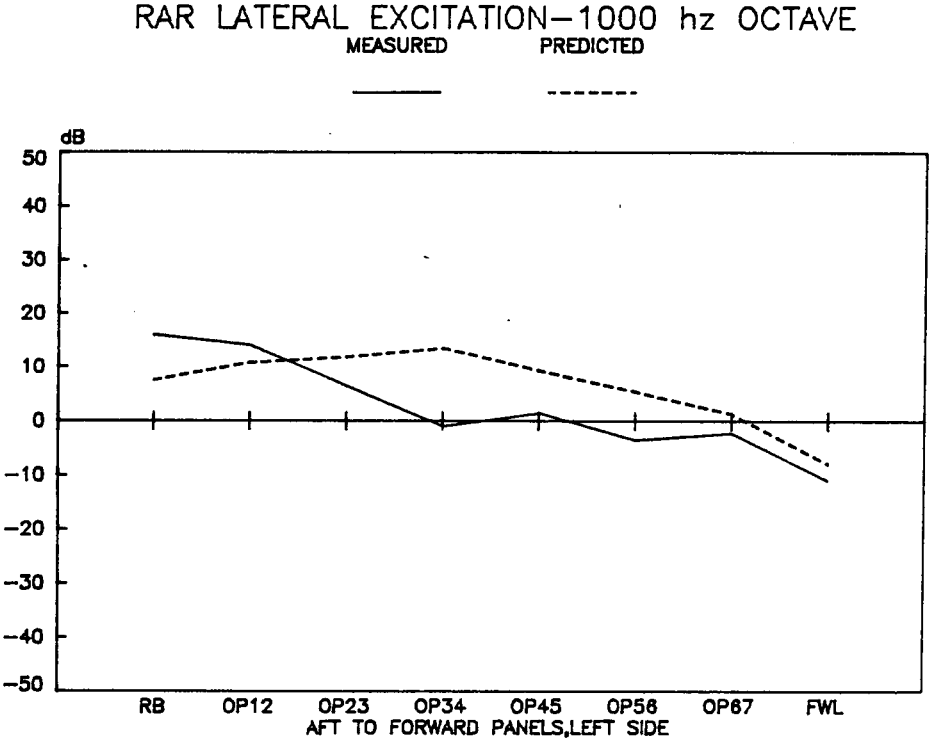

Figure E20b. Measured vs. Predicted Overhead Panel Vibration, Left Side, RAR Lateral Excitation, 1 kHz

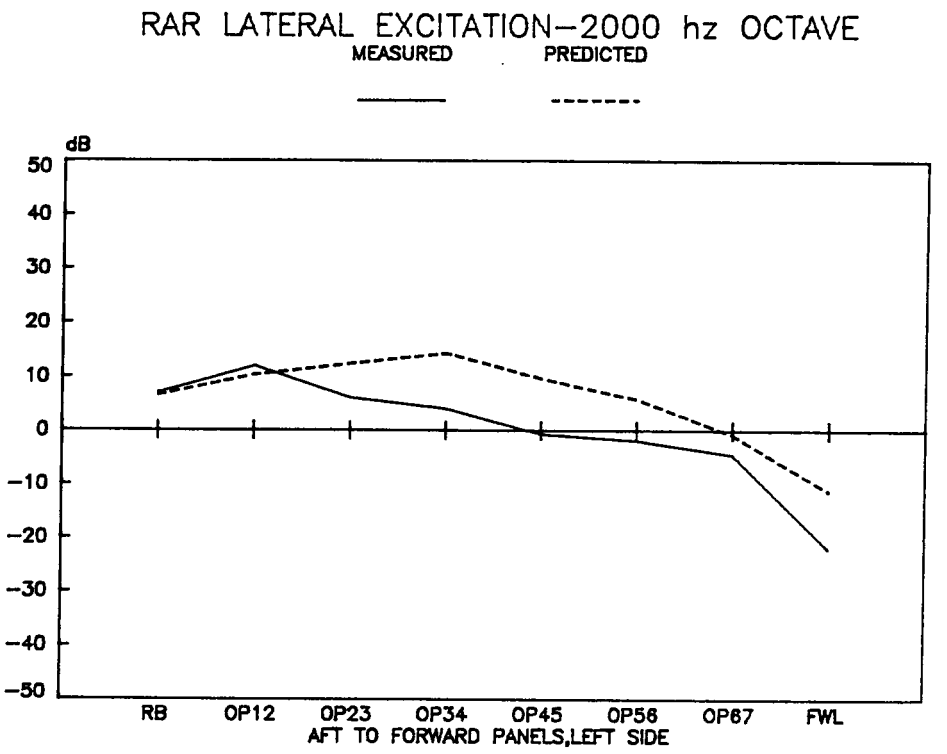

Figure E20c. Measured vs. Predicted Overhead Panel Vibration, Left Side, RAR Lateral Excitation, 2 kHz

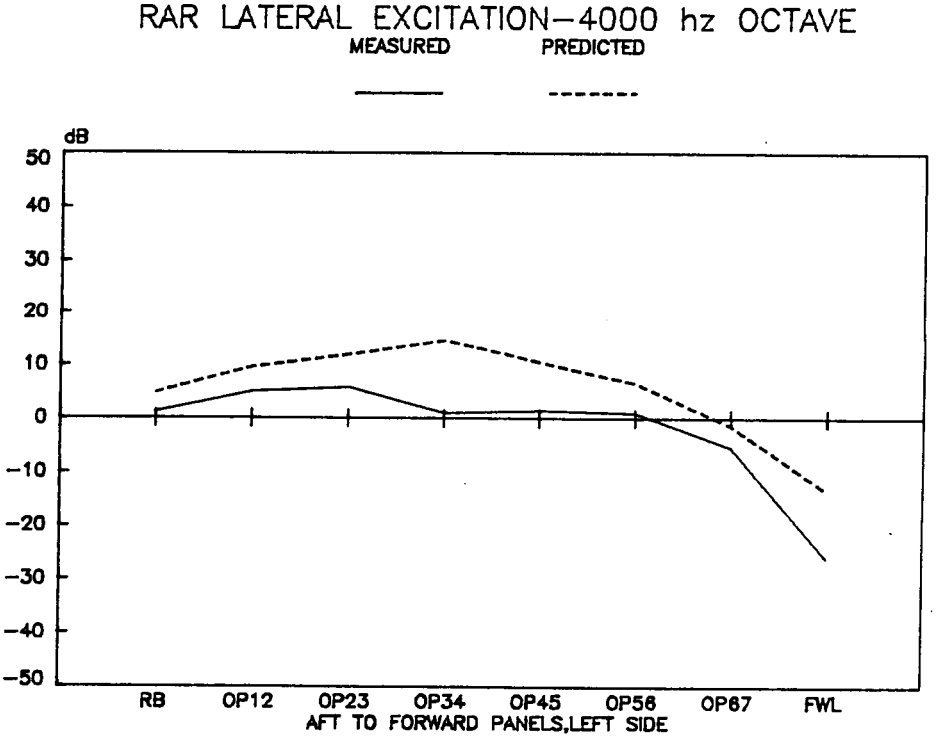

Figure E20d. Measured vs. Predicted Overhead Panel Vibration, Left Side, RAR Lateral Excitation, 4 kHz

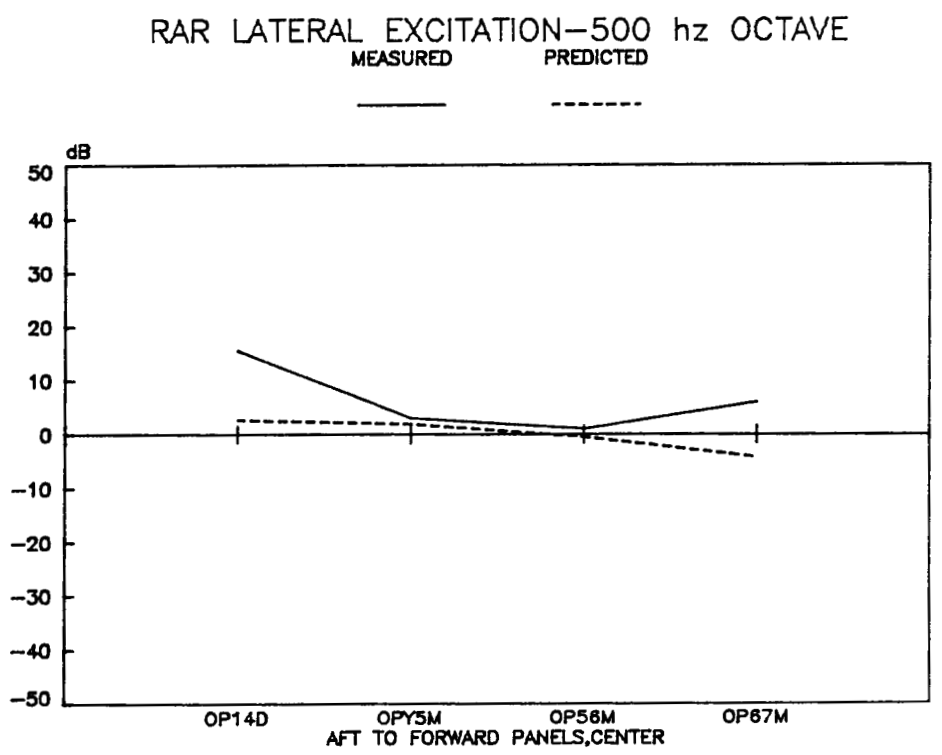

Figure E21a. Measured vs. Predicted Overhead Panel Vibration, Middle, RAR Lateral Excitation, .5 kHz

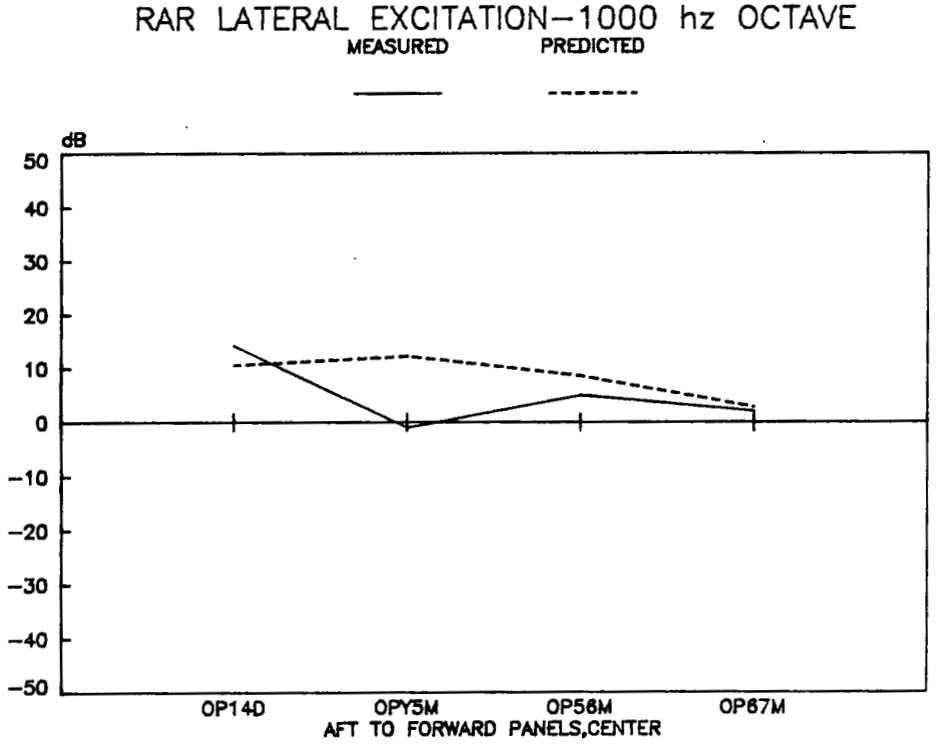

Figure E21b. Measured vs. Predicted Overhead Panel Vibration, Middle, RAR Lateral Excitation, 1 kHz

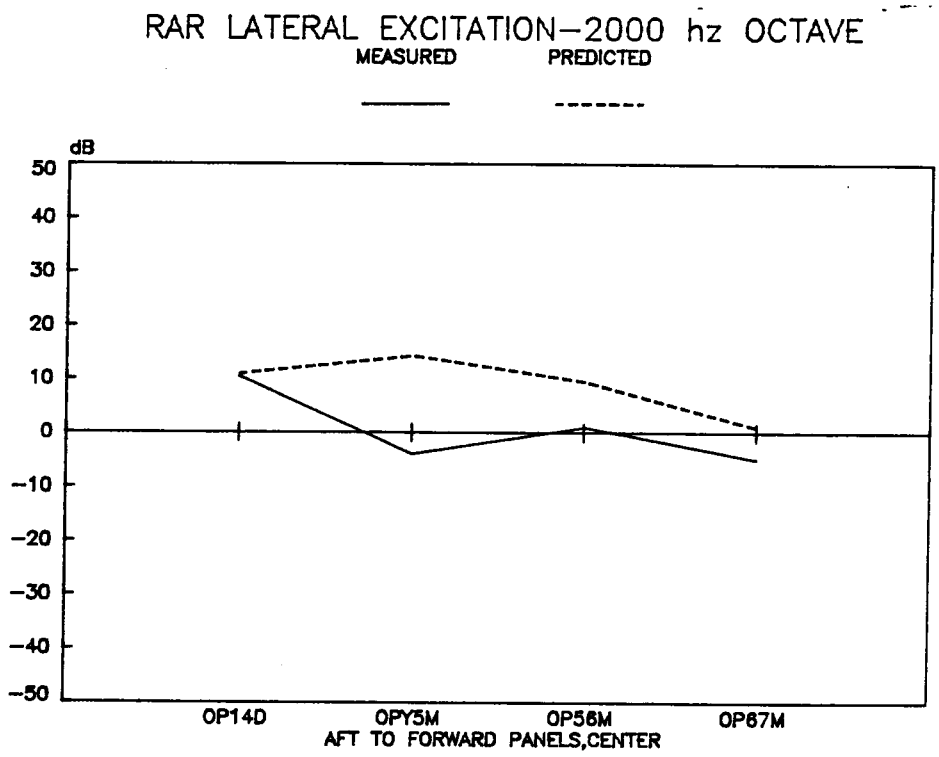

Figure E21c. Measured vs. Predicted Overhead Panel Vibration, Middle, RAR Lateral Excitation, 2 kHz

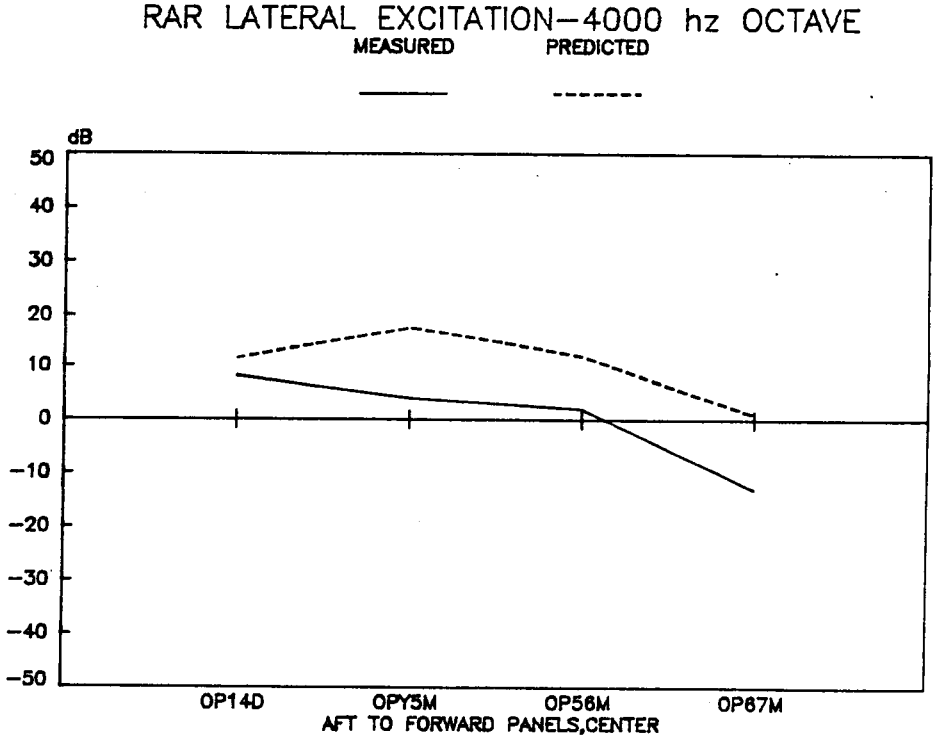

Figure E21d. Measured vs. Predicted Overhead Panel Vibration, Middle, RAR Lateral Excitation, 4 kHz

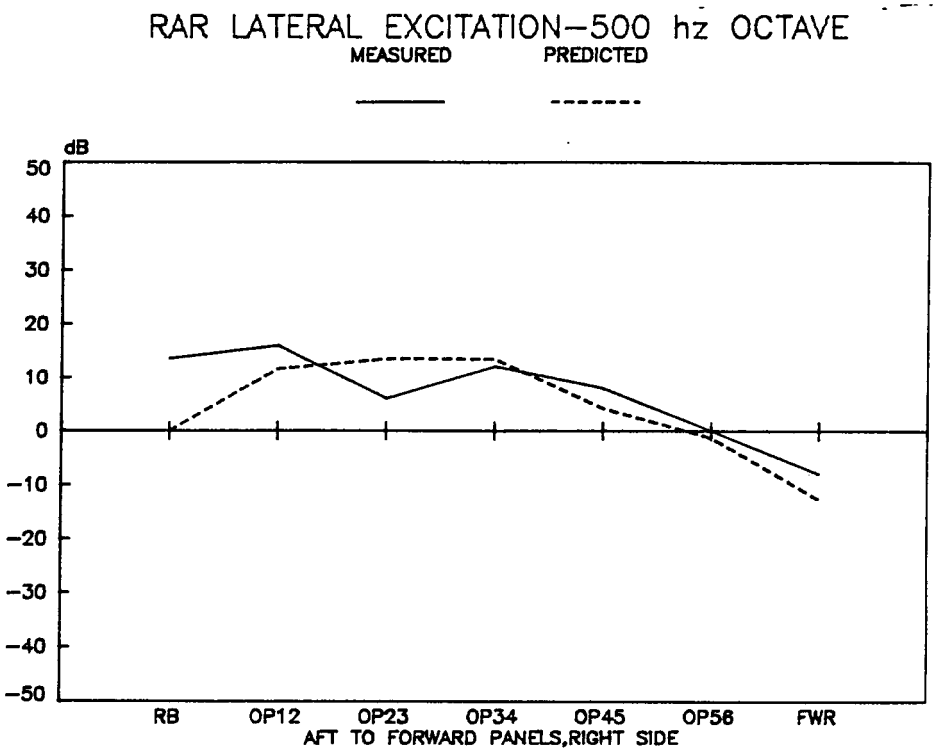

Figure E22a. Measured vs. Predicted Overhead Panel Vibration, Right Side, RAR Lateral Excitation, .5 kHz

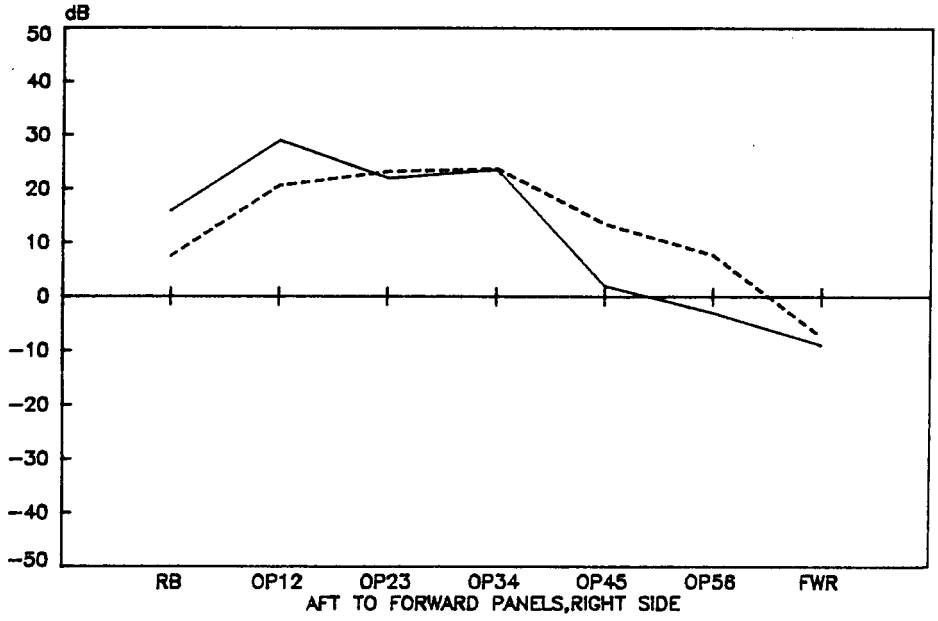

Figure E22b. Measured vs. Predicted Overhead Panel Vibration, Right Side, RAR Lateral Excitation, 1 kHz

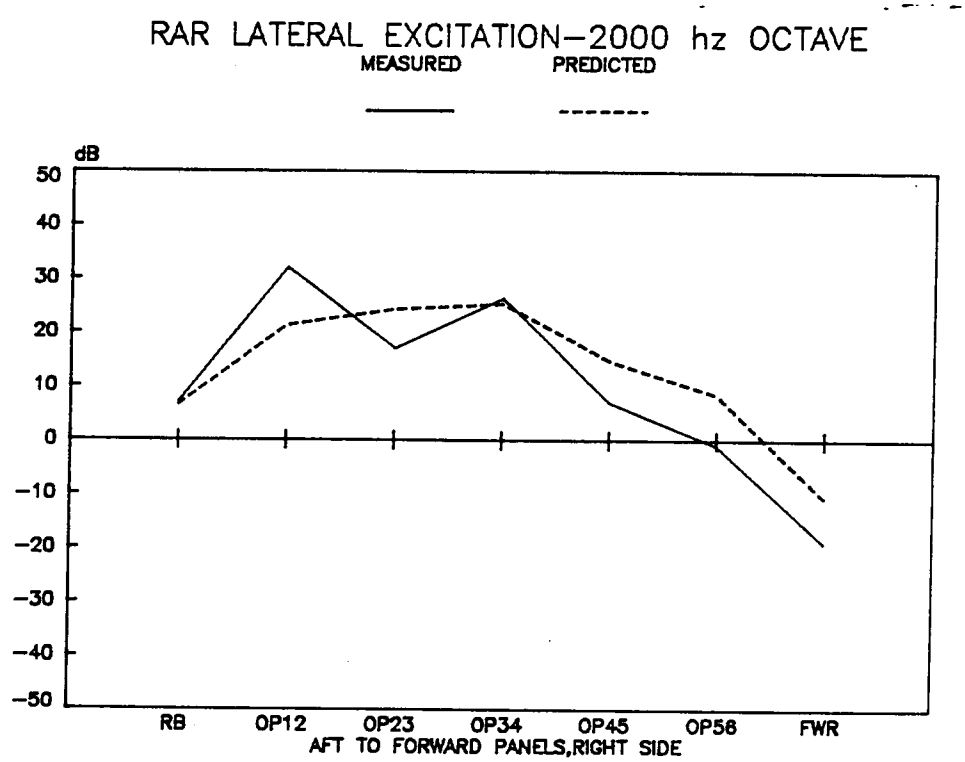

Figure E22c. Measured vs. Predicted Overhead Panel Vibration, Right Side, RAR Lateral Excitation, 2 kHz

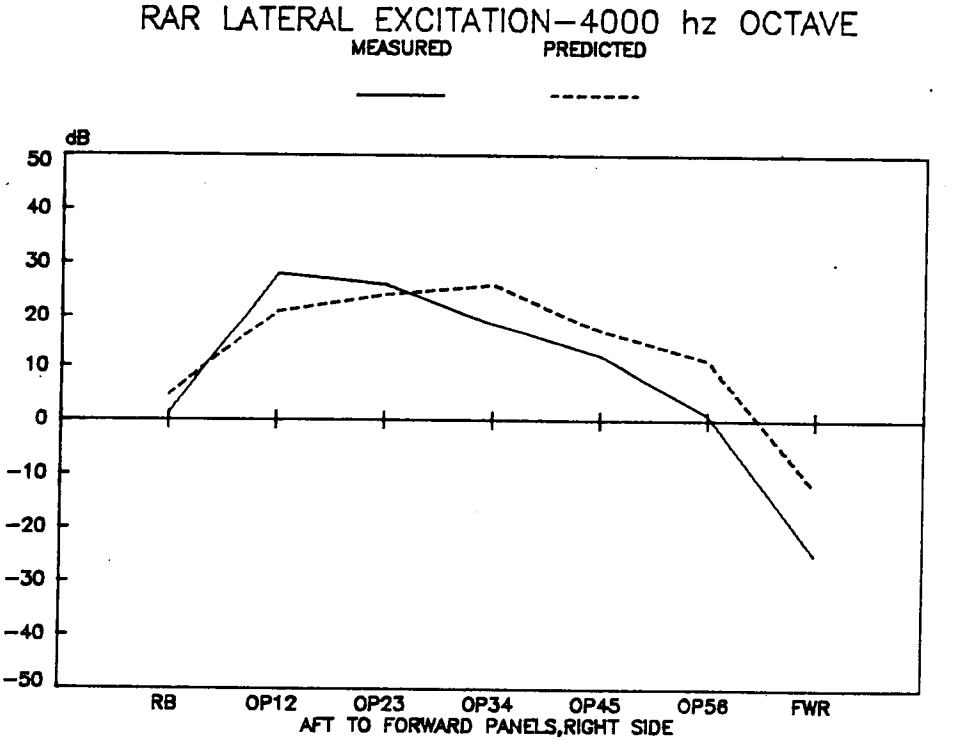

Figure E22d. Measured vs. Predicted Overhead Panel Vibration, Right Side, RAR Lateral Excitation, 4 kHz

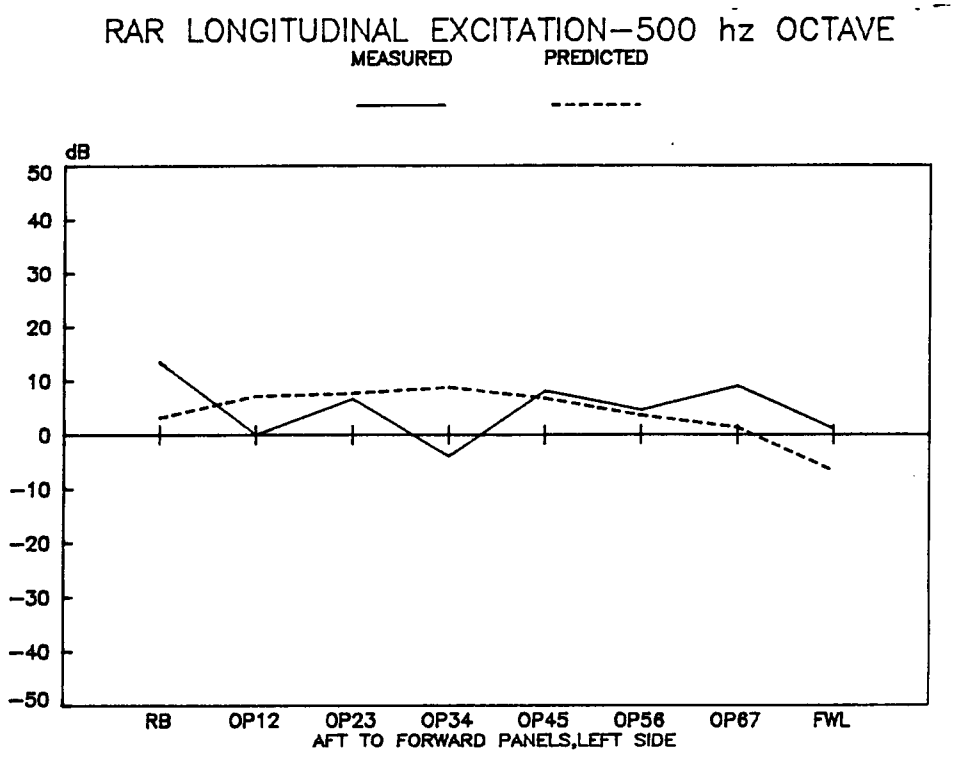

Figure E23a. Measured vs. Predicted Overhead Panel Vibration, Left Side, RAR Longitudinal Excitation, .5 kHz

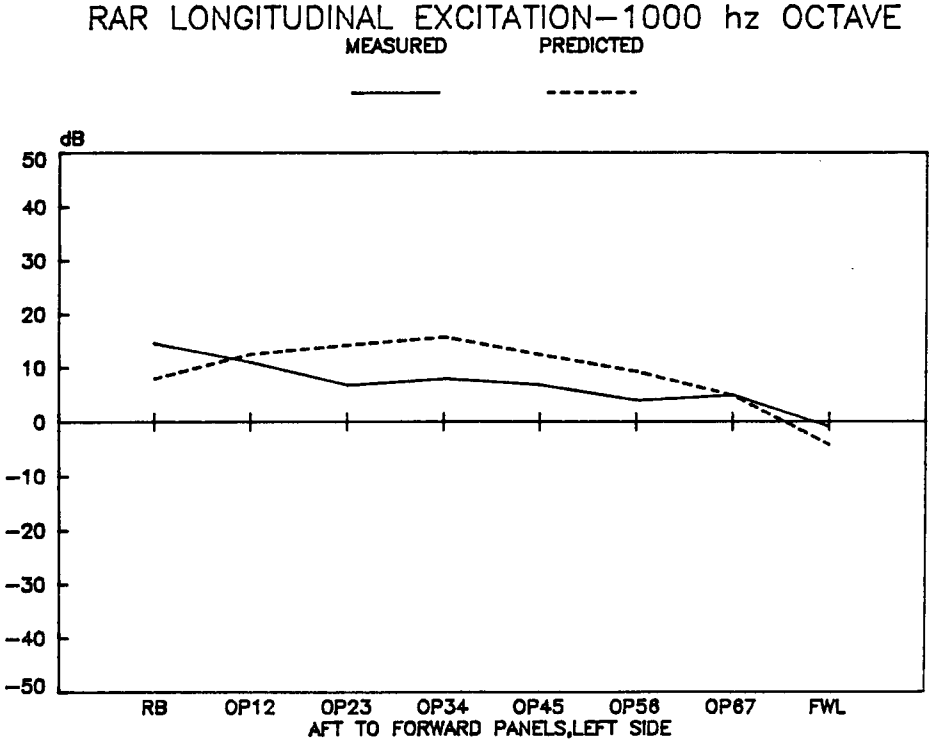

Figure E23b. Measured vs. Predicted Overhead Panel Vibration, Left Side, RAR Longitudinal Excitation, 1 kHz

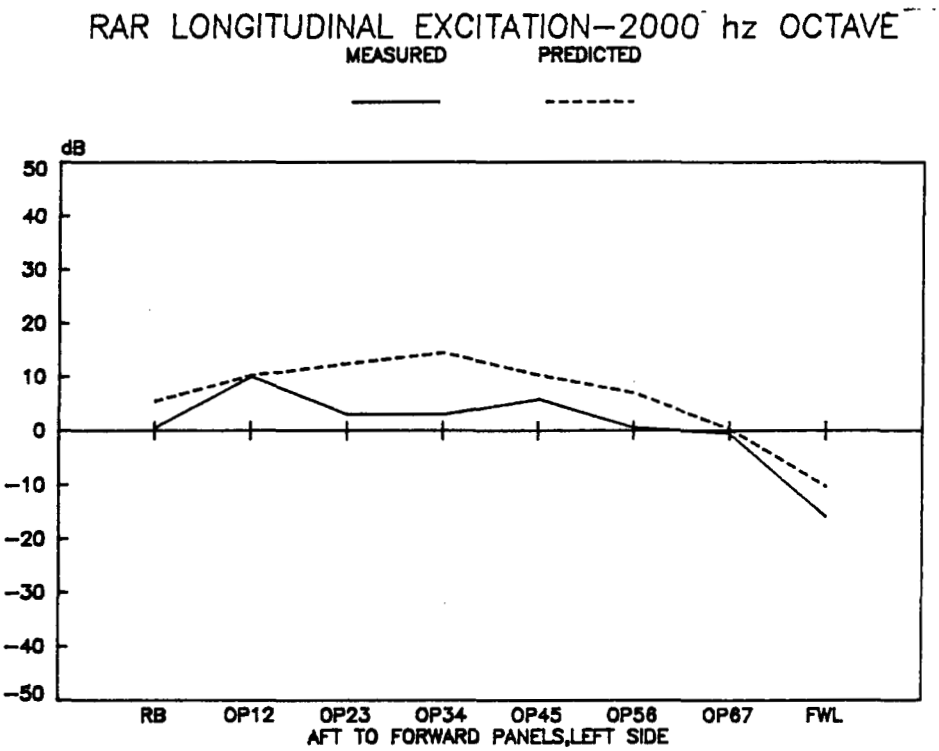

Figure E23c. Measured vs. Predicted Overhead Panel Vibration, Left Side, RAR Longitudinal Excitation, 2 kHz

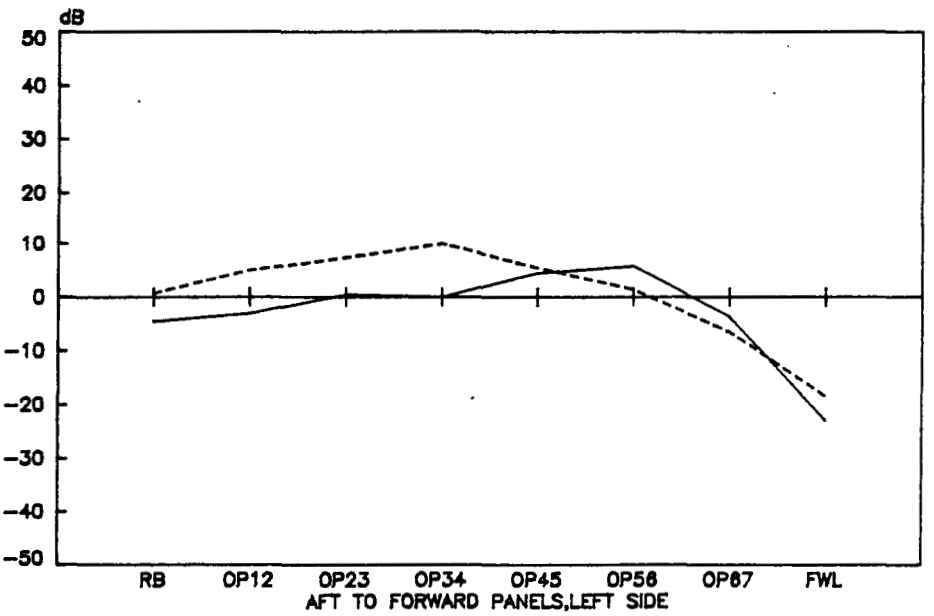

Figure E23d. Measured vs. Predicted Overhead Panel Vibration, Left Side, RAR Longitudinal Excitation, 4 kHz

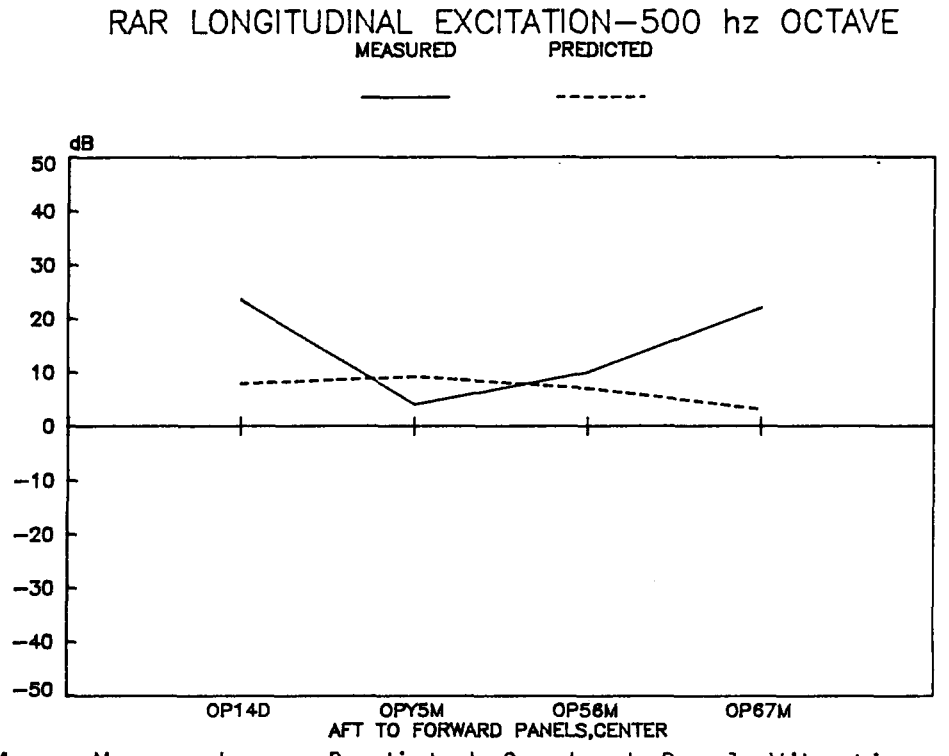

Figure E24a. Measured vs. Predicted Overhead Panel Vibration, Middle, RAR Longitudinal Excitation, .5 kHz

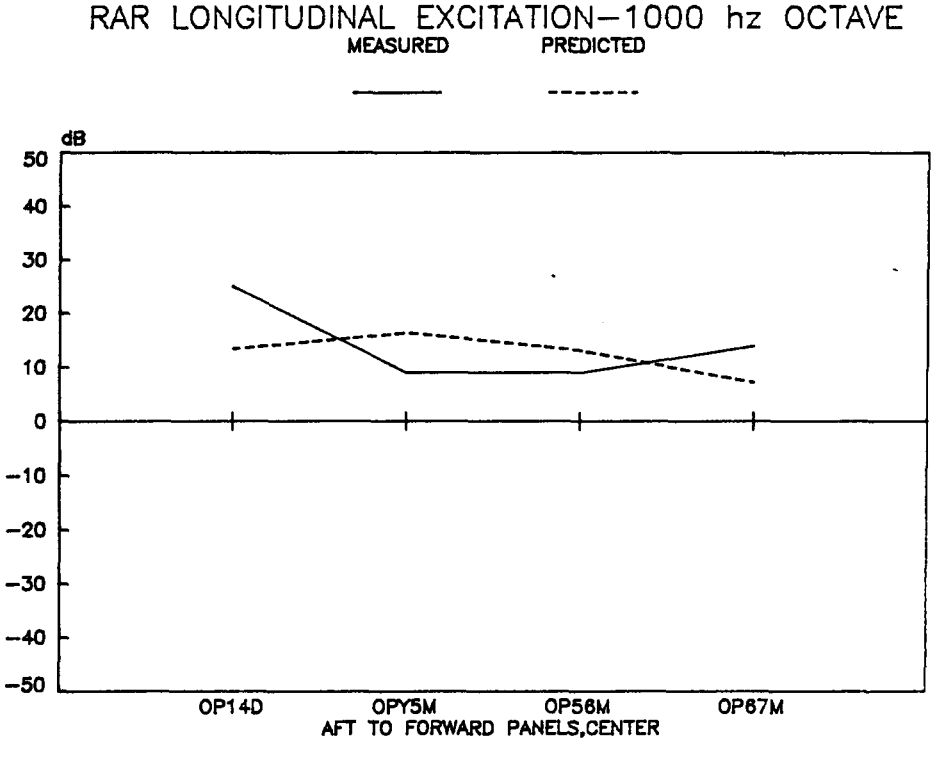

Figure E24b. Measured vs. Predicted Overhead Panel Vibration, Middle, RAR Longitudinal Excitation, 1 kHz

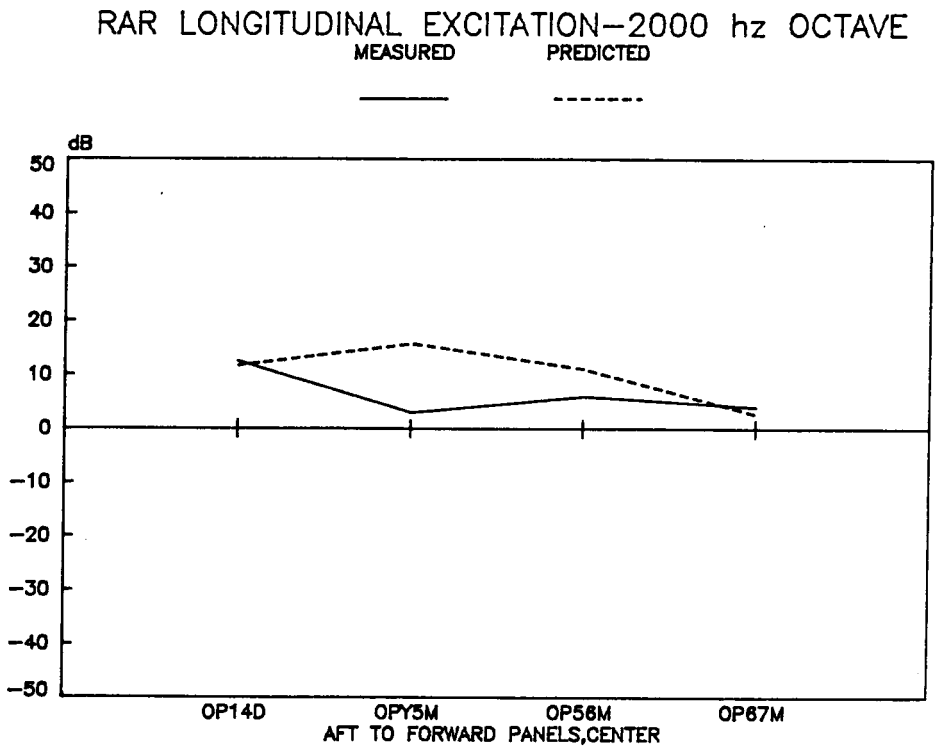

Figure E24c. Measured vs. Predicted Overhead Panel Vibration, Middle, RAR Longitudinal Excitation, 2 kHz

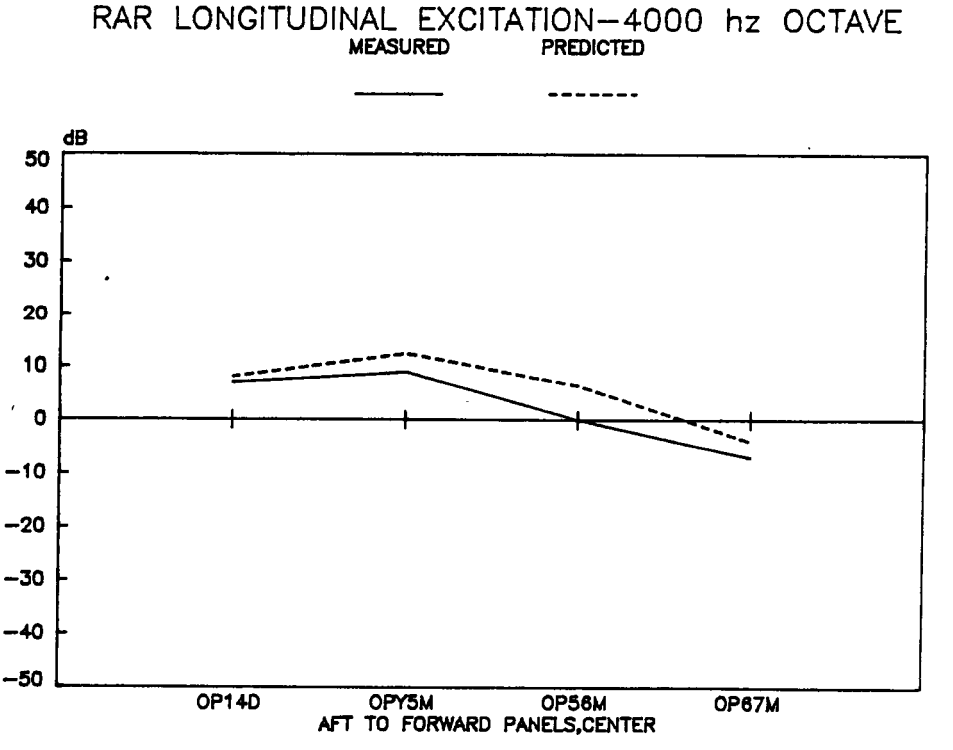

Figure E24d. Measured vs. Predicted Overhead Panel Vibration, Middle, RAR Longitudinal Excitation, 4 kHz

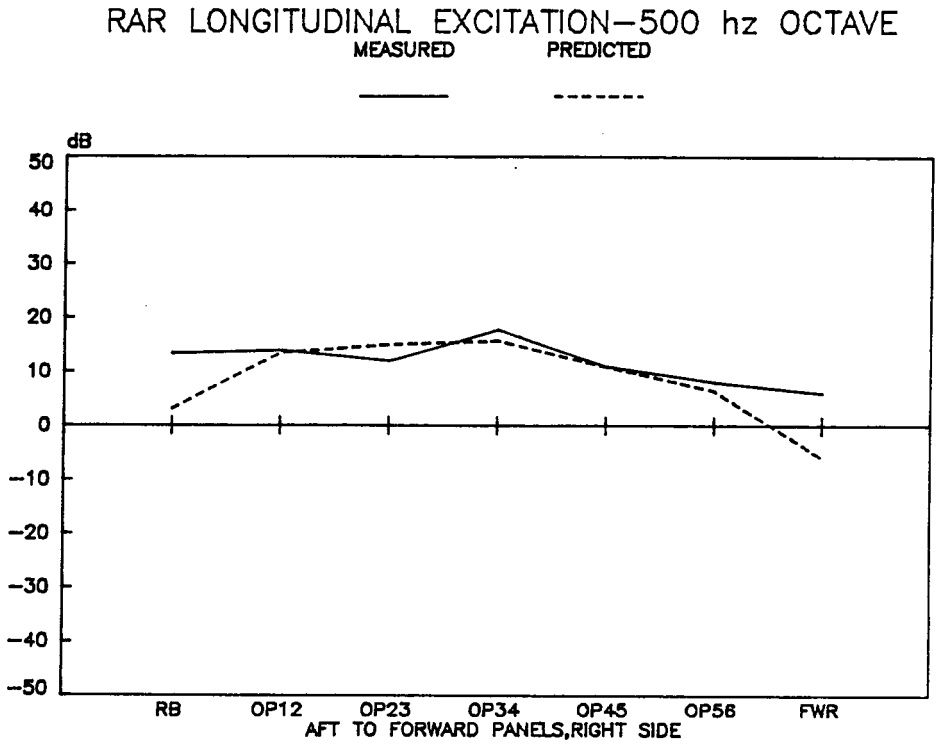

Figure E25a. Measured vs. Predicted Overhead Panel Vibration, Right Side, RAR Longitudinal Excitation, .5 kHz

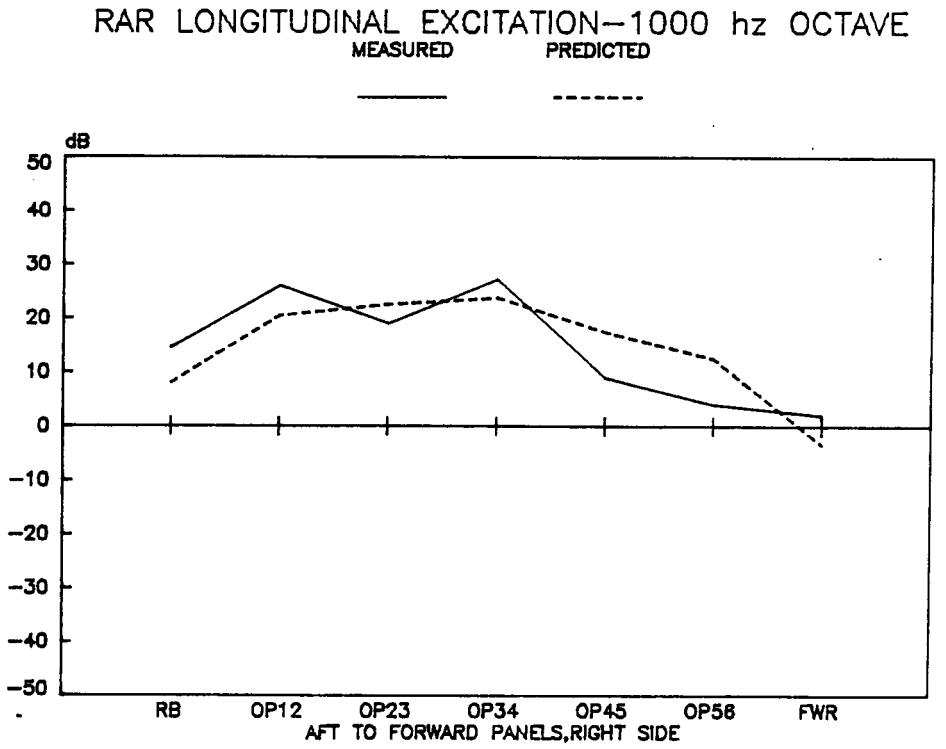

Figure E25b. Measured vs. Predicted Overhead Panel Vibration, Right Side, RAR Longitudinal Excitation, 1 kHz

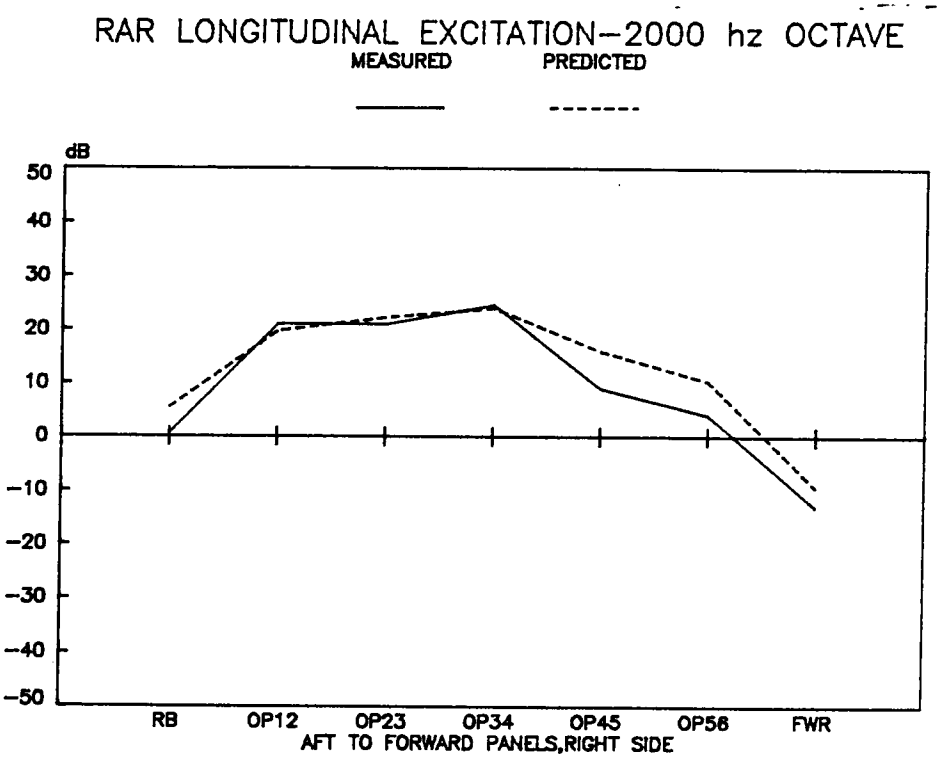

Figure E25c. Measured vs. Predicted Overhead Panel Vibration, Right Side, RAR Longitudinal Excitation, 2 kHz

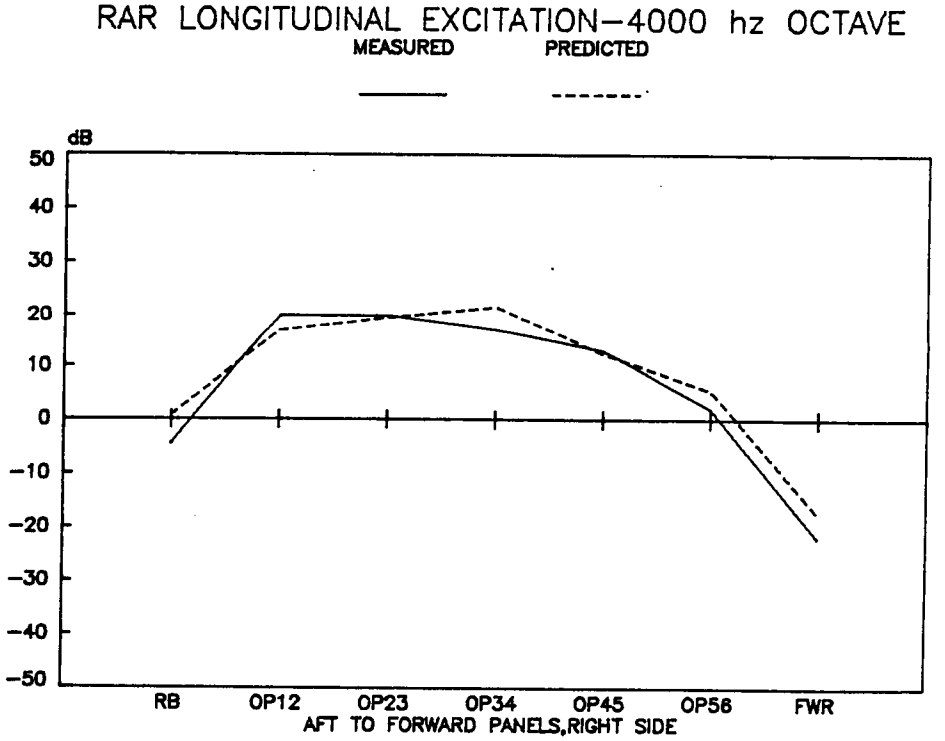

Figure E25d. Measured vs. Predicted Overhead Panel Vibration, Right Side, RAR Longitudinal Excitation, 4 kHz

Hydraulic system attachment locations comparisons are shown in Figures E26 through E31. The hydraulics panel excitation in Figures E29 through E31. Figure E26 shows good correlation between predictions and measurements for some left and middle overhead frames. CPM shows underprediction at 500 and 1000 hz and LF14L shows overprediction at 2000 and 4000 hz by 9 and 11 dB. Figure E27 shows the left side overhead panels. The predictions here follow the general measured trends, but predict a smoother distribution of level with position than the measured data shows. Tendency is for overprediction at the high frequency octaves. Figure E28 shows the right side overhead panels, which tend to be overpredicted in more subsystems with higher frequency. The subsystems adjacent to the source and the RB are underpredicted at 500, 1000 and 2000 hz.

The hydraulics panel excitation results for some left and middle overhead frames is shown in Figure E29. The 500, 1000, and 2000 hz octaves show underprediction by 7, 8, and 10 dB on average, respectively. The 4000 hz octave, however, shows good agreement with 8 dB max variation and no over or underprediction. Figure E30 shows left side overhead panel measurements that show excellent correlation with predictions, with no tendency for over or underprediction. Figure E31 shows the right side overhead panels to be predicted well at 500 and 1000 hz, but some discrepancy shows at 2000 hz in subsystems adjacent to the source and at 4000 hz in distant subsystems.

Ground test statistics. - A statistical breakdown of the measurement minus predictions deltas for each excitation, frequency and subsystem group are shown in Table E1 and Figures E32 to E37. These figures show mean and sample standard deviation of the difference between the measurements and predictions for these groups, as well as the number of comparison points for each group. The overall data represents the entire measured vs. predicted group for each excitation, while the OP1-4 group contains all overhead and side panels up to cross frame 5. The latter group represents the panels adjacent to the aft and mid row seating locations, which are highest in measured in-flight sound pressure level. The in-flight predictions also show this group to contain the major contributors to cabin input power flow (see Appendix E). The remaining groups, OP5-7 and LF, represent the forward cabin and cockpit overhead and side panels, and the overhead cabin longitudinal frames, respectively.

TABLE E1. GROUND TEST STATISTICS

f	500		1000		2000		4000		
	$\bar{x}$	s	$\bar{x}$	s	$\bar{x}$	s	$\bar{x}$	s	n
FALV									
Overall	0.7	5.2	-0.9	5.9	-2.9	6.4	-6.1	5.9	32
OP1-4	1.8	4.8	-0.7	5.0	-2.3	5.9	-5.3	6.7	13
OP5-7	-0.6	6.5	-4.9	3.8	-6.7	2.7	-8.7	4.4	10
LF	2.9	3.3	0.2	1.9	-3.6	2.5	-5.5	5.0	7
FAL Lat									
Overall	7.7	6.3	0.9	6.7	-1.2	5.6	-2.5	5.8	28
OP1-4	4.5	7.0	1.0	4.4	-2.0	4.2	-3.3	4.5	10
OP5-7	8.1	3.2	-1.4	3.1	-2.7	2.7	-4.9	3.5	8
LF	7.9	5.0	-1.6	4.2	-1.5	4.3	-2.1	4.6	6
RARV									
Overall	1.0	5.0	-0.3	6.8	-4.3	5.8	-4.2	6.7	28
OP1-4	0.3	5.1	-0.4	6.2	-3.0	5.4	-2.4	7.4	12
OP5-7	-1.6	2.9	-4.7	3.6	-9.6	3.2	-8.3	3.2	8
LF	2.7	3.1	0.3	3.1	-3.5	2.3	-5.9	4.3	6
RAR Lat									
Overall	4.2	5.6	-3.0	7.7	-5.6	7.2	-7.2	6.9	28
OP1-4	2.1	5.8	-3.8	7.6	-4.9	8.8	-5.6	8.4	12
OP5-7	3.8	3.1	-5.1	3.7	-8.3	2.6	-10.2	3.6	8
LF	6.1	5.7	-4.2	5.9	-7.2	5.1	-8.8	6.4	6
RAR Long									
Overall	3.5	8.0	-1.4	8.1	-4.2	6.4	-3.0	6.7	28
OP1-4	-1.8	5.6	-4.4	6.1	-5.4	6.4	-4.4	8.1	10
OP5-7	6.2	6.8	-1.2	5.9	-4.7	3.7	-2.8	4.3	8
LF	3.9	6.8	-2.9	7.7	-3.9	6.7	-2.8	8.3	6
Hyd Frame									
Overall	-2.6	7.8	-3.0	6.1	-1.5	5.8	-5.7	5.6	16
Hyd Panel									
Overall	2.8	4.9	2.3	5.0	6.4	5.4	-1.2	5.6	16

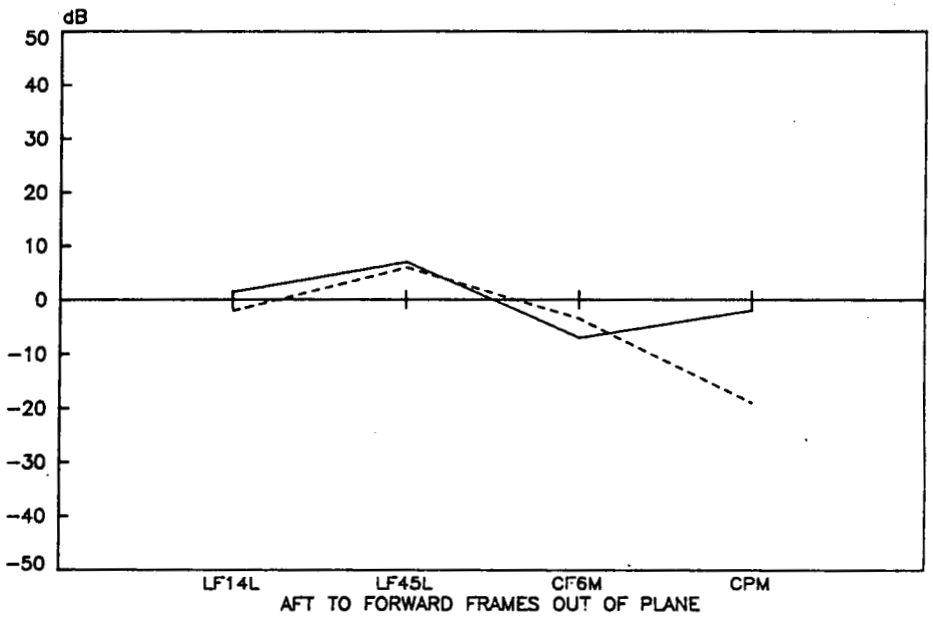

Figure E26a. Measured vs. Predicted Frame Out-of-Plane Vibration, Hydraulics Frame Attachment Excitation, .5 kHz

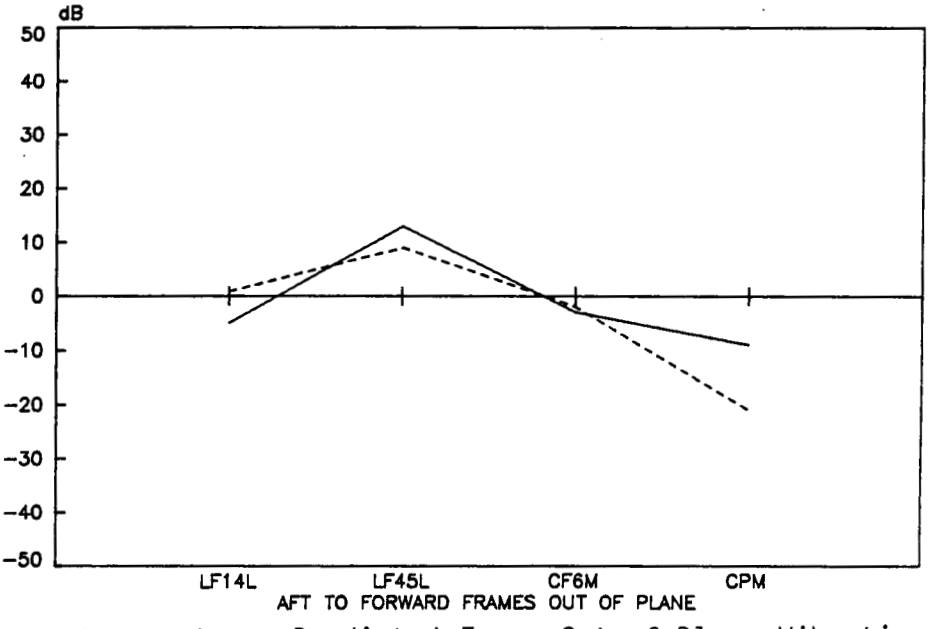

Figure E26b. Measured vs. Predicted Frame Out-of-Plane Vibration, Hydraulics Frame Attachment Excitation, 1 kHz

C-3

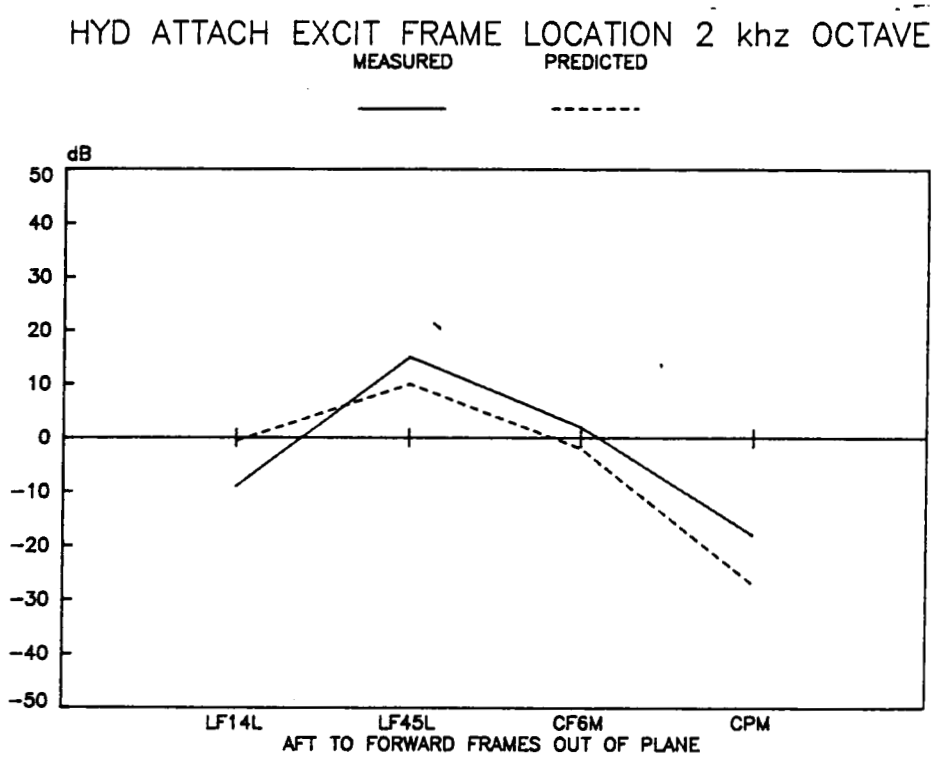

Figure E26c. Measured vs. Predicted Frame Out-of-Plane Vibration, Hydraulics Frame Attachment Excitation, 2 kHz

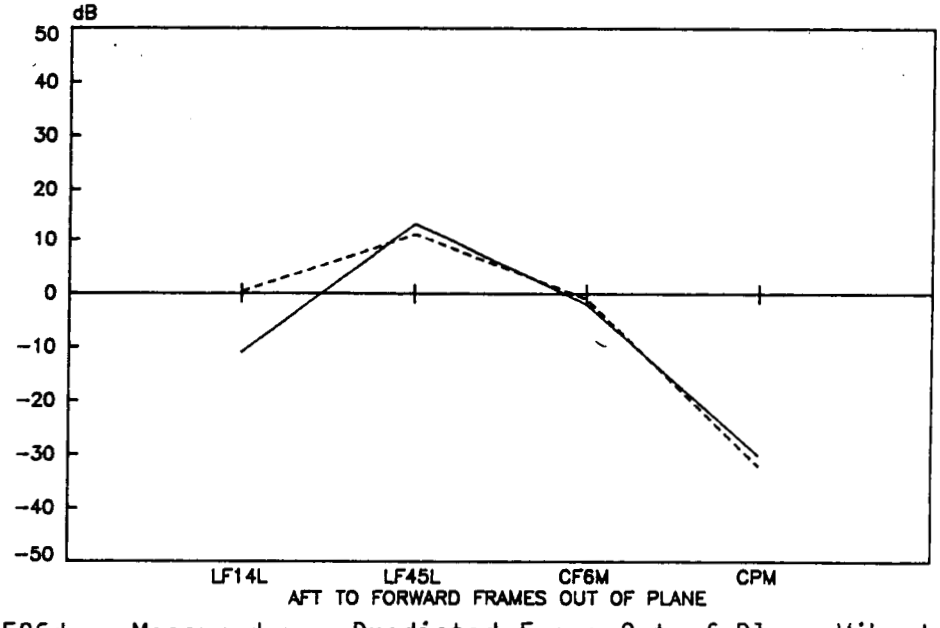

Figure E26d. Measured vs. Predicted Frame Out-of-Plane Vibration, Hydraulics Frame Attachment Excitation, 4 kHz

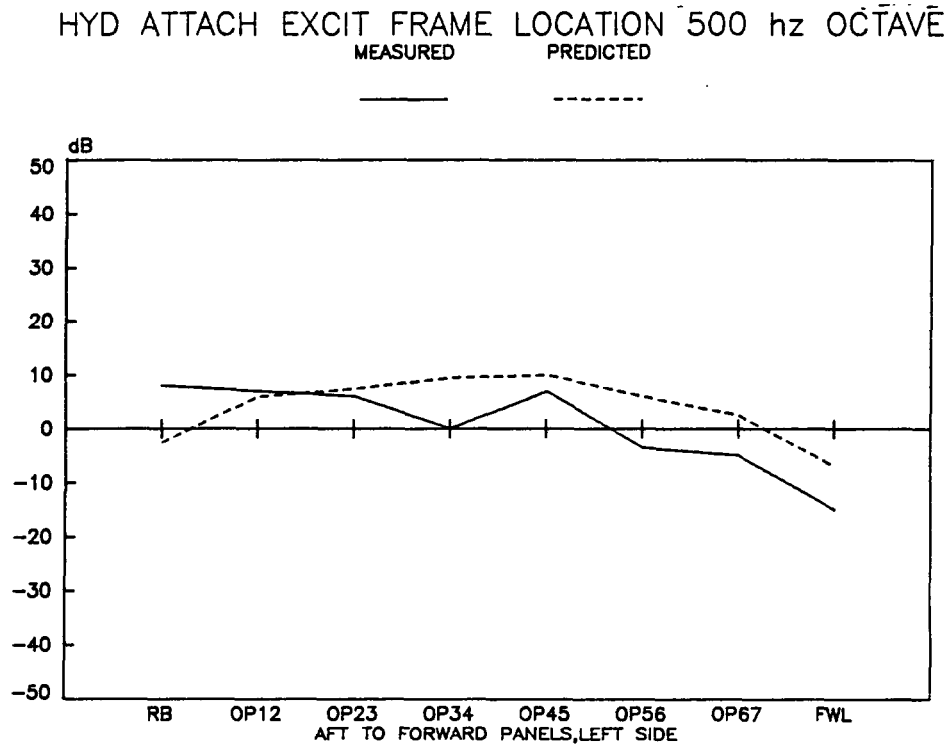

Figure E27a. Measured vs. Predicted Overhead Panel Vibration, Left Side, Hydraulics Frame Attachment Excitation, .5 kHz

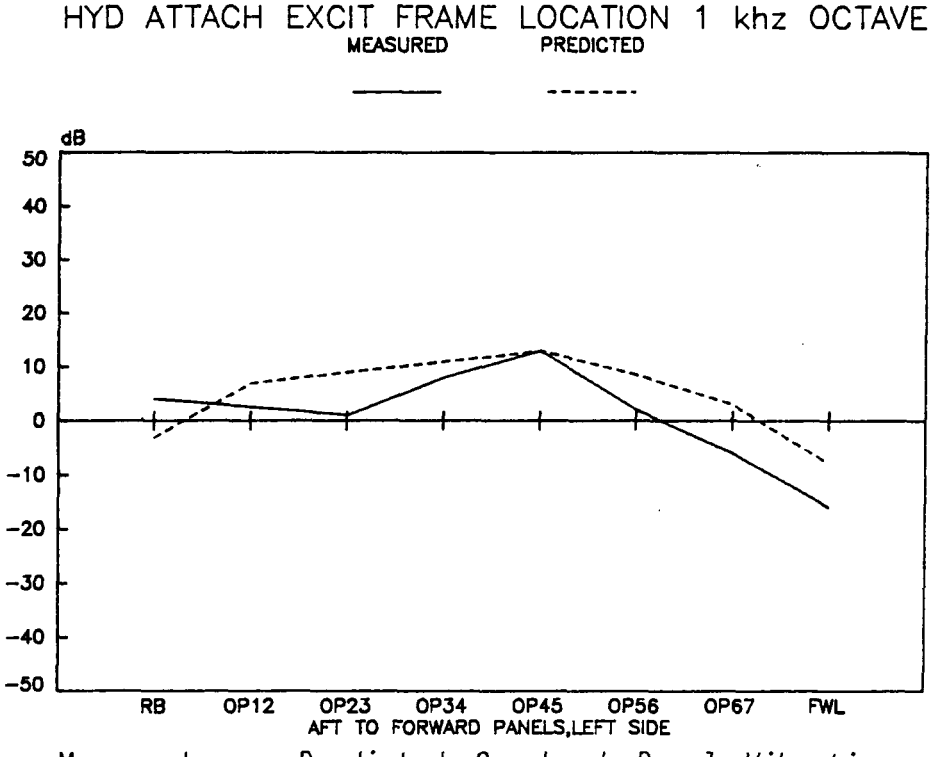

Figure E27b. Measured vs. Predicted Overhead Panel Vibration, Left Side, Hydraulics Frame Attachment Excitation, 1 kHz

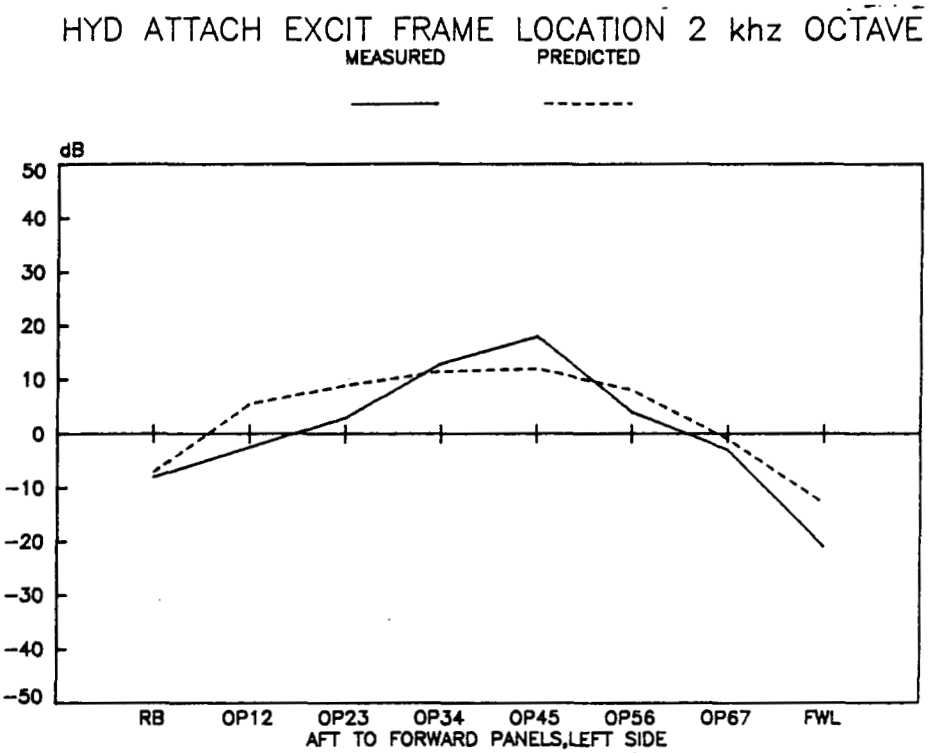

Figure E27c. Measured vs. Predicted Overhead Panel Vibration, Left Side, Hydraulics Frame Attachment Excitation, 2 kHz

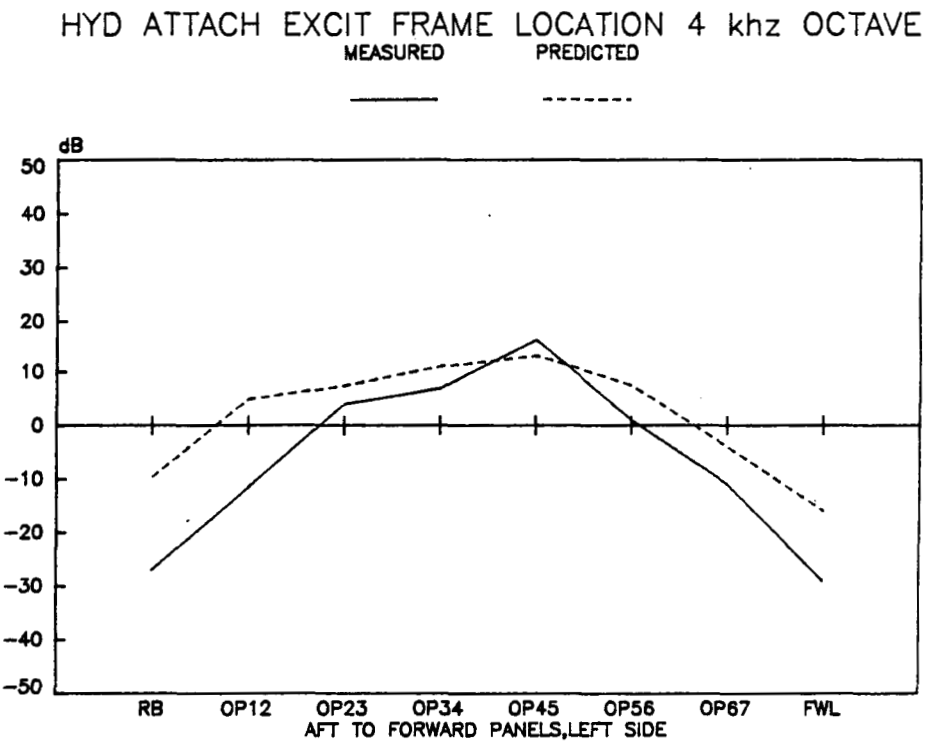

Figure E27d. Measured vs. Predicted Overhead Panel Vibration, Left Side, Hydraulics Frame Attachment Excitation, 4 kHz

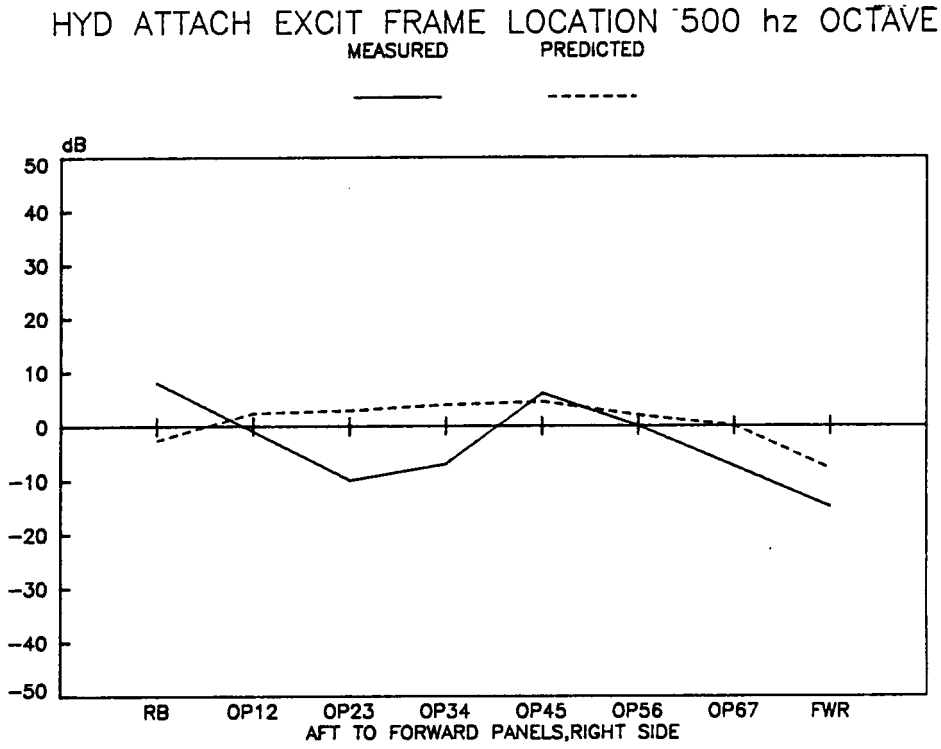

Figure E28a. Measured vs. Predicted Overhead Panel Vibration, Right Side, Hydraulics Frame Attachment Excitation, .5 kHz

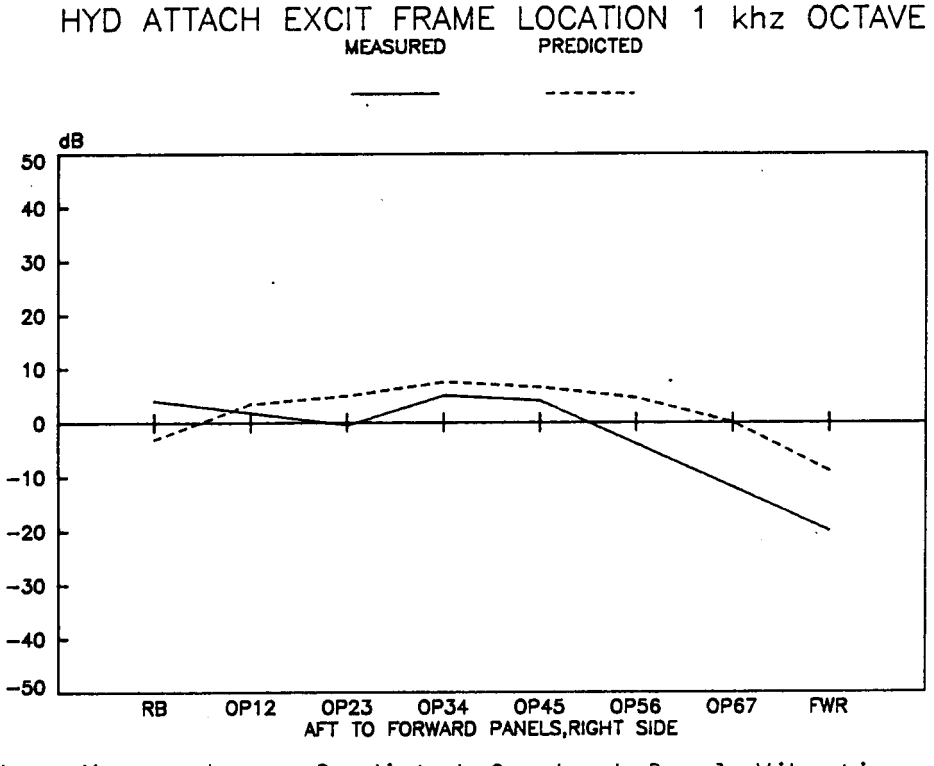

Figure E28b. Measured vs. Predicted Overhead Panel Vibration, Right Side, Hydraulics Frame Attachment Excitation, 1 kHz

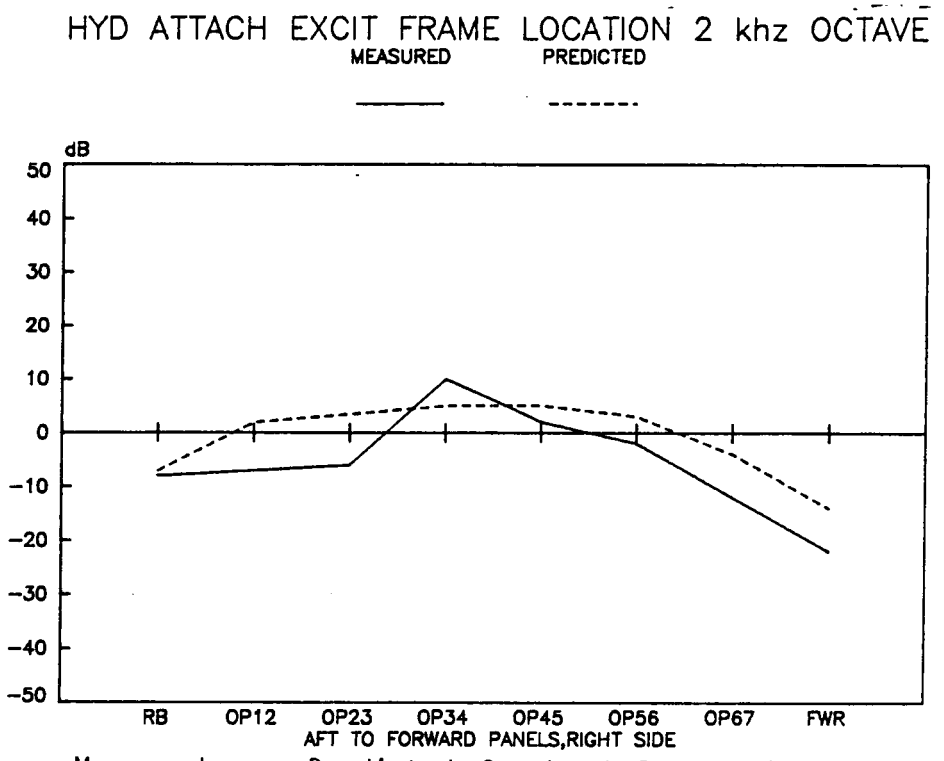

Figure E28c. Measured vs. Predicted Overhead Panel Vibration, Right Side, Hydraulics Frame Attachment Excitation, 2 kHz

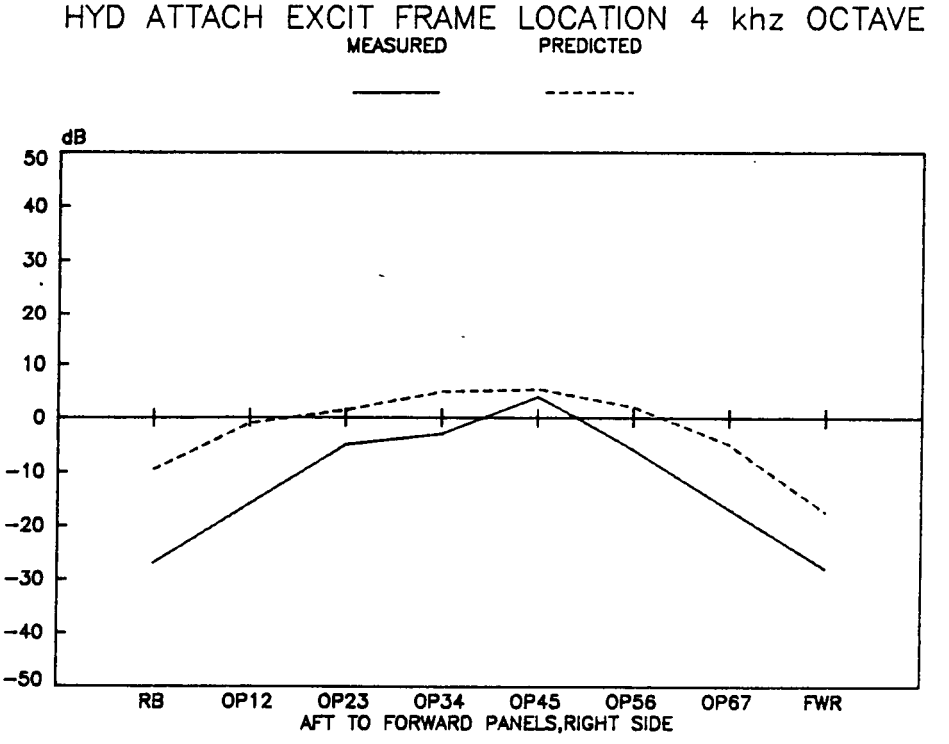

Figure E28d. Measured vs. Predicted Overhead Panel Vibration, Right Side, Hydraulics Frame Attachment Excitation, 4 kHz

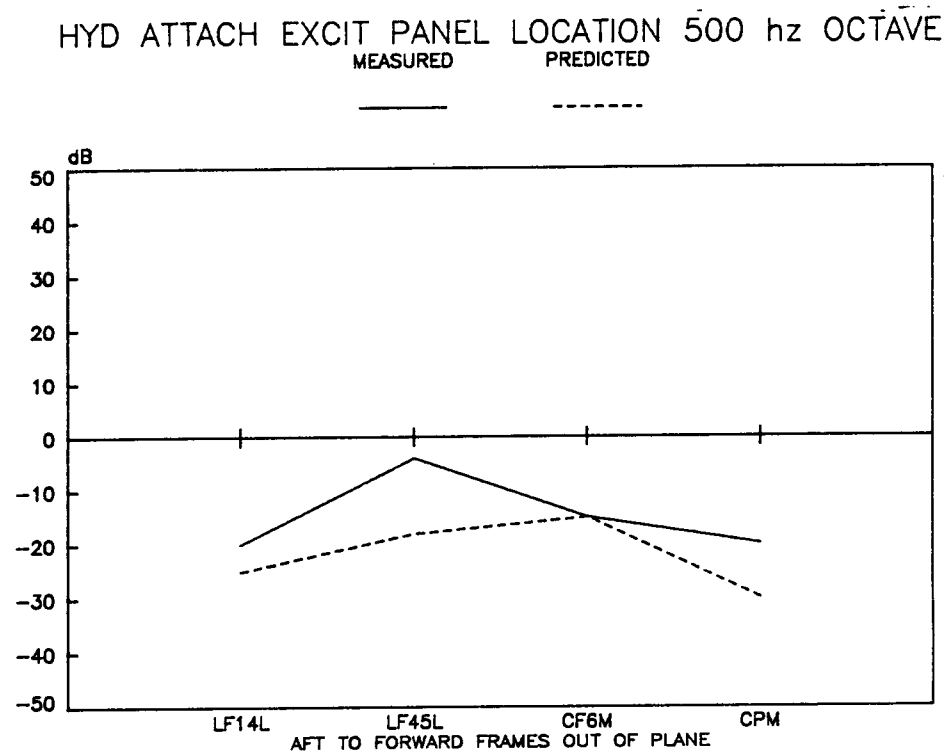

Figure E29a. Measured vs. Predicted Frame Out-of-Panel Vibration, Hydraulics Panel Attachment Excitation, .5 kHz

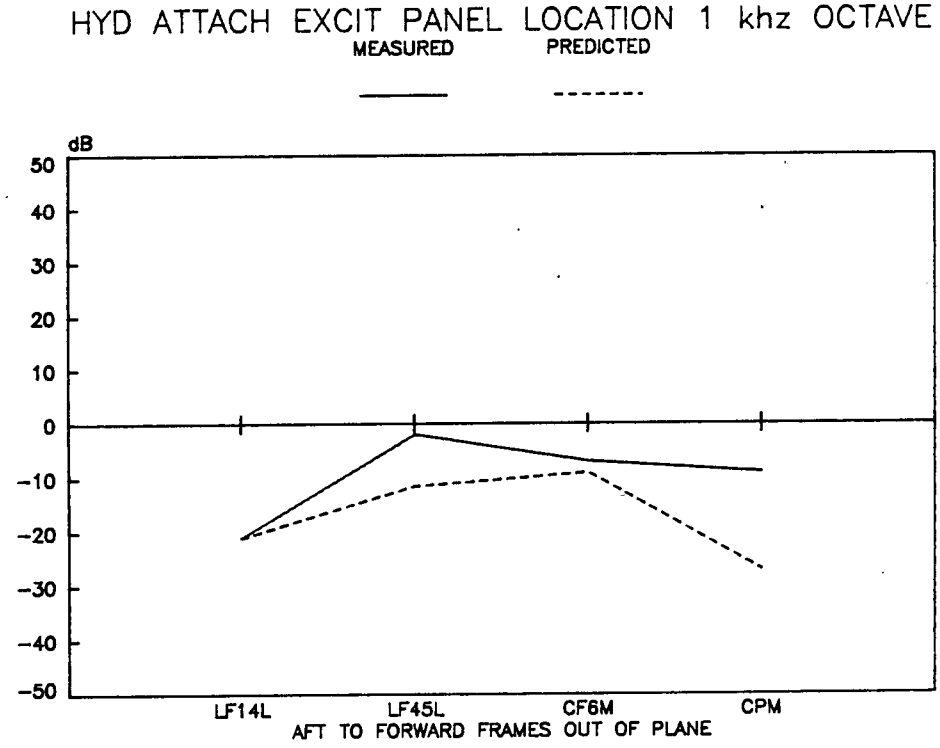

Figure E29b. Measured vs. Predicted Frame Out-of-Panel Vibration, Hydraulics Panel Attachment Excitation, 1 kHz

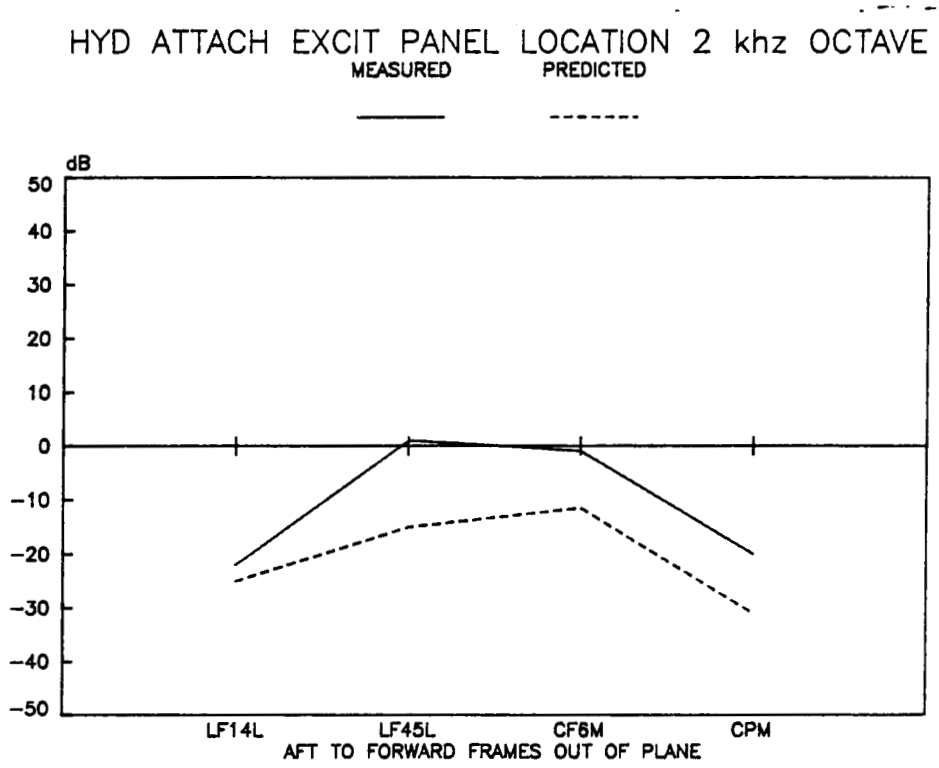

Figure E29c. Measured vs. Predicted Frame Out-of-Panel Vibration, Hydraulics Panel Attachment Excitation, 2 kHz

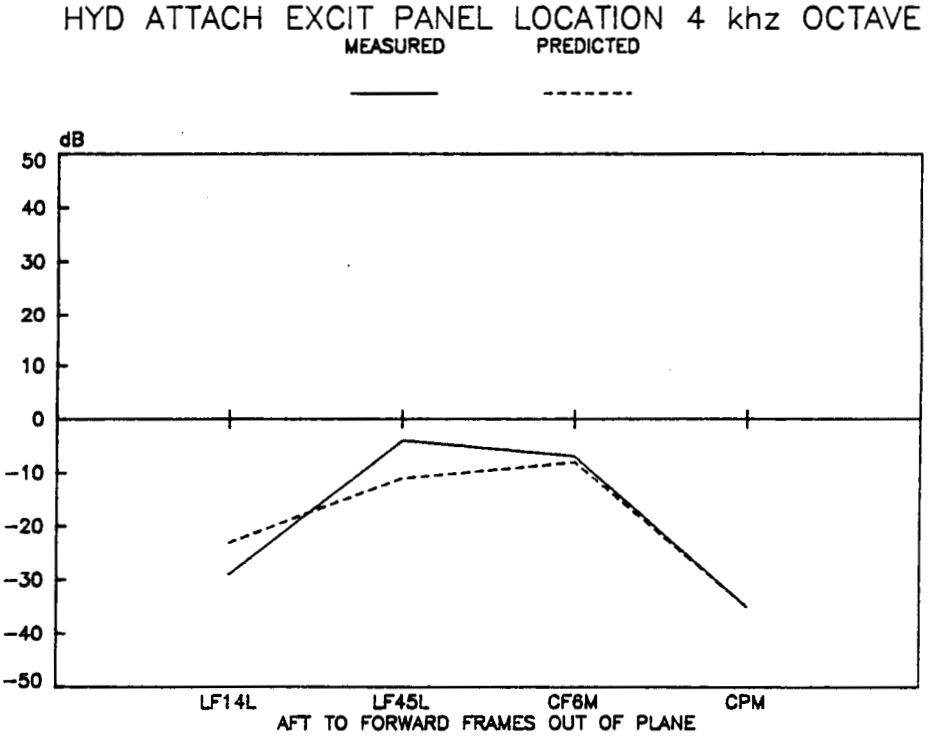

Figure E29d. Measured vs. Predicted Frame Out-of-Panel Vibration, Hydraulics Panel Attachment Excitation, 4 kHz

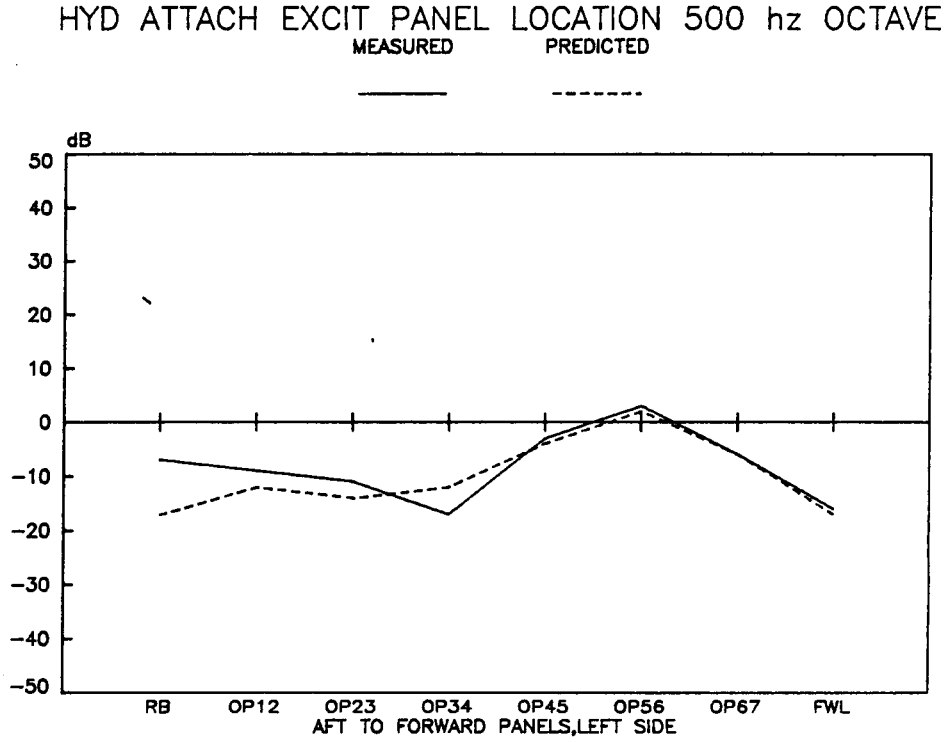

Figure E30a. Measured vs. Predicted Overhead Panel Vibration, Left Side, Hydraulics Panel Attachment Excitation, .5 kHz

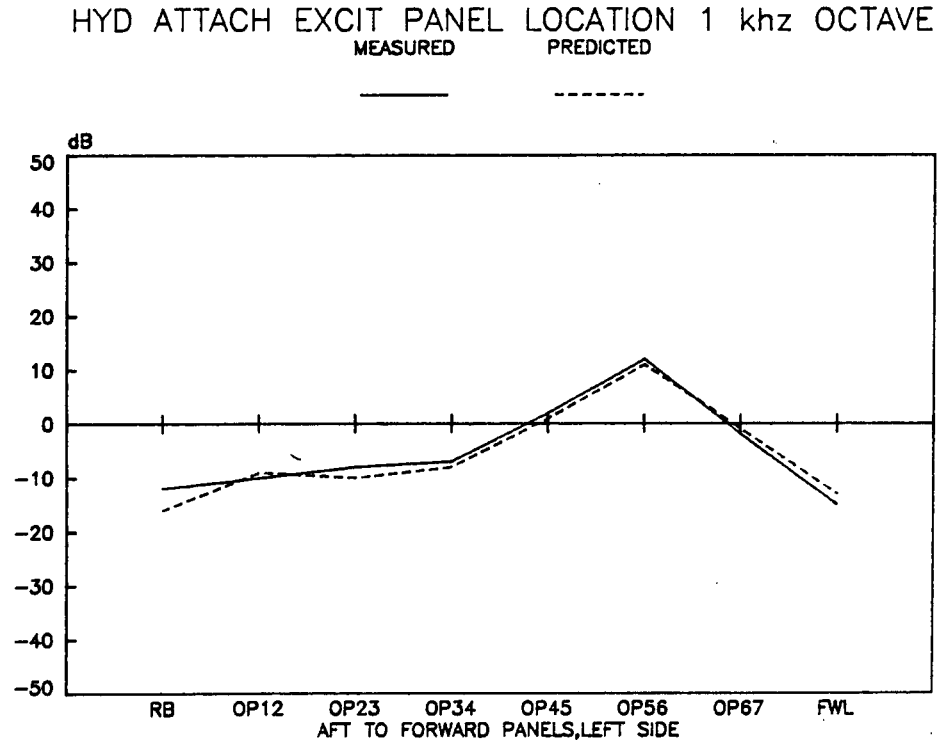

Figure E30b. Measured vs. Predicted Overhead Panel Vibration, Left Side, Hydraulics Panel Attachment Excitation, 1 kHz

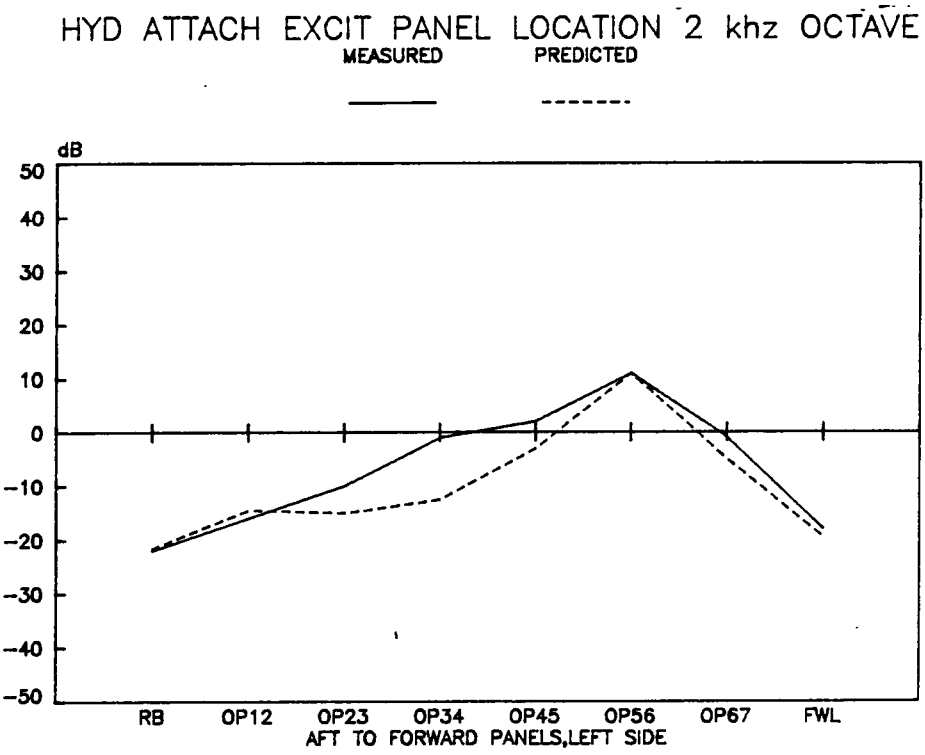

Figure E30c. Measured vs. Predicted Overhead Panel Vibration, Left Side, Hydraulics Panel Attachment Excitation, 2 kHz

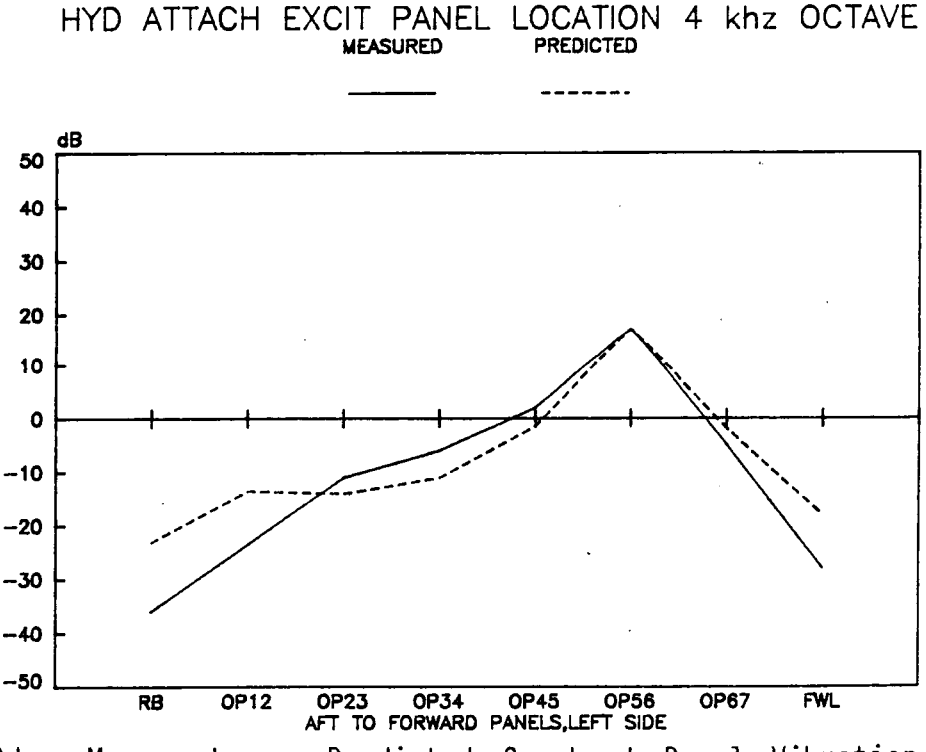

Figure E30d. Measured vs. Predicted Overhead Panel Vibration, Left Side, Hydraulics Panel Attachment Excitation, 4 kHz

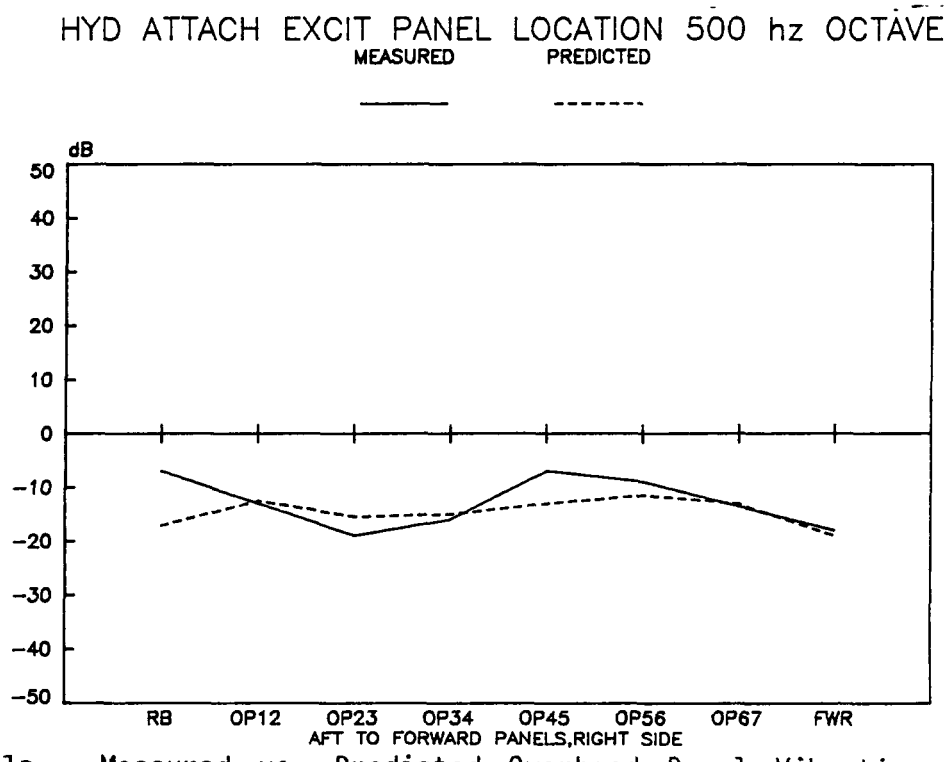

Figure E31a. Measured vs. Predicted Overhead Panel Vibration, Right Side, Hydraulics Panel Attachment Excitation, .5 kHz

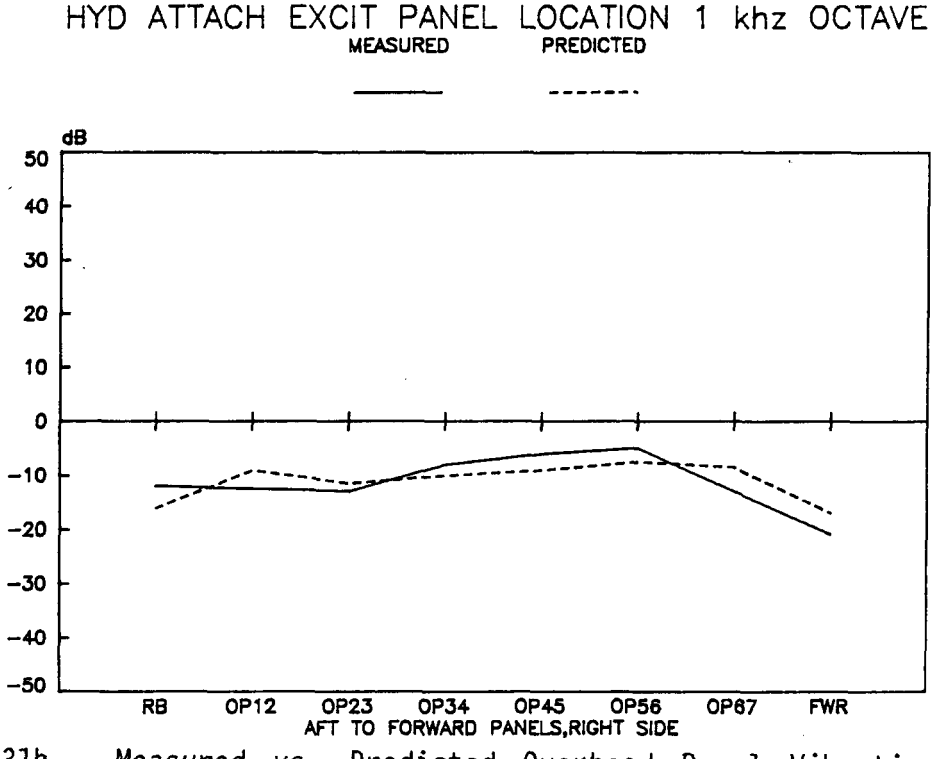

Figure E31b. Measured vs. Predicted Overhead Panel Vibration, Right Side, Hydraulics Panel Attachment Excitation, 1 kHz

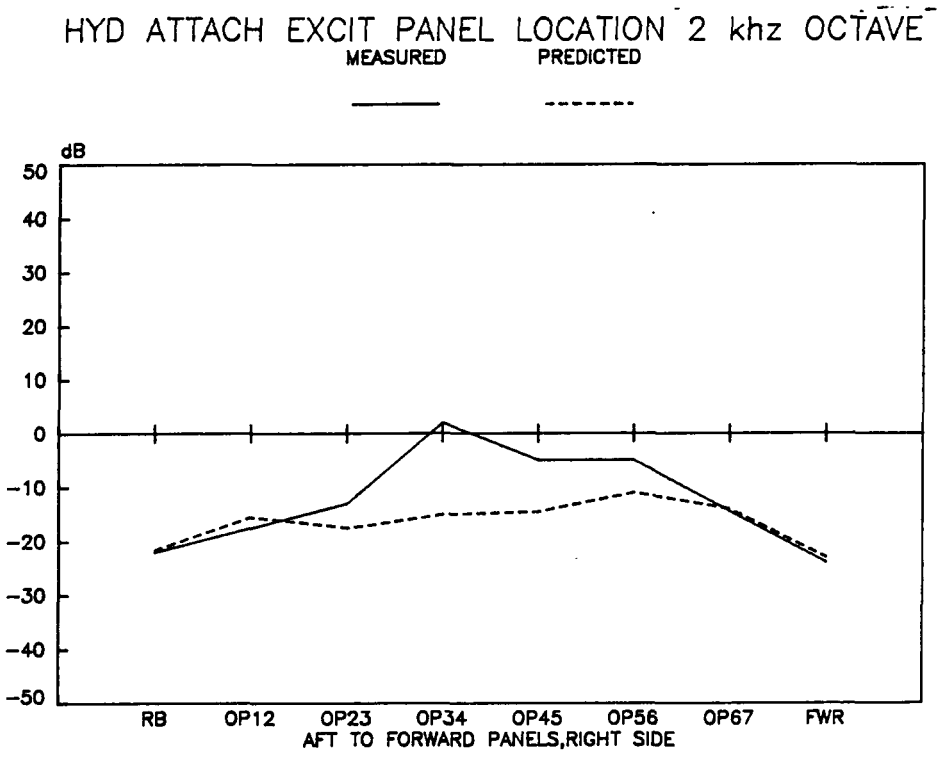

Figure E31c. Measured vs. Predicted Overhead Panel Vibration, Right Side, Hydraulics Panel Attachment Excitation, 2 kHz

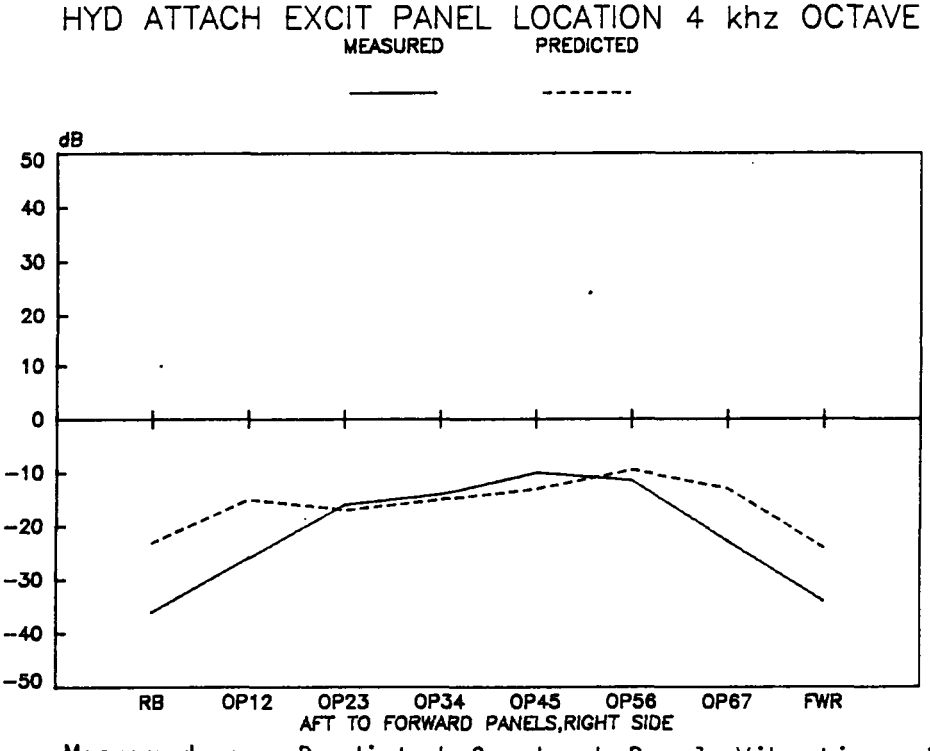

Figure E31d. Measured vs. Predicted Overhead Panel Vibration, Right Side, Hydraulics Panel Attachment Excitation, 4 kHz

The overall average delta (delta-bar) figures range from +7.7 dB at 500 Hz for FAL lateral excitation to -7.2 dB at 4000 hz for RAR lateral. The delta-bar values decrease with increasing frequency, with the five 500 Hz values positive (underprediction) and all but one of the values from the remaining three octaves in all five excitations negative (overprediction). The 1000 Hz octave appears the best predicted, with -3 dB the maximum delta-bar for RAL lateral excitation, and three of the five excitations having less than 1 dB average absolute delta. The corresponding standard deviations for this octave are between 5.9 and 8.1 dB for FAL vertical and RAR longitudinal, respectively. Examination of this data shows that a few subsystems contribute greatly to this deviation for each excitation. The subsystems controlling the FALV deviation are CPM,RB, and OP14D,FAL lateral input by CPM and OP14D,RAR vertical by RB, RAR lateral by CPM,OP12R, and SP14L, and the RAR longitudinal by SP14L. In each case, the subsystems detrimental to the standard deviation for the excitation are either on the side opposite, or far downstream of the source in physical location. Exceptions are OP14D, OP12R and RB, which are in close proximity to each source location but remain poorly predicted. The lightweight construction of these subsystems compared to the relatively stiffer frames and honeycomb skin panels that attach to them may not be handled properly in terms of junction modeling for this type subsystem. Also, it is realized that the input motions assumed for the predictions cannot be realistically duplicated during testing.

The OP1-4 group shows some improved delta-bar values, while the standard deviation values improve only marginally. Delta-bar values range from -5.6 dB for the 4000 Hz octave in the RAR lateral excitation to 4.5 dB for the 500 Hz octave during FAL lateral excitation. In general, the delta-bar values continue to decrease with increasing frequency, much like the overall group. Standard deviation values range from 4.2 dB in the FAL lateral 2000 Hz octave and RAR lateral 2000 Hz octave, respectively. The best predicted excitation appears to be RAR vertical in terms of delta-bar values, with only 0.3 to -3.0 dB range of deltas in the four SIL-4 octaves. This group contains OP14D, one of the consistent problem subsystems for prediction.

The OP5-7 contains subsystems in the forward cabin and cockpit area, including the windshields and forward side panels. The delta-bar values for this group range from 8.1 dB (FAL lateral @ 500 Hz) to -10.2 dB (RAR lateral @ 4000 Hz). The standard deviation values, however, are best for three excitations in this group, FAL lateral, RAR vertical, and RAR lateral, with a range from 2.6 to 3.7 dB across the four octaves of interest. The LF group shows delta-bar values ranging from 7.9 to -8.8 dB, in the FAL and RAR lateral excitations respectively. Standard deviation values are nearly always better than the overall for this group.

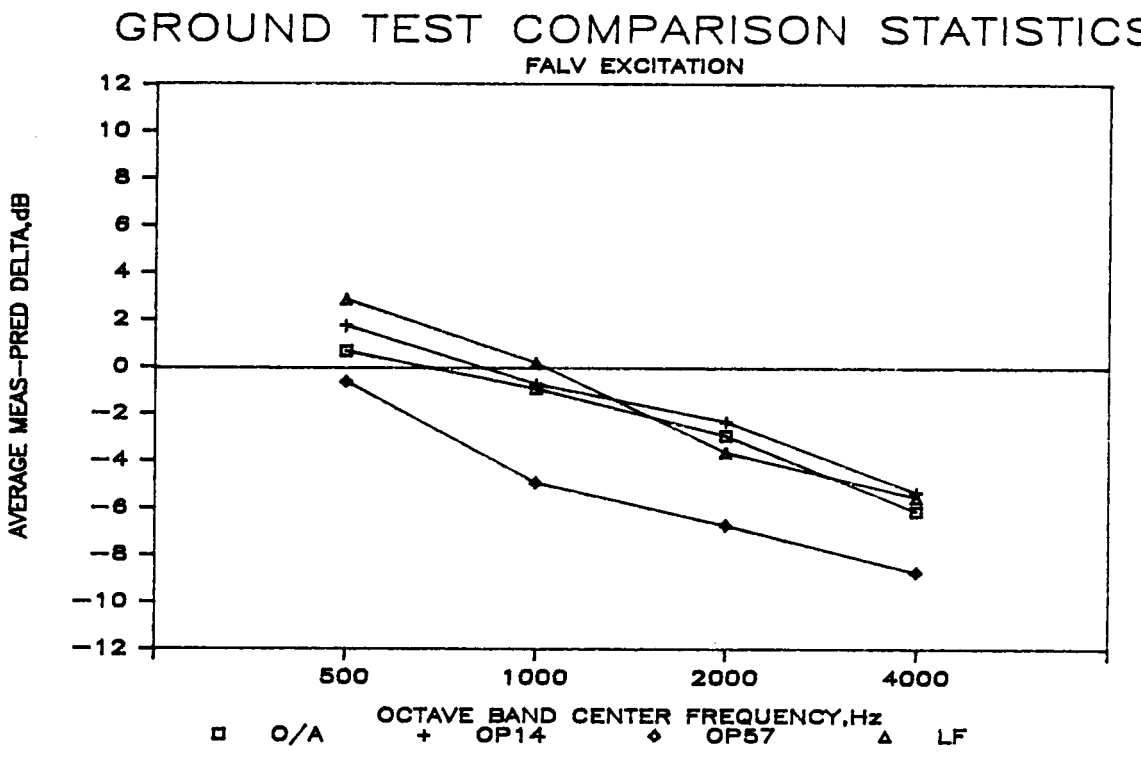

Figure E32. Ground Test Comparison Statistics - FAL Vertical Excitation

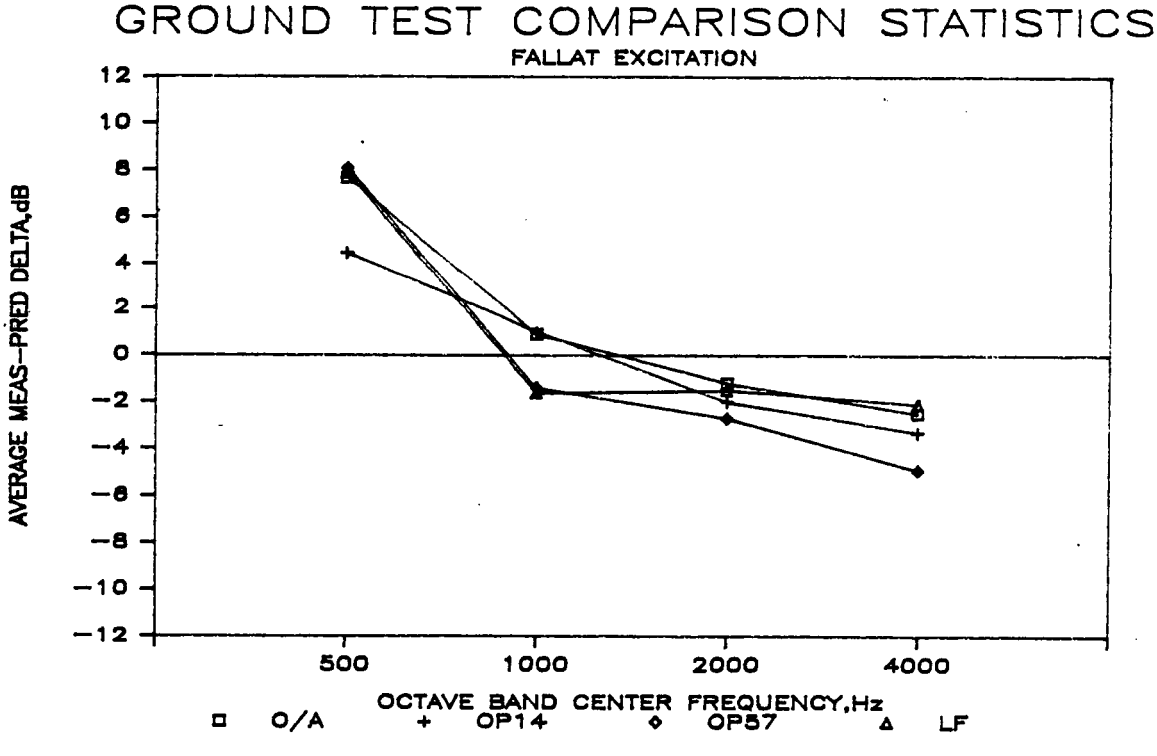

Figure E33. Ground Test Comparison Statistics - FAL Lateral Excitation

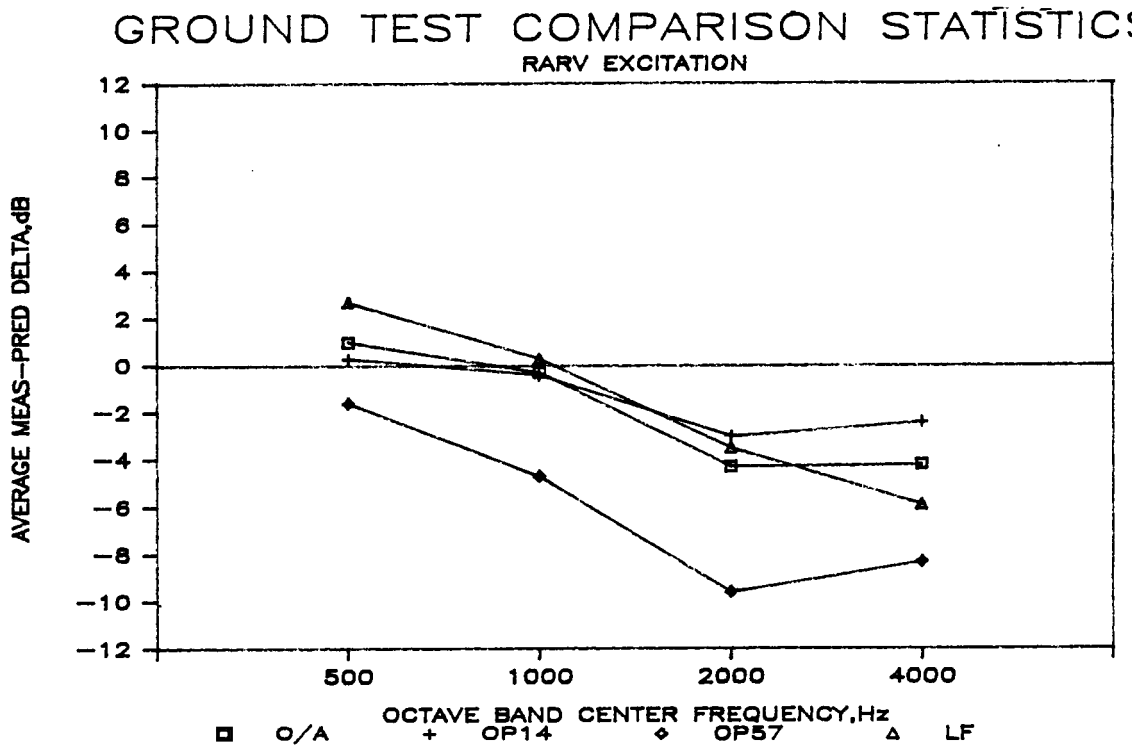

Figure E34. Ground Test Comparison Statistics - RAR Vertical Excitation

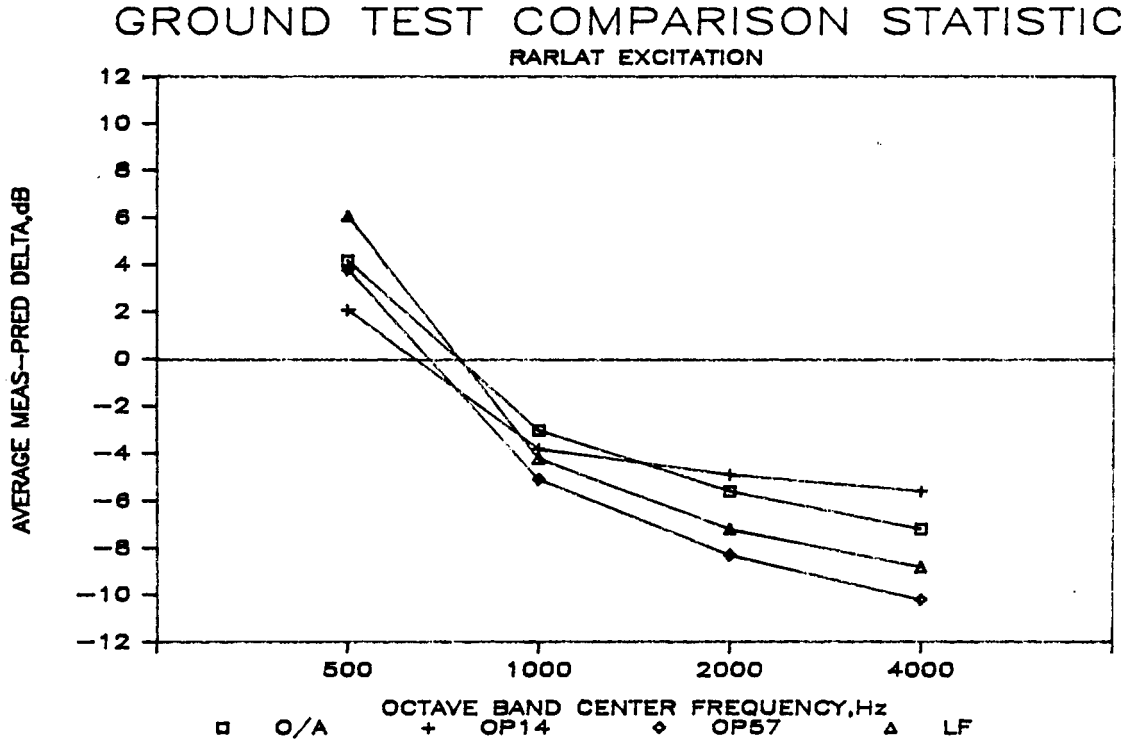

Figure E35. Ground Test Comparison Statistics - RAR Lateral Excitation

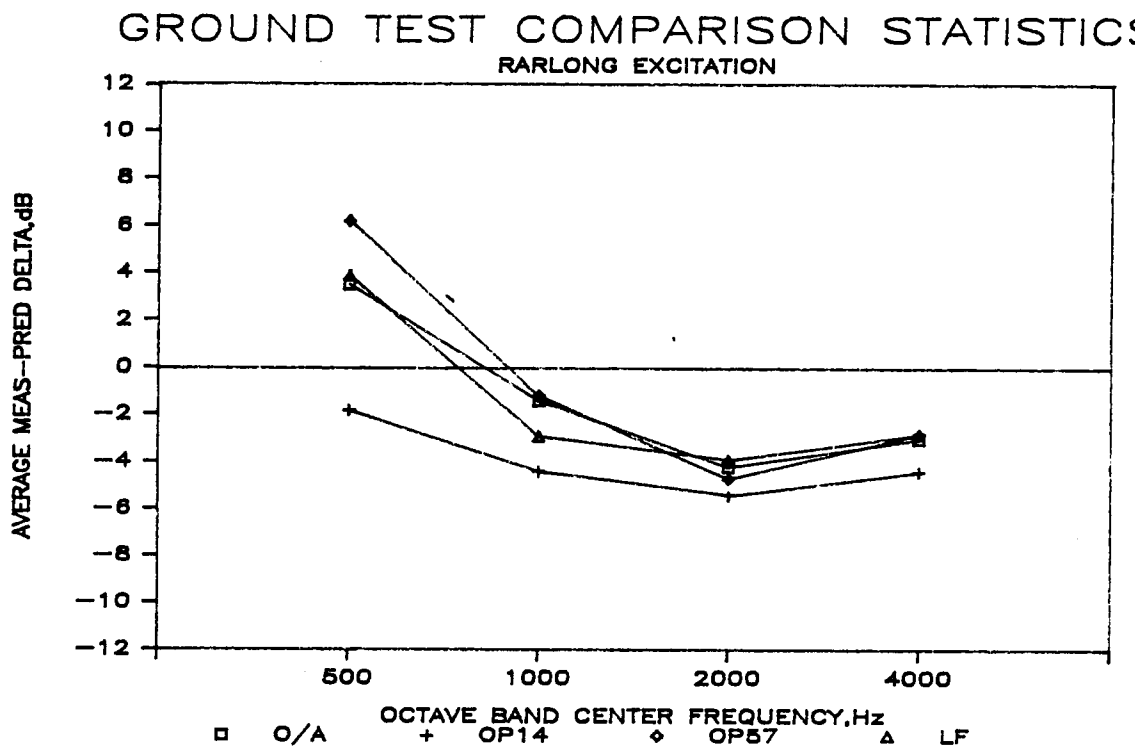

Figure E36. Ground Test Comparison Statistics - RAR Longitudinal Excitation

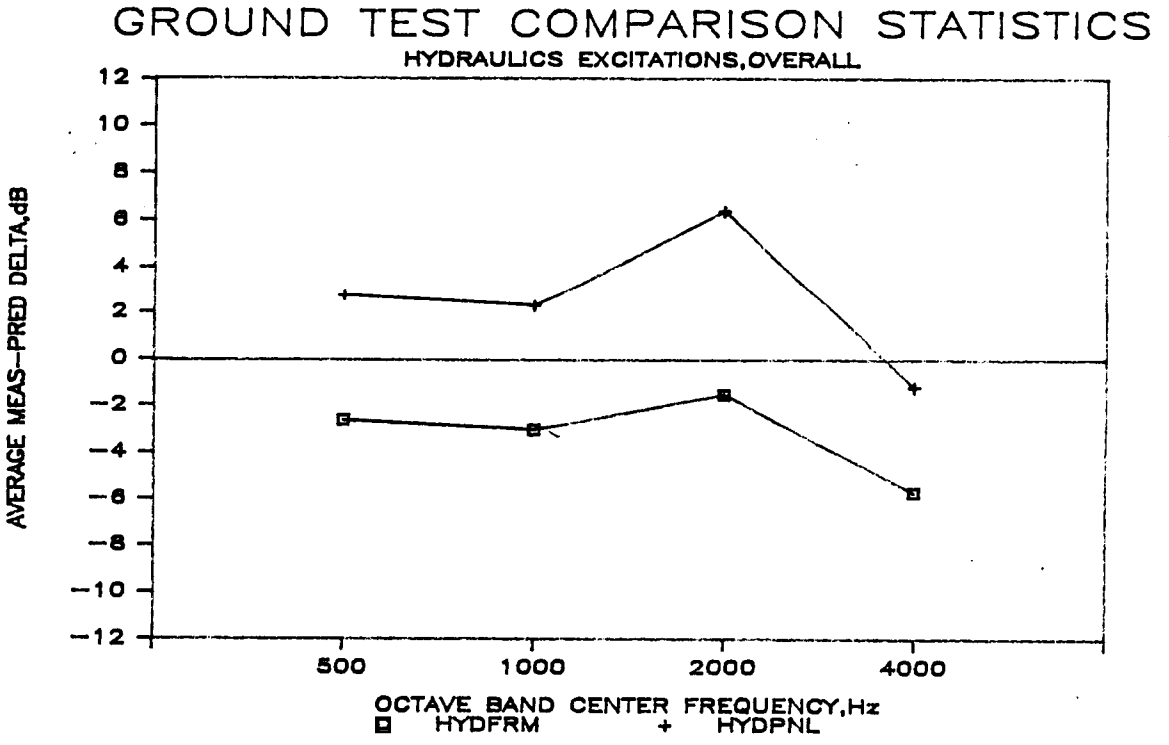

Figure E37. Ground Test Comparison Statistics - Hydraulics Excitations

The hydraulics excitations locations average delta values are shown in Figure E37. These data show less high frequency overprediction tendency than the gearbox attachment data. The frame excitation is overpredicted in all four octaves with delta's of -1.5 to -5.7 dB while the panel excitation is underpredicted up to the 4000 Hz octave with a delta range of -1.2 to 6.4 dB. Standard deviation values for these predictions range from 4.9 to 7.8 dB. Examination of the measurement and prediction data shows RB and CPM drive the deviation figures for both the hydraulics excitations.

Flight Test Measurements

Introduction. - The physical attachment of the main transmission to the airframe is such that the four main transmission mounting feet are attached to two SEA model subsections, LF14L and LF14R, on the left and right sides, respectively. Thus the power input into each of these two subsections must contain the power provided by two main transmission attachments, both front and rear on each side (see Photos P3, P4, and P5). The SEA subsystems that the power is input to are the in-plane and out-of-plane bending motions associated with each of the noted subsections. This means that the three-direction measured vibration levels associated with each of the four input locations must be combined to yield in-plane bending and out-of-plane bending power inputs. This combination of vibration terms is key to the input power approximation.

Flight test measurement data. - The measurement of in-flight vibration levels on near-source subsystems provides the in-flight subsystem response levels which can be equated to the superposition of SEA predictions of subsystem responses for the respective inputs. As with the ground test data, overall scaling is provided by comparison of the near-source subsystem predictions and measurements. However, in the flight configuration, the main gearbox source attachment consists of four locations, each capable of transmitting power in at least three translational degrees of freedom into the airframe. The contribution of each of these must be estimated before overall scaling is performed.

The SEA model requires the assumption that all input power be incoherent. This assumption is appropriate, with reference to the coherent sources investigation detailed in Appendix D. Another assumption involves the approximation that the real portion of the driving point impedance is constant over the frequency range of interest. The values used are calculated from compliance measurements performed on the airframe and gearbox (see Appendix D).

Input vibratory source power determination. - The actual power transmitted across the attachment locations into the airframe is very difficult to measure, and was considered beyond the scope of this program. As a reasonable alternate, measurements of vibration levels at the main transmission attachment locations were multiplied by the value of the real portion of the impedance at that location and direction. This yields an approximate input power quantity

for each of the support frames (LF14L, R) in each of the two degrees of freedom (in-plane and out-of-plane). These are required to provide a total prediction that is the sum of predictions for the various sources.

Vertical and longitudinal power quantities are summed at each attachment location, to yield an out-of-plane input, while lateral power represents the in-plane input. Since two transmission attachment locations occupy the same SEA subsection (both LF14L and LF14R have front and rear attachment), these values are summed front and back on each side to yield inputs to LF14Lo, LF14Li, LF14Ro, and LF14Ri. SEA predictions are then made using these inputs and summed to provide a prediction (still in need of overall scaling). Overall scaling is provided by comparison of measurements and predictions of subsystems adjacent to the source subsystems, and scaling accordingly. The flight prediction process is summarized in Figure E38.

Acoustic level results. - The prediction of cabin sound pressure level was performed by utilizing three near-source subsystems for overall scaling. These subsystems were OP23L, OP34L1, and OP4YM, for which in-flight vibration levels were measured. The first two subsystems have direct connection with frame LF14L, while the third connects to frames CF4M, LF45L and R. These frames directly connect to both LF14L and LF14R. Now that the input power has been scaled, SEA model predictions of bare cabin noise can be made. The results of this prediction are shown in Figure E39.

Comparison of these predictions to the bare cabin measurements performed in flight reveal differences from -3.2 to +3.3 dB in the SIL octaves for the aircraft spatial average, with all octave predictions within the spread of measurements made at eleven positions throughout the aircraft. Under predicting at 500 hz and 1 Khz by 3.2 and 2.1 dB while over predicting the 2 Khz and 4 Khz octaves by 0.9 and 3.3 dB provides an SIL-4 prediction within 0.2 dB. These differences are reasonable when one considers the complexity of the system modeled and that the actual measurement points may, on average, have an expected value which is higher or lower than the expected value of an infinite number of measurement points on that particular subsystem. This infinite point expected value (i.e., subsystem energy level) is what SEA predicts.

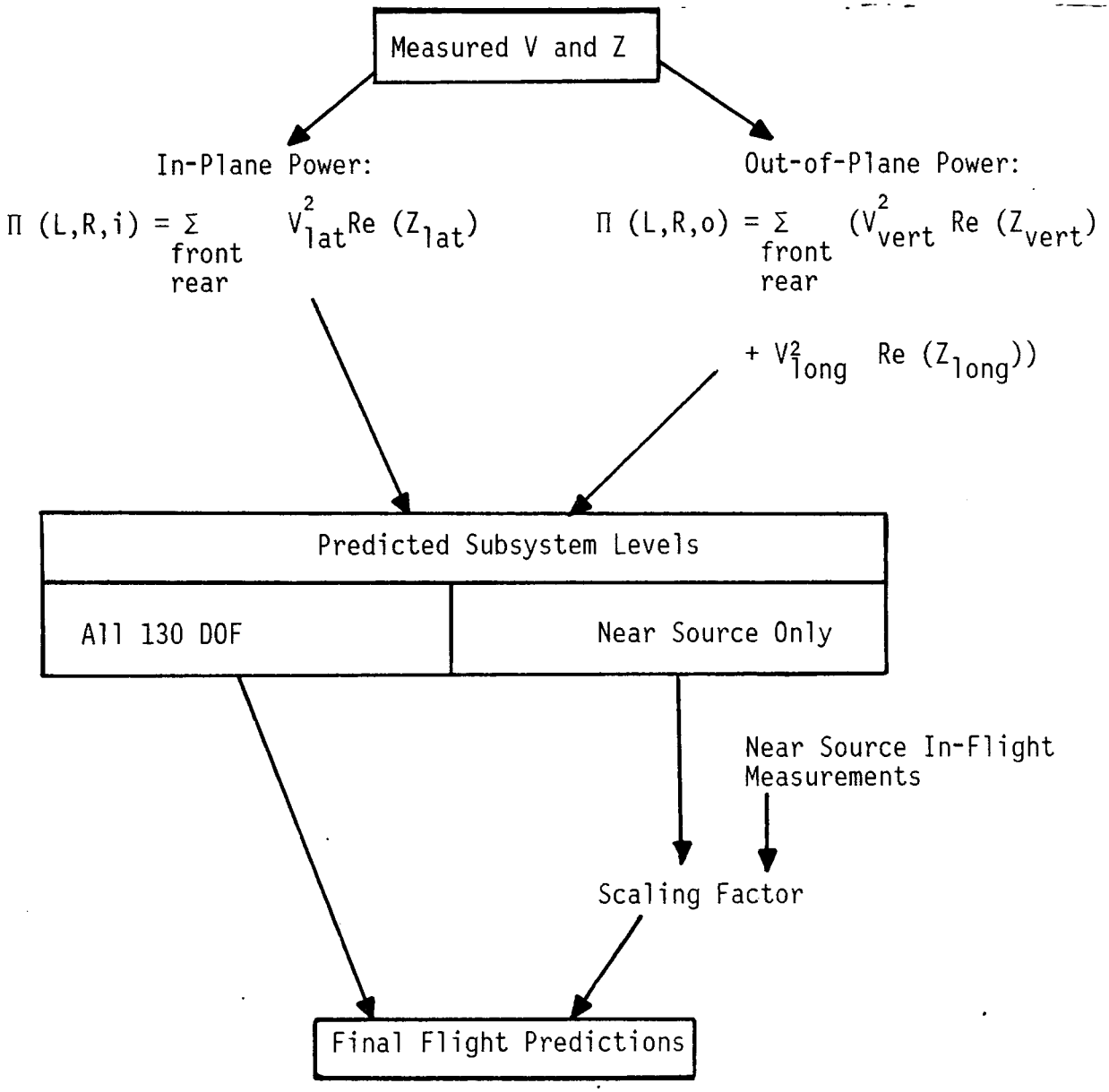

Figure E38. Flight Prediction Procedure

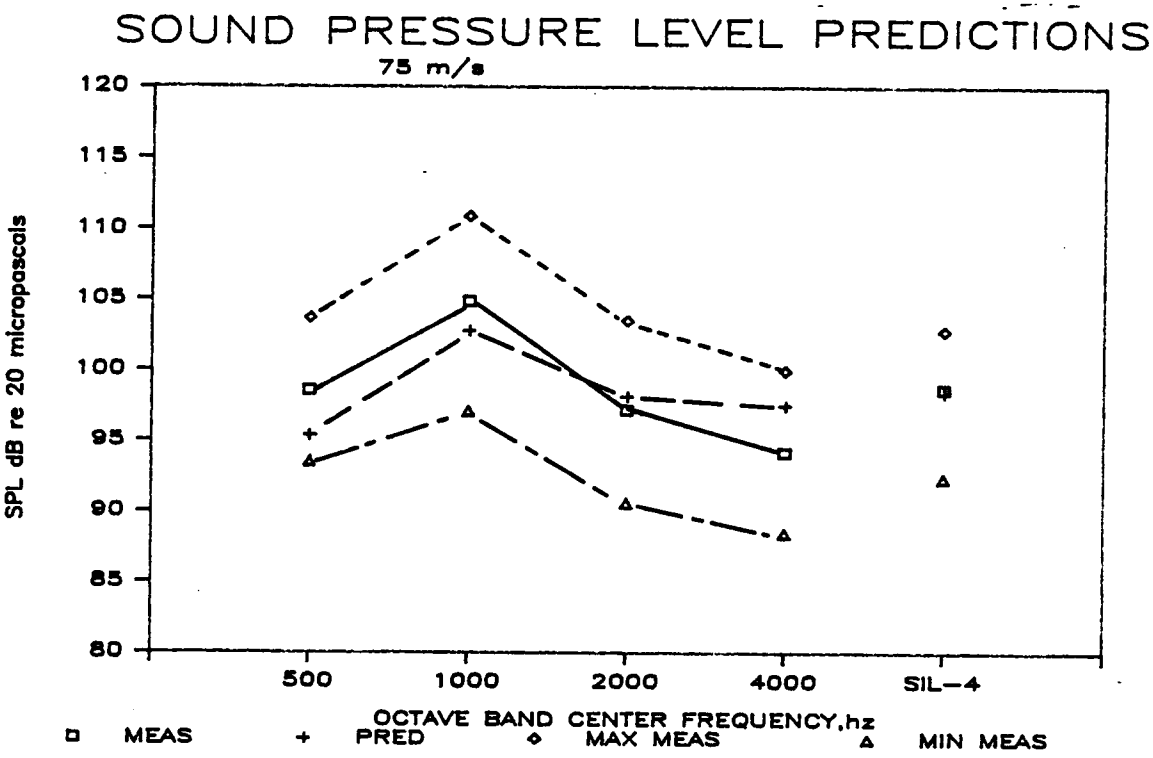

Figure E39. Measured vs. Predicted In-Flight Sound Pressure Level Comparison

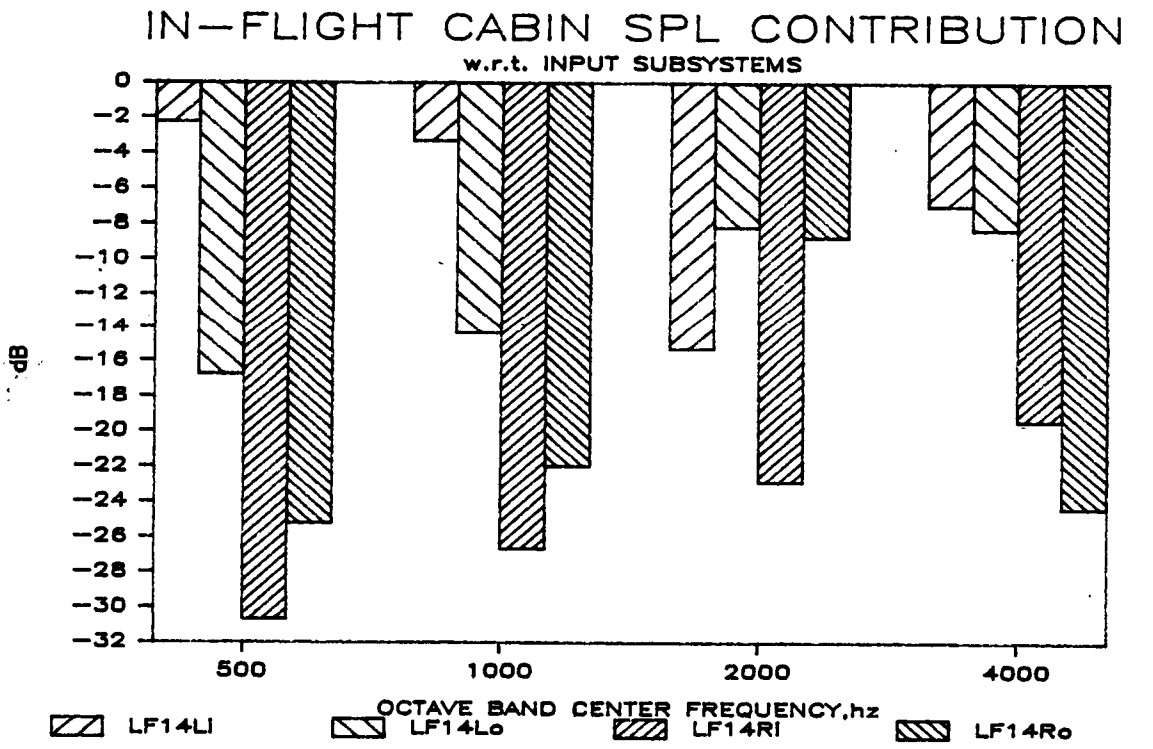

Figure E40. Predicted In-Flight Input Subsystem Cabin Sound Pressure Level Contribution

Cabin Power Flow Prediction

Introduction. - The cabin acoustic space receives its energy by direct radiation from 110 of the 130 subsystems in the model. Clearly, certain subsystems will make a more significant contribution to the cabin sound pressure levels than will other subsystems. One might presume, for instance, that panels near the source would contribute a higher percentage than those further away. There also will be cases when the nearby frame radiation into the cabin will be more significant than the radiation produced by some of the more distant panels.

Once the previously described scaling is completed, one can easily determine the relative in-flight contribution made by each of the source power inputs and the SEA subsystems to the flight cabin noise levels. The following sections describe these relations in more detail.

In-flight cabin SPL contribution. - For each input, the percent contribution to the cabin response level is calculated and shown logarithmically such that the summation of the four inputs in each octave is 0 dB (see Figure E40). Domination of the 500 and 1 Khz octaves is clearly by the input from LF14Li, with -1 and -2 dB contribution levels. LF14Lo is next, approximately 20 dB lower in both octaves. The 2 Khz octave is dominated by LF14Ro (-6.5 dB), with LF14Li and LF14Lo approximately 5 and 6 dB lower. At 4 Khz, LF14Li once again dominates with -5.5 dB contribution, LF14Lo is at -9.5 dB, and the remaining subsystems are both more than 20 dB down. This "left side" dominance may be due to some asymmetries associated with the main gearbox.

In-flight power flow to cabin. - Predicted subsystem contribution to the cabin acoustic response level is shown in Figures E41 and E42, and are sorted in descending order according to SIL-4 contribution. Dominance by the near-source subsystems is evident, with OP23L the largest contributor in all four octaves. In the 500 hz octave, four subsystems are within 6 dB of OP23L (at -5 dB), OP34Lu at -7 dB, SP14L at -10 dB and OP45L and OP4YM both at -11 dB. Only OP34Lu of this set has a junction directly with the source frames, while the remaining have "second generation" connections. That is, they connect to a subsystem that connects to a source frame. At 1 Khz, six subsystems are within 6 dB of OP23L at -5 dB. These are OP34Lu at -7 dB, SP14L at -10 dB, and OP45L, OP4YM, OP12L and OPY5M at -11 dB. Of these, only OP34Lu and OP12L are connected to source frames. At 2 Khz, eleven subsystems are within 6 dB of OP23L (at -8 dB). OP23R, OP4YM, and OP34Lu are at -9 dB, OP34Ru and OPY5m at -10 dB, OP45R and OP45L at -11 dB, and SP14L, OP12L, SP14R, and OP12R are at -13 dB. Five of these subsystems connect directly to the source frames, while the remaining six have second generation connections. At 4 Khz, seven subsystems are within 6 dB of OP23L (at -7 dB). OP34Lu at -8 dB, OP4YM at -9 dB, OP12L and OP45L at -10 dB, OPY5M at -11 dB, and LF45Li and SP14L at -12 dB. Three of these are directly connected to source frames (OP34Lu, OP12L, and LF45Li). Note that the frame LF45Li makes more of a contribution to cabin sound pressure levels than many of the forward and side panels at 4 Khz.

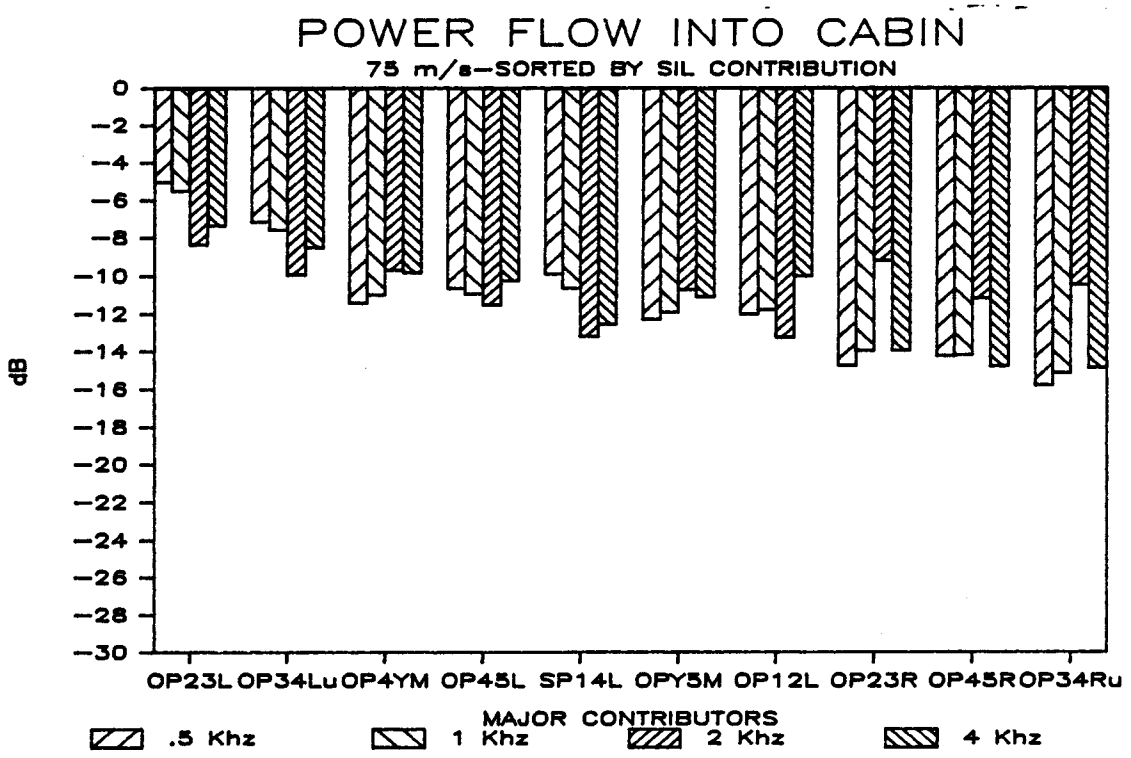

Figure E41. Predicted In-Flight Power Flow to Cabin-Major Contributors

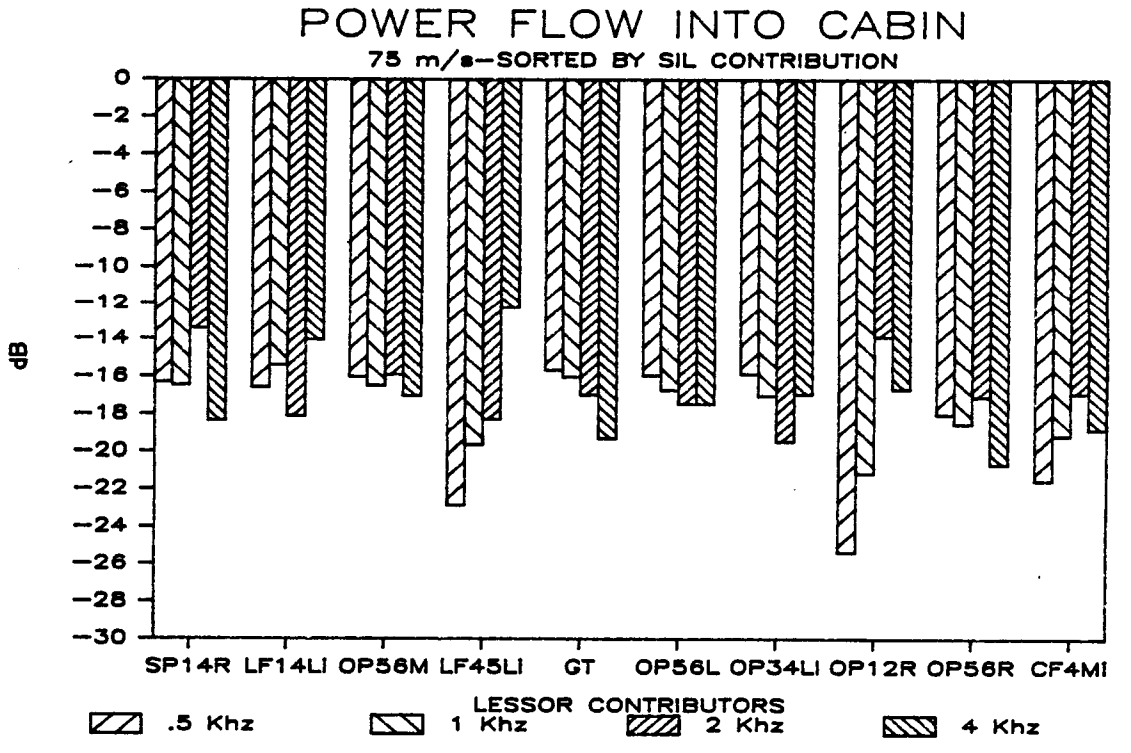

Figure E42. Predicted In-Flight Power Flow to Cabin-Lessor Contributors

The left side subsystem dominance is attributed to the distribution of measured in flight vibration levels at the main transmission attachment, with the lateral levels on the left side 10 to 20 dB higher than the right side. The exception to this is at 2 Khz where the right side out-of-plane source dominates and it is noted that seven out of the twelve major contributing subsystems are on the right or middle.

Power flow to OP23L. - Since OP23L is predicted to be the dominant contributing subsystem to cabin sound pressure (Figure E41), the path by which vibratory power arrives at OP23L is now examined. The major contributing subsystems are shown in Figure E43. This figure reveals that the dominance is shared by the out-of-plane motion of the two cross frames that border OP23L on its forward (CF3L) and aft (CF2L) edge. The predictions also state that LF14L transmits at least 6 dB less in all four SIL octaves than these two cross frames, even though it represents a direct connection from a source subsystem. The junction information shows that CF2L and CF3L each have longer line connections (.470m and .454m) to OP23L than LF14L (.335m). Also, these cross frames have less out-of-plane bending stiffness (approximately one fifth the out-of-plane moment of inertia) than LF14L, which may provide better impedance matching to OP23L and therefore more power transfer.

Power flow to OP34Lu. - The second highest predicted contributor to cabin noise in the 500, 1000, and 4000 hz octaves, OP34Lu, also receives the majority of its input from CF3Lo, in each SIL octave (see Figure E44). Much like OP23L, this subsystem has direct connection to LF14L, but receives its power mainly from the out-of-plane motion of its aft-edge cross frame. Its junction length to LF14L is approximately one-third of the junction length between CF3L and OP34Lu, and has the same impedance situation as OP23L.

Measured sound pressure vs. predicted panel vibration. - As a clue to how well the SEA method would predict the acoustic response level at passenger locations, the aft to forward predicted overhead panel vibration levels during forward flight are compared to the measured in-flight sound pressure levels. This comparison for the left side cabin locations is shown in Figure E45. The aft location considers one-third of the rear bulkhead and the four overhead panels between Sta 215 and 188 including OP12L, OP23L, OP34Lu, and OP34L1 as the contributors to the aft seat location, OP45L for the mid and OP56L for the forward location. For the aft location, the velocity compared is an area weighted average of the in-flight predictions for the aforementioned panels, while the mid and forward are represented by single predictions to their respective overhead panel. These predictions are then superimposed in Figure E45a through d onto the acoustic data to reveal a close agreement in the trend of lower sound pressure levels with distance forward (away from the source). Each of the comparisons agrees very well. The motivation behind these calculations is to provide a means of defining the spatial distribution of sound pressure that would be predicted if the cabin acoustic space were to be subsectioned by seat location. The current cabin response calculated is an average response for the entire cabin volume. These results show promising evidence that seat location predictions are possible using the SEA method.

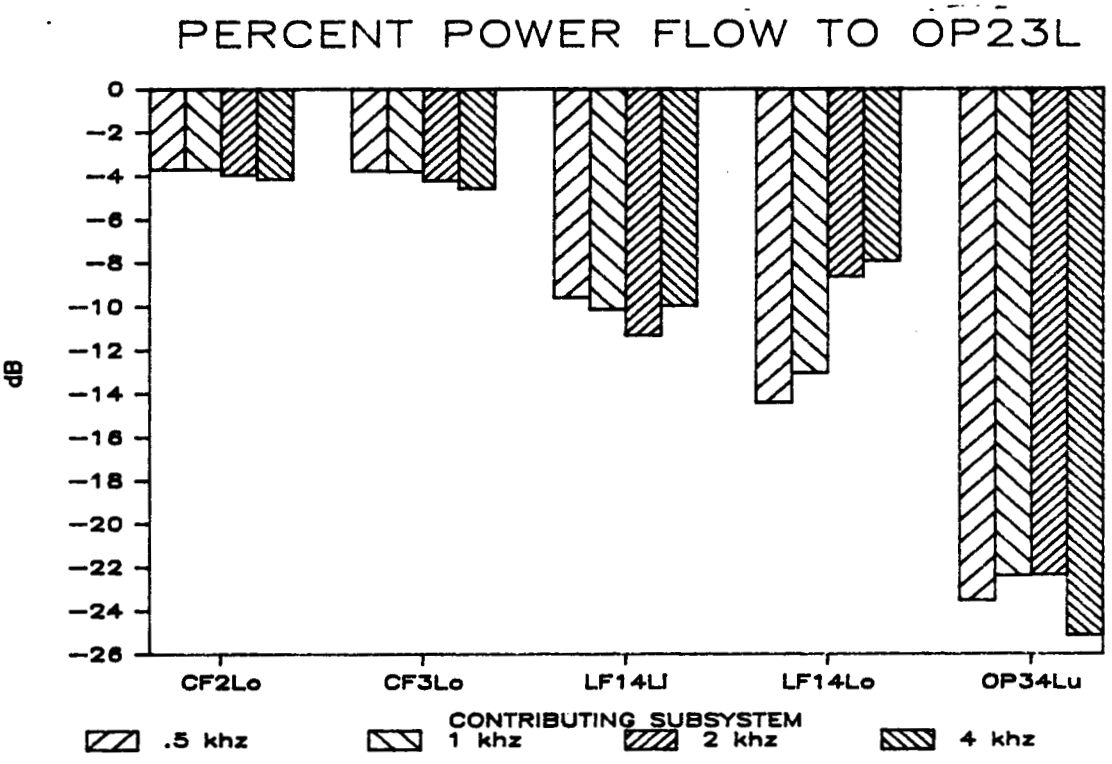

Figure E43. Predicted In-Flight Power Flow to OP23L

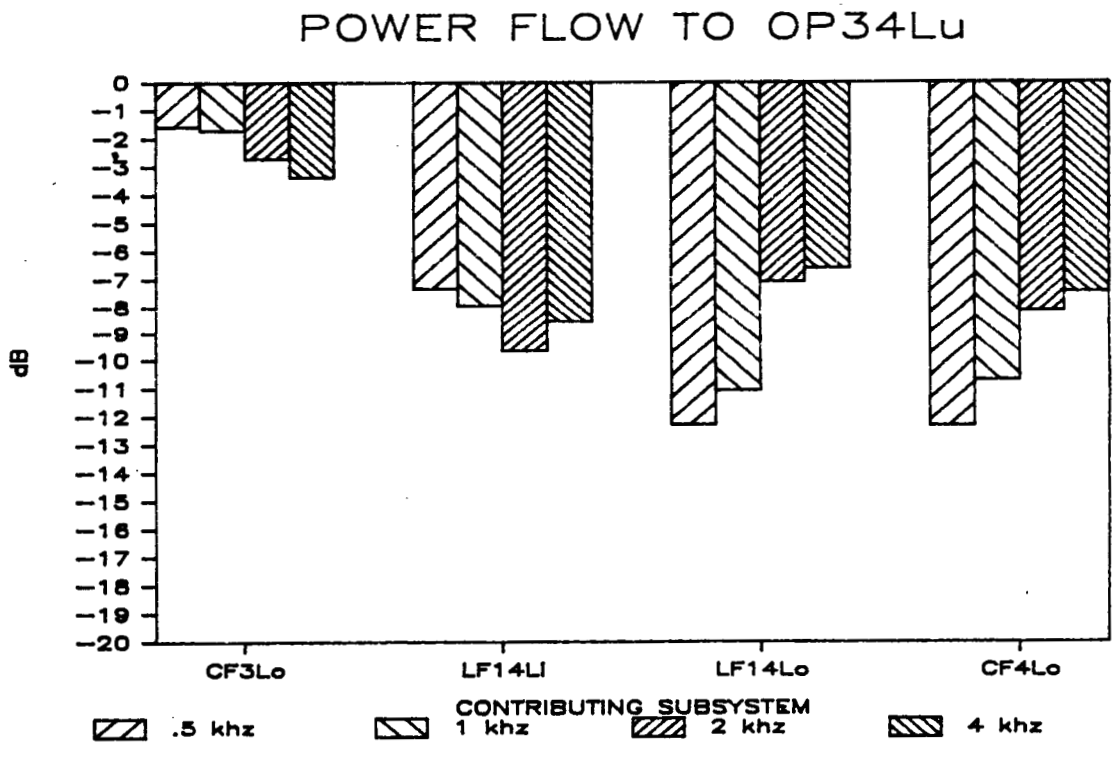

Figure E44. Predicted In-Flight Power Flow to OP34Lu

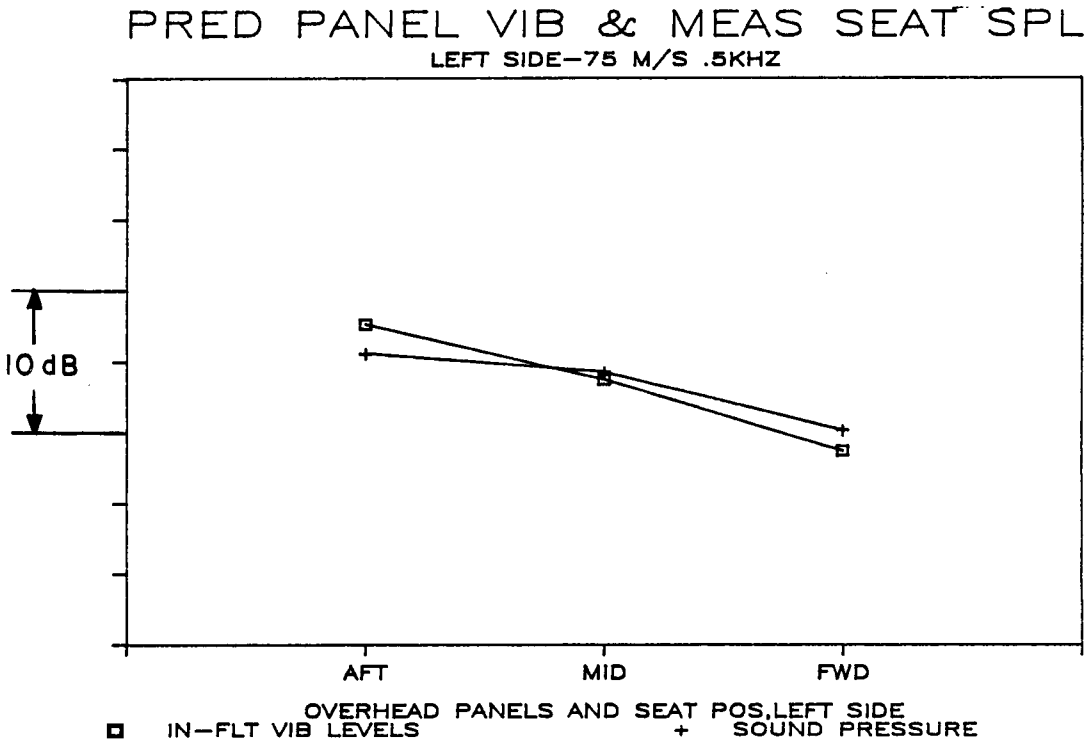

Figure E45a. Predicted In-Flight Panel Vibration Level vs. Measured Seat Location Sound Pressure Level, .5 kHz

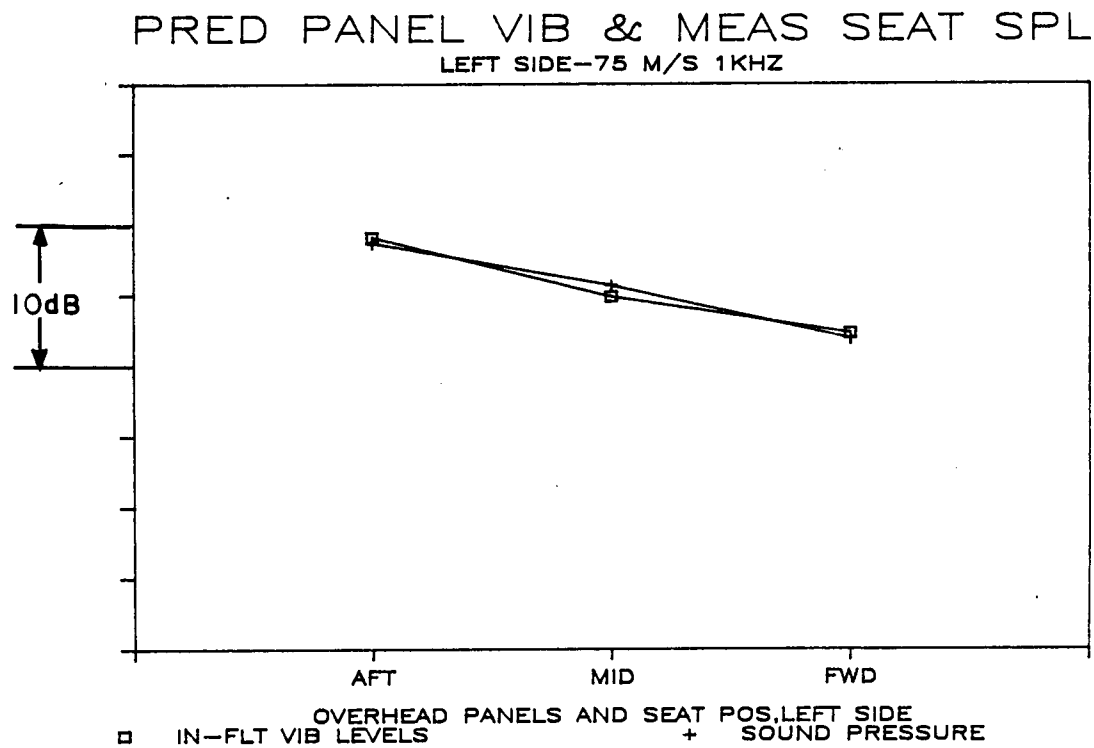

Figure E45b. Predicted In-Flight Panel Vibration Level vs. Measured Seat Location Sound Pressure Level, 1 kHz

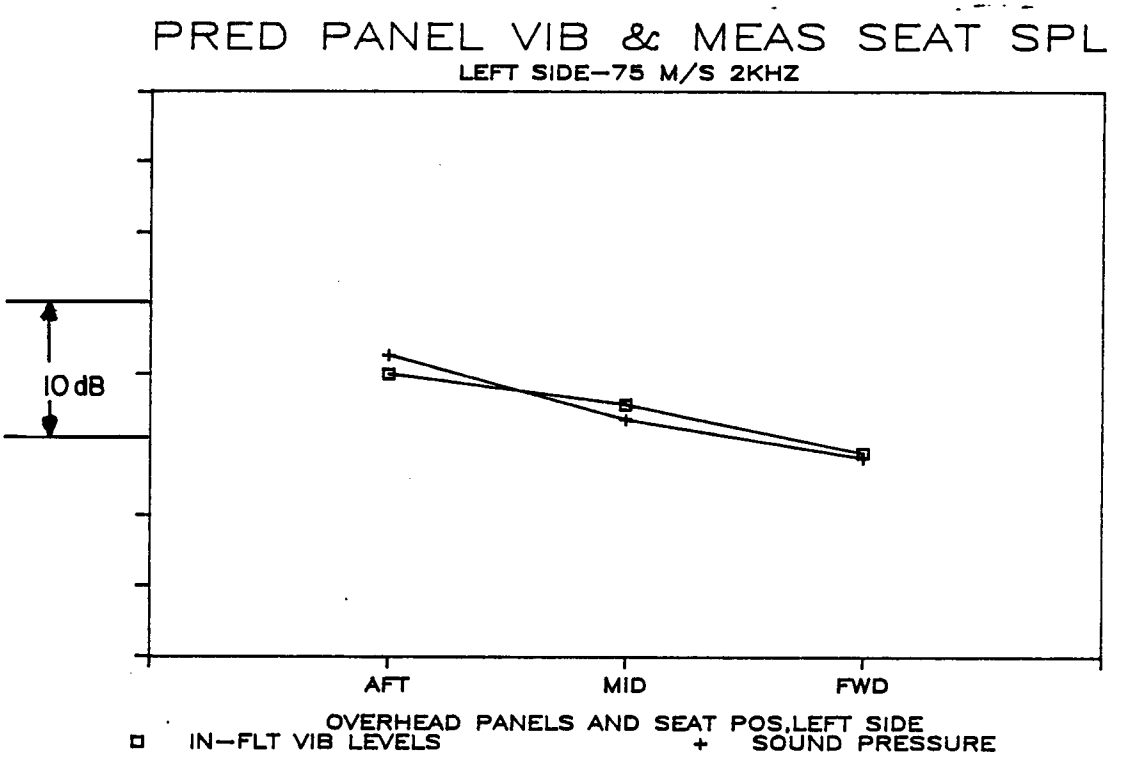

Figure E45c. Predicted In-Flight Panel Vibration Level vs. Measured Seat Location Sound Pressure Level, 2 kHz

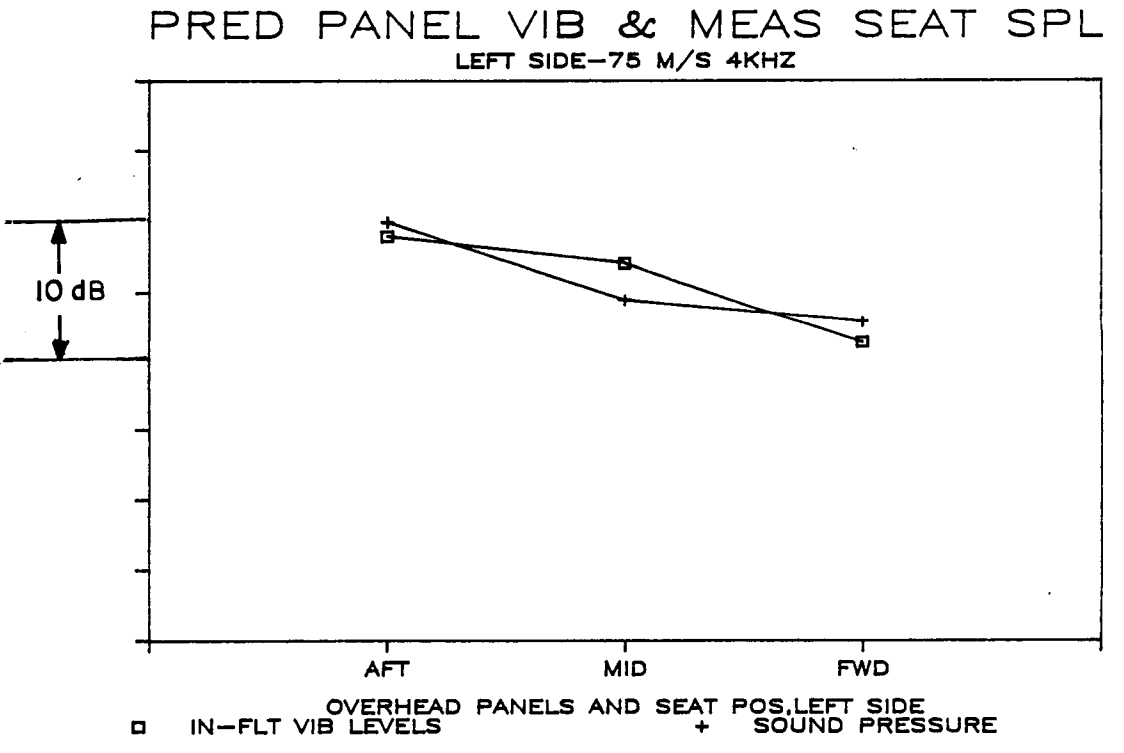

Figure E45d. Predicted In-Flight Panel Vibration Level vs. Measured Seat Location Sound Pressure Level, 4 kHz

APPENDIX F

REFINEMENTS TO THE SEA MODEL

CONTENTS

Frame Junction Vibration Transmission Model

Introduction. - A frame junction consists of the intersection of frame members. The following analysis presumes all frame members lie in the same plane and intersect each other at right angles. The basis for the modeling is to identify the motion types allowed for each frame. The model evaluates the propagation behavior for each motion type. Impedance representations for individual frames are combined in describing the dynamics of the frame junction. The vibration transmission through the frame junction is characterized in terms of an energy transmission coefficient that relates the transmitted to incident energies for particular source and receiving frames and motion types. The coupling loss factor for use in the SEA model of the helicopter airframe is determined from the energy transmission coefficients.

A prior frame junction model developed during Phase I of this study accounted for both in-plane and out-of-plane bending and torsional frame deformations [Reference 1]. It did not reflect potential constraints on the frame motion due to the in-plane impedance of the skin panels which are attached to the frames. The present model, described herein, presumes the skin panels completely restrict the in-plane motion at the top of the frames where they attach to the skin panels.

Helicopter frames are typically of a relatively deep web construction. The original model included a conventional Euler Bernoulli representation of the bending deformation. The revised model accounts for transverse shear deformation, but is not fully representative of a Timoshenko Mindlin bending deformation model in that it does not include the effects of rotary inertia. Including transverse shear deformation in the model limits the increase in the bending wavespeed with increasing frequency, when compared to the previous model.

The limiting wavespeed is nearly equal to the shear wavespeed for the frame material. The transition where transverse shear deformation becomes important occurs near 3 kHz for out-of-plane bending in typical S-76 helicopter frames.

Allowed frame motions. - As stated above, it is presumed that the skin panels effectively prohibit motion at the top edge of the frames in the plane of the skin panels. Figure F1 shows the allowed frame motions, including rotation about the axis where the panel connects to the frame and out-of-plane transverse displacements. The transverse displacement corresponds to out-of-plane bending of the frame for which the neutral axis is along the top of the frame where it connects to the panel. The rotational motion allows for both torsional and in-plane bending deformation of the frame. The frame cross-section is presumed to remain undeformed for all motions.

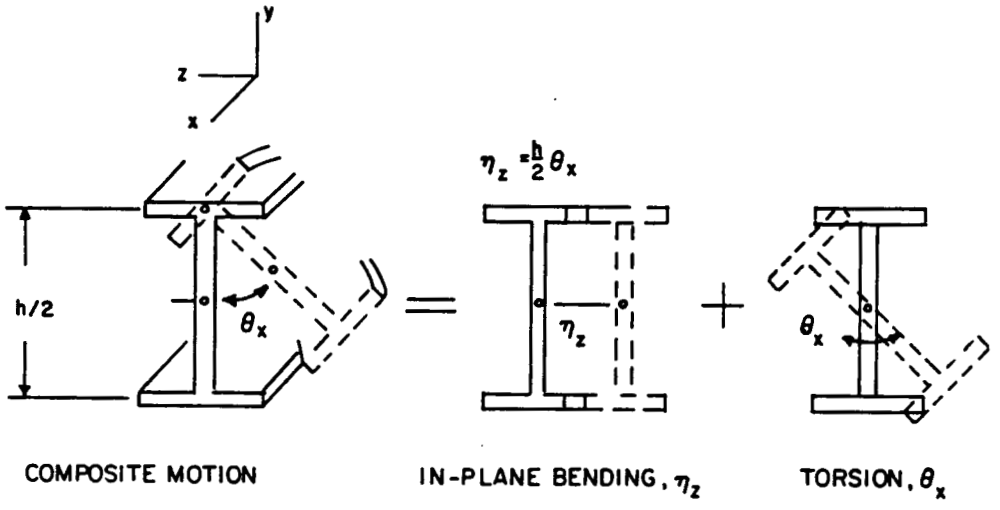

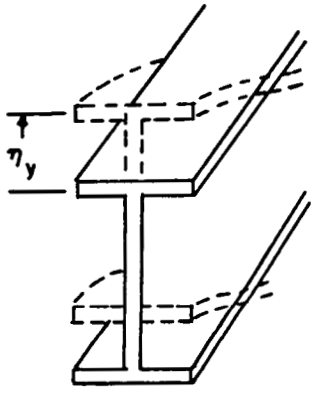

Figure F1. Allowed Motions of Frame Cross-Section

Model for composite in-plane motion. - This motion is characterized by rotation about the top of the frame about an axis parallel to the longitudinal frame axis, θ_x, as shown in Figure F1 and in-plane bending deformation, which is taken into account by the rotation θ_y. All other motions of the cross-section are presumed equal to zero. The θ_y rotation allows the model to account for the effects of transverse shear and rotary inertia for bending deformation. Particle displacements on the frame cross-section corresponding to the rotations θ_x and θ_y are given by:

$$U_z = y\,\theta_x(x) \qquad U_y = -z\,\theta_x(x) \qquad U_x = z\,\theta_y(x) \tag{F1}$$

The strains on a small element dydz of the cross section are described by:

$$\varepsilon_x = \frac{\partial U_x}{\partial x} = z\,\frac{\partial \theta_y}{\partial x}$$

$$\gamma_{xy} = \frac{\partial U_x}{\partial y} + \frac{\partial U_y}{\partial x} = -z\,\frac{\partial \theta_x}{\partial x} \tag{F2a}$$

$$\gamma_{xz} = \frac{\partial U_x}{\partial z} + \frac{\partial U_z}{\partial x} = \theta_y + y\,\frac{\partial \theta_x}{\partial x}$$

while the stresses are described by:

$$\sigma_x = E\,z\,\frac{\partial \theta_y}{\partial x}$$

$$\tau_z = G\,\gamma_{xz} = G\,\{\theta_y + y\,\frac{\partial \theta_x}{\partial x}\} \tag{F2b}$$

$$\tau_y = G\,\tau_{xy} = -G\,z\,\frac{\partial \theta_x}{\partial x}$$

These are integrated over the area of the cross-section to give the shear force in the z direction and resulting moment about the x axis.

$$F_z = GA \{\theta_y - \frac{h}{2} \frac{\partial \theta_x}{\partial x}\}$$

$$M_x = GA \{\frac{h}{2} \theta_y - \frac{I_x^a}{A} \frac{\partial \theta_x}{\partial x}\} \qquad \text{(F3)}$$

$$M_y = -EI_y \frac{\partial \theta_y}{\partial x}$$

A moment balance about the y axis for a frame element of thickness dx yields:

$$F_z = - \frac{\partial M_y}{\partial x}$$

which, when combined with the first and third of Equations (F3), yields:

$$GA \{\theta_y - \frac{h}{2} \frac{\partial \theta_x}{\partial x}\} = EI_y \frac{\partial^2 \theta_y}{\partial x^2} \qquad \text{(F4)}$$

The above results neglect the rotary inertia of the frame cross-section for rotation about the y axis. For rotation about the x axis the moment balance yields:

$$- \frac{\partial M_x}{\partial x} = \rho I_x^a \frac{\partial^2 \theta_x}{\partial t^2}$$

which gives the following, when combined with the second of Equations (F3):

$$- GA \{\frac{h}{2} \frac{\partial \theta_y}{\partial x} - \frac{I_x^a}{A} \frac{\partial^2 \theta_x}{\partial^2 x}\} = \rho I_x^a \frac{\partial^2 \theta_x}{\partial t^2} \qquad \text{(F5)}$$

Propagation characteristics for the composite in-plane motion are obtained from Equations (F4) and (F5) with a plane wave solution of the form:

$$\theta_x = \theta_x^o \, e^{i(kx - \omega t)}$$

$$\theta_y = \theta_y^o \, e^{i(kx - \omega t)} \qquad \text{(F6)}$$

The resulting dispersion relation is fourth order in k and has two distinct roots; one root corresponds to a propagating wave solution, the other to an exponentially decaying solution.

Impedance characteristics looking into a semi-infinite frame are obtained from a superposition of propagating and decaying terms:

$$\dot{\theta}_x = \dot{\theta}_{xp} \, e^{i(k_p x - \omega t)} + \dot{\theta}_{xd} \, e^{(-k_d x - i\omega t)}$$

$$\dot{\theta}_y = \dot{\theta}_{yp} \, e^{i(k_p x - \omega t)} + \dot{\theta}_{yd} \, e^{(-k_d x - i\omega t)} \qquad \text{(F7)}$$

After a fair amount of algebra, Equations (F3), (F4), (F5) and (F7) yield impedances relating the moments and angular velocities at the end of the frame:

$$\begin{Bmatrix} M_x \\ M_y \end{Bmatrix} = \begin{bmatrix} Z_1^{ip} & Z_{12}^{ip} \\ Z_{12}^{ip} & Z_2^{ip} \end{bmatrix} \begin{Bmatrix} \dot{\theta}_x \\ \dot{\theta}_y \end{Bmatrix} \qquad \text{(F8)}$$

where

$$Z_1^{ip} = \frac{GI_x^a}{\omega} \left[\frac{k_p H_d^{ip} + i k_d H_p^{ip}}{H_p^{ip} + H_d^{ip}} \right]$$

$$Z_2^{ip} = \frac{EI_y}{\omega} \left[\frac{i k_d H_d^{ip} + k_p H_p^{ip}}{H_p^{ip} + H_d^{ip}} \right] \qquad \text{(F9a)}$$

$$Z_{12}^{ip} = \frac{EI_y}{\omega}\left[\frac{H_p^{ip}\, H_d^{ip}(k_p - ik_d)}{H_p^{ip} + H_d^{ip}}\right]$$

where

$$H_p^{ip} = \frac{ik_p\, GAh/2}{GA + EI_y\, k_p^2} \quad , \quad H_d^{ip} = \frac{k_d\, GAh/2}{GA - EI_y\, k_d^2} \tag{F9b}$$

Model for out-of-plane bending motion. - This motion is characterized by the transverse displacement of the frame in the y direction, η_y. Accounting for transverse shear deformation also involves an independent rotation of the cross-section about the z axis, θ_z. The development proceeds in a similar fashion to the previous section. Displacements of points on a cross-section are given by:

$$U_x = - y\, \theta_z(x)$$

$$U_y = \eta_y(x) \tag{F10}$$

$$U_z = 0$$

The strains are described by:

$$\varepsilon_x = -y \frac{\partial \theta_x}{\partial x} \tag{F11a}$$

$$\gamma_{xy} = \frac{\partial U_x}{\partial y} + \frac{\partial U_y}{\partial x} = G\{\frac{\partial \eta_y}{\partial x} - \theta_z\}$$

while the stresses are described by:

$$\tau_x = E\, y \frac{\partial \theta_z}{\partial x} \tag{F11b}$$

$$\tau_{xy} = G\{\frac{\partial \eta_y}{\partial x} - \theta_z\}$$

Integrating over the surface area of the cross-section to obtain the resulting forces and moments gives:

$$F_y = -GA\ \{\frac{\partial \eta_y}{\partial x} - \theta_z\ \}$$

$$M_z = -EI_z^a \frac{\partial \theta_z}{\partial x} \tag{F12}$$

Force/moment balances in the y direction and about the z axis for a frame element dx yields:

$$\rho A \frac{\partial^2 \eta_y}{\partial t^2} = GA\{\frac{\partial^2 \eta_y}{\partial x^2} - \frac{\partial \theta_z}{\partial x}\}$$

and

$$-GA\{\frac{\partial \eta_y}{\partial x} - \theta_z\} = EI_z^a \frac{\partial^2 \theta_z}{\partial x^2} \tag{F13}$$

respectively.

These are the governing equations for out-of-plane bending wave propagation in a frame member. Transverse shear deformation was accounted for in the derivation while the effects of rotary inertia were not included. The same approach as for the in-plane motion is followed to obtain propagation characteristics and frame impedances. As before, the dispersion relation yields distinct propagating and decaying wave solutions.

The frame impedances in this case are given by:

$$\begin{Bmatrix} F_y \\ M_z \end{Bmatrix} = \begin{bmatrix} Z_1^{op} & Z_{12}^{op} \\ Z_{12}^{op} & Z_2^{op} \end{bmatrix} \begin{Bmatrix} \dot{\eta}_y \\ \dot{\theta}_z \end{Bmatrix} \tag{F14}$$

where

$$Z_1^{op} = \frac{GA}{\omega} \left[\frac{k_p H_d^{op} + ik_d H_p^{op}}{H_p^{op} + H_d^{op}} \right]$$

$$Z_2^{op} = \frac{EI_z^a}{\omega} \left[\frac{ik_d H_d^{op} + k_p H_p^{op}}{H_p^{op} + H_d^{op}} \right] \tag{F15a}$$

$$Z_{12}^{op} = \frac{EI_z^a}{\omega} \left[\frac{H_p^{op} H_d^{op} (k_p - ik_d)}{H_p^{op} + H_d^{op}} \right]$$

and

$$H_p^{op} = \frac{ik_p GA}{GA + EI_z^a k_p^2} \quad , \quad H_d^{op} = \frac{k_d GA}{GA - EI_z^a k_d^2} \tag{F15b}$$

The impedance expressions are identical in form to those for the in-plane motion. The differences are in the values for the wave-numbers k_p, k_d, the appropriate moment of inertia/area term, and the presence of the frame half-height in the H factors for the in-plane motion.

The procedure for evaluating junction transmission coefficients is to solve for the transmitted powers for an incident power in one of the frames involving only one of the motion types. The incident motion involves only the propagating wave. The junction motions induced by the incident motion result in the transmission of energy through the junction into other frames and motion types. Energy is also reflected back into the source frame into the same motion type as the incident motion and potentially the other motion type as well.

The solution is given by the superposition of the blocked and radiated cases. The blocked case evaluates the source excitation in the form of blocked forces/moments that act on the junction as a result of the incident motion for a rigid junction with zero displacements. Incident motion is removed in the radiated case and the junction is allowed to have its final motion. The transmitted or radiated power into receiving frame and motion combinations is evaluated from the junction motions and individual frame impedances.

The superposition of the two cases is in effect a force/moment balance for motion at the junction. The blocked force/moment that is scaled by the incident motion is balanced by the total reaction force/moment produced by the motion of the attached frames. The reaction force/moment for each frame is determined from the junction motion according to the frame impedances described in Equations (F8) or (F14). The impedances for the different frames are conveniently combined to form a junction impedance matrix. The solution of the force/moment balance gives the junction motions in terms of the amplitude of the incident motion.

Blocked case. - The blocked force/moment expressions are evaluated by superimposing reflected propagating and decaying terms with the incident motion. The amplitudes of the reflected motions are determined in terms of the incident motion amplitude by setting the frame motions equal to zero at the "blocked" junction. The blocked forces/moments are then evaluated from Equations (F3) and (F12).

The blocked moments for the composite in-plane motion are:

$$M_x^{bl} = C_{m_x}^{bl} \dot{\theta}_x^{inc}$$

$$C_{m_x}^{bl} = +2 Z_1^{ip} \qquad \text{(F16)}$$

$$M_y^{bl} = C_{m_y}^{bl} \dot{\theta}_x^{inc}$$

$$C_{m_y}^{bl} = -2 Z_2^{ip} H_p^{ip}$$

where Z_1^{ip}, Z_2^{ip}, and H_p^{ip} are given in Equations (F9a) and (F9b). The blocked force/moment for out-of-plane motion is:

$$F_y^{bl} = C_{f_y}^{bl} \dot{\eta}_y^{inc}$$

$$C_{f_y}^{bl} = +2 Z_1^{op}$$

$$M_z^{bl} = C_{m_z}^{bl} \dot{\eta}_y^{inc} \qquad \text{(F17)}$$

$$C_{m_z}^{bl} = -2 Z_2^{op} H_p^{op}$$

Radiated case. - The incident power is removed for this case and the junction motions take their final values. By appropriately combining impedances for all of the individual frames, including the source frame, a junction impedance matrix involving the allowed motions is developed. It has the following form:

$$\begin{Bmatrix} F_y \\ M_y \\ M_x \\ M_z \end{Bmatrix} = [Z^j] \begin{Bmatrix} \dot{\eta}_y \\ \dot{\theta}_y \\ \dot{\theta}_x \\ \dot{\theta}_z \end{Bmatrix} \qquad \text{(F18)}$$

where

$$[Z^J] = \begin{bmatrix} Z_{f_y} & 0 & Z_{f_y\theta_x} & Z_{f_y\theta_z} \\ 0 & Z_{m_y} & Z_{m_y\theta_x} & Z_{m_y\theta_z} \\ Z_{f_y\theta_x} & Z_{m_y\theta_x} & Z_{m_x} & 0 \\ Z_{f_y\theta_z} & Z_{m_y\theta_z} & 0 & Z_{m_z} \end{bmatrix} \qquad \text{(F19)}$$

and

$$
\begin{aligned}
Z_{f_y} &= Z_1^{op}(1) + Z_1^{op}(2) + Z_1^{op}(3) + Z_1^{op}(4) \\
Z_{m_y} &= Z_2^{ip}(1) + Z_2^{ip}(2) + Z_2^{ip}(3) + Z_2^{ip}(4) \\
Z_{m_x} &= Z_1^{ip}(1) + Z_1^{ip}(3) + Z_2^{op}(2) + Z_2^{op}(4) \\
Z_{m_z} &= Z_2^{op}(1) + Z_2^{op}(3) + Z_1^{ip}(2) + Z_1^{ip}(4) \\
Z_{f_y\theta_z} &= Z_{12}^{op}(1) - Z_{12}^{op}(3) \\
Z_{f_y\theta_x} &= Z_{12}^{op}(2) - Z_{12}^{op}(4) \\
Z_{m_y\theta_x} &= Z_{12}^{ip}(1) - Z_{12}^{ip}(3) \\
Z_{m_y\theta_z} &= Z_{12}^{ip}(4) - Z_{12}^{ip}(2)
\end{aligned}
\qquad \text{(F20)}
$$

The forces and moments for the radiated case are those that must act on the junction in order to produce the final motions.

Junction force/moment balance. - Balancing the frame reaction forces/moments from the radiated case with the blocked force/moment excitation from the blocked case yields the following,

for in-plane incidence:

$$[Z^J]\begin{Bmatrix} \dot{\eta}_y \\ \dot{\theta}_y \\ \dot{\theta}_x \\ \dot{\theta}_z \end{Bmatrix} = \begin{Bmatrix} 0 \\ C^{bl}_{m_y} \\ C^{bl}_{m_x} \\ 0 \end{Bmatrix} \dot{\theta}^{inc}_x \tag{F21}$$

and for out-of-plane incidence:

$$[Z^J]\begin{Bmatrix} \dot{\eta}_y \\ \dot{\theta}_y \\ \dot{\theta}_x \\ \dot{\theta}_z \end{Bmatrix} = \begin{Bmatrix} C^{bl}_{f_y} \\ 0 \\ 0 \\ C^{bl}_{m_z} \end{Bmatrix} \dot{\eta}^{inc}_y \tag{F22}$$

Inverting the matrix yields the solution for the junction displacements.

Transmission coefficient evaluation. - The incident power is determined by the amplitude of the incident wave and includes components associated with both displacement variables for the incident motion type. The displacement variables for in-plane motion are θ_x and θ_y. Considering only a propagating wave these are related by:

$$\dot{\theta}_y = H^{ip}_p \dot{\theta}_x \tag{F23}$$

The variables for out-of-plane incident motion, η_y and θ_z, are related by:

$$\dot{\theta}_z = H_p^{op} \dot{\eta}_y \tag{F24}$$

The power in a propagating wave is given in terms of the frame impedances by the following equations,

for in-plane incidence:

$$\Pi_{inc}^{ip} = \frac{1}{2} \text{Re} \{Z_1^{ip} + Z_2^{ip} |H_p^{ip}|^2\} |\theta_x^{inc}|^2 \tag{F25}$$

and for out-of-plane incidence:

$$\Pi_{inc}^{op} = \frac{1}{2} \text{Re} \{Z_1^{op} + Z_2^{op} |H_p^{op}|^2\} |\eta_y^{inc}|^2 \tag{F26}$$

The transmitted power is calculated from the junction displacements. It is necessary to determine the appropriate displacements for each receiving frame/motion type combination as well as the proper sense for the junction motions. An example would be the right angle frame, number 2, in Figure F1, where in-plane motion is excited by the global displacements, θ_y and $-\theta_z$. The minus sign accounts for the different sense of the global motion θ_z in comparison with the appropriate sense locally looking into frame number 2.

The transmitted power as a result of these junction displacements is given by the following equations,

for in-plane motion:

$$\Pi_{tran} = \frac{1}{2} \text{Re} \{Z_1^{ip} |\dot{\theta}_z|^2 + Z_2^{ip} |\dot{\theta}_y|^2 + Z_{12}^{ip} (\dot{\theta}_y [-\dot{\theta}_z^*] + \dot{\theta}_y^* [-\dot{\theta}_z])\} \tag{F27}$$

The appropriate junction displacements for out-of-plane motion in frame 2 are η_y and θ_x for which the transmitted power is:

$$\Pi_{tran} = \frac{1}{2} \text{Re} \{Z_1^{op} |\dot{\eta}_y|^2 + Z_2^{op} |\dot{\theta}_x|^2 + Z_{12}^{op} (\dot{\theta}_x \dot{\eta}_y^* + \dot{\theta}_x^* \dot{\eta}_y)\} \quad \text{(F28)}$$

The appropriate junction displacements for in-plane or out-of-plane transmission will differ for other frame locations relative to the source frame.

The transmission coefficient, which is the ratio of transmitted to incident power, is given by:

$$\tau = \frac{\Pi_{tran}}{\Pi_{inc}} \quad \text{(F29)}$$

Coupling loss factor evaluation. - The coupling loss factor, η_{ij}, for an SEA calculation relates the stored energy in a structural or acoustic subsystem to the power that is transmitted to attached subsystems as a result of that energy, thus

$$\Pi_{tran} = \eta_{ij} \omega e_i \quad \text{(F30)}$$

The transmitted power is the same in Equations (F29) and (F30) which results in the following:

$$\eta_{ij} = \frac{\tau}{\omega} \frac{\Pi_{inc}}{e_i} \quad \text{(F31)}$$

The standard presumption at this point is that the energy field is highly reverberant with equal propagating power components in all directions. For a one-dimensional subsystem of the length L, the power incident on a junction at one end of the subsystem is simply half the total power propagating within the subsystem. This leads to the following relationship between the subsystem energy, e_i, and the incident power, Π_{inc}:

$$\Pi_{inc} = \frac{c_g e_i}{2L} \tag{F32}$$

where c_g is the group velocity for the particular incident motion being considered. It is obtained for the dispersion relation for the motion type according to:

$$c_g = \frac{d\omega}{dk} \tag{F33}$$

With Equations (F31) and (F32) the final result relating the transmission coefficient and coupling loss factor becomes:

$$\eta_{ij} = \frac{c_g \tau}{2L\omega} \tag{F34}$$

Transmission behavior of typical S-76 frames. - The above analysis was used to investigate the transmission characteristics of frame junctions with frames that are typical of those in the cabin overhead of the Sikorsky S-76. Transmission coefficient plots are shown in Figures F2 to F5 for two frame junction configurations; 1) a symmetric four-frame junction, and 2) an asymmetric three-frame (tee) junction. Corresponding coupling loss factor plots are shown in Figures F6 and F7 for two of the four cases considered.

A comparison of the reflected energy for in-plane and out-of-plane incidence shows that in-plane motion is more significantly reflected at the junction. Impedances for out-of-plane motion are typically larger than for in-plane motion so that the junction impedances, Equations (F19) and (F20), are dominated by the larger out-of-plane impedances. The larger junction impedances relative to the blocked force or moment coefficient, Equations (F16) and (F17), result in smaller junction displacements for in-plane in comparison to out-of-plane incidence.

Removal of one of the frames from the junction results in asymmetries which introduce transmission into motions originally unexcited by the incident energy. For example, in-plane motion does not transmit into out-of-plane motion of the source frame (#1) or in line frame (#3) in the symmetric four-frame junction, but for the asymmetric three-frame junction in-plane incidence results in significant energy transmission into these motions.

The coupling loss factor plots reveal a modified frequency dependence as a result of the group velocity and frequency factors in Equation (F34). The coupling loss factor for the higher impedance out-of-plane motion is relatively large at low frequency, particularly for transmission into the in-line frame.

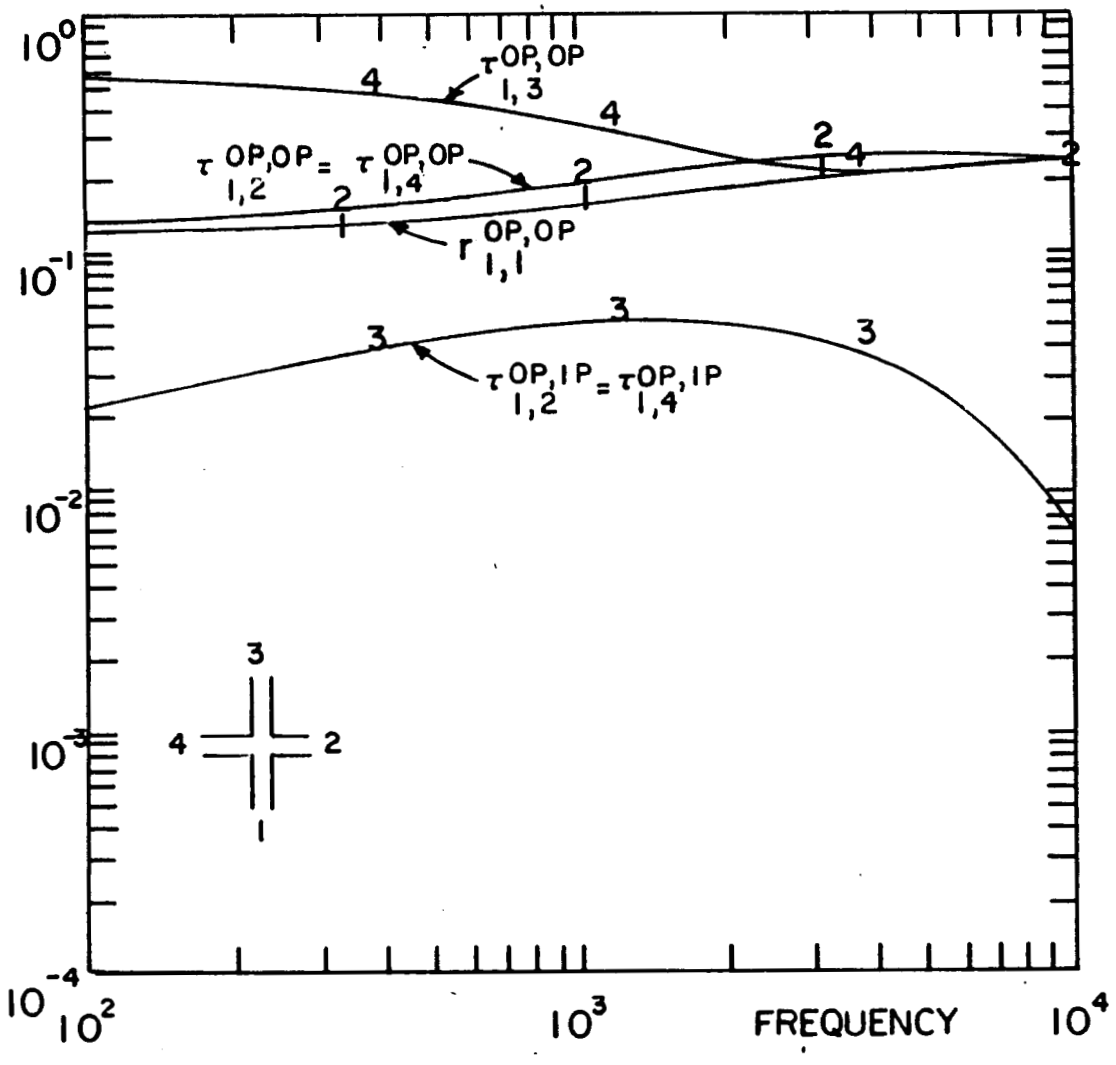

Figure F2. Transmission Coefficients for Out-of-Plane Incident Energy (Frame 1) for a Four-Frame Junction

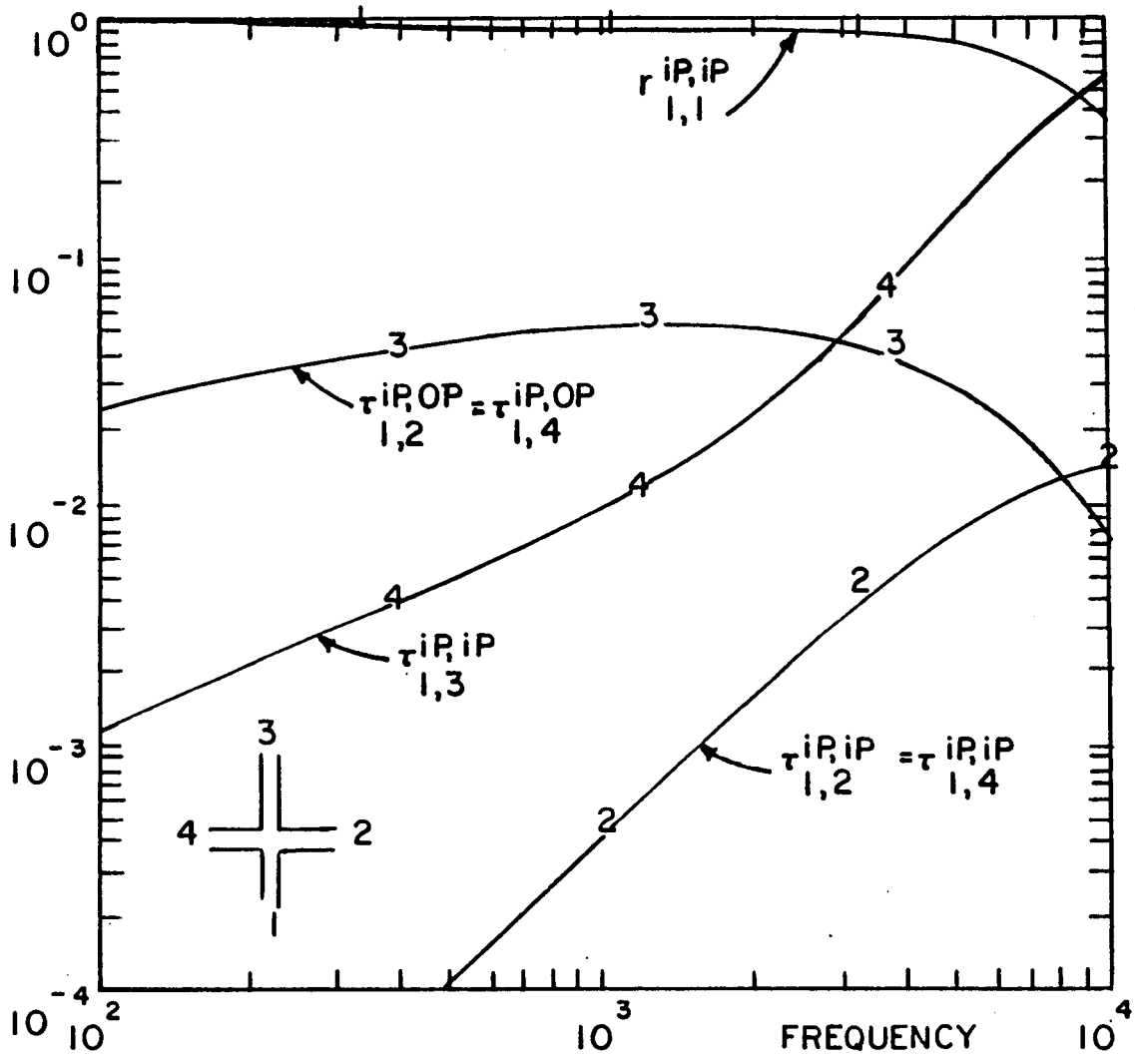

Figure F3. Transmission Coefficients for In-Plane Incident Energy (Frame 1) for a Four-Frame Junction

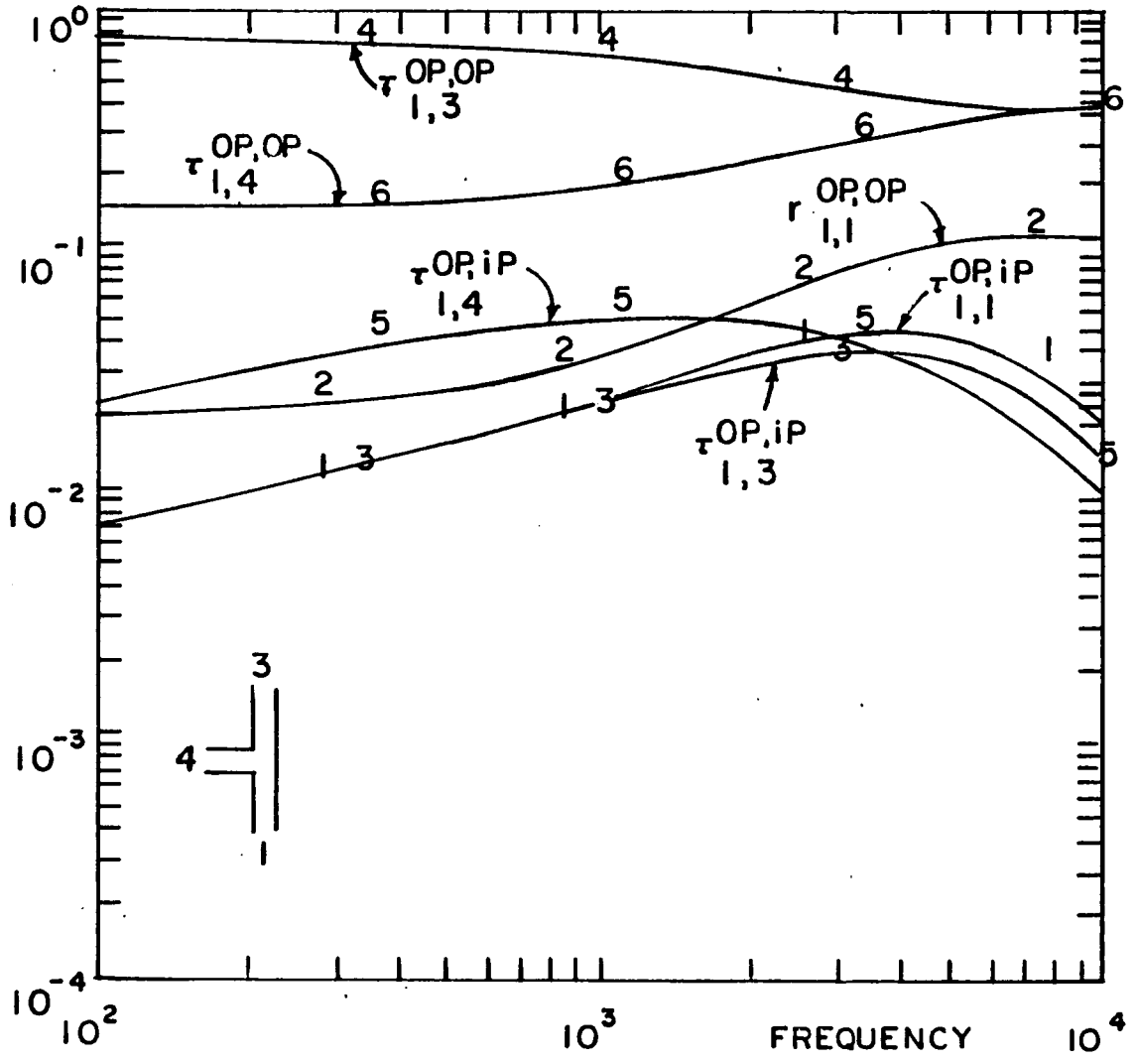

Figure F4. Transmission Coefficients for Out-of-Plane Incident Energy (Frame 1) for a Three-Frame Junction

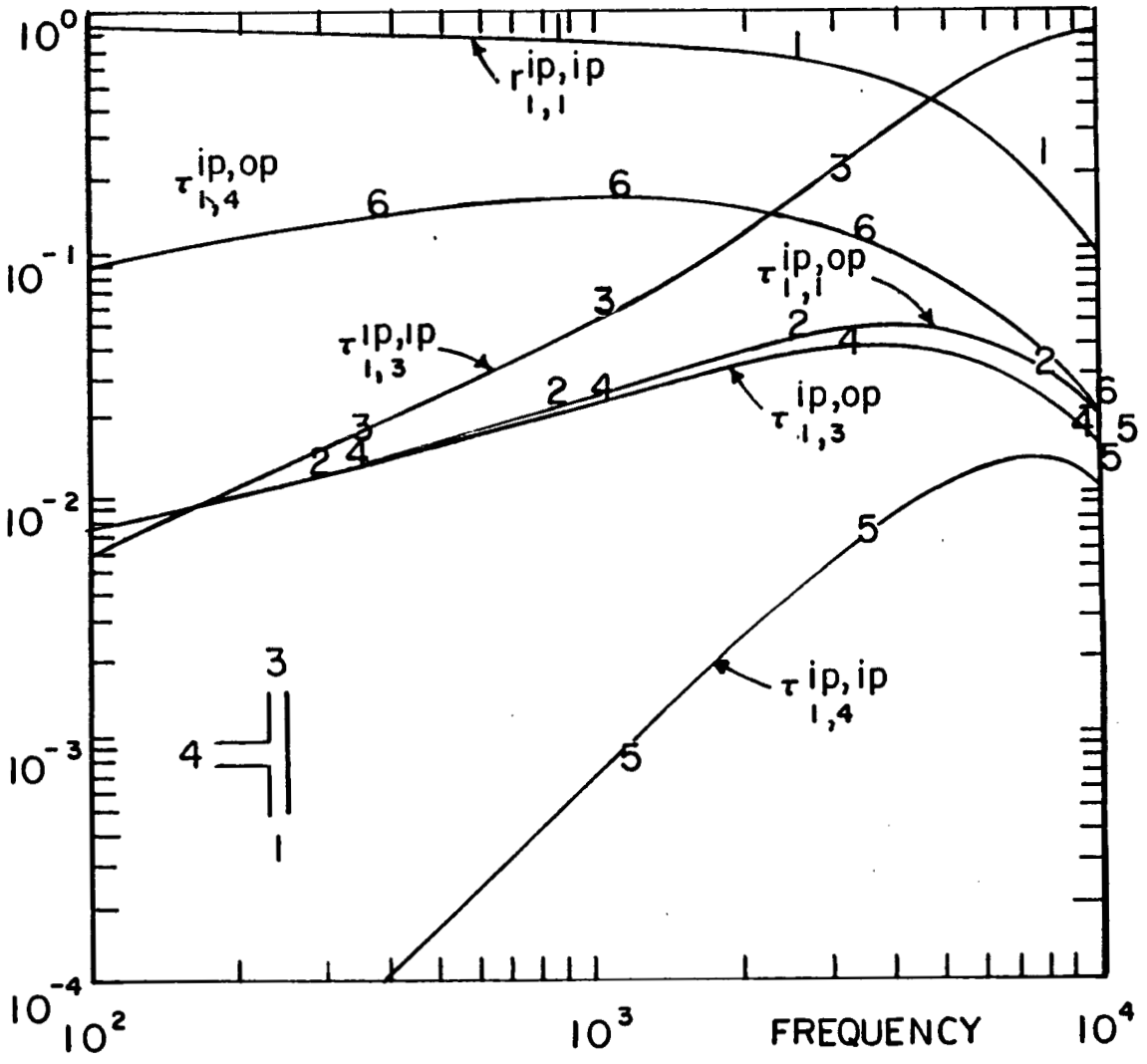

Figure F5. Transmission Coefficients for In-Plane Incident Energy (Frame 1) for a Three-Frame Junction

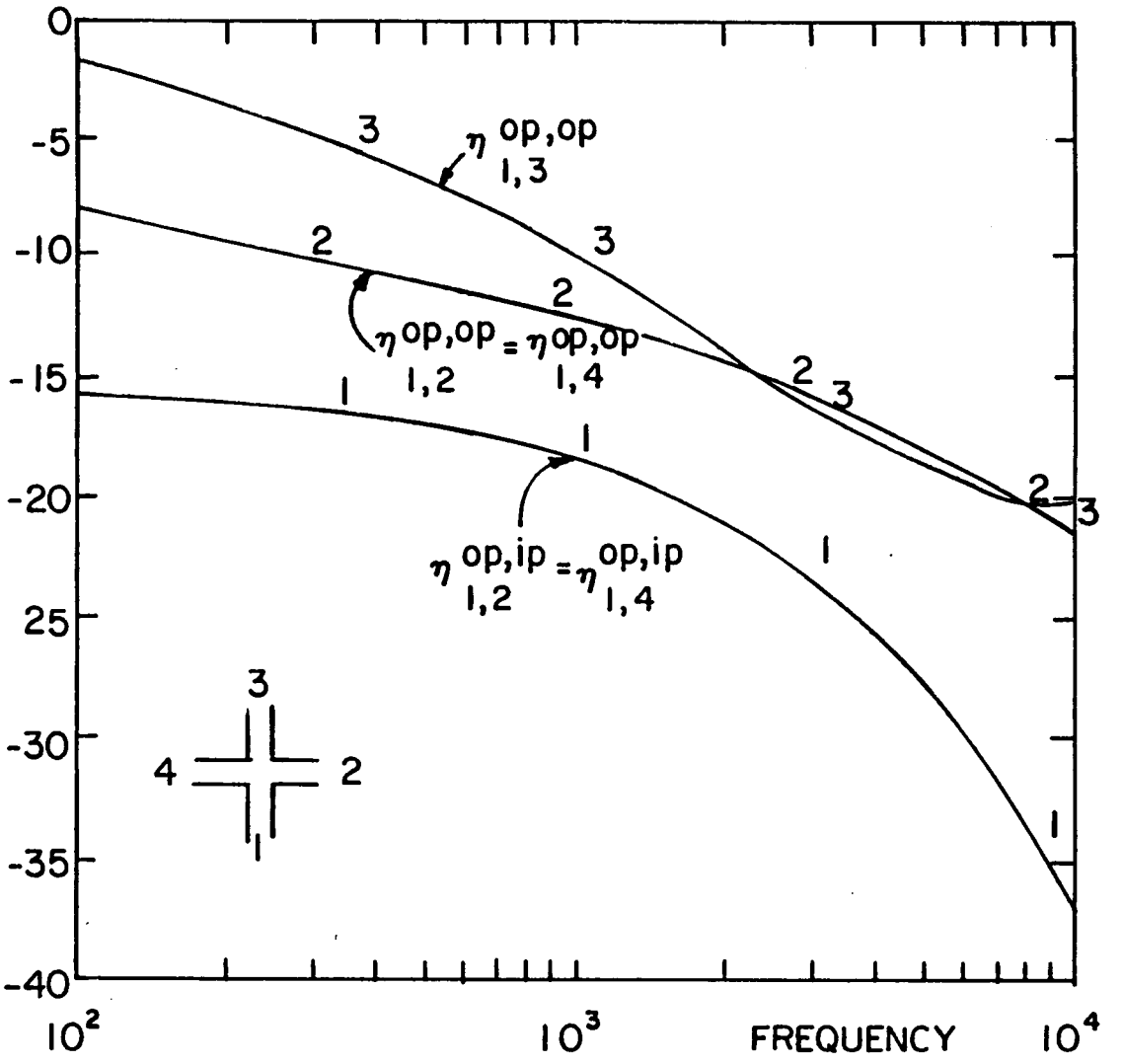

Figure F6. Coupling Loss Factors for a Four-Frame Junction

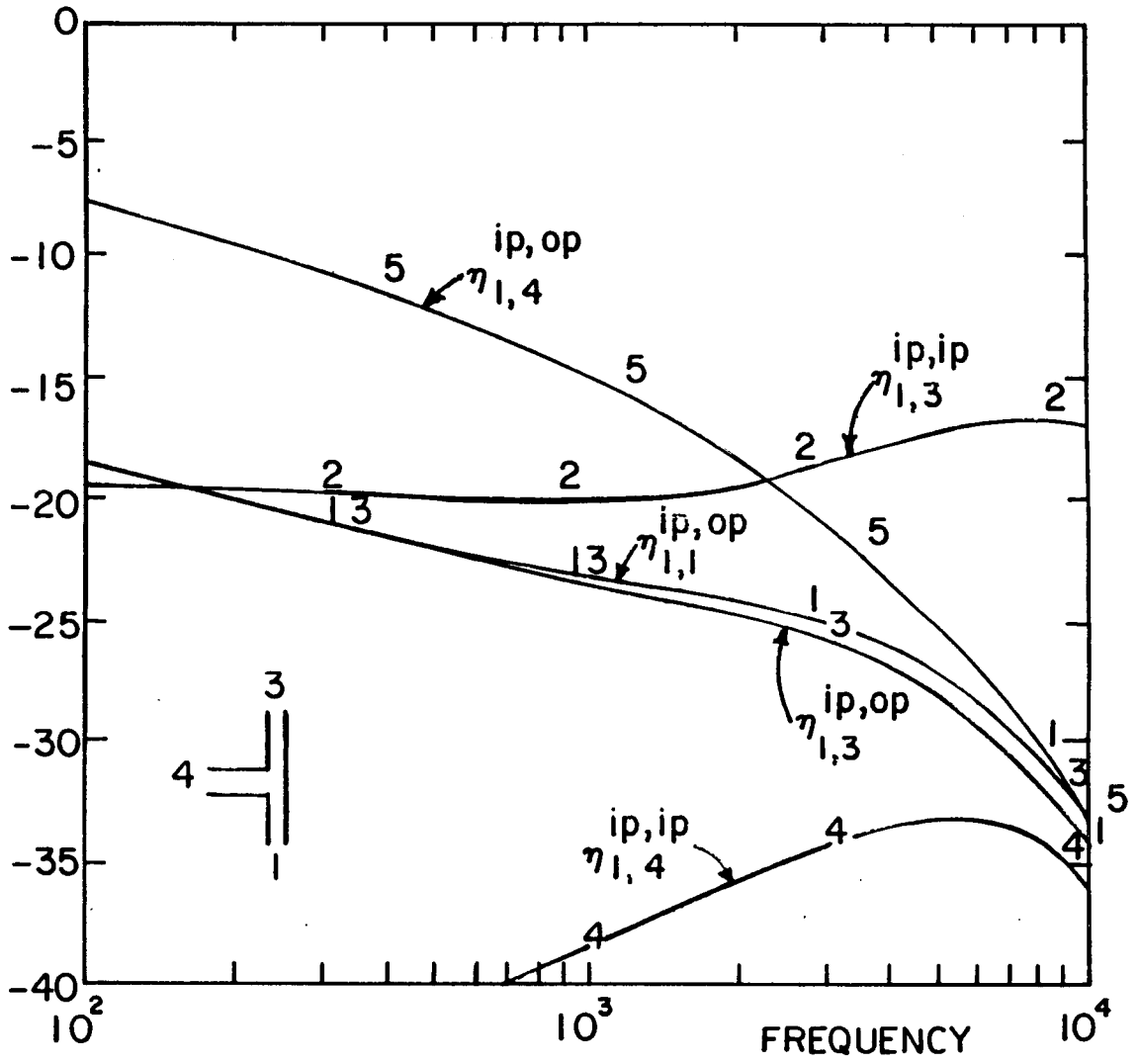

Figure F7. Coupling Loss Factors for a Three-Frame Junction

This may result in an enhanced transmission for out-of-plane motion in the overall SEA model of the S-76 airframe. The transmission of in-plane motion may rely more heavily on the coupling to out-of-plane transmission as opposed to direct transmission through in-plane motion.

Additional Coupling Loss Factor Evaluations

Direct coupling between panels across a frame. - A commonly occurring junction in the S-76 airframe is the connection between skin panels along the top of a frame section. In the SEA model this is a line junction where the connected subsystems include in-plane and out-of-plane motions for the frame and bending in the panels. The coupling loss factors between resonant motions in the frame and panels have preivously been described [1]. Resonant coupling is associated with a coincidence matching of panel trace wavelength along the junction with the wavelength for motion in the frame.

Incidence angles in the panel near normal result in the panel trace wavelength being larger than the frame wavelength and the frame responds non-resonantly where its motion is dependent on its mass reactance. Frame motion is either rotational for in-plane motion or translational, in the vertical direction, for out-of-plane bending. In the former the rotation axis is the line junction along the top of the frame where it connects to the skin panels, thus the appropriate inertial impedance determining the frame response is the moment of inertia about the line junction. For translational out-of-plane motion the response is governed by the mass per unit length of the frame.

Incident motion in one of the skin panels excites a non-resonant or mass law response of the frame and also radiation into the adjoining panel on the other side of the frame. This coupling between panels through non-resonant frame response constitutes a direct coupling between panels in that the non-resonant frame response is not otherwise described by an existing frame subsystem modal energy. The coupling of non-resonant frame motion to other frames at a frame junction is ignored in the current SEA model of the airframe.

The analytical description of the direct coupling proceeds from a representation of the transmission coefficient between panels across the frame:

$$\tau_{ij} = \frac{4\mathrm{Re}(Z_f^{p,i})\mathrm{Re}(Z_f^{p,j})}{|Z_f^{p,i} + Z_f^{p,j} + Z_f^{fr}|^2} \qquad \text{(F35)}$$

where τ_{ij}, is the energy transmission coefficient involving non-resonant translational motion of the frame, $Z_f^{p,i}$ is the line force impedance at the edge of the source panel for transverse motion and Z_f^{fr} is the mass law frame impedance, in this instance for out-of-plane translation. A similar expression occurs occurs for non-resonant in-plane rotation of the frame.

The panel impedances are given by the following expressions:

$$Z_f^p = \frac{B\ k_p^3}{2\omega}\ (1-i) \qquad \text{(force)} \qquad \text{(F36a)}$$

$$Z_m^p = \frac{B\ k_p}{\omega}\ (1+i) \qquad \text{(moment)} \qquad \text{(F36b)}$$

where k_p is the panel bending wave number, B is the panel bending rigidity. The expressions are for normal incidence relative to the line junction with the frame and relate transverse shear forces or moments per unit length along the junction to the transverse or rotational velocities of the junction, respectively. For the frame the mass law impedances are given by:

$$Z_f^{fr} = -i\omega m_{fr} \qquad \text{(F37a)}$$

$$Z_m^{fr} = -i\omega\rho I^a \qquad \text{(F37b)}$$

where I^a is the cross-sectional area moment of inertia of the frame about the line junction along the top of the frame where the panels are attached:

$$I^a = I_p + \frac{Ah}{2} \qquad \text{(F38)}$$

The transmission coefficient is dependent on the angle of incidence on the junction of the bending wave energy in the source panel. The expression given is for normal incidence only. The averaging over angle of incidence has been accounted for by DeJong [2] based on an adaptation of work by Swift [3] in relating the normal incidence transmission coefficient to the coupling loss factor:

$$\eta_{ij}(\omega) = \frac{I_{ij}\ \tau_{ij} L_{fr}^{J}}{\pi\ \omega\ n_i(\omega)\ (2 - \tau_{ij})} \tag{F39}$$

where I_{ij}, is the factor accounting for the averaging, given by:

$$I_{ij} = \frac{k_i k_j}{4} \left[\frac{1}{k_i^4 + k_j^4}\right]^{\frac{1}{4}} \tag{F40}$$

and $n_i(\omega)$ is the mode density of the source panel, and k_i, k_j are the bending wave numbers in the source and receiving panels.

Coupling between frames and acoustic spaces. - Overhead framing in the S-76 cabin is of deep web construction in order to efficiently support the mechanical loads of the airframe while minimizing weight penalties. A typical frame is 0.2 m deep with a representative spacing between adjacent longitudinal and/or cross frames of 0.85 m. The total frame surface area in the cabin overhead that radiates into the cabin is comparable to the panel surface area and must therefore be accounted for in the power flow into the cabin due to radiation from vibrating surfaces.

The conventional expressions for predicting the acoustic power radiated by a vibrating panel are based on analyses of finite simply supported panels vibrating in the plane of a rigid baffle. The lower edge of the frame web for transverse motion can be considered to be unbaffled. Depending on relative wavelengths of the panel motion compared with those of sound in air, the radiation potential of an unbaffled edge can be greatly reduced over the baffled case.

Transverse motion of the frame web is associated with the composite in-plane frame motion in the SEA model. Out-of-plane bending of the frame results in an in-plane motion of the web which is not coupled to the cabin acoustic space. The lower flange of the frame, which is approximately 0.05 m wide, is coupled to the cabin acoustic space for out-of-plane bending but not for the composite in-plane motion. Transverse motion of the lower flange is unbaffled on both edges.

Analytical representation of the coupling to an acoustic space for unbaffled motion of either the frame web or lower flange is based on a derivation by Blake [4] of the radiation from unbaffled vibrating strips or beams. No variation of motion is allowed across the width of the strip. The relevant results from Blake for the present application are the following:

$$\frac{R_r}{L} = 2\rho_o c_o \, h \, \frac{\pi}{192} \, (k_o h)^2 \, \left(\frac{h}{L}\right) \, \left(\frac{k_o}{k_{fr}}\right)^2 \qquad \text{for } k_o < k_{fr} \tag{F41}$$

and

$$\frac{R_r}{L} = 2\rho_o c_o h \qquad \text{for } k_o \geq k_{fr} \tag{F42}$$

where R_r, the radiation resistance of the strip, relates the space average motion of the strip to the radiated power:

$$\Pi_{rad} = R_r < V_f^2 > \tag{F43}$$

and L and h are the length and height of the frame, respectively, while k_o and k_{fr} are the acoustic and frame wavenumbers, respectively where k_{fr} depends on the particular type of frame motion, and $\rho_o c_o$ is the characteristic impedance of sound in air. The factor of 2 in front of the expression takes into account the total radiation, since both sides of the frame surface couple to the acoustic space.

Frequency dependence in Equation (F41) is through the quantities k_o and k_{fr} and the frequency dependence of the phase speed of the particular frame motion type from which k_{fr} is obtained. Simple bending deformation of the frame results in k_{fr} proportional to $\sqrt{f}$ and the value of R_r increases proportional to f. Actual frame motion types are more complicated including transverse shear for out-of-plane bending and transverse shear and torsional deformation for the composite in-plane motion. Both cases result in phase speeds which tend to increase with frequency at a rate slower than proportional to f and therefore R_r will also

increase with frequency. The coupling loss factor, $\eta_{fr,a}$, between frame motion and the cabin acoustic space is given in terms of the radiation resistance by:

$$\eta_{fr,a} = \frac{R_r}{\omega C_m} \tag{F44}$$

where

$$C_m = m_{fr} \tag{F45}$$

is the total mass of the frame for out-of-plane bending, and

$$C_m = I^a L \tag{F46}$$

is the total (rotational) inertia of the frame about an axis at the elevation where the panel joins with the frame for the composite in-plane motion.

Modified Description of the Perimeter Member

The perimeter member refers to the lightweight channel structure at the seam between overhead and side wall skin panels. Its cross-section is open as shown in Figure F8. Originally modeled as a frame member, it contributed in an unrealistically significant manner to the vibration transmission from the gearbox attachment locations forward to the front windshields.

This can be seen from the power flow description given in Table F1 in which the perimeter member is modeled as a frame. The dominant contribution to the power flow into the windshield comes from the perimeter frame member at the seam between the windshield and composite overhead panel above the pilot/co-pilot locations. Traced back towards the gearbox the path is along the perimeter frame with important contributions from cross frames.

The predicted distribution of frame and panel response levels from the S-76 SEA model with the original perimeter frame representation are shown in Figures F9 and F10 along with measured levels from the ground test program. Overhead panel levels forward in the cabin are consistently overpredicted. Based on this discrepancy in comparing panel levels forward in the cabin, a revised description was developed to more realistically represent the transmission through the perimeter members.

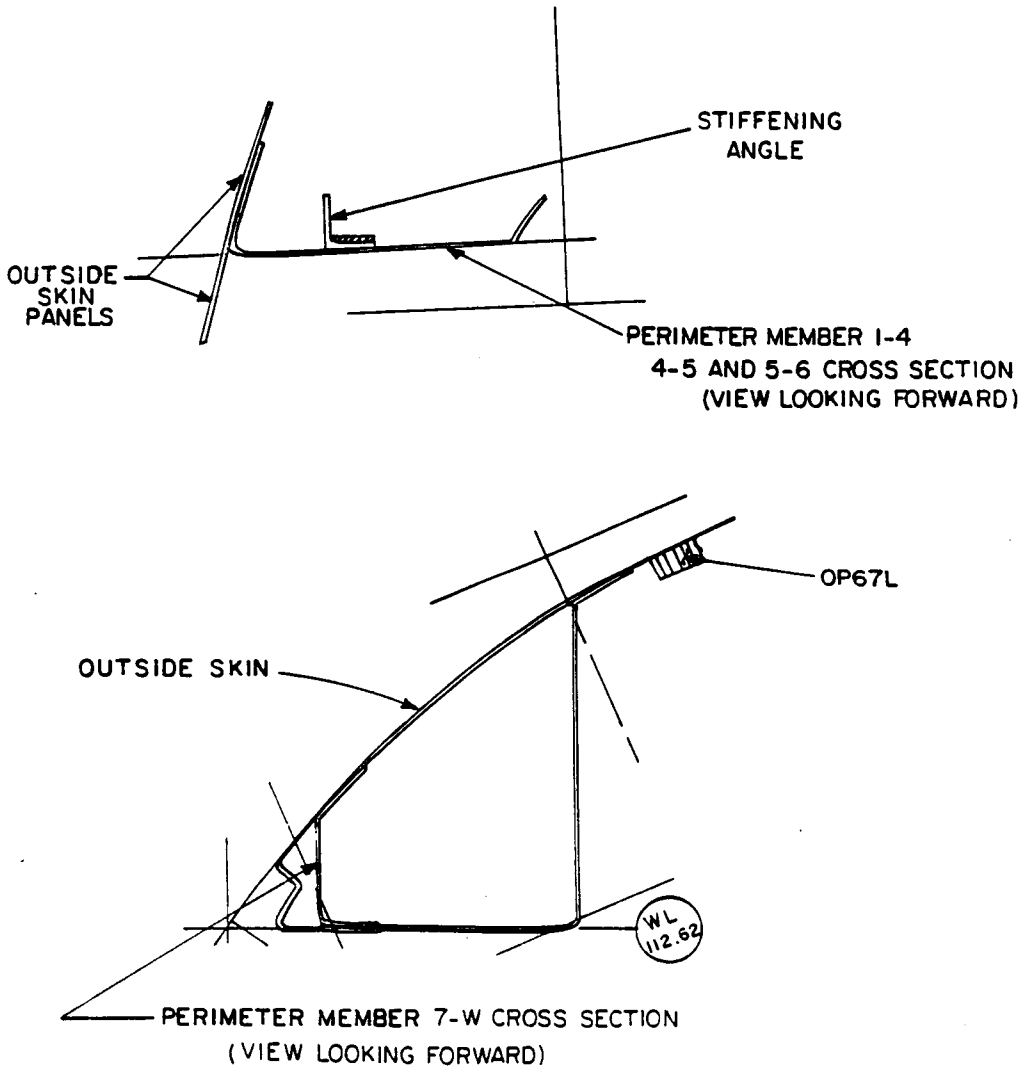

Figure F8. Perimeter Member Cross-Sectional Geometry

In that the perimeter member is of an open, lightweight, sheet metal construction that is riveted to the seam between overhead and side wall skin panels along a common tab (see Figure F8), it was decided to model it as a panel subsystem instead of a frame. The junction now involves connections between three panel subsystems, overhead and side wall skin panels and the panel subsystem characterizing the perimeter structure. The skin panels are of a composite honeycomb construction that are significantly stiffer than the perimeter structure when modeled as a panel.

Comparisons with the revised SEA prediction are shown in Figures E1 and E3 with the revised power flow description given in Table F2. Now the perimeter, when modeled as a panel, does not contribute at all to the power flow into the forward panels and windshields and a more consistent comparison between data and predictions is achieved for both overhead frames and panels. The predictions also reflect an increase in panel damping values in the SEA model that are consistent to a greater extent with the in-situ measured loss factors of panel sections within the airframe.

Table F1. Power Flow Description When the Perimeter Member is Modeled as a Frame

Left Front Windshield (FWL)	% of Total Power Inflow
Power Inflow From:	(1 kHz Octave Band)
Perimeter Frame (PF7WL)	93.0
Main Longitudinal Frame (LF67L)	3.2
Overhead Panel (OP67L)	2.4

Perimeter Frame (PF7WL)	
Power Inflow From:	
Perimeter Frame (PF56L)	46.6
Cross Frame (CF6M)	32.2

Perimeter Frame (PF56L)	
Power Inflow From:	
Perimeter Frame (PF45L)	77.6
Cross Frame (CF5L)	22.0

Conclusion:

Transmission along the outer perimeter frame of the cabin overhead is an important path leading to the windshield.

Perimeter Frame - Lightweight box construction
Modeled as frame in bending

Potential Refinement: Allow plate like deformation of side walls

Softer - Lower impedance propagation behavior

Table F2. Power Flow Description When the Perimeter Member is Modeled as a Panel

Front Windshield (FWL)	% of Total Power Inflow
Power Inflow From:	(1 kHz Octave Band)
Overhead Panel (OP67L)	50.5
Overhead Panel (OP67M)	39.0
Cabin Acoustic Space (CA)	10.5
Overhead Panel (OP67L)	
Power Inflow From:	
Main Longitudinal Frame (LF67L)	54.0
Cross Frame (CF6L)	22.5
Overhead Panel (OP56L)	15.5
Main Longitudinal Frame (LF67L)	
Power Inflow From:	
Main Longitudinal Frame (LF56L)	68.5
Cross Frame (CF6M)	13.5
Cross Frame (CF6L)	10.0
Main Longitudinal Frame (LF56L)	
Power Inflow From:	
Main Longitudinal Frame (LF45L)	100.0
Main Longitudinal Frame (LF45L)	
Power Inflow From:	
Main Longituidnal Frame (LF14L)	98.5
Cross Frame (CF4L)	1.3
Cross Frame (CF4M)	0.1

Photo P1. Sikorsky S-76

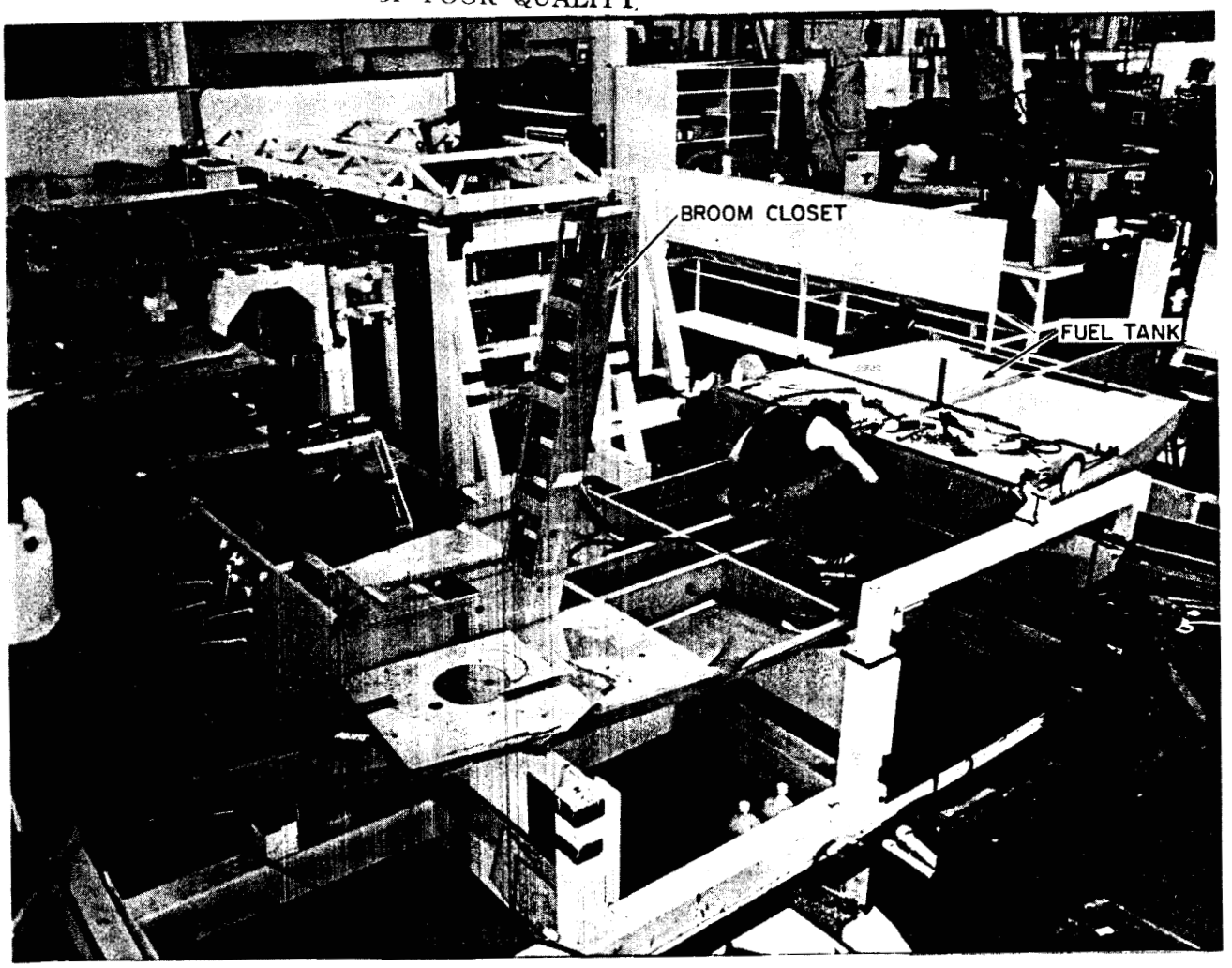

Photo P2. S-76 Lower Airframe During Assembly.

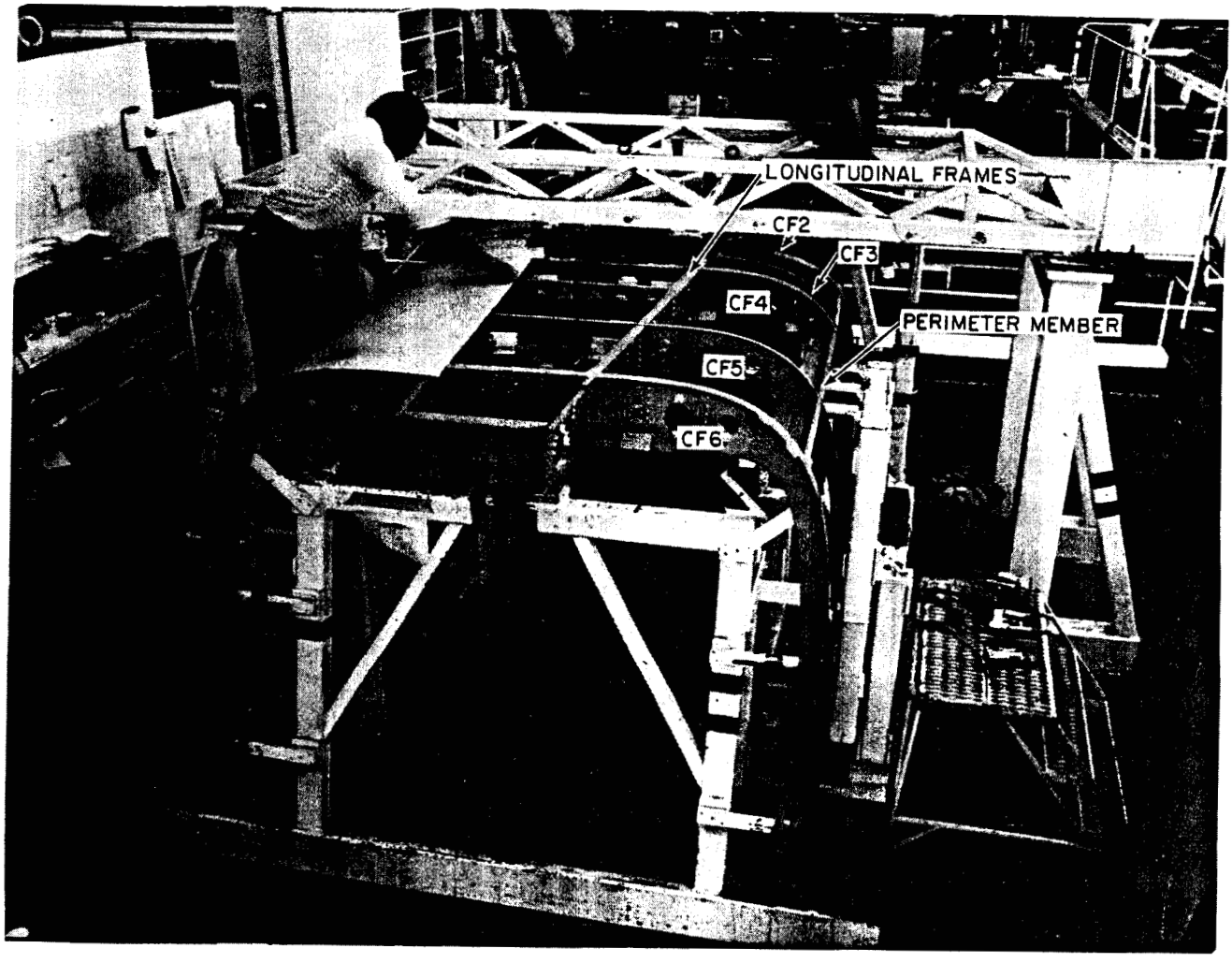

Photo P3. S-76 Upper Airframe (Cabin Section) During Assembly.

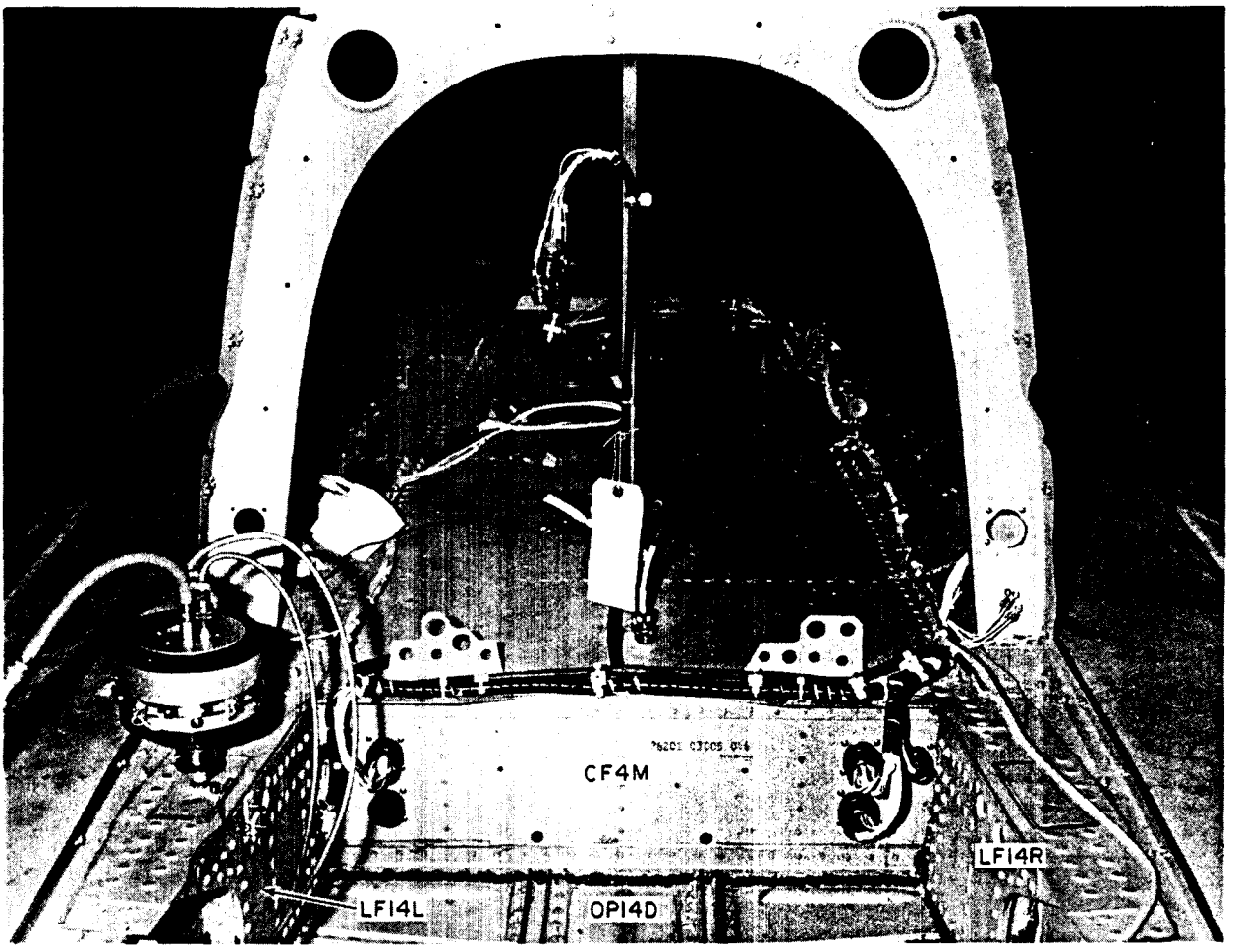

Photo P4. Aircraft Upper Deck (Forward) and Shaker Location.

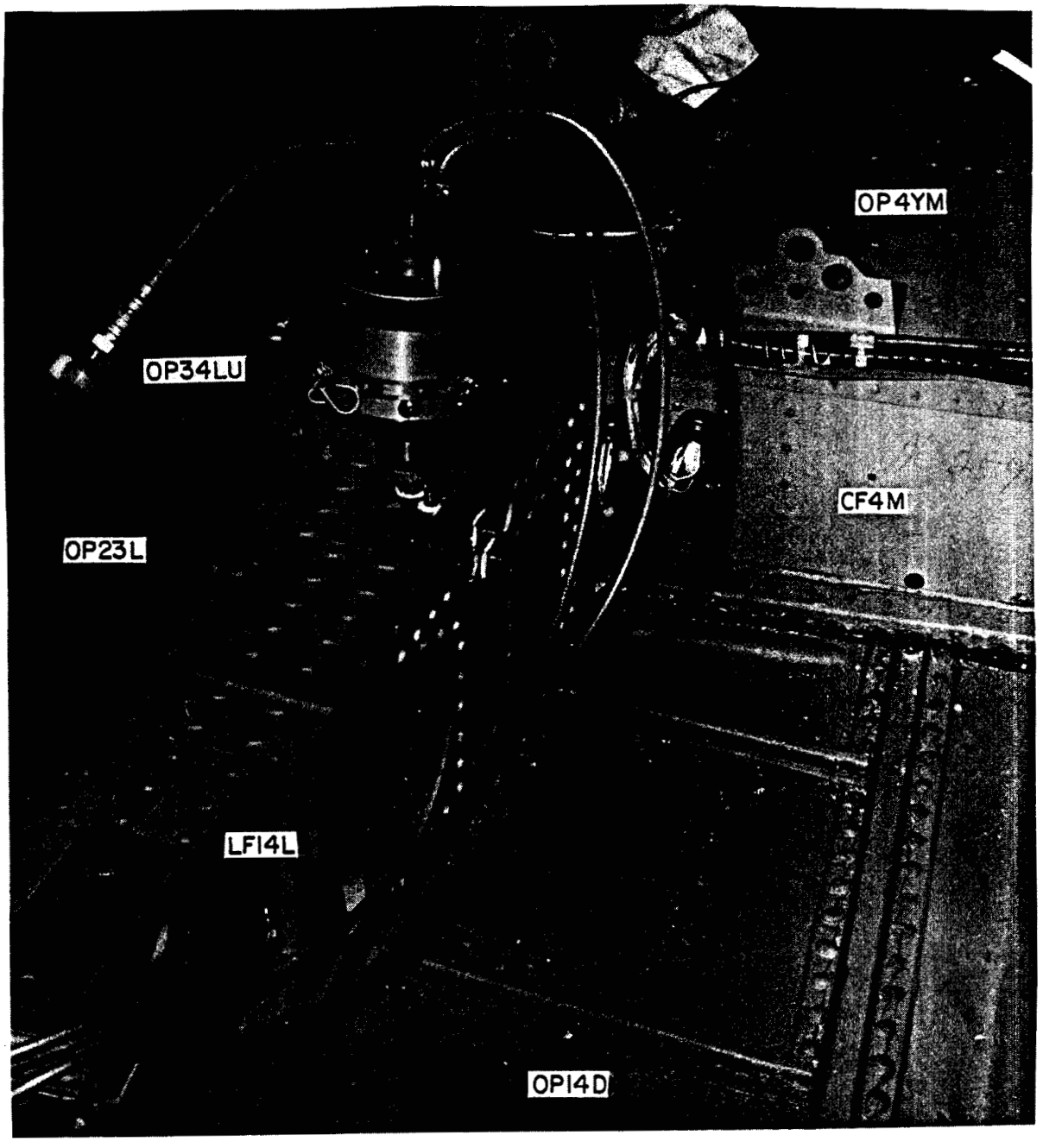

Photo P5. Airframe Shaker Attachment, Vertical and Lateral.

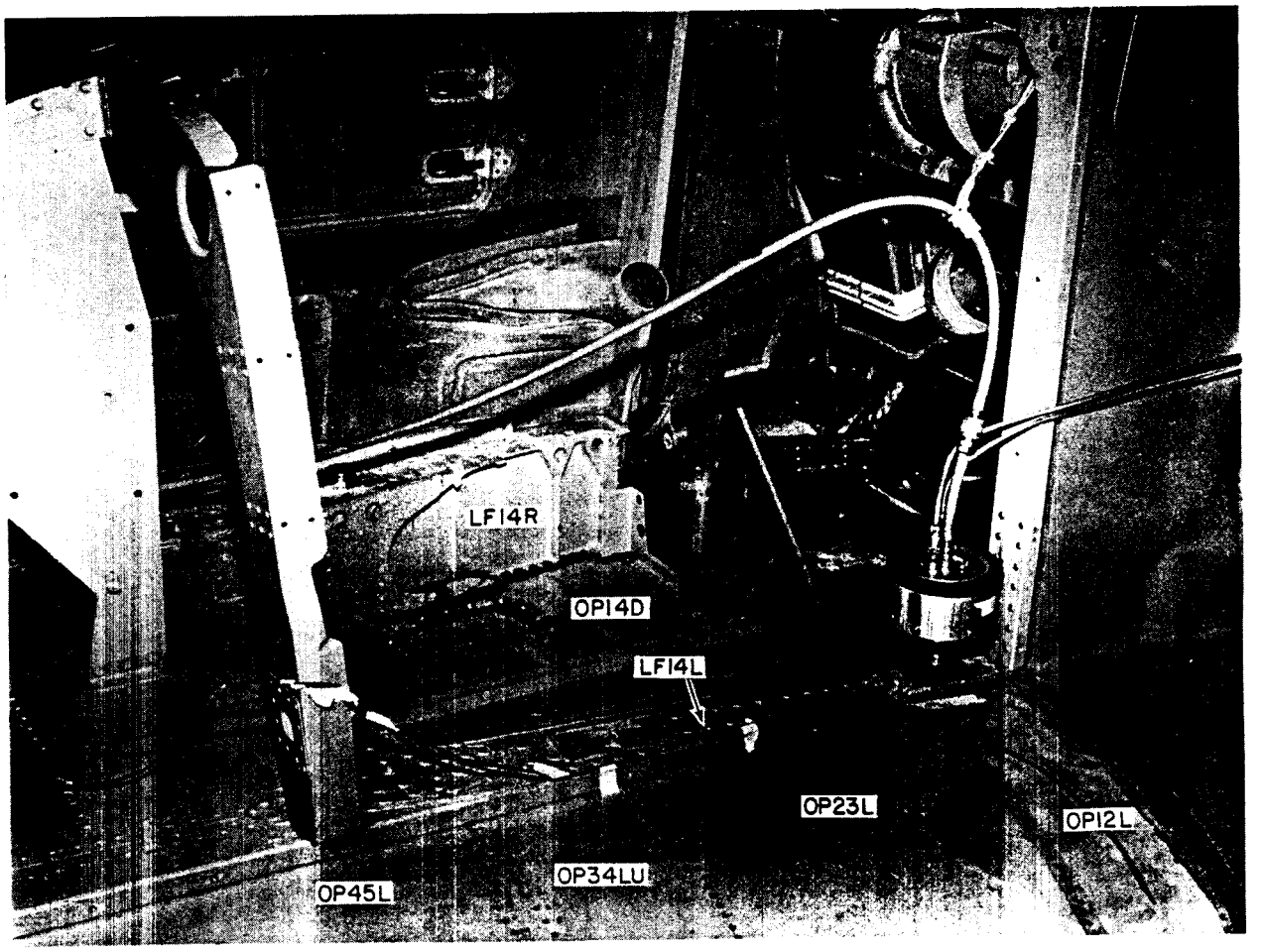

Photo P6. Aircraft Upper Deck (Aft) Turbine Inlet Area.

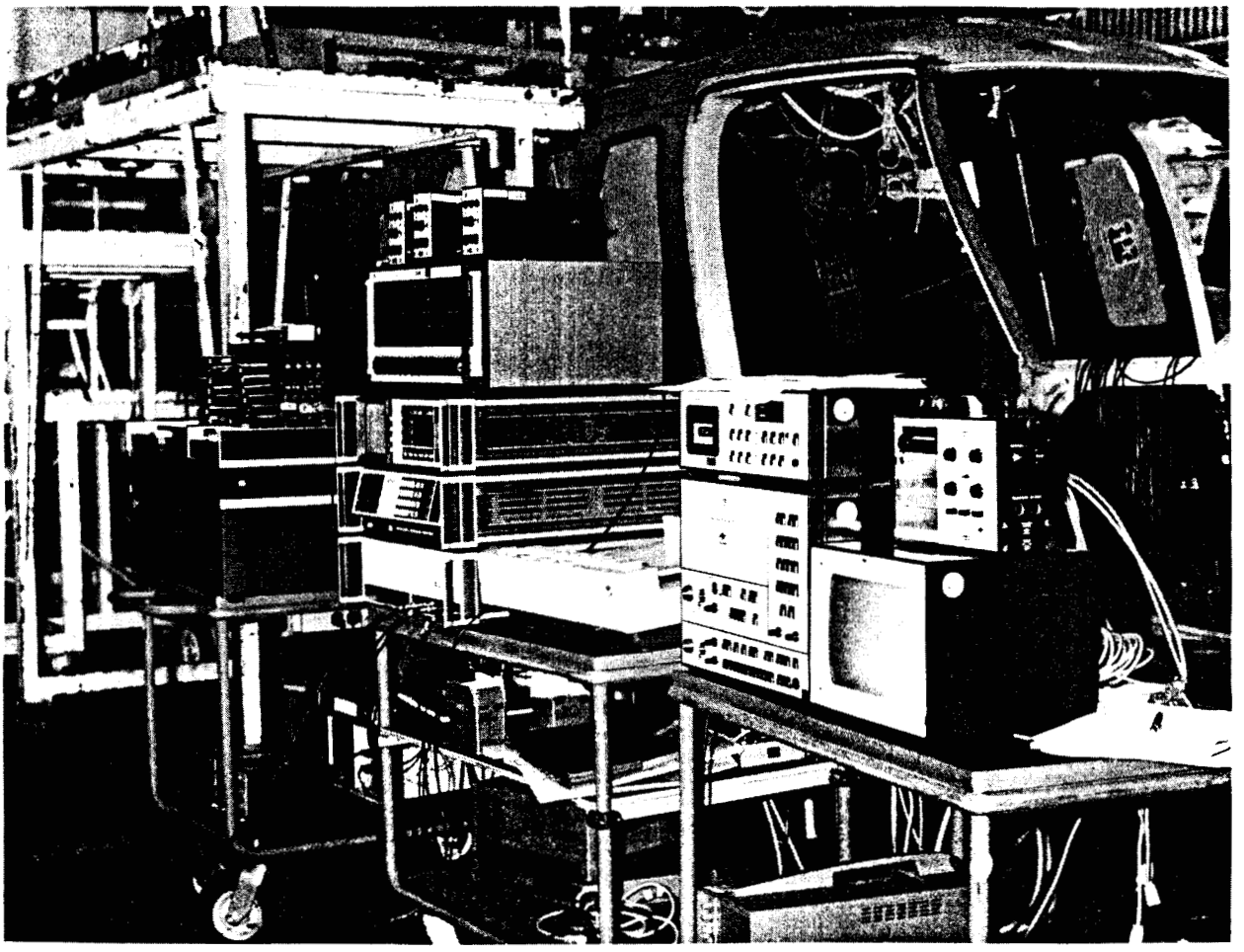

Photo P7. Instrumentation for Ground Test Measurements.

Photo P8. Coherent Sources Test Measurement Instrumentation.

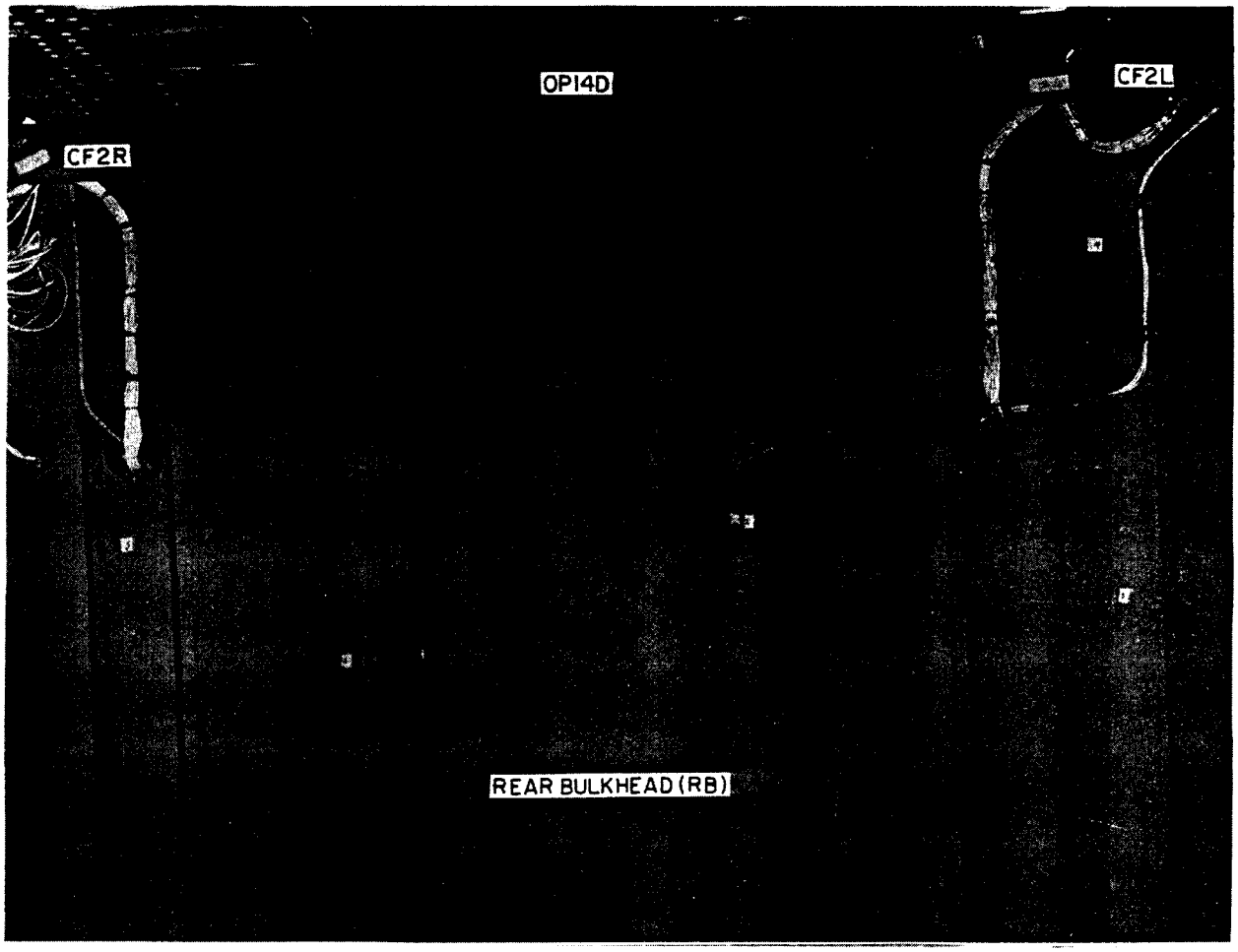

Photo P9. Rear Bulkhead (Aft Cabin).

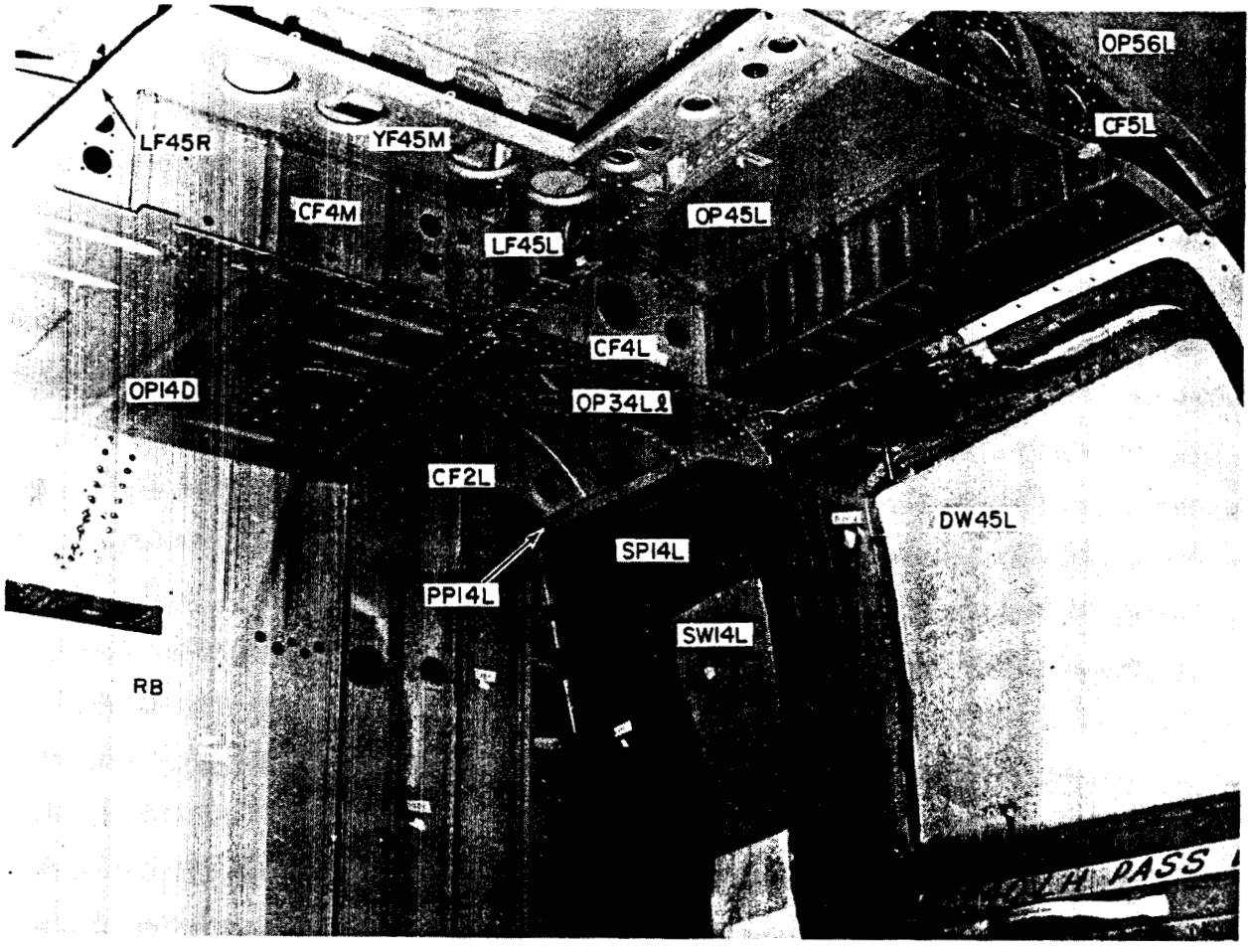

Photo P10. Aft Cabin, Left and Overhead Structure.

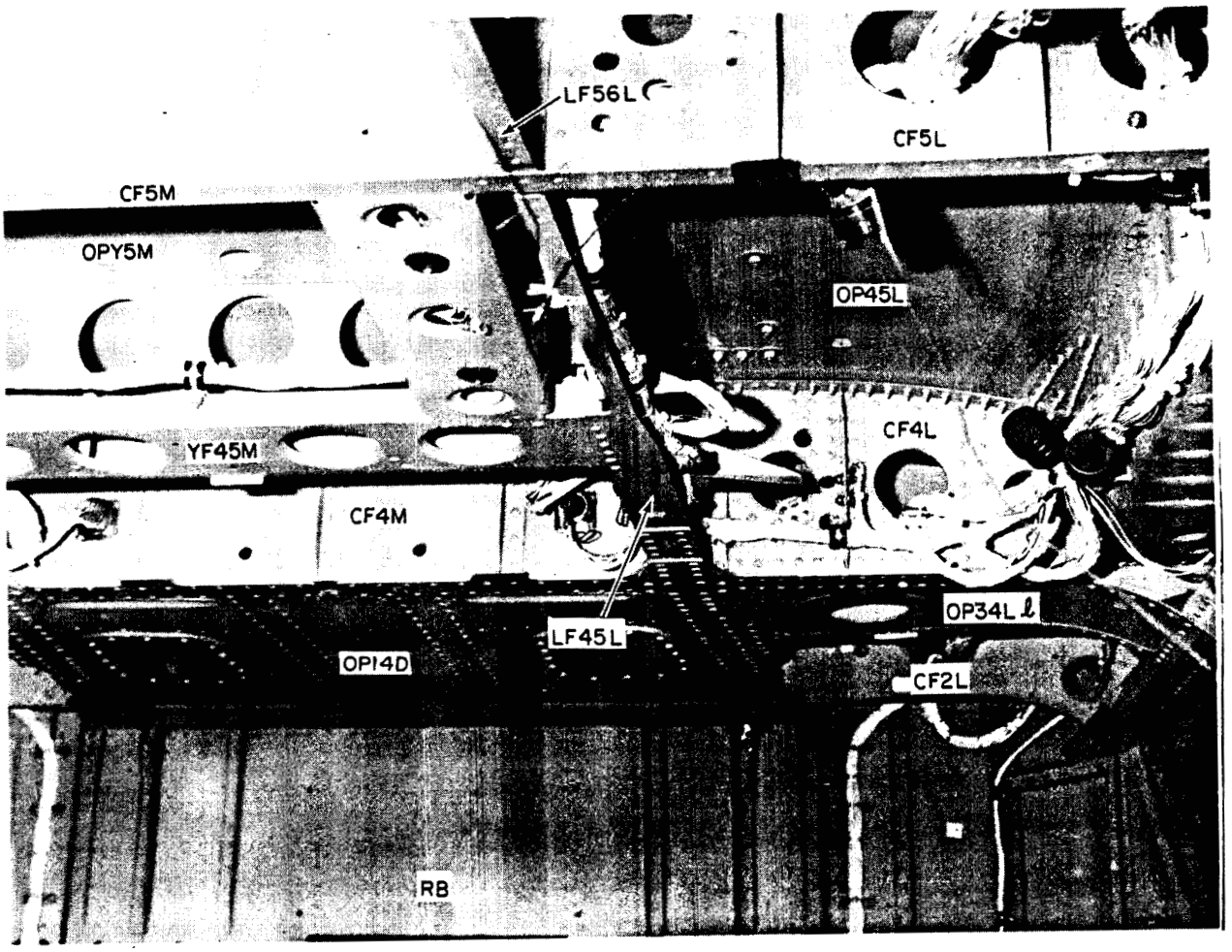

Photo P11. Aft Cabin, Middle, and Left Overhead Structure

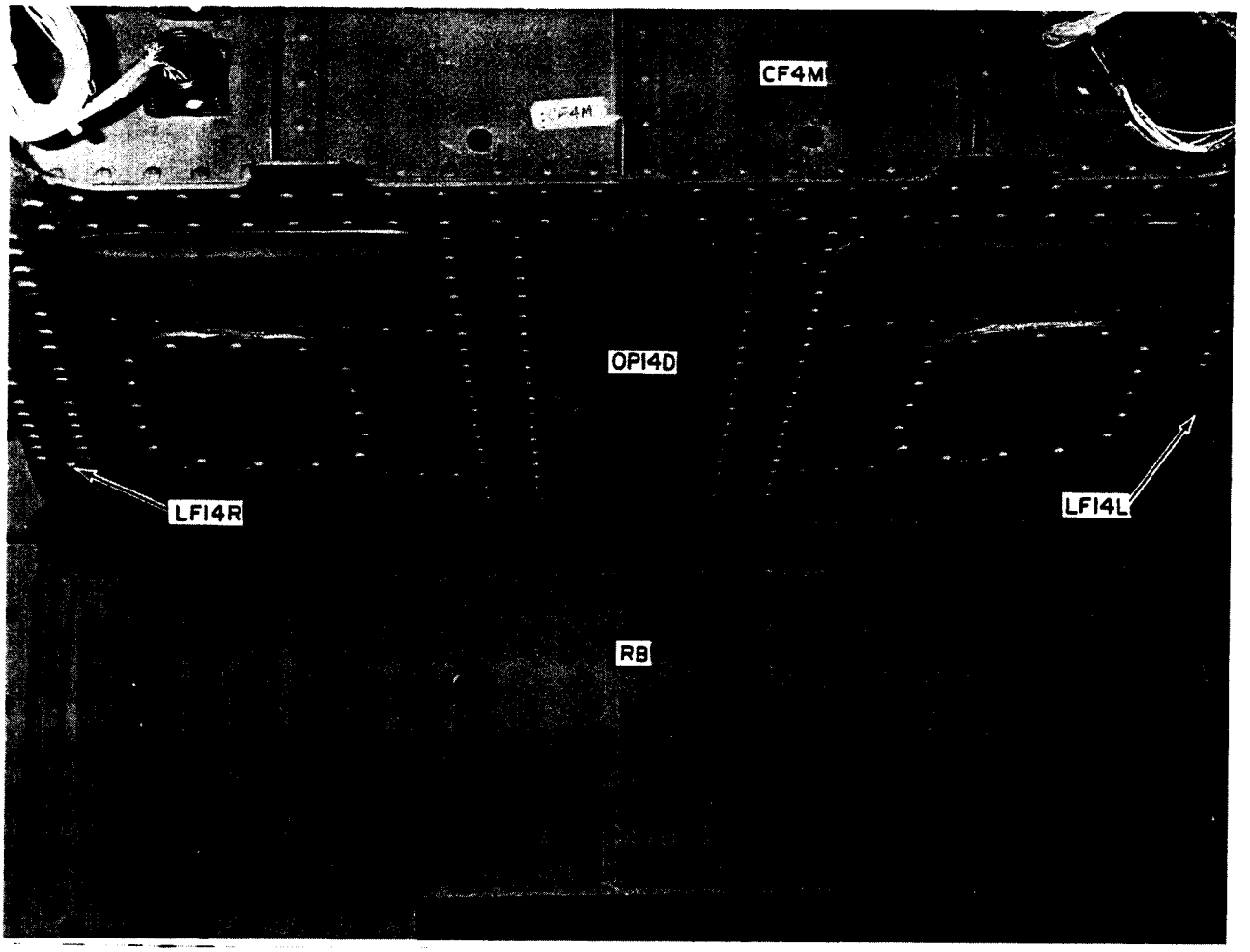

Photo P12. Drip Pan, Rear Bulkhead.

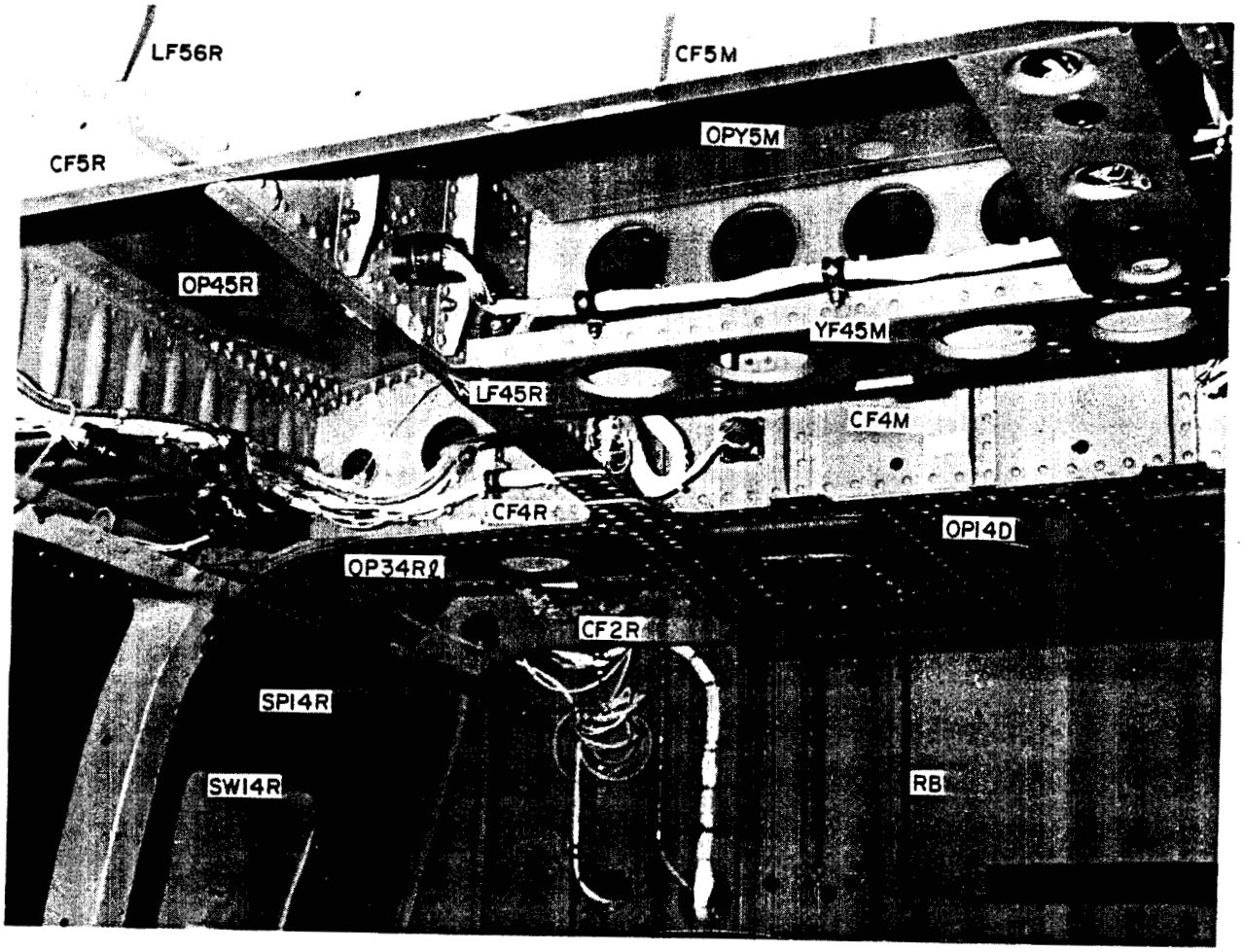

Photo P13. Aft Cabin, Right Side, and Middle Overhead Structure

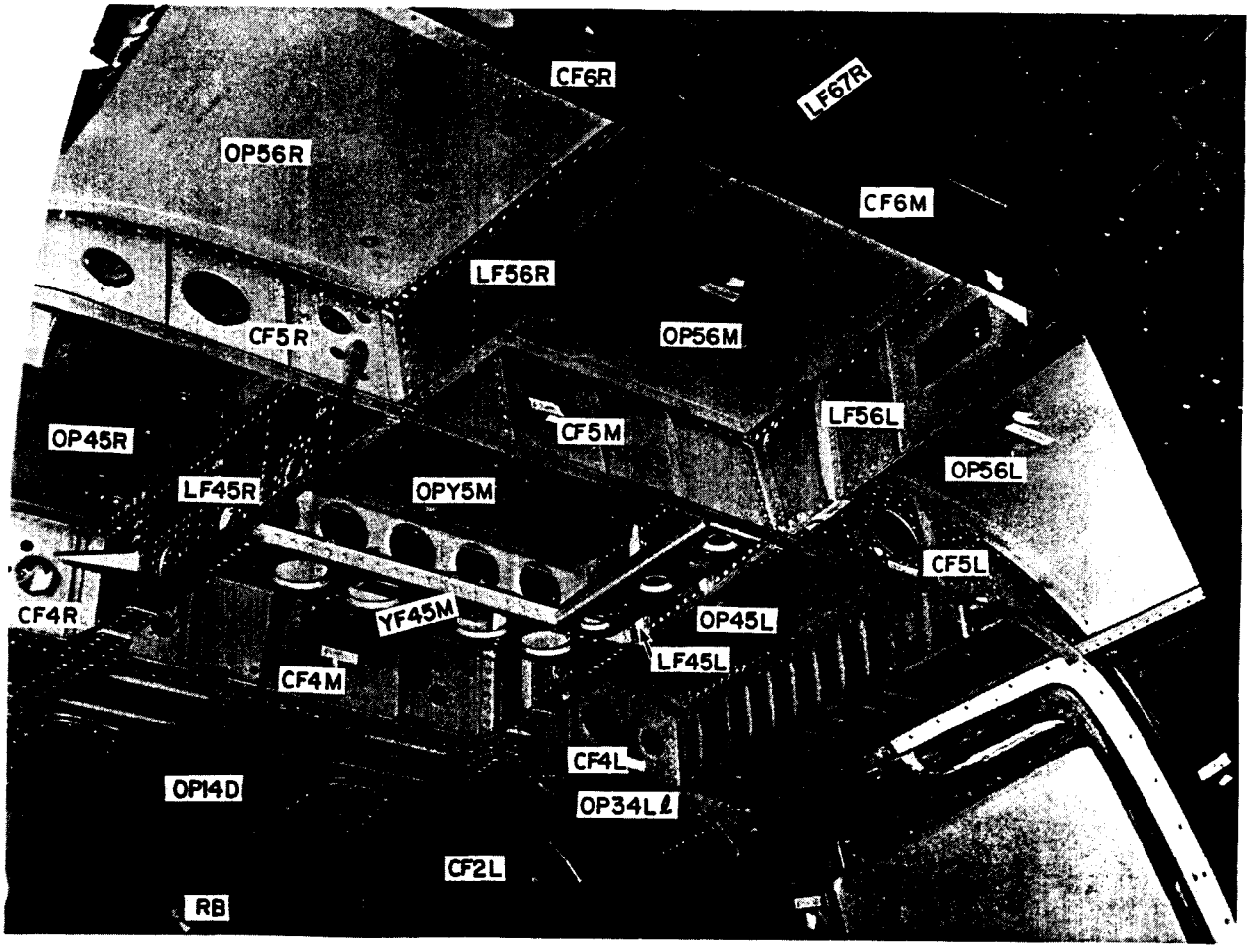

Photo P14. Cabin Overhead Structure.

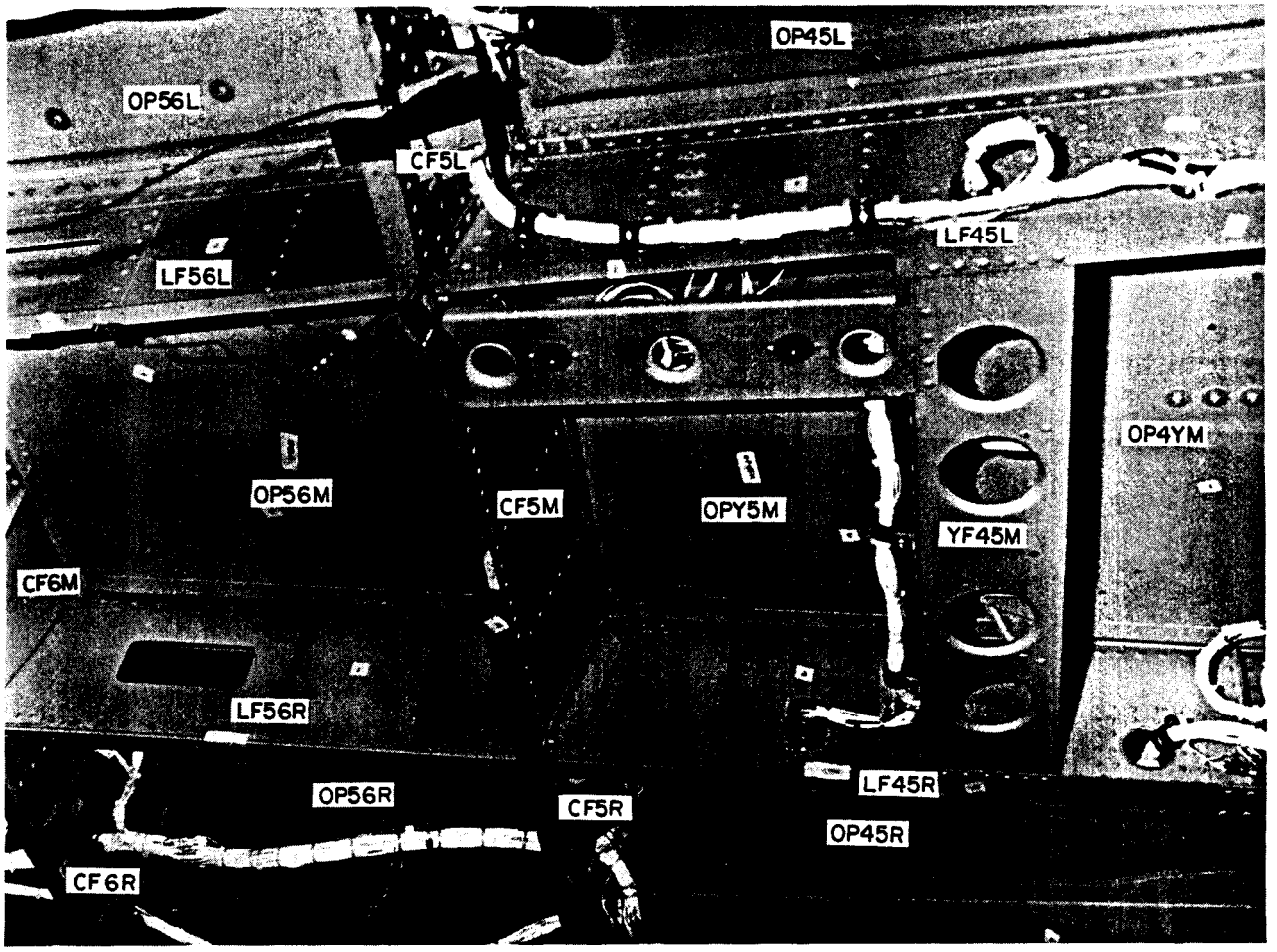

Photo P15. Middle Cabin Overhead Main Longitudinal Frames and Panels.

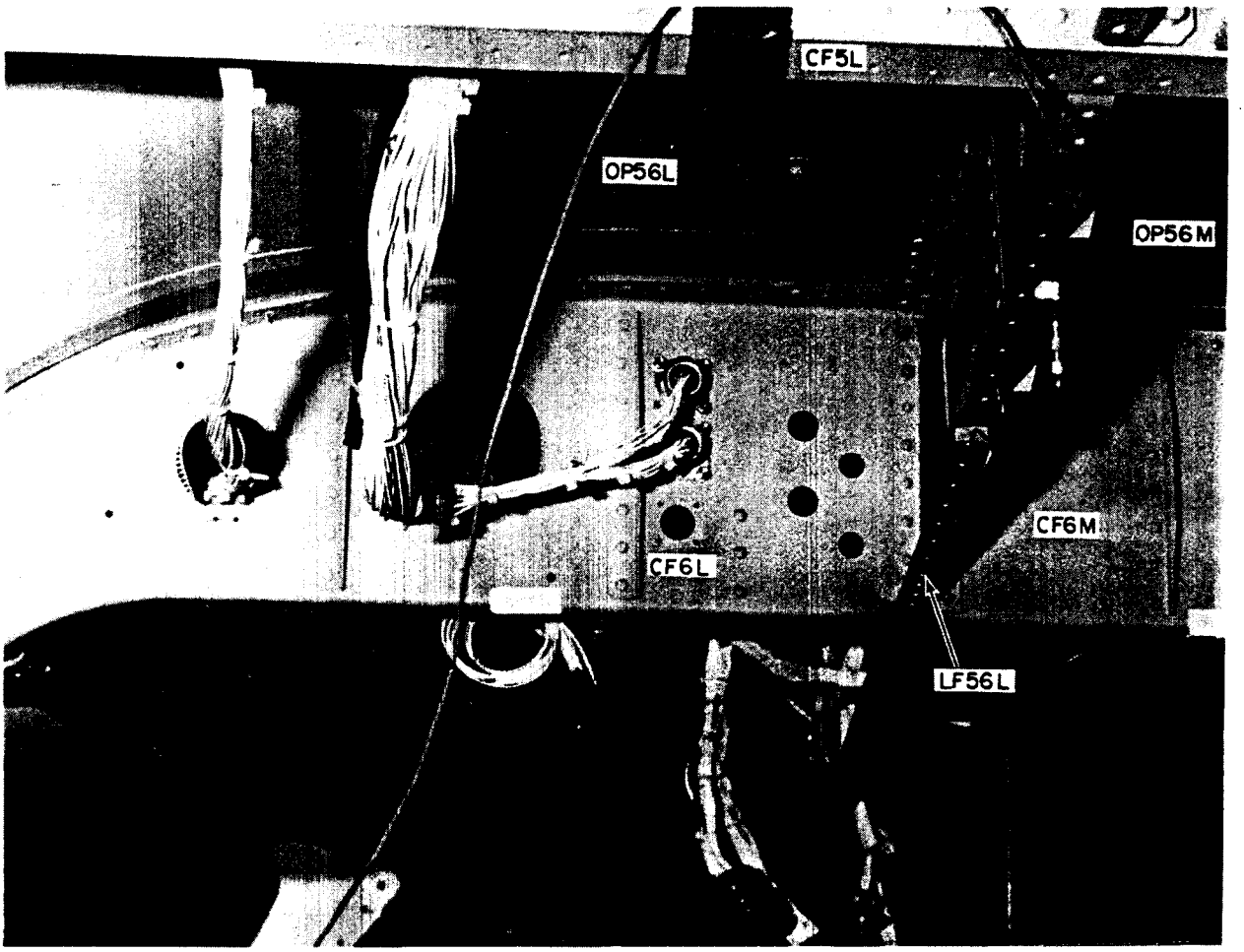

Photo P16. Cross Frame 6 and Cockpit Overhead, Left Side.

Photo P17. Broom Closet, Cockpit Area.

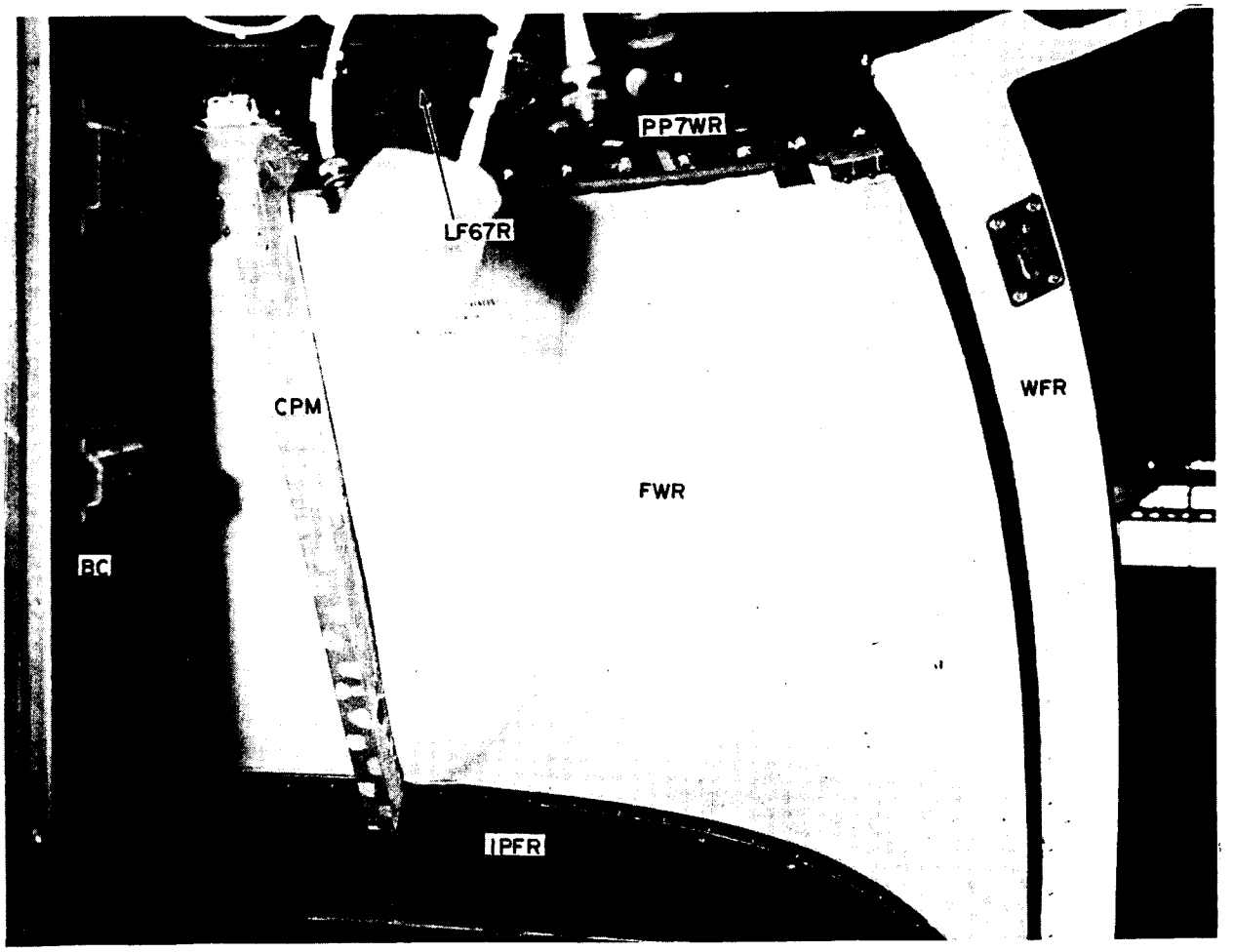

Photo P18. Front Right Windshield and Center Post.

Photo P19. Middle Cabin, Left Side Panel and Passenger Door

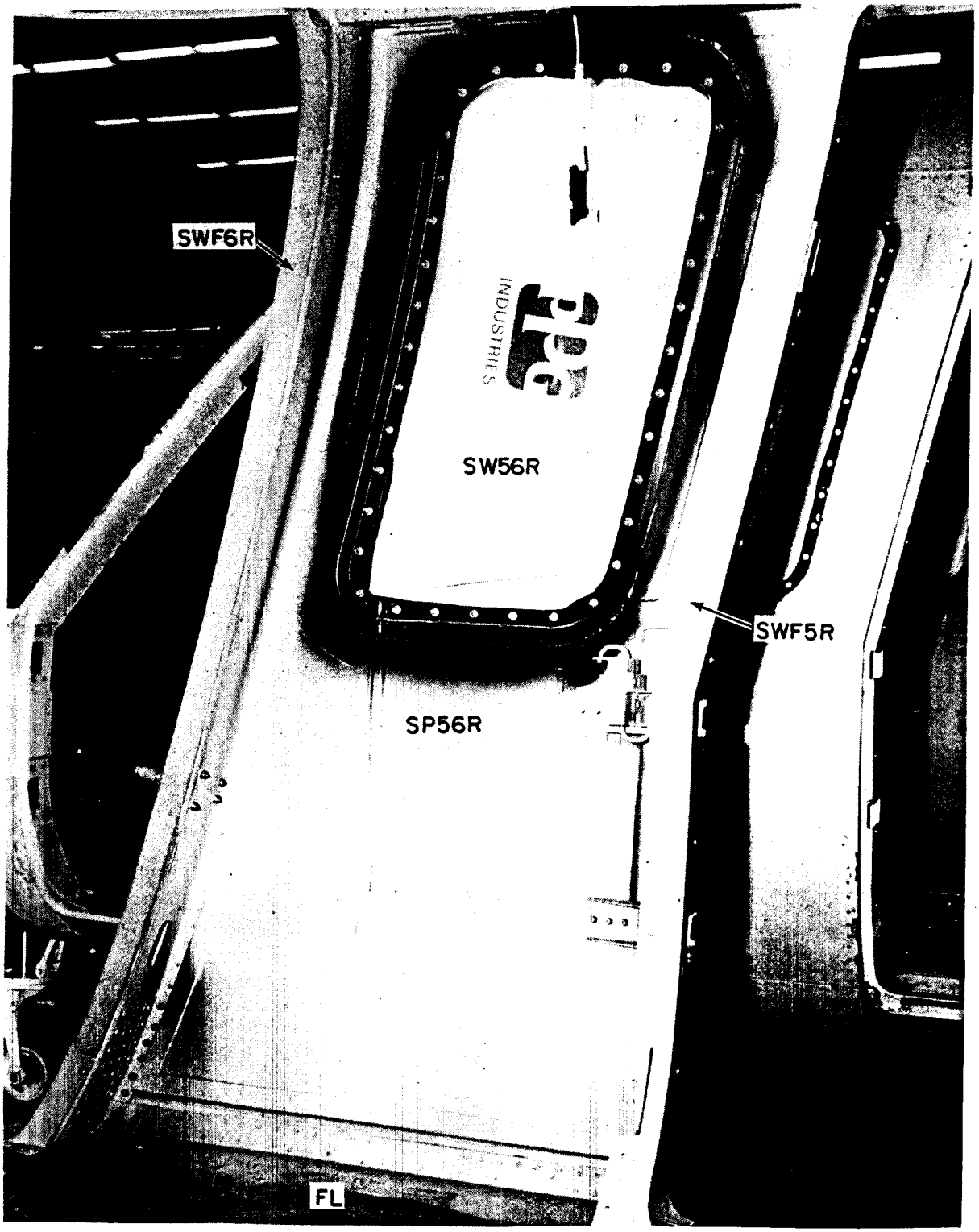

Photo P20. Middle Cabin Right Side Panel.

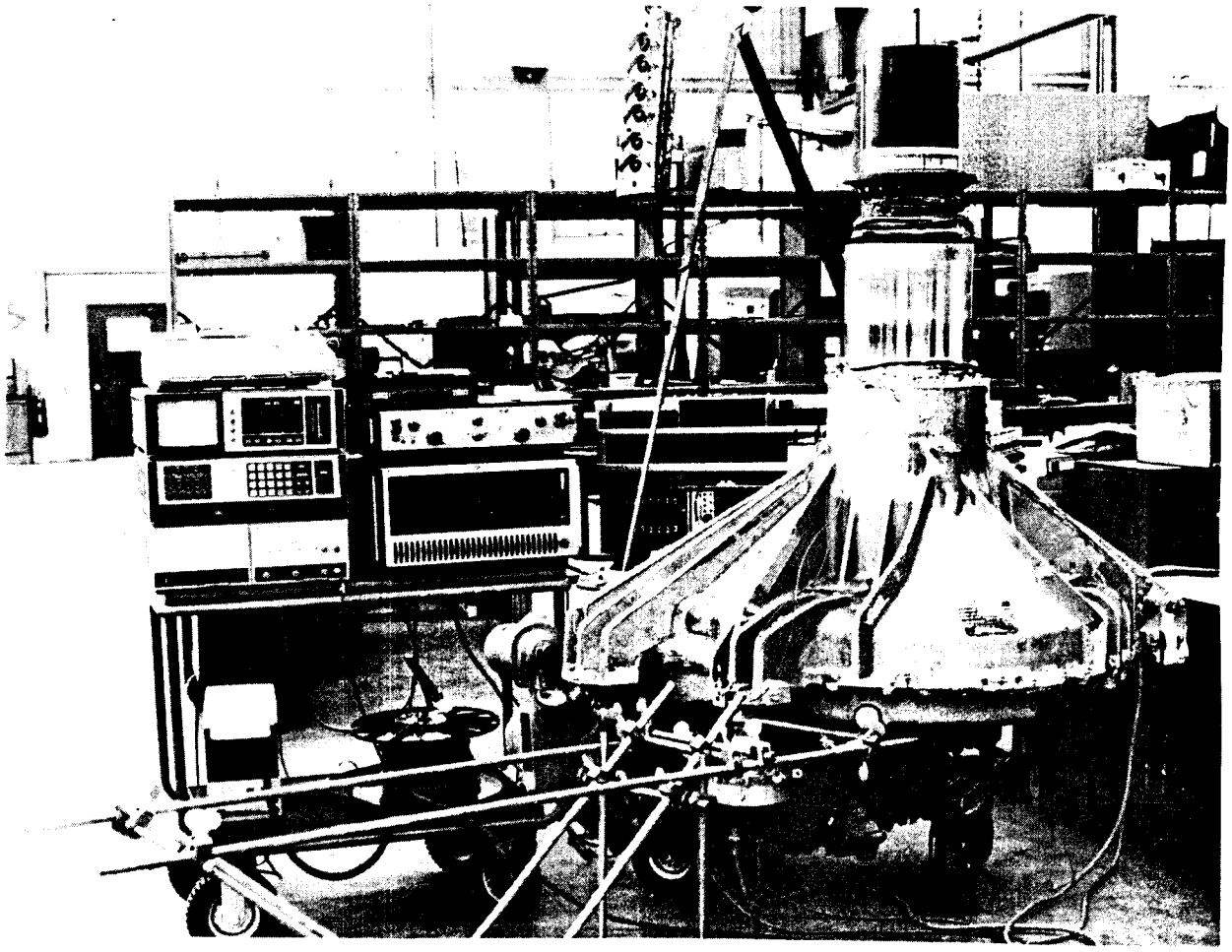

Photo P21. S-76 Main Transmission Gearbox Attachment Point Compliance Measurement Test Setup and Instrumentation.

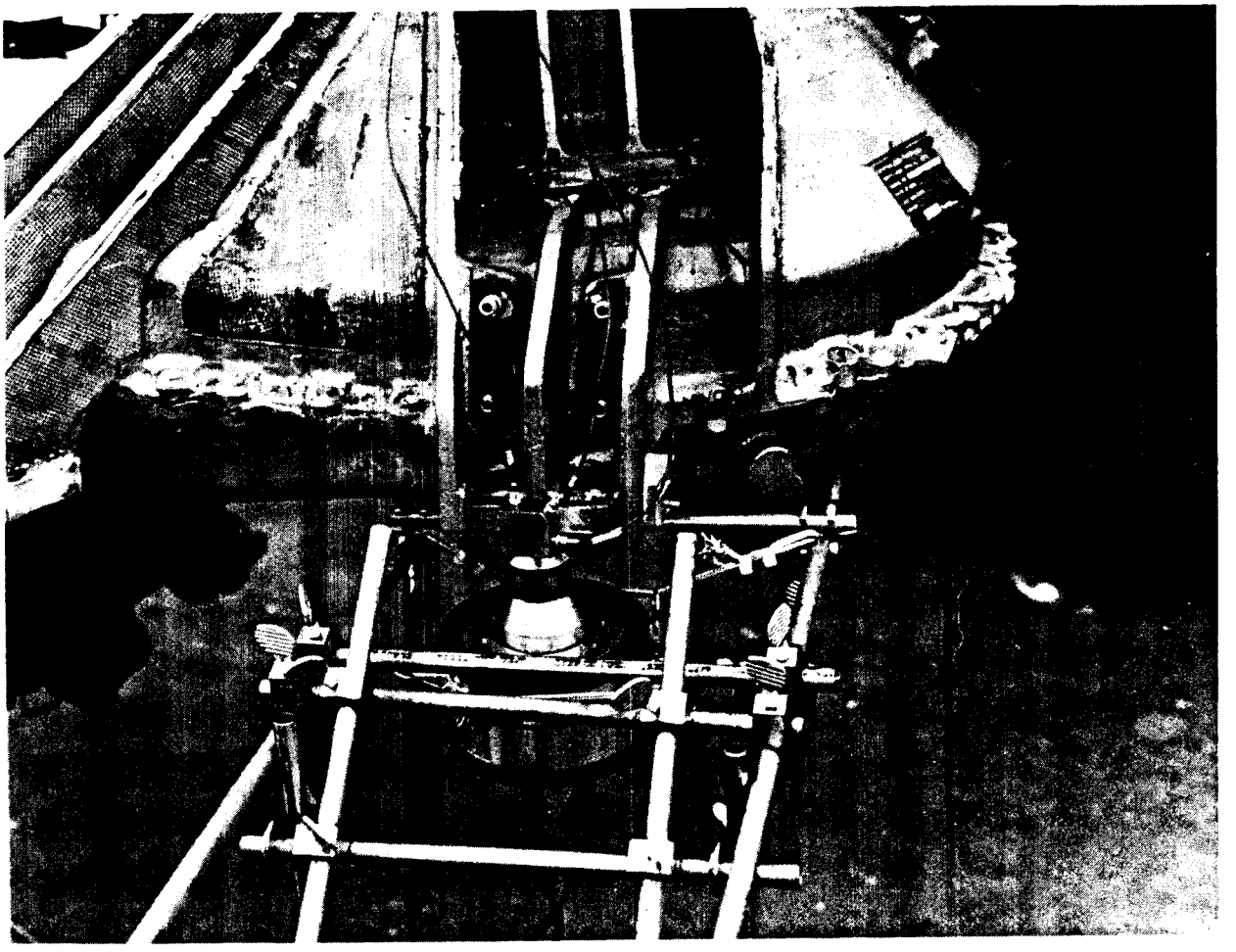

Photo P22. FAR Vertical Shaker and Triaxial Accelerometer Location for S-76 Gearbox Compliance Measurements.

Photo P23. In-flight Measurement Testing.

Photo P24. Typical S-76 Utility Interior Configuration

Photo P25. Typical S-76 Executive (VIP) Interior Configuration

REFERENCES

1. Yoerkie, C.A.; Moore, J.A.; and Manning, J.E.: Development of Rotorcraft Interior Noise Control Concepts - Phase I: Definition Study. NASA CR-166101, May 1983.

2. DeJong, R.D.: A Study of Pump and Piping Generated Ship Noise Using Statistical Energy Analysis. Cambridge Collaborative, Inc., Report to DTNSRDC, Annapolis, MD. Contract No. 00600-77-R-1417, 15 May 1978.

3. Swift, P.B.: The Vibrational Energy Transmission Through Connected Structures. Ph.D. Thesis, The University of Adelaide, Australia, May 1977.

4. Blake, W.K.: The Radiation from Free-Free Beams in Air and in Water. Journal of Sound and Vibration, Vol. 33, No. 4, 1974, pp. 427-450.

1. Report No.	2. Government Accession No.	3. Recipient's Catalog No.
NASA CR-172594		

4. Title and Subtitle	5. Report Date
DEVELOPMENT OF ROTORCRAFT INTERIOR NOISE CONTROL CONCEPTS, PHASE II: FULL SCALE TESTING	February 1986
	6. Performing Organization Code
7. Author(s)	8. Performing Organization Report No.
C.A. Yoerkie, P.J. Gintoli, and J.A. Moore	SER 760703
	10. Work Unit No.
9. Performing Organization Name and Address Sikorsky Aircraft Division United Technologies Corporation Stratford, CT 06601	11. Contract or Grant No. NASA1-16932
	13. Type of Report and Period Covered Contractor Report May 1983-December 1985
12. Sponsoring Agency Name and Address National Aeronautics and Space Administration Langley Research Center Hampton, VA 23665	14. Sponsoring Agency Code

15. Supplementary Notes

LaRC Technical Representative: William H. Mayes

16. Abstract The Phase II effort consisted of a series of ground and flight test measurements to obtain data for validation of the SEA model. Included in the ground tests were various transfer function measurements between vibratory and acoustic subsystems, vibration and acoustic decay rate measurements, and coherent source measurements. The bulk of these, the vibration transfer functions, were used for SEA model validation, while the others provided information for characterization of damping and reverberation time of the subsystems. The flight test program included measurements of cabin and cockpit sound pressure level, frame and panel vibration level, and vibration levels at the main transmission attachment locations (for input power determination and final prediction comparisons). Comparisons between measured and predicted subsystem excitation levels from both ground and flight testing were evaluated. The ground test data show good correlation with predictions of vibration levels throughout the cabin overhead for all excitations. The flight test results also indicate excellent correlation of in-flight sound pressure measurements to sound pressure levels predicted by the SEA model, where the average aircraft speech interference level (SIL-4) is predicted within 0.2 dB.

The material presented represents reasonable verification with the Statistical Energy Analysis method of rotorcraft cabin noise prediction is a feasible and relatively accurate approach. The methodology provides output which, in addition to predicting sound pressure levels, predicts power flow information that reveals vibratory energy paths leading to the creation of cabin noise. It is now possible to assess the influence structural modifications have on energy flow and the resulting changes in cabin acoustic levels. Additionaly, an efficient and systematic approach is available for evaluation of structural damping.

17. Key Words (Suggested by Author(s))	18. Distribution Statement
Statistical Energy Analysis Modeling, Helicopter, Acoustics, Vibration, Cabin Noise, Structureborne Noise, Full Scale Vibro/Acoustic Test	[redacted] Until February 1988

19. Security Classif. (of this report)	20. Security Classif. (of this page)	21. No. of Pages	22. Price
Unclassified	Unclassified	284	